Constraining Earthquake Source Processes through Physics-Based Modeling

Thesis by
Valère Lambert

In Partial Fulfillment of the Requirements for the
Degree of
Doctor of Philosophy

CALIFORNIA INSTITUTE OF TECHNOLOGY
Pasadena, California

2021
Defended April 28, 2021

Valère Lambert

ORCID: 0000-0002-6174-9651

ACKNOWLEDGEMENTS

Numerous individuals have contributed to my development as a researcher and deserve my thanks; many more than those listed here.

First, I would like to thank my advisor Nadia Lapusta for her extraordinary guidance and support over the past five years. I am incredibly grateful for her wisdom and the wealth of opportunities that she has provided me throughout my graduate years at Caltech, both to freely explore different avenues of work and to connect with the broader Earth science and engineering communities. I would also like to thank my committee members Zhongwen Zhan, Mark Simons, and Jean-Philippe Avouac for their advice and generous time throughout my graduate studies. I thank Zhongwen for his infectious enthusiasm and great patience in introducing me to the world of observational seismology. Thank you to Mark for being an excellent academic advisor, who has always been a source of honest feedback and well-grounded perspective. I am also very much indebted to Jean-Philippe, who bravely provided me with my first research experience as a freshman at Caltech, and who has been an amazing source of support throughout the entirety of my academic career.

A substantial highlight of my time with the Caltech Seismolab has been regular discussion with faculty members, post-docs and fellow students during morning coffee hour. My near-daily conversations with Tom Heaton and Hiroo Kanamori have been a particular privilege, and I greatly appreciate their willingness to share their experience and knowledge on so many aspects of geophysics and its history. These coffee hour discussions with Tom and Hiroo have truly been formative experiences throughout my time in Seismolab and have substantially contributed to this thesis.

I would like to thank Victor Tsai and Zachary Ross for being superb life mentors and role models, and for the wealth of career and personal advice that they have shared with me. I would particularly like to thank Victor for highlighting the balance between knowledge and creative freedom, and encouraging me to continuously identify and challenge my areas of needed development.

Throughout my time at Caltech I have been incredibly fortunate to learn and gather advice from a wide community of faculty scholars, including Mike Gurnis, Joann Stock, Rob Clayton, Jennifer Jackson, Pablo Ampuero, Egill Hauksson, Don Helmberger, Ares Rosakis, Jose Andrade, Domniki Asimaki, Dennis Kochmann, and Guillaume Blanquart. I have truly enjoyed the opportunity to gather their perspectives through various courses and discussions. I would also like to thank Dan Faulkner, Eric Dunham, Paul Segall, Harsha Bhat, Camilla Cattania, Ahmed Elbanna and Emily Brodsky for the many instructive conversations and valuable advice and feedback that they have shared with me over the years.

I would like to express special thanks to Sylvain Barbot for introducing me to geophysics,

twice. I would certainly not be where I am today if not for Sylvain's mentorship and friendship. I would also like to thank my colleagues at the Earth Observatory of Singapore for welcoming me into the Earth sciences. In particular, thank you to Rishav Mallick for your incredible friendship and inspiring conversations. I am also immensely grateful to my undergraduate advisors, Maria Spiropulu and Harvey Newman, for their tremendous support throughout my development as a researcher and for introducing me to the world of high performance computing.

Countless individuals and programs at Caltech have been invaluable resources throughout my time here. I would like to thank the GPS and MCE staff who make everything possible. Thank you to Jenn Weaver at the CTLO for inspiring me to become a better teacher-mentor-scientist. Special thanks to the Caltech SFP office for facilitating all of the opportunities that I had to develop as a researcher during my undergraduate years, and for helping me to become a mentor as well.

I am sincerely thankful for the many friendships that I have made at Caltech as well as over various parts of the world, which have all helped me to grow as a researcher and person. Special thanks to Voon Hui Lai for being an endless source of encouragement; Stacy Larochelle for being my academic twin; Jack Muir, Ollie Stephenson and Ethan Williams for the many thought-provoking discussions and challenging questions; Newton Nguyen, Rachel and Muir Morrison for whiskey nights; and Kavya Sudhir, Ying Shi Teh, Taeho Kim, Brittany Pittner, Rob Learsch, Lealia Xiong, Théa Ragon, Sylvain Michel, Marcello Gori, Luca Dal Zilio, and Jonny Smith for all of the wonderful conversations and adventures.

Finally, I would like to thank my family for their unconditional and never-ending support, especially my parents Vicky and Hervé and my brother Max. Any and all successes that I have had, and will have, are possible because of you.

ABSTRACT

Determining principles and conditions governing motion along faults is crucial for assessing how earthquake ruptures start and how large they may ultimately become. This thesis aims to shed light on the physics governing earthquake source processes by (i) developing physics-based numerical models that combine geological observations and laboratory insight with theoretical developments, and (ii) using these models to examine how different physical mechanisms and conditions are reflected in a range of geophysical observations taken together, from heat-flow constraints and seismologically determined properties of earthquakes to geodetic inferences and earthquake frequency-magnitude statistics.

We examine the behavior and observable characteristics of numerically simulated sequences of earthquakes and aseismic slip in fault models designed to reproduce well-known features of mature faults that produce large destructive earthquakes. In part, the models are consistent with the inferred low-stress, low-heat operation of mature faults, which host large earthquakes at much lower levels of stress than their expected static strength. We explore two potential explanations for such behavior, one that faults are indeed quasi-statically strong but experience dramatic weakening during earthquakes, or that faults are persistently weak, e.g., due to fluid overpressure. We find that the two classes of fault models can, in principle, be distinguished based on the amount of seismic energy radiated from earthquake ruptures. Dynamic ruptures in the form of self-healing pulses, which occur on quasi-statically strong but dynamically weak faults, result in much larger radiated energy than inferred teleseismically for megathrust events, whereas crack-like ruptures on persistently weak faults are consistent with the seismological observations. The larger radiated energy of self-healing pulses is similar to limited regional inferences for crustal strike-slip faults. Our results suggest that re-evaluating estimates of radiated energy and static stress drop would provide substantial insight into the driving physics of large earthquakes and the absolute stress conditions on faults, with potential differences between tectonic settings.

The results also have significant implications for seismic hazard, since our modeling shows that fault models that experience efficient dynamic weakening during ruptures tend to predominantly produce large earthquakes, at the expense of smaller earthquakes. Such behavior is consistent with some mature fault segments, such as several segments of the San Andreas Fault in California that have hosted large earthquakes but are currently nearly seismically quiescent. These considerations can provide physical basis for improving earthquake early warning systems. If mature faults in California are indeed governed by enhanced dynamic weakening, then our results suggest that the likelihood of an earthquake on these faults becoming substantially larger is much higher than typical expectations based on Gutenberg-Richter statistics.

By considering average fault stress before simulated earthquake ruptures, we find that critical

stress conditions for earthquake occurrence depend on the size and style of motion (e.g. the degree of slip acceleration at the rupture front) during individual ruptures. In particular, the stress conditions required to propagate large earthquake ruptures can be considerably lower than those required for rupture nucleation, and standard notions of quasi-static fault strength based on laboratory studies. Our results demonstrate that the critical stress for earthquake occurrence is not governed by a simple condition such as a certain level of Coloumb stress, as commonly used in studies of stress interactions among faults and earthquake aftershocks patterns. More robust criteria for critical stress conditions would depend on the strength evolution during dynamic rupture and can be explored in numerical simulations.

Finally, evaluating the predictive power of numerical earthquake models for future hazards is a topic of great importance for physics-based seismic hazard assessment. Towards that end, we investigate the sensitivity of outcomes from numerical simulations of sequences of earthquakes and aseismic slip, including the long-term interaction of fault segments, to choices in numerical discretization and treatment of inertial, wave-mediated effects. In particular, we find that the rate of earthquake ruptures that manage to jump between two fault segments, a parameter routinely used in seismic hazard studies, is highly sensitive to numerical and physical modeling choices. These results suggest the need for developing different parameterization of seismic hazard than currently used, a task for which numerical modeling is well-suited.

PUBLISHED CONTENT AND CONTRIBUTIONS

Chapter 2 has been adapted from:

1) Lambert, V., Lapusta, N., & Faulkner, D. (in review). Scale dependence of earthquake rupture prestress in models with enhanced weakening: Implications for event statistics and inferences of fault stress. *Journal of Geophysical Research: Solid Earth*. DOI: 10.1002/essoar.10506240.1.
CONTRIBUTIONS: V.L. and N.L. contributed to developing the main ideas. V.L. designed, carried out, and analyzed the numerical experiments. All three authors contributed to interpreting the results and producing the paper.

Chapter 3 has been adapted from:

2) Lambert, V. & Lapusta, N. (2020). Rupture-dependent breakdown energy in fault models with thermo-hydro-mechanical processes. *Solid Earth*, 11(6), 2283-2302. DOI: 10.5194/se-11-2283-2020.
CONTRIBUTIONS: V.L. and N.L. both contributed to developing the main ideas, designing the modeling, and producing the paper. V.L. carried out and analyzed the numerical experiments.

Chapters 2 and 3 present continuations of work from:

3) Perry, S.M., Lambert, V. & Lapusta, N. (2020). Nearly magnitude-invariant stress drops in simulated crack-like earthquake sequences on rate-and-state faults with thermal pressurization of pore fluids. *Journal of Geophysical Research: Solid Earth*, 125(3), e2019JB018597. DOI: 10.1029/2019JB018597.
CONTRIBUTIONS: All three authors contributed to developing the main ideas and producing the paper. S.M.P. carried out and analyzed the numerical experiments including only standard rate-and-state friction as well as preliminary simulations of crack-like ruptures including enhanced dynamic weakening. V.L. designed, carried out, and analyzed the final simulations including enhanced dynamic weakening with considerations of thermal constraints on natural mature faults.

Chapter 4 has been adapted from:

4) Lambert, V., Lapusta, N. & Perry, S. (2021). Propagation of large earthquakes as self-healing pulses and mild cracks. *Nature*. DOI: 10.1038/s41586-021-03248-1.

CONTRIBUTIONS: V.L. and N.L. contributed to developing the main ideas, interpreting the results and producing the manuscript. S.P. performed preliminary simulations comparing crack-like ruptures and self-healing pulses. V.L. designed, carried out, and analyzed the numerical experiments in this work.

Chapter 5 has been adapted from:

5) Lambert, V. & Lapusta, N. Absolute stress levels on numerically simulated faults: Definitions, links to seismological observables, and differences for crack-like vs. pulse-like ruptures. in preparation for *Journal of Geophysical Research: Solid Earth*.
CONTRIBUTIONS: V.L. and N.L. both contributed to developing the main ideas and producing the paper. V.L. designed, carried out, and analyzed the numerical experiments.

Chapter 6 has been adapted from:

7) Lambert, V. & Lapusta, N. (in review). Resolving simulated sequences of earthquakes and fault interactions: Implications for physics-based seismic hazard assessment. *Journal of Geophysical Research: Solid Earth*. DOI: 10.1002/essoar.10506727.1.
CONTRIBUTIONS: V.L. and N.L. both contributed to developing the main ideas, designing the modeling, and producing the paper. V.L. carried out and analyzed the numerical experiments.

Chapter 7 has been adapted from:

6) Lambert, V. & Tsai, V.C. (2020). Time-dependent stresses from fluid extraction and diffusion with applications to induced seismicity. *Journal of Applied Mechanics*, 87(8). DOI: 10.1115/1.4047034.
CONTRIBUTIONS: V.L. performed the calculations for the study, analyzed the results, and wrote the manuscript. V.L. and V.C.T. both contributed to the initial conception and design of the study, as well as the discussion of the results and review of the manuscript.

TABLE OF CONTENTS

LIST OF ILLUSTRATIONS

LIST OF TABLES

Chapter 1

INTRODUCTION

Determining conditions that govern fault motion is a key goal for assessing potential societal threats from large destructive earthquakes, as well as developing mitigation strategies for the increasing prevalence of induced seismicity (Lee et al., 2019; McGarr et al., 2015). Several recent great earthquakes have notably challenged our previous knowledge of where large earthquake ruptures may occur and how large they may become. Such examples include the 2004 M_w 9.2 Sumatra-Andaman earthquake, which spread over at least 1200 kilometers to become one of the largest ruptures ever recorded (Ishii et al., 2005; Subarya et al., 2006); the 2011 M_w 9.0 Tohoku-oki earthquake, which produced exceptionally large displacement in the shallow portion of the megathrust that was previously assumed to be stable, causing a massive tsunami and catastrophic ecological disaster (Ide et al., 2011; Simons et al., 2011); the 2013 M_w 8.3 Sea of Okhotsk earthquake, which became the largest deep earthquake recorded, rupturing at least 600 kilometers below Earth's surface, and producing a M_w 6.7 aftershock supershear rupture at comparable depths (Zhan et al., 2014); as well as the 2016 M_w 7.8 Kaikoura earthquake, which developed into a complex multi-fault rupture spanning at least 21 fault segments (Hamling et al., 2017; Litchfield et al., 2018).

A significant limitation in studying the nature of great earthquakes is their infrequent occurrence. For example, the last major earthquakes greater than M_w 7.5 along the San Andreas Fault were the 1857 M_w 7.9 Fort Tejon and 1906 M_w 7.9 San Francisco earthquakes, which both occurred before the age of modern instrumentation. Given the rarity of large earthquakes, we ultimately must look to developing physics-based earthquake models that combine available information from laboratory experiments and physics principals, and are evaluated against modern observations and geologic records. While recent decades have seen a massive revolution in field observations and laboratory techniques, interpreting small-scale laboratory measurements and remote geophysical inferences on Earth's surface

in terms of properties of faults and potential future seismic hazards still remains a substantial challenge.

This thesis presents an exploration of how physics-based modeling of earthquake source processes can be used to study the relationship between different geophysical and geological observations and local fault behavior, and thus how the collective insight from laboratory and field studies can be used to constrain underlying fault physics and inform seismic hazard assessment.

1.1 Classical models for earthquake source processes and evolution of fault stress

Fault constitutive relations that describe the evolution of shear resistance with fault motion are essential ingredients of earthquake source modeling. When coupled with the elasto-dynamic equations of motion, these relations provide insight into the growth and ultimate arrest of ruptures.

Faults are often modeled as frictional interfaces, where the resistance to shear motion across the fault is linearly proportional to the effective normal stress on the fault $\overline{\sigma}$ through a friction coefficient f (Figure 1.1). Here, the effective stress principle is assumed with $\overline{\sigma} = (\sigma - p)$, where σ is the normal stress and p is the pore fluid pressure within the shearing layer (Terzaghi, 1923). A common conceptual model for frictional resistance is to consider a block being pushed or pulled along an interface (Figure 1.1B). The block is originally stuck with no motion until the applied force overcomes the static frictional strength, then sliding continues at a fixed dynamic, or kinetic, friction level (Figure 1.1C). The static and dynamic friction coefficients, f_{static} and f_{dynamic} respectively, are often considered material properties of the interface, such that the difference between the static strength and dynamic resistance, called the stress drop, is essentially fixed assuming constant effective normal stress. In such a model, the block slips by the same amount during each failure event, with characteristic timing under constant loading.

However, even this relatively simple block model, which is often described as a single-degree-of-freedom (SDOF) system, shows rich evolution of motion and hence shear resistance when examined in detail in the laboratory (Ben-David, Cohen, & Fineberg, 2010; Ben-David, Rubinstein, & Fineberg, 2010; Marone, 1998; Rubinstein et al., 2004). First, the block begins to creep, then the motion may accelerate, often in a spatially nonuniform way, and there is no set dynamic resistance level throughout different styles of motion (Ben-David, Cohen, & Fineberg, 2010; Ben-David, Rubinstein, & Fineberg, 2010; Rubinstein et al., 2004). Furthermore, the peak shear resistance reached by the block depends on how long the block was in contact with the interface before the experiment, demonstrating interfacial healing (Dieterich & Kilgore, 1994; Rubinstein et al., 2006).

While the ratio of average shear stress and normal stress along the block may be consistent with typical quasi-static friction coefficients around 0.6–0.85 (aka "Byerlee friction"), the ratio of the local shear stress to normal stress at various points along the interface may exceed or be considerably lower than the expected quasi-static friction for no perceivable slip (Ben-David, Cohen, & Fineberg, 2010; Byerlee, 1978). Such observations highlight the difference between an SDOF system and a continuous object, like the actual physical block. For an SDOF system, the entire object is considered to be rigid and experiencing the same resistance and motion at the same time. For a continuum, the motion of individual particles within the body can occur at different time scales, resulting in a rich evolution of average shear resistance (e.g Hulikal, Bhattacharya, & Lapusta, 2015). The current state-of-the-art understanding of frictional behavior is encapsulated in so-called rate-and-state friction laws which highlight that the resistance to shear is not a fixed material property of the interface, but depends on the rate of deformation and a number of state variables that describe contact populations (Figure 1.1D-E; Dieterich, 1979; Marone, 1998; Ruina, 1983).

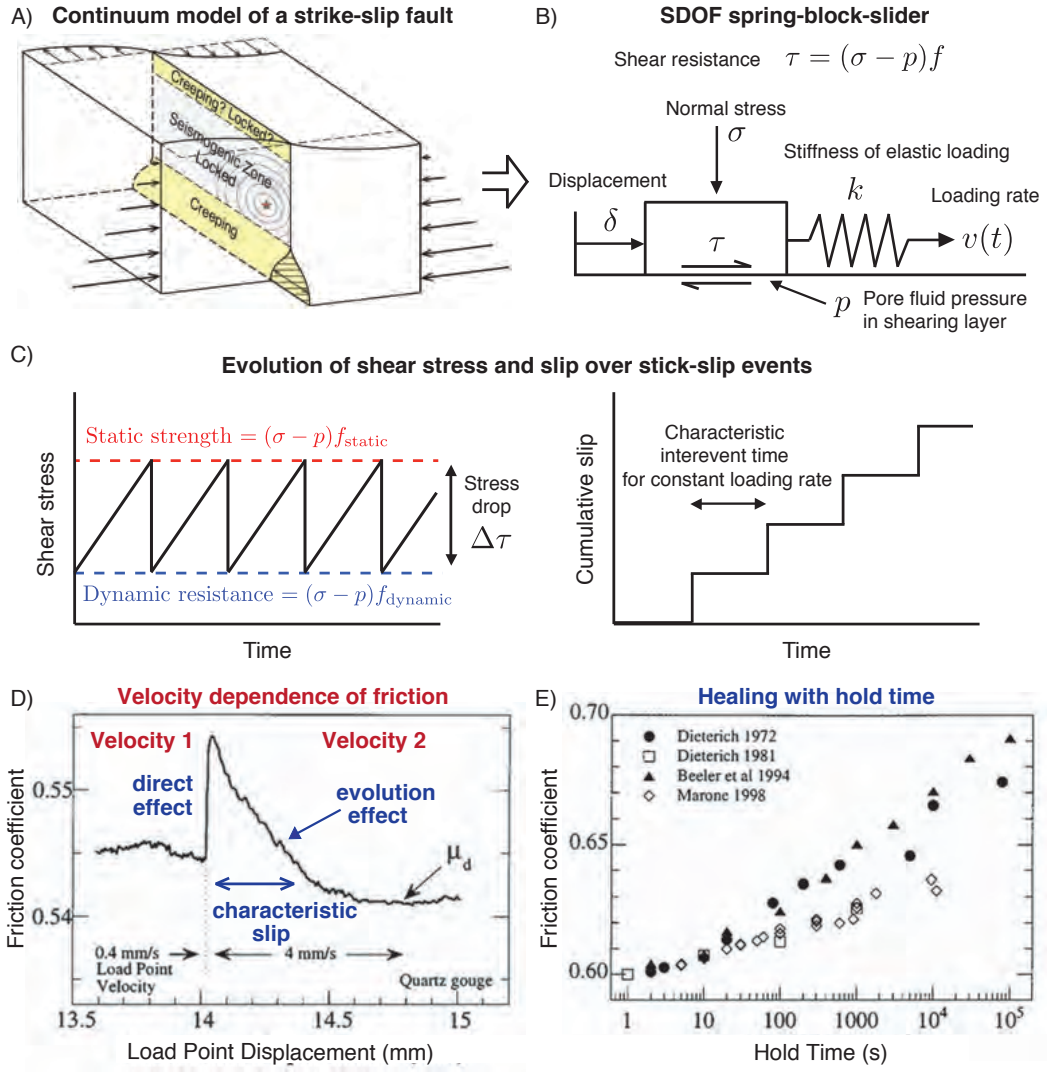

Figure 1.1: Classical spring-slider model of fault friction. (A) Schematic continuum model of a generic strike-slip fault segment where an earthquake rupture nucleates in a region (red star) and propagates along the fault. (B) Single-degree of freedom (SDOF) model for a block undergoing frictional sliding as it is continuously loaded through a spring. (C) Evolution of shear stress and slip for the block throughout stick-slip events. The block remains motionless with no slip for a period of time during which stress is brought up to the static frictional strength through constant loading, then the frictional resistance drops to the dynamic resistance level and slip occurs to unload the spring. (D-E) Laboratory experiments that study the evolution of the shear resistance on rock surfaces and granular layers at low sliding rates show more involved descriptions of frictional behavior where a positive slip-rate jump is always accompanied by an increase in shear resistance, followed by its evolution with characteristic slip. Moreover, the peak friction coefficient reached upon a jump in slip rate depends on the preceding period of negligible motion, increasing with longer hold times. These features have been combined into widely used rate-and-state friction laws. Adapted from Marone (1998).

In order to account for the spatio-temporal evolution of motion and stress during earthquake ruptures, earthquake source processes are often considered in the framework of dynamic fracture mechanics, where the rupture is considered as a dynamically propagating shear crack or pulse (Figure 1.2; Freund, 1990; Heaton, 1990; Ida, 1972; Kanamori & Brodsky, 2004; Kanamori & Heaton, 2000; Kostrov & Das, 1988; Madariaga, 1976; Palmer & Rice, 1973; Rice, 1980, 2000; Rubin & Ampuero, 2005). Classical models from fracture mechanics that assume a constant stress change on the crack surface are often used to determine the average stress drop due to an earthquake rupture. By analogy to cohesive-zone relations for Mode I opening cracks, slip-weakening friction laws have been commonly used to describe the dynamic decrease in shear resistance during sliding (Bouchon, 1997; Bouchon et al., 1998; Cruz-Atienza et al., 2009; Gallovic et al., 2019; Ida, 1972; Ide & Takeo, 1997; Kanamori & Brodsky, 2004; Kaneko et al., 2017; Kostrov & Das, 1988; Madariaga, 1976; Olsen et al., 1997; Palmer & Rice, 1973). Linear slip weakening is one of the simplest and most commonly used versions, in which the shear resistance decreases linearly with slip from a peak of τ_{peak} to a constant dynamic level τ_{dyn} achieved at slip of D_c (Fig. 1.3).

The breakdown energy G is associated with the evolution of shear resistance from the initial shear stress τ_{ini} to the peak shear resistance τ_{peak} and then breakdown to the minimum dynamic shear resistance τ_{min}. It is a part of the overall energy partitioning for dynamic ruptures, with the total strain energy change throughout the ruptured region (ΔW) being separated into the radiated energy E_R, breakdown energy G, and other residual dissipated energy (Kanamori & Rivera, 2013). The breakdown energy is analogous to fracture energy from cohesive zone models of fracture mechanics (Freund, 1990; Palmer & Rice, 1973; Rice, 1980; Tinti et al., 2005) and hence it is thought to be relevant to rupture dynamics, e.g., rupture speed. For linear slip-weakening friction, it is given by $G = (\tau_{\text{peak}} - \tau_{\text{dyn}})D_c/2$. The term "fracture energy," while initially associated with the creation of free surfaces during tensile fracture, has been routinely used to refer broadly to inelastic dissipation relevant to the crack-tip motion for both tensile and shear cracks, including contributions from off-fault damage creation, plastic work, and frictional heat (e.g. Freund, 1990; Rice, 1980, 2006). However, in this thesis we follow the work of Tinti et al. (2005) in referring to this quantity

as the "breakdown" work, or energy, to further emphasize that G can incorporate various physical sources of energy dissipation.

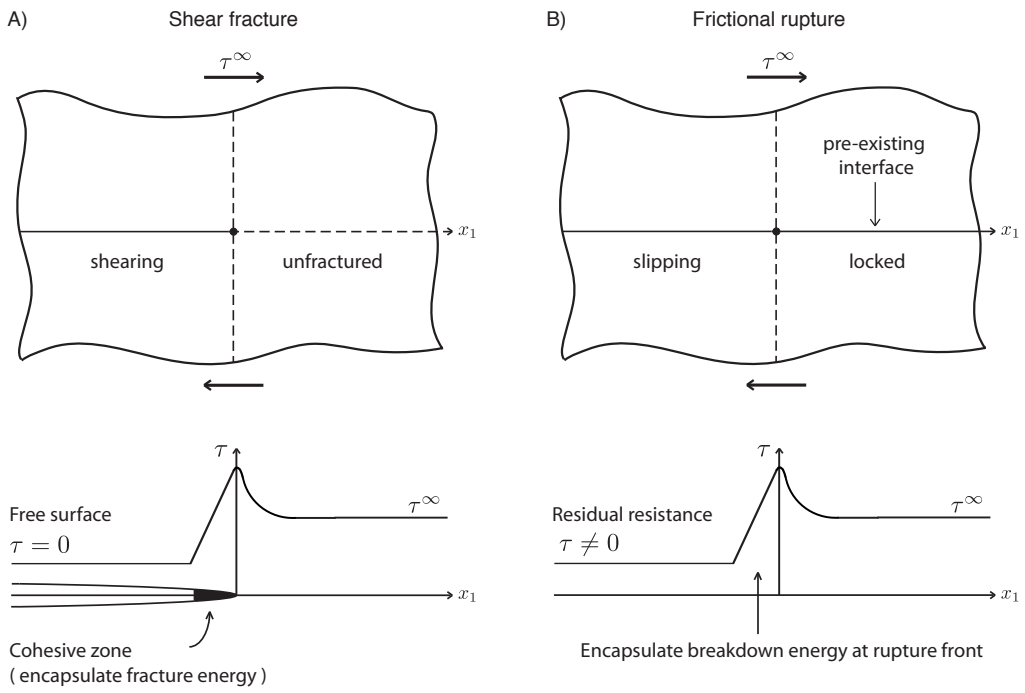

Figure 1.2: Analogy between shear fracture and frictional rupture. Consider an elastic body undergoing far-field shear loading. (A) For shear fracture, shearing occurs within the crack with unfractured material ahead of the crack tip. In cohesive-zone models of fracture, the stress concentration ahead of the crack tip breaks down to a traction-free surface over a small region called the cohesive zone, with the energy consumed to advance the crack tip called the fracture energy. (B) For frictional rupture, we consider the difference between slipping and locked regions of a pre-existing interface, with the stress concentration at the boundary between the two. If the shear resistance breaks down to a fixed residual level within the slipping region over a small enough region (small-scale yielding), then we can consider this breakdown energy required to advance the rupture front analogous to fracture energy.

As observed for the block, more involved rate-and-state fault-constitutive laws are generally required to explain a number of aspects of faulting behavior, most notably the restrengthening of faults in between earthquakes. A number of previous studies have used models on rate-and-state faults to provide insight into a number of earthquake and slow slip observations, such as sequences of earthquakes on an actual fault segment and repeating earthquakes (Barbot et al., 2012; T. Chen & Lapusta, 2009; Dieterich, 2007, and references therein).

While incorporating a more involved dependence of shear resistance on long-term healing, standard Dieterich-Ruina rate-and-state friction has been shown to resemble linear slip weakening during dynamic rupture (Cocco & Bizzarri, 2002; Lapusta & Liu, 2009; P. G. Okubo, 1989), providing further reinforcement of the notion that the breakdown of shear resistance during dynamic rupture may be adequately described by linear slip-weakening behavior.

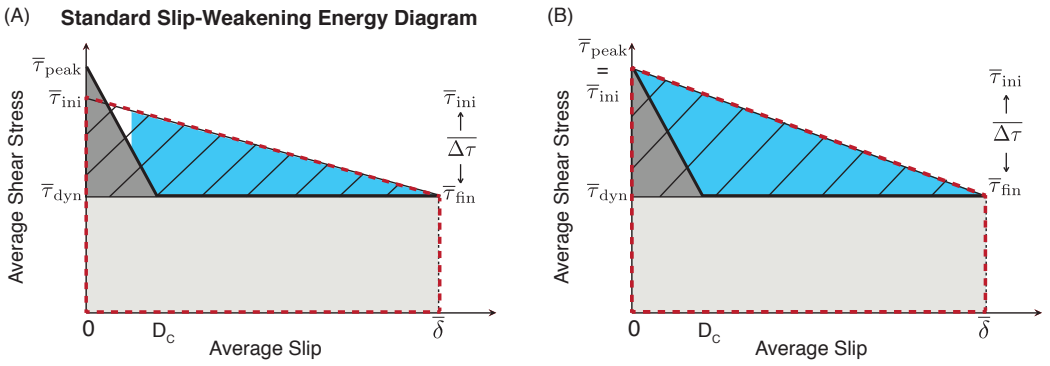

Figure 1.3: Standard linear slip-weakening average stress vs slip diagram which represents the standard energy partitioning of frictional ruptures. (A) The average shear stress is assumed to increase from an initial to peak stress with no slip and then linearly decrease to a dynamic resistance level over a critical slip distance D_c. The difference between the average initial and final shear stress levels is called the static stress drop. The average stress vs. slip diagram is used to represent the energy partitioning of the total strain energy change per unit rupture area (dashed red trapezoid) into the breakdown energy (dark grey triangle), residual dissipated energy per unit area (light gray rectangle), and radiated energy per unit area (blue region). The additional dissipation associated with the initial strengthening outside of the red trapezoid comes at expense of the radiated energy (white triangle inside the red-dashed trapezoid). (B) The case of the initial stress equal to the peak stress. Note that this diagram is an approximation even if the local behavior is governed by linear slip-weakening friction, since different points of the rupture would have different slip, including near-zero slip close to the rupture edges, and averaging over the dynamic rupture would produce a different curve from the local behavior (Noda & Lapusta, 2012).

Two key assumptions for the analogy between between shear fracture and frictional ruptures are that the breakdown of shear resistance is concentrated in a small region near the rupture front (referred to as small-scale yielding) and that there exists a constant residual stress level $\tau_{dyn} = \tau_{min}$ throughout the ruptured region during sliding (Figure 1.2; Freund, 1990; Palmer & Rice, 1973). Implicit in these assumptions is that the rupture dynamics do not depend

on the residual dissipated energy below the dynamic resistance level, and thus the absolute levels of stress on the fault. In practice, at least part of this dissipated energy is converted to heat, which can have profound effects on the evolution of shear resistance during rupture.

1.2 Assessing stress levels on faults

The absolute levels of stress on a fault dictate the maximum amount of stress, and hence mechanical potential energy, that may be released during earthquake ruptures, which translates into both static surface deformation due to fault slip and strong shaking due to the radiation of seismic waves during rapid motion. Determining the absolute level and controlling factors of the stress state on faults is a topic of many geological and geophysical investigations, with profound implications for earthquake physics, seismic hazard assessment, and the role of faulting in plate tectonics and geodynamics.

One of the most notable constraints on the stress state of faults is the abundance of field observations suggesting that the average shear stress acting on mature plate boundary faults, where the largest earthquakes typically occur, must be on the order of 20 MPa or less (Brune et al., 1969; Fulton et al., 2013; Gao & Wang, 2014; Henyey & Wasserburg, 1971; Lachenbruch & Sass, 1980; Nankali, 2011; Rice, 2006; Sibson, 1975; Suppe, 2007; Tanikawa & Shimamoto, 2009; Townend & Zoback, 2004). This is substantially lower than the expected shear resistance of 100–200 MPa averaged over seismogenic depths where earthquakes occur, given rock overburden and hydrostatic pore fluid pressure, along with typical Byerlee friction values measured in laboratory experiments. Such evidence includes the lack of a substantial heat flow anomaly around mature faults that would be expected for fault slip at 100 MPa or more (Brune et al., 1969; Gao & Wang, 2014; Henyey & Wasserburg, 1971; Lachenbruch & Sass, 1980; Nankali, 2011), inferences of steep angles between the principal stress direction and fault plane (Townend & Zoback, 2004), analyses of the fault core obtained by drilling through shallow parts of faults that have experienced major recent events, including the 2011 M_w 9.0 Tohoku-oki event (Fulton et al., 2013; Tanikawa & Shimamoto, 2009), the geometry of thrust-belt wedges (Suppe, 2007), and the existence of long-lived narrow shear zones that do not exhibit any evidence of melting (Rice, 2006; Sibson, 1975).

Note that such evidence for apparent fault weakness pertains predominantly to mature plate boundary faults, whereas some studies suggest that smaller, less mature active faults may sustain the expected higher shear stresses given Byerlee friction values and overburden minus hydrostatic pore pressure (e.g. Townend & Zoback, 2000).

A relatively straightforward explanation for the low-stress operation of mature faults is that they may be persistently weak (Figure 1.4), due to the presence of anomalously low quasi-static friction coefficients and/or low effective normal stress from pervasive fluid overpressure (Bangs et al., 2009; Brown et al., 2003; Collettini et al., 2009; Faulkner et al., 2006; Lockner et al., 2011). However, most materials with low quasi-static friction coefficients (less than 0.5) under laboratory conditions tend to exhibit velocity-strengthening behavior (Ikari et al., 2011), which would favor stable sliding and preclude spontaneous nucleation of dynamic ruptures. Moreover, while evidence of substantial fluid overpressure has been documented for some subduction zones (Bangs et al., 2009; Brown et al., 2003), there remains much debate over the ubiquity of chronic near-lithostatic fluid overpressurization along faults in other tectonic settings, such as continental faults, with borehole measurements suggesting fluid pressure levels more consistent with hydrostatic conditions (Townend & Zoback, 2000; Zoback et al., 2010).

An alternative hypothesis for explaining such low-stress, low-heat operation is that mature faults are indeed strong at slow, quasi-static sliding rates but undergo considerable enhanced dynamic weakening at seismic slip rates, which has been widely hypothesized in theoretical studies and documented in laboratory experiments (Figure 1.4, dashed black line; Acosta et al., 2018; Di Toro et al., 2011; Noda et al., 2009; Rice, 2006; Sibson, 1973; Tsutsumi & Shimamoto, 1997; Wibberley et al., 2008). The standard rate-and-state laws are the most established representation of fault shear resistance that we have for relatively low slip rates from tectonic plate rates of 10^{-9} m/s to around 10^{-3} m/s (Dieterich, 1979; Ruina, 1983). At higher slip rates, further enhanced dynamic weakening of fault frictional resistance can occur due to a variety of physical mechamisms, for example, due to rapid shear heating.

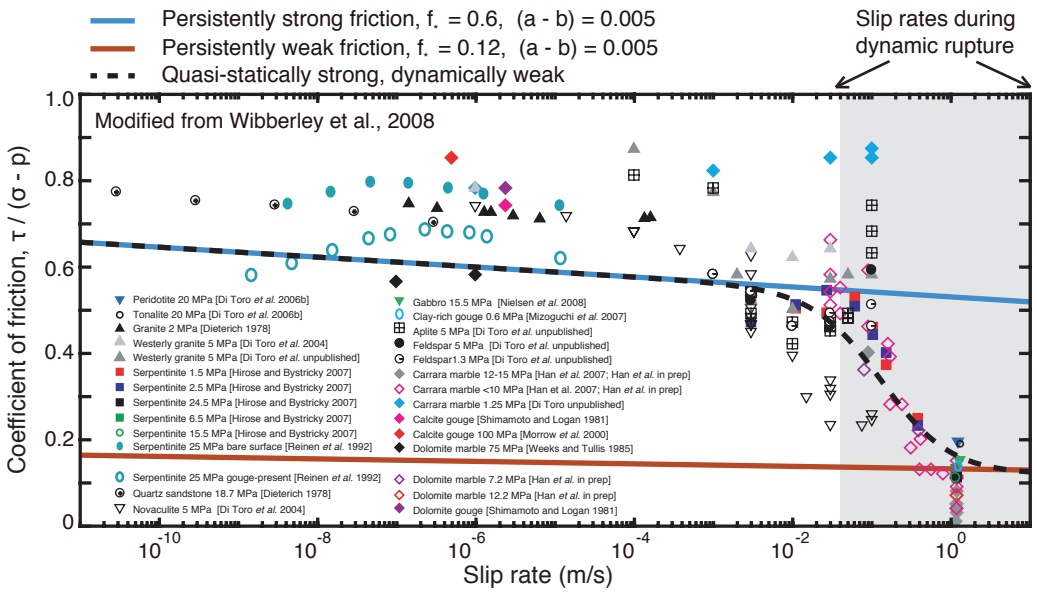

Figure 1.4: Field observations suggest that the average effective friction on mature faults must be low (< 0.1). One explanation for this inferred low effective friction would be that mature faults are persistently weak, such as from the presence of fault materials with persistently low friction coefficients $\tau/(\sigma - p)$ (red). Faults may also be persistently weak while having actual friction coefficients that are persistently high (> 0.2, blue), but require substantial chronic fluid overpressure in order to maintain low effective fault friction. A number of laboratory experiments indicate that the coefficient of friction for many materials relevant to seismogenic faults is around 0.6-0.8 at low sliding rates, but drops dramatically to lower values (< 0.2) at higher slip rates relevant to seismic slip, consistent with the notion of quasi-statically strong, but dynamically weak behavior (dashed black line).

One particular mechanism for such enhanced weakening is the thermal pressurization of pore fluids, which occurs when pore fluids within the fault shearing layer heat up, expand, and pressurize during dynamic rupture, reducing the effective normal stress, and therefore shear resistance (Noda & Lapusta, 2010; Rice, 2006; Sibson, 1973). Other mechanisms can act in the fault shear zone to produce similar enhanced weakening effects to thermal pressurization, including the thermal decomposition of rocks (Han et al., 2007; Sulem & Famin, 2009), macroscopic melting (Di Toro et al., 2004, 2011; Goldsby & Tullis, 2002), elastohydrolubrication (Brodsky & Kanamori, 2001), and silica gel formation (Brodsky & Kanamori, 2001; Di Toro et al., 2004; Goldsby & Tullis, 2002).

Constraining the degree to which natural faults undergo enhanced dynamic weakening during earthquake ruptures has substantial implications for assessing the stability of different fault regions and the maximum extent to which a rupture may grow. Numerical models have shown that the incorporation of thermally-activated enhanced weakening mechanisms during dynamic rupture can have profound effects on the evolution of individual ruptures, as well as the long-term behavior of fault segments, with the potential to make seemingly stable creeping regions fail violently during earthquakes (Noda & Lapusta, 2013), and for the deeper penetration of large ruptures, which may explain the seismic-quiescence of mature faults that have historically hosted large earthquakes (Jiang & Lapusta, 2016).

The presence of enhanced dynamic weakening on natural faults has been questioned by the expectation that enhanced weakening would produce much larger static stress drops than typical values of 1 to 10 MPa inferred from earthquakes on natural faults (Allmann & Shearer, 2009; Gao & Wang, 2014; Ye et al., 2016b). The expectation is based on a common assumption that the shear prestress over the entire rupture area should be near the static strength of the fault while the final shear stress should be near the dynamic resistance of the fault, resulting in a large static stress change (Figures 1.1C and 1.3B). However, a number of numerical and laboratory studies have demonstrated that, once nucleated, dynamic ruptures can propagate under regions with prestress conditions that are well below the expected static strength, based on prescribed or measured quasi-static friction coefficients and confining conditions (Dunham et al., 2011a; Fineberg & Bouchbinder, 2015; Gabriel et al., 2012; Lu et al., 2010; Noda et al., 2009; Zheng & Rice, 1998). Indeed, numerical studies have shown that models with enhanced weakening can be consistent with magnitude-invariant static stress drops, despite the evolving dynamic resistance (Perry et al., 2020).

A substantial challenge in relating laboratory and field studies of average fault stress is the discrepancy in scales and styles of motion involved (Figure 1.5). Typical laboratory friction experiments study the rich evolution of shear resistance on relatively small, centimeter-scale samples where relatively uniform motion may be imposed (e.g. Acosta et al., 2018; Di

Toro et al., 2011; Dieterich, 1979; Goldsby & Tullis, 2011; Marone, 1998; Wibberley et al., 2008). Such well-controlled experiments are invaluable for determining fault constitutive relations under slow and fast sliding conditions, however special consideration is needed when evaluating their implications for the slip and stress occuring at larger scales on natural faults. The evolution of fault slip and stress during earthquake ruptures can be highly variable as the rupture nucleates in one region and then propagates elsewhere along the fault. Intermediate-scale experiments aim to capture some aspects of the spatially and temporally varying motion during rupture generation and propagation (e.g. Gori et al., 2018; Ke et al., 2018; McLaskey et al., 2014; Rubino et al., 2017; Yamashita et al., 2015), however their interpretation still requires consideration of experimental conditions, such as loading configuration, nucleation procedures, as well as the use of analog materials, which are dictated in part by the size of the apparatus.

Many geophysical studies seek to shed light on fault physics and earthquake source processes by measuring the motion on Earth's surface and estimating earthquake source properties. Seismological and geodetic measurements are routinely used to perform kinematic inversions of earthquake source processes in order to illuminate complex finite-fault aspects of the rupture process. In particular, numerous kinematic inversions suggest that large earthquakes ($M_w > 7$) tend to propagate as slip pulses, skipping along the fault surface with only a small portion of the rupture area slipping at a given time, like a wrinkle in a rug (e.g. K. Chen et al., 2020; Galetzka et al., 2015; Heaton, 1990; Pritchard, Ji, & Simons, 2006; Subarya et al., 2006; Ye et al., 2016b). However, the solutions to finite-fault earthquake source inversions are non-unique and the resulting images can be sensitive to inherent smoothing as well as a priori assumptions in the physics of the earthquake source and wave propagation (Bletery et al., 2016; Duputel et al., 2015; Minson et al., 2013, 2014; Ragon & Simons, 2020; Ragon et al., 2019).

Given the remote nature of surface measurements and the non-uniqueness in the source inversion process, the most robust geophysical inferences typically represent single averaged

source quantities, such as average static stress drop, radiated energy, radiation efficiency, and average breakdown energy. The estimation of such quantities often relies on the use of idealized rupture models, often inspired by dynamic fracture mechanics (Abercrombie & Rice, 2005; Allmann & Shearer, 2009; Ide & Beroza, 2001; Rice, 2006; Viesca & Garagash, 2015; Ye et al., 2016b). The relationship between remote geophysical observations and the actual local fault behavior at depth can therefore be model-dependent and is not directly evident.

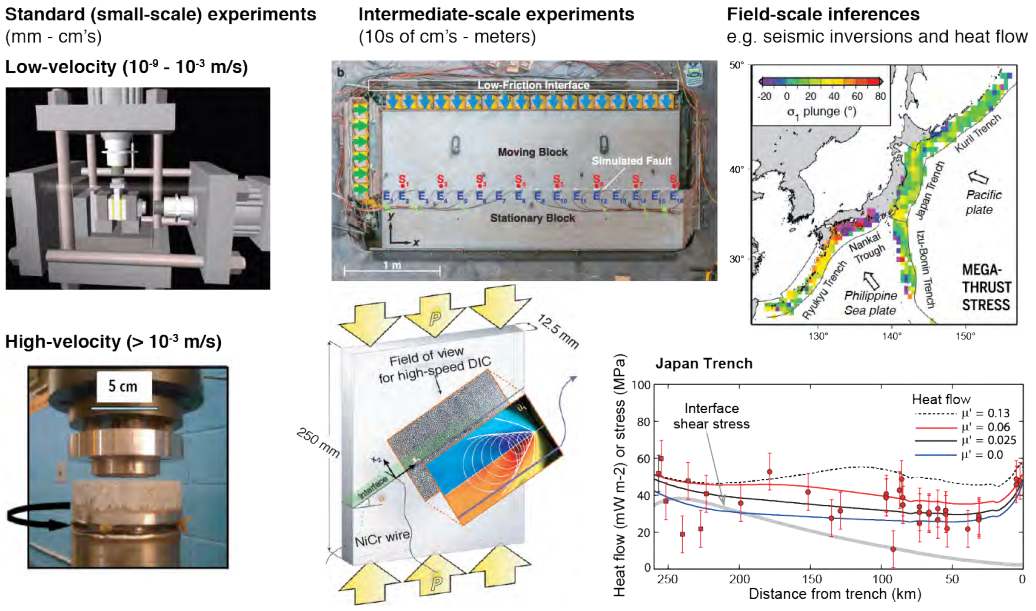

Figure 1.5: Wide range of scales spanning laboratory and field studies of fault stress. (Left) Laboratory friction experiments study the evolution of shear resistance at low and high velocities with relatively uniform motion applied over centimeter-scale samples. Such experiments form the basis for fault constitutive equations (illustration of double direct shear experiment courtesy of Chris Marone; high-speed rotary shear apparatus from Tullis & Goldsby, 2003). (Center) Larger, intermediate-scale experiments on the order of 10s of centimeters to meters study aspects of spatially-varying motion consistent with rupture generation and propagation, sometimes using analog materials (Gori et al., 2018; Ke et al., 2018). (Right) Field observations, including inversions of earthquake focal mechanisms and heat flow measurements (e.g. Gao & Wang, 2014; Hardebeck, 2015), represent measures of average stress over much larger areas of 100s of meters or kilometers).

1.3 Overview

Improving our understanding of the evolution of shear stress on faults over periods of slow and fast motion is crucial for assessing how earthquakes start, grow, and ultimately stop. Numerical simulations of sequences of earthquakes and aseismic slip (SEAS) are well-suited to explore the physical conditions governing these problems and their relation to a wide range of geophysical observables, as they can resolve all styles of the deformation history on faults. In this thesis, we utilize such SEAS simulations to examine how average fault stress, seismologically-inferable rupture properties, and earthquake population statistics such as frequency-magnitude statistics, relate to the heterogeneous motion and stress conditions that naturally evolve in fault models with differing physical conditions. The particular goal of this work is to examine how the characteristics of physical models for "weak" mature faults are reflected in a range of geophysical observations, and thus how such observations can be used to constrain the physical conditions on faults and potentially improve the predictive capabilities of earthquake models.

We begin in Chapter 2 by investigating how laboratory friction measurements and field studies of fault stress can be reconciled by accounting for the scale- and motion-dependence of average fault shear resistance. We study the stress conditions preceding simulated earthquake ruptures (aka prestress) of different sizes that spontaneously evolve in numerical SEAS simulations on fault models with laboratory-derived rate-and-state friction and enhanced dynamic weakening due to thermal pressurization (TP) of pore fluids. We also examine how such stress conditions vary in faults models with increasingly efficient dynamic weakening and the relation to the resulting complexity of earthquake sequences, in terms of the variability of rupture sizes. Our modelling allows us to examine the implications of the laboratory-derived constitutive behaviors for the larger-scale behavior of faults, and demonstrates the importance of accounting for finite-fault effects when relating measurements from small-scale laboratory experiments to field observations.

In Chapters 3 and 4, we review the application of traditional fracture mechanics theory

to frictional ruptures and discuss when such applications appear valid, and when they are not, particularly in the presence of pore fluids and shear heating. In Chapter 3, we use SEAS simulations including enhanced weakening due to TP to study how accounting for thermo-hydro-mechanical processes during dynamic shear ruptures alters the underlying assumptions between shear fracture and frictional ruptures. In particular, we examine how both the average and local breakdown energy no longer reflect fixed material properties of the fault, but depend on the amount of slip attained during rupture, as well as how that slip is achieved through the history of slip rate and dynamic stress changes throughout rupture.

Chapter 4 examines the energy partitioning of simulated earthquake rupture scenarios of different rupture style and their relation to competing theories for earthquake ruptures that satisfy the well-known observations of 1–10 MPa static stress drops and low-stress, low-heat conditions along mature faults. In that regime, quasi-statically strong but dynamically weak faults mainly host relatively sharp, self-healing pulse-like ruptures, with only a small portion of the fault slipping at a given time, whereas persistently weak faults host milder ruptures with more spread-out slip, which are called crack-like. We demonstrate how notable differences in the evolution of average stress throughout these different styles of rupture propagation can be reflected in seismologically-observable properties, such as the relationship between radiated energy, static stress drop, and seismic moment. We then compare the results of our simulated ruptures with existing seismological estimates from large earthquakes from different tectonic settings.

In Chapter 5, we expand on the exploration of the previous chapters to study the similarities and differences among different measures of average fault stress associated with dynamic rupture, their scaling with rupture size, dependence on earthquake rupture style, and their relationship with seismologically inferable quantities. We also examine the significance of rapid dynamic weakening and healing of shear resistance during ruptures, such as from the diffusion of pore fluids for TP, in order to maintain relatively high interseismic stresses while accommodating low dynamic resistance during earthquakes. Moreover, we demon-

strate how seismological observations may be used to differentiate between mechanisms for pulse-like rupture propagation and, together with shear-heating constraints, can in principle can be used to constrain the average stress conditions on faults before, during and after large ruptures.

Assessing the predictive power of numerical earthquake models for future hazards remains an important topic of ongoing debate. In Chapter 6, we investigate the sensitivity of outcomes from numerical SEAS simulations, including the long-term interaction of fault segments, to choices in numerical discretization and treatment of inertial effects, using a simplified 2-D crustal fault model with two co-planar segments separated by a creeping barrier. We use this model to explore how conditions for adequate numerical resolution and convergence depend on the physical assumptions and complexity of earthquake sequences, as well as on the modeling outcome of interest. We particularly focus on the rate of earthquake ruptures that manage to jump between the two fault segments, its sensitivity to numerical and physical modeling choices, and whether reproducing comparable earthquake frequency-magnitude statistics and static stress drops provides sufficient predictive power for the jump rate, a quantity of interest to seismic hazard studies (Field, 2019).

Finally, Chapter 7 presents a different focus on induced seismicity and examines the implications of the time-dependent diffusion of pore fluids for the poroelastic stresses and seismicity resulting from fluid extraction (or injection) from (or into) a buried reservoir, with particular relevance to energy resource practices. We perform a quantitative analysis of the stresses surrounding a horizontal reservoir resulting from fluid extraction and diffusion and examine how the the spatial pattern and magnitude of imposed stresses is controlled by the ratio between the volumetric rate of fluid extraction and the reservoir diffusivity. We further study the impact of the diffusion of pore fluids for the evolution of the perturbed principle stress directions, with potential implications for interpreting temporal variations in seismicity trends around producing regions.

Chapter 2

SCALE DEPENDENCE OF EARTHQUAKE RUPTURE PRESTRESS IN MODELS WITH ENHANCED WEAKENING: IMPLICATIONS FOR EVENT STATISTICS AND INFERENCES OF AVERAGE FAULT STRESS

This chapter has been adapted from:

Lambert, V., Lapusta, N., & Faulkner, D. (in review). Scale dependence of earthquake rupture prestress in models with enhanced weakening: Implications for event statistics and inferences of fault stress. *Journal of Geophysical Research: Solid Earth*. DOI: 10.1002/essoar.10506240.1.

2.1 Introduction

Recent numerical studies of earthquake sequences have shown that fault models incorporating some chronic fluid overpressure as well as mild-to-moderate enhanced dynamic weakening due to the thermal pressurization of pore fluids are able to reproduce a range of seismological observations (Perry et al., 2020), including reasonable static stress drops between 1–10 MPa nearly independent of earthquake magnitude, the seismologically inferred increase in average breakdown energy with rupture size, and low heat flow as observed around mature faults. The near magnitude-invariance of average static stress drop arises in these fault models because enhanced dynamic weakening results in both lower average prestress and lower average final shear stress for larger ruptures with larger slip, with the average static stress drops being nearly magnitude-independent. These studies suggest that distinguishing between the conditions required for rupture nucleation and propagation is important for assessing the relationship between laboratory friction measurements, seismological observations and the absolute stress conditions on faults.

Here, we expand upon the set of models from Perry et al. (2020) to document the variability of prestress on a fault that arises from the history of previous ruptures, and to study the

relation between the size of dynamic rupture events and the average shear prestress over the rupture area. We also examine how the complexity of earthquake sequences, in terms of the variability of rupture size, differs with the efficiency of dynamic weakening. We study these behaviors in the context of simulations of sequences of earthquakes and slow slip, which allow the prestress conditions before earthquakes to be set by the loading conditions, evolving fault shear resistance (including weakening and healing), and stress redistribution by prior slip, as would occur on natural faults. Moreover, our simulations resolve the spontaneous nucleation process with the natural acceleration of slow unsteady slip prior to dynamic rupture. The constitutive relations for the evolving fault resistance and healing adopted in our models have been formulated as a result of a large body of laboratory, field and theoretical work (e.g Di Toro et al., 2011; Dieterich, 1979; Rice, 2006; Ruina, 1983; Sibson, 1973; Wibberley et al., 2008). Indeed, laboratory experiments of fault shear resistance at both slow and fast slip rates have been indispensible for our understanding of fault behavior and for formulating fault models such as the ones used in this study. The modelling allows us to examine the implications of the laboratory-derived constitutive behaviors for the larger-scale behavior of faults, and we compare our inferences of average shear prestress from relatively large-scale finite-fault modeling to field measurements of crustal stresses acting on mature faults and small-scale laboratory measurements of the shear resistance of typical fault materials.

2.2 Building on laboratory constraints to model larger-scale fault behavior

Laboratory experiments have been instrumental for exploring aspects of fault resistance during both slow and fast sliding (10^{-9} m/s - 1 m/s, Figure 1.4). Experiments with slow sliding velocities ($< 10^{-3}$ m/s) are critical for formulating fault constitutive laws that form the basis for understanding the nucleation of earthquake ruptures. High-velocity laboratory friction experiments have demonstrated enhanced dynamic weakening of faults and elucidated a range of mechanisms by which this dynamic weakening can occur (e.g. Acosta et al., 2018; De Paola et al., 2015; Di Toro et al., 2011; Faulkner et al., 2011; Goldsby & Tullis, 2011; Han et al., 2007; Wibberley et al., 2008). Most slow- and high-velocity experiments measure or infer the relevant quantities –slip, slip rate, shear stress etc –averaged over the sample and ex-

amine the evolution of shear resistance corresponding to a particular history of loading, such as imposed variations in the displacement rate of the loading piston, and the particular fault conditions (normal stress, temperature, pore fluid pressure, etc.). Some experimental studies imposed the expected sliding motion during earthquakes in order to directly relate laboratory stress measurements to seismological quantities, such as static stress drop and breakdown energy (e.g. Fukuyama & Mizoguchi, 2010; Nielsen et al., 2016; Sone & Shimamoto, 2009).

To understand the full implications of the evolution of shear resistance measured in small-scale experiments for slip at larger scales along natural faults, they are synthesized into mathematical formulations and used in numerical modeling, for the following reasons. During slipping events on a finite fault over scales of tens of meters to kilometres –much larger than the experimental scale –the fault does not slip uniformly with a predetermined slip-rate history. Rather, the slip event initiates on a portion of the fault and then spreads along the fault, with varying slip-rate histories and final slips at different points along the fault. This is captured in inversions of large earthquakes (e.g. Heaton, 1990; Simons et al., 2011; Tinti et al., 2016; Ye et al., 2016a) and, to a degree, in larger-scale experiments, sometimes involving analog materials (Lu et al., 2010; McLaskey et al., 2014; Rubino et al., 2017; Svetlizky & Fineberg, 2014; Yamashita et al., 2015). In the process, the slip (1) transfers stress to the more locked portions of the fault and (2) enters portions of the fault with different conditions –such as levels of shear pre-stress, pore fluid pressure, etc –and potentially different friction and hydraulic properties. Hence the resulting coupled evolution of shear resistance and slip rate at different locations on the fault is often quite different and, through stress transfer, strongly dependent on the entire slip process at all locations throughout the rupture. These nonlinear and often dynamic feedback processes on the scales of tens of meters to kilometers can currently be only captured through numerical modeling.

Many numerical models of earthquake source processes utilize insight from laboratory experiments that indicate that the resistance to shear τ along a fault depends on the sliding rate V and the quality and/or lifetime of the local contacts, typically parameterized by a state variable θ with units of time, as well as on the effective normal stress $\overline{\sigma} = \sigma - p$ acting on

the fault, with σ being the normal stress and p being the pore fluid pressure localized within the shearing layer (Figure 1.1D-E, e.g. Dieterich, 1979; Marone, 1998). For continuum problems involving frictional sliding, the motion within the continuum is governed by the balance of linear momentum, subject to the boundary condition that tractions are given by the constitutive law of the interface. For frictional sliding without changes in the elastodynamic normal stress, which is the case considered in this work, the boundary condition reduces to the shear stress being equal to the shear resistance on the interface ($y = 0$):

$$\begin{aligned} \tau_{\text{stress}}(x, y = 0, z; t) &= \tau_{\text{resistance}}(x, y = 0, z; t) \\ &= f(V, \theta)(\sigma - p). \end{aligned} \tag{2.1}$$

An important concept in the rate-and-state formulation of the friction coefficient $f(V, \theta)$ is that the friction coefficient is not a fixed property of the interface but evolves over time, facilitating the time-dependent changes of shear resistance and hence shear stress along the fault during shear.

The most commonly used formulation of rate-and-state laws is the Dieterich-Ruina formulation (Dieterich, 1979; Ruina, 1983):

$$f(V, \theta) = \left[f_* + a \ln \frac{V}{V_*} + b \ln \frac{\theta V_*}{D_{\text{RS}}} \right], \tag{2.2}$$

where f_* is a reference steady-state friction coefficient at the reference sliding rate V_*, D_{RS} is the characteristic slip distance, and a and b are the direct effect and evolution effect parameters, respectively. Our fault models are governed by a form of the laboratory-derived Dieterich-Ruina rate-and-state friction law regularized for zero and negative slip rates (Lapusta et al., 2000; Noda & Lapusta, 2010). The evolution of the state variable can be described by various evolution laws; we employ the aging law (Ruina, 1983):

$$\dot{\theta} = 1 - \frac{V\theta}{D_{\text{RS}}}, \tag{2.3}$$

which describes evolution during sliding as well as time-dependent healing in near-stationary contact. In our models, the shear resistance and shear stress also change due to the evolution of pore fluid pressure p.

We conduct numerical simulations following the methodological developments of Lapusta et al. (2000), Noda and Lapusta (2010) and Lambert et al. (2021) in order to solve the elastodynamic equations of motion with the fault boundary conditions, including the evolution of pore fluid pressure and temperature on the fault coupled with off-fault diffusion. The simulations solve for mode III slip on a 1-D fault embedded into a 2-D uniform, isotropic, elastic medium (Figure 2.1). The potential types of slip on the fault include sequences of earthquakes and aseismic slip (SEAS) and they are simulated in their entirety, including the nucleation process, dynamic rupture propagation, postseismic slip that follows the event, and interseismic period between seismic events that can last up to tens or hundreds of years and host steady and transient slow slip (Figure 2.1).

The simulated fault in our models contains a 24-km-long segment with velocity-weakening (VW) frictional properties where earthquake ruptures may nucleate and propagate, surrounded by velocity-strengthening (VS) segments that inhibit rupture nucleation and propagation. Our simulations include enhanced dynamic weakening due to the thermal pressurization of pore fluids, which occurs when pore fluids within the fault shearing layer heat up and pressurize during dynamic rupture, reducing the effective normal stress and shear resistance (Noda & Lapusta, 2010; Rice, 2006; Sibson, 1973). Thermal pressurization is one potential mechanism for enhanced weakening; qualitatively similar results should hold for models with other types of enhanced dynamic weakening. We follow the thermal pressurization formulation of Noda and Lapusta (2010) (Appendix Section 2.10.1).

For the purpose of comparing local frictional behavior with the average prestress for dynamic ruptures of varying sizes, we focus this study on simulated ruptures that arrest within the VW region, where the friction properties are uniform with a quasi-static reference friction of 0.6, consistent with many materials exhibiting VW behavior in laboratory experiments (Ikari et al., 2011). We examine the evolution of the apparent friction coefficient, or the ratio of the current shear stress τ to the interseismic drained effective normal stress $(\sigma - p_{\text{int}})$, where p_{int} is the interseismic drained value of the pore pressure. The "drained" refers to the effective stress with ambient pore pressure unaffected by slip processes such as dilatancy, compaction, or thermal pressurization.

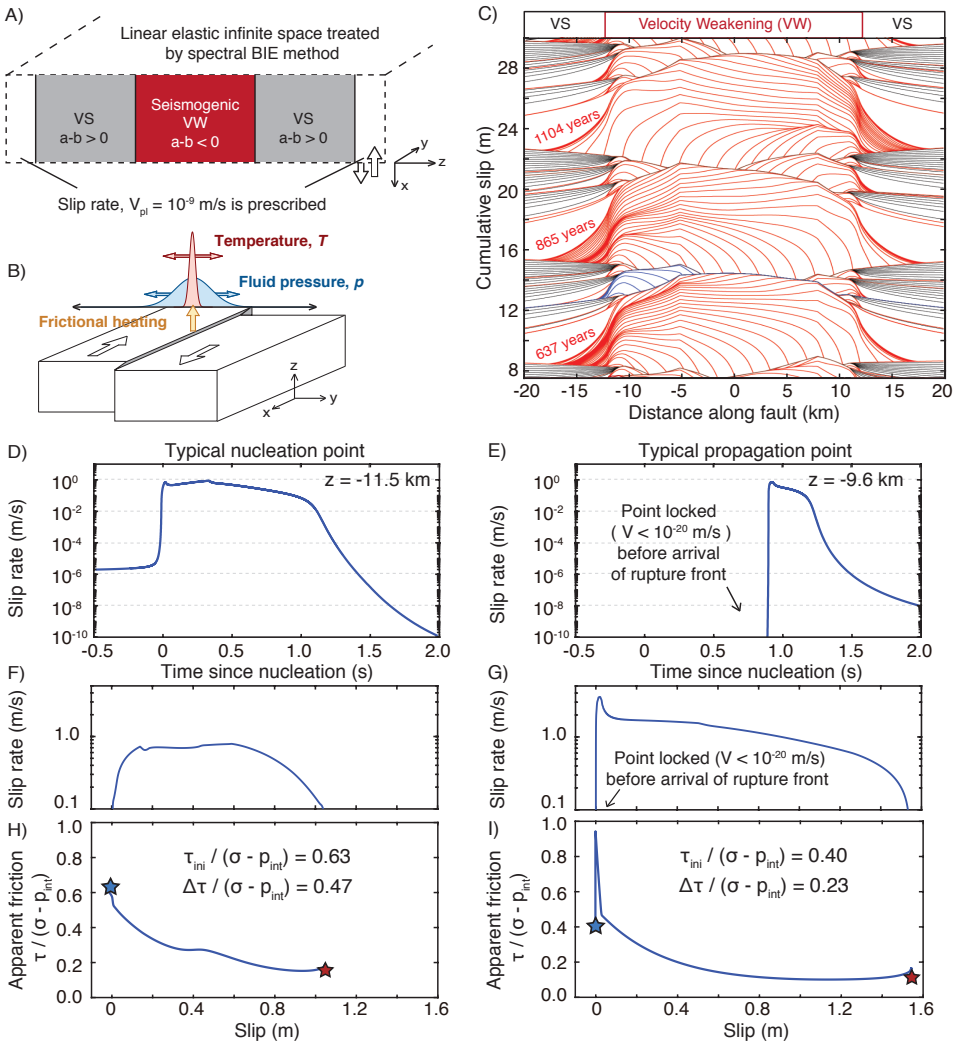

Figure 2.1: Modeling of sequences of earthquakes and aseismic slip on a rate-and-state fault with (A) a velocity-weakening (VW) seismogenic region surrounded by two velocity-strengthening (VS) sections and (B) enhanced dynamic weakening due to the thermal pressurization of pore fluids. The evolution of temperature and pore fluid pressure due to shear heating and off-fault diffusion is computed throughout our simulations. (C) A short section of the accumulated slip history in fault model TP3 (Table 2.2). Seismic events are illustrated by red lines plotted every 0.5 s while aseismic slip is shown by black lines plotted every 10 years. (D-G) Evolution of local slip rate with time and slip at points representative of nucleation and typical rupture propagation behavior within a crack-like rupture (colored blue in C). Points throughout rupture propagation (E & G) are initially locked and are driven to rupture by the concentration of dynamic stresses at the rupture front, thus experiencing more rapid acceleration of slip compared to points within the nucleation region (D & F). (H-I) The difference in local slip rate history contributes to a difference in the evolution of shear stress with slip. (H) Evolution of the apparent coefficient of friction $\tau/(\sigma - p_{\text{int}})$ with slip in the nucleation region is consistent with the laboratory notion of quasi-statically strong, dynamically weak behavior, with the apparent friction coefficient initially close to the reference value of 0.6 and dropping to a low dynamic resistance below 0.2 with slip. (I) Evolution of the apparent friction coefficient at points throughout rupture propagation is more complicated as the scaled prestress can be much lower than the reference friction before the arrival of the dynamic stress concentration.

We examine fault models with varying levels of ambient fluid overpressure in terms of the effective normal stress, as well as varying degrees of efficiency in enhanced weakening due to thermal pressurization. The parameter values we have chosen (Tables 2.1 - 2.3) are motivated by prior studies that have reproduced a range of seismological observations as well as low-stress, low-heat operation of mature faults (Lambert et al., 2021; Perry et al., 2020). The parameter values also facilitate our goal of examining ruptures in fault models with a range of efficiency in enhanced dynamic weakening. We define the beginning and end of dynamic rupture, t_{ini} and t_{fin} respectively, as well as the ruptured area Ω, using a slip velocity threshold (V_{thresh} = 0.01 m/s) for seismic slip, based on previous studies (Lambert et al., 2021; Perry et al., 2020). Note that t_{ini} and t_{fin} refer to the beginning and end of the entire rupture event, which starts when one location on the fault reaches the threshold velocity and ends when all points on the fault drop below the threshold velocity. In the following, we use "rupture" to refer to such dynamic slip events, unless noted otherwise. Further description of the numerical methodology can be found in the Appendix (Section 2.10.1)

2.3 Evolution of local slip and shear resistance and notions of failure

Our simulations capture the evolution of motion and shear stress across the fault over sequences of earthquakes spanning several thousands of years (Figure 2.1C). The initial distributions of shear stress and other quantities such as the slip rate are assumed to be uniform along most of the VW region of the fault at the start of our simulations, other than a small region of initially high prestress near the VW-VS boundary to nucleate the first rupture in the earthquake sequence. The distributions of shear stress and slip along the fault evolve to become highly variable throughout periods of fast earthquake-producing slip as well as slow aseismic slip and fault locking. Below we review how the rate-and-state friction framework allows the model to represent both creeping, locked, and seismically slipping fault areas as well as transitions between these different styles of slip.

During dynamic rupture, the evolution of slip rate and shear stress can be particularly complex and variable along the fault. At points where individual ruptures nucleate, the slip rate gradually accelerates towards seismic slip rates and shear stress at the beginning of rupture, t_{ini}, is relatively high, with the apparent friction coefficient $\tau/(\sigma - p_{int})$ close to the quasi-static reference friction of 0.6. As seismic slip rates are reached, $\tau/(\sigma - p_{int})$ drops substantially due to thermal pressurization of pore fluids in a manner qualitatively consistent with the enhanced dynamic weakening observed in high-velocity laboratory friction experiments (Figure 2.1H). The evolution of slip rate and shear stress outside of the nucleation region is even more complicated: The shear stress at t_{ini}, prior to the arrival of the rupture front, can be much lower than the shear stress levels where the rupture nucleates, then increases to a higher peak shear stress that reflects the interseismic fault healing and rate-and-state direct effect and is achieved due to the dynamic stress concentration at the rupture front, and then decreases due to weakening with seismic slip (Figure 2.1H vs. I). Consistently, the slip rate rapidly increases to seismic values at the beginning of slip and then decreases, as in a typical Yoffe-like behavior for dynamic ruptures (Figure 2.1G; e.g Tinti et al., 2005). Thus, even with the uniform normal stress and uniform parameters of the assumed friction and pore pressure equations within the seismogenic VW region, the prestress conditions throughout the rupture area can be highly variable and, in part, substantially different between regions of rupture nucleation and rupture propagation.

Note that the peak shear stress during dynamic rupture of fault locations outside the nucleation zone can correspond to much higher apparent friction coefficient (e.g., 0.95 in Figure 2.1I) than the reference friction coefficient ($f_* = 0.6$ in this study). This is due to both the direct effect at the rupture tip and the high, interseismically "healed" value of the state variable θ, as discussed in Lambert and Lapusta (2020) (Chapter 3) and Appendix Section 2.10.1 (Equation 2.9). As follows from the first line of equation 2.9, the difference between the peak friction coefficient and f_* due to the direct effect of $a \ln(V_{peak}/V_*)$ would be 0.14 to 0.16 for $V_{peak} = 1$ to 10 m/s and other parameters of our model, with the rest due to the much larger value of the "healed" state variable than that for sliding at the reference sliding

rate.

The local evolution of shear stress throughout the VW seismogenic zone differs among points based on the long-term history of motion, including both local slip as well as slip across the entire fault. For example, a point at the center of the VW region (z = 0 km) in one of our simulations (fault model TP 3 in Table 2.2, as shown in Figure 2.1C) experiences substantial slip only during the largest earthquake ruptures that span the entire VW domain, resulting in a relatively simple and quasi-repetitive pattern of stress accumulation and weakening over sequences of earthquakes (Figure 2.2A & C). In contrast, another point in the VW region closer to the VS boundary (z = -9.6 km) experiences different amounts of slip during dynamic ruptures of varying size, resulting in a more complicated evolution of shear stress with accumulating slip (Figure 2.2B & D).

In between individual earthquakes, the VS regions of the fault creep (i.e., slowly slip) with the slip rate close to the prescribed tectonic plate rate, due to that rate being imposed on the fault areas nearby, with occasional quasi-static accelerations due to post-seismic slip (Figure 2.3, left column). The creep penetrates into the VW regions nearby, creating fault areas prone to earthquake nucleation (Jiang & Lapusta, 2016; Michel et al., 2017) (Figure 2.3, right column). These points of the VW region close to the VS region (within one or so nucleation length) are reloaded due to creep and post-seismic slip from previous rupture within the VS regions. The loading rate at these points near the VS-VW boundary varies over time depending on the rate of motion in the VS region, which in turn depends on the previous history of co-seismic slip during dynamic ruptures in the VW region.

The slip rate and apparent friction at points close to the VW-VS boundary are typically brought to near steady conditions around the loading plate rate, however both exhibit small oscillations as these points continue to be loaded by creep in the VS region, resulting in further acceleration, slip and weakening, and thus the transmission of stress further into the VW region until a sufficiently large area is loaded to sustain rupture nucleation and acceleration

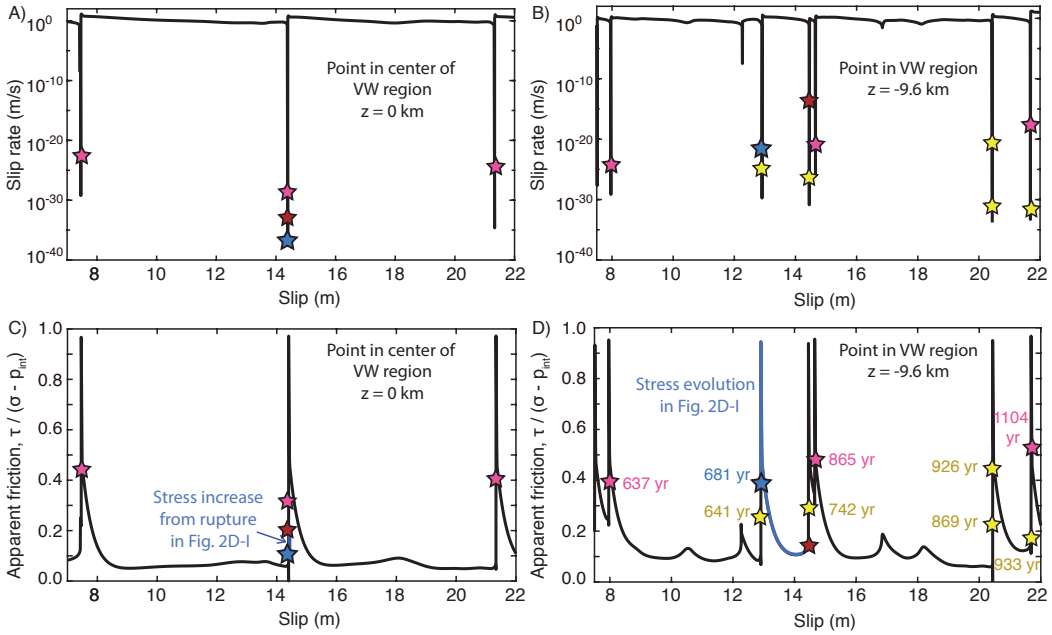

Figure 2.2: Evolution of the local slip rate and apparent friction coefficient at points within the velocity-weakening (VW) region with accumulating slip in fault model TP3 (Table 2.2). The stars denote instances in the earthquake sequence in Figure 2.1C, with pink stars marking the initiation of the three large model-spanning ruptures, the blue and red stars denoting the beginning and end of the moderate-sized rupture illustrated by blue contours, respectively. The yellow stars denote small to moderate-sized ruptures occurring along the VW-VS boundary at $z = -12$ km. (A & C) The point in the center of the VW region (z = 0 km) ruptures and experiences substantial slip only in large ruptures. The point exhibits an increase in shear stress over time due to the stress transfer from smaller ruptures that do not penetrate into the center of the VW region (such as the rupture colored blue in Fig. 2.1C). (B & D) Points closer to the boundary between the VW and VS regions can rupture during both smaller and large ruptures depending on the prestress conditions when ruptures arrive, resulting in a more complicated evolution of shear stress with accumulating slip. For both points in the VW region, the shear stress is brought to the peak stress and failure during ruptures by the dynamic stresses at the rupture front.

to seismic slip rates (Figure 2.3E-G). This oscillatory behavior is consistent with predictions from the stability analysis of a single degree-of-freedom spring-slider undergoing frictional slip, where the amplitude of the oscillations is expected to grow as the spring stiffness decreases below a critical stiffness value until (Gu et al., 1984). The effective stiffness of the slipping fault zone in a continuum model is inversely proportional to the slipping zone size (Rice & Ruina, 1983), decreasing with the increasing slipping region. Note that this rate-and-state nucleation process has been used to explain the period-dependent response of

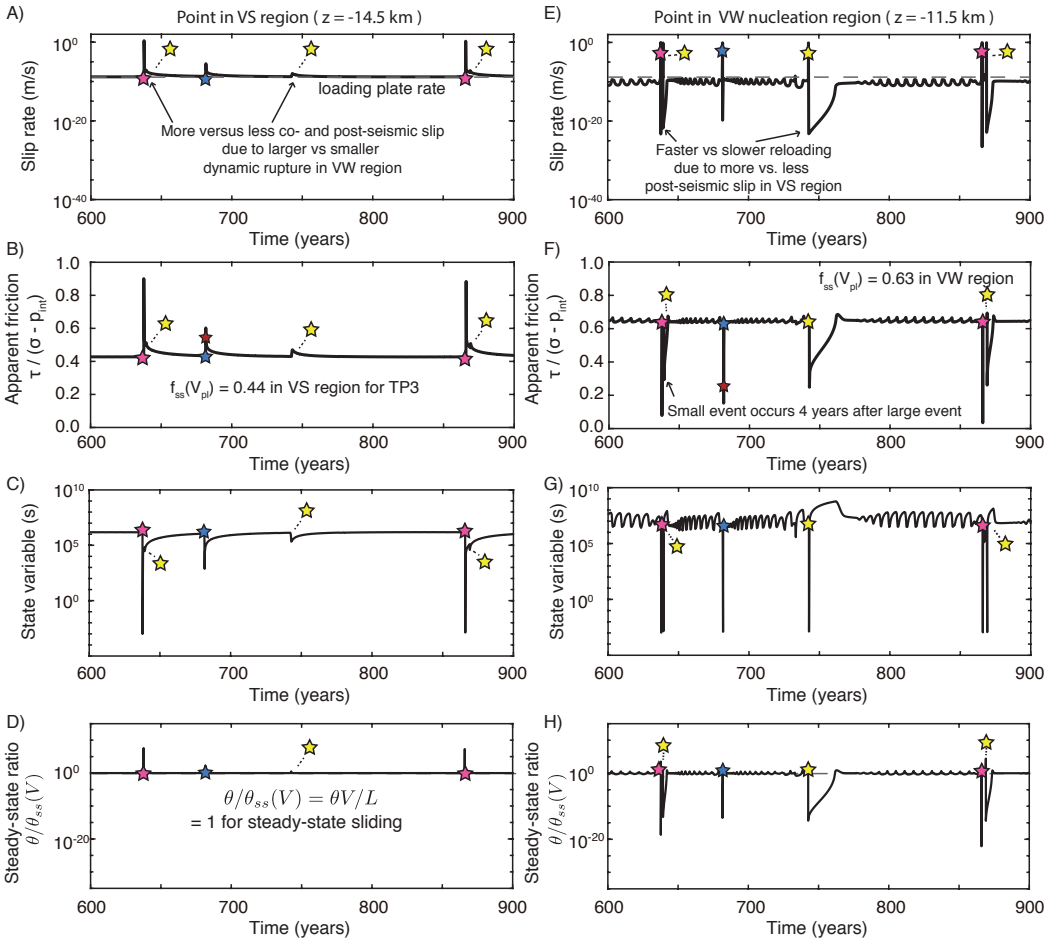

Figure 2.3: Evolution of local slip rate, apparent friction, and state variable at points near rupture nucleation between two model-spanning ruptures. The stars denote instances in the earthquake sequence in Figure 2.1C, with pink stars marking the initiation of the first two large model-spanning ruptures, the blue star denoting the beginning of the moderate-sized rupture illustrated by blue contours and the yellow stars denoting smaller ruptures. (A) Points within the VS region typically slip near the loading plate rate but can experience transient accelerated slip during and following ruptures occurring within the VW region. (B-D) The apparent friction coefficient and state variable in the VS region is typically near steady state, except during accelerated slip. (E-F) Slow slip penetrates into the VW region, driving points near the VW-VS boundary close to the loading slip rate, with the apparent friction coefficient being close to the corresponding steady-state value $f_{\rm ss}(V_{\rm pl})$. The slip rate and apparent friction exhibit small oscillations as the points near the VW-VS boundary continue to be loaded by slow slip in the VS region, accelerate, and weaken, thus transmitting stress further into the VW region until a sufficiently large region is loaded to sustain rupture nucleation and acceleration to seismic slip rates. The loading rate of the VW region also depends on the amount of accelerated slip in the VS due to previous ruptures (e.g. A & E $\sim$ 650 vs. 750 years). (G-H) Following dynamic rupture, the state variable heals close to the steady-state value around the prescribed loading rate $\theta_{ss}(V_{\rm pl})$ but continues to oscillate along with the unsteady slip resulting from the penetration of creep into the VW region, as seen in (E).

microseismicity to periodic stress perturbations in Nepal, where seismicity shows significant variations in response to annual monsoon-induced stress variations but not to semidiurnal tidal stresses of the same magnitude (Ader et al., 2014).

In contrast, much of the VW region further away from the VS regions is essentially locked, which is expressed in the rate-and-state formulation as sliding at very low, but still non-zero, slip rates that are many orders of magnitude smaller than the loading rate (Figure 2.4A-B). This differential motion between the VS and VW regions loads points in the VW region (Figure 2.4C-D), gradually increasing shear stress there (e.g., between 700 and 800 years in Figure 2.4C). Note that the interseismic stressing rate is higher at locations closer to the creeping regions than further away from it (Figures 2.4C vs. 2.4D vs. 2.3F), as one would expect. At the same time, the essentially locked points within the VW region experience time-dependent healing of the local shear resistance encapsulated in the increase of the state variable θ (Figure 2.4E-F). One of the manifestations of this healing is that larger interseismic increases in the state variable generally lead to higher peak shear stress during dynamic rupture propagation (Chapter 3; Lambert & Lapusta, 2020). Despite the increase in the state variable, its value is far below the steady-state one for the very low interseismic slip rates, consistent with continuing healing prior to dynamic rupture (Figure 2.4G-H). Depending on whether the local shear stressing rate (which increases the shear stress τ on the left of equation 2.1) is larger or smaller than the rate of healing (expressed by the last, θ term on the right hand side of equation 5.1), the local slip rate (that enters the second term of equation 5.1) increases (as between 700 and 800 years in Figure 2.4A) or decreases, i.e., the fault is accelerating towards failure or becomes even more locked. However, most of the locked points of the fault never accelerate close to failure interseismically; rather, they fail due to stress concentrations from dynamic events, seen as vertical lines in Figure 2.4C-D.

We note that healing on natural faults, in the presence of fluids and depth-dependent elevated temperatures, can be affected by a number of mechanisms that are not captured by the basic state evolution equation (J. Chen et al., 2015a, 2015b; Tenthorey & Cox, 2006; Yasuhara

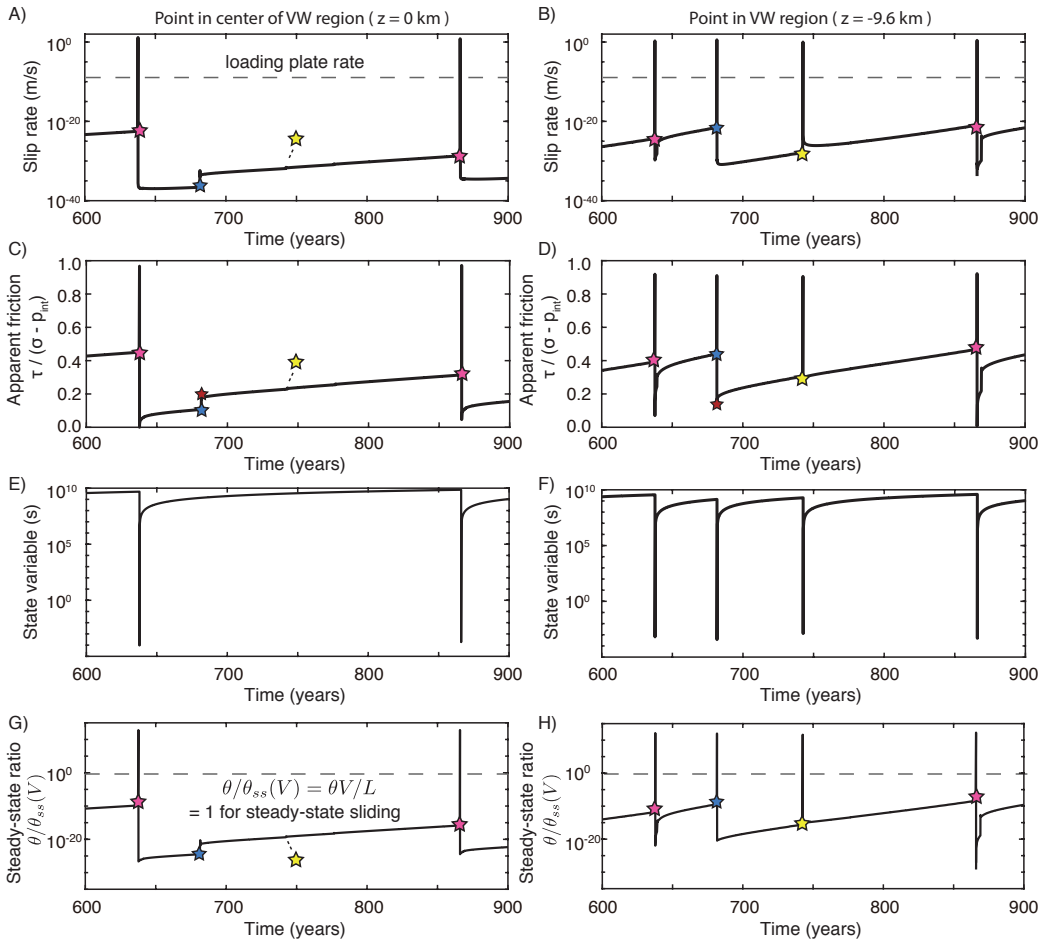

Figure 2.4: Evolution of local slip rate, apparent friction, and state variable at points within the VW region between two model-spanning ruptures. The stars denote instances in the earthquake sequence in Figure 2.1C, with pink stars marking the initiation of the first two large model-spanning ruptures, the blue star denoting the beginning of the moderate-sized rupture illustrated by blue contours and the yellow stars denoting smaller ruptures. (A-B) Points within the VW region are typically locked in between earthquake ruptures, sliding at slip rates far below the loading plate rate. (C-D) Loading from the VS regions as well as slip in neighboring ruptures leads to a time-dependent increase in shear stress. However, the points are still near-locked when dynamic rupture arrives from elsewhere, bringing a significant stress concentration and weakening on the timescale of the event which here collapses onto a vertical line. (E-F) The evolution of the state variable shows increase in the interseismic periods which encapsulate the fault healing and decrease to low values during earthquake rupture. (G-H) The ratio of the current value of the state variable θ to the steady-state value $\theta_{ss}(V)$, corresponding to the current local slip rate V, is much smaller than 1 during the interseismic periods, indicating the continued healing of shear resistance prior to rupture. As the slip rate rapidly accelerates during dynamic rupture, the state variable temporarily exceeds the new much lower steady-state values corresponding to the dynamic slip rate $\theta_{ss}(V_{\mathrm{dyn}})$, then evolves to this lower steady-state value, and then falls to values below steady-state during the interseismic periods, indicating fault healing.

et al., 2005). Incorporating more realistic healing into shear resistance formulations and numerical modelling is an important goal for future work. This can be done by modifying the evolution of the state variable θ or adding other state variables that would encode healing. Yet, qualitatively, additional healing mechanisms would have similar effects on the simulations as the current rate-and-state healing, in that the healing would modify the peak shear resistance and the subsequent evolution of the resistance based on the interseismic fault state, potentially further amplifying differences in shear resistance evolution for different points along the fault (e.g., nucleation points vs. locked points) that our simulations already highlight.

The presence of time-dependent healing as well as persistent, potentially unperceivable, slow (quasi-static) motion and its acceleration under variable levels of shear stress illustrate how the concepts of failure, and hence strength, are not easily defined for frictional sliding. For realistic frictional interfaces, the precise value of a static friction coefficient is ill-defined, since no interface loaded in shear is perfectly static; rather creep processes occur at slow, unperceivable slip rates at any level of shear loading (Bhattacharya et al., 2017; Dieterich & Kilgore, 1994) and/or over parts of the contacting interfaces (Ben-David, Cohen, & Fineberg, 2010; Rubinstein et al., 2004, 2006). Hence the transition from locked interfaces to detectable slip is always a gradual process (although it may be occurring faster than the time scales of interest/observation in many applications). This reality is reflected in lab-derived fault constitutive relations such as rate-and-state friction. Since failure typically refers to the presence of irreversible or inelastic deformation, frictional interfaces may be considered failing under any style or rate of motion, be it during slow steady sliding, transient slow slip, or dynamic rupture. Therefore, any meaningful notion of strength first requires definition of the failure of interest, e.g., reaching seismic slip rates of the order of 1 m/s. Without such explicit definition, failure is then implicitly defined as transition from locked to slipping and corresponds to sliding with a detectable velocity; for laboratory experiments or observational studies, this would imply that whether the interface is locked or slipping depends on the instrumental precision for detectable motion.

In this study, we would like to compare the shear stress values required for aseismic slip nucleation and for dynamic rupture propagation. During spontaneous aseismic slip nucleation, the slip rates evolve from very low to seismic, passing in the process through the slip rate equal to the tectonic loading rate V_{pl}. In the standard rate-and-state friction, at each fixed sliding rate V, the friction coefficient eventually evolves to a steady-state value $f_{ss}(V)$ (equation 5.3; for very small slip rates, the regularized formulation of equation 2.11 needs to be considered). Under slow loading, aseismic earthquake nucleation on a finite fault is typically a gradual process, with many points within the nucleation zone being close to the steady state (Figure 2.3; Kaneko & Lapusta, 2008; Rubin & Ampuero, 2005). While the steady-state values of friction depend on the sliding rate, the dependence is relatively minor at the low, quasi-static slip rates between the plate rate of approximately 10^{-9} m/s and sub-seismic slip rates of $< 10^{-3}$ m/s (Figure 1.4) which are relevant for fault creep and earthquake nucleation, and for which the standard rate-and-state formulation is (approximately) valid. The product of this collection of steady-state quasi-static friction coefficients and the interseismic drained effective stress gives the shear resistance of faults at sustained slow sliding rates, which we call the *steady-state quasi-static fault shear resistance* (referred to in short as local SSQS shear resistance). As the representative value of such local SSQS shear resistance, we choose the shear resistance of the fault steadily creeping at the prescribed long-term tectonic plate rate V_{pl} (which the fault would have long-term if it were slipping stably), with the interseismic drained value of the pore pressure p_{int}:

$$\tau_{ss}^{V_{\mathrm{pl}}}(z,t) = (\sigma - p_{\mathrm{int}})\, f_{ss}(V_{\mathrm{pl}}). \tag{2.4}$$

In our models, $\tau_{ss}^{V_{\mathrm{pl}}}/(\sigma - p_{\mathrm{int}}) = 0.63$ within the VW region. Note that choosing V_* instead of V_{pl} would result in a similar value of $\tau_{ss}^{V_{\mathrm{pl}}}/(\sigma - p_{\mathrm{int}}) = f_* = 0.6$.

In the following section, we compare this representative value of local SSQS shear resistance to the spatial distribution of shear stress prior to dynamic ruptures in our simulations. Note that the local SSQS shear resistance is similar to what is typically viewed as "frictional fault

strength" in the sense of Byerlee (1978), i.e., this is the resistance that needs to be met for noticeable quasi-static slip with the loading rate or another reference rate.

2.4 Larger ruptures associated with lower shear prestress over the rupture scale but higher prestress over smaller scales near nucleation

The interseismic periods in between individual earthquake ruptures in our simulations vary from months to decades, depending on the size of the rupture and the stress state resulting from the history of prior slip along the fault. Our earthquake sequence simulations produce a wide variety of rupture sizes due to heterogeneous prestress conditions along the fault that spontaneously arise in our models.

Let us consider the evolution of slip and shear stress in representative simulated spontaneous ruptures of increasing sizes within the same simulation (Figure 2.5). Over sequences of rupture events, the shear stress conditions prior to and after individual dynamic ruptures become spatially heterogeneous. This stress heterogeneity is due in part to the history of spatially variable slip and local static stress drop produced in previous ruptures, as well as stress relaxation and redistribution due to aseismic slip. In addition, while our simulated fault models are loaded by a constant long-term loading rate of V_{pl}, the effective loading conditions along the fault interface vary in space and time due to differences in slip rate along the fault. Ruptures nucleate preferentially in regions with the highest shear prestress, which in our models occur near the creeping regions as discussed in section 2.3 (Figure 2.5). The ruptures then propagate into the less stressed areas of the fault. Put another way, the average prestress over the nucleation region is higher than the average prestress over the entire ruptured region (Figure 2.7A vs. B), as we quantify in the following.

We compute the average shear prestress right before a dynamic rupture event over the entire future rupture area (which we do as post-processing of data in our simulation). We also compute the average shear prestress over the slow-slip nucleation zone, which we call the *nucleation stress*. We compare these average shear stress measures with the *local steady-state*

quasi-static (SSQS) fault shear resistance $\tau_{ss}^{V_{pl}}$, which is related to the local fault constitutive properties during slow slip and given by Equation 2.4.

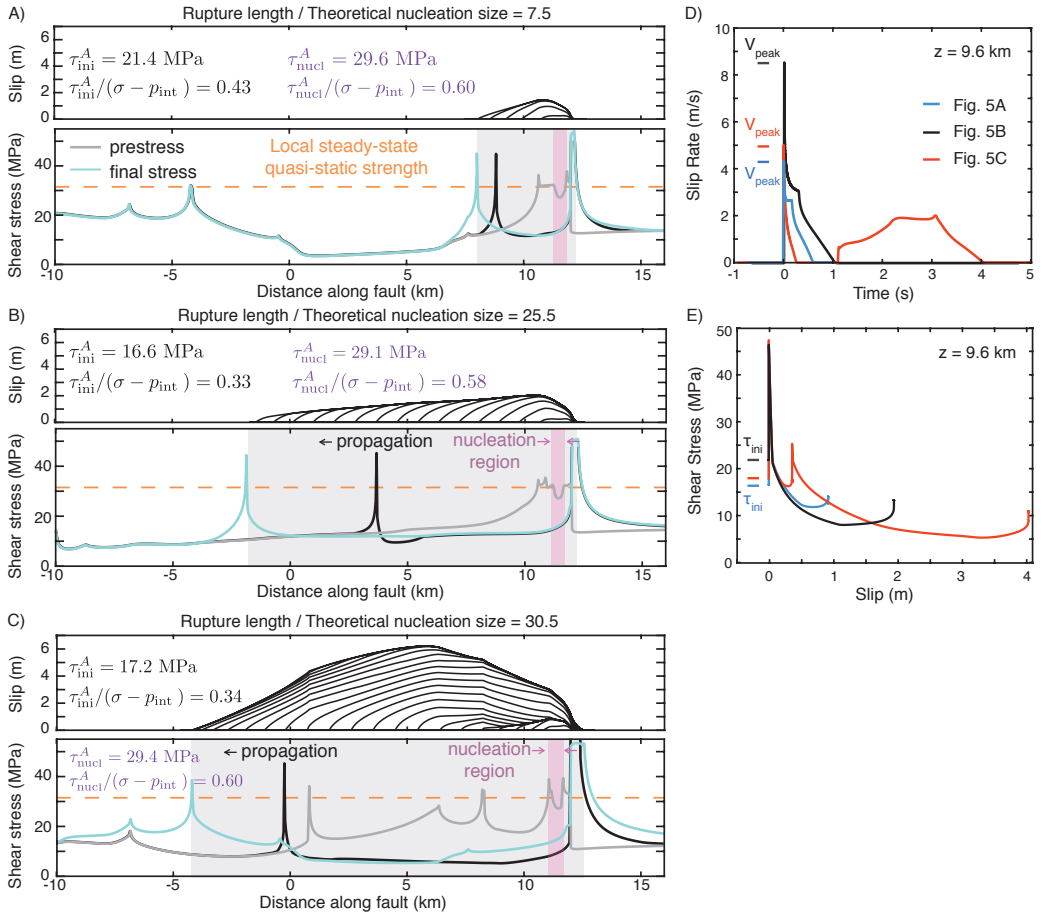

Figure 2.5: Spatial distribution of slip (top) and prestress and final shear stress (bottom) during three ruptures (A-C) with different rupture lengths in the same fault model (TP4 from Table 2.2). Slip contours are plotted every 0.25 s. The purple and gray shading illustrates the extent of the nucleation and ruptured regions, respectively, over which the prestress is averaged. While the ruptures nucleate in regions with stress levels near the local steady-state quasi-static shear resistance (dashed orange line), larger ruptures propagate over lower prestressed areas, resulting in lower average prestress and lower average coefficients of friction $\tau_{ini}^A/[\sigma - p_{int}]$. The shear stress distribution for a typical moment during rupture propagation is shown in black, demonstrating the stress concentration at the rupture front that brings the fault stress to values comparable to the SSQS shear resistance. The peak stress is even higher since the fault is initially dynamically stronger due to the rate-and-state direct effect. (D-E) Significant differences in local evolution of slip and stress at the same fault location ($z = 9.6$ km) for different ruptures that depend on the prestress conditions due to previous slip events and the dynamic stress interactions during the individual ruptures.

Averaging of spatially variable stress fields can be done in several different ways (Noda & Lapusta, 2012; Noda et al., 2013). The simplest definition of the average shear prestress over the rupture region Ω is the spatially averaged prestress τ^A_{ini} acting in the overall slip direction at the beginning of the rupture t_{ini}, given by:

$$\tau^A_{\text{ini}} = \frac{\int_\Omega \tau(z, t_{\text{ini}}) dz}{\int_\Omega dz}. \tag{2.5}$$

We can similarly define the spatially averaged nucleation stress τ^A_{nucl} within the nucleation region. We define the nucleation region to be the fault segment between the expanding stress fronts at the initiation of dynamic rupture; the size of the nucleation regions in our simulations is comparable to the theoretical nucleation size estimate h^*_{RA} of Rubin and Ampuero (2005) (Equation 2.12, Figure 2.6).

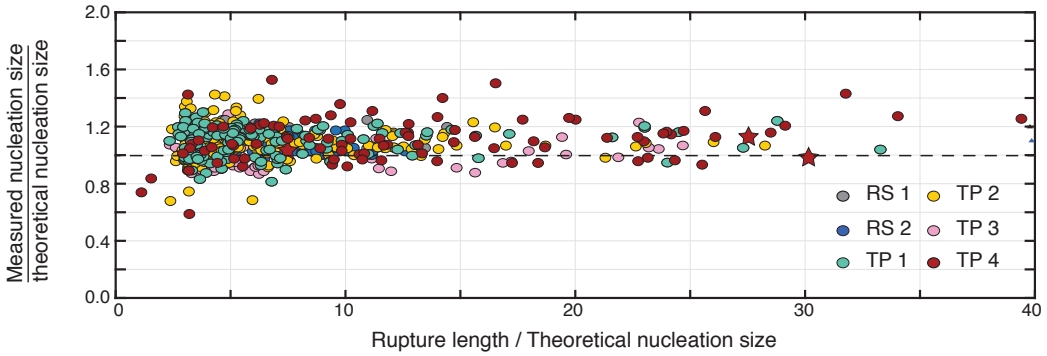

Figure 2.6: The measured nucleation sizes of the simulated ruptures (models RS1-2 and TP1-4 from Tables 2.2-2.3) are comparable to the theoretical estimate h^*_{RA}, within a factor of 2.

Not surprisingly and consistent with prior studies, we find that the spatially averaged nucleation stress τ^A_{nucl} for our simulated ruptures is comparable to the local SSQS shear resistance $\tau^{V_{\text{pl}}}_{ss}$ (Figure 2.7A). As a consequence, it does not significantly depend on the ultimate rupture size or slip. Since the nucleation stress here is computed at the beginning of dynamic rupture, it is then the shear stress within the nucleation zone at the end of the nucleation, when parts of the zone slip with near-dynamic slip rates approaching 10^{-2} m/s. That is why the nucleation stress is systematically slightly lower than the local SSQS shear resistance

defined as the steady-state shear resistance to slip with the (lower) plate rate. The difference between the nucleation stress and local SSQS shear resistance could be more substantial if dynamic weakening were efficient enough to affect some portion of the earthquake nucleation region (Segall & Rice, 2006).

In contrast, the spatially averaged prestress over the entire ruptured area τ^A_{ini} tends to decrease with the rupture size and increasingly deviate from the local SSQS shear resistance and nucleation stress for increasingly efficient dynamic weakening (Figures 2.5 & 2.7B). Such behavior is also true for another average prestress measure, the energy-based average prestress $\overline{\tau}^E_{\text{ini}}$ (Noda & Lapusta, 2012), which is the average shear prestress weighted by the final slip of the rupture, and hence represents the average prestress associated with the potency of the impending rupture:

$$\overline{\tau}^E_{\text{ini}} = \frac{\int_\Omega \tau(z, t_{\text{ini}})\delta_{\text{fin}}(z)dz}{\int_\Omega \delta_{\text{fin}}(z)dz} \tag{2.6}$$

where $\delta_{\text{fin}}(z) = \delta(z, t_{\text{fin}}) - \delta(z, t_{\text{ini}})$ is the final local slip accrued in the rupture. We denote $\overline{\tau}^E$ with a bar as it not only represents an average over space, but also requires knowledge of the final slip of the rupture. $\overline{\tau}^E_{\text{ini}}$ differs from the spatially-averaged prestress τ^A_{ini} over the rupture area when the resulting slip distribution is not uniform. We find that $\overline{\tau}^E_{\text{ini}}$ and τ^A_{ini} for our simulated ruptures are comparable and vary similarly with the rupture size and efficiency of dynamic weakening, with the values of $\overline{\tau}^E_{\text{ini}}$ being slightly larger (Figure 2.8).

The finding that larger ruptures are associated with smaller average shear prestress over the ruptured area may appear counterintuitive. Why do smaller ruptures not become larger if they are more favorably prestressed? To understand this behavior, let us consider the prestress averaged over several fixed scales around the nucleation region for ruptures of different sizes. We locate the VW-VS boundary next to which each of our simulated ruptures nucleate and average the prestress along the VW region over fixed distances (1, 2, 4, 8, 12, and 16 km) from the corresponding VW-VS boundary (Figure 2.9; shown for fault model TP4 from Table 2.2). While the spatially-averaged prestress over the entire rupture length decreases with increasing rupture size, we see that the prestress spatially-averaged over smaller fixed

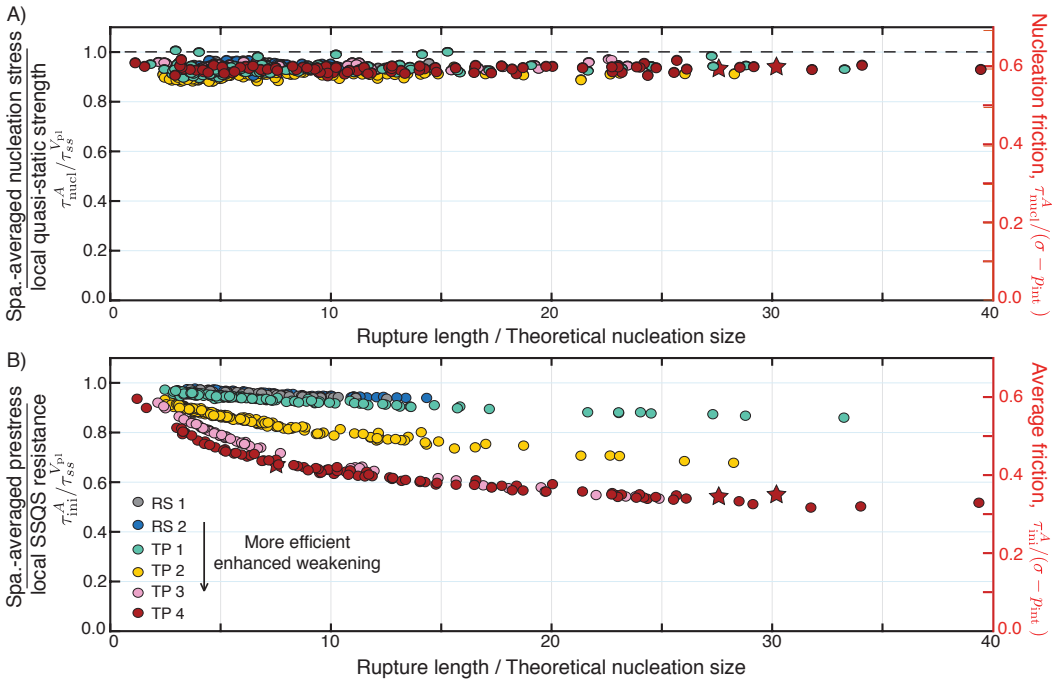

Figure 2.7: The difference between average shear stress needed for rupture nucleation vs. dynamic propagation. (A) The spatially-averaged nucleation stress $\tau^A_{\rm nucl}$ for ruptures is comparable to the average local steady-state quasi-static shear resistance $\tau_{ss}^{V_{\rm pl}}$, regardless of the final rupture size. (B) The spatially-averaged prestress $\tau^A_{\rm ini}$ and average friction coefficient $\tau^A_{\rm ini}/(\sigma - p_{\rm int})$ decrease with increasing rupture size; the effect is more pronounced with increasing efficiency of weakening. The three ruptures shown in Figure 2.5 are denoted by red stars.

scales is generally higher for larger ruptures than for smaller ruptures (Figure 2.9 warmer vs cooler colored triangles). For smaller ruptures, the average shear stress over scales just larger than their total rupture length is lower than the average prestress of larger ruptures with comparable length to the fixed averaging scales (Figure 2.9, triangles below the circles). This confirms that the smaller ruptures arrest because the prestress conditions ahead of the rupture are too low to sustain further rupture propagation. For larger ruptures, the average prestress levels at scales smaller than their total rupture length are generally higher or comparable to the average prestress over smaller ruptures with the length comparable to the fixed averaging scales (Figure 2.9, triangles above the circles). This finding suggests that larger ruptures have higher, more favorable average prestress conditions at smaller scales compared to smaller ruptures, which facilitates continued rupture propagation. Hence we

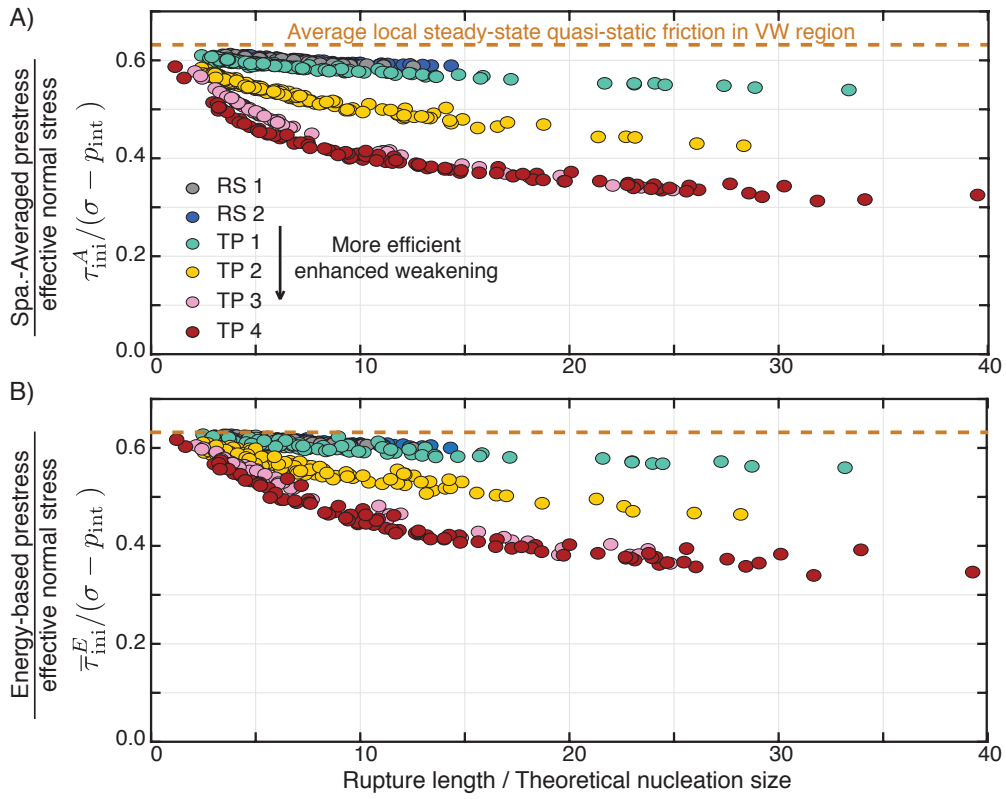

Figure 2.8: The spatially-averaged prestress $\tau^A_{\rm ini}$ and energy-averaged prestress $\overline{\tau}^E_{\rm ini}$ are generally comparable and decrease with increasing rupture size and efficiency of weakening.

find that the shear prestress prior to our simulated ruptures of varying sizes self-organizes into a spatial distribution of scale-dependent average shear stress that governs the rupture occurrence.

2.5 Role of dynamic stress transfers and motion-dependent local shear resistance

Such scale- and motion-dependent average fault shear prestress before ruptures results from two related and interacting factors. First, as dynamic rupture propagates, some of the released energy is carried by waves along the fault, creating a substantial stress concentration near the rupture tip that is a well-known feature of dynamic rupture (e.g., Freund, 1990). The stress concentration enables rupture propagation over regions where the prestress is lower than the local SSQS shear resistance, drawing the local shear stress up to the peak stress before the subsequent stress drop due to local weakening (black lines in Figure 2.5). The dynamic stress concentration increases with the rupture dimension and/or slip and

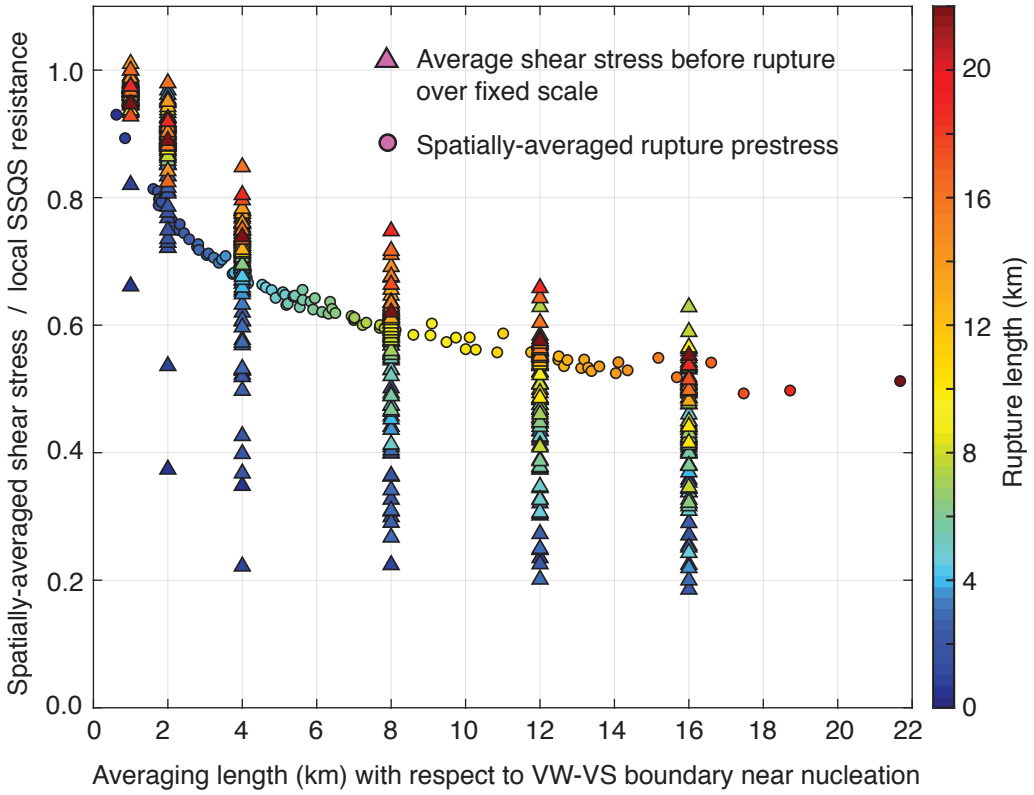

Figure 2.9: Comparison of the spatially averaged prestress over several fixed scales (1, 2, 4, 8, 12, and 16 km) and the average prestress over ruptures of varying size. As shown in Figure 2.7, the spatially-averaged prestress over the total rupture area τ_{ini}^{A} (circles) decreases considerably with rupture size in fault model TP4 from Table 2.2 with moderate enhanced dynamic weakening. However, larger ruptures have generally higher average shear stresses over smaller fixed scales around the nucleation region compared to smaller ruptures (red vs. blue triangles). The spatially-averaged shear stress over 1 km from the VW-VS boundary near the nucleation region of ruptures (triangles on the far-left) is relatively high (comparable to the local SSQS resistance) for both small and large ruptures, indicating that ruptures nucleate in regions of relatively high prestress compared to the average prestress over the entire rupture area (circles). For smaller ruptures, the average prestress at the fixed scales just larger than their total rupture length is lower than the average prestress of ruptures with comparable length to the fixed scale, suggesting that the prestress levels were too low to sustain further rupture propagation.

thus allows larger ruptures to continue propagating over regions with lower, and hence less favorable, prestress conditions (Figure 2.5). This is illustrated in this work for largely crack-like ruptures that occur in the presented models with mild to moderate enhanced dynamic weakening (Lambert et al., 2021), but similar conclusions would be reached for pulse-like ruptures provided that they satisfy the observational constraint of magnitude-independent

stress drops, which implies that ruptures with larger magnitudes would have larger average slip and hence larger stress concentrations. Note that a pulse-like rupture with the same or similar spatial distribution of the slip rate (and hence the same local slip) propagating along the fault would result in a similar stress concentration at the rupture tip regardless of the rupture length; however, in that scenario, pulses with larger rupture propagation lengths would have systematically lower static stress drops, as the stress drops would be proportional to the (uniform) pulse slip divided by ever increasing propagation lengths.

Second, the evolving local shear resistance substantially depends on both the prior history of slip events on the fault through fault prestress and on the motion during the current rupture event through dynamic stress transfers that add substantial time-dependent loading. This pronounced dependence is due to strong coupling between the evolving motion, the resulting shear heating, and the evolving shear resistance. As a result, the evolution of local slip rate and local shear resistance (1) significantly differs at different fault locations of each rupture (despite uniform constitutive properties) and (2) significantly differs at the same fault location for different ruptures (Figures 2.1D-I and 2.5D-E).

These two factors create a substantial positive feedback, in which larger ruptures with more slip generate larger stress concentrations, leading to faster and larger slip, which dynamically causes more fault weakening, which in turn promotes more/faster slip, more energy release, larger stress concentrations, and increasing rupture sizes.

The result that larger ruptures are associated with lower average prestress indicates the need for increasingly less favorable stress conditions to arrest growing ruptures. For a given rupture size, if the prestress ahead of the rupture is favorable, then the rupture would continue to grow until it experiences sufficiently unfavorable prestress conditions, thus lowering the overall average prestress. Alternatively, the rupture may be forcibly arrested by other means such as strong geometric or rheological barriers. For example, ruptures propagating over higher prestress conditions within the VW region can be arrested by fault regions with VS

properties; in those cases, the overall average prestress conditions would depend on the properties of the VS regions (Perry et al., 2020). Detailed study of the implications of fault geometry and heterogeneity for rupture arrest and the average stress conditions prior to rupture is an important topic for future work.

2.6 Comparison of finite-fault modeling to single-degree-of-freedom representations

As captured in field observations of natural earthquakes and reflected in our simulations, sufficiently large earthquake ruptures nucleate on a subsection of the fault and then propagate through other sections of the fault. Capturing such space-dependent behavior is typically called "finite-fault" modeling, in contrast to the point source that considers a spatially averaged representation of an event, as if it occurs at one "point." A typical numerical model of a point source is the single-degree-of-freedom system (SDOF) of a slider with friction pulled by a spring (e.g. Dieterich, 1979; Rice & Ruina, 1983; Ruina, 1983). Small-scale laboratory experiments often measure properties averaged over a sample and are typically modeled as a SDOF spring-slider systems.

The significant role of spatially varying prestress conditions and dynamic stress transfers during rupture propagation in determining the rupture behavior implies that capturing the finite-fault nature of the process is essential for determining the stress evolution characteristic of dynamic rupture. For example, several laboratory studies applied variable slip rates histories inferred from natural earthquakes to rock samples, measured the resulting shear resistance, and then related laboratory stress measurements to seismological source properties such as breakdown energy and stress drops (e.g. Fukuyama & Mizoguchi, 2010; Nielsen et al., 2016; Sone & Shimamoto, 2009). Such experiments have provided invaluable data about the local shear resistance of faults, specifically enhanced dynamic weakening, that have informed theoretical and numerical modeling of finite faults (e.g. Dunham et al., 2011a; Gabriel et al., 2012; Lambert et al., 2021; Noda et al., 2009; Noda & Lapusta, 2010; Perry et al., 2020; Rice, 2006; Zheng & Rice, 1998), including the current study. However, the interpretation of such experiments needs to take into account their SDOF nature. For example, to improve alignment etc, the experiments often impose pre-sliding at slow slip rates

(of the order of micron/s) prior to imitating seismic motion. That procedure results in the shear prestress before seismic slip comparable to the local SSQS shear resistance (equation 2.4) and near steady-state values of the state variable, as appropriate for a location within a nucleation zone. In contrast, our simulations show that most points on a fault through which the rupture propagates have much lower shear prestress and much larger values of the state variable corresponding to well-healed fault (Figures 2.5 and 2.10B). Furthermore, the experiments often apply smoothened slip-rate histories obtained from finite-fault inversions, while the stress concentration at the tip of dynamic rupture makes the slip rate variation much more dramatic.

To illustrate the differences for the shear resistance evolution obtained with such experimental procedures versus the one from our simulated finite-fault models, let us compare the local fault behavior during one of our dynamic ruptures with a SDOF calculation. In the SDOF calculation, we use the same fault properties (Equations 3.2, 2.10 and 5.6-5.5) and same parameter values as in the finite-fault VW regions, but apply quasi-static presliding and modified, smoothened slip rates motivated by the laboratory procedures of Fukuyama and Mizoguchi (2010) (further details in Supplementary Materials). We conduct the comparison for two fault locations, one in the nucleation region and one within dynamic rupture propagation region (Figure 2.10). These SDOF calculations are successful at reproducing the presence of the enhanced dynamic weakening with slip as occurs during dynamic ruptures and generally capture the more moderate slip evolution and behavior of points within the nucleation region of our simulated dynamic ruptures. At the same time, the overall shear stress evolution during typical propagation of the dynamic rupture substantially differs from that of the SDOF calculation, with notable features including the low initial stress (which depends on prior slip history) relative to the SSQS shear resistance, the much more dramatic increase in shear stress associated with the dynamic rupture front (which arises due to the more healed fault coupled with the dynamic stress concentration), and the shear stress evolution at the end of slip (which depends on the final slip distribution over the entire finite fault) (Figure 2.10).

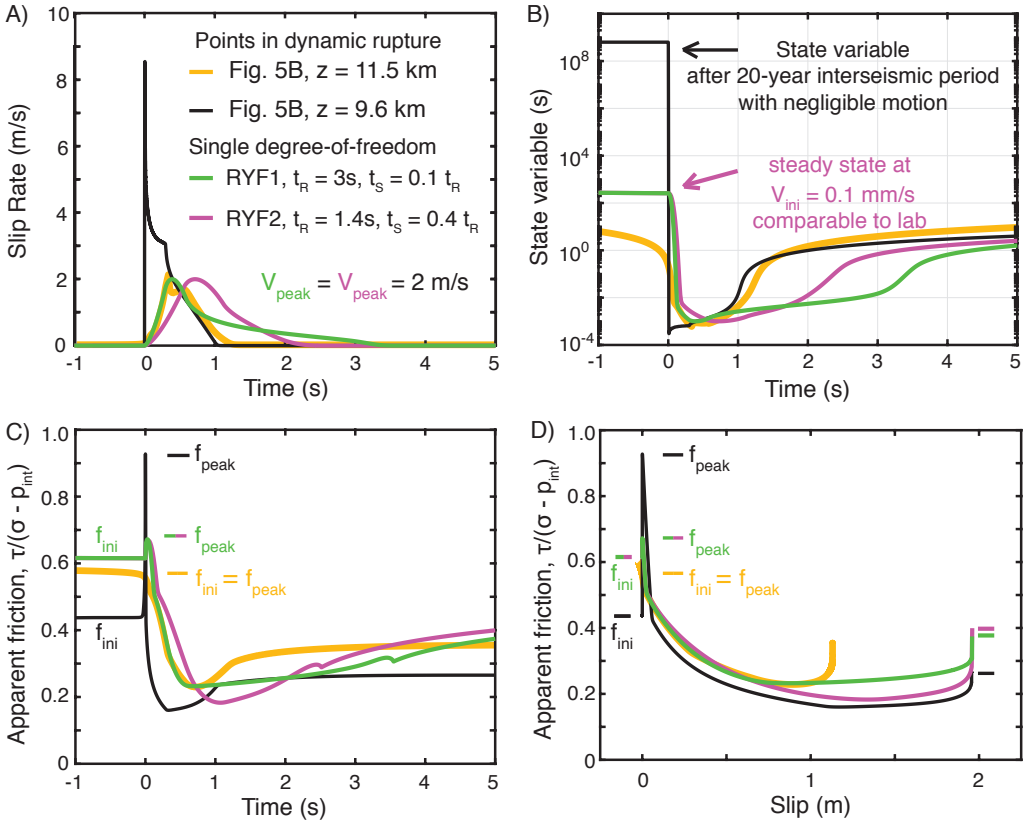

Figure 2.10: Comparison of the results of our dynamic modeling with what would be obtained in laboratory experiments given the same constitutive properties and typical lab procedures. (A) Comparison of the local slip rate during nucleation (z = 11.5 km, yellow) and typical propagation (z = 9.6 km, black) of the simulated dynamic rupture of Figure 2.5B with the slip rate evolution that could be imposed in lab experiments represented by two regularized Yoffe functions (Tinti et al., 2005) with peak slip rate of 2 m/s and comparable slip to the point at z = 9.6 km. The imposed regularized Yoffe functions are generally comparable to the evolution of slip within the nucleation region (z = 11.5 km), however they do not capture the rapid acceleration of slip associated with the arrival of the rupture front at points of typical propagation, as observed at z = 9.6 km. (B) Comparison of the state variable evolution from our simulation and the lab experiment which we simulate using the single-degree of freedom (SDOF) equations. The simulated lab experiment starts with the steady-state conditions for 0.1 mm/s based on the experiments of Fukuyama and Mizoguchi (2010), which results in a much lower initial state value compared to the point z = 9.6 km in our simulations which, prior to dynamic rupture, had negligible motion over a 20-year interseismic period. (C-D) Evolution of the local apparent coefficient of friction with time and slip for the point in our simulated finite-fault dynamic rupture and SDOF lab experiments. The dynamic weakening is generally comparable between the points in the finite rupture and the SDOF experiments, however the evolution of shear stress substantially differ with regards to the much lower prestress at z = 9.6 km before the finite dynamic rupture and the abrupt increase and then decrease in stress due to the arrival of the dynamic rupture front and the associated rapid weakening.

2.7 Implications for earthquake statistics

A notable feature of the scale dependence of average prestress before dynamic rupture is that, as an earthquake grows larger, the prestress needed for further propagation decreases (Figure 2.7B). In addition, the higher the weakening rate, the easier it should be for a rupture to have favorable prestress conditions to continue growing, rather than arresting as a smaller earthquake. Hence one could hypothesize that the more efficient the enhanced dynamic weakening, the smaller the complexity of the resulting earthquake sequences, with increasing representation of larger events at the expense of smaller events.

This is exactly what our modeling shows (Figure 2.11). The fault models with increasingly more efficient weakening produce earthquake sequences with increasingly fewer small events and decreasing b-values of the cumulative size distribution (Figure 2.11). Fault models with even more efficient dynamic weakening than considered in this study, such as those that produce sharp self-healing pulses, result in relatively simple earthquake sequences consisting of only large events (Chapter 4; Lambert et al., 2021). The fault models governed by relatively mild to more moderate weakening as considered in this work develop a wider range of earthquake sizes, due to a feedback loop of more likely rupture arrest due to milder weakening creating stress heterogeneity that in turn makes rupture arrest more likely. This result is consistent with those of previous quasi-dynamic earthquake sequence simulations demonstrating complex earthquake sequences with b-values around 0.75 on faults with standard rate-and-state friction only and milder quasi-dynamic stress transfer (Cattania, 2019). Our study shows that the b-values decrease to 0.5 for fully dynamic simulations without enhanced dynamic weakening, and further decrease to 0.25 or so for the most efficient weakening considered in this study.

While the frequency-magnitude distribution of seismicity over relatively large regions, such as Northern or Southern California, is generally well-described by Gutenberg-Richter scaling with typical b-values near unity (Field et al., 2013), whether such scaling applies to individual fault segments and/or their immediate surroundings is a topic of active research

(Field et al., 2017; Ishibe & Shimazaki, 2012; Kagan et al., 2012; Page & Felzer, 2015; Page & van der Elst, 2018; Wesnousky, 1994). Estimates of b-values associated with individual fault segments can exhibit considerable variability (e.g. between 0.5 and 1.5 along faults in California; Tormann et al., 2014), and are sensitive to a number of factors, including the magnitude of completeness of the relevant earthquake catalog and the choice of observation region and time window (Ishibe & Shimazaki, 2012; Page & Felzer, 2015; Page & van der Elst, 2018; Tormann et al., 2014). A number of studies suggest that the rate of large earthquakes on major faults, such as the San Andreas Fault, is elevated above what would be expected given typical Gutenberg-Richter scaling from smaller magnitude events (Field et al., 2017; Schwartz & Coppersmith, 1984). In particular, some mature fault segments that have historically hosted large earthquakes, such as the Cholame and Carrizo segments of the San Andreas Fault, exhibit substantial deviations from typical Gutenberg-Richter scaling, being nearly absent of small earthquakes (Bouchon & Karabulut, 2008; Hauksson et al., 2012; Jiang & Lapusta, 2016; Michailos et al., 2019; Sieh, 1978; Wesnousky, 1994). Our findings suggest that the paucity of microseismicity on such mature fault segments may indicate that they undergo substantial dynamic weakening during earthquakes ruptures.

2.8 Discussion

Our simulations demonstrate that the average shear prestress required for rupture propagation can be considerably lower than the average shear stress required for the rupture nucleation. This is because the quasi-static nucleation process is governed by relatively small stress changes and hence requires favorable prestress conditions –close to the local steady-state quasi-static shear resistance –to proceed. In contrast, during dynamic rupture, the rupture front is driven by larger wave-mediated dynamic stress concentrations, which are more substantial for larger ruptures and facilitate rupture propagation over less favorably stressed regions, resulting in the spatially-averaged prestress over the ruptured area being much lower than the average local SSQS shear resistance. More efficient weakening facilitates larger dynamic stress changes at the rupture front, allowing propagation over even less favorable prestress conditions. Our results highlight the significance of heterogeneity in prestress, or shear resistance, for the nucleation and ultimate arrest of finite ruptures, even in fault models

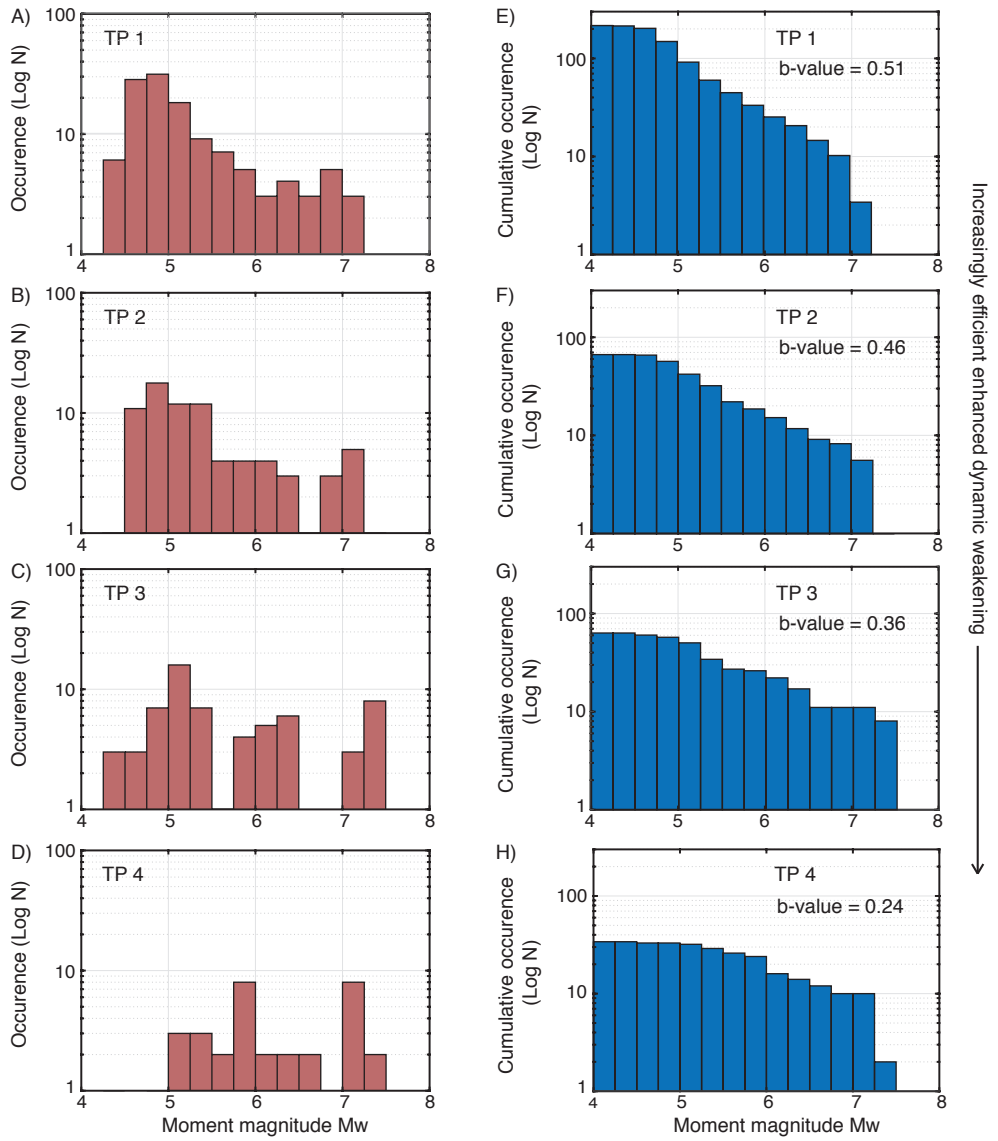

Figure 2.11: Fault models with more efficient weakening result in less earthquake sequence complexity, producing fewer smaller events (left column) and smaller b-values (right column). (A-D) Frequency-magnitude and (E-H) cumulative frequency-magnitude statistics for simulations with increasing efficiency of enhanced dynamic weakening (TP1-4 from Table 2.2).

that have otherwise uniform material and confining properties.

The decrease in averaged prestress with rupture length can be interpreted as a decrease in the average quasi-static friction coefficient $\tau^A_{\text{ini}}/(\sigma - p_{\text{int}})$ with rupture size (Figure 2.7). The

average quasi-static friction coefficients for ruptures on the scale of the nucleation size are consistent with the prescribed quasi-static reference friction coefficient near typical Byerlee values. However, as we average the prestress over larger rupture lengths, the average quasi-static friction coefficient can considerably decrease depending on the efficiency in weakening.

The presence of enhanced dynamic weakening draws the average shear stress along larger regions of the fault below the local SSQS consistent with earthquake nucleation, resulting in lower average shear stress conditions in terms of both the average prestress for larger ruptures and the average dynamic resistance associated with shear heating during ruptures (Figure 2.12). The models presented in this study with mild-to-moderate enhanced weakening include considerable persistent fluid overpressurization to maintain low-heat, low-stress conditions with average dynamic shear resistance during seismic slip rates below 10 MPa; however the degree of fluid overpressure required to maintain low-heat conditions is less than that with comparable rate-and-state properties but no enhanced weakening. The presence of some enhanced dynamic weakening is also needed for persistently weak fault models due to chronic fluid overpressure in order to ensure that static stress drops are not too small, as they would otherwise be with low effective stress and small changes in the friction coefficient due to standard rate-and-state laws (Figures 2.12 and 2.13; Lambert et al., 2021). Fault models with more efficient dynamic weakening have been shown to be able to reproduce low-stress operation and reasonable static stress drops with quasi-static friction coefficients around Byerlee values and higher effective normal stress (e.g. $\geq$ 100 MPa; Dunham et al., 2011a; Lambert et al., 2021; Noda et al., 2009). Earthquake sequence simulations of such fault models typically consist of only large ruptures (Lambert et al., 2021), consistent with the notion that large fault areas governed by efficient weakening maintain substantially lower average shear stresses than that required for nucleation. These findings further strengthen the conclusion of prior studies that enhanced dynamic weakening can help explain the discrepancy between laboratory values of (quasi-static) friction coefficients around 0.6 and geophysical inferences of low effective coefficients of friction ($<$ 0.2), along with mild

average static stress drops of 1 to 10 MPa, over fault areas that host large earthquakes (e.g Allmann & Shearer, 2009; Dunham et al., 2011a; Gao & Wang, 2014; Ikari et al., 2011; Lambert et al., 2021; Marone, 1998; Noda et al., 2009; Perry et al., 2020; Suppe, 2007; Ye et al., 2016b).

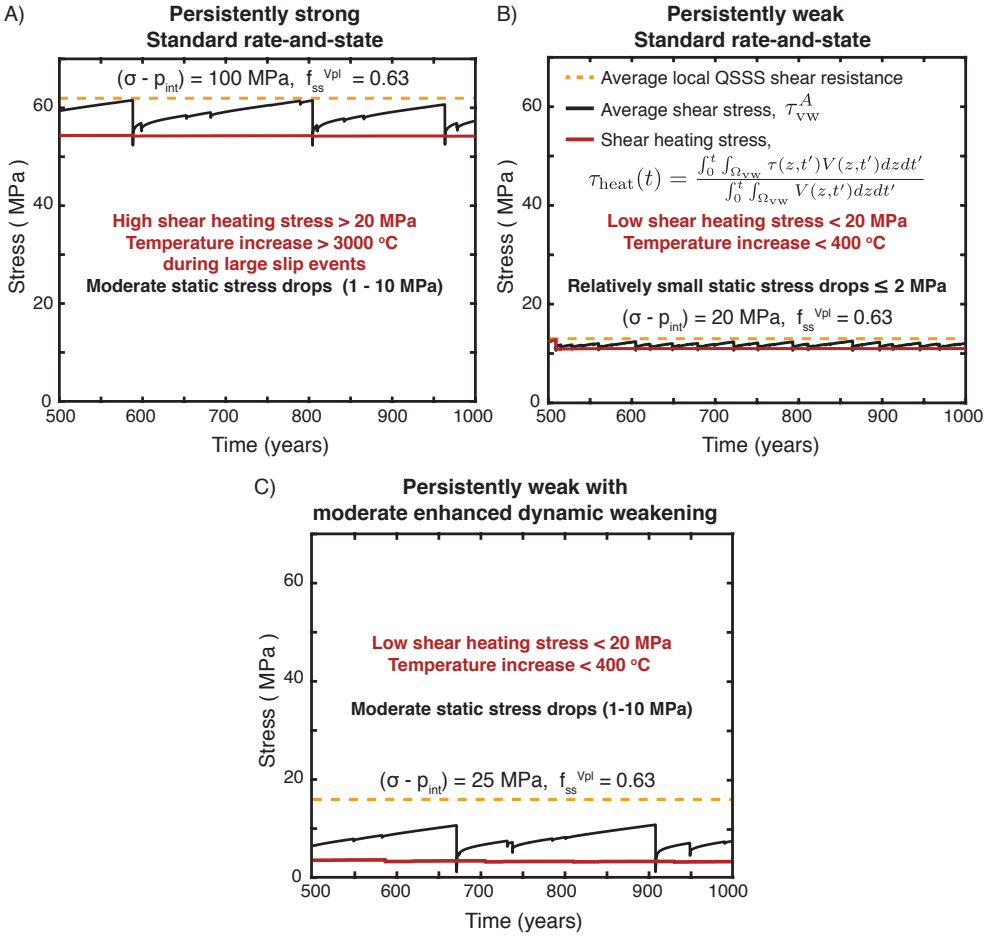

Figure 2.12: Evolution of the spatially averaged shear stress in the VW region $\tau_{\rm vw}^A$ (black line) over earthquakes sequences. (A-B) Standard rate-and-state friction results in modest changes in shear resistance from the average local steady-state quasi-static (SSQS) shear resistance (orange line). Ruptures on persistently strong faults produce realistic static stress drops (A); however, the fault temperature would increase by more than 3000 ^{o}C during a dynamic event for a shear-zone half-width of 10 mm. (B) Persistently weak fault models due to low effective normal stress but with no enhanced weakening (RS 1 of Table 2.2) can maintain modest fault temperatures, but produce relatively small static stress drops $\leq$ 2 MPa. (C) Persistently weak models with mild to moderate enhanced dynamic weakening (TP3 of Table 2.2) are capable of maintaining modest fault temperatures and producing more moderate average stress drops between 1 - 10 MPa.

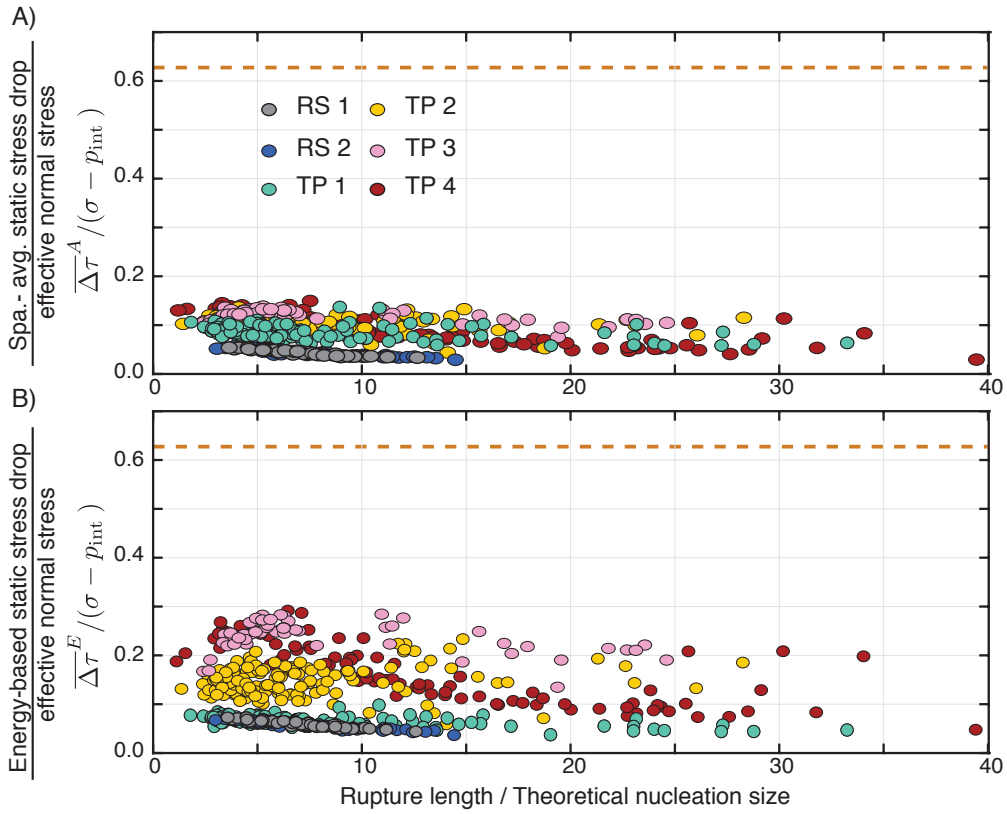

Figure 2.13: The (A) spatially-averaged and (B) energy-based average static stress drops for ruptures represent relatively mild decreases in average shear stress with respect to the effective normal stress. Persistently weak fault models with low effective normal stress ≤ 20 MPa and relatively mild weakening, such as from standard rate-and-state friction (RS1 and RS2) produce potentially too small average static stress drops ≤ 2 MPa, whereas models with mild to moderate enhanced weakening (TP1-4) produce realistic average static stress drops of 1–10 MPa.

The scale dependence of average prestress before ruptures can also be interpreted as a scale dependence of *average fault strength*, since the average prestress represents a measure of how much shear stress that fault region can hold before failing in a rupture. Given this interpretation, our simulations suggest that faults maintain lower average shear stresses, and hence appear weaker, at larger scales than at smaller scales. This interpretation is conceptually consistent with laboratory measurements of scale-dependent yield stress for rocks and a number of engineering materials, which demonstrate decreasing material strength with increasing scale (Bandis et al., 1981; Greer et al., 2005; Jaeger & Cook, 1976; Pharr et al., 2010; Thom et al., 2017; Uchic et al., 2004; Yamashita et al., 2015). Note that our larger

simulated ruptures, even with more efficient weakening, still require higher average shear stresses over smaller scales in order to nucleate and grow. Thus the lower average prestress levels that allow continued failure in dynamic ruptures at larger scales only become relevant once the rupture event has already nucleated and sufficiently grown over smaller scales. This consideration suggests that the critical stress conditions for rupture occurrence are governed not by a single stress quantity but by a distribution of scale-dependent stress criteria for rupture nucleation and continued propagation. An important implication of our findings is that the critical stress for earthquake occurrence may not be governed by a simple condition such as a certain level of Coulomb stress. Given our findings, in order to reason about the stress conditions critical for a rupture to occur, it is important to consider both the size of the rupture and the weakening behavior, and hence the style of motion, that may occur throughout rupture propagation.

The scale dependence of fault material strength has also been hypothesized to explain the measured scaling of roughness on natural fault surfaces (Brodsky et al., 2016). Dynamic rupture simulations on geometrically irregular faults motivated by such roughness measurements have indicated an additional contribution to fault shear resistance arising from roughness drag during rupture propagation (Fang & Dunham, 2013). Further examination of the scale dependence of average shear resistance across faults including realistic fault geometry is an important topic for future work.

A common assumption is that the shear prestress over the entire ruptured area must be near the local static (or quasi-static) strength, comparable to the SSQS shear resistance discussed in this study. We demonstrate that the assumption is not necessarily valid and that faults with enhanced dynamic weakening and history of large earthquake ruptures would, in fact, be expected to have low average shear stress over large enough scales. At the same time, the state of stress needs to be heterogeneous, with the average stresses over small scales (comparable to earthquake nucleation) being close to the (much higher) local SSQS shear resistance in some places. Thus, while individual measurements of low resolved shear stress

onto a fault may suggest that those locations appear to not be critically stressed for quasi-static failure, those regions, and much of the fault, may be sufficiently stressed to sustain dynamic rupture propagation and hence large earthquake ruptures. In addition, our findings suggest that inferences of stress levels on faults may differ if they are obtained over different scales or influenced by different rupture processes. For example, low-stress conditions on mature faults from observations of low heat flow may not only represent average shear stress conditions over large fault segments as a whole but also be dominated by low dynamic resistance during fast slip, whereas averages over smaller scales would be expected to reflect the heterogeneity of the underlying prestress distribution, as perhaps reflected in varying stress rotations inferred over scales of tens of kilometers (Hardebeck, 2015; Hardebeck & Hauksson, 1999, 2001).

Our modeling shows that increasingly efficient dynamic weakening leads to different earthquake statistics, with fewer small events and an increasing number of large events. Another factor that can significantly affect the ability of earthquake ruptures to propagate is fault heterogeneity. Some dynamic heterogeneity in shear stress spontaneously develops in our simulations, leading to a broad distribution of event sizes for cases with mild to moderate enhanced dynamic weakening. Our findings suggest that the effects of pre-existing types of fault heterogeneity need to be considered with respect to the size of the rupture and weakening behavior on the fault. For example, faults that experience more substantial weakening would require the presence of larger amplitudes of small-wavelength heterogeneity in shear stress or resistance to produce small events. Examining the relationship between earthquake sequence complexity and varying levels of fault heterogeneity and enhanced dynamic weakening is an important topic for future work.

2.9 Conclusions

Our modeling of faults with rate-and-state friction and enhanced dynamic weakening indicates that average shear prestress before dynamic rupture –which can serve as a measure of average fault strength –can be scale-dependent and decrease with the increasing rupture size. Such decrease is more prominent for faults with more efficient dynamic weakening.

The finding holds for faults with the standard rate-and-state friction only, without any additional dynamic weakening, although the dependence is relatively unremarkable in that case (Figures 2.7 and 2.14). However, the scale-dependent decrease in average prestress is quite pronounced even for fault models with mild to moderate enhanced dynamic weakening that satisfy a number of other field inferences, including nearly magnitude-invariant static stress drops of 1-10 MPa, increasing average breakdown energy with rupture size, radiation ratios between 0.1 and 1.0, and low-heat fault operation (Lambert et al., 2021; Perry et al., 2020).

Our simulations illustrate that both critical fault stress required for rupture propagation and static stress drops are products of complex finite-fault interactions, including wave-mediated stress concentrations at the rupture front and redistribution of stress post-rupture by dynamic waves. Hence it is important to keep in mind the finite-fault effects - and their consequences in terms of the spatially variable fault prestress, slip rate, and shear stress evolution - when interpreting single-degree-of-freedom representations, such as spring-slider models and small-scale laboratory measurements. This consideration highlights the need to continue developing a better physical understanding of faulting at various scales through a combination and interaction of small-scale and intermediate-scale lab and field experiments, constitutive relations formulated based on such experiments, and finite-fault numerical modeling constrained by inferences from large-scale field observations. Our comparison of local fault behavior in SDOF and dynamic rupture simulatons also demonstrate how small-scale experiments can be used in conjunction with finite-fault modeling to improve our understanding of the earthquake source: the finite-fault modeling can suggest the initial conditions and slip-rate histories for the small-scale experiments to impose, and then the shear stress evolution from the small-scale experiments can be compared to the numerically obtained ones, which would allow to validate and improve the constitutive laws used in finite-fault modeling.

We find that increasingly efficient dynamic weakening leads to different earthquake statistics, with fewer small events and increasingly more large events. This finding is consistent with

the interpretation of average fault prestress before rupture as average fault strength, in that lower fault strength over larger scales leads to an increasing number of larger events. It also adds to the body of work suggesting that enhanced dynamic weakening may be responsible for deviations –inferred for large, mature fault segments –of earthquake statistics from the Gutenberg-Richter scaling (Bouchon & Karabulut, 2008; Hauksson et al., 2012; Jiang & Lapusta, 2016; Michailos et al., 2019; Sieh, 1978). For example, fault models with efficient dynamic weakening are consistent with mature faults that have historically hosted large earthquakes but otherwise appear seismically quiescent, such as the Cholame and Carrizo segments of the San Andreas Fault, which hosted the 1857 Fort Tejon earthquake (Jiang & Lapusta, 2016). In contrast, the presence of a wider range of rupture sizes and styles of slip transients on other faults, such as the Japan trench (e.g. Ito et al., 2013), may suggest that they undergo more mild to moderate enhanced weakening during dynamic ruptures, and/or exhibit more pronounced fault heterogeneity.

Such considerations may be useful for earthquake early warning systems, which currently do not take into account the potential physics-based differences in the event size distribution. Under the assumption of Gutenberg-Richter statistics, the probability that a smaller, Mw 5 or 6 event becomes a much larger earthquake is not great; however, that probability may be substantially larger on mature faults if they are indeed governed by enhanced dynamic weakening.

Our results indicate that critical stress conditions for earthquake occurrence cannot be described by a single number, but rather present as complex spatial distribution with scale-dependent averages. When considering the critical stress conditions, it is essential to take into account both the size of the rupture and the weakening behavior, and hence the style of motion, that may occur throughout rupture propagation. These results warrant further investigation, specifically how the weakening behavior during dynamic rupture would interact with different degrees of fault heterogeneity as well as implications for earthquake early warning.

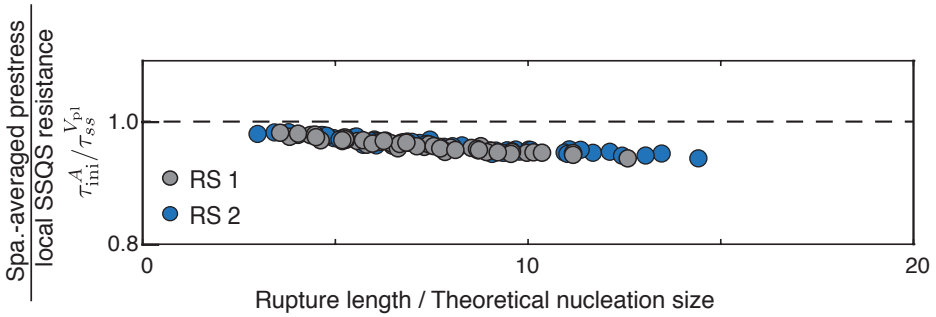

Figure 2.14: Ruptures on fault models with relatively mild weakening due to standard rate-and-state friction also exhibit a mild decrease in the spatially-averaged prestress $\tau^A_{\rm ini}$ with increasing rupture size.

Parameter	Symbol	Value
Loading slip rate	V_{pl}	10^{-9} m/s
Shear wave speed	c_s	3299 m/s
Shear modulus	μ	36 GPa
Thermal diffusivity	α_{th}	10^{-6} m^2/s
Specific heat	ρc	2.7 MPa/K
Shear zone half-width	w	10 mm
Rate-and-state parameters		
Reference slip velocity	V_*	10^{-6} m/s
Reference friction coefficient	f_*	0.6
Rate-and-state direct effect (VW)	a	0.010
Rate-and-state evolution effect (VW)	b	0.015
Rate-and-state evolution effect (VS)	b	0.003
Length scales		
Fault length	λ	96 km
Frictional domain	λ_{fr}	72 km
Velocity-weakening region	λ_{VW}	24 km
Cell size	Δz	3.3 m
Quasi-static cohesive zone	Λ_0	84 m
Nucleation size (Rice & Ruina, 1983)	h^*_{RR}	226 m
Nucleation size (Rubin & Ampuero, 2005)	h^*_{RA}	550 m

Table 2.1: Model parameters used in all simulations in Ch. 2 unless otherwise specified.

Parameter	Symbol	TP 1	TP 2	TP 3	TP 4
Interseismic effective normal stress (MPa)	$\bar{\sigma} = (\sigma - p_{\text{int}})$	25	25	25	50
Rate-and-state direct effect (VS)	a	0.050	0.050	0.025	0.050
Characteristic slip (mm)	D_{RS}	1	1	1	2
Coupling coefficient (MPa/K)	Λ	0.1	0.34	0.34	0.34
Hydraulic diffusivity m^2/s	α_{hy}	10^{-3}	10^{-3}	10^{-4}	10^{-3}

Table 2.2: Parameters for models in Ch.2 including thermal pressurization of pore fluids.

Parameter	Symbol	RS 1	RS 2
Interseismic effective normal stress (MPa)	$\bar{\sigma} = (\sigma - p_{\text{int}})$	10	20
Rate-and-state direct effect (VS)	a	0.050	0.050
Characteristic slip (mm)	D_{RS}	0.5	1
Quasi-static cohesive zone (m)	Λ_0	106	106
Nucleation size (m), Rice & Ruina, 1983	h^*_{RR}	282	282
Nucleation size (m), Rubin & Ampuero, 2005	h^*_{RA}	688	688

Table 2.3: Parameters for models in Ch. 2 including only standard rate-and-state friction.

2.10 Appendix

2.10.1 Methodology for simulations of sequences of earthquakes and aseismic slip with and without the thermal pressurization of pore fluids

In order to conduct numerical simulations of sequences of spontaneous earthquakes and aseismic slip, we utilize the spectral boundary integral method to solve the elastodynamic equations of motion with the friction boundary conditions, including the evolution of pore fluid pressure and temperature on the fault coupled with off-fault diffusion (Lapusta et al., 2000; Noda & Lapusta, 2010). Our fault models are governed by a form of the laboratory-derived Dieterich-Ruina rate-and-state friction law regularized for zero and negative slip rates, with the state evolution governed by the aging law (Noda & Lapusta, 2010; Rice & Ben-Zion, 1996). The most commonly used formulation of rate-and-state laws is the Dieterich-Ruina formulation (Dieterich, 1979; Ruina, 1983):

$$\tau = \overline{\sigma} f(V, \theta) = (\sigma - p) \left[f_* + a \ln \frac{V}{V_*} + b \ln \frac{\theta V_*}{D_{\text{RS}}} \right], \tag{2.7}$$

where f_* is a reference steady-state friction coefficient at reference sliding rate V_*, D_{RS} is the characteristic slip distance, and a and b are the direct effect and evolution effect parameters,

respectively. During steady-state sliding ($\dot{\theta} = 0$), the friction coefficient is expressed as:

$$f_{ss}(V) = f_* + (a - b) \ln \frac{V}{V_*}, \tag{2.8}$$

where the combination of frictional properties $(a - b) > 0$ results in steady-state velocity-strengthening (VS) behavior, where stable slip is expected, and properties resulting in $(a - b) < 0$ lead to steady-state velocity-weakening (VW) behavior, where accelerating slip and hence stick-slip occur for sufficiently large regions.

The peak shear stress during dynamic rupture propagation can correspond to a much higher apparent friction coefficient than the reference friction coefficient f_* or the similar steady-state friction coefficient at seismic slip rates of the order of 1 m/s. Assuming that the fault has been locked interseismically with the state variable healing to a value θ_{int} and the slip rate rapidly accelerates to the peak slip rate V_{peak} upon arrival of the rupture front with negligible evolution of the state variable $\theta \approx \theta_{\text{int}}$, the peak friction can be approximately given as:

$$\begin{aligned} \tau_{\text{peak}}/(\sigma - p_{\text{int}}) &= f_* + a \ln \frac{V_{\text{peak}}}{V_*} + b \ln \frac{\theta_{\text{int}}}{\theta_{\text{ss}}(V_*)} \\ &= \frac{\tau_{\text{ss}}(V_{\text{peak}})}{(\sigma - p_{\text{int}})} + b \ln \frac{\theta_{\text{int}}}{\theta_{\text{ss}}(V_{\text{peak}})} \\ &= \frac{\tau_{\text{ss}}(V_{\text{pl}})}{(\sigma - p_{\text{int}})} + (a - b) \ln \frac{V_{\text{peak}}}{V_{\text{pl}}} + b \ln \frac{\theta_{\text{int}}}{\theta_{ss}(V_{\text{peak}})}. \end{aligned} \tag{2.9}$$

Note that $V_{\text{peak}} \gg V_* \gg V_{\text{pl}}$ and $\theta_{\text{int}} \gg \theta_{\text{ss}}(V_*) \gg \theta_{\text{ss}}(V_{\text{peak}})$ for typical seismic slip rates and interseismic durations of healing. The last two terms on the third line gives the difference between the local SSQS shear resistance described in the main text and the peak shear resistance, where the last term typically dominates for periods of extending healing and higher values of θ_{int}. Consequently, for a given dynamic slip rate V_{peak}, the better healed the interface with higher θ_{ini}, the higher the peak friction during dynamic rupture (Chapter 3 Lambert & Lapusta, 2020).

The standard Dieterich-Ruina formulation (Equation 5.1) has been empirically-determined from laboratory experiments at sliding rates between 10^{-9} m/s to around 10^{-3} m/s. Under

the standard logarithmic formulation, friction becomes negative as the slip rate V approaches zero and is undefined for zero or negative slip rates (Figure 2.15). The standard formulation may be regularized near $V = 0$ such that the shear resistance remains positive for all positive values of V (Rice & Ben-Zion, 1996):

$$\tau(V,\theta) = a\overline{\sigma}\sinh^{-1}\left[\frac{V}{2V_*}\exp\left(\frac{f_* + b\log(\theta V_*/L)}{a}\right)\right], \tag{2.10}$$

with the steady-state shear resistance given by:

$$\tau_{ss}(V) = a\overline{\sigma}\sinh^{-1}\left[\frac{V}{2V_*}\exp\left(\frac{f_* + b\log(V_*/V)}{a}\right)\right]. \tag{2.11}$$

Theoretical justification for such regularization has been provided by drawing analogy between the direct velocity effect and the exponential formulation of thermally-activated creep at contact junctions, where the contact shear stress acts as a biasing factor (Rice et al., 2001). The standard logarithmic rate-dependent formulation is derived when only considering forward activated jumps, which may be dominant under significant shear stress and conditions relevant to most laboratory experiments. The regularized formulation (Equation 2.10) arises when including the presence of backward jumps, which are equally probable as forward jumps for $\tau = 0$, as in the full thermally-activated creep theory. The logarithmic and regularized formulations are equivalent for conditions consistent with laboratory experiments, and differ only for very low slip rates (Figure 2.15).

Earthquakes may nucleate only if the VW region is larger than the nucleation size h^*. For 2D problems, two theoretical estimates of the nucleation size in mode III are (Rice & Ruina, 1983; Rubin & Ampuero, 2005):

$$h^*_{RR} = \frac{\pi}{4}\frac{\mu D_{\mathrm{RS}}}{(b-a)(\sigma - p)};\ h^*_{RA} = \frac{2}{\pi}\frac{\mu D_{\mathrm{RS}} b}{(b-a)^2(\sigma - p)}, \tag{2.12}$$

where μ is the shear modulus. The simulated fault in our models contains a 24-km region with VW frictional properties surrounded by VS regions to create a 72-km frictional region. Outside of this frictional regions, the fault moves with a prescribed plate rate V_{pl} to provide tectonic-like loading (Figure 2.1A).

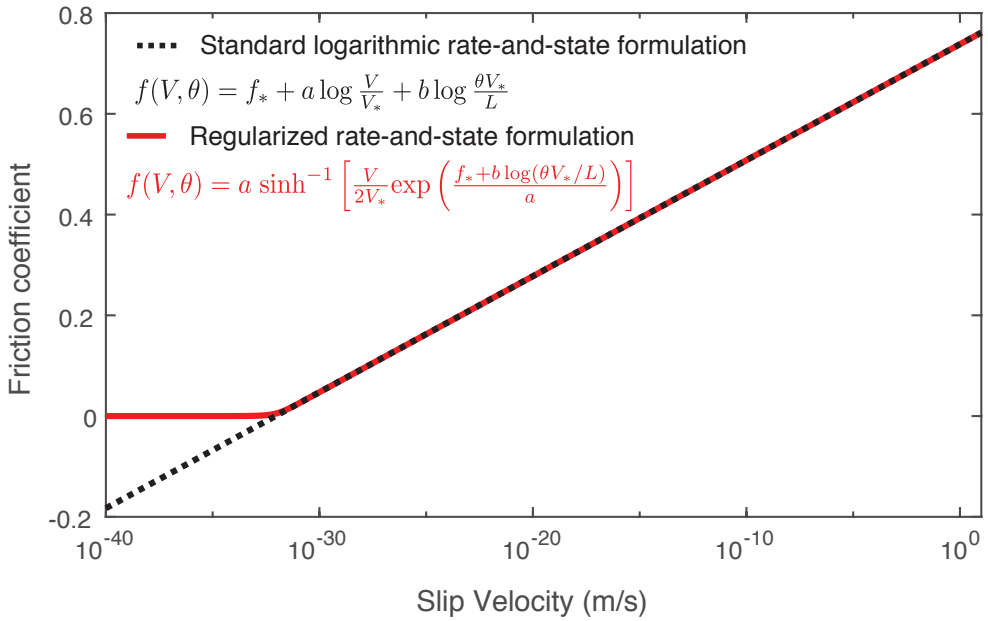

Figure 2.15: Comparison of the standard logarithmic (black) and regularized (red) formulations for rate-and-state friction given fixed $\theta = D_{RS}/V_*$ with $V_* = 1$ μm/s, $f_* = 0.6$, and $(a - b) = 0.004$. The two formulations are equivalent for slip rates relevant to most laboratory experiments, but differ as V approaches 0 m/s.

The thermal pressurization of pore fluids is governed in our simulations by the following coupled differential equations for temperature and pore pressure evolution (Noda & Lapusta, 2010):

$$\frac{\partial T(y,z;t)}{\partial t} = \alpha_{\text{th}}\frac{\partial^2 T(y,z;t)}{\partial y^2} + \frac{\tau(z;t)V(z;t)}{\rho c}\frac{\exp(-y^2/2w^2)}{\sqrt{2\pi}w}, \tag{2.13}$$

$$\frac{\partial p(y,z;t)}{\partial t} = \alpha_{\text{hy}}\frac{\partial^2 p(y,z;t)}{\partial y^2} + \Lambda\frac{\partial T(y,z;t)}{\partial t}, \tag{2.14}$$

where T is the temperature of the pore fluid, α_{th} is the thermal diffusivity, τV is the shear heating source distributed over a Gaussian shear layer of half-width w, ρc is the specific heat, y is the distance normal to the fault plane, α_{hy} is the hydraulic diffusivity, and Λ is the coupling coefficient that gives pore pressure change per unit temperature change under undrained conditions. To approximate the effects of off-fault yielding, we employ a velocity limit of $V_{\text{max}} = 15$ m/s, as discussed in detail in Lambert et al. (2021). This approximation is motivated by detailed dynamic rupture simulations with off-fault yielding (Andrews, 2004), with the value of velocity limited corresponding to a representative seismogenic depth of

10 km.

Our simulations include fault models with varying levels of ambient fluid overpressure in terms of effective normal stress and as well as degrees of efficiency due to enhanced weakening due to thermal pressurization. Parameters for the simulations are given in Tables 2.1-2.3. Note that the stress changes associated with standard rate-and-state friction have a relatively mild logarithmic dependence on slip rate and are directly proportional to the effective confining stress. As such, persistently weak rate-and-state fault models with low effective normal stress and no enhanced weakening result in generally mild static stress drops ($\leq$ 2 MPa) for typical frictional parameters measured in the laboratory (Figure 2.1). Thus, the inclusion of at least mild enhanced dynamic weakening is required for fault models with low effective normal stress, such as due to substantial fluid overpressurization, to produce average static stress drops between 1–10 MPa, as typically inferred for natural earthquakes (Figures 2.12-2.13; Lambert et al., 2021).

In order to examine the prestress at the beginning of dynamic ruptures, we define the beginning and end of dynamic rupture, as well as the ruptured area, based on a slip velocity threshold (V_{thresh} = 1 cm/s) for seismic slip. We have found in previous studies that varying V_{thresh} between by 10^{-3} to 10^{-1} m/s results in minor variations of the determined rupture timing and area, within 1% (Lambert et al., 2021; Perry et al., 2020).

Our fault models with more efficient enhanced dynamic weakening produce fewer smaller events than those with mild to moderate enhanced weakening, as can be observed in the frequency-magnitude statistics (Figure 2.11). To create frequency-magnitude histograms, we compute the seismic moment $M_0 = \mu A \bar{\delta}$ for ruptures, where μ is the shear modulus, A is the rupture area and $\bar{\delta}$ is the average slip in the rupture. As our simulations are 2-D, we compute the moment by assuming a circular rupture area $A = \pi(\lambda_{\text{rupt}}/2)^2$, where λ_{rupt} is the rupture length.

2.10.2 Single-degree-of-freedom representation of laboratory experiments

We compare the evolution of local slip rate and shear stress in our simulated dynamic ruptures with single-degree-of-freedom (SDOF) calculations motivated by high-velocity laboratory experiments that impose variable seismic slip rates to infer shear resistance evolution and often compare their findings with seismological observations (Fukuyama & Mizoguchi, 2010; Sone & Shimamoto, 2009). The SDOF calculations are governed by the same rate-and-state friction with enhanced dynamic weakening due to thermal pressurization as in our fault model TP4. Our SDOF calculations impose a slip-rate history, as typically done in laboratory experiments, and solve for the evolution of shear stress, state variable, temperature, and pore pressure using Equation 3.2 and Equations 2.10 and 5.6-5.5 given the initial state. We assume initial conditions where sliding has been maintained until steady-state conditions at the slip rate of $V = 0.1$ mm/s, comparable to the initial conditions of Fukuyama and Mizoguchi (2010). We then impose two different slip rate functions characterized by regularized Yoffe functions (Tinti et al., 2005), with total slip of 1.95 m (comparable to our simulated slip) and maximum slip rate of 2 m/s. Tinti et al. (2005) regularized the stress singularity in the analytical Yoffe function by convolving it with a triangular function of half-width t_s. The regularized Yoffe functions are characterized by two time-scales, the half-width t_s and the rise time t_r. For the two examples shown in Figure 9 of the main text, we choose values of $t_r = 3$s with $t_s = 0.1t_r$ for RYF1 and $t_r = 1.4$s with $t_s = 0.4t_r$ for RYF2, in order to compare pulses with more pronounced and gradual accelerations that produce the same slip and peak slip rate.

Chapter 3

RUPTURE-DEPENDENT BREAKDOWN ENERGY IN FAULT MODELS WITH THERMO-HYDROMECHANICAL PROCESSES

This chapter has been adapted from:

Lambert, V. & Lapusta, N. (2020). Rupture-dependent breakdown energy in fault models with thermo-hydro-mechanical processes. *Solid Earth*, 11(6), 2283-2302. DOI: 10.5194/se-11-2283-2020.

3.1 Introduction

Many seismological studies consider earthquake source processes in the framework of dynamic fracture mechanic and have attempted to infer parameters of the slip-weakening shear resistance from the strong-motion data resulting from natural earthquakes (Bouchon, 1997; Bouchon et al., 1998; Cruz-Atienza et al., 2009; Gallovic et al., 2019; Ide & Takeo, 1997; Kaneko et al., 2017; Olsen et al., 1997). Such studies have noted substantial trade-offs in the inferred parameters during such inversions, such as between the slip-weakening distance D_c and strength excess $\tau_{\text{peak}} - \tau_{\text{ini}}$, where τ_{ini} is the initial stress (Fig. 1.3). It has been presumed that the spatial distribution of static stress drop and breakdown energy may be the most reliably determined features, as the stress drop can be inferred from the spatial distribution of slip and remaining variations in rupture speed are largely controlled by the breakdown energy in such linear slip-weakening representations (Guatteri & Spudich, 2000).

One of the most notable features of seismologically-inferred breakdown energies from natural earthquakes is that the average breakdown energy from the rupture process has been inferred to increase with the earthquake size (Abercrombie & Rice, 2005; Brantut & Viesca, 2017; Cocco & Tinti, 2008; Rice, 2006; Viesca & Garagash, 2015). Increase in breakdown energy with slip has also been observed in high-speed friction experiments (Nielsen et al.,

2016; Selvadurai, 2019), although in some experiments the increase saturates after a given amount of weakening (Nielsen et al., 2016). Such findings are inconsistent with the breakdown energy being a fixed fault property as often assumed in linear slip-weakening laws and as approximately follows from standard rate-and-state friction with uniform characteristic slip-weakening distance (Perry et al., 2020), unless strong and very special heterogeneity is assumed in fault properties. For example, some modeling studies have assigned strongly heterogeneous D_c and hence G values to the fault, as if they are properties of the interface, with larger patches having significantly larger values of D_c and hence G, and considered sequences of events over such interfaces (e.g. Aochi & Ide, 2011; Ide & Aochi, 2005).

Several theoretical and numerical studies have demonstrated that enhanced dynamic weakening, as widely observed at relatively high slip rates ($> 10^{-3}$ m/s) in laboratory experiments (Di Toro et al., 2011; Tullis, 2007), may explain the inferred increase in breakdown energy with slip (Brantut & Viesca, 2017; Perry et al., 2020; Rice, 2006; Viesca & Garagash, 2015). A number of different mechanisms have been proposed for such enhanced weakening, many of them due to shear heating. For example, thermal pressurization may occur due to the rapid shear heating of pore fluids during slip (Andrews, 2002; Rice, 2006; Sibson, 1973); if pore fluids are heated fast enough and not allowed to diffuse away, they pressurize and reduce the effective normal stress on the fault. Flash heating is another thermally-induced weakening mechanism, where the effective friction coefficient is rapidly reduced due to local melting of highly stressed micro-contacts along the fault (Goldsby & Tullis, 2011; Passelegue, Goldsby, & Fabbri, 2014; Rice, 1999). Considerations of heat production during dynamic shear ruptures provide a substantial constraint for potential fault models, as field studies show no correlation between faulting and heat flow signatures and rarely suggest the presence of melt (Lachenbruch & Sass, 1980; Sibson, 1975). Models with enhanced weakening have been successful in producing fault operation at low overall prestress and low heat production (Lambert et al., 2021; Noda et al., 2009; Rice, 2006) as supported by several observations (Brune et al., 1969; Hickman & Zoback, 2004; Williams et al., 2004; Zoback et al., 1987).

At the same time, accounting for thermo-hydro-mechanical processes during dynamic rupture can clearly weaken or even remove the analogy between frictional shear ruptures and idealized shear cracks of fracture mechanics. The analogy is based on two key assumptions: 1) that the breakdown of shear resistance is concentrated in a small region near the rupture front, referred to as small-scale yielding, and 2) that there exists a constant residual stress level $\tau_{dyn} = \tau_{min}$ throughout the ruptured region during sliding (Freund, 1990; Palmer & Rice, 1973). For example, the relationship between rupture speed and fracture energy of linear elastic fracture mechanics is only valid under these assumptions. Clearly, these assumptions can become invalid when thermo-hydro-mechanical processes are considered. For example, shear heating can raise the pore fluid pressure in regions away from the rupture front and weaken the fault there, contributing to the breakdown of fault resistance away from the rupture tip and varying the dynamic resistance level. Furthermore, the shear heating itself would depend on the overall dissipated energy, making the fault weakening behavior, and hence "breakdown," depend on the absolute stress levels, and not just the stress changes, as typically considered by analogy with traditional fracture mechanics. Moreover, studies that infer dynamic parameters from natural earthquakes using dynamically-inspired kinematic models suggest more complicated evolutions of shear stress with slip, including heterogeneous dynamic resistance levels (Bouchon et al., 1998; Causse, Dalguer, & Mai, 2013; Ide & Takeo, 1997; Tinti et al., 2005)

In this study, we use numerical models of earthquake sequences with enhanced weakening due to thermal pressurization to illustrate how the inclusion of thermo-hydro-mechanical processes during dynamic shear ruptures makes breakdown energy rupture-dependent, in that the value of both local and average breakdown energy vary among ruptures on the same fault, even with spatially uniform and time-independent constitutive properties. As such, the breakdown energy is not an intrinsic fault property, but develops different values at a given location, depending on the details of the rupture process, which in part depend on the prestress before the dynamic rupture achieved as a consequence of prior fault slip history.

Moreover, the local breakdown energy is not uniquely defined by the amount of slip attained during rupture, but depends on how that slip was achieved through the complicated history of slip rate and dynamic stress changes throughout the rupture process. Additional fault characteristics that we do not consider here, such as heterogeneity in fault properties and dynamically-induced, evolving, inelastic off-fault damage (Dunham et al., 2011a, 2011b; Roten et al., 2017; Withers et al., 2018) should result in qualitatively similar effects and add even more variability to the breakdown energy.

3.2 Description of numerical models

We conduct numerical simulations of spontaneous sequences of earthquakes and aseismic slip (SEAS) utilizing the spectral boundary integral method to solve the elastodynamic equations of motion coupled with friction boundary conditions, including the evolution of pore fluid pressure and temperature on the fault coupled with off-fault diffusion (Lapusta et al., 2000; Noda & Lapusta, 2010). Our simulations consider mode III slip on a 1-D fault embedded into a 2-D uniform, isotropic, elastic medium slowly loaded with a long-term slip rate V_{pl} (Fig. 3.1). The simulations resolve the full slip behavior throughout earthquake sequences, including the nucleation process, the propagation of individual dynamic ruptures, as well as periods of post-seismic and the interseismic slip between events that can last from months to hundreds of years.

Our fault models adopt the laboratory-derived Dieterich-Ruina rate-and-state friction law with the state evolution governed by the aging law (Dieterich, 1979; Ruina, 1983):

$$\tau = \overline{\sigma} f(V, \theta) = (\sigma - p) \left[f_* + a \log \frac{V}{V_*} + b \log \frac{\theta V_*}{D_{\text{RS}}} \right], \tag{3.1}$$

$$\dot{\theta} = 1 - \frac{V\theta}{D_{\text{RS}}}, \tag{3.2}$$

where $\overline{\sigma}$ is the effective normal stress, σ is the normal stress, p is the pore fluid pressure, f_* is the reference steady-state friction coefficient at reference sliding rate V_*, D_{RS} is the characteristic slip distance, and a and b are the direct effect and evolution effect parameters, respectively. Other formulations for the evolution of the state variable exist, such as the slip law (Ruina, 1983) as well as various composite laws, and the formulation that best describes

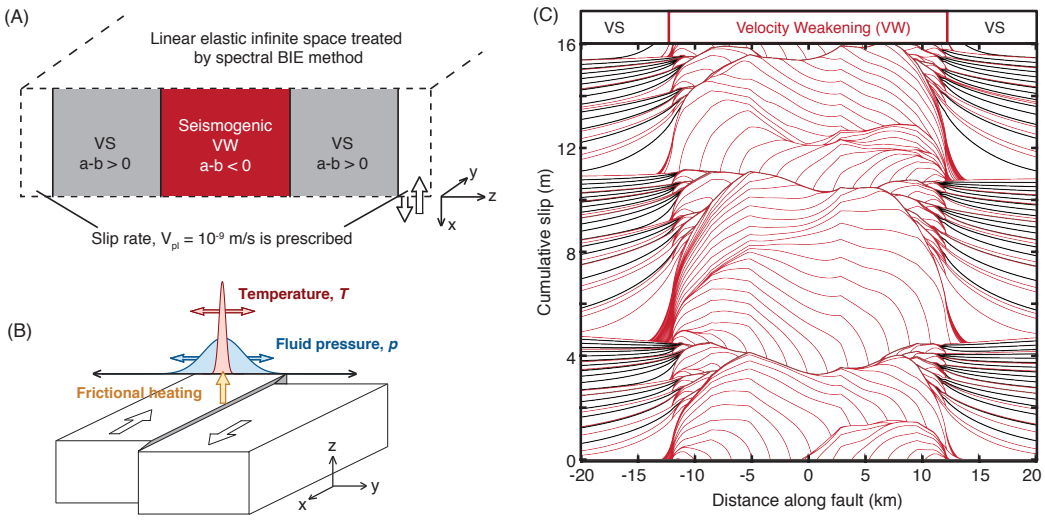

Figure 3.1: Fault model for simulated sequences of earthquakes on a rate-and-state fault including enhanced weakening due to thermal pressurization of pore fluids. (A) The fault model incorporates a velocity-weakening (VW) seismogenic region surrounded by two velocity-strengthening (VS) sections. A fixed plate rate is prescribed outside of these regions. (B) We incorporate enhanced dynamic weakening due to the thermal pressurization of pore fluids by calculating the evolution of temperature and pore fluid pressure due to shear heating and off-fault diffusion throughout our simulations. (C) The beginning of the accumulated slip history for simulated sequences of crack-like earthquake ruptures and aseismic slip. Seismic events are illustrated by red lines with slip contours being plotted every 0.5 seconds while interseismic slip is plotted in black every 10 years. The total simulated slip history spans 2675 years corresponding to cumulative slip of 84 m and contains 200 seismic events.

various laboratory experiments remains a topic of ongoing research (Bhattacharya et al., 2015, 2017; Shreedharan et al., 2019). However, the choice of the state evolution law should not substantially influence the results of this study, as the evolution of shear resistance during dynamic rupture within our simulations is dominated by the presence of enhanced weakening mechanisms. We use the version of the expressions (3.1) and (3.2) regularized for zero and negative slip rates (Noda & Lapusta, 2010).

During conditions of steady-state sliding ($\dot{\theta} = 0$), the friction coefficient is expressed as:

$$f_{ss}(V) = f_* + (a - b) \log \frac{V}{V_*}. \tag{3.3}$$

The combination of frictional properties $(a - b) > 0$ results in steady-state velocity-strengthening (VS) behavior, where stable slip is expected, and properties resulting in

$(a - b) < 0$ lead to steady-state velocity-weakening (VW) behavior, where accelerating slip and hence stick-slip occur for sufficiently large regions (Rice et al., 2001; Rice & Ruina, 1983; Rubin & Ampuero, 2005).

An important, yet often underappreciated, implication of the rate- and state-dependent effects observed in laboratory experiments is that notions of static and dynamic friction coefficients, as well as the slip-weakening distance, are not well-defined and fixed quantities, as would be considered by standard linear slip-weakening laws (Ampuero & Rubin, 2008; Barras et al., 2019; Cocco & Bizzarri, 2002; Lapusta & Liu, 2009; Perry et al., 2020; Rubin & Ampuero, 2005). Instead, they depend on the history and current style of motion. For example, the dynamic friction, comparable to the steady-state friction at dynamic slip rates, depends on slip rate (Eq. 3.3), which can vary substantially throughout rupture and between different ruptures. Moreover, the peak friction and effective slip-weakening distance under standard rate-and-state friction depend on the history of motion through the state variable θ, as well as the sliding rate during fast slip (Fig. 3.2). Let us consider a point with the same initial friction but different periods of inter-event healing, captured by increasingly larger values of the pre-rupture state variable. If the point is now driven to slide at a fixed sliding rate, the peak friction and slip-weakening distance would be larger for points that (i) have higher pre-rupture value of the state variable, representing better healed interfaces, and/or (ii) sliding at faster slip rates (Fig. 3.2). For standard rate-and-state friction, these effects typically translate into generally mild variations in dynamic/static stress drop and breakdown energy, due to the logarithmic dependence of the shear stress evolution on slip rate, resulting in both static stress drop and breakdown energy being effectively rupture-independent (Ampuero & Rubin, 2008; Cocco & Bizzarri, 2002; Lapusta & Liu, 2009; Perry et al., 2020; Rubin & Ampuero, 2005), at least compared to the large variations of breakdown energy with slip inferred from natural earthquakes as discussed in the introduction. However, such variations in stress evolution become more substantial with enhanced dynamic weakening mechanisms that lead to stronger rate-dependent weakening.

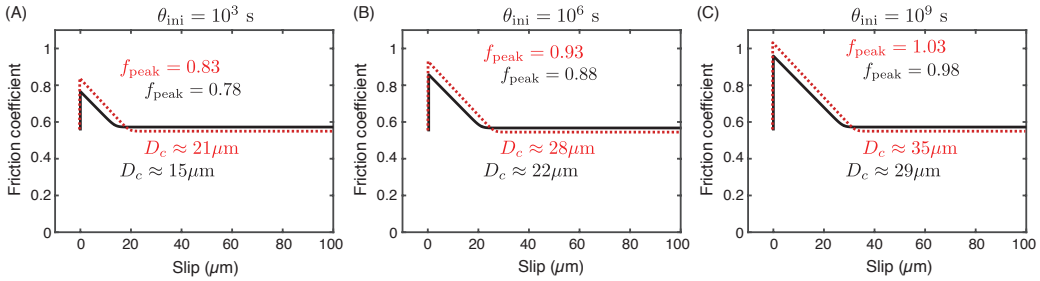

Figure 3.2: Illustration of the rate- and state-dependence of peak and dynamic friction coefficients, f_{peak} and f_{dyn}, respectively, as well as the effective slip-weakening distance D_c. (A-C) Evolution of friction coefficient with slip for points with the same initial friction coefficient of 0.58 but different values of initial state variable θ_{ini}, corresponding to different histories of previous motion. The initially locked point slips at an imposed slip rate of V = 1 cm/s (black) or V = 1 m/s (red), to approximately reproduce transition from the locked state to dynamic sliding as the rupture propagates through. For a given slip rate, the friction evolves to a new steady-state level, $f_{dyn} = 0.54$ and $f_{dyn} = 0.56$ for V = 1 m/s and V = 1 cm/s, respectively. These levels are similar, as expected from the logarithmic dependence on the slip rate and a narrow range of dynamic slip rates. The peak friction coefficient and effective slip-weakening distance vary more significantly with θ_{ini}, where the peak friction coefficient increases for higher θ_{ini} associated with longer inter-event healing times. The example uses typical laboratory values of $(a - b) = 0.004$, $f_* = 0.6$, $D_{RS} = 1\mu$m, and $V_* = 10^{-6}$ m/s.

Laboratory experiments indicate that the standard rate-and-state laws (Eqs. 3.1 - 3.2) provide good descriptions of frictional behavior at relatively slow slip rates (10^{-9} to 10^{-3} m/s). However, at higher sliding rates, including average seismic slip rates of ~1 m/s, additional enhanced weakening mechanisms can occur, such as the thermal pressurization of pore fluids. Thermal pressurization is governed in our simulations by the following coupled differential equations for the evolution of temperature and pore fluid pressure (Noda & Lapusta, 2010):

$$\frac{\partial T(y,z;t)}{\partial t} = \alpha_{th}\frac{\partial^2 T(y,z;t)}{\partial y^2} + \frac{\tau(z;t)V(z;t)}{\rho c}\frac{\exp(-y^2/2w^2)}{\sqrt{2\pi}w}, \tag{3.4}$$

$$\frac{\partial p(y,z;t)}{\partial t} = \alpha_{hy}\frac{\partial^2 p(y,z;t)}{\partial y^2} + \Lambda\frac{\partial T(y,z;t)}{\partial t}, \tag{3.5}$$

where T is the pore fluid temperature, α_{th} is the thermal diffusivity, τV is the shear heating source which is distributed over a Gaussian shear layer of half-width w, ρc is the specific heat, y is the fault-normal distance, α_{hy} is the hydraulic diffusivity, and Λ is the coupling coefficient that provides the change in pore pressure per unit temperature change under

undrained conditions.

The total fault domain of size λ is partitioned into a frictional region of size λ_{fr} where we solve for the balance of shear stress and frictional resistance, as well as loading regions at the edges where the fault is prescribed to slip at a tectonic plate rate (Fig. 3.1A). The frictional interface is composed of a 24-km region with VW frictional properties of size λ_{VW}, surrounded by a velocity-strengthening domain. The majority of the seismic events arrest within the VW region, which we refer to as "partial ruptures," however some span the entire VW region, which we refer to as "complete ruptures" (Fig. 3.1C). Weakening due to thermal pressurization is confined to the region with the VW properties. The parameter values used for the simulations presented in this work are motivated by prior studies (Noda & Lapusta, 2010; Perry et al., 2020; Rice, 2006) and provided in Table 3.1.

3.3 Energy partitioning and notion of breakdown energy G

In the earthquake energy budget, the total strain energy change per unit source area $\Delta W/A$ is partitioned into the dissipated energy per unit area, E_{Diss}/A, and the radiated energy per unit area, E_R/A:

$$\Delta W/A = E_{\text{Diss}}/A + E_R/A. \tag{3.6}$$

The total strain energy released per unit area $\Delta W/A$ is given by:

$$\Delta W/A = \frac{1}{2}(\bar{\tau}_{\text{ini}} + \bar{\tau}_{\text{fin}})\bar{\delta}, \tag{3.7}$$

where $\bar{\delta}$ is the average final slip for the event, and $\bar{\tau}_{\text{ini}}$ and $\bar{\tau}_{\text{fin}}$ are the average initial and final shear stress weighted by the final slip (Noda & Lapusta, 2012), respectively,

$$\bar{\tau}_{\text{ini}} = \frac{\int_\Omega \tau_{\text{ini}}(z)\delta_{\text{fin}}(z)dz}{\int_\Omega \delta_{\text{fin}}(z)dz}, \tag{3.8}$$

$$\bar{\tau}_{\text{fin}} = \frac{\int_\Omega \tau_{\text{fin}}(z)\delta_{\text{fin}}(z)dz}{\int_\Omega \delta_{\text{fin}}(z)dz}. \tag{3.9}$$

Here, Ω represents the ruptured domain. The static stress drop is a measure of the difference in average stress before and after the rupture. The relevant definition of average static stress drop for energy considerations is the energy-based or slip-weighted stress drop (Noda et al.,

2013):

$$\overline{\Delta\tau} = \overline{\tau}_{\text{ini}} - \overline{\tau}_{\text{fin}} = \frac{\int_\Omega \left[\tau_{\text{ini}}(z) - \tau_{\text{fin}}(z)\right] \delta_{\text{fin}}(z) dz}{\int_\Omega \delta_{\text{fin}}(z) dz}. \tag{3.10}$$

The dissipated energy per unit rupture area can be computed from the evolution of shear resistance with slip:

$$E_{\text{Diss}}/A = \frac{\int_\Omega \left[\int_0^{\delta_{\text{fin}}(z)} \tau(\delta') d\delta'\right] dz}{\int_\Omega dz}. \tag{3.11}$$

The dissipated energy E_{Diss}/A is often further partitioned into the average breakdown energy G (Palmer & Rice, 1973; Rice, 1980; Tinti et al., 2005) and residual dissipated energy (dark grey triangle and light grey rectangle in Fig. 1.3, respectively). The average breakdown energy represents the spatial average of the local breakdown energy G_{loc} within the source region,

$$G = \frac{\int_\Omega G_{\text{loc}}(z) dz}{\int_\Omega dz} \tag{3.12}$$

where the local breakdown energy is defined as,

$$G_{\text{loc}}(z) = \int_0^{D_c(z)} [\tau(\delta') - \tau_{\text{min}}(z)] d\delta', \tag{3.13}$$

and $\tau_{\text{min}}(z)$ is the minimum local shear resistance during seismic slip after the initial strengthening from the initial to peak shear resistance via the direct effect. D_c is defined as the critical slip distance during the rupture such that $\tau(D_c(z)) = \tau_{\text{min}}(z)$.

Seismological studies have attempted to estimate the average breakdown energy for natural earthquakes based on the standard energy partitioning diagram (Fig. 1.3) as follows (Abercrombie & Rice, 2005; Rice, 2006):

$$G' = \frac{\overline{\delta}}{2}\left(\overline{\Delta\tau} - \frac{2\mu E_R}{M_0}\right), \tag{3.14}$$

where G' is the approximation for the average breakdown energy G, $\overline{\delta}$ is the average slip during the rupture, $\overline{\Delta\tau}$ is the seismologically-inferred average static stress drop, μ is the shear modulus, E_R is the radiated energy and M_0 is the seismic moment. The definition of G' assumes that the rupture area exhibits negligible stress overshoot/undershoot, or that the average level of dynamic resistance during sliding is the same as the final average shear

stress. Numerical studies have shown that G' may indeed provide a reasonable estimate of the average breakdown energy (within a factor of 2) for crack-like ruptures, which exhibit mild overshoot/undershoot compared to the static stress drop (Perry et al., 2020), however such estimates can dramatically differ from the true values for ruptures that experience a considerable stress undershoot, as is the case of self-healing pulse-like ruptures (Chapter 4 Lambert et al., 2021).

Note that the energy balance shown in Eq. 3.6 reflects the energy partitioning over the rupture process as a whole. While the dissipated energy is a local quantity along the fault, the radiated energy is not and can only be related to the stress-slip behavior in the averaged sense over the entire rupture process (Fig. 1.3). Seismological estimates of the average breakdown energy can be made assuming the standard energy partitioning following the slip-weakening diagram (Fig. 1.3) and using Eq. 3.14 with the total radiated energy, with the results dependent on the accuracy of the radiated energy estimates and validity of the assumed energy partitioning model, which has been shown to breakdown for self-healing pulse-like ruptures (Chapter 4; Lambert et al., 2021). Estimating the local breakdown energy is more challenging. One approach is to use finite-fault slip inversions to determine the stress evolution during rupture and hence the breakdown work (e.g. Tinti et al., 2005), with the results dependent on the accuracy of finite-fault inversions that are known to be non-unique and affected by smoothing.

3.4 Breakdown energy in models with thermal pressurization of pore fluids

The local slip and stress evolution are determined at every point along the fault within our simulations at all times, thus we can calculate the local dissipation and breakdown energy throughout each rupture as well as study these quantities evolve in different ruptures throughout the sequence. We can also compute the average energy quantities and construct the average stress vs. slip curves for the total rupture process in a manner that preserves the overall energy partitioning (Noda & Lapusta, 2012). We define seismic slip to occur when the local slip velocity exceeds a velocity threshold $V_{\text{thresh}} = 0.01$ m/s. As slip rates during sliding are typically around 1 m/s or higher and drop off rapidly during the arrest of

slip, modest changes of this velocity threshold by an order of magnitude produce very mild differences in D_c and G, by less than 1%.

The average breakdown energy G computed from our simulations increase with average slip and matches estimates of breakdown energy for natural events (Fig. 3.3), as expected from the simplified theoretical considerations (Rice, 2006). As demonstrated in previous numerical studies (Perry et al., 2020), when our fault models combine moderately efficient thermal pressurization with persistently weak conditions, such as from relatively low interseismic effective normal stresses (25 MPa) due to substantial chronic fluid overpressurization, the models produce mostly crack-like ruptures that reproduce all main observations about earthquakes, including magnitude-invariant average static stress drops of 1–10 MPa, breakdown energy values that are quantitatively comparable to estimates from natural earthquakes, and fault temperatures well below representative equilibrium melting temperatures near 1000^o C for wet granitic compositions in the shallow crust (Rice, 2006). It is important to note that the presence of enhanced dynamic weakening is critical for producing reasonable values of static stress drop (> 1 MPa) in such fault models with chronic fluid overpressurization; otherwise, the stress changes due to the standard rate-and-state friction would be too low (as they are proportional to the effective normal stress). As such, dynamic weakening due to thermal pressurization still dominates the overall weakening behavior during dynamic rupture. These results suggest that fault models incorporating chronic fault weakness and enhanced weakening may be plausible representations of rupture behavior on mature faults. The work of Perry et al. (2020) and Lambert et al. (2021) provide a broader exploration of models with different parameters, including different levels of interseismic effective stresses and efficiency of enhanced dynamic weakening. Here, we use a representative model to illustrate the resulting properties of the breakdown energy in such models.

Let us examine the spatial distribution of shear stress and breakdown energy in three ruptures of varying sizes within the same simulated sequence of earthquakes (Fig. 3.4). All three ruptures nucleate, propagate, and arrest predominantly in the VW region that has uniform

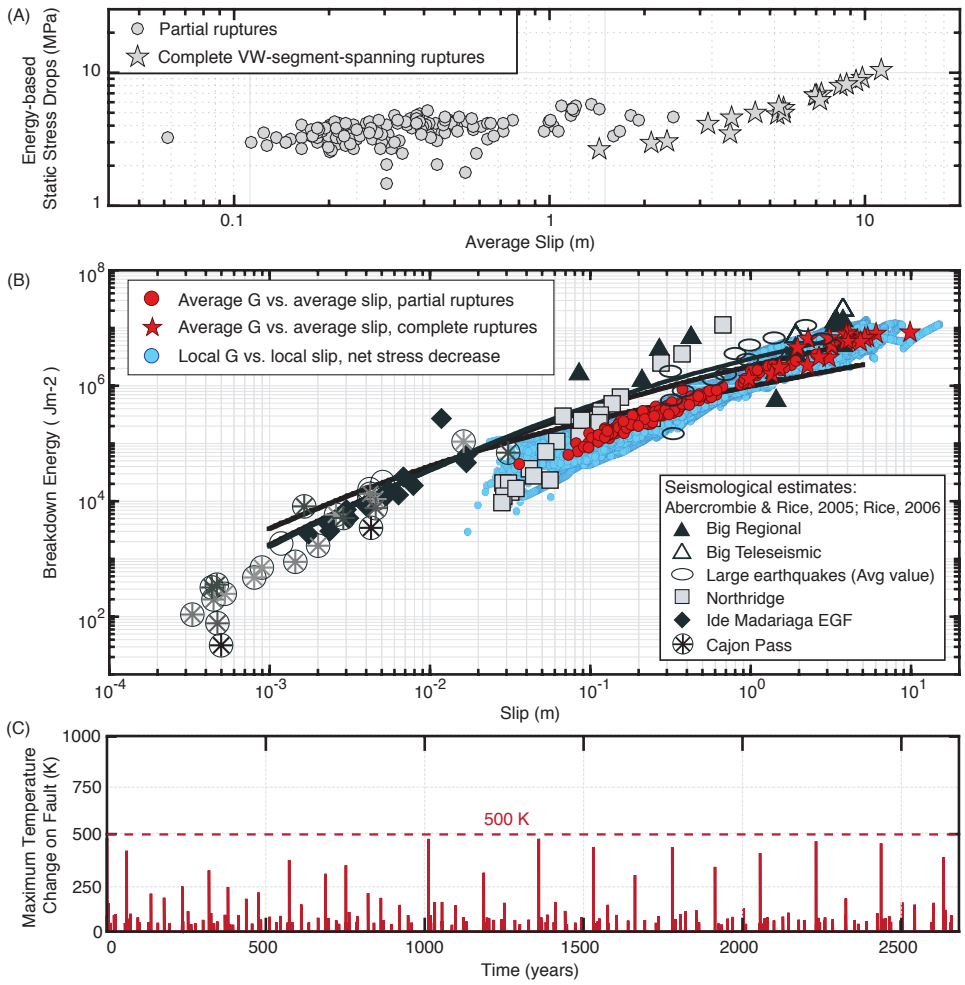

Figure 3.3: Fault models including TP reproduce seismologically-inferred magnitude invariance of stress drops and increasing average breakdown energy with slip. (A) The simulations result in a sequence of mostly crack-like ruptures that, despite including dynamic weakening due to thermal pressurization of pore fluids, are capable of reproducing nearly-magnitude invariant average static stress drops, with values between 1–10 MPa. (B) These crack-like ruptures display the overall increasing trend in average breakdown energy with average slip, as inferred for natural earthquakes (Abercrombie & Rice, 2005; Rice, 2006). (C) The simulated fault maintains reasonable temperatures and avoids melting, due to relatively low interseismic effective normal stress of 25 MPa (and hence chronic fluid overpressurization) and sufficiently efficient enhanced weakening due to thermal pressurization of pore fluids.

fault properties, the only difference being how big the events become. The distribution of shear stress along the fault before each rupture is heterogeneous due to the stress drop from previous ruptures. While each earthquake nucleates in a region with approximately the same locally-high initial stress, the ruptures propagate and arrest over regions with lower prestress.

Larger ruptures with more slip experience greater weakening and larger local stress drops in some regions, which facilitates further rupture propagation over areas of lower prestress. As such, while the final average shear stress decreases for larger ruptures, the average initial stress also decreases, resulting in nearly magnitude-invariant average stress drops.

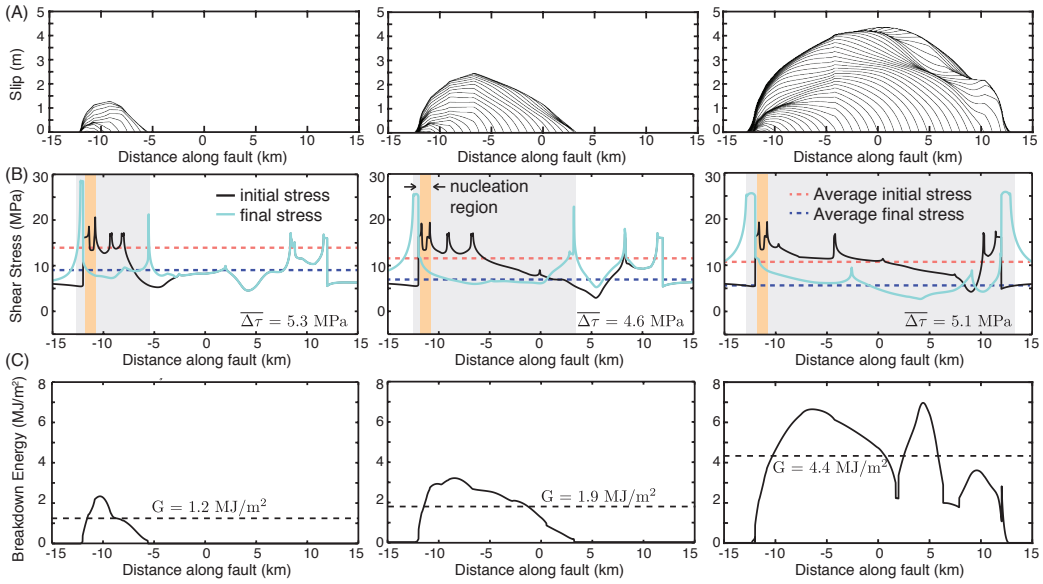

Figure 3.4: Comparison of three earthquake ruptures of different sizes nucleating over the same fault area. (A) Slip distributions for the three ruptures. (B) Distributions of initial (solid black) and final (solid blue) shear stress for the three ruptures. Gray shading denotes the ruptured region and orange shading denotes the region where each rupture nucleates. The dashed red and blue lines denote the average initial and final shear stress in the ruptured region. Large events have smaller initial and smaller final average stress, resulting in similar stress drops. (C) Distribution of breakdown energy (solid black) and average breakdown energy for each event (dashed line). The average breakdown energy generally increases with the rupture size.

Despite the fault constitutive properties being uniform and constant in time, the breakdown energy varies spatially within each event as well as differs at each location for different ruptures (Figs. 3.4C and 3.5). Larger ruptures that experience larger average slip also exhibit more weakening, resulting in the average breakdown energy generally increasing with the rupture size (Fig. 3.4C). If we examine individual points that are common among all three ruptures, we see that the local breakdown energy also varies as the points experience different degrees of slip and overall weakening behavior (Fig. 3.5). This suggests that the local

and average breakdown energy is not just a function of the local fault material properties, but a more complicated evolution of effective weakening behavior and stress throughout the rupture.

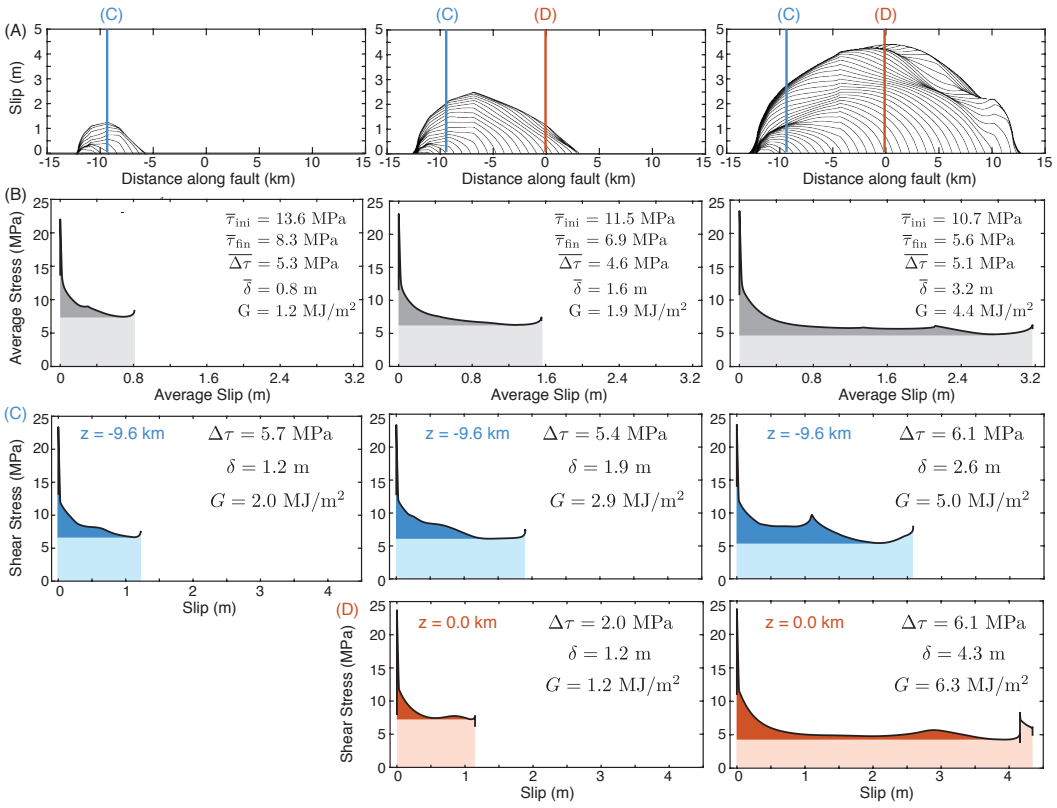

Figure 3.5: The dependence of shear stress on slip for the three ruptures of Figure 3.4. A) Slip distributions with locations examined in detail marked. (B) Average shear stress versus slip curves illustrating the energy partitioning of the ruptures, based on the averaging methodology of Noda and Lapusta (2012) that attempts to preserve local rupture behavior. The curves capture the continuous weakening with slip experienced by most rupture locations. (C-D) Local shear stress versus slip curves at two points within the three ruptures, illustrating the general trend in increasing breakdown energy with increasing slip at the same point.

Note that the breakdown energy illustrated in Fig. 3.5 is dominated by the thermal pressurization of pore fluids, with negligible contribution from the weakening due to standard rate-and-state friction. The breakdown energy due to rate-and-state friction can be estimated

as (Perry et al., 2020):

$$G = \frac{1}{2} b\overline{\sigma} D_{\mathrm{RS}} \left(\log \frac{\theta_{\mathrm{ini}} V_{\mathrm{dyn}}}{D_{\mathrm{RS}}} \right)^2 \tag{3.15}$$

where the effective normal stress $\overline{\sigma}$ is assumed to be constant, θ_{ini} is the value of the state variable at the beginning of slip, and V_{dyn} is the representative dynamic slip rate. Assuming that $\overline{\sigma}$ is still approximately given by the interseismic value at the beginning of slip (which would produce a upper bound), θ_{ini} is given by the representative inter-event time of 10 years, and V_{dyn} is given by the representative peak rate of 10 m/s, the breakdown energy due to the standard rate-and-state friction in our simulation has the upper bound of 0.15 MJ/m^2. This is an order of magnitude smaller than the values of 1 to 6 MJ/m^2 of Fig. 3.5.

3.5 Overall increase of breakdown energy with slip and significant rupture-dependent scatter

Previous theoretical work has demonstrated how the incorporation of thermo-hydro-mechanical processes such as the thermal pressurization of pore fluids can explain the inferred increase in breakdown energy with increasing event size (Rice, 2006). The work of Rice (2006) presented solutions for two end-member cases for the evolution of shear resistance and breakdown energy with thermal pressurization, illustrating how continuous weakening occurs with slip and results in breakdown energy increasing with slip.

If slip occurs within a layer of thickness h that is large enough to justify the neglect of heat and fluid transport, conditions may be considered adiabatic and undrained, which may be relevant for relatively short slip durations (Rice, 2006; Viesca & Garagash, 2015). Under such conditions, the weakening behavior is controlled by the ratio of the coupling coefficient Λ and specific heat ρc, as well as the thickness of the shearing layer h which controls the efficiency of heat production. Assuming a constant friction coefficient f and slip rate V, one can express the evolution of shear resistance τ and breakdown energy G as functions of

slip (Rice, 2006),

$$\tau(\delta) = f\,(\sigma - p_0)\exp\left(-\frac{f\Lambda}{\rho c}\frac{\delta}{h}\right), \tag{3.16}$$

$$G(\delta) = \frac{\rho c\,(\sigma - p_0)\,h}{\Lambda}\left[1 - \left(1 + \frac{f\Lambda\delta}{\rho c h}\right)\exp\left(-\frac{f\Lambda\delta}{\rho c h}\right)\right]. \tag{3.17}$$

Under such conditions, increasing slip results in continued weakening of the shear resistance and increasing values of breakdown energy. The continued weakening is the result of shear heating and subsequent pressurization, which remains active as long as the slip rate and shear stress are non-zero.

The inclusion of thermal and hydraulic diffusion introduces a diffusion time-scale to the problem, which governs the efficiency of weakening over extended slip durations. If one considers slip on a mathematical plane, a characteristic weakening time-scale t^* may be defined assuming a constant friction coefficient and slip rate (Mase & Smith, 1987):

$$t^* = \frac{4}{f^2}\left(\frac{\rho c}{\Lambda}\right)^2 \frac{\left(\sqrt{\alpha_{\mathrm{hy}}} + \sqrt{\alpha_{\mathrm{th}}}\right)^2}{V^2}. \tag{3.18}$$

Rice (2006) demonstrated that this may be related to a characteristic slip-weakening distance for thermal pressurization,

$$L^* = \frac{4}{f^2}\left(\frac{\rho c}{\Lambda}\right)^2 \frac{\left(\sqrt{\alpha_{\mathrm{hy}}} + \sqrt{\alpha_{\mathrm{th}}}\right)^2}{V}, \tag{3.19}$$

such that the evolution of shear resistance and breakdown energy for slip on a plane may also be expressed as a function of slip (Rice, 2006):

$$\tau(\delta) = f(\sigma - p_0)\exp\left(\frac{\delta}{L^*}\right)\operatorname{erfc}\left(\sqrt{\frac{\delta}{L^*}}\right), \tag{3.20}$$

$$G(\delta) = f(\sigma - p_0)L^*\left[\exp\left(\frac{\delta}{L^*}\right)\operatorname{erfc}\left(\sqrt{\frac{\delta}{L^*}}\right)\left(1 - \frac{\delta}{L^*}\right) - 1 + 2\sqrt{\frac{\delta}{\pi L^*}}\right]. \tag{3.21}$$

Unlike the case of a critical slip-weakening distance D_c in standard slip-weakening models, the weakening of shear resistance is continuous with increasing slip (Fig. 3.6a), with L^* providing a measure of how much slip is needed to weaken by a certain degree. Note that the evolution of stress in Eqs. (3.16) and (3.20) do not consider the elastic interactions

that occur due to non-uniform slip within finite ruptures, and therefore assume that the slip velocity is not only temporally constant, but spatially uniform over the fault.

Both of these thermal pressurization solutions have the convenient feature of expressing the breakdown of shear resistance as a function of slip, drawing familiarity to standard slip-weakening notions of shear fracture. As pointed out by Rice (2006), the representation of breakdown energy purely as a function of slip is a considerable simplification, whereas the physics underlying the mechanisms for weakening require that τ is a complicated function of the slip rate history up to the current time. During dynamic rupture, the local slip rate experiences considerable acceleration near the rupture front, resulting in a more pronounced weakening rate (Fig. 3.6), which in turn facilitates large dynamic stresses and higher slip rates in other parts of the rupture. As the rupture front passes, both the slip rate and weakening rate decrease. However, the slip rate may persists around typical seismic values of 1 m/s until the arrival of arrest waves from the edges of the rupture or local healing. Note that while the slip rates behind the rupture front in our models appear more or less stable around 1 m/s (Fig. 3.6E and G), they may vary depending on the arrival of wave-mediated dynamic stresses from other slipping regions in the rupture, which drive prolonged slip and therefore modulate the weakening rate due to shear heating mechanisms like thermal pressurization. In general, the friction coefficient may also vary considerably with the slip rate, particularly when accounting for additional enhanced weakening processes such as flash heating (Goldsby & Tullis, 2011; Passelegue et al., 2014; Rice, 1999).

The continued weakening with slip due to thermal pressurization is an important factor that drives rupture propagation and allows ruptures to propagate under lower, and hence less favorable, prestress conditions. Let us consider two fault models with the same initial prestress and the same rate-and-state frictional parameters, but with and without enhanced weakening due to thermal pressurization (Fig. 3.7). The rupture governed by only standard rate-and-state friction exhibits relatively mild stress variations with slip rate and thus requires higher prestress conditions to propagate. While the local slip rate evolution varies

among points throughout the rupture, the evolution of shear resistance with slip associated with the breakdown process is generally comparable throughout the rupture with uniform rate-and-state properties (Fig. 3.7 left column). In contrast, the rupture that is driven by enhanced weakening due to thermal pressurization experiences a stronger feedback between the evolution of shear stress and slip rate, resulting in a much larger rupture that propagates over lower prestress conditions. The evolution of slip rate is highly variable for different points throughout the crack-like rupture, with long tails of seismic slip behind the rupture front that experience periods of acceleration and deceleration due to dynamic stress interactions from neighboring points. This variability in local slip rate translates into further variability in local weakening, even for points with the same initial prestress. This emphasizes that the local weakening behavior, and the associated breakdown energy, depend not only on the local prestress and weakening properties, but also the distribution of prestress and weakening behavior throughout the entire rupture process.

An important consequence of continued fault weakening is that much of the additional dissipated energy, which leads to the increase of breakdown energy with continued slip, is not concentrated near the rupture front (Fig. 3.6). Moreover, weakening may not actually be strictly monotonic, but local points can experience transient increases in shear stress as they begin to arrest, but then are loaded by neighboring slipping regions and forced to slip and weaken further (Fig. 3.5 and 3.8). The continued and variable weakening of shear resistance behind the rupture front emphasizes a critical difference between dynamic shear ruptures and mode I fracture, where the crack surface is typically traction-free behind the cohesive zone at the rupture front. The attribution of the continually dissipated energy to the breakdown process governing rupture propagation is also inconsistent with the assumption of small-scale yielding, which facilitated the original mathematical analogy based on laboratory constitutive relations derived at lower slip-rates (Palmer & Rice, 1973).

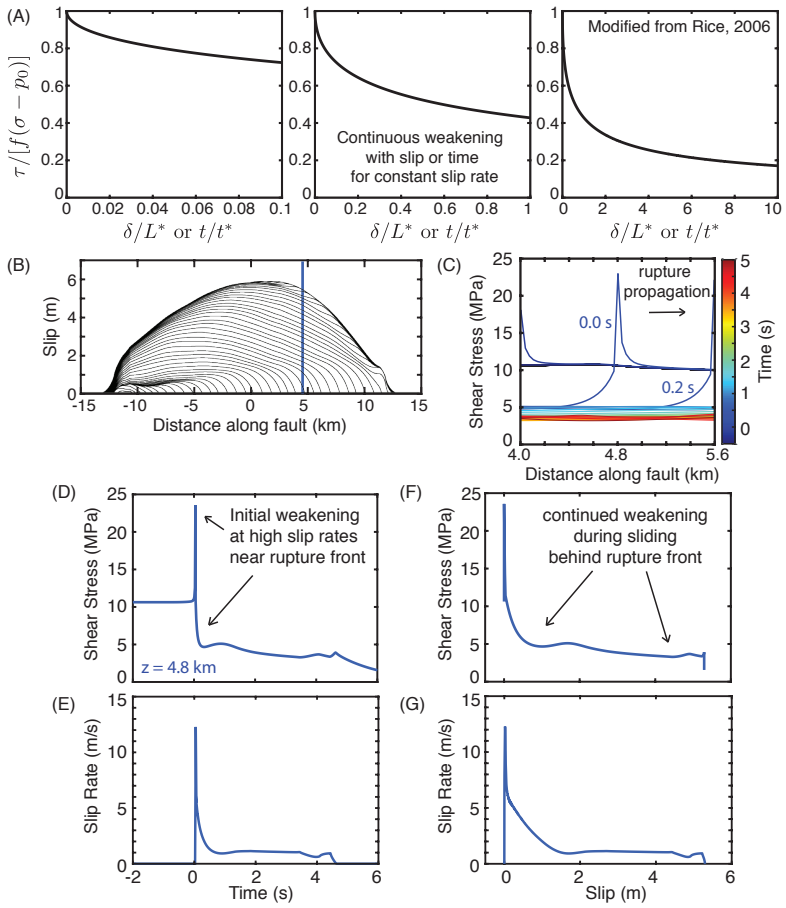

Figure 3.6: Comparison of predicted continuous weakening due to thermal pressurization at constant slip rate versus local behavior during dynamic rupture. (A) Prediction of continuous weakening of shear resistance with slip or time due to the thermal pressurization of pore fluids during slip on a plane at constant slip rate V and constant friction coefficient f (Rice, 2006). (B) Evolution of slip during a dynamic rupture, slip contoured every 0.2 s. (C) Evolution of shear stress localized around the point z = 4.8 km within the rupture. The time window shown corresponds to the duration of sliding at seismic slip rates at z = 4.8 m. (D-E) Evolution of local shear stress and slip rate with time at the point indicated by the blue line in (B). (F-G) Evolution of local shear stress and slip rate with slip at the same point. While qualitatively consistent with (A) in terms of the continued weakening with slip and time, the evolution of shear resistance during dynamic ruptures depends on the more complicated history of slip rate, which varies throughout the rupture process. Most of the initial local weakening occurs at slip rates higher than 1 m/s as the rupture front passes by, followed by more gradual weakening behind the rupture front at lower, but still seismic, slip rates.

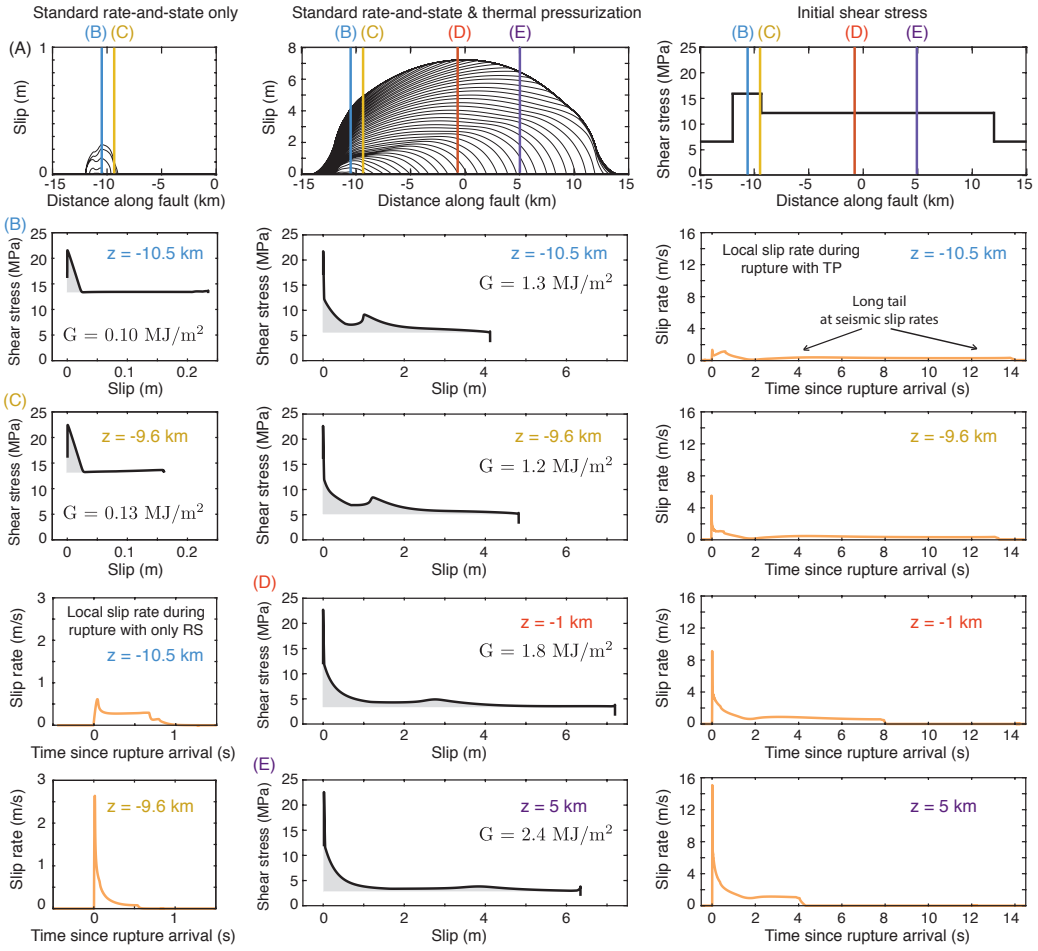

Figure 3.7: Comparison of accumulated slip, local shear stress vs. slip, and local slip rate vs. time for ruptures with rate-and-state (RS) friction with and without enhanced weakening due to thermal pressurization (TP). The two ruptures occur with the same initial shear stress distribution (top right), which results in a relatively small rupture in the RS-only model that is localized within the relatively highly prestressed nucleation region (top left) The inclusion of TP allows the rupture to grow and propagate over lower prestress conditions (top center). (Left column) For the rupture governed by only RS, the breakdown of shear resistance is generally comparable at different locations with the same fault properties, despite differences in local slip rate. This is due to the relatively mild dependence of RS friction on slip rate. (Center and right columns) The rupture governed by RS and TP exhibits a more complex evolution of local shear stress and slip rate throughout the rupture, which depends not only on the local prestress but also the prestress and weakening behavior over the entire rupture through dynamic stress interactions.

While breakdown energy does not appear to be a constant material property, one may ask if the effects of local weakening due to thermal pressurization may be adequately encapsulated into a slip-weakening formulation such as Eqs. (3.16-3.20). To gain insight into such pos-

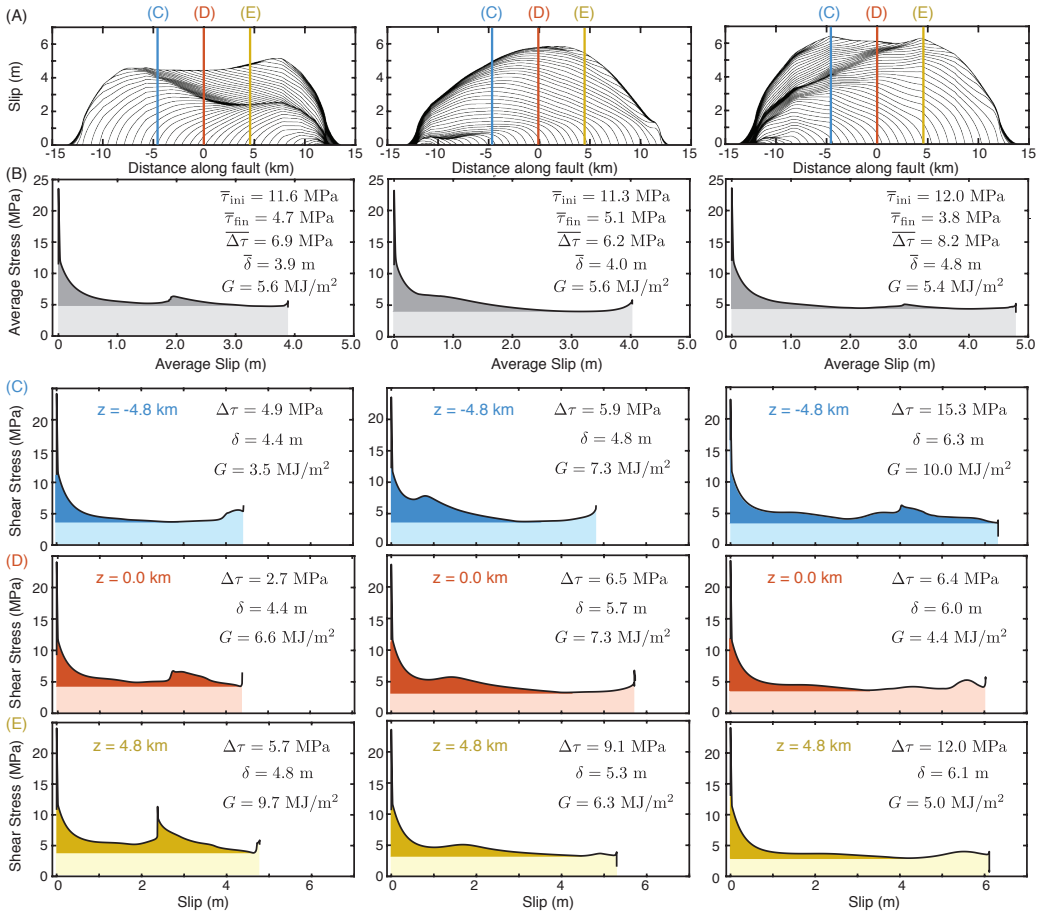

Figure 3.8: Comparison of local breakdown energy for three large earthquake ruptures with nearly the same average breakdown energy and comparable average slip. (A) Slip distributions for the three ruptures. (B) Average shear stress versus slip curves illustrating the energy partitioning of the ruptures. (C-E) Local shear stress versus slip curves at three points within the ruptures. There is not a strictly increasing trend of breakdown energy with slip for all points. In (C), the point $z = -4.8$ km experiences increasing G with increasing slip. However, in (E), the point $z = 4.8$ km experiences lower values of G in ruptures with larger local slip.

sibility, let us examine three large ruptures in our simulations that have comparable average slip and breakdown energy (Fig. 3.8). If we consider the evolution of local shear stress and slip at points shared among the three ruptures, we can see that the local breakdown energy differs even for comparable local slip. Moreover, the three points, which share the same constitutive description, do not exhibit a systematic scaling relationship between local slip and breakdown energy. For example, the point at $z = -4.8$ km exhibits a generally increasing trend in local G with increasing slip, whereas the point at $z = 4.8$ km shows

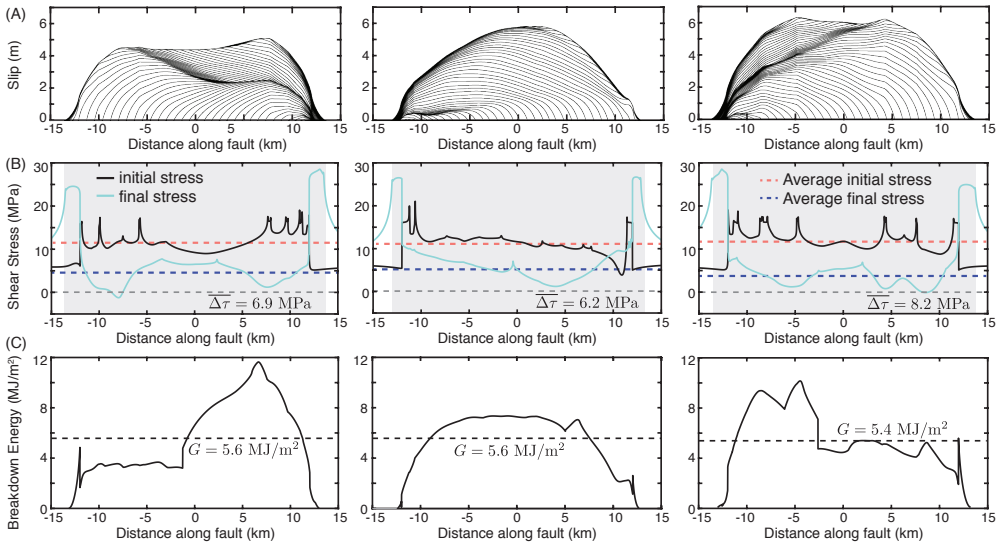

Figure 3.9: Comparison of the spatial breakdown energy distribution for the three large earthquake ruptures with nearly the same average breakdown energy and comparable average slip of Fig. 3.8. (A) Slip distributions for the three ruptures. (B) Spatial distributions of initial (solid black) and final (solid blue) shear stress for the three ruptures. Gray shading denotes the ruptured region and dashed red and blue lines indicate the average initial and final shear stresses, respectively. (C) Spatial distributions of the local breakdown energy. While the three ruptures have comparable average breakdown energy, the spatial variation throughout the rupture process considerably differs. Furthermore, the same spatial locations can have significantly different breakdown energy values in different rupture events of comparable size.

decreasing values of G for increasing slip among the three ruptures (Fig. 3.8C vs. E). The point in the center of the rupture ($z = 0$) does not even exhibit a monotonic trend, as G both increases and decreases for ruptures with increasing slip (Fig. 3.8D). Indeed, if we examine the spatial distribution of local stress and breakdown energy within each rupture, we see that while the three ruptures have comparable average G and slip, they achieve both in different ways (Fig. 3.9).

The general trend of increasing breakdown energy with slip qualitatively holds for most local points within our simulated ruptures, however there is considerable variability for individual values of G at a given slip (Fig. 3.10). While values of average breakdown energy and slip for individual ruptures appear to demonstrate a consistent scaling relationship, these average values smooth out the greater variability in local breakdown energy and slip. For points

within our simulated ruptures that experience a net decrease, or breakdown, in shear stress, the local G is generally within a factor of 3 of the scaling relationship between average G and average slip. This variation adds up to approximately an order of magnitude variation in local G for some values of slip.

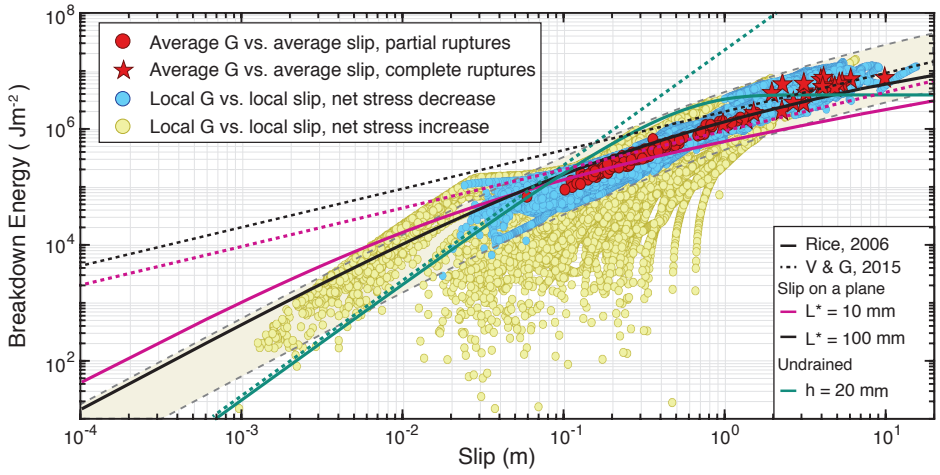

Figure 3.10: The average and local breakdown energy values for the simulated ruptures show an increasing trend with average and local slip, consistent with inferences from natural earthquakes (Fig. 3.3). The general trend of increasing breakdown energy with slip qualitatively holds for local points within our simulated ruptures; however, there is considerable variability for individual values of G at a given slip. For points that exhibit net weakening behavior in our simulated ruptures (blue circles), local values of G tend to vary within a factor of 3 from the scaling relationship between average G and average slip. The shaded band bordered by grey dashed lines illustrates the variation in G at a given value of slip. Local values of G are more variable for regions that experience a net increase in stress during the rupture process (yellow circles), e.g., regions close to rupture arrest. Theoretical curves for G vs. slip are indicated by solid lines for Eqs. (3.17) and (3.21) based on Rice (2006) and dashed lines for Eqs. (3.22 - 3.23) based on Viesca and Garagash (2015), with the coefficient of friction of $f = 0.53$ and values otherwise indicated in Table 3.1. In both cases, the magenta and black lines correspond to the solutions for slip on a plane with two different values of L^* while the green line corresponds to the solution for an adiabatic and undrained shear band of width 20 mm.

For frictional ruptures, substantial slip may occur in regions that experience a net increase in shear stress, particularly in the regions near the rupture arrest (Fig. 3.5B). We find that points in our simulated ruptures that experience a net increase in shear stress exhibit greater variability in G with slip (Fig. 3.10, yellow circles), potentially due to the greater variability

in slip rate during rupture deceleration and arrest. These points illustrate the challenge of partitioning the dissipated energy into components that are thought to be, and not be, relevant to the dynamic rupture process. These points exhibit no net local breakdown of shear resistance but rather a net strengthening. A more appropriate approach may be to distinguish between concepts of breakdown energy and "restrengthening energy," as discussed in Tinti et al. (2005). However, the physical relevance for either component, or their distinction, during the rupture process is not directly evident. Understanding the physical significance of different components of dissipated energy for dynamic rupture propagation is an important topic of active research.

The theoretical considerations of Rice (2006) have been extended to the spatially and temporally variable slip rate associated with steady rupture propagation (Viesca & Garagash, 2015). Approximate expressions for the scaling of breakdown energy with slip can be presented for end-member conditions of undrained $G_u(\delta)$ and drained $G_d(\delta)$ weakening as:

$$G_u(\delta) \approx f(\sigma - p_0)\frac{f\Lambda\delta^2}{2\rho c h}, \qquad \text{undrained, small slip} \tag{3.22}$$

$$G_d(\delta) \approx (12\pi)^{-1/3} f(\sigma - p_0) L^{*1/3} \delta^{2/3}, \qquad \text{slip on a plane, large slip.} \tag{3.23}$$

Similar to the solutions (3.17) and (3.21) that assume constant slip rate, the steady-state solutions (3.22-3.23) do not capture the variability of the local breakdown energy with slip seen in our simulated dynamic ruptures (Fig. 3.10). This is because our simulated dynamic ruptures do not exhibit steady rupture propagation, but rather have considerable spatial variations in slip rate evolution, as likely the case for natural earthquake ruptures. This comparison illustrates a limitation of steady-state rupture solutions for examining rupture properties that are highly sensitive to spatial heterogeneity in slip motion, such as breakdown energy in the presence of thermal pressurization.

While the general increase in breakdown energy with slip is qualitatively consistent among the theoretical solutions and our simulated dynamic ruptures in 2D models with 1D faults

(Fig. 3.10), the scaling relationship between breakdown energy and slip would be best studied in 3D models of dynamic rupture with 2D faults. For example, for ruptures on 2D faults would have a larger fraction of the ruptured area associated with rupture arrest and hence may demonstrate a wider scatter in local G, as seen by points in our simulated ruptures that experience a net increase in shear stress. In addition, it would be prudent to examine any differences in scaling behavior for ruptures that are geometrically confined along a given direction, as may be representative of large crustal earthquakes. However, we expect that the main results of this work –that the local and average breakdown energy can vary among ruptures and are not unique functions of slip –would be consistent with 2D rupture scenarios in 3D models.

3.6 Conclusions

The average breakdown energy for our simulated ruptures tends to increase with increasing rupture size and average slip in a manner consistent with inferences from field observations and simplified theoretical models (Rice, 2006; Viesca & Garagash, 2015). At the same time, the values of local breakdown energy for a given amount of slip have a wide spread in our simulations, even though the constitutive properties are uniform and time-independent along the fault, highlighting the reality that breakdown energy in models with thermo-hydro-mechanical mechanisms is not fundamentally a function of slip. In fact, ruptures with near-uniform slip can have local values of the breakdown energy vary by as much as a factor of 4 (Fig. 3.9C), making a homogeneous fault appear to be heterogeneous. This is because the breakdown energy depends on the specific history of motion and dynamic stress changes that occur throughout individual rupture processes. Furthermore, since the history of rupture motion is determined, in part, by the fault prestress before the dynamic rupture, the breakdown energy also depends on the history of other slip events on the fault that determine the prestress.

The analytic formulations for the evolution of shear resistance with slip for the thermal pressurization presented by Rice (2006) provide profound insight into the first-order behavior of such thermally-activated hydro-mechanical weakening mechanisms. However, they are

based on the kinematic assumptions of a *spatially uniform and temporally constant* slip velocity, as well as a constant friction coefficient, that allow for the weakening rate to be determined as a function of slip. In the fully dynamic statement of the problem, the evolving and spatially non-uniform slip rate is a key part of the solution which leads to the evolution in the associated shear heating and weakening/strengthening of the fault that depend not only on the amount of slip, but also on how that slip is achieved through the complex history of slip velocity. Our results demonstrate that the extension to steady-state rupture solutions with non-constant slip rate (Viesca & Garagash, 2015) similarly does not capture the variability in local breakdown energy associated with the complex and evolving history of slip velocity and dynamic stress interactions in non-steady ruptures, even in fault models with uniform fault properties like ours.

Note that this variability in local G for a given slip is achieved among points with uniform and constant constitutive properties. Such variability in the effective weakening rate and G may become more pronounced in the presence of fault heterogeneity, such as for geometrically rough faults with variable effective normal stress, or if the hydraulic properties of the shearing layer and surrounding rock were to evolve during the rupture process, such as from changes in rock permeability due to off-fault damage. The evolution of permeability during dynamic rupture may have considerable implications for the role of thermo-hydro-mechanical processes in the evolution of shear resistance on faults and it is an important topic for future work.

While we follow the assumption that most of the breakdown energy occurs on the shearing surface (Rice, 2006; Viesca & Garagash, 2015), additional dissipation may also come from the production of damage and off-fault inelastic deformation (Andrews, 2005; K. Okubo et al., 2019; Poliakov, Dmowska, & Rice, 2002), especially on rough, non-planar faults (Dunham et al., 2011b). Such sources of additional dissipated energy may contribute to the inferred increase in average breakdown energy with average slip for natural earthquakes. Estimates from laboratory and field measurements suggest that the contribution of damage

and other off-fault processes to dissipation may be relatively small, <10 % (Aben et al., 2019; J. S. Chester et al., 2005; Rockwell et al., 2009), however, this remains an area of active research. Since the off-fault damage would be rupture-dependent as well, adding it to the consideration of the breakdown energy would likely further reinforce the conclusion of this study that breakdown energy is not an intrinsic fault property, but rather is rupture-dependent.

The finding that the breakdown energy –as well as the weakening rate –can vary substantially along a given rupture and among subsequent ruptures, even for comparable values of slip, suggests that caution is needed in using the inferred breakdown energies from natural events for modeling of future earthquake scenarios. Some dynamic rupture simulations account for thermo-hydro-mechanical effects (Andrews, 2002; Bizzarri & Cocco, 2006; Noda et al., 2009; Schmitt et al., 2015) and/or incorporate the effects of inelastic off-fault damage (Dunham et al., 2011a, 2011b; Roten et al., 2017; Withers et al., 2018) that should result in qualitatively similar effects on the breakdown energy. However, many employ simplified shear resistance evolutions that prescribe the breakdown energy and/or weakening rate directly, as a local fault property (Dalguer et al., 2020; Gallovic et al., 2019; Richards-Dinger & Dieterich, 2012; Shaw et al., 2018). Future work is needed to investigate whether and how the complexity of the local weakening/strengthening behavior experienced by the simulated faults with thermo-hydro-mechanical and other mechanismscan be translated into simulations with more simplified local relations, e.g. slip-dependent, and still result in similar rupture dynamics.

Furthermore, several features of faulting in the presence of thermo-hydro-mechanical effects call into question the overall analogy with cohesive-zone dynamic fracture theory and hence the significance of the breakdown energy as the quantity that controls rupture dynamics. The analogy between breakdown and fracture energies, and more broadly frictional faulting and shear cracks of traditional fracture mechanics, requires that the breakdown process be confined close to the rupture tip (small-scale yielding) and that the dynamic resistance level be constant; under such conditions, the conclusions of dynamic fracture theory apply,

including on the significance of breakdown energy (Freund, 1990). However, neither of these assumptions holds for the faults with thermo-hydro-mechanical processes. The weakening –and hence breakdown process –typically continues with ongoing slip at seismic slip rates on such faults, long after the rupture front passes. As a result, the breakdown process is not confined to the rupture tip and the dynamic resistance level is not constant. Moreover, the total dissipated energy –not just the energy included in the notion of breakdown energy –contributes to shear heating and hence fault weakening in thermo-hydro-mechanical fault models. That is why the entire dissipated energy may affect rupture dynamics as well. These considerations emphasize the need for better understanding of rupture dynamics and its controls in the presence of thermo-hydro-mechanical processes and for more systematic incorporation of such processes in earthquake source modeling.

Table 3.1: Model parameters used in Ch. 3 with the thermal pressurization of pore fluids.

Parameter	Symbol	Value
Loading slip rate	V_{pl}	10^{-9} m/s
Shear wave speed	c_s	3299 m/s
Shear modulus	μ	36 GPa
Rate-and-state parameters		
Reference slip velocity	V_*	10^{-6} m/s
Reference friction coefficient	f_*	0.6
Characteristic slip	D_{RS}	1 mm
Rate-and-state direct effect (VW)	a	0.010
Rate-and-state evolution effect (VW)	b	0.015
Rate-and-state direct effect (VS)	a	0.050
Rate-and-state evolution effect (VS)	b	0.003
Thermal pressurization parameters		
Interseismic effective normal stress	$\bar{\sigma} = (\sigma - p)$	25 MPa
Coupling coefficient (when TP present)	Λ	0.34 MPa/K
Thermal diffusivity	α_{th}	10^{-6} m^2/s
Hydraulic diffusivity	α_{hy}	10^{-3} m^2/s
Specific heat	ρc	2.7 MPa/K
Shear zone half-width	w	10 mm
Length scales		
Fault length	λ	96 km
Frictional domain	λ_{fr}	72 km
Velocity-weakening region	λ_{VW}	24 km
Cell size	Δz	3.3 m
Quasi-static cohesive zone	Λ_0	75 m
Nucleation size (Rice & Ruina, 1983)	h^*_{RR}	200 m
Nucleation size (Rubin & Ampuero, 2005)	h^*_{RA}	490 m

Chapter 4

PROPAGATION OF LARGE EARTHQUAKES AS SELF-HEALING PULSES OR MILD CRACKS

This chapter has been adapted from:

Lambert, V., Lapusta, N. & Perry, S. (2021). Propagation of large earthquakes as self-healing pulses and mild cracks. *Nature*. DOI: 10.1038/s41586-021-03248-1.

4.1 Competing theories for low-stress faults

Accumulating geophysical evidence suggests that shear stress acting on mature faults must be low, 20 MPa or less, in comparison to the expected shear resistance of 100-200 MPa at depths where earthquakes occur, given rock overburden and hydrostatic pore fluid pressure, along with typical friction coefficients measured at low-sliding rates in laboratory experiments (Brune et al., 1969; Fulton et al., 2013; Gao & Wang, 2014; Henyey & Wasserburg, 1971; Lachenbruch & Sass, 1980; Nankali, 2011; Rice, 2006; Sibson, 1975; Suppe, 2007; Tanikawa & Shimamoto, 2009; Townend & Zoback, 2004). One of the most compelling lines of evidence is the lack of substantial heat flow anomaly around mature faults that would be expected for fault slip at 100 MPa or more, the so-called "heat paradox" (Brune et al., 1969; Gao & Wang, 2014; Henyey & Wasserburg, 1971; Lachenbruch & Sass, 1980; Nankali, 2011). The "heat paradox" is documented along prominent plate boundary faults such as the San Andreas Fault and Japan Trench, which have hosted large earthquakes such as the 1857 Fort Tejon and 2011 M_w 9.0 Tohoku-oki earthquakes, respectively (Figure 4.1). Other lines of evidence include inferences of steep angles between the principal stress direction and fault trace (Townend & Zoback, 2004), analyses of the fault core obtained by drilling through shallow parts of faults that have experienced major recent events, including the 2011 M_w 9.0 Tohoku-oki event (Fulton et al., 2013; Tanikawa & Shimamoto, 2009), the geometry of thrust-belt wedges (Suppe, 2007), and the existence of long-lived narrow shear zones that do not exhibit any evidence of melting (F. M. Chester & Chester, 1998; Rice,

2006; Sibson, 1975).

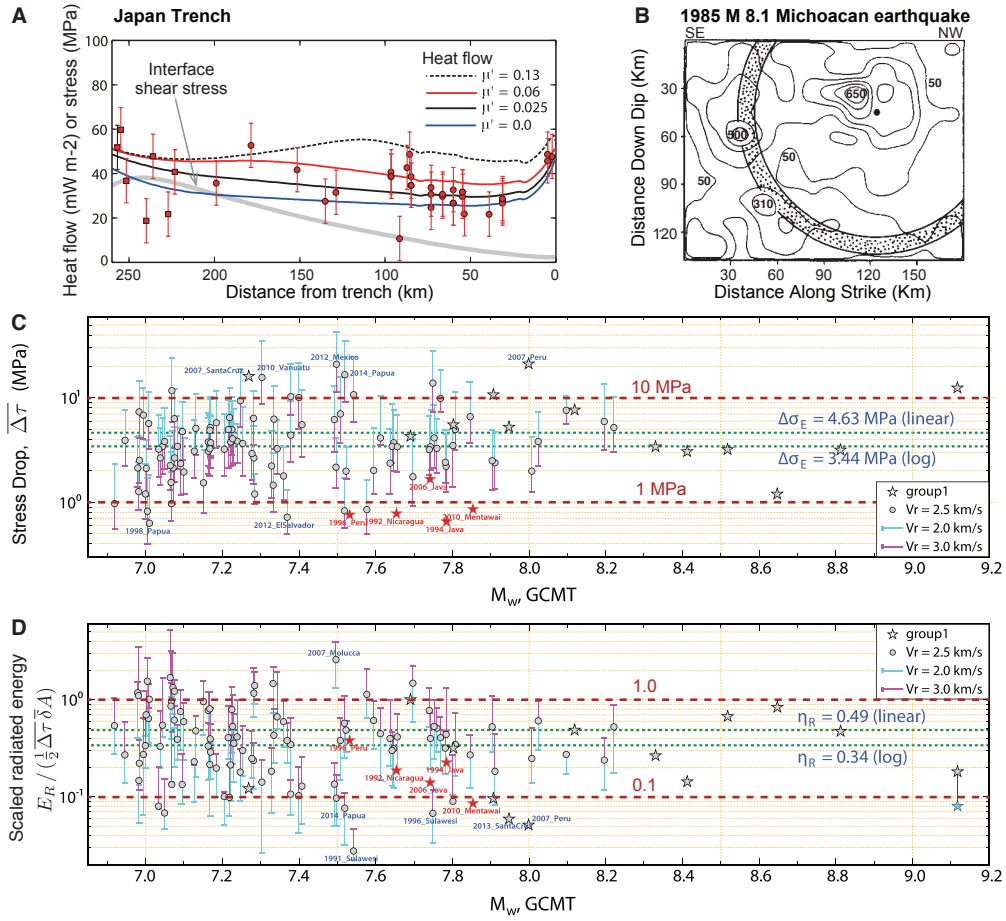

Figure 4.1: Geophysical inferences from large earthquakes that can be used to constrain earthquake physics. (A) Heat flow measurements from mature faults such as the Japan trench suggest that dynamic shear stress levels at seismogenic depths are low (< 20 MPa) (Gao & Wang, 2014). Red bars indicate assigned errors on observed heat flow. (B) Slip inversions of high-frequency ground motion indicate that the local slip durations of large earthquakes are quite short, suggesting that large earthquakes propagate as slip pulses (Heaton, 1990). (C) Inferred average stress drops from 114 large ($M_w \geq 7.0$) earthquakes between 1990 and 2015 are generally between 1 to 10 MPa (Ye et al., 2016b). (D) Inferred radiated energy values scaled by the product of average slip and stress drop, called radiation efficiency, are generally between 0.1 and 1, although some exceed values of 1 (Ye et al., 2016b). Error bars indicate differences in source parameter estimates with the assumed rupture speed V_r in the finite-fault inversions.

Two contrasting hypotheses are used to explain such low-stress, low-heat operation: either (H1) mature faults are strong at slow, quasi-static sliding rates, but undergo considerable enhanced dynamic weakening at seismic slip rates, as widely observed in laboratory exper-

iments (Di Toro et al., 2011; Tullis, 2007; Wibberley & Shimamoto, 2005), or (H2) mature faults are chronically weak, including at slow, quasi-static slip rates, due to anomalously low quasi-static friction coefficients and/or low effective confinement from pervasive fluid overpressure (Bangs et al., 2009; Brown et al., 2003; Collettini et al., 2009; Faulkner et al., 2006; Lockner et al., 2011). Slip inversions of high-frequency ground motions from large earthquakes indicate that their local slip duration is much shorter than the total duration of the rupture event (Heaton, 1990), suggesting that large earthquake ruptures may propagate as self-healing slip pulses (Figure 4.1). Numerical and theoretical studies have shown that self-healing slip pulses with realistic static stress drops can indeed occur on quasi-statically strong but dynamically weak faults, promoting hypothesis (H1) (Noda et al., 2009). In contrast, simplified earthquake source theories are based on the assumption that earthquake ruptures are crack-like, with the local slip duration comparable to the total duration of the rupture event. Finite-fault inversions of earthquakes are non-unique and cannot conclusively distinguish between crack-like and pulse-like ruptures. A sharper pulse-like rupture may be smeared by smoothing inherent in inversions while a crack-like rupture may look more pulse-like if the inversion cannot capture a long tail of low slip rates. Hence, we must examine alternative methods for their distinction.

To shed light on the physics governing earthquake ruptures, seismological studies seek to estimate source properties such as static stress drop, radiated energy, apparent stress, radiation efficiency, and average breakdown energy. Global comparisons of static stress drops suggest that the average stress change within the rupture area of earthquakes is generally independent of the magnitude of the rupture (Allmann & Shearer, 2009; Ye et al., 2016b), with typical values between 1 to 10 MPa (Figure 4.1). Earthquake sources are also often characterized by the apparent stress, which is defined as the rigidity μ multiplied by the ratio E_R/M_0, that relates the total radiated energy E_R to the seismic moment M_0. Both the apparent stress and E_R/M_0 are inferred to be magnitude-independent, with typical values for E_R/M_0 clustering around 10^{-5} (Ide & Beroza, 2001; Ye et al., 2016b). Average breakdown energy G has been inferred to increase with earthquake size, which is consistent with continued decrease of

shear resistance with slip due to enhanced dynamic weakening (Abercrombie & Rice, 2005; Perry et al., 2020; Rice, 2006; Viesca & Garagash, 2015). The relative importance of the radiated energy and breakdown energy is sometimes represented as a radiation efficiency η_R^{inf}, with values inferred from large earthquakes typically ranging from 0.1 to 1.0 (Figure 4.1 Ye et al., 2016b). These source parameters aim to characterize ruptures through single averaged quantities and are inferred indirectly from seismological observations, often based on simplified rupture models.

Here, we show that self-healing pulses that propagate on quasi-statically strong, dynamically weak faults (hypothesis H1) radiate much more seismic energy than crack-like ruptures on persistently weak faults (hypothesis H2), given similar static stress drop. This is because self-healing pulses have lower dynamic stress levels during seismic slip than the final shear stress –a property called stress undershoot –allowing for low heat production and mild static stress drops in comparison to their dynamic stress drops (Beeler et al., 2003; Kanamori & Rivera, 2013; Viesca & Garagash, 2015). In contrast, crack-like ruptures are typically characterized by a stress overshoot, where dynamic stress during seismic slip is higher than the final shear stress, meaning that the static stress drop is larger than the dynamic stress drop (Kanamori & Rivera, 2013; Madariaga, 1976; Viesca & Garagash, 2015). Self-healing pulses should then radiate more energy than crack-like ruptures with the same static stress drop, since the radiated energy from earthquakes should be proportional to the dynamic stress changes.

4.2 Simulated pulse- vs. crack-like ruptures

To verify this conjecture and examine the seismological observables for different types of ruptures, we conduct numerical simulations in earthquake source models representative of the two hypotheses for the low-stress, low-heat operation of mature faults. Our simulation approach is capable of simulating sequences of earthquakes and slow slip under slow, tectonic-like loading, while accounting for full inertial effects and shear heating effects during each earthquake rupture (Noda & Lapusta, 2010, Section 4.5). In our models, the faults are governed by laboratory-derived rate-and-state friction laws, which have been success-

fully used to explain and simulate a number of earthquake-related phenomena, including earthquake nucleation, post-seismic slip, continuing creep of stable segments, repeating earthquakes, and aftershock rates (Dieterich, 2007). Such laws are the most established representation of fault shear resistance that we have for slow, quasi-static slip rates from tectonic plate rates of 10^{-9} m/s to 10^{-2} m/s. At higher slip rates, enhanced dynamic weakening of fault frictional resistance can occur, for example, due to rapid shear heating, as widely documented in high-velocity laboratory experiments (Di Toro et al., 2011; Tullis, 2007; Wibberley & Shimamoto, 2005) and supported by theoretical studies (Rice, 2006). Most of our models include enhanced dynamic weakening due to thermal pressurization of pore fluids and one includes flash heating of contact asperities. The models of persistently weak faults additionally incorporate fluid overpressure and/or low quasi-static friction coefficients. The faults are embedded into an elastodynamic domain, with all inertial effects captured during simulated sequences of earthquake ruptures. To approximate the effects of off-fault yielding –which may increase dissipated energy, reduce sliding rates, and hence reduce shear heating –we impose a limit on the fault slip rate as suggested by detailed dynamic rupture simulations (Andrews, 2004). To illustrate the overall behavior and energy budget of the simulated earthquake ruptures, we average the local on-fault behavior for each dynamic rupture in a manner that preserves the overall energy partitioning within the rupture (Noda & Lapusta, 2012). The numerical methodology, model parameters, and analyses of simulated ruptures are further described in Section 4.5.

Let us compare two characteristic ruptures resulting from our dynamic simulations: a self-healing pulse-like rupture obtained in a quasi-statically strong but dynamically weak fault model (hypothesis H1 with effective normal stress of 100 MPa and efficient thermal pressurization of pore fluids, model TP1 from Table 4.3) and a crack-like rupture produced in a persistently weak model (hypothesis H2 with low effective normal stress of 25 MPa and relatively mild thermal pressurization of pore fluids, model TP6a from Table 4.3) (Figure 4.2). The two ruptures have similar average static stress drop $\overline{\Delta\tau}$ (~8 MPa) and slip $\overline{\delta}$ (~4 m), while being consistent with low heat production. Only a small portion of the fault slips

at a given time during the self-healing pulse-like rupture, resulting in a relatively short local sliding duration (or rise time). For the crack-like rupture, a considerable portion of the fault slips at most times during the rupture and the local sliding duration is comparable to the total rupture duration.

Perhaps not surprisingly, the physical behavior on the fault, as illuminated by the averaged shear stress versus slip plots (Figure 4.2), is significantly different in the two types of ruptures (and hence two types of fault models). The self-healing pulse occurs when the average fault shear prestress is relatively low, ~30 MPa, in comparison to the fault representative quasi-static frictional strength of ~70 MPa. Note that, to nucleate the rupture, the prestress needs to be comparable to the (high) quasi-static frictional strength in the nucleation region, but the size of the nucleation region is small in comparison to the overall rupture extent, and hence the average prestress is still low (Figure 4.5, Supplementary Video S1). In each initially low-stressed but ruptured location, the fault experiences a large dynamic stress increase, brought by seismic waves, to overcome the (high) static strength, with the average peak shear stress of ~100 MPa. The fault resistance then plummets, due to enhanced dynamic weakening, to much lower dynamic levels below 10 MPa, consistent with the quasi-statically strong but dynamically weak fault hypothesis (H1). As slip stops, the fault experiences a rapid stress increase due to the combination of fault healing and stress increase brought from nearby sliding regions by seismic waves, with the final average shear stress being appreciably higher than the dynamic stress level, in what is known as stress undershoot (Beeler et al., 2003; Kanamori & Rivera, 2013; Viesca & Garagash, 2015). The resulting average static stress drop of ~8 MPa is much smaller than the dynamic stress changes described.

In contrast, the static and dynamic stress changes are more comparable for the milder crack-like rupture that occurs in a model of a persistently weak fault (Figure 4.2D vs. C). Notably, there is no significant difference between the dynamic shear stress during slip and final shear stress; close examination reveals that the final stress is actually slightly lower than the dynamic resistance, a mild stress overshoot characteristic of crack-like ruptures (Figures

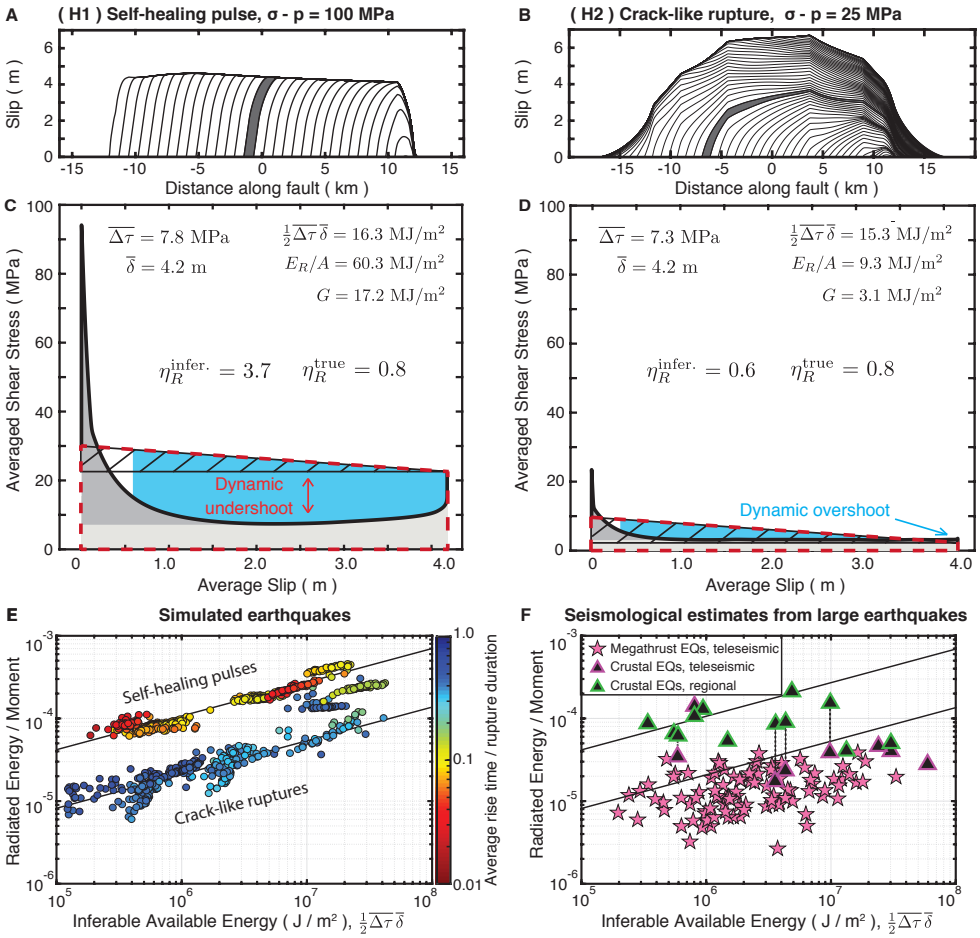

Figure 4.2: Simulated self-healing pulses on quasi-statically strong but dynamically weak faults vs. crack-like ruptures on chronically weak faults: energy partitioning and comparison with field observations. (A-B) Characteristic evolution of slip for the two rupture types. Contours are plotted every 0.25 s. (C-D) The corresponding average evolution of shear stress vs. slip that also illustrates the energy budget (see text), with the radiated energy in blue. The self-healing pulse experiences substantial stress undershoot, with the dynamic shear stress much lower than the final stress. (E-F) The radiated energy to moment ratios for the simulated pulses (vs. crack-like ruptures) are much larger than (vs. comparable to) inferences for large earthquakes from teleseismic measurements (pink stars and triangles). The higher values of radiated energy for the self-healing pulses are compatible with limited regional estimates from large crustal earthquakes (green triangles, Table 4.6). Dashed lines connect teleseismic and regional estimates for the same earthquakes.

4.2D and 4.6, and Supplementary Videos 2 and 3; Kanamori & Rivera, 2013; Madariaga, 1976; Viesca & Garagash, 2015). In order to maintain low heat production, as well as similar average static stress drop to the self-healing pulse, the crack-like rupture requires persistently lower stress levels, achieved in this case by a (low) effective normal stress of 25

MPa, consistent with hypothesis (H2).

4.3 Large differences in radiated energy

While the two types of ruptures exhibit similar stress drop and average slip, their energy partitioning substantially differs. In particular, the radiated energy from the self-healing pulse is over six times larger than that of the crack-like rupture. Through an extensive suite of simulations with different fault properties (Tables 4.1-4.5), we find that this is a generic result: the ratio of the radiated energy to seismic moment, which is proportional to apparent stress (Ide & Beroza, 2001; Ye et al., 2016b), is almost an order of magnitude larger for the self-healing pulses than for crack-like ruptures with comparable stress drop and slip (Figure 4.2E). Note that the crack-like ruptures in our simulations produce radiated energy values comparable to those seismologically inferred for natural megathrust earthquakes (Figure 4.2E-F), while the self-healing pulse-like ruptures result in about an order-of-magnitude higher values of radiated energy. The higher radiated energy of self-healing pulses is consistent with limited estimates from large crustal earthquakes, which seem to exhibit higher apparent stress than megathrust earthquakes (Figure 4.2F; Choy & Boatwright, 1995; Perez-Campos & Beroza, 2001). Note that higher radiated energy for earthquakes with the same moment is commonly interpreted in terms of higher static stress drops (Figure 4.2E; Ide & Beroza, 2001; Ma & Archuleta, 2006; Perez-Campos & Beroza, 2001). Our results show that ruptures with the same, or even lower, static stress drop and moment would have considerably higher radiated energy if they have higher undershoot (and hence are more pulse-like) (Figures 4.2E and 4.7, Section 4.6). This result is independent of the absolute stress levels on the fault (Figures 4.7 - 4.8). Intraplate earthquakes are an interesting example of ruptures with relatively high radiated-energy-to-moment ratios which may be achieved by higher static stress drops than the typical values of 1-10 MPa (Allmann & Shearer, 2009; Choy & Boatwright, 1995; Perez-Campos & Beroza, 2001). We do not focus on intraplate earthquakes here since they may not occur under low-stress, low-heat conditions which are predominately evidenced for mature plate-boundary faults.

The reason for the substantial difference in radiated energy is the completely different rela-

tion between the dynamic resistance and final level of stress for the self-healing pulses in comparison to the crack-like ruptures, which significantly modifies their overall energy partitioning (Kanamori & Rivera, 2013). Earthquake ruptures release part of the elastic strain energy stored in the surrounding medium; some of the energy is consumed in dissipation on and around the fault (dissipated energy), and the rest is radiated away from the fault (radiated energy). The average shear resistance vs. slip curves used to examine the average behavior of the representative pulse-like and crack-like earthquake ruptures also serve as illustrations of the energy budget, due to their special construction (Noda & Lapusta, 2012). The total strain energy released per unit rupture area $\Delta W/A$ is the trapezoid encompassed by red dashed lines in Figure 4.2; the dissipated energy is shaded by gray; and the difference, illustrated by blue, is the radiated energy. Because the dynamic resistance dips significantly below the final level of stress for self-healing pulse-like ruptures while the average static stress drop and slip are the same, the difference between the strain energy released and dissipated energy –i.e., the radiated energy –is significantly larger for the self-healing pulse-like ruptures than for the crack-like ruptures of the same average static stress drop and slip (Section 4.6). Note that the additional dissipation associated with the dynamic shear stress increase at the rupture tip above the initial stress level comes at the expense of the radiated energy, resulting in white regions inside the red-dashed trapezoid that depicts the total energy available for dissipation and radiation.

Our simulations show that progressively sharper self-healing pulses, with shorter local slip durations compared to total rupture duration, experience increasingly larger average stress undershoot, and, as a consequence, result in increasingly more radiated energy for the same stress drop and moment (Figure 4.3). Note that the increasing stress undershoot is a generic feature of increasingly sharper self-healing pulse-like ruptures that should develop regardless of the exact governing physics, for the following reasons. Consider a self-healing slip pulse of a certain local duration that achieves approximately spatially uniform local slip. As the slip pulse propagates over longer fault stretches, it becomes relatively sharper (i.e., the ratio of the local duration to the overall event duration becomes smaller). While

its dynamic stress drop (defined as the difference between the initial stress and dynamic shear resistance) stays approximately the same, governed by its local behavior, its static stress drop –related to the slip divided by the increasing rupture length –becomes smaller. It then follows that undershoot, equal to the difference between the dynamic and static stress drops, increases for progressively sharper pulses. Physically speaking, as the pulse of slip propagates through and then away from a location on the fault, the waves from the regions slipping elsewhere reload the just-slipped portions of the fault, causing the increase in the final shear stress level and hence the growing undershoot. To stay locked under such increasing shear stress, the fault needs to exhibit sufficiently rapid healing (Perrin et al., 1995). Similar considerations should apply to any physical fault mechanisms and conditions that generate sharp pulse-like ruptures, with potential candidates including geometric restrictions of the rupture area, strong heterogeneities, or elastic contrasts across the interface (Andrews & Ben-Zion, 1997; Beroza & Mikumo, 1996; Day, 1982). The results of our study would qualitatively apply to all slip-pulse ruptures with a substantial stress undershoot.

The generic mismatch between sliding resistance and final shear stress highlights the potential limitation of the commonly used approach to infer the earthquake energy balance (Kanamori & Brodsky, 2004; Ye et al., 2016b). In the common approach, the average shear stress drop is assumed to drop from an initial average shear stress $\bar{\tau}_{\text{ini}}$ down to a dynamic level of shear resistance $\bar{\tau}_{\text{dyn}}$, which is assumed to be equal to the final average shear stress $\bar{\tau}_{\text{fin}}$ (Figure 4.4). In this approximation, subtracting the shear stress $\bar{\tau}_{\text{dyn}}$ from the problem creates a mathematical analogy with traction-free cracks of fracture mechanics, with the remaining dissipated energy G (dark grey triangle) being analogous to the notion of fracture energy (Cocco et al., 2004). G is also called breakdown energy (Cocco et al., 2004). In general, the strain energy available for the breakdown energy and radiation can be defined as $\Delta W_0^{\text{true}}/A = E_R/A + G$, and the relative importance of radiated energy in that sum can be described by a radiation efficiency (Kanamori & Brodsky, 2004):

$$\eta_R^{\text{true}} = \frac{E_R/A}{E_R/A + G}. \tag{4.1}$$

For the commonly used simplified energy diagram (Figure 4.4A), the available energy is

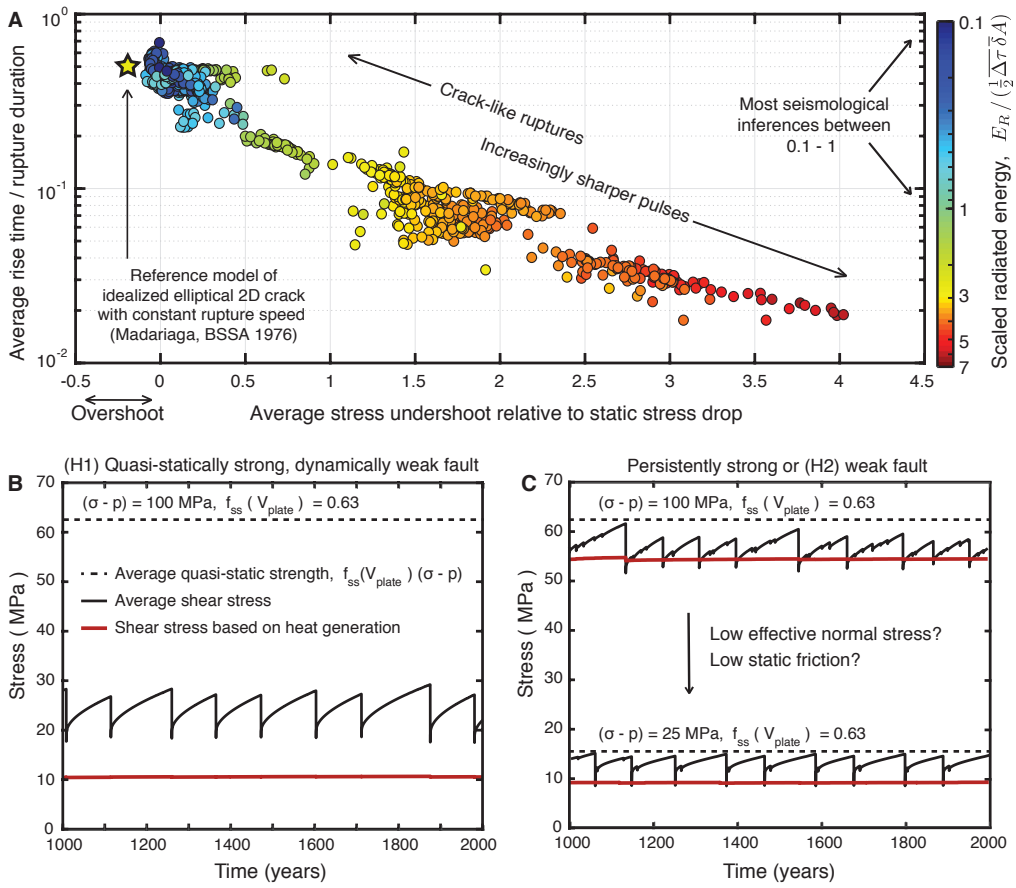

Figure 4.3: The relationship between the rupture mode, radiated energy, and stress state on simulated faults. (A) Progressively sharper self-healing pulses, with shorter local slip durations compared to total rupture duration, experience larger average stress undershoots and, as a consequence, result in more radiated energy for the same static stress drop and moment. (B-C) The evolution of average shear stress and shear heating stress over sequences of ruptures simulated on a quasi-statically strong but dynamically weak fault (B) and a persistently weak/strong fault (C). The average shear stress is far from the quasi-static strength in the former case but comparable to it in the latter case.

given by $\Delta W_0^{\text{inf}}/A = (\overline{\Delta\tau}\,\overline{\delta})/2$ and hence becomes seismologically inferable. The radiation efficiency and breakdown energy can then be inferred as:

$$\eta_R^{\text{inf}} = \frac{E_R/A}{\frac{1}{2}\overline{\Delta\tau}\,\overline{\delta}} \tag{4.2}$$

and

$$G^{\text{inf}} = \Delta W_0^{\text{inf}}/A - E_R/A. \tag{4.3}$$

The inferable radiation efficiency is also sometimes referred to as the Savage-Wood effi-

ciency (Savage & Wood, 1971).

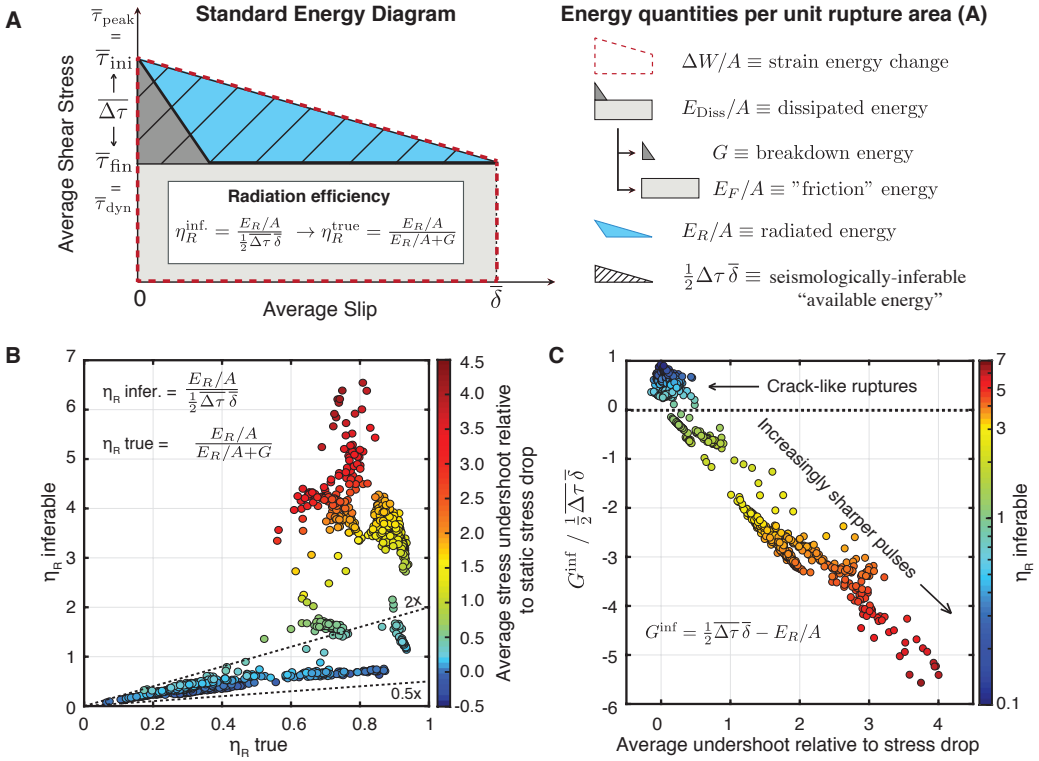

Figure 4.4: Energy-related values for self-healing pulses are substantially different from seismological inferences based on the standard energy budget. (A) The standard diagram for the earthquake energy budget from which seismological inferences are defined. (B-C) Self-healing pulse-like ruptures with larger average stress undershoot relative to static stress drop result in greater radiated energy for the same seismologically-inferable available energy, leading to inferable radiation efficiencies much greater than 1 and estimated breakdown energies that are increasingly negative. Crack-like ruptures are well described by the standard energy diagram.

A critical assumption in deriving relations (2) and (3) is that the final average shear stress after the rupture $\overline{\tau}_{\mathrm{fin}}$ is the same as the average dynamic level of shear resistance $\overline{\tau}_{\mathrm{dyn}}$, which holds relatively well for crack-like ruptures (e.g. Figure 4.2D) but not for self-healing pulse-like ruptures. Due to the substantial stress undershoot typical for self-healing pulses, seismological inferences would significantly underestimate the available energy, resulting in inferable radiation efficiencies much greater than 1 and inferable breakdown energies G^{inf} that are negative (Figure 4.4B and C) (Section 4.6). While several seismological studies

have indeed recorded radiation efficiencies greater than 1 and negative estimates of G^{inf} for some earthquake ruptures (Abercrombie & Rice, 2005; Viesca & Garagash, 2015; Ye et al., 2016b), such inferences are uncommon. Note that some prior studies of self-healing pulses assumed that the extra available energy can be spent as breakdown energy (Viesca & Garagash, 2015), whereas our simulations show that much of it translates into radiated energy. Our simulation results also call into question the relevance for finite faults of models with steady-state slip pulses propagating on infinite faults; such infinite-fault slip pulses have zero radiated energy as well as zero static stress drop, in clear contradiction with seismic observations (Rice et al., 2005). Our simulations show that pulses on finite faults generated as part of spontaneous earthquake sequences result in evolving pulse shape, non-zero local static stress changes and significant seismic radiation (Figures 4.9 - 4.11), despite sometimes having near-uniform slip distribution. We have verified that these results do not depend on the numerical resolution.

Crack-like rupture propagation can also occur in models with quasi-statically strong but dynamically weak friction for high enough levels of shear prestress (Noda et al., 2009); however, such simulated ruptures typically have static stress drops that are too large in comparison to field inferences of 1-10 MPa. However, for sufficiently efficient enhanced weakening, we find that crack-like ruptures can propagate over considerably lower stress levels than the local quasi-static strength, resulting in reasonable stress drops (Figures 4.12–4.13). While theoretically possible, the physical plausibility of such ruptures on natural faults warrants further study, as they require considerably more efficient weakening than the more generic self-healing pulses, and such special weakening may potentially be easily suppressed, for example, by dynamically induced changes in rock permeability or additional energy loss due to off-fault damage during dynamic rupture. Ruptures with more efficient weakening may be potentially distinguished by their production of considerably stronger high-frequency ($>$ 1 Hz) near-fault ground motions (Figures 4.14 - 4.15). Similarly, pulse-like ruptures can and do occur in models of chronically weak faults, for the right combination of fault prestress and weakening. However, such ruptures may have static stress drops (and hence

slips) that are too low compared to observations. Regardless of the absolute stress levels, such pulse-like ruptures still produce high levels of radiated energy relative to their seismic moment (Figure 4.16) and they are included in Figures 4.2 and 4.3.

Both prevailing types of ruptures –self-healing pulses on quasi-statically strong but dynamically weak faults and crack-like ruptures on persistently weak faults –indeed result in low-stress, low-heat fault operation as intended (Figure 4.3B-C, models TP1 and TP8 from Table 4.3). A crucial difference between the two models is the relation of the fault-averaged shear stress to the representative local quasi-static strength (defined in Section 4.5), i.e., how ready is the fault to fail in the quasi-static sense. In the quasi-statically strong but dynamically weak fault models, the fault is always far, on average, from the representative local quasi-static strength (Figure 4.3B), with the difference being a large multiple of the typical static stress drop. Such behavior elevates the importance of earthquake nucleation, which can only occur in special locations (either locally highly stressed or locally weak), and hence is potentially rare, perhaps leading to seismic quiescence as observed on some major strike-slip faults (Jiang & Lapusta, 2016). For the persistently weak models, the fault is always close, on average, to the local quasi-static strength (within one static stress drop).

4.4 Megathrust vs. crustal earthquakes

Crack-like ruptures in our simulations of persistently weak faults reproduce a number of seismological observables for natural earthquakes, including stress drops between 1 and 10 MPa, radiation efficiencies between 0.1 and 1.0 (Figures 4.3 and 4.4), positive seismologically inferable breakdown energies (Figure 4.4), and ratios of radiated energy to moment around 10^{-5} (Figure 4.2). Moreover, the energy partitioning for crack-like ruptures is well captured by the standard energy analysis, with radiation efficiencies and average breakdown energy inferred using seismological approaches being comparable to the true, simulated values, within a factor of two (Figure 4.4 and 4.17). These results suggest that fault models incorporating chronic fault weakness may be plausible representations of natural faults, particularly megathrusts in subduction zones which have documented evidence of fluid overpressure (Bangs et al., 2009; Brown et al., 2003) and which dominate the inferences of radiated

energy. While the ruptures in such models propagate mainly as crack-like ruptures or mildly self-healing pulses, they may appear somewhat more pulse-like in finite-fault inversions, either because the inversions may not be able to resolve weak "tails" of the continuing lower slip rates or because the slip-rate tails have been further reduced or arrested by the geometric effects of healing waves from the boundaries of the seismogenic region (Day, 1982). Note that even for chronically weak faults, additional enhanced dynamic weakening can be critical for reproducing available seismological inferences, such as realistic static stress drops (> 1 MPa) under persistently weak conditions and inferred increase in breakdown energy with slip (Perry et al., 2020; Rice, 2006; Viesca & Garagash, 2015).

The higher radiated energy for pulse-like ruptures, however, is consistent with regional estimates for crustal strike-slip earthquakes (Figure 4.2E). Our results show that the discrepancy of 5–10 times between the radiated energy estimates for large megathrust and strike-slip events, if real, may signify a difference in physical behavior of faults in different tectonic environments, with mature strike-slip faults being quasi-statically strong but dynamically weak and hosting mostly self-healing pulse-like ruptures, consistent with hypothesis H1, and megathrust faults being chronically weak due to pore fluid overpressure (potentially with additional milder dynamic weakening due to shear heating), consistent with hypothesis H2. Such an interpretation would be consistent with sharp pulse-like ruptures inferred by slip inversions of high-frequency ground motions from large, mostly crustal earthquakes (Heaton, 1990). The validity of this insight critically depends on the accuracy of the radiated energy estimates, which need to be further verified (Kanamori et al., 2020; Ma & Archuleta, 2006; Perez-Campos & Beroza, 2001), especially since different methods produce different results. The (much higher) radiated energy estimates for strike-slip events are typically obtained from regional (nearby) data, while the (lower) radiated energy estimates for megathrust events are obtained from teleseismic (distant) data. The estimates can be affected by a number of factors, including attenuation, rupture directivity, and focal mechanism (Ide & Beroza, 2001; Kanamori et al., 2020; Ma & Archuleta, 2006; Perez-Campos & Beroza, 2001; Ye et al., 2016b). The approaches for estimating radiated energy can be evaluated

using synthetic data from various physics-based models, such as the simulations in this work.

In summary, we find that two commonly invoked physical models for low-heat, low-stress operation of mature faults can be distinguished based on radiated energy, under the constraint of static stress drops of 1–10 MPa consistent with finite-fault inversions of large earthquakes. Self-healing pulse-like ruptures have relatively high radiated energy per seismic moment, similar to limited regional estimates for crustal earthquakes but 5 to 10 times higher than numerous teleseismic estimates for megathrust earthquakes. The teleseismic estimates for megathrusts are consistent with radiated energy from crack-like ruptures, which need to occur on chronically weak faults in order to result in low-heat, low-stress operation. Hence, either large megathrust earthquake ruptures rarely propagate as self-healing pulses, or their radiated energy is substantially underestimated by current teleseismic seismological techniques. Our findings, although conceptually promising, are based on geometrically simplified two-dimensional models with piecewise uniform fault properties; they motivate systematic exploration of the relation between rupture mode and seismic radiation in geometrically realistic three-dimensional fault models with heterogeneity. Our results also suggest that re-examining the validity of the seismological estimates of radiated energy and static stress drop from large earthquake ruptures of various types (including self-healing pulses), using in part numerically simulated sources, would provide significant further insight into earthquake source physics, driving mechanisms of large earthquakes, and hence seismic hazard.

4.5 Materials and methods

4.5.1 Supplementary figures

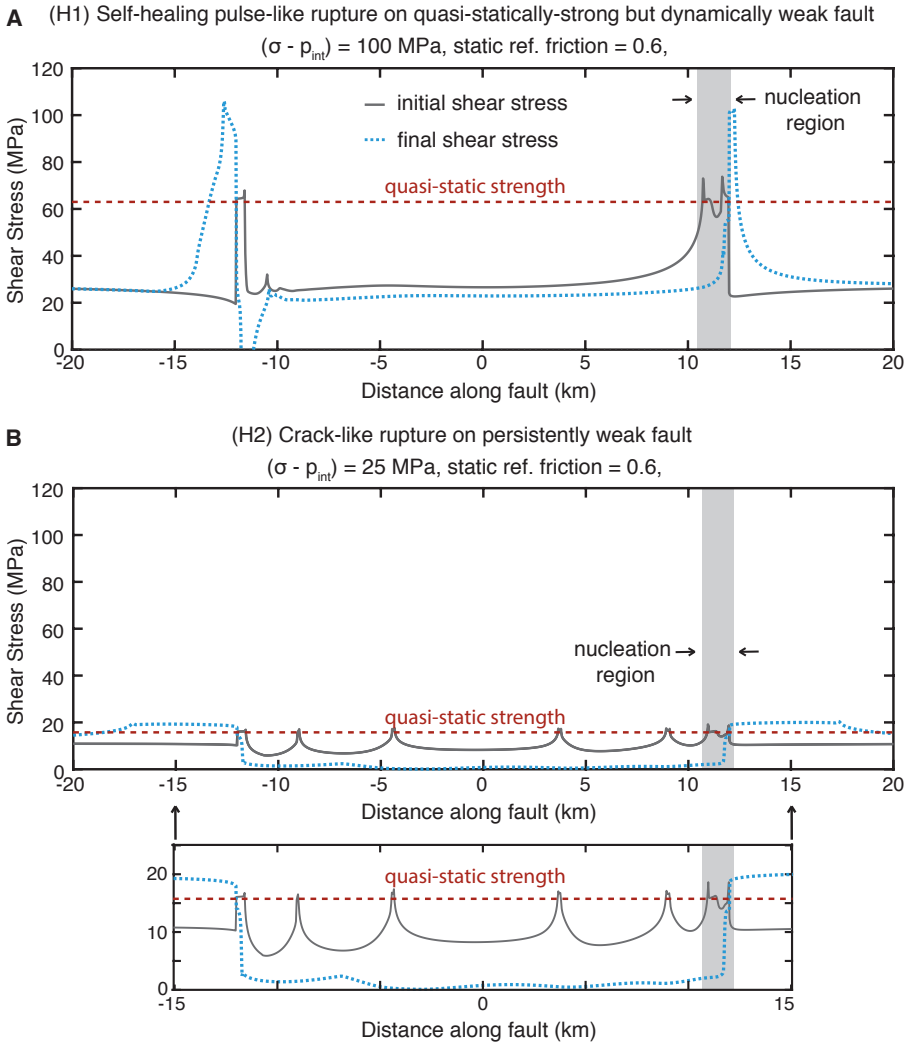

Figure 4.5: Stress distributions before and after dynamic rupture for models of low-stress, low heat fault operation. Distribution of the initial (grey) and final (blue) shear stress along the fault for (A) a self-healing pulse-like rupture on a (H1) quasi-statically strong but dynamically weak fault, and (B) a crack-like rupture on a (H2) persistently weak fault. Both ruptures have similar average static stress drops around 7-8 MPa, and nucleate in a region with stress levels close to their respective quasi-static strength (grey bar). For the self-healing pulse (A), most of the fault is far below the quasi-static strength, whereas for the crack-like rupture the entire rupture region is within 1-2 times the static stress drop from the quasi-static strength.

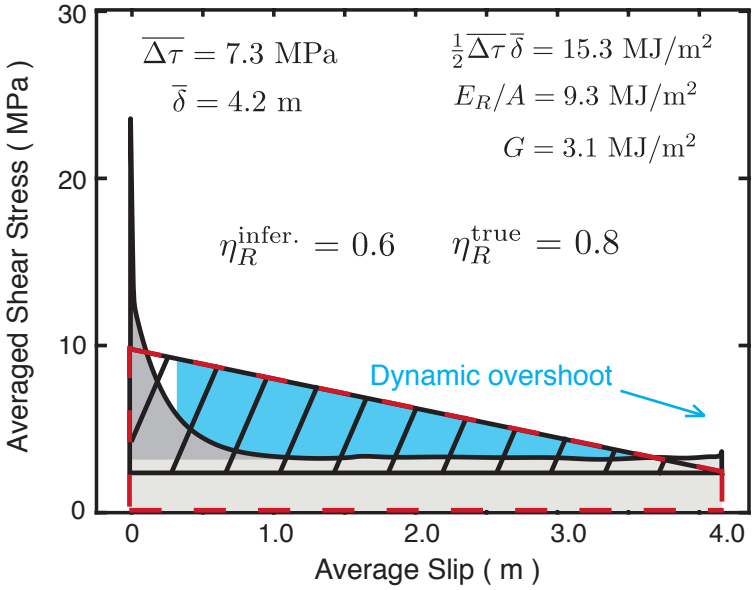

Figure 4.6: Average shear stress versus slip for a representative crack-like rupture (same as Figure 4.2D but on enlarged scale). The average shear stress versus slip curve also serves as the energy partitioning diagram for the crack-like rupture. Crack-like ruptures typically exhibit a mild dynamic overshoot where the final average shear stress is lower than the average dynamic resistance.

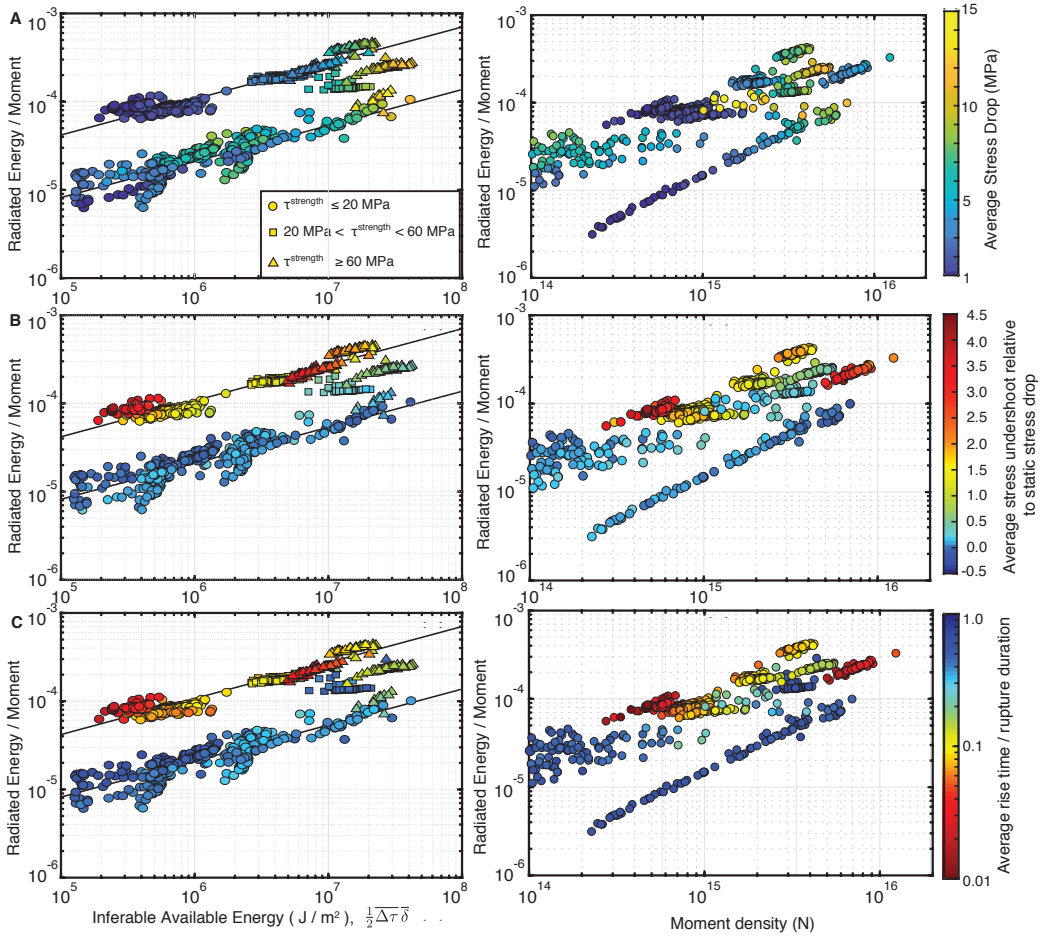

Figure 4.7: Relationship between radiated energy, seismic moment, static stress drop and stress undershoot. (Left) Ratio of radiated energy to moment versus seismologically inferable available energy for simulated ruptures. Circles indicate models with average quasi-static strength τ^{strength} below 20 MPa, squares indicate those with τ^{strength} between 20 and 60 MPa and triangles indicate models with τ^{strength} greater than 60 MPa. (Right) Radiated energy to moment ratio versus 2D moment density for simulated ruptures. Ruptures are colored by A) average static stress drop, B) average stress undershoot, and C) the ratio of the average rise time to rupture duration.

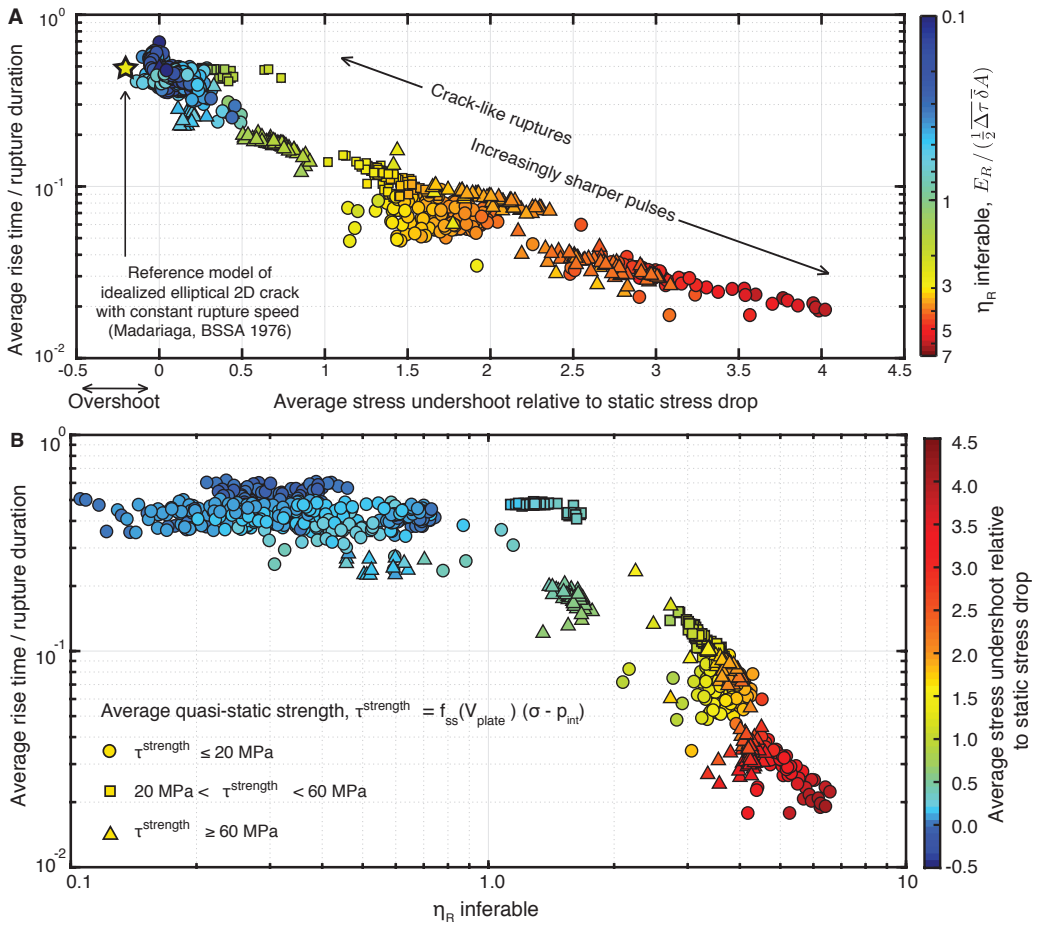

Figure 4.8: The relationship between rupture mode and inferable radiation efficiency. (A) The relationship between inferable radiation efficiency and undershoot does not depend on the absolute stress levels. Circles indicate models with average quasi-static strength τ^{strength} below 20 MPa, squares indicate those with τ^{strength} between 20 and 60 MPa and triangles indicate models with τ^{strength} greater than 60 MPa. B) Our simulated crack-like ruptures result in inferable radiation efficiencies between 0.1 and 1.0, whereas self-healing pulses produce radiation efficiencies greater than 1.

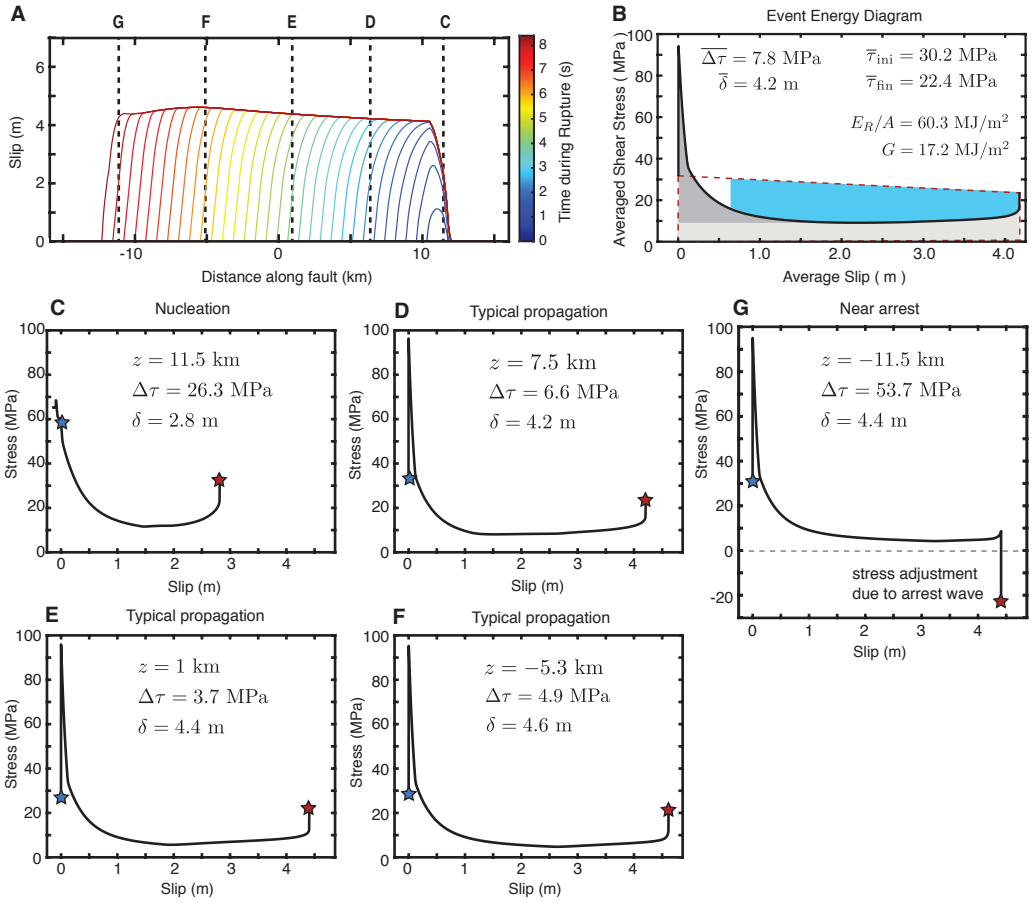

Figure 4.9: Relationship between local and average stress versus slip behavior for a self-healing pulse. (A) Evolution of accumulated slip during a representative self-healing pulse-like rupture with thermal pressurization TP1. Slip is contoured every 0.25 s. (B) Average shear stress vs. slip behavior. The local behavior in all ruptures is variable, however we use the averaging methodology of Noda and Lapusta (2012) to construct the average shear stress vs. slip behavior and illustrate averaged source parameters. (C-G) The local evolution of shear stress with slip at five different points throughout the rupture.

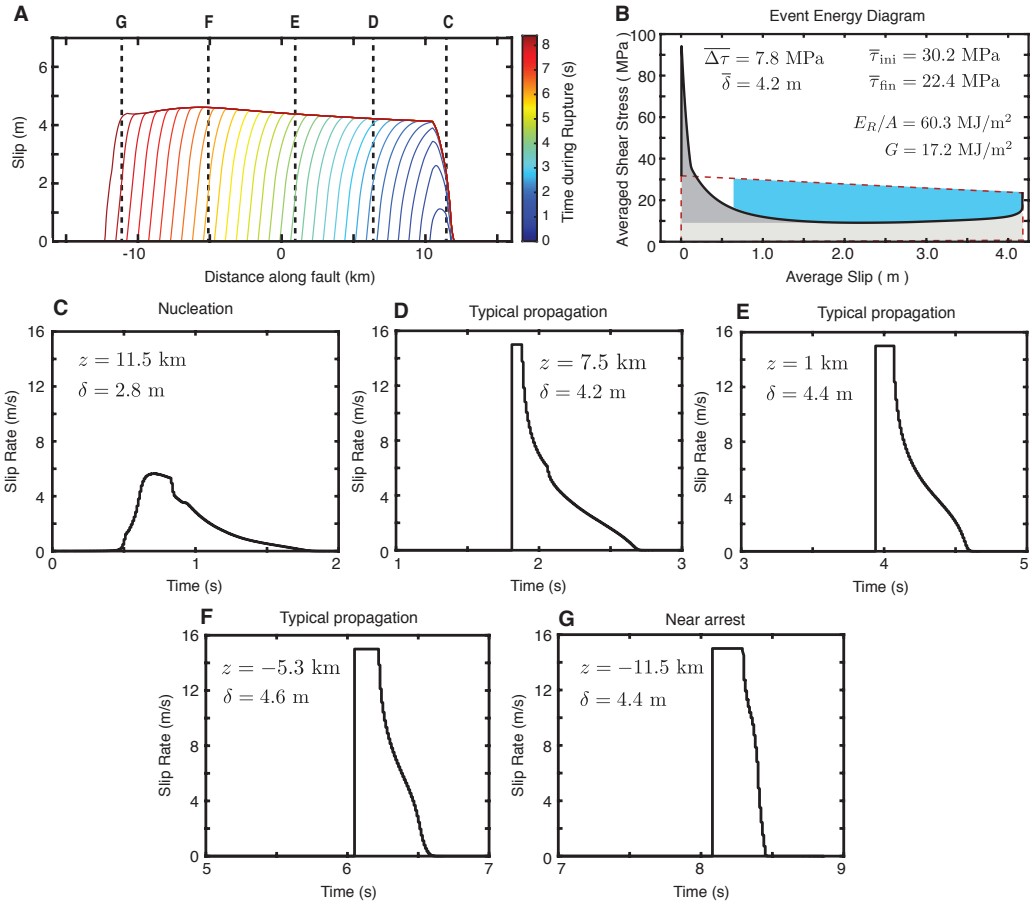

Figure 4.10: Evolution of slip pulse throughout the rupture process. (A) Evolution of accumulated slip during a representative self-healing pulse-like rupture with thermal pressurization TP1. Slip is contoured every 0.25 s. (B) Average shear stress vs. slip behavior. (C-G) The local evolution of slip rate with time at five different points throughout the rupture indicating the development of pulse and non-steady local behavior. As the rupture accelerates, the pulse becomes sharper, with shorter local slip duration compared to the total rupture duration.

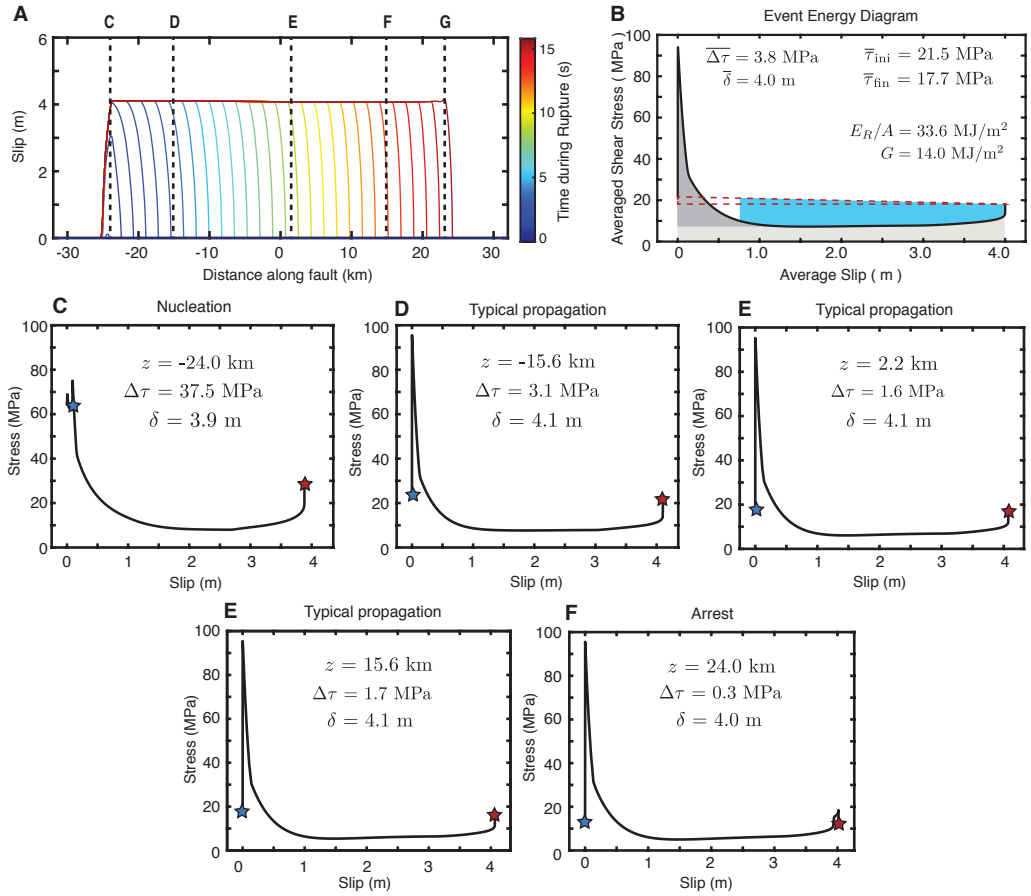

Figure 4.11: Relationship between local and average stress versus slip behavior for a self-healing pulse on a longer fault. (A) Evolution of accumulated slip during a representative self-healing pulse-like rupture with thermal pressurization TP1 on a longer fault with a 50-km VW region. Slip is contoured every 0.5 s. (B) Average shear stress vs. slip behavior. The local behavior in all ruptures is variable, however we use the averaging methodology of Noda and Lapusta (2012) to construct the average shear stress vs. slip behavior and illustrate averaged source parameters. (C-E) The local evolution of shear stress with slip at five different points throughout the rupture. The general behavior is qualitatively similar to the self-healing pulses with similar properties on the shorter fault with a 24-km VW region.

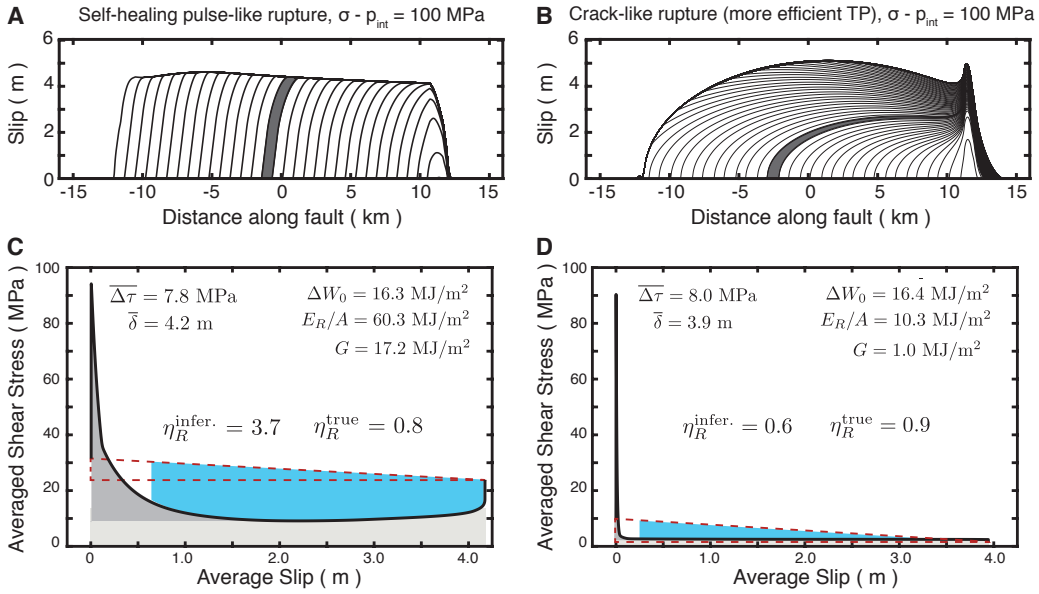

Figure 4.12: (A-B) Evolution of slip along the fault for a self-healing pulse-like rupture (A) and crack-like rupture (B) with more efficient enhanced weakening. Contours are plotted every 0.25 s and the gray shading illustrates a portion of the fault that is slipping during a 0.25-second interval. (C-D) The corresponding average evolution of shear stress vs. slip illustrating the radiated energy (blue shading), as well as the dissipated energy, which is further separated into the average breakdown energy (dark gray shading) and residual dissipated energy (light gray shading). The seismologically-inferable available energy (red-dashed triangle) illustrates that the two ruptures have similar static stress drop and average slip. The crack-like rupture with efficient enhanced weakening experiences large dynamic stress changes at the rupture front but remains at very low stress levels, experiencing a mild stress overshoot and no healing in contrast to the self-healing pulse.

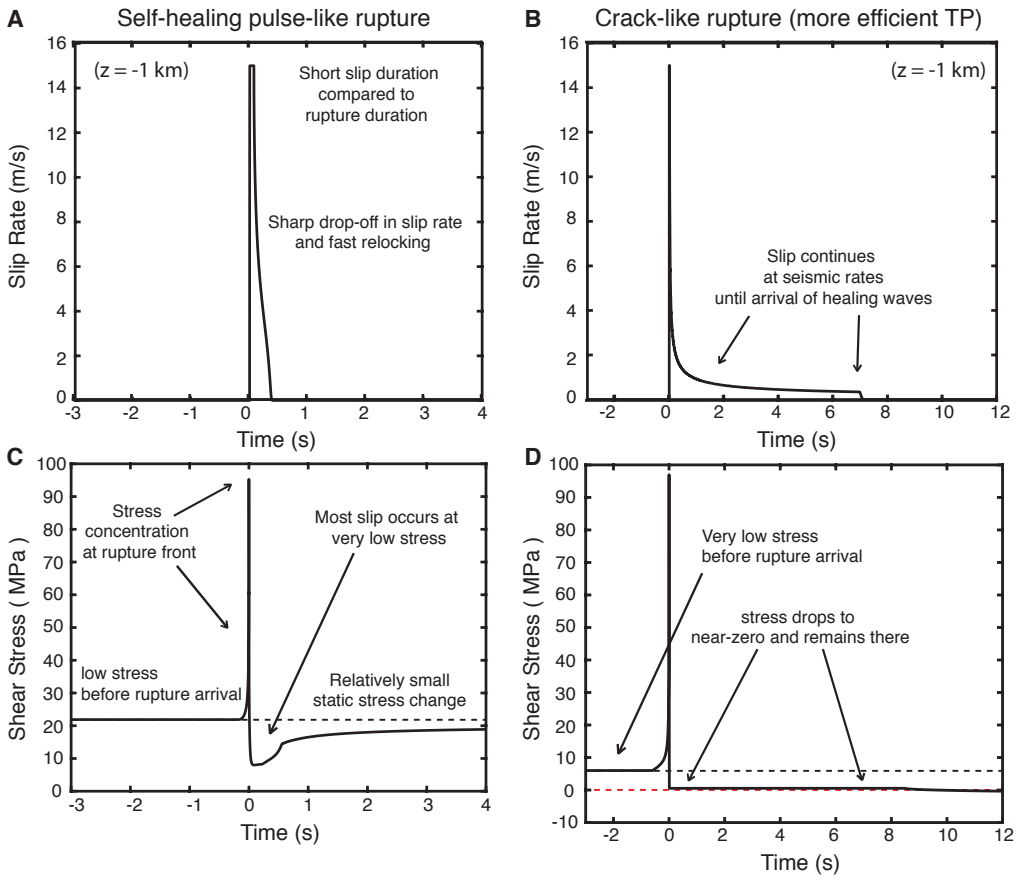

Figure 4.13: Local behavior during a self-healing pulse and crack-like rupture. (A-B) Evolution of slip rate with time at an individual point in the center of a self-healing pulse-like rupture (A) and crack-like rupture (B) with more efficient enhanced weakening. Both ruptures experience a rapid acceleration of slip as the rupture front arrives, however, local sliding is very short in the self-healing pulse-like rupture before the point quickly relocks, whereas the point continues to slip with seismic slip rates (1 m/s) until the arrival of healing waves from the boundary in the crack-like rupture. (C-D) Evolution of shear stress with time for the same points as in (A-B). Both points have initially low prestress before the arrival of the stress concentration at the rupture front. The self-healing pulse dramatically weakens and then heals such that the static stress change is much smaller than the dynamic stress change. In contrast, the shear stress at the point in the crack-like rupture drops dramatically and stays low, such that the local static and dynamic stress drops are comparable.

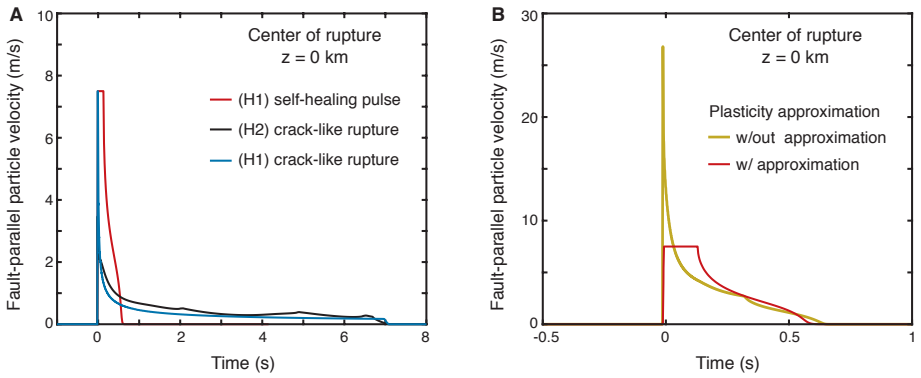

Figure 4.14: Particle motion for self-healing pulse and crack-like ruptures. (A) Particle velocity vs. time in the center of the rupture region (z = 0) for a representative self-healing pulse on a quasi-statically strong, dynamically weak fault (H1,red, Figure 4.2C), crack-like rupture on a persistently weak fault (H2, black, Figure 4.2D), and crack-like rupture on a quasi-statically strong, dynamically weak fault (H1, blue, Figure 4.12). (B) The approximation of off-fault plasticity (V_{lim} = 15 m/s) reduces the sharp peak in particle velocity associated with the passing of the rupture front, which corresponds to high frequency motion above 1 Hz (Figure 4.15C-D).

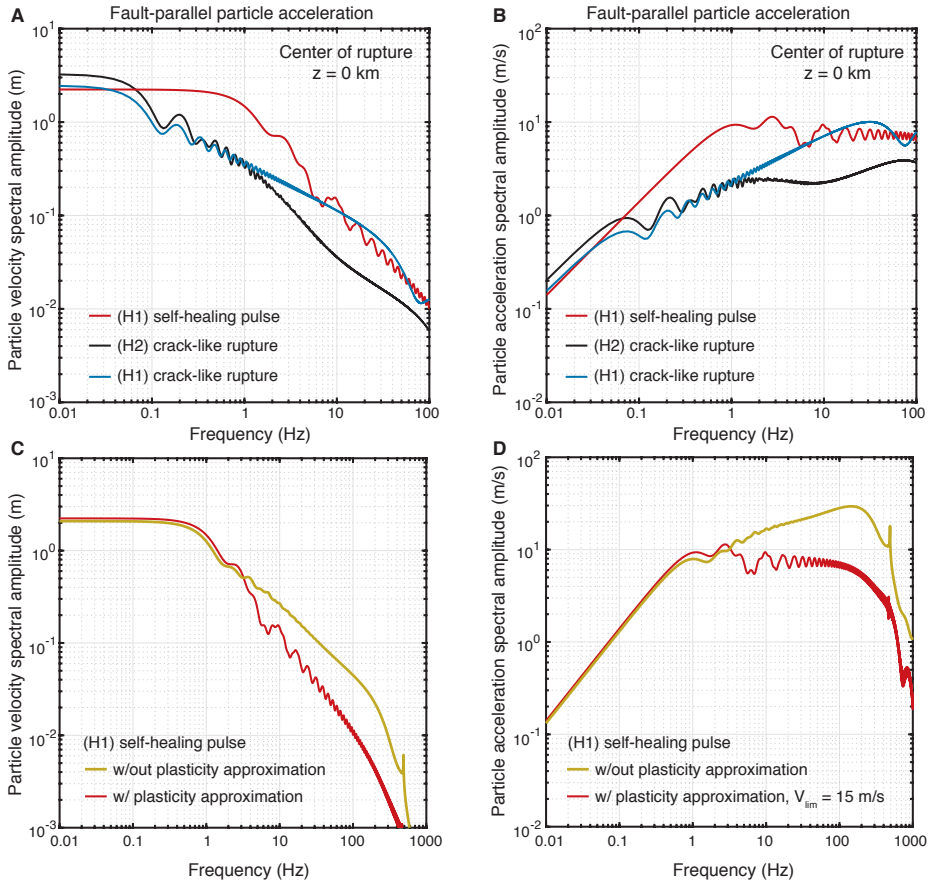

Figure 4.15: Particle motion spectra for self-healing pulse and crack-like ruptures. (A-B) Particle velocity and acceleration spectral amplitudes in the center of the rupture region (z = 0) for a representative self-healing pulse on a quasi-statically strong, dynamically weak fault (H1, red, Figure 4.2C), crack-like rupture on a persistently weak fault (H2, black, Figure 4.2D), and crack-like rupture on a quasi-statically strong, dynamically weak fault (H1, blue, Figure 4.12D). Both ruptures on quasi-statically strong, dynamically weak faults experience larger and more rapid dynamic stress changes resulting in more pronounced high-frequency ground motion above 1 Hz. (C-D) High-frequency motions can be considerably damped by the inclusion of approximations for off-fault plasticity (V_{lim} = 15 m/s), however this may be concentrated towards higher frequencies than typically considered for many seismological and strong ground motion studies.

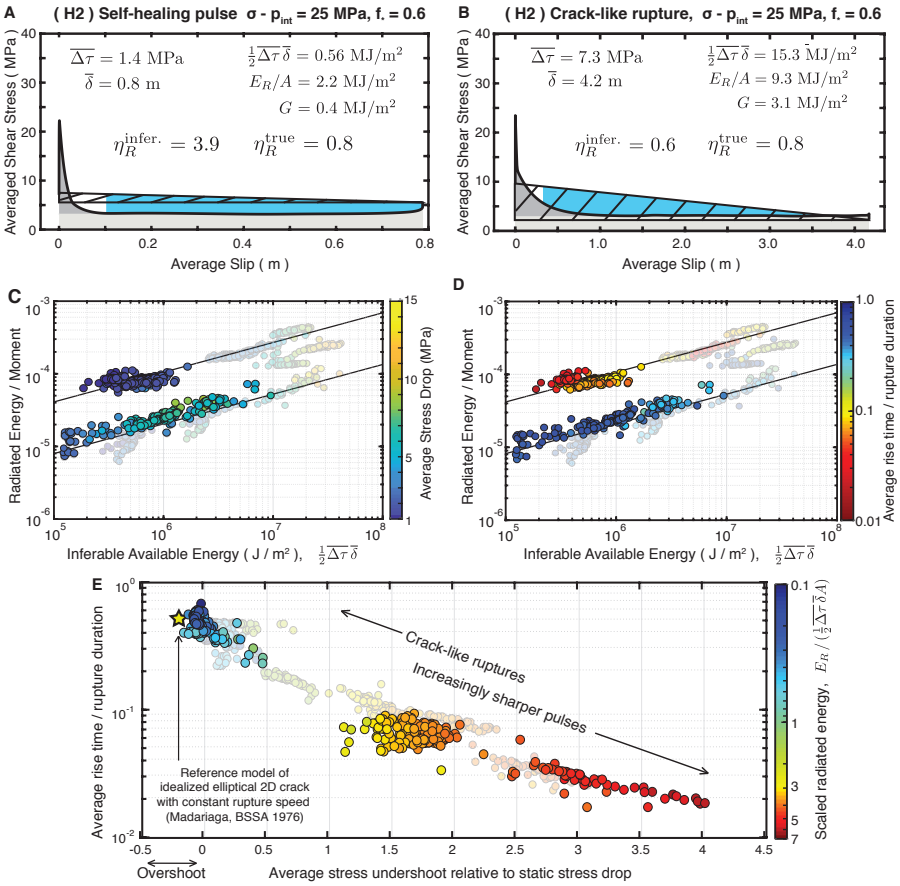

Figure 4.16: Self-healing pulses and crack-like ruptures in models with comparable quasi-static strength. (A-B) The average evolution of shear stress vs. slip for a representative self-healing pulse and crack-like rupture with the same low quasi-static strength conditions (the effective normal stress of 25 MPa, models TP6a and TP 7b. The self-healing pulse results in a smaller static stress drop and average slip than the crack-like rupture with similar quasi-static strength and comparable dynamic resistance. However, the self-healing pulse has a considerable undershoot compared to its static stress drop. (C-D) Despite simulated self-healing pulses having lower average static stress drops than crack-like ruptures with the same quasi-static strength and comparable dynamic resistance, the radiated energy to moment ratios for the pulse-like ruptures are much larger than those for the crack-like ruptures. E) Progressively sharper pulses experience greater average stress undershoot, resulting in more radiated energy for the same static stress drop and moment. In panels (C-E), the grayed-out backgrounds show results from all models as in Figure 4.2.

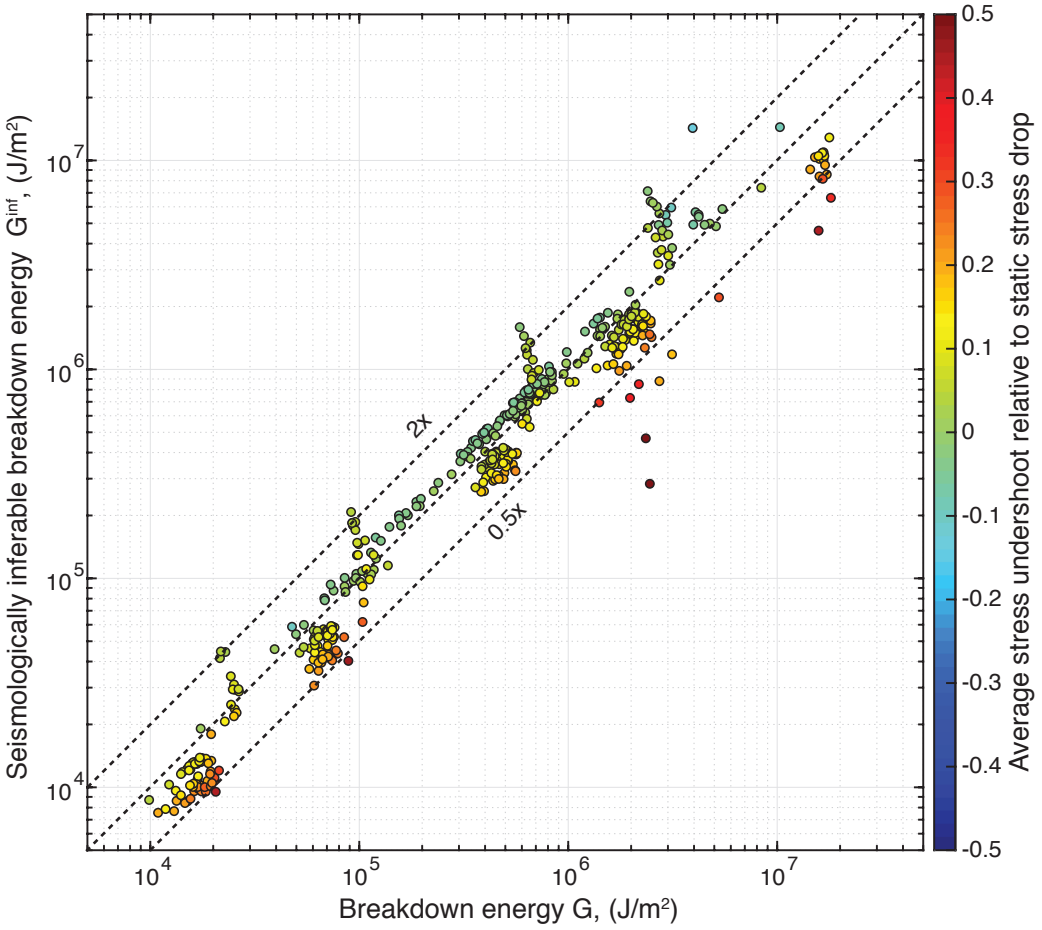

Figure 4.17: Comparison of seismologically-inferable and true average breakdown energies for simulated crack-like ruptures with average stress overshoot/undershoot within $0.5\overline{\Delta\tau}$. Inferable breakdown energies are comparable to the true values, within a factor of two.

4.5.2 Model description

To conduct numerical simulations of long-term fault behavior including earthquake sequences and aseismic slip, we utilize the spectral boundary integral method to solve the elastodynamic equations of motion coupled with friction boundary conditions, including the evolution of pore fluid pressure and temperature on the fault coupled with off-fault diffusion (Lapusta et al., 2000; Noda & Lapusta, 2010). Our simulations consider mode III slip on a 1-D fault embedded into a 2-D uniform, isotropic, elastic medium. At each time step, slip rates and shear tractions are calculated for each cell of the discretized fault by equating fault shear stress to frictional shear resistance. The evolution of shear stress at each cell depends on loading conditions as well as coupled interactions with slip at other fault cells through wave-mediated static and dynamic stress transfers. The use of adaptive time-stepping in our methodology allows us to resolve earthquake sequences in their entirety, including the spontaneous nucleation process, dynamic rupture propagation, postseismic slip following rupture events, and the interseismic period between events that can last up to tens or hundreds of years.

In all of our fault models, we use the laboratory-derived Dieterich-Ruina rate-and-state friction law with the state evolution governed by the aging law (Dieterich, 1979; Marone, 1998; Ruina, 1983):

$$\tau = \overline{\sigma} f(V, \theta) = (\sigma - p)\left[f_* + a \log \frac{V}{V_*} + b \log \frac{\theta V_*}{D_{\mathrm{RS}}}\right], \tag{4.4}$$

$$\dot{\theta} = 1 - \frac{V\theta}{D_{\mathrm{RS}}}, \tag{4.5}$$

where $\overline{\sigma}$ is the effective normal stress, σ is the normal stress, p is the pore fluid pressure, f_* is the reference steady-state friction coefficient at reference sliding rate V_*, D_{RS} is the characteristic slip distance, and a and b are the direct effect and evolution effect parameters, respectively. Other formulations for the evolution of the state variable exist, such as the slip law (Ruina, 1983) as well as various composite laws, and the formulation that best describes various laboratory experiments remains a topic of ongoing research (Bhattacharya et al., 2015). However, the choice of the state evolution law should not substantially influence the

results of this study, as the evolution of shear resistance during dynamic rupture within our simulations is dominated by the presence of enhanced weakening mechanisms. We use the version of the expressions (4.4-4.5) regularized for zero and negative slip rates (Noda & Lapusta, 2010).

During conditions of steady-state sliding ($\dot{\theta} = 0$), the friction coefficient is expressed as:

$$f_{ss}(V) = f_* + (a - b) \log \frac{V}{V_*}. \tag{4.6}$$

The combination of frictional properties $(a - b) > 0$ results in steady-state velocity-strengthening (VS) behavior, where stable slip is expected, and properties resulting in $(a - b) < 0$ lead to steady-state velocity-weakening (VW) behavior, where accelerating slip and hence stick-slip occur for sufficiently large regions. The total fault domain of size λ is partitioned into a frictional region of size (Figure 4.18). The frictional interface is composed of a region with velocity-weakening frictional properties of size λ_{VW}, surrounded by a velocity-strengthening domain. Most simulations are performed on a fault with a 24-km VW region, however we perform some additional studies with a 50-km VW region to verify that our results are consistent for longer fault models. Values for parameters used in our simulations are provided in Tables 4.1 - 4.5.

Note that the concept of "static strength" is not uniquely defined in such rate-and-state formulations of shear resistance in which slip rate is non-zero for any non-zero shear stress of the regularized friction formulation. Even if slip is prescribed at a fixed sliding rate, friction depends on the history of previous slip through the evolution of the state variable, which aims to capture the evolution of local contacts. However, at each fixed sliding rate V, the friction eventually evolves to the steady-state value $f_{ss}(V)$ given by (4.6). While that steady-state value depends on the sliding rate, the dependence is relatively minor, as it is logarithmic and $(a - b) \sim 0.01$ or less. We refer to this collection of similar friction values at slow slip rates appropriate for fault creep and earthquake nucleation as "quasi-static" friction coefficient. The product of this quasi-static friction coefficient and the effective confining stress (normal stress minus pore fluid pressure p) gives the shear resistance of

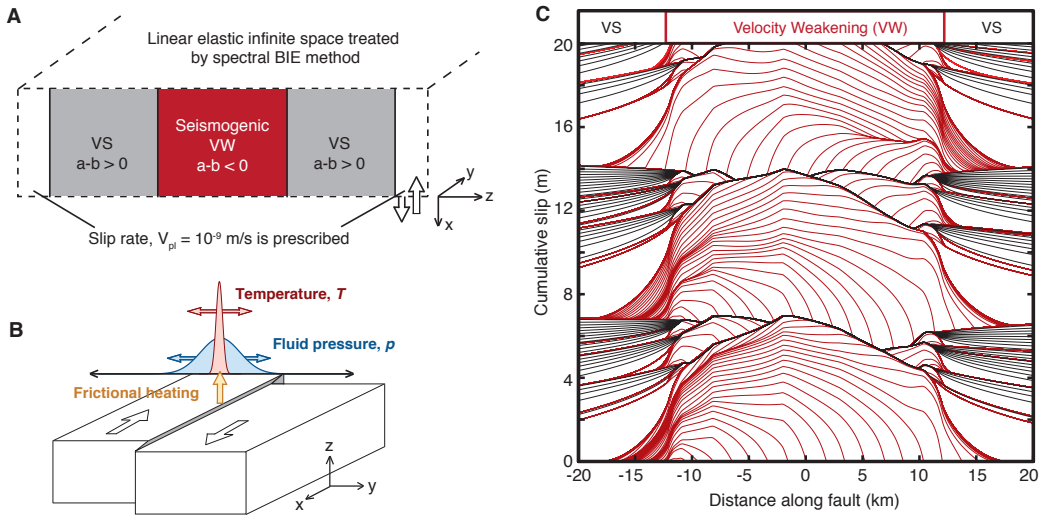

Figure 4.18: Model set up for simulations of earthquake sequences and slow slip with and without enhanced dynamic weakening. (A) The fault is composed of a velocity-weakening (VW) seismogenic region surrounded by two velocity-strengthening (VS) sections. A fixed plate rate is prescribed outside of these regions. (B) We incorporate enhanced dynamic weakening due to the thermal pressurization of pore fluids by calculating the evolution of temperature and pore fluid pressure due to shear heating and off-fault diffusion throughout our simulations. (C) A short section of the accumulated slip history for simulated sequences of crack-like earthquake ruptures and aseismic slip from the same simulation as rupture of Figure 4.2. Seismic events are illustrated with red lines plotted every 0.5 seconds while interseismic slip is plotted in black every 10 years.

faults at slow sliding rates, which we call quasi-static strength. As the representative value of such quasi-static strength, we choose the shear resistance of the fault steadily creeping at the prescribed long-term tectonic plate rate V_{plate} with the interseismic value of the pore pressure p_{int} (i.e. the value of pore pressure not affected by thermal pressurization of pore fluids):

$$\tau^{\text{strength}}_{\text{quasi-static}} = \tau_{ss}(V_{\text{plate}}) = (\sigma - p_{\text{int}}) \left[f_* + (a-b) \log \left(\frac{V_{\text{plate}}}{V_*} \right) \right]. \tag{4.7}$$

Laboratory experiments have shown that the standard rate-and-state laws (Equations 4.4-4.5) work well for relatively slow slip rates (10^{-9} to 10^{-3} m/s). However, at higher slip rates, including average seismic slip rates of ~1 m/s, additional dynamic weakening mechanisms, such as thermal pressurization, can be present. Thermal pressurization occurs when pore fluids within the fault shearing layer heat up, expand, and pressurize during dynamic rupture,

reducing the effective normal stress, and therefore shear resistance (Noda & Lapusta, 2010; Rice, 2006; Sibson, 1973). Thermal pressurization is governed in our simulations by the following coupled differential equations for pore pressure and temperature evolution (Noda & Lapusta, 2010):

$$\frac{\partial p(y,z;t)}{\partial t} = \alpha_{\text{hy}} \frac{\partial^2 p(y,z;t)}{\partial y^2} + \Lambda \frac{\partial T(y,z;t)}{\partial t}, \tag{4.8}$$

$$\frac{\partial T(y,z;t)}{\partial t} = \alpha_{\text{th}} \frac{\partial^2 T(y,z;t)}{\partial y^2} + \frac{\tau(z;t)V(z;t)}{\rho c} \frac{\exp(-y^2/2w^2)}{\sqrt{2\pi}w}, \tag{4.9}$$

where T is the temperature of the pore fluid, α_{hy} is the hydraulic diffusivity, α_{th} is the thermal diffusivity, τV is the source of shear heating distributed over a Gaussian shear layer of half-width w, ρc is the specific heat, y is the distance normal to the fault plane, and Λ is the coupling coefficient that gives pore pressure change per unit temperature change under undrained conditions.

The efficiency of the thermal pressurization process depends on the interplay of several parameters, where it may be the dominant weakening mechanism during unstable slip for some physical regimes (Rice, 2006; Segall et al., 2010). Shear heating, τV, must be strong enough to raise the temperature, given both the specific heat of the rock, ρc, and the half-width of the shear zone, w. Furthermore, this heat generation must not be dissipated too quickly by the thermal diffusivity, α_{th}, of the system. If sufficient heat is generated, the temperature of the system increases, and this increase is coupled into an increase in pressure of the fluid. The fluid then pressurizes as long as the hydraulic diffusivity, α_{hy}, is not too large. Some of these parameters are relatively well constrained from laboratory experiments: $\alpha_{\text{th}} = 10^{-6}$ m/s and $\rho c = 2.7$ MPa K (Noda & Lapusta, 2010; Rempel & Rice, 2006; Wibberley & Shimamoto, 2005). The change in pore pressure given a degree increase in temperature is described by the coupling coefficient Λ, which depends on the extent of damage and inelastic dilation around the shearing layer, with typical values ranging from 0.1 for highly damaged wall rock to 1 MPa/K for intact wall rock (Rempel & Rice, 2006; Rice, 2006). Two other parameters that substantially control the efficiency of thermal pressurization are the half-width of the shear zone w and hydraulic diffusivity α_{hy}, which can vary significantly: w can vary from 10^{-3} m to 10^{-1} m and α_{hy} can vary from 10^{-2} m^2/s to 10^{-6} m^2/s (Rice,

2006). Changing these two parameters within these ranges can make thermal pressurization either very efficient or completely negligible. The values we have chosen are motivated by prior studies (Noda & Lapusta, 2010; Rice, 2006) as well as our goal of examining ruptures with both efficient and inefficient enhanced dynamic weakening. In our simulations, we use uniform values for all hydrothermal properties other than w throughout the entire domain, as indicated in Tables 4.1-4.3. w is set to the values shown in Table 4.3 within the VW region, and then smoothly expands, over a 1 km region at the transition to the VS regions, to a 1-m shearing layer, so that thermal pressurization is effectively disabled in the VS regions.

In addition to thermal pressurization, we also consider a model with enhanced dynamic weakening due to flash heating (Rice, 2006), which has been shown to be efficient at generating self-healing pulses (Dunham et al., 2011a; Noda et al., 2009). Flash heating occurs when highly stressed microcontacts heat up dramatically during rapid slip and weaken dynamically. This process is often modeled with a characteristic slip velocity V_w at which flash heating activates. The friction coefficient then evolves to a residual level f_w and remains there during rapid sliding. To model flash heating, we make slight modifications to our steady-state rate-and-state equations to take into account the weakening following (Noda, 2008):

$$f_{ss}(V) = f(V, \theta_{ss}(V)) = \frac{f(V, D_{\mathrm{RS}}/V) - \frac{V}{|V|} f_w}{1 + |V|/V_w} + \frac{V}{|V|} f_w \tag{4.10}$$

where V is the slip rate on the fault, V_w is the characteristic slip velocity at which flash heating becomes effective, and f_w is the residual friction coefficient. Values for parameters used in our simulations with flash heating are provided in Table 4.4.

We use thermal pressurization in most of our simulations to demonstrate the effects of enhanced dynamic weakening, however the effects should be qualitatively consistent for other weakening mechanisms.

Earthquakes can nucleate only if the steady-state velocity-weakening region is larger than the nucleation size h^*. For 2-D problems, two theoretical estimates of the nucleation size in

mode III are (Rice & Ruina, 1983; Rubin & Ampuero, 2005):

$$h^*_{RR} = \frac{\pi}{4}\frac{\mu D_{\mathrm{RS}}}{(b-a)(\sigma-p)}; h^*_{RA} = \frac{2}{\pi}\frac{\mu D_{\mathrm{RS}} b}{(b-a)^2(\sigma-p)} \tag{4.11}$$

where μ is the shear modulus. Another important physical length-scale is the cohesive zone which represents the region at the rupture front under which the primary breakdown in shear resistance occurs. The quasi-static estimate of the cohesive zone Λ_0 is given as:

$$\Lambda_0 = C_1 \frac{\mu}{W} \tag{4.12}$$

with C_1 being a constant and the weakening rate $W = \frac{b\overline{\sigma}}{D_{\mathrm{RS}}}$ for the standard rate-and-state friction law. As the rupture speed increases to the limiting wave speed c_L (c_L is the shear wave speed in mode III), the cohesive zone collapses towards zero. Stronger rate-weakening mechanisms, such as thermal pressurization and flash heating, result in much larger weakening rates and reductions in the cohesive zone size, such that the criterion for sufficient numerical resolution becomes far more restrictive.

Previous studies established that $\Lambda_0/\Delta z$ of 3 to 5 is required to resolve dynamic ruptures with relatively mild weakening imposed through linear slip-weakening friction (Day et al., 2005). However we find that this is not sufficient with more efficient enhanced dynamic weakening, such as that which results in self-healing pulses. If one considers adiabatic and undrained conditions, then an upper bound for the weakening rate due to thermal pressurization can be expressed as (Noda & Lapusta, 2010),

$$W_{TP} = \frac{f\tau\Lambda}{\sqrt{2\pi}w\rho c}. \tag{4.13}$$

For the simulations with the most efficient thermal pressurization in this study ($f_{\mathrm{peak}} \approx 0.9$, $\tau_{\mathrm{peak}} \approx 45$ MPa, $\Lambda = 0.34$ MPa/K and $w = 1$ mm), W_{TP} is about 2035 MPa/m, which is five to six times larger than the weakening rate from rate-and-state friction $W_{RS} = 375$ MPa/m. We therefore use a spatial discretization of $\Delta z = 3.3$ m which resolves the quasi-static cohesive zone estimate by at least 25 cells and the nucleation size with more than 88 cells. This more stringent resolution criterion motivates the choice of 2-D calculations for this study. We have compared the results of our 2-D simulations with fully dynamic 3-D

Parameter	Symbol	Value
Loading slip rate	V_{plate}	10^{-9} m/s
Shear wave speed	c_s	3299 m/s
Shear modulus	μ	36 GPa
Thermal diffusivity	α_{th}	10^{-6} m^2/s
Specific heat	ρc	2.7 MPa/K
Rate-and-state parameters		
Reference slip velocity	V_*	10^{-6} m/s
Reference friction coefficient	f_*	0.6
Rate-and-state direct effect (VW)	a	0.010
Rate-and-state evolution effect (VW)	b	0.015
Rate-and-state direct effect (VS)	a	0.050
Rate-and-state evolution effect (VS)	b	0.003
Length scales		
Fault length	λ	96 km
Frictional domain	λ_{fr}	72 km
Velocity-weakening region	λ_{VW}	24 km
Cell size	Δz	3.3 m
Quasi-static cohesive zone	Λ_0	84 m
Nucleation size (Rice & Ruina, 1983)	h^*_{RR}	226 m
Nucleation size (Rubin & Ampuero, 2005)	h^*_{RA}	550 m

Table 4.1: Parameters for all simulations unless specified otherwise.

Parameter	Symbol	RS 1	RS 2	RS 3	RS 4
Interseismic effective normal stress	$\bar{\sigma} = (\sigma - p_{\text{int}})$	100 MPa	50 MPa	20 MPa	10 MPa
Reference friction coefficient	f_*	0.12	0.12	0.6	0.6
Characteristic slip	D_{RS}	5 mm	2.5 mm	1 mm	0.5 mm
Shear zone half-width	w	10 mm	1 mm	10 mm	1mm
Quasi-static cohesive zone	Λ_0	106 m	106m	106 m	106 m
Nucleation size (Rice & Ruina, 1983)	h^*_{RR}	282 m	282 m	282 m	282 m
Nucleation size (Rubin & Ampuero, 2005)	h^*_{RA}	688 m	688 m	688 m	688 m

Table 4.2: Parameters for models with only standard rate-and-state friction, without enhanced dynamic weakening.

simulations for models with milder enhanced dynamic weakening and found qualitatively similar results.

Parameter	Symbol	TP 1	TP 2	TP3
Interseismic effective normal stress	$\bar{\sigma} = (\sigma - p_{\text{int}})$	100 MPa	100 MPa	100 MPa
Rate-and-state direct effect (VS)	a	0.05	0.05	0.05
Characteristic slip	D_{RS}	4 mm	4 mm	4 mm
Shear zone half-width	w	10 mm	10 mm	10 mm
Hydraulic diffusivity	α_{hy}	10^{-3} m^2/s	10^{-4} m^2/s	10^{-5} m^2/s
Coupling coefficient	Λ	0.34 MPa/K	0.34 MPa/K	0.34 MPa/K
		TP 4ab	TP 5	
Interseismic effective normal stress	$\bar{\sigma} = (\sigma - p_{\text{int}})$	50 MPa	50 MPa	
Rate-and-state direct effect (VS)	a	0.025, 0.05	0.05	
Characteristic slip	D_{RS}	2 mm	2 mm	
Shear zone half-width	w	1 mm	1 mm	
Hydraulic diffusivity	α_{hy}	10^{-4}m^2/s	10^{-5} m^2/s	
Coupling coefficient	Λ	0.34 MPa/K	0.34 MPa/K	
		TP 6ab	TP 7abc	TP8
Interseismic effective normal stress	$\bar{\sigma} = (\sigma - p_{\text{int}})$	25 MPa	25 MPa	25 MPa
Rate-and-state direct effect (VS)	a	0.025, 0.05	0.0125, 0.025, 0.05	0.05
Characteristic slip	D_{RS}	1 mm	1 mm	1 mm
Shear zone half-width	w	10 mm	1 mm	10 mm
Hydraulic diffusivity	α_{hy}	10^{-4}m^2/s	10^{-4}m^2/s	10^{-4} m^2/s
Coupling coefficient	Λ	0.34 MPa/K	0.34 MPa/K	0.1 MPa/K

Table 4.3: Parameters for models with thermal pressurization of pore fluids.

Parameter	Symbol	FW1
Interseismic effective normal stress	$\bar{\sigma} = (\sigma - p_{\text{int}})$	25 MPa
Characteristic slip	D_{RS}	1 mm
Shear zone half-width	w	1 mm
Characteristic weakening velocity	V_w	0.14 m/s
Residual dynamic friction	f_w	0.12

Table 4.4: Parameters for models with flash weakening.

Parameter	Symbol	M2
Fault length	λ	192 km
Frictional domain	λ_{fr}	168 km
Velocity-weakening region	λ_{VW}	50 km
Cell size	Δz	3.3 m

Table 4.5: Length scales for longer fault model with thermal pressurization parameters TP1.

4.5.3 Methodologies for computing seismological inferences

In our dynamic simulations, the slip and stress evolution is computed at every point along the fault at all times. As such, we are able to calculate the the local and average energy quantities, stress and slip directly in our models (Figure 4.19). We utilize the averaging methodology of Noda and Lapusta (2012) to compute the energetically averaged properties directly from the local properties along the fault. The initial distribution of shear traction on the fault before an earthquake is denoted by $\tau^{\text{ini}}(z)$. An earthquake produces a slip distribution $\delta(z)$ and the traction along the fault changes to $\tau^{\text{fin}}(z)$. In our models, there is small non-zero slip everywhere on the fault during every event due to the nature of the rate-and-state framework. In terms of determining the area associated with the dynamic rupture process, it is appropriate to only consider points where the inertial term becomes significant. However, there is no exact quantitative criterion to define that. Hence we follow prior studies (Jiang & Lapusta, 2016; Lapusta et al., 2000; Noda & Lapusta, 2013; Noda et al., 2013) by defining the ruptured domain Σ to consist of locations that exceed a threshold slip rate of V_{th}:

$$\Sigma = \{\underline{z} \in \Omega | \underline{V}(\underline{z}) > V_{\text{th}}\}. \tag{4.14}$$

There is a sharp falloff in slip rate outside the ruptured area down to the creeping rate many orders of magnitude below the seismic slip rate. Thus, changing the threshold by even an order of magnitude or two does not change the rupture size appreciably. For the simulations presented in this study, we use a threshold of $V_{\text{th}} = 0.01$ m/s. We have explored the sensitivity of the rupture area calculated based on V_{th} ranging from 10^{-3} to 10^{-1} m/s and find minor variations, within 1%. Given this criterion for the rupture area, we are able to calculate all of the averaged and energetic quantities directly from the local properties along the fault.

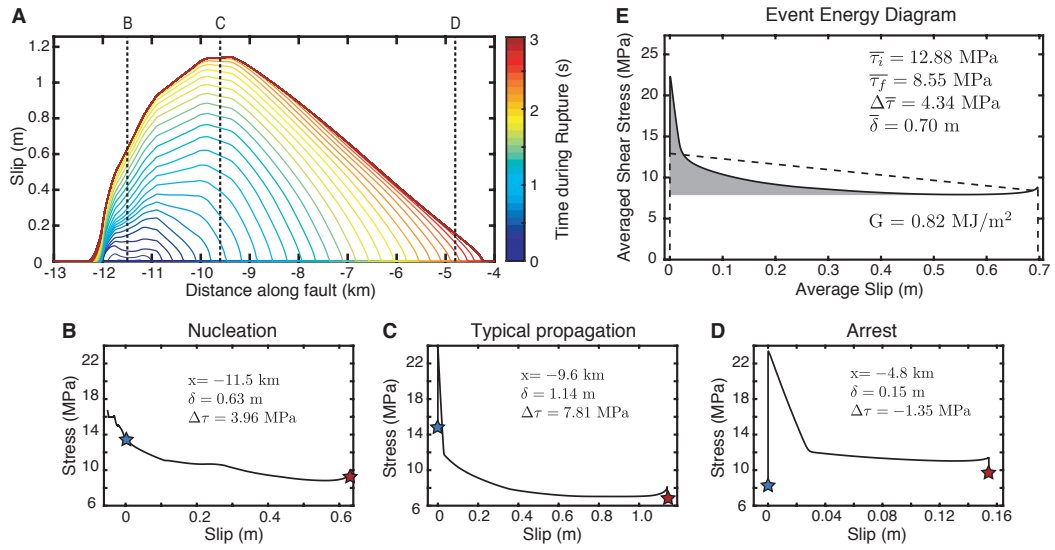

Figure 4.19: Averaging local on-fault behavior for entire rupture, for comparison with seismological observations. (A) Evolution of accumulated slip during a representative crack-like rupture with thermal pressurization. (B-D) The local evolution of shear stress with slip at three representative points showing: (B) the milder stress evolution during initial nucleation including preslip, (C) stress concentration followed by continuous weakening during typical rupture propagation, and (D) negative static stress drop near the arrest of the rupture. (E) Average shear stress vs. slip behavior which resembles the shape of the typical propagation location. The local behavior in all ruptures is variable, however we use the averaging methodology of Noda and Lapusta (2012) to construct the average shear stress vs. slip behavior and illustrate averaged source parameters.

For natural earthquakes, it is difficult to precisely determine the rupture area due to non-uniqueness and smoothing during inversion procedure. For large events, the rupture shape and dimension may be determined from finite-fault inversions, along with the corresponding local changes in slip and stress, depending on the parameterization of the inversion, including the choice of a minimum slip threshold for a given region to slip before being considered part of the ruptured area (P. Liu & Archuleta, 2000; Noda et al., 2013; Tinti et al., 2016; Ye et al., 2016b). Note that many seismological studies infer average slip, moment-based stress drops, and rupture dimensions for earthquakes based on spectral representations of the seismic waveforms fitted by a model based on a circular crack with constant rupture speed (Abercrombie & Rice, 2005; Rice, 2006; Viesca & Garagash, 2015). The stress drop consistent with energy partitioning is the energy-based or slip-weighted stress drop, which

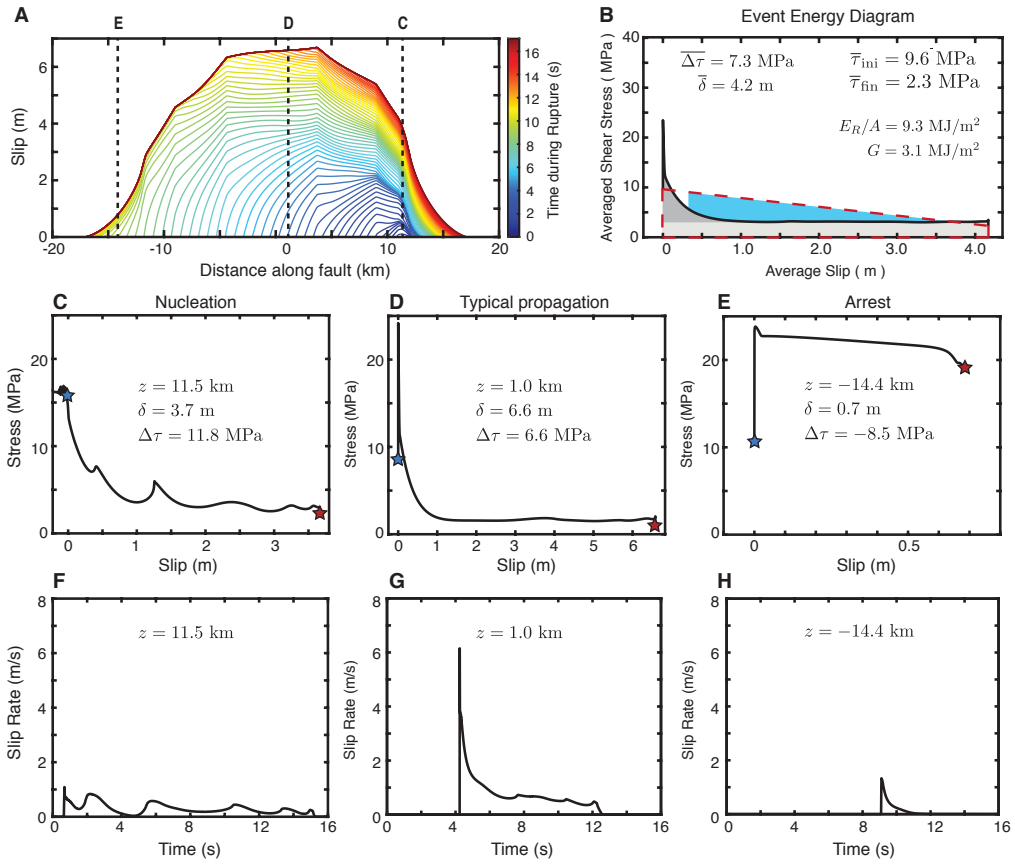

Figure 4.20: Relationship between local and average stress versus slip behavior for a crack-like rupture. (A) Evolution of accumulated slip during a representative crack-like rupture with thermal pressurization TP6a. Slip is contoured every 0.25 s. (B) Average shear stress vs. slip behavior. The local behavior in all ruptures is variable, however we use the averaging methodology of Noda and Lapusta (2012) to construct the average shear stress vs. slip behavior and illustrate averaged source parameters. (C-E) The local evolution of shear stress with slip at three different points throughout the rupture. (F-H) The local evolution of slip rate with time at the same points.

was proven to always be larger than the moment-based estimate (Noda et al., 2013). This reality, along with resolution limitations and the application of smoothing during inversions, suggest that seismologically estimated average stress drops most likely provide lower estimates for the needed energy-based stress drops for energy partitioning (Adams et al., 2016; Noda et al., 2013). Some recent studies used finite-fault inversions to estimate energy-based stress drops directly (Ye et al., 2016b).

In this study, we compare the averaged source properties from our simulated ruptures with published seismological inferences from 114 large ($M_w \geq 7.0$) megathrust earthquakes between 1990 and 2015 (Ye et al., 2016b), as well as inferences from the large crustal earthquakes shown in Table 4.6. The inferences for megathrust earthquakes, such as the energy-based stress drops, are based on teleseismic finite fault inversions, where the final rupture models depend on the choice of rupture speed in the parameterization of the inversion. For the comparisons in this study, we utilize the results of published finite fault inversions with a rupture speed of 2.5 km/s (Ye et al., 2016b).

Only moment-based estimates of static stress drop can be determined for the large crustal earthquakes, given published inferences of seismic moment and rupture dimensions. The estimates of the moment-based stress drop vary by about a factor of 2 given the assumed geometry of the source region and the dimensions inferred from published finite fault inversions. These estimates of moment-based stress drop most likely represent lower bounds for the energy-based stress drop, which is the more appropriate stress drop for considerations of energy partitioning. Published teleseismic and regional estimates of radiated energy for the large crustal earthquakes in Table 4.6 vary by about a factor of 4 within the published references.

4.5.4 Shear heating during frictional sliding

We aim to explore conditions compatible with the inferred low-stress, low-heat operation of mature faults. In addition, as the constitutive behavior in our simulations does not account for the production of macroscopic melt, maintaining temperatures below those for which substantial melt formation would be expected is important for producing models that are physically self-consistent. Frictional formulations such as standard rate-and-state laws as well as flash heating do not depend on macroscopic temperature changes and are therefore mathematically agnostic to the localization of shear and corresponding shear heating. We monitor the temperature changes throughout all of our simulations and use the results from only those simulations in which temperatures remain below 1000 ^{0}C, a representative equilibrium melting temperature for granitic compositions in Earth's crust (Rice, 2006).

Earthquake	Refs	E_R^t (J)	E_R^r (J)	M_0 (N-m)	L x W (km)	$\overline{\delta}$ (m)	$\overline{\Delta\tau}_M$ (MPa)
San Fernando 1971	(Bolt, 1986; Heaton, 1990; K. D. Smith et al., 1991)	–	1.5e+15	7.0e+18	12 x 14	1.2	8.1
Coyote Lake 1979	(Bolt, 1986; Heaton, 1990; K. D. Smith et al., 1991)	–	4.6e+13	3.5e+17	6 x 6	0.5	4.1
Imperial Valley 1979	(Abercrombie & Rice, 2005; Archuleta, 1984)	–	5.9e+14	6.7e+18	35 x 15	0.4	1.7
Morgan Hill 1986	(Bolt, 1986; Heaton, 1990; K. D. Smith et al., 1991)	–	1.4e+14	2.1e+18	20 x 8	0.4	2.9
Loma Prieta 1989	(Abercrombie & Rice, 2005; Wald et al., 1991)	5.4e+14	2.7e+15	3.1e+19	40 x 17	1.5	4.8
Landers 1992	(Abercrombie & Rice, 2005; Wald & Heaton, 1994)	3.0e+15	1.2e+16	7.7e+19	65 x 15	2.6	7.6
Northridge 1994	(Abercrombie & Rice, 2005; Wald et al., 1996)	3.1e+14	1.2e+15	1.3e+19	15 x 20	1.4	6.3
Kobe 1995	(Abercrombie & Rice, 2005; Wald, 1995)	8.5e+14	1.5e15	2.4e+19	60 x 20	0.7	1.7
Hector Mine 1999	(Abercrombie & Rice, 2005; Ji et al., 2002)	2.6e+15	3.2e+15	6.3e+19	41 x 13	3.9	15.5
Tottori 2000	(Choy & Boatwright, 2009; Tinti et al., 2005)	1.8e+15	1.3e+15	1.2e+19	30 x 20	0.7	2.3
Denali 2002	(Asano et al., 2005; Choy & Boatwright, 2004)	3.6e+16	–	7.6e+20	292 x 18	4.8	10.4
Fukuoka 2005	(Asano & Iwata, 2006; Yoo et al., 2010)	–	6.5e+14	1.2e+19	26 x 18	0.9	3.3
Kumamoto 2016	(Asano & Iwata, 2016; Kanamori et al., 2020)	–	2.1e+15	5.1e+19	40 x 15	2.8	9.5
Izmit 1999	(Kanamori & Ross, 2019; Yagi & Kikuchi, 2000)	6.0e+15	–	2.1e20	70 x 15	6.7	18.6

Table 4.6: Radiated energy estimate is denoted as regional E_R^r or teleseismic E_R^t, where available. The rupture length L and width W are approximated from slip distributions of finite fault inversions in the given references. Average slip is estimated from these parameters as $\overline{\delta} = M_0/(\mu A)$, with rigidity $\mu = 3 \times 10^{10}$ N-m^{-2}, and the moment-based stress drop is estimated as a rectangular source region as $\overline{\Delta\tau}_M = CM_0/A^{3/2}$, where C takes values of 2.53, 3.02, and 5.21 for aspect ratios of 1, 4 and 16, respectively (Noda et al., 2013).

Figure 4.21 illustrates the evolution of maximum fault temperature change over sequences of earthquakes and slow slip for the three models shown in Figure 4.3.

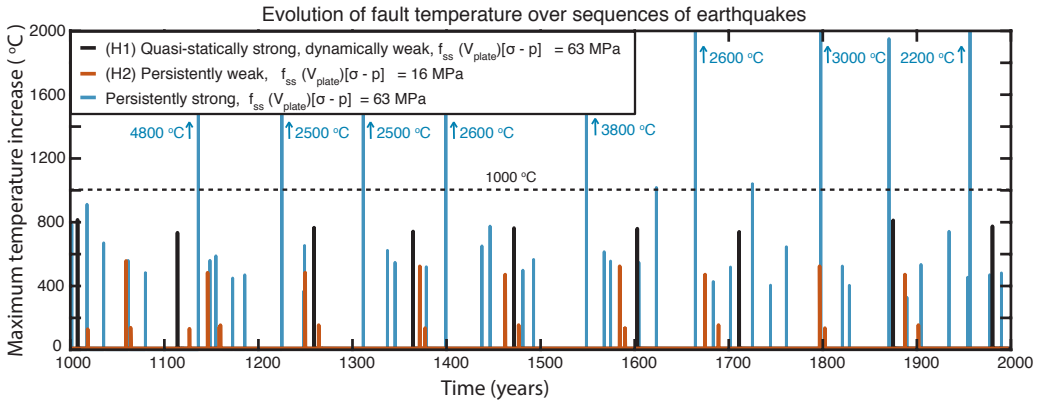

Figure 4.21: The history of maximum temperature increase along the fault during the three simulations shown in Figure 4.3B-C. The three fault models are representative cases for (H1) a quasi-statically strong, dynamically weak fault (black lines), (H2) a persistently weak fault (red lines), and a persistently strong fault (blue lines). The models consistent with low-heat, low-stress hypothesis (H1) and (H2) maintain maximum temperature changes below 1000^o C, whereas the temperature changes for the persistently strong fault routinely increases over 2000^o C during large ruptures, given the shear zone width of 10 mm. Note that we can reduce the maximum fault temperatures in the persistently strong fault model by increasing the width of the shearing zone.

The rate of shear heating during sliding on a frictional interface is proportional to the shear resistance and sliding rate, τV, and the average shear stress associated with dissipation and heat generation can be calculated as:

$$\tau_{\text{heat}}(t) = \frac{\int_0^t \int_\Omega \tau(z,t')V(z,t')dzdt'}{\int_0^t \int_\Omega V(z,t')dzdt'} \tag{4.15}$$

where Ω is the area of the fault interface. The associated temperature increase due to distributed shear within a shearing layer heavily depends upon the degree of localization. Let us consider the temperature rise due to slip distributed over a Gaussian shear layer with half-width, w. The temperature rise at the center of the layer as a function of time can be expressed as (Rice, 2006):

$$T(0,t) = \frac{1}{\rho c}\int_0^t \frac{\tau(t')V(t')dt'}{\sqrt{2\pi}\sqrt{w^2 + 2\alpha_{th}(t-t')}} \tag{4.16}$$

where α_{th} is the thermal diffusivity and ρc is the specific heat. In the simplified case of dissipation due to sliding at a fixed slip rate and a fixed residual stress level, ignoring any dissipation associated with the breakdown process during a rupture, the peak temperature change as a function of the shear zone half-width and the prescribed dynamic resistance level, assuming 1 and 5 meters of slip at $V = 1$ m/s, is shown in Figure 4.22. Substantial temperature increase is expected as the shearing layer becomes localized between 1 - 10 mm, except for very low dynamic resistance levels. For $w = 1$ mm, temperatures would be expected to increase by over 1000^o C if the dynamic resistance is greater than 3 MPa. Even for a much broader layer of $w = 10$ mm, substantial temperature increase would be expected for sliding at stress levels above 10 MPa. Note that, for slip rates higher than 1 m/s as commonly observed in dynamic rupture simulations, the shear heating production rate increases, leading to even higher temperatures. In addition, this consideration ignores the dissipation associated with the breakdown process, which may be comparable to or even greater than the dissipation at low residual stress levels.

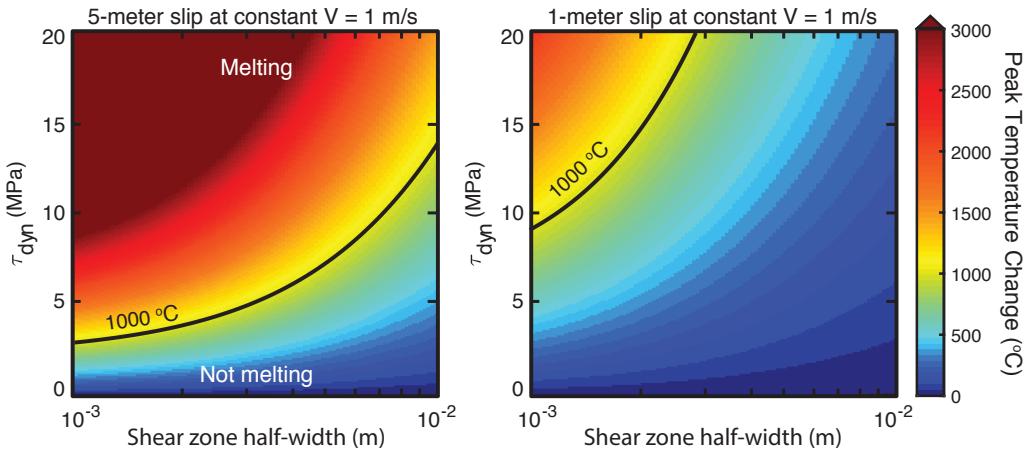

Figure 4.22: Peak temperature rise at varying dynamic levels of shear resistance and degrees of shear localization after 5 meters (right) and 1 meter (left) of slip at a fixed slip velocity of 1 m/s. For shear localized within layers of 1 mm half-width, resistance levels must be lower than 10 MPa even for 1 meter of slip to avoid temperature rises above 1000 ^{0}C.

4.5.5 Approximation for off-fault plasticity

As enhanced dynamic weakening can lead to rapid and large dynamic stress changes, the slip rates in models with perfectly linear elastic bulk materials can reach unphysical levels (> 100 m/s), particularly for fault models with higher effective normal stress (e.g. $\overline{\sigma}$ = 100 MPa). In real rocks, such high slip rates, and hence strain rates, would be mitigated by the onset of additional inelastic deformation around the rupture front, which is not explicitly included in the spectral boundary integral method that we use.

Numerical studies of dynamic rupture propagation with off-fault Drucker-Prager plasticity have shown that imposing a maximum slip velocity can mimic the effect of off-fault energy loss due to the plastic yielding of the off-fault materials under high strain rates (Andrews, 2004). In full consideration of plasticity, the yielding conditions depend upon the bulk material properties and confining conditions. For consistency and simplicity, here we employ a fixed value of $V_{\max}$ = 15 m/s, motivated by yielding considerations at a representative seismogenic depth of 10 km (Andrews, 2004). We have explored a range of maximum velocities in our simulations and found that the qualitative behavior of the resulting ruptures, including the relationships among seismological parameters of interest, such as radiated energy, apparent stress, radiation efficiencies, stress drop, and average slip, do not substantially change for velocity limits of 10 m/s or above.

Interestingly, we find that the effect of mimicking the off-fault dissipation through the slip velocity limit is much larger for single ruptures with a given prestress than for ruptures in sequences of earthquakes and slow slip. Limiting slip velocities for single ruptures with the same prestress conditions can result in slower rupture propagation and diminished slip (Figure 4.23). In the context of sequences of events, however, the additional dissipation is balanced by ruptures nucleating at slightly higher average shear prestress in the cases that we have examined. This compensation, in turn, results in similar kinematics, such as average slip and stress drops, but mildly different energy partitioning (Figure 4.24). Simulations of single dynamic ruptures with the explicit incorporation of off-fault plasticity as

well as enhanced dynamic weakening due to flash heating have also shown that the addition of off-fault plasticity increases the prestress levels at which self-healing pulses may occur (Dunham et al., 2011a). In our simulations, we find that, following the first several events (Figure 4.24), the average stress drop and slip tend to be comparable for simulations with and without the velocity limit, though the average breakdown energy and radiated energy differ. The initial weakening rate during ruptures is generally similar (Figure 4.24), but it is eventually slightly restricted by the velocity limit, leading to mildly larger G, which is expected with the incorporation of off-fault plasticity. However, while $\overline{\Delta\tau}$ is similar, $\overline{\tau}_{\text{ini}}$ and $\overline{\tau}_{\text{fin}}$ are both higher for ruptures including the velocity limit, though the dynamic level $\overline{\tau}_{\text{dyn}}$ is more or less the same, resulting in a larger undershoot and therefore more radiated energy for the same static stress drop and slip (Figure 4.24).

These results highlight the importance of studying effects of off-fault plasticity on rupture propagation within the context of earthquake sequences where stress conditions evolve in a self-consistent manner based on previous slip events. Note that much more stringent and perhaps unreasonable limits (e.g., $V_{\text{max}} = 1$ m/s) favor higher prestress conditions and predominantly crack-like rupture propagation. The specific effects of off-fault plasticity on rupture propagation and energy partitioning merits much more detailed study.

4.5.6 Reference to idealized crack model

In comparing local slip duration of crack-like and pulse-like ruptures (Figure 4.3), we refer to the idealized case of a 2-D antiplane rupture expanding as a symmetric elliptical crack with constant rupture speed and stress drop, which has been extensively studied both analytically and numerically (Kostrov, 1964; Madariaga, 1976). The rupture expands with constant rupture speed v_r to a crack half-length a, then abruptly arrests at $t = t^{\text{arr}} = \frac{a}{v_r}$, producing the slip profile (Kostrov, 1964):

$$\delta_1(z, t^{\text{arr}}) = \frac{1}{E\left(\sqrt{1 - v_r^2/c_s^2}\right)} \frac{\Delta\tau}{\mu} \left(a^2 - z^2\right)^{1/2} \tag{4.17}$$

where μ is the shear modulus, $\Delta\tau$ is the stress drop which is uniform over the rupture length, c_s is the shear wave speed, and E is the complete elliptic integral of the second

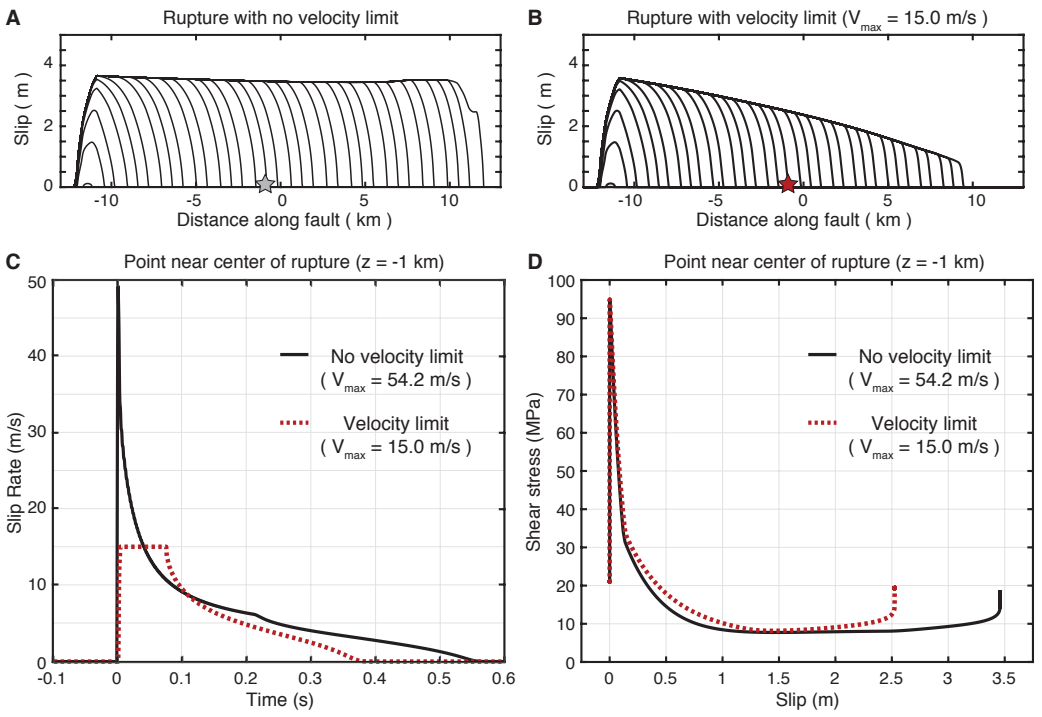

Figure 4.23: Using local velocity limit as an approximation for off-fault plasticity. (A-B) Accumulation of slip during two dynamic ruptures with the same prestress in simulations without (A) and with (B) an imposed velocity limit utilized to mimic effects of off-fault plasticity. (C-D) Local slip rate versus time (C) and shear stress versus slip (D) at a point near the center of the simulated ruptures (denoted by star in A and B). The initial weakening behavior is preserved for a velocity limit of 15 m/s, however, the restricted dynamics lowers the weakening rate, increases the breakdown energy G, limits the amount of slip during the rupture, resulting in a milder pulse.

kind. Following the abrupt arrest is a period of wave-mediated stress redistribution along with the propagation of healing waves from the ends of the rupture. This period of stress redistribution leads to an adjustment of the final (static) slip profile to:

$$\delta_1(z, t^{\text{fin}}) = \frac{\Delta\tau}{\mu}\left(a^2 - z^2\right)^{1/2}. \tag{4.18}$$

The wave-mediated stress adjustment following rupture arrest results in a stress overshoot where the final stress is lower than the dynamic sliding level. This stress overshoot can vary from 15 percent at $v_r = 0.6c_s$ to about 20 percent at $v_r = 0.9c_s$ from the static solution (Madariaga, 1976).

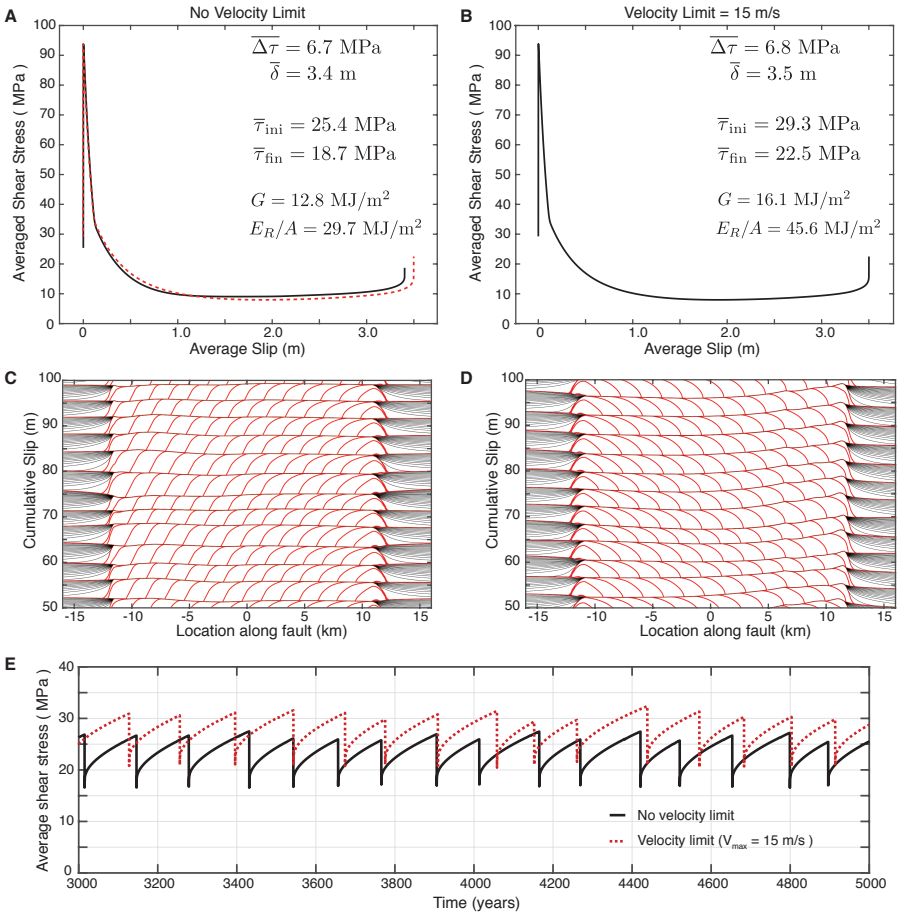

Figure 4.24: Long-term behavior of simulations with velocity limit. (A-B) Average shear stress vs. slip diagrams for events with similar stress drop and slip after long-term simulations of sequences of seismic and aseismic slip without (A) and with (B) a velocity limit to mimic the effects of off-fault plasticity. The average curve for the rupture with the velocity limit in (B) is overlain on (A) as a red-dashed contour for comparison. Initial weakening is generally consistent but is constrained by the velocity limit, resulting in more continuous weakening and mildly larger G. The higher initial stress also results in greater overall undershoot and higher E_R/A. (C-D) The general accumulation of slip within each event is similar for the long-term behavior of simulations without (C) and with (D) the velocity limit. (E) The average shear stress is higher in simulations with the velocity limit, which overcompensates for the additional effects due to limited velocity

After the abrupt arrest at the rupture boundary, slip continues within the center of the ruptured region until the arrival of healing waves propagating from the boundaries. Accounting for the propagation of healing waves, assumed to propagate at speed c_h, the total slip duration

can be estimated as:

$$T = a\left(\frac{1}{v_r} + \frac{1}{c_h}\right). \tag{4.19}$$

Similarly, the local sliding duration or rise time as a function of location can be estimated as,

$$t(x_3) = \left(\frac{1}{v_r} + \frac{1}{c_h}\right)(a - |z|)\,. \tag{4.20}$$

The spatial average of the rise time over the ruptured region is then,

$$\bar{t} = \frac{\left(\frac{1}{v_r} + \frac{1}{c_h}\right)\int_{-a}^{a}(a - |z|)dz}{2a} = \frac{a}{2}\left(\frac{1}{v_r} + \frac{1}{c_h}\right) \tag{4.21}$$

giving the ratio $\bar{t}/T = 0.5$. Note that for similar considerations with a perfectly symmetric rupture in 3D, the average rise time would be,

$$\bar{t} = \frac{\left(\frac{1}{v_r} + \frac{1}{c_h}\right)\int_0^{2\pi}\int_0^{a}(a - r)r\,dr\,d\theta}{\pi a^2} = \frac{a}{3}\left(\frac{1}{v_r} + \frac{1}{c_h}\right) \tag{4.22}$$

with the same total duration T. The spatial average of the rise time is smaller in 3D given that a greater proportion of the rupture area consists of near-arrest portions of the rupture where slip durations are relatively short compared to the interior. In this case, the ratio of the average rise time to duration is $\bar{t}/T = 0.33$, which is a modest adjustment of the 2D solution.

4.6 Supplementary text

4.6.1 Energy budget for earthquakes

The earthquake energy budget considers the partitioning of the total strain energy change ΔW into the dissipated energy, E_{Diss}, and the energy radiated away from the source region to the far-field, E_R:

$$\Delta W = E_{\text{Diss}} + E_R. \tag{4.23}$$

This relation can also be written per unit source area as:

$$\Delta W/A = E_{\text{Diss}}/A + E_R/A. \tag{4.24}$$

The total strain energy change per unit area on the fault $\Delta W/A$ is given by (Kostrov, 1974):

$$\Delta W/A = \frac{1}{2}(\bar{\tau}_{\text{ini}} + \bar{\tau}_{\text{fin}})\bar{\delta}, \tag{4.25}$$

where $\bar{\tau}_{\text{ini}}$ is the average initial stress, $\bar{\tau}_{\text{fin}}$ is the average final stress, $\bar{\delta}$ is the average final slip, and where (Noda & Lapusta, 2012):

$$\bar{\tau}_{\text{ini}} = \frac{\int_{\Sigma} \tau_{\text{ini}}(z)\delta_{\text{fin}}(z)dz}{\int_{\Sigma} \delta_{\text{fin}}(z)dz}, \tag{4.26}$$

$$\bar{\tau}_{\text{fin}} = \frac{\int_{\Sigma} \tau_{\text{fin}}(z)\delta_{\text{fin}}(z)dz}{\int_{\Sigma} \delta_{\text{fin}}(z)dz}. \tag{4.27}$$

In this study, we follow the work of Noda and Lapusta (2012), which provides an averaging methodology for constructing the average shear stress vs. slip diagrams, $\overline{\tau}(\delta')$. The dissipated energy within the source volume can then be calculated by integrating the area under the average stress-slip curve in the energy diagram,

$$E_{\text{Diss}} = \int_0^{\overline{\delta}} \overline{\tau}(\delta')d\delta', \tag{4.28}$$

and the energy that is radiated outside of the source region as seismic waves is determined by the difference between the strain energy change and dissipated energy within the volume,

$$E_R = \Delta W - E_{\text{Diss}}. \tag{4.29}$$

While it is presumed that the radiated energy can be inferred from seismological observations (Boatwright & Choy, 1986; Dahlen, 1977; Husseini & Randall, 1976; Kanamori & Brodsky, 2004; Kanamori & Rivera, 2013; Kostrov, 1974; Kostrov & Das, 1988; Venkataraman & Kanamori, 2004; Ye et al., 2016b), determining the total strain energy change and dissipated energy is challenging as it requires knowledge of the absolute stress levels throughout the source process. The dissipated energy is often partitioned further into the breakdown energy G (Cocco et al., 2004; Palmer & Rice, 1973) and the "frictionally dissipated" energy E_F/A. The breakdown energy G is thought to be the part of the dissipated energy that controls the dynamics of the rupture, often considered as the frictional analog of fracture energy from singular and cohesive-zone models of dynamic fracture theory. The so-called frictionally dissipated energy E_F is the remaining portion of the dissipated energy which is assumed to not affect the dynamics of the source process. Note that while the only source of dissipation in our simulations is through frictional resistance, natural shear ruptures can also experience contributions from dissipation within the surrounding volume, such as from the activation

or production of damage during ruptures. We partially approximate this effect by imposing the velocity limit, as discussed in the Section 4.5.

The averaging methodology for the representative shear stress vs. slip evolution during dynamic rupture can serve as the energy partitioning diagram as it preserves the total event energy quantities such as strain energy change, dissipated energy, and therefore radiated energy. However it does not necessarily precisely preserve the average breakdown energy. The true average breakdown energy can be defined as the spatial average of the local breakdown energy with respect to the local stress minima $\tau_{\min}(x)$:

$$G = \frac{1}{A}\int_{\Sigma}\left[\int_{0}^{\delta(\tau_{\min(x)})}\tau(\delta) - \tau_{\min}(\delta)d\delta\right]dz \tag{4.30}$$

which is how we compute the average breakdown energy in our models. This is not necessarily equivalent to the breakdown energy reflected in the average diagram, since the minimum shear stress of the average curve does not have a simple relation to the minima of the curves of each ruptured point. Numerical studies of crack-like ruptures including thermal pressurization found that these two averaged quantities give similar, but not identical results (Perry et al., 2020). Therefore, the representation of G from the average energy diagram can illustrate the average breakdown energy, but does not represent its exact value.

4.6.2 Standard analysis of earthquake energy balance

The standard earthquake energy analysis considers an idealized average stress vs. slip rupture model (Figure 4.4) in order to express energy-related quantities that are thought to be relevant to the source dynamics in terms of potentially seismologically-inferable quantities, namely stress drop, average slip, and radiated energy. An important aspect of the analysis is the concept of "available energy," or the energy associated with the breakdown process and radiation, effectively the energy thought to be relevant to the dynamics of the earthquake rupture (Dahlen, 1977; Husseini & Randall, 1976; Kanamori & Brodsky, 2004; Kanamori & Rivera, 2013; Kostrov, 1974; Kostrov & Das, 1988; Venkataraman & Kanamori, 2004; Ye et al., 2016b). We can define the true available energy per unit area $\Delta W_0^{\text{true}}/A$ as the sum of the breakdown energy (defined per unit source area) and radiated energy per unit source

area:

$$\Delta W_0^{\text{true}}/A = G + E_R/A. \tag{4.31}$$

Given this definition, one can also compare the relative magnitudes of the breakdown and radiated energy through a quantity known as radiation efficiency (Venkataraman & Kanamori, 2004):

$$\eta_R^{\text{true}} = \frac{E_R/A}{G + E_R/A} = \frac{E_R/A}{\Delta W_0^{\text{true}}/A}. \tag{4.32}$$

The determination of the available energy is fairly straight forward given the idealized energy diagram of Figure 4.4 (Kanamori & Heaton, 2000; Kanamori & Rivera, 2013; Venkataraman & Kanamori, 2004). In this idealized model, the shear stress evolution follows simplified linear slip weakening where stress drops linearly from an initial value $\overline{\tau}_{\text{ini}}$ until slip reaches a critical value D_c, at which the stress remains constant at $\overline{\tau}_{\text{dyn}}$ for the remainder of slip, with $\overline{\tau}_{\text{fin}} = \overline{\tau}_{\text{dyn}}$. The available energy in this case can be represented by:

$$\Delta W_0^{\text{inf}}/A = \frac{1}{2}\overline{\Delta\tau}\,\overline{\delta}, \tag{4.33}$$

which we call the seismologically-inferable available energy, as it is based on quantities that can be inferred seismologically. Here $\overline{\delta}$ is the average slip and $\overline{\Delta\tau}$ is the energy-based stress drop (Noda & Lapusta, 2012; Noda et al., 2013):

$$\overline{\Delta\tau} = \bar{\tau}_{\text{ini}} - \bar{\tau}_{\text{fin}} = \frac{\int_\Sigma \Delta\tau(z)\delta_{\text{fin}}(z)dz}{\int_\Sigma \delta_{\text{fin}}(z)dz}. \tag{4.34}$$

Given this definition, one defines the seismologically-inferable radiation efficiency as:

$$\eta_R^{\text{inf}} = \frac{E_R}{\Delta W_0^{\text{inf}}/A} = \frac{E_R/A}{\frac{1}{2}\overline{\Delta\tau}\,\overline{\delta}}. \tag{4.35}$$

This quantity can, and has been, estimated from seismological observations (Venkataraman & Kanamori, 2004; Ye et al., 2016b). Note that while $0 \le \eta_R^{\text{true}} \le 1$ by definition, η_R^{inf} can in principle exceed 1. In that sense, η_R^{true} can be called a radiation efficiency, but η_R^{inf} is more accurately a radiation ratio (Noda et al., 2013).

Within the context of the idealized rupture model represented by the standard energy diagram (Figure 4.4), it can be seen that:

$$\Delta W_0^{\text{inf}}/A \equiv \frac{1}{2}\overline{\Delta\tau}\,\bar{\delta} = \Delta W - E_F = E_R/A + G \equiv \Delta W_0^{\text{true}}/A. \tag{4.36}$$

Given this notion of available energy, there have also been attempts to estimate the average breakdown energy G for natural earthquakes based on $\Delta W_0^{\text{inf}}/A$ and E_R/A (Abercrombie & Rice, 2005; Rice, 2006; Ye et al., 2016b). Assuming relations equivalent to the standard energy diagram, one can subtract the radiated energy E_R/A from the seismologically-inferred available energy $\Delta W_0^{\text{inf}}/A$, thus leading to the seismologically-estimated breakdown energy G^{inf}:

$$G^{\text{inf}} = \Delta W_0^{\text{inf}}/A - E_R/A. \tag{4.37}$$

Substituting values that can be inferred seismologically, we can define the inferable quantity (Abercrombie & Rice, 2005; Rice, 2006):

$$G' = \frac{1}{2}\bar{\delta}\left(\overline{\Delta\tau} - \frac{2\mu E_R}{M_0}\right), \tag{4.38}$$

where μ is the shear modulus and M_0 is the seismic moment of the event. The last term is proportional to the apparent stress, $\sigma_A = \mu\frac{E_R}{M_0}$ (Wyss & Brune, 1968).

4.6.3 Discrepancy between dynamic fault resistance and final post-earthquake stress: consequences for estimating energy-related quantities

In our simulations, the final average shear stress is typically not the same as the dynamic level of shear stress, which is a potential issue with the standard energy analysis. This mismatch is due to either a dynamic stress undershoot, as typical for self-healing pulses, or a dynamic stress overshoot, as often the case for crack-like ruptures (Figure 4.6; Kanamori & Rivera, 2013; McGarr, 1999; Viesca & Garagash, 2015). Note that the two levels of stress are not expected to be linked physically, since the dynamic shear resistance is determined by a host of mechanisms acting during slip, such as rate-and-state friction, shear heating, fluid effects, etc, while the final static stress depends only on the initial stress and the final static slip.

The discrepancy between the final stress and dynamic fault resistance can significantly affect the considerations of the earthquake energy balance. Here, we consider a few relevant

simple modifications of the standard energy diagram and the resulting relationship between the inferable and true available energies, ΔW_0^{inf} and ΔW_0^{true}, respectively. Recall that the frictionally dissipated energy E_F is defined as the energy dissipated below the lowest average dynamic level of shear stress $\overline{\tau}_{\text{dyn}}$ in the average stress vs. slip diagram. We can define an alternative form of the true available energy $\Delta \hat{W}_0^{\text{true}}$ based on the average stress vs. slip diagram:

$$\Delta \hat{W}_0^{\text{true}}/A = \Delta W/A - E_F/A = \frac{1}{2}(\bar{\tau}_{\text{ini}} + \bar{\tau}_{\text{fin}})\bar{\delta} - \bar{\tau}_{\text{dyn}}\bar{\delta}. \tag{4.39}$$

Note that this expression for the true available energy is not necessarily the same as the previous definition $\Delta W_0^{\text{true}}/A \equiv E_R/A + G$, as mentioned earlier due to the complicated relationship between the minimum of the average curve and the average of the local stress-slip curves which provide G. In addition, the relationship assumes that the fault does not recover appreciably from the minimum level of average dynamic stress before the final slip. Additional energy may be dissipated after the rupture reaches its minimum dynamic level of stress if it restrengthens with slip rather than only at the final slip. In our simulations, we find that this effect is normally negligible compared to the other energy quantities and $\Delta \hat{W}_0^{\text{true}} \approx \Delta W_0^{\text{true}}$.

If the rupture behavior includes a stress undershoot of size $\gamma\overline{\Delta\tau}$, as occurs in self-healing pulse-like ruptures, $\Delta \hat{W}_0^{\text{true}}$ may be written in terms of $\gamma\overline{\Delta\tau}$ and ΔW_0^{inf}:

$$\begin{aligned}\Delta \hat{W}_0^{\text{true}}/A &= \frac{1}{2}\overline{\Delta\tau}\bar{\delta} + (\bar{\tau}_{\text{fin}} - \bar{\tau}_{\text{dyn}})\bar{\delta} \\ &= \Delta W_0^{\text{inf}}/A + \gamma\overline{\Delta\tau}\bar{\delta}.\end{aligned} \tag{4.40}$$

We see then that the ratio between the true and seismologically-inferable available energies depends on the extent of the over- or undershoot:

$$\frac{\Delta \hat{W}_0^{\text{true}}}{\Delta W_0^{\text{inf}}} = 1 + 2\gamma. \tag{4.41}$$

If $\gamma = 0$, we have the idealized case and $\Delta \hat{W}_0^{\text{true}} = \Delta W_0^{\text{inf}}$. If there is a non-negligible undershoot, then $\gamma > 0$ and $\Delta \hat{W}_0^{\text{true}} > \Delta W_0^{\text{inf}}$. The ratio between the true and seismologically-inferable available energies can also be expressed as the ratio between η_R^{inf} and η_R^{true} (Figure

4.25):

$$\frac{\Delta \hat{W}_0^{\text{true}}}{\Delta W_0^{\text{inf}}} = \frac{E_R/A + G}{\frac{1}{2}\overline{\Delta\tau}\,\overline{\delta}} = \frac{\eta_R^{\text{inf}}}{\eta_R^{\text{true}}}. \tag{4.42}$$

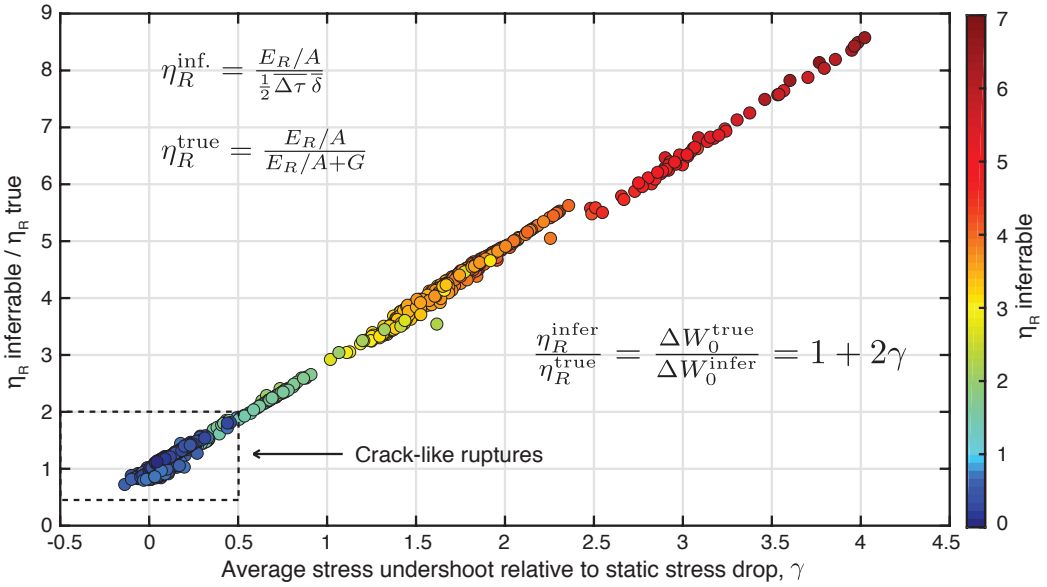

Figure 4.25: Comparison of seismologically-inferable and true radiation efficiencies as a function of stress undershoot. As the average undershoot exceeds 0.5 of the static stress drop, the inferable radiation efficiency exceeds the true efficiency by more than a factor of 2.

Note that, for rupture behavior with a non-zero increase from $\overline{\tau}_{\text{ini}}$ to $\overline{\tau}_{\text{peak}}$ (called strength excess), the additional dissipated energy does not alter the available energy. This initial increase affects how available energy is partitioned into breakdown energy G and radiated energy E_R/A, but does not change the actual available energy ΔW_0^{true} of the rupture. The strength excess increases the breakdown energy G at the expense of radiated energy E_R/A.

The same argument can be made for rupture behaviors with an overshoot as is often the case with crack-like ruptures, and equation (S37) still applies, with negative values of γ. This behavior would result in $\Delta \hat{W}_0^{\text{true}} < \Delta W_0^{\text{inf}}$, but in most simulations $|\gamma| \ll 1$ for crack-like ruptures, and thus $\Delta W_0^{\text{true}} \approx \Delta W_0^{\text{inf}}$. Numerical studies have shown that the seismologically estimated breakdown energy G^{inf} agrees well (within a factor of 2) with the true breakdown energy G for crack-like events incorporating thermal pressurization (Perry et al., 2020),

which is consistent with the simulations in this study (Figure 4.17).

As we have seen, if the fault experiences a substantial stress undershoot, the available energy for radiation and breakdown would be significantly underestimated. Let us consider the case where the fault experiences a stress undershoot of magnitude $\gamma\overline{\Delta\tau}$ and we can approximate the breakdown energy as $G \approx \frac{1}{2}(1+\gamma)\overline{\Delta\tau}D_c$. Then:

$$\begin{aligned} E_R/A &= \Delta\hat{W}_0^{\text{true}}/A - G \\ &= \frac{1}{2}\overline{\Delta\tau}\bar{\delta} + \gamma\overline{\Delta\tau}\bar{\delta} - \frac{1}{2}(1+\gamma)\overline{\Delta\tau}D_c, \end{aligned} \tag{4.43}$$

$$\eta_R^{\text{inf}} = \frac{E_R}{\Delta W_0^{\text{inf}}/A} = 1 + 2\gamma - (1+\gamma)D_c/\bar{\delta}. \tag{4.44}$$

Thus, E_R will exceed ΔW_0^{inf} for any undershoot such that:

$$\gamma > \frac{D_c/\bar{\delta}}{2 - D_c/\bar{\delta}}, \tag{4.45}$$

which would lead to inferable radiation efficiencies (more appropriately called ratios) of $\eta_R^{\text{inf}} > 1$. If $\gamma > 1$, meaning that the undershoot is larger than the average stress drop, then the stress undershoot is large enough that E_R/A would always exceed ΔW_0^{inf}, no matter the slip-weakening distance D_c. If $\Delta W_0^{\text{inf}} \approx \Delta W_0^{\text{true}}$, as is the case for crack-like ruptures, then $\eta_R^{\text{inf}} \approx \eta_R^{\text{true}}$. However, for a substantial undershoot, as is the case for self-healing pulse-like ruptures, one would expect $\eta_R^{\text{inf}} \gg \eta_R^{\text{true}}$.

Notice that G^{inf} is also directly related to η_R^{inf}:

$$G^{\text{inf}} = \Delta W_0^{\text{inf}}/A - E_R/A \rightarrow \frac{G^{\text{inf}}}{\Delta W_0^{\text{inf}}/A} = 1 - \eta_R^{\text{inf}}. \tag{4.46}$$

Hence, if ΔW_0^{inf} underestimates ΔW_0^{true}, and we still subtract E_R/A, then we are left with a significant underestimation of the true breakdown energy G. Indeed, in the case of substantial undershoot, $\gamma > 0.5$, the radiated energy can exceed ΔW_0^{inf}, therefore estimates of G^{inf} will also be negative (Figure 4.4c), which is physically inconsistent with the concept of breakdown energy.

There is no simple way to calculate G reliably for self-healing pulse-like ruptures using current seismological observations. One approach has considered the case of a stress undershoot and additionally assumed a complete coseismic stress loss ($\overline{\tau} = 0$) during large pulse-like events (Viesca & Garagash, 2015). In that work, $G_{\max}$ is defined as:

$$G_{\max} = G^{\inf} + \bar{\tau}_{\text{fin}}\bar{\delta} = \frac{1}{2}\bar{\delta}\left(\overline{\Delta\tau} - \frac{2\mu E_R}{M_0}\right) + \bar{\tau}_{\text{fin}}\bar{\delta}. \tag{4.47}$$

To calculate $G_{\max}$, the absolute final stress on the fault must be known (or assumed) and the dynamic level of stress is assumed to be zero, thereby assuming that the available energy is the total strain energy change. This metric assumes that all of the dissipated energy is incorporated into the breakdown energy, hence it represents the maximum potential breakdown energy given the assumed absolute stress levels. Note that $G_{\max}$ can dramatically overestimate G if the fault does not weaken to zero strength.

4.6.4 Discrepancy between dynamic fault resistance and final post-earthquake stress: consequences for apparent stress

The existence of stress undershoot/overshoot also affects the interpretation of apparent stress. A number of seismological studies have associated variations in apparent stress with differences in static stress drop (Ide & Beroza, 2001; Ma & Archuleta, 2006; McGarr, 1999; Perez-Campos & Beroza, 2001). We can approximate the relationship between apparent stress and static stress drop by dividing equation (S40) by average slip:

$$\sigma_A = \frac{E_R}{\bar{\delta}A} = \overline{\Delta\tau}\left[\frac{1+2\gamma}{2} - \frac{1+\gamma}{2}\frac{D_c}{\bar{\delta}}\right]. \tag{4.48}$$

This relation shows that increasing static stress drop $\overline{\Delta\tau}$ indeed leads to increasing apparent stress, for the same γ and $D_c/\bar{\delta}$. However, even if two ruptures have comparable static stress drop, the apparent stress would considerably differ if the two ruptures exhibit different undershoot/overshoot. For the idealized case with no substantial undershoot ($\gamma = 0$), $\sigma_A \approx \overline{\Delta\tau}\left[1/2 - D_c/2\bar{\delta}\right]$, whereas for an undershoot of $\gamma = 1$, $\sigma_A \approx \overline{\Delta\tau}\left[3/2 - D_c/\bar{\delta}\right]$. Assuming again that D_c is similar for the two cases, this would result in over a factor of 3 greater apparent stress for the undershoot of $\gamma = 1$. For $\gamma = 2$, this increases to at least a factor of 5.

Our simulations indeed show that the ratio of radiated energy to moment, and thus apparent stress, increases for both increasing static stress drop and undershoot (Figure 4.7). In fact, ruptures with smaller static stress drops but considerable undershoot can have higher apparent stress than ruptures with larger static stress drops but mild to no undershoot. For example, if we examine crack-like ruptures and self-healing pulses in models with the same quasi-static strength, our simulated self-healing pulses tend to have smaller average static stress drops but higher ratios of radiated energy to moment in comparison to simulated crack-like ruptures (Figure 4.16).

As the apparent stress is sensitive to both the static stress drop and degree of undershoot, according to our simulations, a (relatively high) radiated energy to moment ratio around 10^{-4} may be indicative of either a moderately sharp self-healing pulse with a standard stress drop around 2 - 3 MPa and undershoot $\gamma \approx 1.5$, or a crack-like rupture with negligble undershoot/overshoot and a larger stress drop of 10 - 15 MPa. The seismologically-inferable radiation efficiency scales the radiated energy by both the potency $\overline{\delta}A$ and static stress drop $\overline{\Delta\tau}$, resulting in a single scalar quantity that may provide insight into the degree of stress undershoot and rupture style. While the inferable radiation efficiency is not a true efficiency, it describes a scaled energy measure with reference to an idealized fracture model, providing a useful metric for how compatible the average source process is with a crack-like rupture (Figures 4.3A and 4.8). Note that the discussed relationships between radiated energy, moment, static stress drop, and average slip depend on stress changes during the rupture but not the absolute stress levels (Figures 4.7-4.9).

The relationship between apparent stress, stress undershoot and static stress drop emphasizes the need for improving constraints on static stress drops from large earthquakes. For example, apparent stress is inferred to be systematically higher for intraplate earthquakes, which also are typically inferred to have higher static stress drops (Allmann & Shearer, 2009; Choy & Boatwright, 1995; Perez-Campos & Beroza, 2001). The apparent stress is sometimes used as a constraint for inversions of static stress drop, where it is assumed that the static

stress drop must be larger than the apparent stress, consistent with a stress overshoot for crack-like ruptures (Savage & Wood, 1971; M. Wei & McGuire, 2014). The uncertainty of stress drops can be quite high; for example a Mw 6.5 intraplate earthquake offshore Northern California in 2010 has been inferred static stress drops between 2 and 20 MPa, with a high value of apparent stress around 7 MPa (M. Wei & McGuire, 2014). Note that the 7 MPa apparent stress with a lower-end estimate of static stress drop at 2 MPa results in a seismologically-inferable radiation efficiency (or radiation ratio) around 3, consistent with our relatively sharp simulated self-healing pulses and considerable undershoot. However, if the apparent stress is lower than the static stress drop, then the radiation ratio would be less than 1, consistent with crack-like ruptures and dynamic overshoot.

4.6.5 Radiated energy from self-healing pulses: relation to local rupture behavior, qualitative consistency for different rupture arrest and for longer faults

The average stress-slip curves that we produce for our ruptures, including pulse-like, are representative of typical local behavior (Figures 4.9 and 4.19). At the same time, the simulated pulses in this study are not steady but exhibit variations in local slip, slip rate, and rupture speed, resulting in seismic radiation and non-zero local static stress changes throughout the rupture process (Figures 4.9-4.10). Hence our simulated slip pulses are quite different from the theoretical case of an infinitely propagating steady pulse in which all the total strain energy change is dissipated within the source region, implying no net radiated energy. Note, however, that there is no notion of far-field radiation for an infinite fault given that the entire infinite domain is the source region. Moreover, the relevance of the infinitely propagating steady pulse model for natural earthquakes is not readily apparent, as not only the radiated energy but also static stress drop are zero for such models (Rice et al., 2005). Several theoretical and numerical studies have examined such steady pulse propagation and shown that it is highly unstable, with pulses eventually dying or growing as a result of small perturbations in prestress (Brantut et al., 2019; Gabriel et al., 2012).

To study the effect of rupture nucleation and arrest on the radiated energy, we conduct simulations with different properties of the VS regions that surround our seismogenic region.

Modifying the VS properties modifies the nucleation process as well as allows for smoother or more forcible arrest. We find that models with significantly different properties of the arresting regions produce qualitatively similar results for the radiated energy per moment (Figure 4.26).

Our simulations are performed with a 24-km velocity-weakening region due to computational limitations, given the long simulations to generate long earthquake sequences and resolution required for such simulations with efficient enhanced weakening. The conclusions should hold for a longer fault as well, as we illustrate by considering a twice longer, 50-km velocity-weakening region (Figures 4.11 and 4.27). In general, while the specific values of the average source properties such as average stress drop, slip, radiated energy, and average breakdown energy may vary based on the geometry and properties of the fault, the main findings presented in this study should be qualitatively consistent, in that any conditions that result in an average stress undershoot, or larger average dynamic stress changes than static stress changes, would result in higher radiated energy for the same average slip and static stress drop.

4.6.6 On crack-like vs. pulse-like ruptures

We find that self-healing pulses require higher average prestress than crack-like ruptures to achieve the same average dynamic stress levels and static stress drops. Crack-like ruptures within our simulations experience relatively minor under/overshoot with respect to their static stress drop, therefore the average initial stress in the rupture area is around one static stress drop away from the average dynamic resistance level:

$$\overline{\tau}_{\text{ini}} \approx \overline{\tau}_{\text{dyn}} + \overline{\Delta\tau}. \tag{4.49}$$

In contrast, self-healing pulse-like ruptures experience a substantial undershoot γ, such that the average initial stress is significantly more than one stress drop away from the average dynamic resistance level:

$$\overline{\tau}_{\text{ini}} = \overline{\tau}_{\text{dyn}} + (1+\gamma)\overline{\Delta\tau}, \tag{4.50}$$

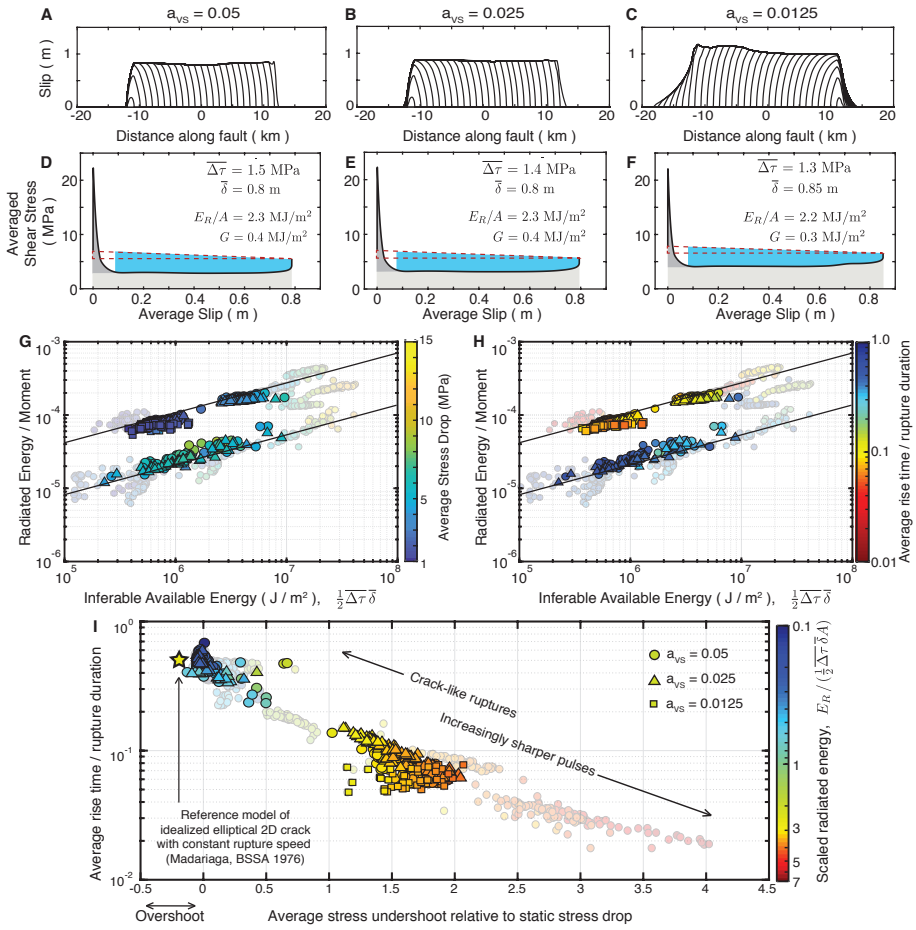

Figure 4.26: Effect of velocity-strengthening regions on average source properties. (A-C) Representative self-healing pulses with comparable average slip in models TP7 with varying VS properties. (D-F) Corresponding average stress-slip diagrams that illustrate the energy partitioning for the ruptures in (A-C). Regions with strong VS properties (a_{VS} = 0.05) arrest rupture propagation over shorter distances than those with relatively weaker VS properties (a_{VS} = 0.0125), resulting in mild differences in average source properties such as the average slip and stress drop. (G-I) The scaling relationships between the average source properties are generally consistent among models with varying VS properties (TP 4,6 and 7), with ruptures exhibiting larger average undershoot radiating more energy for the same static stress drop and average slip. Models with relatively strong VS properties (a_{VS} = 0.05) are denoted by circles, while models with a_{VS} = 0.025 and a_{VS} = 0.0125 are denoted by triangles and squares, respectively. The grayed-out backgrounds show results from all models as in Figure 4.2.

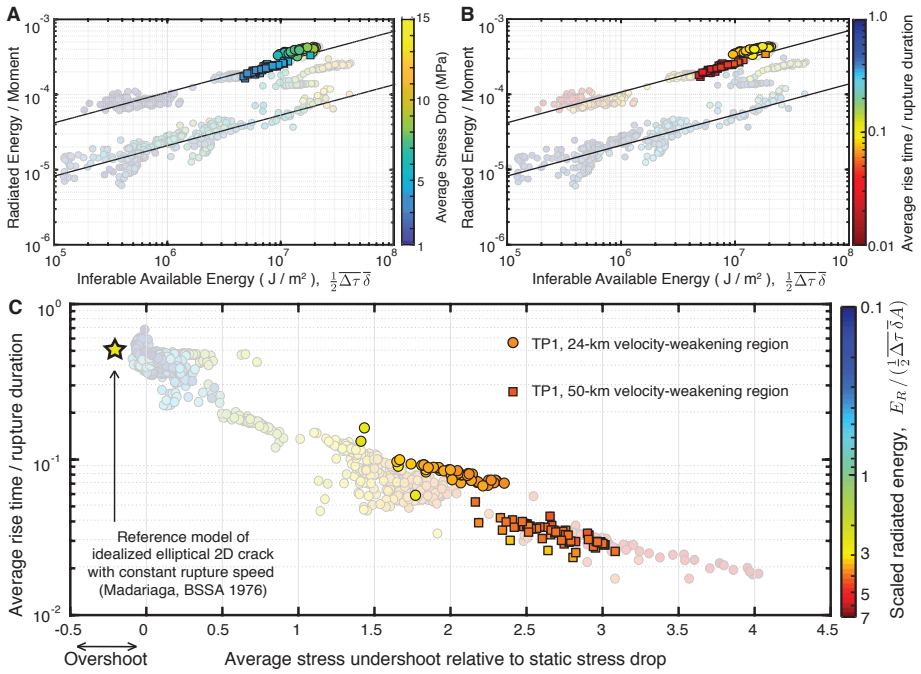

Figure 4.27: Consistency of radiated energy scaling for different fault lengths. (A-B) Self-healing pulses propagating over a 50-km VW region (squares) result in systematically lower static stress drops than those propagating over a 24-km VW region and result in mildly sharper pulses with shorter rise time to rupture duration. C) While the specific slip and stress distributions for different rupture sizes vary, they exhibit a consistent trend in higher radiated energy with increasing stress undershoot for the same average slip and stress.

where $\gamma \geq 0.5$. Therefore, self-healing pulses have higher average prestress than crack-like ruptures, for the same average dynamic stress levels and static stress drops. This consideration implies a minimum average initial stress that is needed for self-healing pulses; if we take $\overline{\tau}_{\text{dyn}} = 0$ MPa as the minimum dynamic stress level, then the minimum average initial stress for a self-healing pulse is $\overline{\tau}_{\text{ini}}^{\text{min}} = (1+\gamma)\overline{\Delta\tau}$. So for a minimum stress drop of 1 MPa, the average initial stress must be $\overline{\tau}_{\text{ini}} \geq (1+\gamma)$ MPa.

Another implication is that crack-like ruptures have larger stress drops than self-healing pulses, for the same average initial stress and dynamic stress levels (Figure 4.27). This is because $\overline{\Delta\tau}^{\text{pulse}} = \left(\overline{\tau}_{\text{ini}} - \overline{\tau}_{\text{dyn}}\right)/(1+\gamma)$, whereas $\overline{\Delta\tau}^{\text{crack}} \approx \overline{\tau}_{\text{ini}} - \overline{\tau}_{\text{dyn}}$, resulting in the relation,

$$\overline{\Delta\tau}^{\text{crack}} \approx (1+\gamma)\overline{\Delta\tau}^{\text{pulse}}, \tag{4.51}$$

given the same average initial and dynamic stress levels. It is then apparent that the crack-like ruptures must have lower average initial stress for crack-like ruptures and self-healing pulse-like ruptures to have similar average dynamic stress levels and static stress drops.

Note that all ruptures nucleate in regions of relatively high stress, close to the quasi-static strength (Figure 4.5). However, enhanced weakening allows for larger dynamic stress changes at the rupture front which facilitates rupture propagation over regions of the fault with lower prestress. In the case of persistently weak faults, the stress changes at the rupture front are more mild, requiring prestress levels to be not too far from the quasi-static strength for the rupture to propagate (Figure 4.5B).

We find that fault models with high quasi-static strength and ultra-efficient dynamic weakening can support crack-like ruptures at fairly low levels of shear prestress, in which case they can have reasonable stress drops. The reasoning is as follows. Theoretical and numerical studies have shown that ruptures can take the form of self-healing pulses, provided that the background shear stress is around or below a critical stress level τ^{pulse} that depends on the properties of dynamic weakening (Noda et al., 2009; Zheng & Rice, 1998). In other words, there exists a critical background stress level τ^{pulse}, below which, if a rupture is to propagate, it can only propagate as a self-healing pulse. As the efficiency of the weakening increases, τ^{pulse} decreases. Hence if the weakening is quite efficient, then τ^{pulse} can be near-zero, and crack-like ruptures may be able to propagate at fairly low levels of shear stress (even though the levels would have to be higher than τ^{pulse}).

Let us consider a fault model (Model A) with an effective confining stress of 100 MPa and efficient thermal pressurization (Λ = 0.34 MPa/K and $\alpha_{\text{hy}} = 10^{-3}$ m^2/s), resulting in self-healing pulses. Now consider another fault model (Model B) with similar physical conditions, except with more efficient thermal pressurization (Λ = 0.5 MPa/K and $\alpha_{\text{hy}} = 10^{-6}$ m^2/s). In such conditions, the crack-like rupture in Model B is able to propagate with an average initial stress that is even lower than the self-healing pulse in Model A (Figure 4.12),

with both ruptures propagating through average prestress well below the quasi-static strength (~70 MPa), and therefore consistent with (H1) quasi-statically strong but dynamically weak fault operation. Both ruptures experience large dynamic stress changes at the rupture front, increasing to peak stress levels around 100 MPa, and then dramatically weakening to shear resistance levels around or below 10 MPa due to thermal pressurization. The self-healing pulse dramatically weakens and then heals such that the static stress change is much smaller than the dynamic stress change (Figure 4.13). In contrast, the local shear stress within the crack-like rupture drops dramatically and stays low, with comparable local static and dynamic stress changes (Figure 4.13). The two ruptures have comparable static stress drops and average slip, and are compatible with (H1), operating at sliding resistance levels well below the same quasi-static strength. However, the self-healing pulse results in a substantial stress undershoot and therefore radiates considerably more energy, whereas the radiated energy for the crack-like rupture in Model B is comparable to those of milder crack-like ruptures with similar stress drop and slip, as well as seismological inferences.

While this example illustrates that the propagation of crack-like ruptures at stress levels much lower than the quasi-static strength is theoretically possible, the physical plausibility of such mechanism on natural faults is a topic for further exploration. In particular, such behavior would require substantially more efficient enhanced weakening than typically considered (Noda & Lapusta, 2010; Rempel & Rice, 2006; Rice, 2006; Wibberley & Shimamoto, 2005), which may be potentially suppressed, for example by the evolution of rock permeability or energy loss from damage production, during dynamic rupture.

One implication of the possibility for crack-like ruptures with efficient enhanced weakening propagating on quasi-statically strong, but dynamically weak faults is that they may exhibit comparable average source properties, such as static stress drops, average slip, radiated energy, apparent stress, and seismologically inferable breakdown energies, as more mild crack-like ruptures on persistently weak faults (Figure 4.2D vs. 4.12D). This poses a challenge for discriminating the local physical behavior of natural earthquakes from more

remote teleseismic observations alone. However, the larger dynamic stress changes near the rupture front for both self-healing pulse-like ruptures and crack-like ruptures with efficient enhanced weakening would likely result in stronger near-fault ground motion (Figures 4.14A and 4.15). Indeed, the fault-parallel particle acceleration spectral amplitudes near the center of these ruptures on quasi-statically strong, dynamically weak faults in our models can be about a factor of 5 times those for the milder crack-like rupture on a persistently weak fault between 1–10 Hz (4.13B). Note that high-frequency motions may also be considerably damped by the presence of off-fault inelastic deformation (Figure 4.14B and Figure 4.15 C-D) and attenuation, as well as enhanced by the presence of strong heterogeneities in both the rupture process and elastic bulk (Dunham et al., 2011a, 2011b). The expected near-fault ground motions from models with varying degrees of efficiency in enhanced weakening and rupture styles warrants more detailed study.

4.6.7 Captions for supplementary videos

Video S1: Evolution of shear stress during a self-healing pulse-like rupture on a quasi-statically strong but dynamically weak fault.

Evolution of shear stress (black line) along the fault during a self-healing pulse-like rupture on a quasi-statically strong but dynamically weak fault (H1). The video illustrates the changes in shear stress with respect to the initial (gray) and final (blue) shear stresses, as well as the quasi-static strength (red). The initial stress on the majority of the fault is far below the quasi-static strength, except for the region in which the rupture nucleates, which is small compared to the total rupture area. As the rupture front crosses the seismogenic (VW) region, each point experiences a large dynamic stress increase towards ~100 MPa, and then drops to low levels below 10 MPa. Only a small portion of the fault slips at a given time as the shear resistance heals behind the rupture front and the fault relocks, resulting in higher final stress levels than the level of shear resistance at which most of the slip occurred.

Video S2: Evolution of shear stress during a crack-like rupture on a persistently weak fault.

Evolution of shear stress (black line) along the fault during a mild crack-like rupture on a

persistently weak fault (H2). The initial shear stress over the entire rupture region is within 1–2 times the static stress drop (7.3 MPa) away from the quasi-static strength. Slip continues within the regions behind the rupture front until the rupture front is arrested in the VS region on the other side of the seismogenic (VW) region, and healing waves redistribute stress and arrest slip. All conventions follow Video S1.

Video S3: Scaled evolution of shear stress during a crack-like rupture on a persistently weak fault.

Evolution of shear stress (black line) along the fault for the same mild crack-like rupture as shown in Video S2, however with the shear stress axis rescaled to emphasize the dynamic stress changes during the rupture. Slip continues within the regions behind the rupture front until the rupture front is arrested in the VS region on the other side of the seismogenic (VW) region, and healing waves redistribute stress and arrest slip, resulting in a dynamic overshoot throughout most of the ruptured region. All conventions follow Videos S1 and S2.

Chapter 5

ABSOLUTE STRESS LEVELS ON NUMERICALLY SIMULATED FAULTS: DEFINITIONS, LINKS TO SEISMOLOGICAL OBSERVABLES, AND DIFFERENCES FOR CRACK-LIKE VS. PULSE-LIKE RUPTURES

This chapter has been adapted from:

Lambert, V. & Lapusta, N. Absolute stress levels on numerically simulated faults: Definitions, links to seismological observables, and differences for crack-like vs. pulse-like ruptures. in preparation for *Journal of Geophysical Research: Solid Earth*.

5.1 Introduction

The low-stress operation of mature faults indicate that the average shear resistance must be low during periods of substantial fault motion. For example, thermal measurements surrounding mature faults are in principle related to the average shear stress associated with dissipation and shear heating. Such observations can thus provide constraints for the average dynamic shear resistance at seismic slip rates during large earthquakes (Brune et al., 1969; Fulton et al., 2013; Gao & Wang, 2014; Henyey & Wasserburg, 1971; Lachenbruch & Sass, 1980; Nankali, 2011; Tanikawa & Shimamoto, 2009). Studies of exhumed mature faults suggest that shear motion can be accommodated within narrow layers, less than one to several millimeters wide (e.g. F. M. Chester & Chester, 1998; Wibberley & Shimamoto, 2003). Higher bounds for the average shear stress associated with shear heating during dynamic rupture are expected to be on the order of 10 MPa for shear localized between 1 to 10 mm, in order to avoid substantial heat flow and pervasive melt production (Lambert et al., 2021; Rice, 2006). Laboratory and theoretical studies suggest that the shear resistance at seismic slip rates can be significantly lower than the quasi-static shear resistance on faults during periods of slow aseismic slip and interseismic locking with negligible motion, particularly if the fault undergoes enhanced dynamic weakening at seismic slip rates (Acosta et al., 2018; Di Toro et al., 2011; Noda et al., 2009; Rice, 2006; Sibson, 1973; Tsutsumi & Shimamoto,

1997; Wibberley et al., 2008). As such, field evidence for the low-heat, low-stress operation of faults are not inherently indicative of the average shear resistance on faults during periods of quasi-static motion, which may be of particular relevance to tectonic and geodynamic studies.

Given constraints that the average dynamic shear resistance associated with shear heating should be low (< 10 MPa), a long-standing question in earthquake physics is how representative the average static stress drop of large earthquakes is for the average pre-rupture shear stress (i.e. prestress), which may be considered a measure of the average fault strength at the scale of the rupture (Kanamori, 1994; Lambert et al., in review; McGarr, 1999; Scholz, 2000; Townend & Zoback, 2000). Theoretical studies have suggested that the presence of substantial topography on Earth's surface provides evidence that the ambient shear stress in the crust is around 100 MPa at some localities (Jeffreys, 1959), though how this is accommodated along faults and the upper mantle remains a topic of active research (Behr & Platt, 2014; Dielforder, 2017; Dielforder et al., 2020; Luttrell & Smith-Konter, 2017; Luttrell et al., 2011). Several studies have estimated the absolute stress levels along major plate boundary faults, such as the San Andreas Fault system, by considering the force balance of tectonic block motion, topography, and mantle buoyancy (Fay & Humphreys, 2006; Fialko et al., 2005; Luttrell & Smith-Konter, 2017), inferring shear stress levels of 20 to 30 MPa averaged over seismogenic depths. Similar studies suggest that the topography associated with most collisional megathrusts can be maintained by average shear stresses ranging from 7 to 25 MPa (Dielforder, 2017; Dielforder et al., 2020; Lamb, 2006; Luttrell et al., 2011). However, some calculations suggest that regions with more substantial topography, such as the North Chilean subduction zone and portions of the San Andreas and San Jacinto fault zones, may require average shear stresses up to 40 MPa (Fay & Humphreys, 2006; Lamb, 2006). These estimates are all lower than the expected shear resistance given typical quasi-static friction measurements in the lab and confining conditions assuming rock overburden and hydrostatic fluid pressures (Byerlee, 1978; Ikari et al., 2011), however some are significantly higher than the constraint of less than 10-20 MPa based on heat flow and other shear heating

considerations. This distinction suggests that the difference between the average earthquake prestress and the shear resistance during rapid slip could be more than one average static stress drop (Fay & Humphreys, 2006; Heaton, 1990).

A substantial challenge in relating inferences of average shear stress and resistance among laboratory and field studies is the wide range of scales and styles of motion involved. Recent numerical studies have demonstrated that some measures of average shear stress, such as the spatially-averaged and energy-based prestress before dynamic ruptures, depend on both the size of the rupture and efficiency of dynamic weakening on the fault (Lambert et al., in review, 2021; Perry et al., 2020). In particular, such studies highlight that the shear prestress levels required for the relatively slow, unstable sliding consistent with rupture nucleation can be substantially different from those needed to sustain dynamic rupture propagation, emphasizing the importance of considering fault heterogeneity and finite-fault effects when relating laboratory and field measurements of fault stress. A key component of this disparity between rupture nucleation and propagation is the significant role of dynamic stress interactions during dynamic rupture propagation, suggesting that the motion-dependence of shear resistance as well as inertial effects during dynamic rupture are crucial for understanding the evolution of average absolute shear stress on faults.

A number of studies combine seismological inferences with insights into frictional rupture behavior from lab experiments and dynamic fracture theory in order to infer characteristics of the stress evolution and energy partitioning on faults during earthquake ruptures (Abercrombie & Rice, 2005; McGarr, 1999; Rice, 2006; Savage & Wood, 1971; Venkataraman & Kanamori, 2004; Viesca & Garagash, 2015; M. Wei & McGuire, 2014; Ye et al., 2016b). These studies often assume idealized source representations and make specific assumptions about the average dynamic resistance level during sliding. Recent numerical studies have demonstrated that the physical interpretation of some inferences of average earthquake source properties, such as the average static stress drop, average breakdown energy, and radiation ratio, depends on whether rupture propagation occurs as a dynamic crack or self-

healing pulse, and special consideration is needed when relating them to the local stress evolution during ruptures (Lambert & Lapusta, 2020; Lambert et al., 2021; Perry et al., 2020). Hence the interpretation of such average source quantities in terms of the local fault physics depends on the rupture model.

As a variety of methods and considerations are used to infer the absolute levels of shear stress before, during, and after ruptures, here we review different measures of average shear stress on faults, and study their relationship with one another and with geophysical inferences. We consider three different notions of average shear stress: 1) the spatially-averaged stress τ^A, 2) the dissipation-based stress τ^D, and 3) the energy-based stress $\overline{\tau}^E$. We use numerical simulations of sequences of earthquakes and aseismic slip (SEAS) on rate-and-state faults with enhanced dynamic weakening due to the thermal pressurization of pore fluids to compare these three different measures of average fault shear stress and relate them to seismologically inferable source properties, such as the average static stress drop and apparent stress, in simulated ruptures of differing rupture style.

5.2 Fault models with rate-and-state friction laws and thermal pressurization of pore fluids

5.2.1 Model formulation

We conduct numerical simulations of sequences of spontaneous earthquakes and aseismic slip following the methodological developements of Lapusta et al. (2000), Noda and Lapusta (2010), and Lambert et al. (2021). Most of our simulations consider mode III slip on a 1-D fault embedded into a 2-D uniform, isotropic, elastic medium. We also perform a selection of 3-D simulations with 2-D faults in order to explore the impact of fault geometry on our modeling conclusions. The resulting slip on the fault includes sequences of earthquakes and aseismic slip (SEAS) simulated in their entirety, including the nucleation process, dynamic rupture propagation, postseismic slip that follows each seismic event, and interseismic period between seismic events that can last up to tens or hundreds of years and host steady and transient slow slip.

Our fault models are governed by a form of the laboratory-derived Dieterich-Ruina rate-and-state friction law (Dieterich, 1979; Ruina, 1983):

$$\tau = \overline{\sigma} f(V, \theta) = (\sigma - p) \left[f_* + a \log \frac{V}{V_*} + b \log \frac{\theta V_*}{D_{\mathrm{RS}}} \right], \tag{5.1}$$

where $\overline{\sigma}$ is the effective normal stress given normal stress σ and pore fluid pressure p, f_* is a reference steady-state friction coefficient at reference sliding rate V_*, D_{RS} is the characteristic slip distance, and a and b are the direct effect and evolution effect parameters, respectively. In our simulations, we use a form of the Dieterich-Ruina law regularized for zero and negative slip rates (Lapusta et al., 2000; Noda & Lapusta, 2010; Rice & Ben-Zion, 1996).

We use the aging form of the state variable evolution (Ruina, 1983):

$$\dot{\theta} = 1 - \frac{V\theta}{D_{\mathrm{RS}}}, \tag{5.2}$$

which aims to incorporate the evolution of contacts during sliding as well as time-dependent healing during sufficiently slow motion. During steady-state sliding ($\dot{\theta} = 0$), the friction coefficient is expressed as:

$$f_{ss}(V) = f_* + (a - b) \log \frac{V}{V_*}, \tag{5.3}$$

where the combination of frictional properties $(a - b) > 0$ results in steady-state velocity-strengthening (VS) behavior that leads to stable slip and $(a - b) < 0$ results in steady-state velocity-weakening (VW) behavior that can leads to spontaneously accelerating slip and hence seismic events for sufficiently large regions.

Earthquake ruptures can nucleate only if the VW region is larger than the nucleation size h^*. For 2-D problems, two theoretical estimates of the nucleation size in mode III are (Rice & Ruina, 1983; Rubin & Ampuero, 2005):

$$h^*_{RR} = \frac{\pi}{4}\frac{\mu L}{(b-a)(\sigma-p)};\ h^*_{RA} = \frac{2}{\pi}\frac{\mu L b}{(b-a)^2(\sigma-p)}, \tag{5.4}$$

where μ is the shear modulus. h^*_{RR} is the estimate of spatial scale that can host accelerating slip (Dal Zilio et al., 2020; Rice & Ruina, 1983). h^*_{RA} is the upper bound, for the parameter regime $1/2 < b/a > 1$, on the size of the quasi-statically expanding nucleation zone before it transitions to dynamic rupture (Rubin & Ampuero, 2005); numerical studies find that this is a good estimate of the nucleation size, which increases by about a factor of $\pi^2/4$ in 3-D problems (T. Chen & Lapusta, 2009).

The simulated 1-D fault in our 2-D models contains a 24-km region with VW frictional properties where earthquakes may nucleate and propagate, surrounded by VS regions that inhibit rupture nucleation and propagation (Figure 5.1). Our 3-D models include a VW region with a length of 32 km and a down-dip width of 8 km, resulting in an aspect ratio of 4. The properties of the VW regions are such (Tables 5.1 - 5.3) that the smallest dimension of the VW regions are roughly 6 times larger than the estimated nucleation size in our 3-D models and 44 times larger in our 2-D models, ensuring that the regions would be seismogenic. We refer to ruptures that span the entire VW region and arrest in the VS region as model-spanning ruptures. Outside of these frictional regions, the fault moves with a prescribed plate rate V_{pl} to provide tectonic-like loading. We define the beginning and end of dynamic rupture, t_{ini} and t_{fin}, respectively, as well as the ruptured region Ω_{rupt}, in our simulations using a slip velocity threshold ($V_{\text{thresh}} = 1$ cm/s) for seismic slip, based on previous studies (Lambert et al., 2021; Perry et al., 2020).

Such rate-and-state laws are the most established representation of fault shear resistance for relatively low slip rates from tectonic plate rates of 10^{-9} m/s to around 10^{-3} m/s. At higher slip rates, further enhanced dynamic weakening of fault frictional resistance can occur, for example, due to rapid shear heating, as widely documented in high-velocity laboratory experiments (Acosta et al., 2018; Di Toro et al., 2011; Tullis, 2007; Wibberley et al., 2008) and supported by theoretical studies (Rice, 2006). One particular mechanism for such

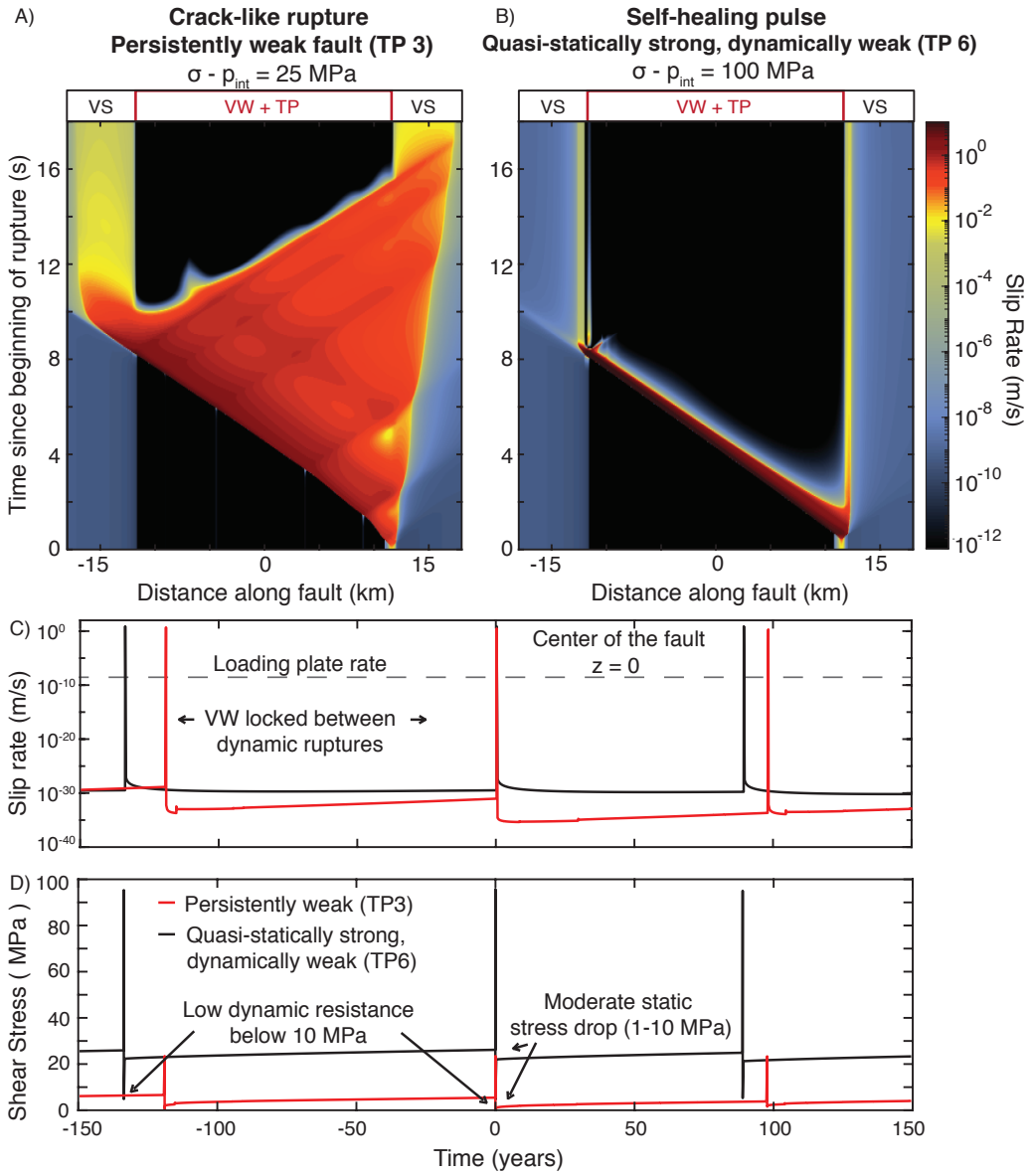

Figure 5.1: Evolution of slip rate and shear stress with time for representative fault models hosting crack-like (fault model TP3) and self-healing pulse-like (fault model TP6) ruptures. (A-B) The fault models are composed of a velocity-weakening (VW) seismogenic region surrounded by two velocity-strengthening (VS) sections. Local seismic slip duration during (A) crack-like ruptures is proportional to the overall rupture duration where as only a small portion of the fault slips at a given time during (B) self-healing pulse-like ruptures. (C-D) Evolution of local slip rate and shear stress at the center of the fault over sequences of earthquakes with low dynamic resistance and moderate static stress drops. Time series are centered at t=0 corresponding to the ruptures shown in (A-B). (C) Most points within the VW region are locked, with slip rates far below the loading plate rate, during the interseismic period between dynamic ruptures. (D) The shear stress over the persistently weak fault model (TP3) which hosts the crack-like rupture is always low (< 20 MPa). For self-healing pulse-like ruptures on quasi-statically strong, dynamically weak fault model (TP6), the shear stress before the rupture is relatively high compared to the persistently weak fault (> 30 MPa), then drops to low values below 10 MPa during seismic slip, and recovers to around 20 MPa over most of the ruptured region.

enhanced weakening is the thermal pressurization of pore fluids, which occurs when pore fluids within the fault shearing layer heat up, expand, and pressurize during dynamic rupture, reducing the effective normal stress, and therefore shear resistance (Noda & Lapusta, 2010; Rice, 2006; Sibson, 1973).

Our simulations also incorporate enhanced dynamic weakening due to the thermal pressurization of pore fluids, which is governed by the following coupled differential equations for pore pressure and temperature evolution (Noda & Lapusta, 2010):

$$\frac{\partial p(y,z;t)}{\partial t} = \alpha_{\text{hy}} \frac{\partial^2 p(y,z;t)}{\partial y^2} + \Lambda \frac{\partial T(y,z;t)}{\partial t}, \tag{5.5}$$

$$\frac{\partial T(y,z;t)}{\partial t} = \alpha_{\text{th}} \frac{\partial^2 T(y,z;t)}{\partial y^2} + \frac{\tau(z;t)V(z;t)}{\rho c} \frac{\exp(-y^2/2w^2)}{\sqrt{2\pi}w}, \tag{5.6}$$

where T is the temperature of the pore fluid, α_{hy} is the hydraulic diffusivity, α_{th} is the thermal diffusivity, τV is the source of shear heating distributed over a Gaussian shear layer of half-width w, ρc is the specific heat, y is the distance normal to the fault plane, and Λ is the coupling coefficient that gives pore pressure change per unit temperature change under undrained conditions.

We also approximate the effects of off-fault yielding during dynamic rupture in our models by employing a velocity limit of $V_{\text{max}} = 15$ m/s, as discussed in detail in Lambert et al. (2021). This approximation is motivated by detailed dynamic rupture simulations with off-fault yielding (Andrews, 2004), with the value of the velocity limit corresponding to a representative seismogenic depth of 10 km.

Note that for realistic, lab-derived fault constitutive relations such as rate-and-state friction, the concept of a local "static friction" coefficient is ill-defined, since slip rate is non-zero for any non-zero shear stress (Rice et al., 2001). In order to examine how average shear stress measures vary with styles of motion and rupture size, we choose a representative value for the classical notion of local quasi-static fault strength, which we call the local steady-state quasi-static (SSQS) shear resistance and define as the product of the interseismic drained

effective normal stress and the quasi-static friction coefficient during steady creep at the prescribed tectonic plate rate V_{pl}:

$$\tau_{ss}^{V_{\text{pl}}}(z,t) = (\sigma - p_{\text{int}})\, f_{ss}(V_{\text{pl}}). \tag{5.7}$$

The "drained" refers to the effective stress with ambient interseismic pore pressure p_{int} unaffected by slip processes such as dilatancy or thermal pressurization. Previous numerical studies have shown that the local SSQS shear resistance $\tau_{ss}^{V_{\text{pl}}}$ is comparable to the spatially-averaged prestress consistent with rupture nucleation (Lambert et al., in review). The quasi-static reference friction in all of our simulations has a uniform value of 0.6, consistent with many materials exhibiting VW behavior in laboratory experiments (Ikari et al., 2011).

We aim to study the evolution of shear stress and average stress measures in fault models consistent with low heat production, where the stresses associated with shear heating are below 20 MPa. We conduct simulations with varying levels of background fluid overpressure in terms of the effective normal stress, as well as varying degrees of efficiency in enhanced weakening due to thermal pressurization. The parameter values we have chosen (Tables 5.1 - 5.3) are motivated by prior studies (Lambert et al., 2021; Noda & Lapusta, 2010; Perry et al., 2020; Rice, 2006) and our goal of examining ruptures with varying efficiency in enhanced dynamic weakening and different rupture styles.

5.2.2 Crack-like versus self-healing pulse-like ruptures

One potential explanation for the inferred low-stress, low-heat operation of mature faults is that faults may be persistently weak due to the presence of anomalously low quasi-static friction coefficients and/or low effective confinement from pervasive fluid overpressure (Bangs et al., 2009; Brown et al., 2003; Collettini et al., 2009; Faulkner et al., 2006; Lockner et al., 2011). Another end-member model is that mature faults may indeed be strong at slow, quasi-static sliding rates, but undergo considerable enhanced dynamic weakening at seismic slip rates (Lambert et al., 2021; Noda et al., 2009; Rice, 2006). Previous numerical studies have shown that ruptures in persistently weak fault models that produce typical static stress

Parameter	Symbol	Value
Loading slip rate	V_{pl}	10^{-9} m/s
Shear wave speed	c_s	3299 m/s
Shear modulus	μ	36 GPa
Thermal diffusivity	α_{th}	10^{-6} m^2/s
Specific heat	ρc	2.7 MPa/K
Shear zone half-width	w	10 mm
Rate-and-state parameters		
Reference slip velocity	V_*	10^{-6} m/s
Reference friction coefficient	f_*	0.6
Rate-and-state direct effect (VW)	a	0.010
Rate-and-state evolution effect (VW)	b	0.015
Rate-and-state direct effect (VS)	a	0.050
Rate-and-state evolution effect (VS)	b	0.003
Length scales for 2-D simulations		
Fault length	λ	96 km
Frictional domain	λ_{fr}	72 km
Velocity-weakening region	λ_{vw}	24 km
Cell size	Δz	3.3 m
Quasi-static cohesive zone	Λ_0	84 m
2D Nucleation size (Rice & Ruina, 1983)	h^*_{RR}	226 m
2D Nucleation size (Rubin & Ampuero, 2005)	h^*_{RA}	550 m
Cell size	Δz	3.3 m
Quasi-static cohesive zone	Λ_0	84 m
Length scales for 3-D simulations		
Fault dimensions	$\lambda_{\text{z}} \times \lambda_{\text{x}}$	80×40 km
Frictional domain	$\lambda_{\text{fr,z}} \times \lambda_{\text{fr,x}}$	60×20 km
Velocity-weakening region	$\lambda_{\text{vw,z}} \times \lambda_{\text{vw,x}}$	32×8 km
Cell size	$\Delta z = \Delta x$	25 m

Table 5.1: Model parameters used in simulations in Ch. 5 unless otherwise specified.

drops between 1 to 10 MPa propagate as crack-like ruptures, in which seismic slip at each fault location, once initiated, continues until arrest waves arrive from the edges of the fault or other heterogeneities in the problem; as a result, the portion of the fault that slips at a given time during rupture is comparable to the final rupture size and the local slip duration at different points is comparable to the total rupture duration (Figure 5.1A; Lambert et al., 2021). The word "crack" in the name refers to analogy with opening cracks that also typically continue to open until that crack arrests at a barrier. In contrast, ruptures in quasi-statically strong, dynamically weak fault models with 1 to 10 MPa static stress drops typically propagate as self-healing pulses in which slip spontaneously arrests behind the

Parameter	Symbol	TP 1	TP 2	TP 3
Interseismic drained effective stress	$\bar{\sigma} = (\sigma - p_{\text{int}})$	25 MPa	25 MPa	25 MPa
Shear zone half-width	w	10 mm	10 mm	10 mm
Characteristic slip	D_{RS}	1 mm	1 mm	1 mm
Rate-and-state direct effect (VS)	a	0.05	0.05	0.025
TP coupling coefficient	Λ	0.1 MPa/K	0.34 MPa/K	0.34 MPa/K
Hydraulic diffusivity	α_{hy}	10^{-3} m^2/s	10^{-3} m^2/s	10^{-4} m^2/s
Parameter	Symbol	TP 4	TP 5	
Interseismic drained effective stress	$\bar{\sigma} = (\sigma - p_{\text{int}})$	50 MPa	25 MPa	
Shear zone half-width	w	10 mm	1 mm	
Characteristic slip	D_{RS}	2 mm	1 mm	
Rate-and-state direct effect (VS)	a	0.05	0.025	
TP coupling coefficient	Λ	0.34 MPa/K	0.34 MPa/K	
Hydraulic diffusivity	α_{hy}	10^{-3} m^2/s	10^{-4} m^2/s	
Parameter	Symbol	TP 6	TP 7	
Interseismic drained effective stress	$\bar{\sigma} = (\sigma - p_{\text{int}})$	100 MPa	100 MPa	
Shear zone half-width	w	10 mm	10 mm	
Characteristic slip	D_{RS}	4mm	4 mm*	
Rate-and-state direct effect (VS)	a	0.05	0.05	
TP coupling coefficient	Λ	0.34 MPa/K	0.5 MPa/K	
Hydraulic diffusivity	α_{hy}	10^{-3} m^2/s	10^{-6} m^2/s	
Parameter	Symbol	TP 8	TP 9	
Interseismic drained effective stress	$\bar{\sigma} = (\sigma - p_{\text{int}})$	25 MPa	25 MPa	
Shear zone half-width	w	1 mm	1 mm	
Characteristic slip	D_{RS}	1mm	1 mm	
Rate-and-state direct effect (VS)	a	0.025	0.025	
TP coupling coefficient	Λ	0.34 MPa/K	0.34 MPa/K	
Hydraulic diffusivity	α_{hy}	10^{-5} m^2/s	10^{-6} m^2/s	

Table 5.2: Parameters for models in Ch. 5 including the thermal pressurization of pore fluids. *Models of crack-like ruptures with very efficient TP (Figure 5.2C) include two 100-m patches of lower characteristic slip distance (D_{RS} = 1mm) placed at the VW to VS transition in order to provide favorable heterogeneity for nucleation while maintaining moderate weakening rates throughout the VW that are more practically resolved numerically.

Parameter	Symbol	RS 1	RS 2
Interseismic drained effective stress	$\bar{\sigma} = (\sigma - p_{\text{int}})$	10 MPa	20 MPa
Characteristic slip	D_{RS}	0.5 mm	1 mm
Quasi-static cohesive zone	Λ_0	106 m	106 m
2D Nucleation size (Rice & Ruina, 1983)	h^*_{RR}	282 m	282 m
2D Nucleation size (Rubin & Ampuero, 2005)	h^*_{RA}	688 m	688 m

Table 5.3: Parameters for models in Ch. 5 including only standard rate-and-state friction.

rupture front due to rapid local healing; as a result, only a small portion of the fault slips at a given time and the local slip duration is short relative to the rupture duration (Figure 5.1B).

The shear resistance, and hence shear stress, along a fault can substantially vary over time, such as before, during and after different rupture events, depending on the efficiency of weakening during rapid fault slip as well as fault healing (Figures 5.1 - 5.3). For persistently weak faults, the shear stress is always low (< 20 MPa, Figures 5.1C-D). In contrast, the local shear resistance on quasi-statically strong, dynamically weak faults, and hence the local shear stress, may be relatively high during periods of negligible motion before and after ruptures, but drop dramatically to lower values below 10 MPa during seismic slip (Figures 5.1C-D).

Crack-like and self-healing pulse-like ruptures differ in terms of the evolution of shear stress during rupture propagation. For crack-like ruptures, the local shear resistance drops at high slip rates and remains low throughout the remainder of the rupture process (Figure 5.2A & C). As the result, the dynamic stresses arriving from neighboring slipping regions continue to drive slip until the arrival of arrest waves with opposite stress polarity from the adges of the rupture (Figure 5.3A & C). The continuation of slip until the arrival of these arrest waves can result in a dynamic stress overshoot, where the final shear stress post-slip can be adjusted by the waves to be lower than the typical shear stress during sliding (Figures 5.3A & C; Kanamori & Rivera, 2013; Lambert et al., 2021; Madariaga, 1976; Viesca & Garagash, 2015). The overshoot is typically minor, i.e., a small fraction of the final static stress change, and can be typically ignored.

In contrast, the arrest of slip during a self-healing pulse occurs due to local healing of the shear resistance independent of the arrival of arrest waves, such as from the diffusion of pore fluids in the case of enhanced weakening due to thermal pressurization, as in our models. In this case, the dynamic stresses arriving from fault slip elsewhere may be balanced by local healing, allowing the slip to arrest. Due to the presence of rapid healing, self-healing

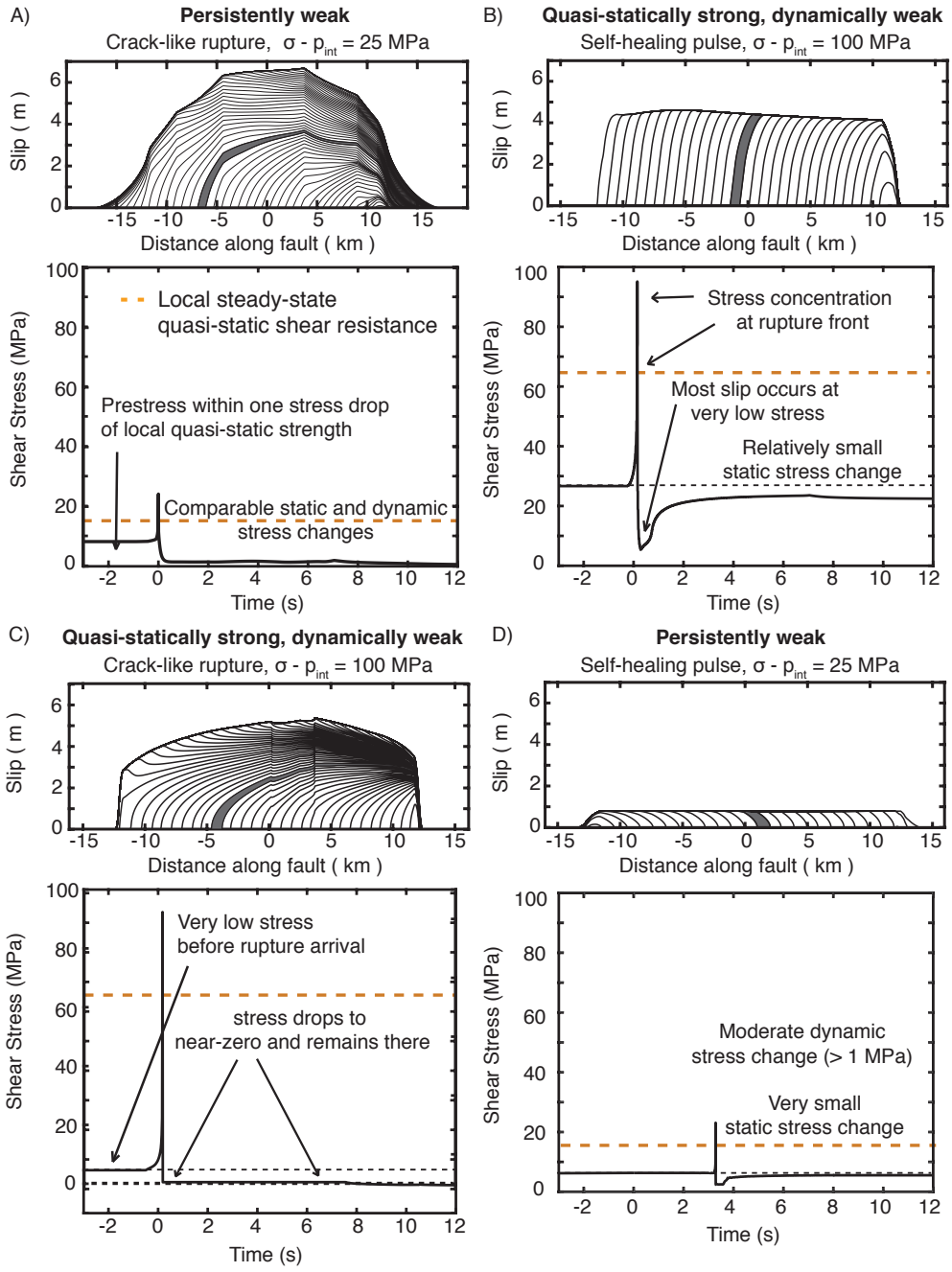

Figure 5.2: Evolution of slip and local shear stress with time throughout four characteristic ruptures. (Top) Characteristic evolution of slip along the fault for (A & C) crack-like ruptures and (B & D) self-healing pulses in persistently weak (TP 3 & 5) and quasi-statically strong, dynamically weak (TP 6 & 7) fault models. Slip contours are plotted every 0.25 s and the gray shading illustrates a portion of the fault that is slipping during a 0.25-second interval. (Bottom) The local evolution of shear stress with time at a point in the center of the fault (z = 0 km), in the four representative ruptures. The stress concentration at the rupture front is much larger for the ruptures with more efficient weakening on quasi-statically strong, dynamically weak behavior (B & C) than for the ruptures with more moderate weakening on persistently weak faults (A & D). The self-healing pulses (B & D) experience rapid healing resulting in dynamic stress variations that are much larger than the static stress change.

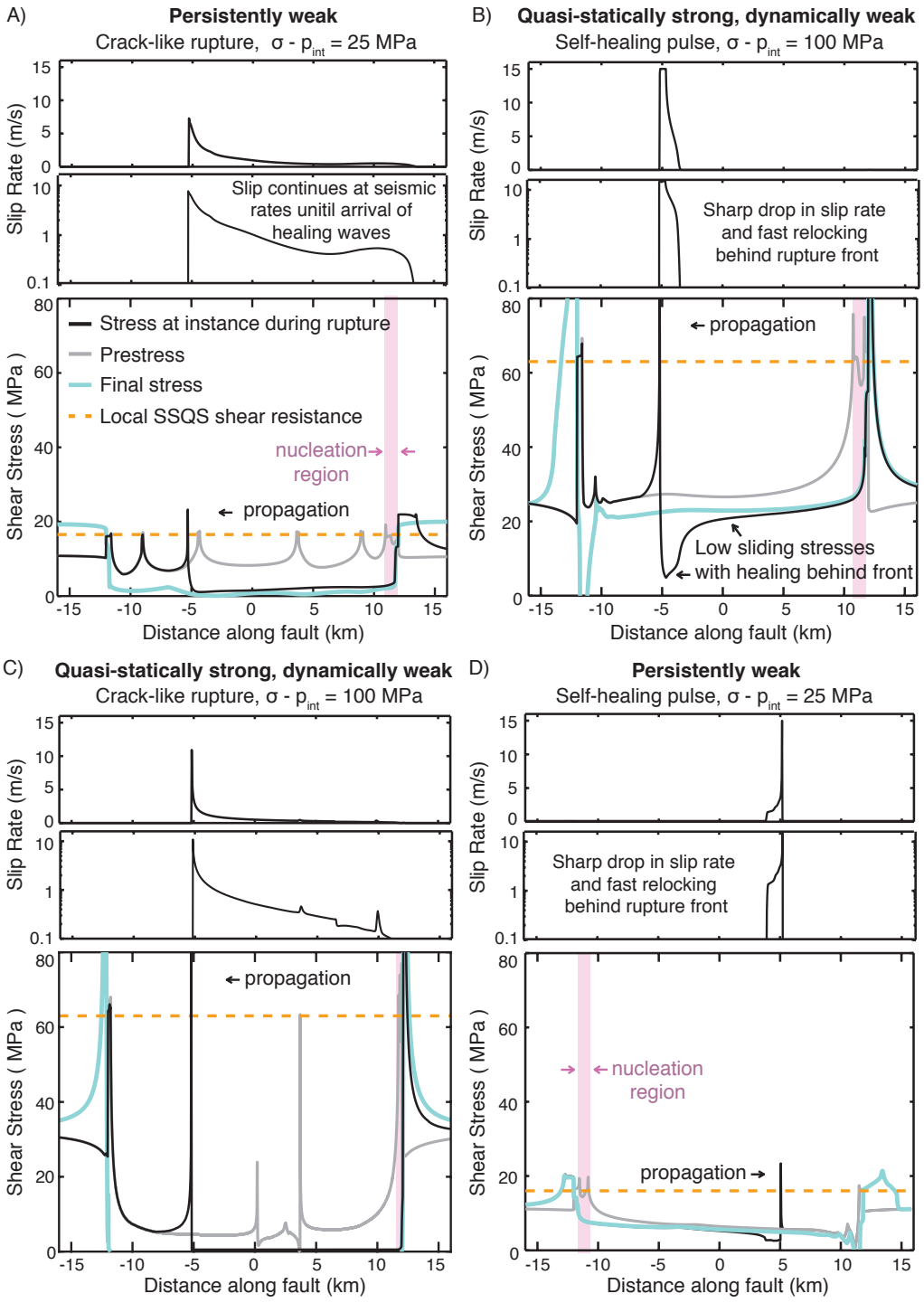

Figure 5.3: Spatial distribution of slip rate (top) and shear stress (bottom) for the same representative ruptures as in Figure 5.2. All four ruptures nucleate with prestress levels (gray line) that are near the local steady-state quasi-static shear resistance (dashed orange line), however the ruptures propagate over lower prestress conditions depending on the efficiency of weakening. The slip rate and shear stress at the same instance are shown by the black lines, illustrating the concentrated stress changes at the rupture front, with slip continuing throughout the entirety of the rupture for the crack-like ruptures (A-B), but not the pulse-like ruptures (C-D).

pulses exhibit a dynamic stress undershoot, or a larger dynamic stress drop than static stress drop, with the final shear stress being higher than the local shear resistance during sliding (Figures 5.1D and 5.3B & D; Heaton, 1990; Lambert et al., 2021). This undershoot can be quite significant, comparable to the static stress drop or even several times larger, increasing for sharper self-healing pulses (Lambert et al., 2021). The presence of this undershoot can significantly modify the average stress on faults as we discuss in the following.

Both crack-like and self-healing pulse-like ruptures can propagate in persistently weak and dynamically weak conditions, though the different modes of rupture result in considerably different styles of motion and evolution of shear stress (Figures 5.2-5.3; Lambert et al., 2021). The spatial distribution of shear stress along faults can be highly variable depending on the current style of motion as well as the history of motion in previous slip events. For example, despite our fault models having uniform frictional properties and interseismic effective stress within the VW region, the shear stress distribution evolves to become spatially heterogeneous due to spatially varying histories of slip over sequences of earthquakes (Figure 5.3). For quasi-statically strong, dynamically weak faults, the prestress along much of the fault can be substantially lower then the local SSQS shear resistance. Ruptures nucleate in regions of locally high prestress close to the local SSQS shear resistance, however points elsewhere throughout the rupture are brought to failure from initially low prestress levels by the concentration of stresses at the dynamic rupture front (Figures 5.2B & C and 5.3B & C). In fact, all of our simulated ruptures nucleate in regions with locally high prestress near the corresponding local SSQS resistance. Ruptures then propagate over areas of potentially much lower prestress conditions depending on the efficiency of dynamic weakening (Figure 5.3; Lambert et al., in review, 2021). For larger ruptures, the relatively high-stressed nucleation region is small compared to the total rupture area, such that the prestress over much of the ruptured fault area can be substantially lower than the local SSQS, or the shear stress required to initiate unstable quasi-static slip (Lambert et al., in review).

5.3 Measures of average fault shear stress

Here, we review different methods for averaging the shear stress along a fault over space and time. We denote methods for averaging shear stress over space with supercripts (e.g. τ^A), whereas quantities that represent temporal averages or require information about the full time-dependent slip process are denoted by a bar (e.g. $\overline{\tau}$). The formulations for average stress measures are presented in this section for a 1-D fault; the generalization of the average stress measures to 2-D interfaces in 3-D media are presented in Noda and Lapusta (2012).

In calculating average stress measures for individual dynamic ruptures, we define the rupture domain as the collection of points over the entire fault domain Ω where the local slip velocity exceeds the seismic velocity threshold:

$$\Omega_{\text{rupt}} = \{z \in \Omega | V(z) \geq V_{\text{thresh}}\}. \tag{5.8}$$

One may also compute the averages over the entire VW domain Ω_{vw} with velocity-weakening frictional properties:

$$\Omega_{\text{vw}} = \{z \in \Omega | (a(z) - b(z) < 0\} = \{|z| \leq \ 12\text{km}\}. \tag{5.9}$$

For our 2-D models with 1-D faults, the spatial averaging is performed over the fault length, such as the rupture length λ_{rupt} and length of the velocity-weakening region λ_{vw}:

$$\lambda_{\text{rupt}} = \int_{\Omega_{\text{rupt}}} dz; \qquad \lambda_{\text{vw}} = \int_{\Omega_{\text{vw}}} dz = 24 \text{ km}. \tag{5.10}$$

For model-spanning ruptures in our earthquake sequence simulations, the rupture length λ_{rupt} is comparable to the length of the VW region λ_{vw}. Thus average shear stress measures taken over the scale of the model-spanning earthquakes are expected to be comparable to averages over the total VW domain.

5.3.1 Spatially-averaged shear stress

The simplest definition of average shear stress along an interface is the spatially-averaged shear stress $\tau^A(t)$, which is just the spatial average of shear stress $\tau(z, t)$ acting in the overall

slip direction. For example, the spatially-averaged shear stress over the entire VW region in our models at time t is given by:

$$\tau^A_{\text{vw}}(t) = \frac{\int_{\Omega_{\text{vw}}} \tau(z,t)dz}{\lambda_{\text{vw}}}. \tag{5.11}$$

For a given rupture, the spatially-averaged prestress τ^A_{ini} and final stress τ^A_{fin} are given by:

$$\tau^A_{\text{ini}} \equiv \tau^A_{\text{rupt}}(t_{\text{ini}}) = \frac{\int_{\Omega_{\text{rupt}}} \tau(z,t_{\text{ini}})dz}{\lambda_{\text{rupt}}} \quad \text{and} \quad \tau^A_{\text{fin}} \equiv \tau^A_{\text{rupt}}(t_{\text{fin}}) = \frac{\int_{\Omega_{\text{rupt}}} \tau(z,t_{\text{fin}})dz}{\lambda_{\text{rupt}}}. \tag{5.12}$$

The spatially-averaged rupture stress $\overline{\tau}^A_{\text{rupt}}$, averaged over both the rupture area and duration, is given by:

$$\overline{\tau}^A_{\text{rupt}} = \frac{\int_{t_{\text{ini}}}^{t_{\text{fin}}} \int_{\Omega_{\text{rupt}}} \tau(z,t)dz}{\lambda_{\text{rupt}} T_{\text{rupt}}}, \tag{5.13}$$

where $T_{\text{rupt}} = t_{\text{fin}} - t_{\text{ini}}$ is the rupture duration.

While simple to define, the spatially-averaged shear stress is not generally the most useful definition. As the other average stress measures discussed below, it is impossible to directly compute, as generally we cannot infer the spatial distribution of absolute stress from remote observations. But this measure is also difficult to put constraints on or interpret, as it does not directly characterize the dissipation or describe the local frictional behavior (Noda & Lapusta, 2012).

5.3.2 Dissipation-based average shear stress

A more physically meaningful definition of average fault shear stress is the dissipation-based average shear stress $\tau^D(t)$, which is the spatial average of shear stress $\tau(z,t)$ acting in the overall slip direction weighted by the slip rate distribution. The dissipation-based average shear stress at time t over the entire VW region and a given rupture area Ω_{rupt} are given by:

$$\tau^D_{\text{vw}}(t) = \frac{\int_{\Omega_{\text{vw}}} \tau(z,t)V(z,t)dz}{\int_{\Omega_{\text{vw}}} V(z,t)dz} \quad \text{and} \quad \tau^D_{\text{rupt}}(t) = \frac{\int_{\Omega_{\text{rupt}}} \tau(z,t)V(z,t)dz}{\int_{\Omega_{\text{rupt}}} V(z,t)dz}, \tag{5.14}$$

respectively. The dissipation-based average prestress at the beginning of a rupture τ^D_{ini} is thus given by:

$$\tau^D_{\text{ini}} \equiv \tau^D_{\text{rupt}}(t_{\text{ini}}) = \frac{\int_{\Omega_{\text{rupt}}} \tau(z, t_{\text{ini}}) V(z, t_{\text{ini}}) dz}{\int_{\Omega_{\text{rupt}}} V(z, t_{\text{ini}}) dz}. \tag{5.15}$$

τ^D is equal to the increment in dissipation per increment in potency. The potency per unit length P over a given domain Ω in our 2-D models is related to the average slip $\overline{\delta}$ in the principal slip direction and fault length λ. The potency over the VW region Ω_{vw} and a given ruptured region Ω_{rupt} are given by:

$$P_{\text{vw}} = \int_{\Omega_{\text{vw}}} \int_0^t V(z, t') dt' dz = \overline{\delta}_{\text{vw}} \lambda_{\text{vw}} \quad \text{and} \quad P_{\text{rupt}} = \int_{\Omega_{\text{rupt}}} \int_{t_{\text{ini}}}^{t_{\text{fin}}} V(z, t') dt' dz = \overline{\delta}_{\text{rupt}} \lambda_{\text{rupt}}, \tag{5.16}$$

respectively. Here, $\overline{\delta}_{\text{vw}}$ is the cumulative average slip across the VW region up to time t and $\overline{\delta}_{\text{rupt}}$ is the average final slip accrued in the rupture between the initiation and termination of the rupture, t_{ini} and t_{fin}, respectively.

The cumulative dissipation per unit potency within the region Ω up to time t may generally be determined by integrating τ^D over the history of average slip within the region, and is often interpreted as the shear stress associated with heat generation (Noda & Lapusta, 2012). We define the shear heating stress in our simulations to be equal to the cumulative dissipation-based average shear stress over the VW seismogenic region, which is thought to be consistent with the shear stress averaged over seismogenic depths inferred from heat flow measurements around faults:

$$\overline{\tau}^D_{\text{heat}}(t) = \frac{\int_0^t \int_{\Omega_{\text{vw}}} \tau(z, t') V(z, t') dz dt'}{\int_0^t \int_{\Omega_{\text{vw}}} V(z, t') dz dt'} = \frac{\int_0^{\overline{\delta}_{\text{vw}}} \tau^D_{\text{vw}}(t(\delta')) d\delta'}{\overline{\delta}_{\text{vw}}}. \tag{5.17}$$

One can similarly define the dissipation-based average rupture stress $\overline{\tau}^D_{\text{rupt}}$ as the average shear stress associated with dissipation throughout a rupture. $\overline{\tau}^D_{\text{rupt}}$ is then related to the total dissipated energy per unit potency within the rupture, $E_{\text{Diss}}/P_{\text{rupt}}$, by integrating τ^D over the average slip of the rupture process:

$$\overline{\tau}^{D}_{\text{rupt}} = \frac{E_{\text{Diss}}}{P_{\text{rupt}}} = \frac{\int_{t_{\text{ini}}}^{t_{\text{fin}}} \int_{\Omega_{\text{rupt}}} \tau(z,t')V(z,t')dzdt'}{\int_{t_{\text{ini}}}^{t_{\text{fin}}} \int_{\Omega_{\text{rupt}}} V(z,t')dzdt} = \frac{\int_{0}^{\overline{\delta}_{\text{rupt}}} \tau^{D}_{\text{rupt}}(t(\delta'))d\delta'}{\overline{\delta}_{\text{rupt}}}. \tag{5.18}$$

The relationship between dissipated energy and heat generation assumes that most of the dissipation is localized near the principal shearing layer and converted into heat, with the energy dissipated by the generation of new fracture surfaces or chemical processes being relatively small. This assumption is supported by some laboratory and field measurements which suggest that the contribution of off-fault dissipation may indeed be small, $< 3\%$ (Aben et al., 2019; J. S. Chester et al., 2005; Rockwell et al., 2009).

One can see that τ^D and τ^A are equivalent when the slip rate V is uniform over the interface ($dV/dz = 0$), as may be the case in well-controlled laboratory experiments where loading displacements may be practically uniformly applied over the sample. In contrast, for interfaces experiencing spatially-varying slip rates, such as during ruptures or larger meter-scale laboratory experiments which experience spatially variable loading and slip (McLaskey et al., 2015; McLaskey & Lockner, 2014; Mclaskey & Yamashita, 2017; Yamashita et al., 2015), the value of $\tau^D(t)$ is controlled by the local shear resistance opposing regions of fastest motion, hence the regions dissipating most of the work imposed on the system. Thus, τ^D is a more useful definition for the *average shear resistance on the fault*, which can potentially be inferred from heat measurements. However, similarly to τ^A, the dissipation-based average shear stress τ^D is not directly related to the average local frictional behavior on the interface (Noda & Lapusta, 2012).

5.3.3 Energy-based average stress

The energy-based average rupture stress $\overline{\tau}^{E}_{\text{rupt}}$ is related to the average shear stress associated with the work, or strain energy change ΔW, given the potency of the rupture:

$$\overline{\tau}^{E}_{\text{rupt}} = \frac{\Delta W}{P_{\text{rupt}}} = \frac{1}{2}\left[\overline{\tau}^{E}_{\text{ini}} + \overline{\tau}^{E}_{\text{fin}}\right]. \tag{5.19}$$

Here, $\overline{\tau}^{E}_{\text{ini}}$ and $\overline{\tau}^{E}_{\text{fin}}$ refer to average shear stresses at the beginning and end of rupture, weighted by the final slip:

$$\overline{\tau}^E_{\text{ini}} = \frac{\int_{\Omega_{\text{rupt}}} \tau(z, t_{\text{ini}})\delta_{\text{rupt}}(z)dz}{\int_{\Omega_{\text{rupt}}} \delta_{\text{rupt}}(z)dz}; \qquad \overline{\tau}^E_{\text{fin}} = \frac{\int_{\Omega_{\text{rupt}}} \tau(z, t_{\text{fin}})\delta_{\text{rupt}}(z)dz}{\int_{\Omega_{\text{rupt}}} \delta_{\text{rupt}}(z)dz}. \tag{5.20}$$

The energy-based average shear stress can be related to the shear tractions and slip along the interface by integrating the work rate along a virtual quasi-static process connecting the beginning and termination of a rupture (Noda & Lapusta, 2012). One can construct a version of this process that results in an average curve with slip that aims to preserve the local shear resistance behavior as well as serve as an energy-partitioning diagram. By considering the average slip $\overline{\delta}_{\text{rupt}}$ in the overall slip direction after a rupture, one can scale the final slip throughout the rupture area $\tilde{\delta}(z) = \delta_{\text{rupt}}(z)/\overline{\delta}_{\text{rupt}}$ to provide a weighting based on the relative contribution of the local final slip at each point to the average slip or potency. One can then introduce the integration variable δ' which represents the increment in average slip from 0 to $\overline{\delta}_{\text{rupt}}$. If the slip and slip rate on the fault is always parallel to the overall slip direction, as it is in our 2-D models with 1-D faults, then the energy-based average stress can be written as a function of δ':

$$\overline{\tau}^E(\delta') = \frac{\int_{\Omega_{\text{rupt}}} \tau(z, \delta'\tilde{\delta}(z))\delta_{\text{rupt}}(z)dz}{\int_{\Omega_{\text{rupt}}} \delta_{\text{rupt}}(z)dz}. \tag{5.21}$$

$\overline{\tau}^E$ has been shown to represent the average local frictional behavior on the interface (Noda & Lapusta, 2012). Its plot vs. the accumulating slip can represent the energy partitioning during ruptures, with the area under the curve equal to the dissipated energy per unit fault area and the initial and final points contributing to the trapezoid illustrating the strain energy released (Figure 5.4).

Note that the energy-based average stress cannot be determined from the distribution of shear stress and slip along the interface at individual instants in time during dynamic rupture, but requires knowledge of the entire rupture event after the dynamic process is over. Therefore all energy-based average stress quantities require knowledge of the final slip, and hence are denoted by a bar, as in $\overline{\tau}^E(\delta')$. Note also that the average of $\overline{\tau}^E(\delta')$ as δ' varies from 0

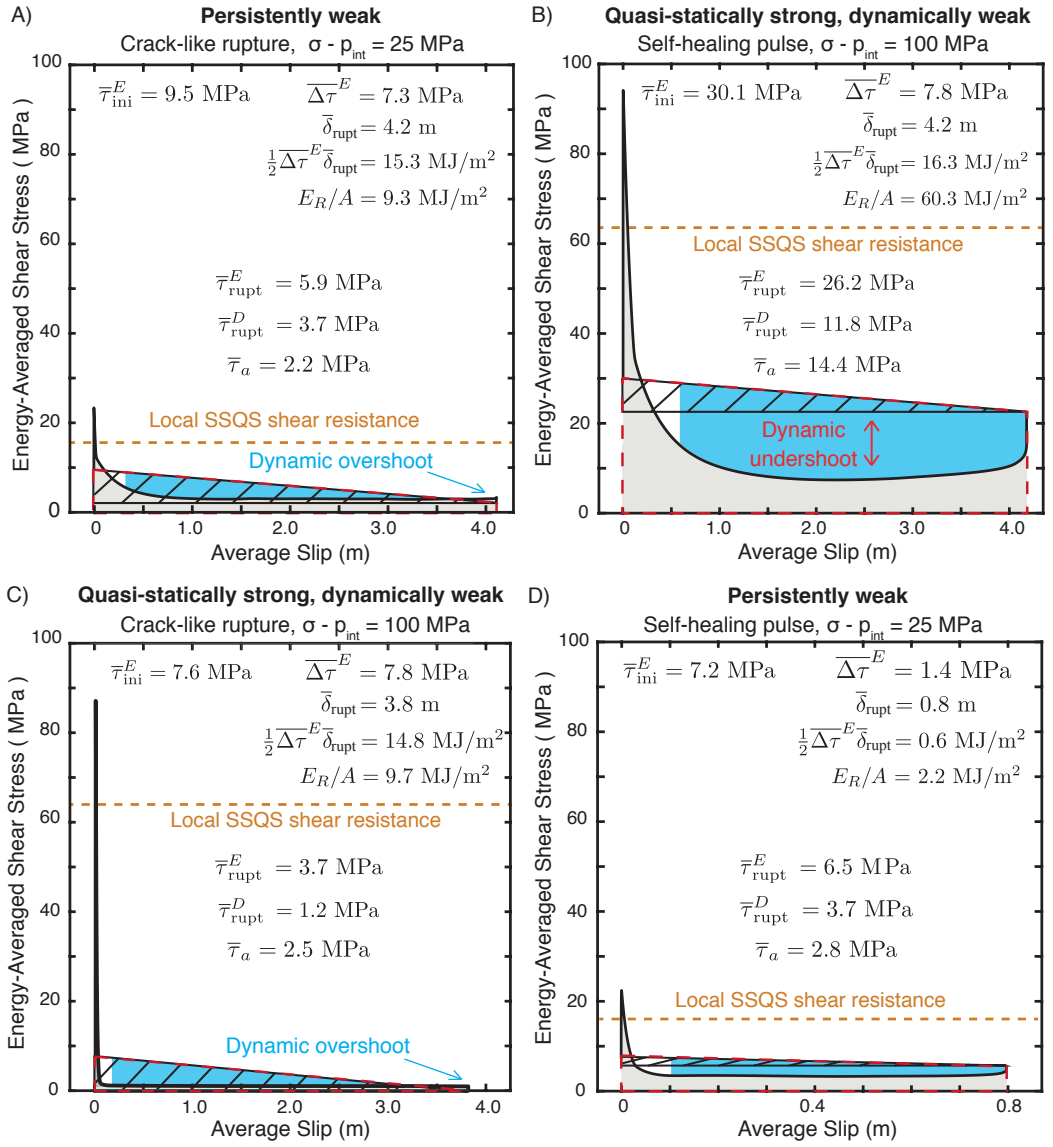

Figure 5.4: The energy-averaged shear stress vs. slip for the same representative ruptures as in Figure 5.2, illustrating the energy budget of each rupture. The two crack-like ruptures (A & C) and the self-healing pulse on the quasi-statically strong, dynamically weak fault (B) have comparable static stress drop and average slip, while the self-healing pulse under persistently weak conditions (D) has smaller average slip and static stress drop. The total strain energy change (dashed red trapezoid) is partitioned into radiated energy (blue shading), and dissipated energy (gray shading). (A & C) For both crack-like ruptures, the average static and dynamic stress drops are comparable. (B & D) The self-healing pulses experiences rapid healing resulting in average dynamic stress variations that are much larger than the average static stress change, and hence radiate more energy for the same average slip and static stress drop as the crack-like ruptures (B vs. A & C).

to the average rupture slip $\overline{\delta}_{\text{rupt}}$ is equal to $\overline{\tau}^D_{\text{rupt}}$ as the construction of $\overline{\tau}^E(\delta')$ preserves the dissipated energy.

5.3.4 Relationship between energy-averaged rupture stress, dissipation-averaged rupture stress, and apparent stress

The strain energy change W per unit rupture area A can be partitioned into the energy dissipated within the ruptured source region E_{Diss} and the energy that is radiated away to the far-field E_R:

$$\Delta W/A = \frac{1}{2}\left[\overline{\tau}^E_{\text{ini}} + \overline{\tau}^E_{\text{fin}}\right]\overline{\delta}_{\text{rupt}} = E_{\text{Diss}}/A + E_R/A. \tag{5.22}$$

For our 2-D simulations of ruptures on 1-D faults, we consider the average energy partitioning per unit rupture length λ_{rupt} rather than rupture area A. By dividing both sides of equation (5.22) by the average slip of the rupture, we can relate the energy-based average rupture stress $\overline{\tau}^E_{\text{rupt}}$ from equation (5.19) to the dissipation-based average rupture stress $\overline{\tau}^D_{\text{rupt}}$ and the seismologically-inferable apparent stress $\overline{\tau}_a = E_R/(\overline{\delta}_{\text{rupt}}A)$ (Wyss & Brune, 1968):

$$\overline{\tau}^E_{\text{rupt}} = \frac{E_{\text{Diss}}}{A\overline{\delta}_{\text{rupt}}} + \frac{E_R}{A\overline{\delta}_{\text{rupt}}} \tag{5.23}$$

$$= \overline{\tau}^D_{\text{rupt}} + \frac{E_R}{A\overline{\delta}_{\text{rupt}}} \tag{5.24}$$

$$= \overline{\tau}^D_{\text{rupt}} + \overline{\tau}_a \tag{5.25}$$

$\overline{\tau}^D_{\text{rupt}}$ represents the average dynamic shear resistance localized along the interface, whereas $\overline{\tau}^E_{\text{rupt}}$ includes the contribution from inertial resistance during dynamic rupture. This additional resistance, which is represented by the apparent stress $\overline{\tau}_a$, is sometimes referred to as the radiation resistance Savage and Wood (1971). For purely quasi-static processes where the radiated energy is negligible, the energy-based average rupture stress $\overline{\tau}^E_{\text{rupt}}$ is equivalent to the dissipation-based average dynamic resistance $\overline{\tau}^D_{\text{rupt}}$. $\overline{\tau}^D_{\text{rupt}}$ can, in principle, be inferred from heat flow measurements; while this may be difficult to accomplish for a single rupture, the long-term constraints on heat flow near mature faults, such as less than 10-20 MPa discussed in the introduction, may be a relevant stand-in for large dynamic ruptures.

$\overline{\tau}^E_{\text{rupt}}$ can then be inferred from $\overline{\tau}^D_{\text{rupt}}$ and remote inferences of earthquake source properties. The energy-based averages are, by definition, the physically relevant average shear stress measures for the work done to impose slip along a fault, and therefore may represent best the overall average shear resistance along the fault to external loading.

The energy-based average prestress before a rupture, $\overline{\tau}^E_{\text{ini}}$, can, in principle, be inferred from thermal constraints (to constrain $\overline{\tau}^D_{\text{rupt}}$), the apparent stress $\overline{\tau}_a$, and the energy-based static stress drop: $\overline{\Delta\tau}^E$:

$$\begin{aligned}\overline{\tau}^E_{\text{ini}} &= \overline{\tau}^E_{\text{rupt}} + \overline{\Delta\tau}^E/2 \\ &= \overline{\tau}^D_{\text{rupt}} + \overline{\tau}_a + \overline{\Delta\tau}^E/2. \end{aligned} \tag{5.26}$$

Ruptures with the same dissipation-based average dynamic resistance $\overline{\tau}^D_{\text{rupt}}$ but larger static stress drops and/or apparent stress thus have higher prestresses $\overline{\tau}^E_{\text{ini}}$. Note that the relevant definition of static stress drop for comparison with energy considerations is the energy-based, or slip-weighted, static stress drop $\overline{\Delta\tau}^E = \overline{\tau}^E_{\text{ini}} - \overline{\tau}^E_{\text{fin}}$, which has been shown to be greater than or equal to standard moment-based estimates of static stress drop from seismological inferences (Noda et al., 2013).

5.4 Relation among average shear stress measures associated with dynamic rupture

5.4.1 Average shear prestress

Let us begin by comparing average measures of shear prestress before our simulated ruptures. The energy-averaged prestress $\overline{\tau}^E_{\text{ini}}$ represents the average prestress associated with the potency of the impending rupture. $\overline{\tau}^E_{\text{ini}}$ differs from the spatially-averaged prestress τ^A_{ini} over the rupture area when the resulting slip distribution is not uniform. For our simulated partial ruptures that arrest within the VW region with uniform fault properties, the energy-based prestress τ^E_{ini} is typically slightly higher than the spatially-averaged prestress τ^A_{ini} (Figures 5.5). This is likely because regions of higher prestress tend to exhibit larger local static stress drop, and hence more slip, for the same efficiency of weakening, thus having a larger contribution to the energy-based average prestress. For larger ruptures that

propagate substantially into the VS regions, the spatially-averaged prestress can be larger than the energy-based prestress, depending on the VS properties and the amount of slip that occurs within the VS regions (Figures 5.5-5.6).

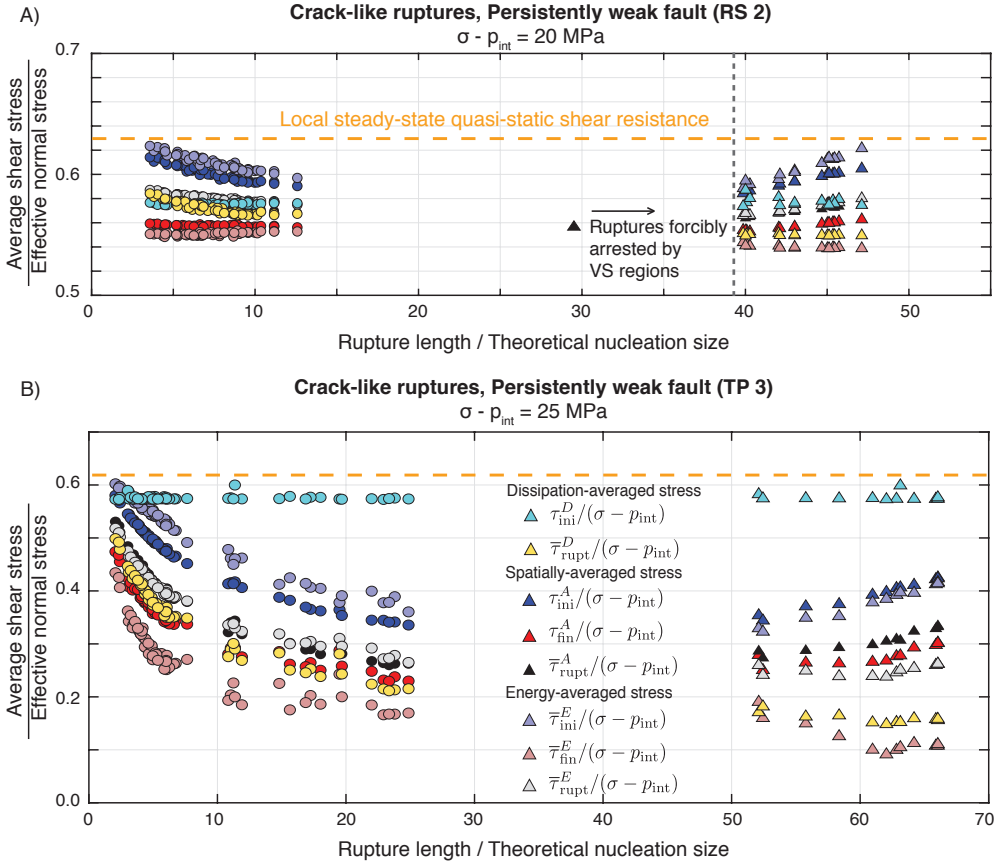

Figure 5.5: Comparison of average stress measures with rupture length for persistently weak fault models that produce crack-like ruptures (A) without and (B) with enhanced weakening due to thermal pressurization. (A) Standard rate-and-state friction results in relatively mild changes in friction and hence modest variation in the average shear stress measures for ruptures. (B) For fault models including at least mild enhanced dynamic weakening, average shear stress measures, except for the dissipation-based average prestress τ_{ini}^{D}, exhibit a notable decreasing trend with increasing rupture size. For crack-like ruptures, the dissipation-based rupture stress $\overline{\tau}_{\text{rupt}}^{D}$ is greater than energy-based average final stress $\overline{\tau}_{\text{fin}}^{E}$, due to the presence of a dynamic overshoot.

Overall, we find that τ_{ini}^{A} and $\overline{\tau}_{\text{ini}}^{E}$ for our simulated ruptures are generally comparable and decrease with increasing rupture size and efficiency of weakening behavior, becoming substantially lower than the average local SSQS shear resistance for increasingly larger ruptures

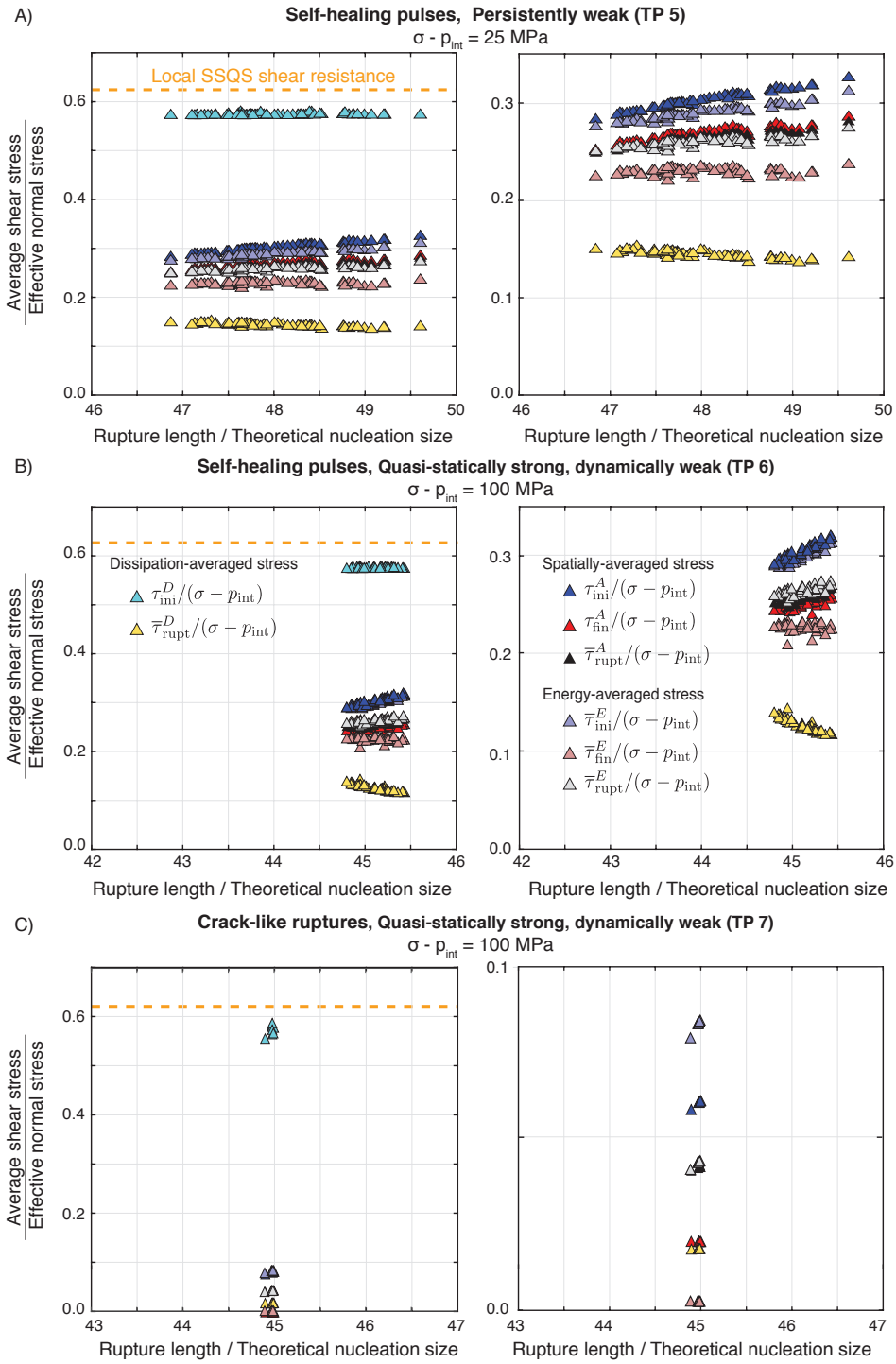

Figure 5.6: Comparison of average stress measures with rupture length for fault models producing self-healing pulses and crack-like ruptures with more efficient enhanced weakening. Stress measures are shown with (left) the same scale and (right) zoomed in to examine differences within individual simulations. (A-B) For self-healing pulses, the dissipation-based dynamic resistance $\overline{\tau}^D_{\rm rupt}$ (yellow) is lower than the other average stress measures, particularly the energy-based final stress $\overline{\tau}^E_{\rm fin}$ (light red). (C) In contrast, $\overline{\tau}^D_{\rm rupt}$ for crack-like ruptures is greater than $\overline{\tau}^E_{\rm fin}$, due to the presence of a dynamic overshoot.

in cases with efficient enhanced dynamic weakening, consistent with previous numerical studies (Figures 5.5-5.6, 5.7A vs. C; Lambert et al., in review).

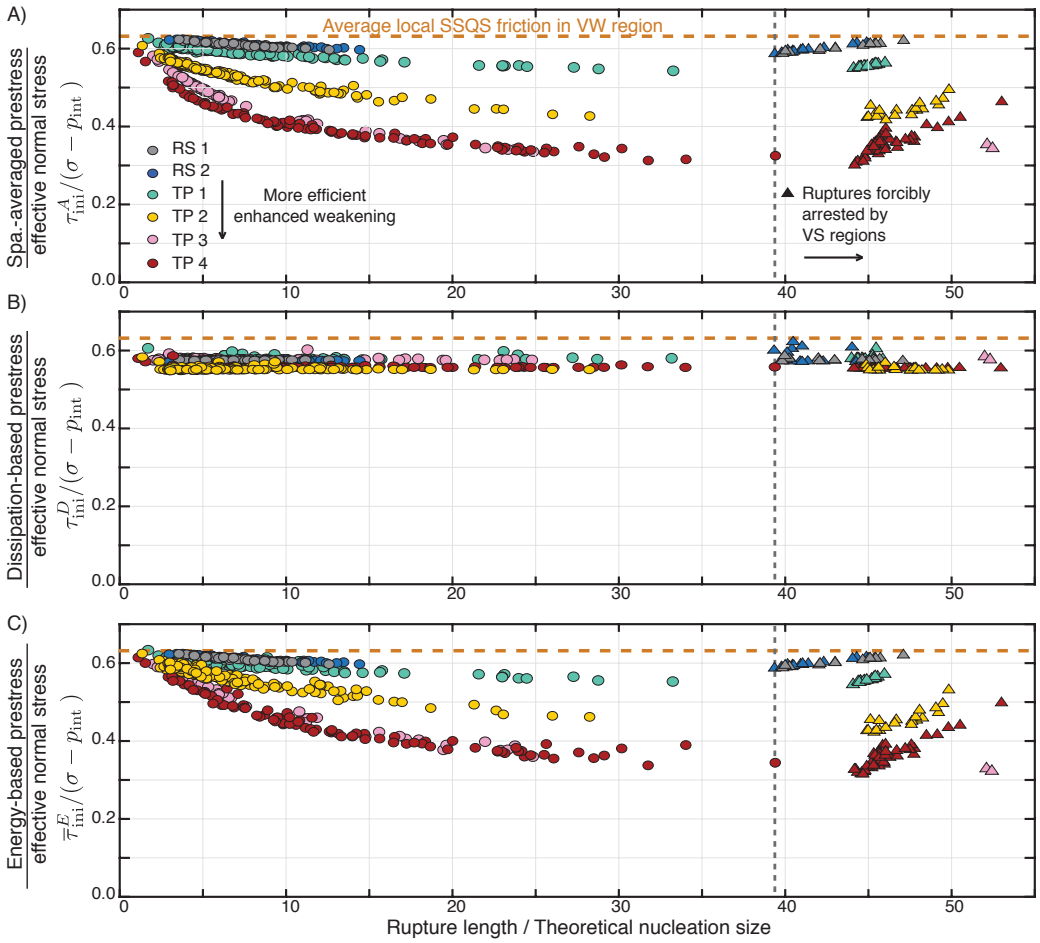

Figure 5.7: Scaling of measures of average rupture prestress with rupture length. (A) The spatially-averaged prestress $\tau^A_{\rm ini}$ for ruptures arresting in the VW region decreases with increasing rupture size. For ruptures that are forcibly arrested in the VS region, the average prestress increases as the average effective weakening decreases. (B) The dissipation-averaged stress $\tau^D_{\rm ini}$ at the initiation of ruptures is generally comparable to the average local SSQS shear resistance $\tau^{V_{\rm pl}}_{ss}$ (orange dashed line), and consistent among simulated ruptures of varying size and weakening behavior. (C) The energy-averaged prestress $\overline{\tau}^E_{\rm ini}$ is comparable spatially-averaged prestress $\tau^A_{\rm ini}$.

In contrast, we find that the dissipation-based prestress over the entire rupture area $\tau^D_{\rm ini}$ is determined by the average shear stresses in the nucleation region $\tau^D_{\rm nucl}$ (Figure 5.8A) and hence does not exhibit a notable dependence on the final rupture length (Figures 5.5 &

5.7B). We define the nucleation region for our simulated ruptures as the region between the expanding stress fronts at the initiation of dynamic rupture and refer to the measures of average shear prestress over this nucleation region at the initiation of rupture as the *nucleation stress*. The similarity between τ^D_{ini} and τ^D_{nucl} is due to the fact that the motion within the nucleation region is orders of magnitude faster than within the remainder of the impending rupture area which is locked during nucleation. Moreover, we find that the dissipation-based and spatially-averaged nucleation stresses, τ^D_{nucl} and τ^A_{nucl}, are comparable to each other (Figure 5.8) as well as to the average local SSQS resistance. Note that the spatially-averaged and dissipation-based nucleation stresses, τ^A_{nucl} and τ^D_{nucl}, as well as the dissipation-based prestress over the entire rupture area τ^D_{ini} may be more variable among different ruptures in fault models with more heterogeneous nucleation conditions.

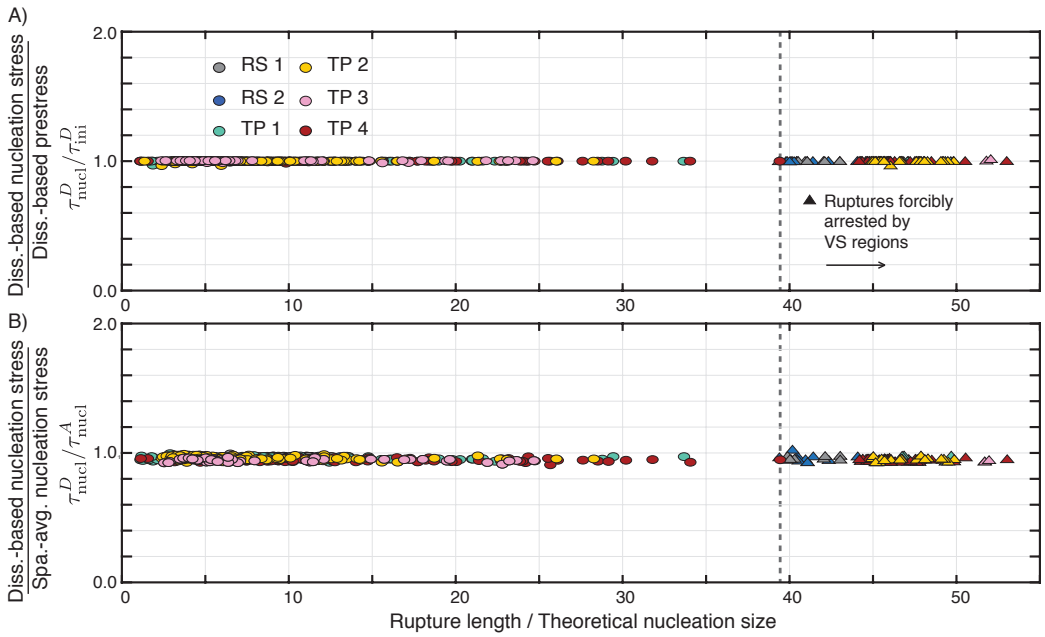

Figure 5.8: Relationship among dissipation and spatially-averaged nucleation stress, and dissipation-based rupture prestress. (A) The dissipation-based average prestress over the nucleation region τ^D_{nucl} is comparable to the dissipation-based average prestress over the entire rupture region τ^D_{ini}. (B) τ^D_{nucl} is also comparable to the spatially-averaged prestress within the nucleation region τ^A_{nucl}. Thus, τ^D_{ini}, τ^D_{nucl}, and τ^A_{nucl} are all comparable to the average local steady-state quasi-static shear resistance $\tau_{ss}^{V_{\text{pl}}}$ (Figure 5.7B), and are consistent among simulated ruptures of varying size and weakening behavior.

5.4.2 Relationship between average dynamic shear resistance and average stress measures for cracks and self-healing pulses

$\overline{\tau}^{E}_{\text{rupt}}$ is always greater than or equal to $\overline{\tau}^{D}_{\text{rupt}}$, since the difference between the two is given by the apparent stress $\overline{\tau}_{a}$ which must be positive (equation 5.23). Our simulations reproduce that (Figures 5.5-5.6). For our simulated ruptures, the spatially-averaged shear stress throughout the rupture process $\overline{\tau}^{A}_{\text{rupt}}$ is generally comparable to the energy-based rupture stress $\overline{\tau}^{E}_{\text{rupt}}$.

The relationship between the dissipation-based rupture stress $\overline{\tau}^{D}_{\text{rupt}}$ and other average stress measures can substantially depend on the style of rupture propagation. For crack-like ruptures, the dissipation-based average rupture stress $\overline{\tau}^{D}_{\text{rupt}}$ is within one static stress drop of the spatially and energy-averaged stresses before (τ^{A}_{ini} and $\overline{\tau}^{E}_{\text{ini}}$) and during ($\overline{\tau}^{A}_{\text{ini}}$ and $\overline{\tau}^{E}_{\text{rupt}}$) the rupture (Figures 5.5 and 5.6C). This is because the final and dynamic stress levels are comparable for the crack-like ruptures and a considerable portion of the total rupture area is slipping and dissipating energy at a given time (Figures 5.1A-B & 5.3 A-B top). In addition, $\overline{\tau}^{D}_{\text{rupt}}$ is higher than the energy-based final stress $\overline{\tau}^{E}_{\text{fin}}$ for crack-like ruptures (Yellow vs. light red in Figures 5.5, 5.6C, and 5.9A), due to the presence of the dynamic overshoot (Figure 5.4B & D). As the shear heating stress $\overline{\tau}^{D}_{\text{heat}}$ across the VW region is dominated by the dissipation during large model-spanning earthquakes, $\overline{\tau}^{D}_{\text{heat}}$ is also within one static stress drop of the spatially and energy-averaged stresses before and during large crack-like ruptures (Figure 5.10A & C).

Fault models with relatively mild weakening maintain average stress levels closer to the local SSQS shear resistance $\tau_{ss}^{V_{\text{pl}}}$ (Figures 5.3A, 5.5 & 5.10A). Such models require chronically weak fault conditions, such as through increased pore fluid pressure or low quasi-static friction, to maintain low values of the dissipation-based average rupture stress $\overline{\tau}^{D}_{\text{rupt}}$, and thus low shear heating stresses (Figure 5.10A). Crack-like ruptures with reasonable stress drops may also occur in fault models with very efficient weakening (Figure 5.3C), where that spatially-averaged average shear stress is far below (several static stress drops) the lo-

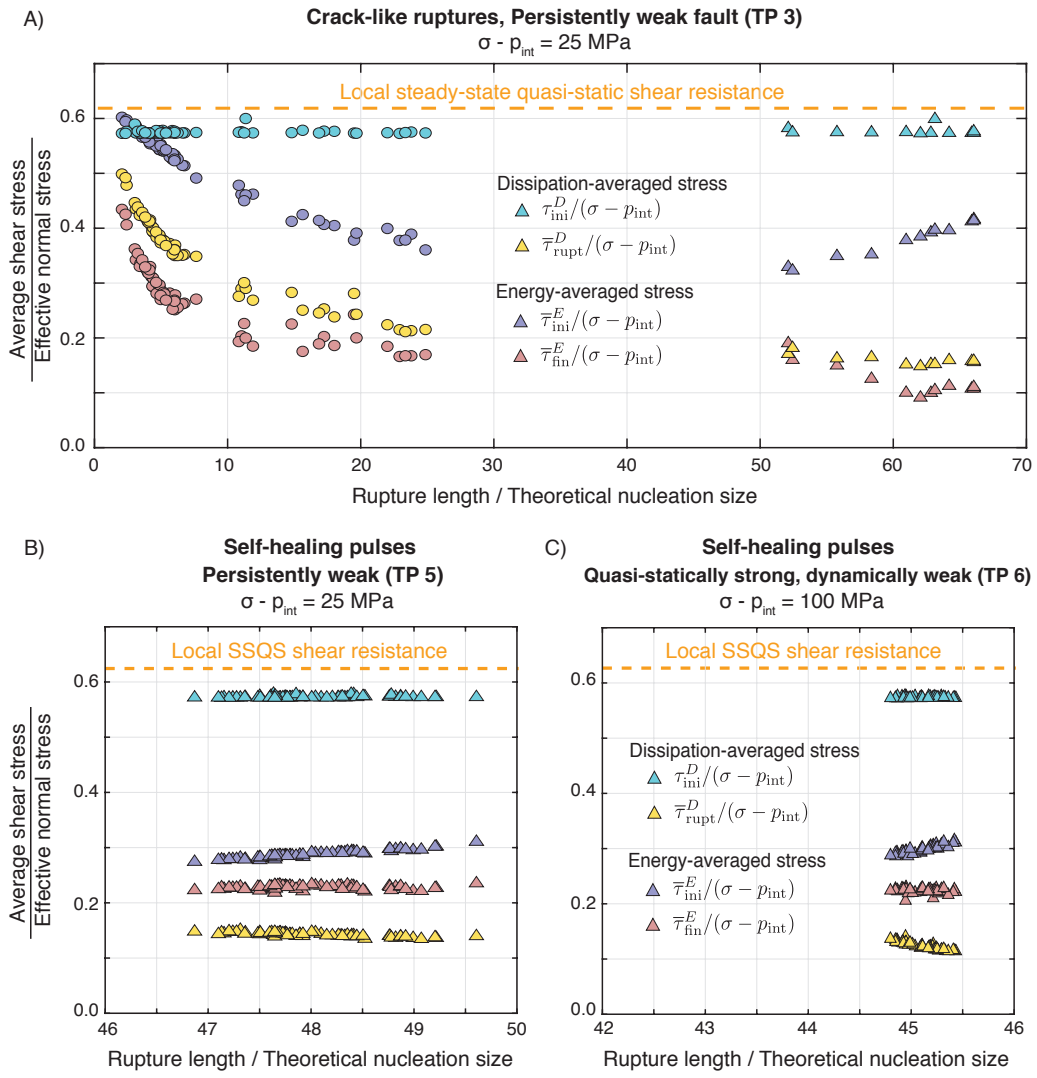

Figure 5.9: Comparison of the dissipation-based dynamic resistance and energy-based average pre-rupture and final shear stresses for crack-like and self-healing pulse-like ruptures. (A) For crack-like ruptures, the dissipation-based average rupture stress $\overline{\tau}^D_{\rm rupt}$ (yellow) –a measure of the average dynamic shear resistance –is higher than the energy-based final stress $\overline{\tau}^E_{\rm fin}$ (pink) due to the presence of a dynamic stress overshoot after rupture arrest. (B-C) In contrast, for self-healing pulses, the dissipation-based average rupture stress is lower than the energy-based final stress due to the presence of a dynamic undershoot. Thus, the energy-based static stress drop ($\overline{\Delta\tau}^E = \overline{\tau}^E_{\rm ini} - \overline{\tau}^E_{\rm fin}$) can substantially underestimate the difference between the energy-based pre-rupture stress and dissipation-based average dynamic resistance for self-healing pulse-like ruptures, whereas the average static stress drop is more comparable or may even overestimate the average dynamic stress drop for crack-like ruptures.

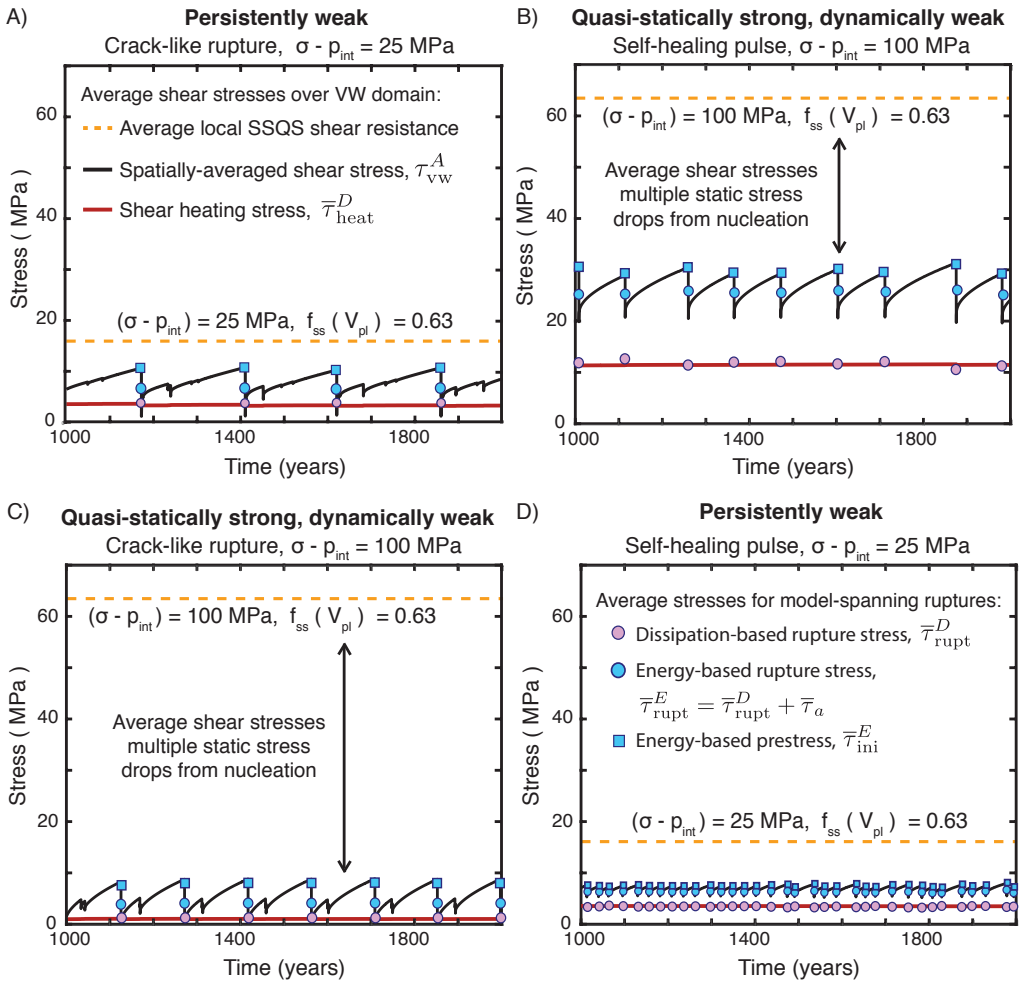

Figure 5.10: The evolution of average shear stress in the VW region over sequences of events for the four fault models shown in Figure 5.2. The spatially-averaged shear stress $\tau^A_{\rm vw}$ for the chronically weak fault producing crack-like ruptures (A) is always within 1-2 static stress drops from the average local SSQS shear resistance (orange line), whereas the average shear stress is far below the average local SSQS shear resistance for models exhibiting dynamically weak behavior (B - D). The dissipation-based stress $\overline{\tau}^D_{\rm rupt}$ from large VW-segment spanning earthquakes (pink circles) is consistent with the shear heating stress, which provides a lower bound of the average shear stress $\tau^A_{\rm vw}$. The energy-based prestress $\overline{\tau}^E_{\rm ini}$ and rupture stress $\overline{\tau}^E_{\rm rupt}$ from large VW-segment spanning earthquakes (blue squares and circles, respectively) provide a reasonable description of the spatially-averaged shear stress before large ruptures and throughout earthquake sequences, independent of the style of rupture.

cal SSQS shear resistance (Figures 5.3C, 5.10C, and 5.6C). While crack-like ruptures may exhibit chronically weak or locally quasi-statically strong, dynamically weak behavior, the spatial and energy-averaged prestresses (τ^A_{ini} and $\overline{\tau}^E_{\text{ini}}$) are constrained to be within one static stress drop of the dissipation-based average dynamic resistance $\overline{\tau}^D_{\text{rupt}}$ (Figures 5.10A-B).

In contrast, for self-healing pulses, the dissipation-based average rupture stress $\overline{\tau}^D_{\text{rupt}}$ can be several static stress drops below the spatially and energy-averaged stresses before (τ^A_{ini} and $\overline{\tau}^E_{\text{ini}}$) and during ($\overline{\tau}^A_{\text{ini}}$ and $\overline{\tau}^E_{\text{rupt}}$) the rupture (Figures 5.6A-B and 5.9B-C). Moreover, $\overline{\tau}^D_{\text{rupt}}$ is lower than both the spatial and energy-based average final stresses, τ^A_{fin} and $\overline{\tau}^E_{\text{fin}}$, respectively (yellow vs. red in Figures 5.6A-B and 5.9B-C). This is because only a small portion of the fault slips at a given time and the level of dynamic resistance is much lower than the final stress after healing (Figures 5.1B & D and 5.3B & D). As such, the fault can sustain substantially higher spatial and energy-averaged prestresses and final stresses, while still maintaining low levels of dynamic resistance and producing moderate average static stress drops (Figures 5.4B & 5.10B). Note that the same relationship holds for self-healing pulses that propagate on faults with persistently weak conditions, such as with low effective normal stress due to chronic fluid overpressurization, however such pulses result in relatively small average slip and static stress drops (Figures 5.4D & 5.10D).

Thus, we find that the dissipation-based stress averages $\overline{\tau}^D_{\text{rupt}}$ and $\overline{\tau}^D_{\text{heat}}$ provide lower bounds for the spatial and energy-averaged shear stress on the fault. How much larger can the spatial and energy-averaged shear stress be depends on the degree of stress undershoot (Figures 5.5, 5.6 & 5.10). The sharper the self-healing pulse-like ruptures, the larger the undershoot and apparent stress (Lambert et al., 2021), and hence the larger the average rupture prestress can be compared to the average dissipation-based shear stress.

5.4.3 Comparison of average static stress drop and average dissipation-based quasi-static versus dynamic shear resistance

If one compares the difference between the dissipation-based average prestress τ_{ini}^{D} and rupture stress $\overline{\tau}_{rupt}^{D}$ –measures of average quasi-static and dynamic shear resistance, respectively –the apparent coefficient of friction can indeed drop from $\tau_{ini}^{D}/(\sigma - p_{int})$ near typical Byerlee values around 0.6, down to values of $\overline{\tau}_{rupt}^{D}/(\sigma - p_{int})$ less than 0.2, depending on the rupture size, and hence amount of slip, as well as the efficiency of weakening (Figures 5.5-5.6). This observation is consistent with large changes in the apparent friction coefficient associated with the presence of enhanced dynamic weakening in high-speed laboratory friction experiments (Di Toro et al., 2011; Tullis, 2007; Wibberley et al., 2008).

However, this large change in average shear stress associated with dissipation does not correspond to large spatial or energy-based average static stress drops for our simulated ruptures. As our simulated ruptures grow larger with respect to their nucleation size, the spatial and energy-averaged prestresses, τ_{ini}^{A} and $\overline{\tau}_{ini}^{E}$, become considerably lower than the dissipation-based prestress τ_{ini}^{D} (Figures 5.5-5.6). The spatial and energy-based average final shear stresses, τ_{fin}^{A} and $\overline{\tau}_{fin}^{E}$, remain comparable to or greater than the dissipation-based rupture stress $\overline{\tau}_{rupt}^{D}$ (Figures 5.5-5.6). In particular, as the final shear stress for self-healing pulses can be much higher than the dissipation-based rupture stress $\overline{\tau}_{rupt}^{D}$, the overall difference between the spatial and energy-based average prestresses and final stresses can be considerably smaller than the difference between the dissipation-based prestress and rupture stress (Figure 5.6A-B and 5.9B-C). Thus, while the difference between average quasi-static and dynamic shear resistance may substantially increase with rupture size, and hence average slip, the resulting spatially-averaged and energy-based static stress drops can be relatively mild (Figure 5.11).

5.4.4 Impact of VW to VS transition for the scale-dependence of average shear stress measures

For simulated ruptures that span the entire VW domain and propagate substantially into the VS regions, the energy-based and spatially-averaged prestress, $\overline{\tau}_{ini}^{E}$ and τ_{ini}^{A}, respectively,

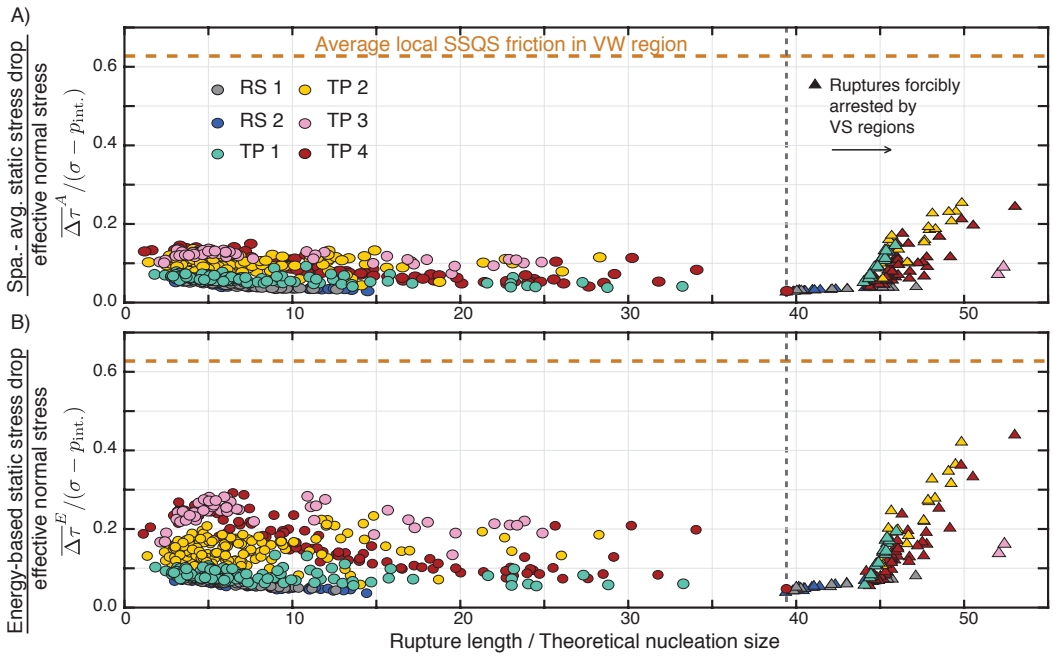

Figure 5.11: Scaling of spatial and energy-based average static stress drops with rupture length. The (A) spatially-averaged and (B) energy-based average static stress drops for ruptures represent relatively mild decreases in average shear stress with respect to the effective normal stress and are nearly magnitude-invariant for ruptures that arrest within the VW region. The average stress drops for ruptures that penetrate into the VS region increase with rupture size, depending the VS properties (Perry et al., 2020).

increase with rupture size beyond the extent of the VW domain (Figures 5.5 and5.7A & C). In contrast, the energy-based rupture stress $\overline{\tau}^E_{\text{rupt}}$ and spatially-averaged rupture stress $\overline{\tau}^A_{\text{rupt}}$ continue to decrease with increasing rupture size (Figures 5.5 and 5.12). The scaling of the spatial and energy-based final stress with rupture size can consequently vary depending on the properties of the VS region as well as co-seismic healing. The increase in average prestress can result in both the spatially-averaged and energy-based average static stress drops increasing for larger ruptures that propagate substantially into the VS regions (Figure 5.11).

Previous numerical studies have shown that the scaling of average static stress drops with rupture size for ruptures that are arrested predominantly by the VS regions depends on the VS properties (Perry et al., 2020). The VW to VS boundary marks a strong transition in

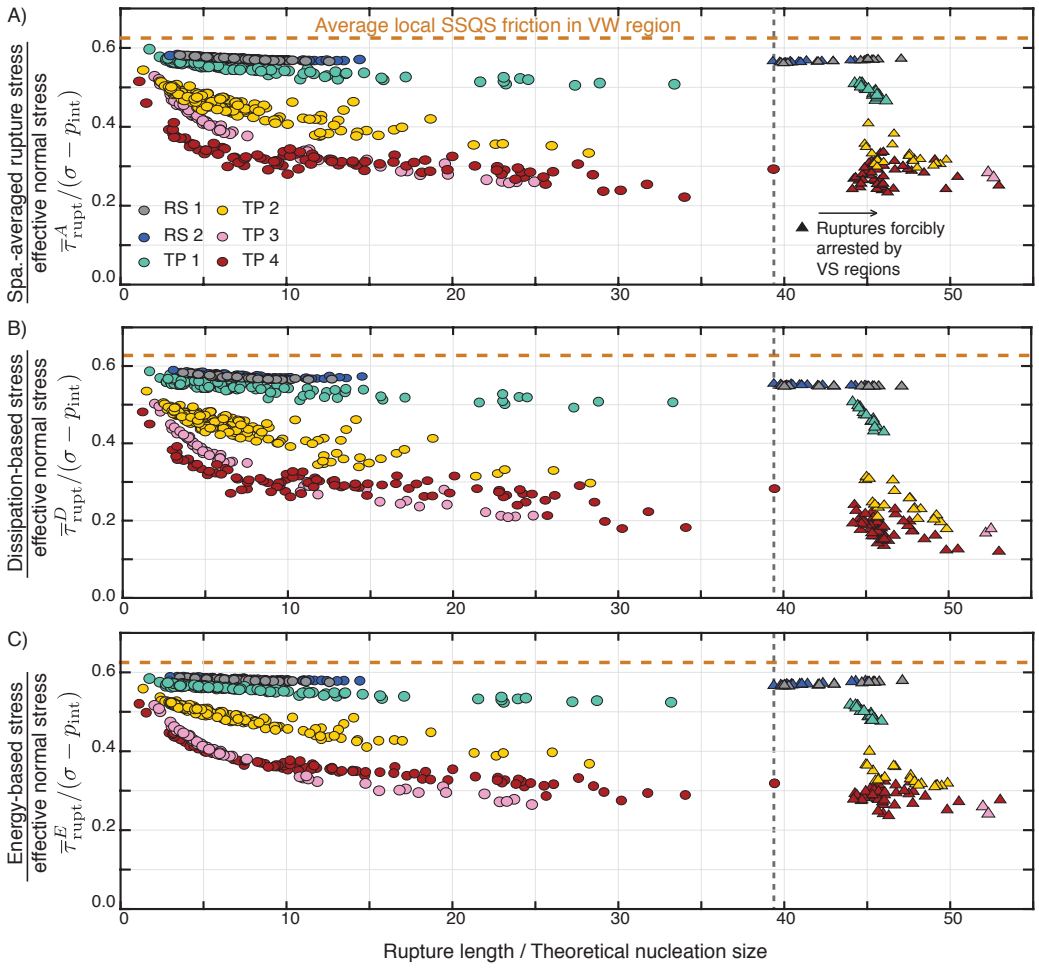

Figure 5.12: Scaling of measures of average rupture shear stress with rupture length. The (A) spatially-averaged rupture stress $\overline{\tau}^{A}_{\mathrm{rupt}}$, (B) dissipation-based rupture stress $\overline{\tau}^{D}_{\mathrm{rupt}}$, and (C) energy-based rupture stress $\overline{\tau}^{E}_{\mathrm{rupt}}$ decrease with increasing rupture size, similar to the spatially- and energy-averaged prestresses in Figure 5.7.

weakening behavior, where ruptures are arrested due to increased dissipation in the VS regions. As localities with VS properties experience increasing shear resistance with slip rate, the "weakening" behavior would in fact be negative. The increase in average prestress with rupture penetration into the VS region is consistent with the notion that fault models with more efficient weakening require lower average prestress for rupture propagation, and those with less efficient weakening require higher average prestress levels for continued rupture propagation, as demonstrated in previous numerical studies (Lambert et al., in review). For our models that include weakening due to thermal pressurization, the continued weakening

with increasing rupture size is a result of continued slip behind the rupture front which produces further pore fluid pressurization at non-zero levels of dynamic shear resistance, thus continuing to drop the effective normal stress. The continued weakening due to thermal pressurization is confined to the VW region in our fault models. Numerical studies based on laboratory measurements of natural fault properties have also shown that enhanced dynamic weakening may facilitate net VW behavior as ruptures propagate through VS regions, raising questions about the relative role of VS properties and prestress conditions for the ultimate arrest of large earthquakes (Jiang & Lapusta, 2016; Noda & Lapusta, 2013). Examining the details of the properties at the rheological transition from VW to VS regions is beyond the scope of this study, but an important topic for future work.

5.5 Relationship among earthquake source observations, rupture styles, and absolute stress levels on faults

5.5.1 Relationship between static stress drop, apparent stress, and absolute stress levels

The discrepancy between the energy-based and the dissipation-based average rupture stresses, $\overline{\tau}^{E}_{\text{rupt}}$ and $\overline{\tau}^{D}_{\text{rupt}}$, respectively, is described by the apparent stress $\overline{\tau}_a$ (equation 5.22), which reflects the additional inertial resistance during dynamic rupture. Apparent stress has commonly been associated with the static stress drop in seismological analyses (Ide & Beroza, 2001; Ma & Archuleta, 2006; McGarr, 1999; Perez-Campos & Beroza, 2001). It has sometimes been used as a constraint for inversions of static stress drop, where it is assumed that the static stress drop must be larger than the apparent stress, consistent with a dynamic stress overshoot for crack-like ruptures (Savage & Wood, 1971; M. Wei & McGuire, 2014). However, this need not be the case as dynamic stress can be considerably larger than the static stress changes for self-healing pulse-like ruptures.

The ratio of the apparent stress to average static stress drop can be described by a radiation ratio, sometimes referred to as the radiation efficiency or Savage-Wood efficiency, which is also equal to the ratio of the radiated energy to the seismologically inferable available energy (Kanamori & Brodsky, 2004; Lambert et al., 2021; Noda et al., 2013; Savage & Wood, 1971):

$$\eta_R = \frac{E_R/A}{\frac{1}{2}\overline{\Delta\tau}^E \overline{\delta}_{\text{rupt}}} = \frac{2\overline{\tau}_a}{\overline{\Delta\tau}^E}. \tag{5.27}$$

Previous numerical simulations have shown that crack-like ruptures typically exhibit a relatively mild dynamic overshoot compared to the average static stress drop, meaning that crack-like ruptures result in comparable average static and dynamic stress drops, within a factor of two (Lambert et al., 2021). Thus, crack-like ruptures result in radiation ratios less than or around 1. Lambert et al. (2021) also demonstrate that sharper self-healing pulses, with shorter local slip durations compared to the rupture duration, result in increasingly greater stress undershoot and higher values of apparent stress than crack-like ruptures with the same static stress drop. Therefore self-healing pulses produce higher radiation ratios, greater than 1 (Figure 5.13, Lambert et al., 2021).

The relationship between the radiation ratio and rupture style demonstrates that whether the static stress drop adequately represents the average dynamic stress changes during a rupture depends on the degree of overshoot/undershoot, and hence the rupture model (Figures 5.4 & 5.13). In contrast, the apparent stress, which is derived from the radiated energy and thus more adequately describes the dynamic stress changes, is independent of the source model (McGarr, 1999).

5.5.2 Self-healing versus geometric pulses

A number of physical mechanisms can produce kinematically pulse-like rupture propagation, where a relatively small portion of the fault slides at a given time with shorter apparent local sliding duration compared to the total rupture duration. This includes self-healing pulse-like rupture propagation associated with enhanced dynamic weakening and rapid healing (Heaton, 1990; Lambert et al., 2021; Lu et al., 2007; Noda et al., 2009; Viesca & Garagash, 2015), as well as other mechanisms for creating pulse-like ruptures such as geometric restrictions of the seismogenic zone, strong frictional or stress heterogeneity, and elastic contrast across the fault interface (Ampuero & Ben-Zion, 2008; Andrews & Ben-Zion, 1997; Beroza & Mikumo, 1996; Day, 1982; Johnson, 1992; Michel et al., 2017; Olsen

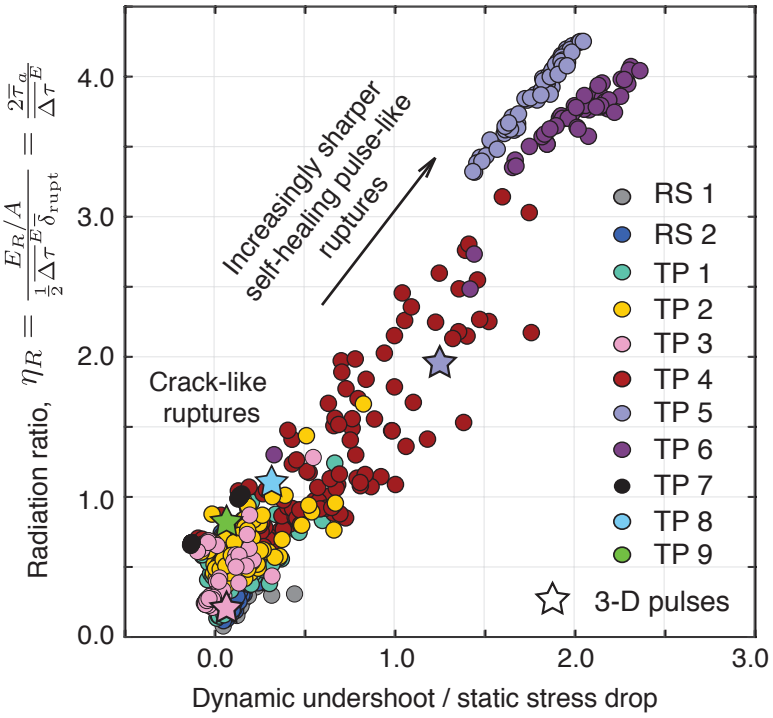

Figure 5.13: The radiation ratio, or ratio of apparent stress to energy-based static stress drop, increases for ruptures that experience larger average dynamic undershoot with respect to the static stress drop. Crack-like ruptures typically result in mild stress overshoot/undershoot whereas sharp self-healing pulses may experience a substantial stress undershoot and radiation ratios greater than 1 (Lambert et al., 2021). 3-D simulations of geometric (TP3, 8, 9) and self-healing pulses (TP5) are denoted by stars, showing that geometric pulses that exhibit mild to no undershoot exhibit comparable radiation ratios with crack-like ruptures.

et al., 1997). However, it is not clear that all mechanisms for pulse-like rupture propagation produce substantial dynamic stress undershoot, as exhibited by self-healing pulses.

A defining feature of self-healing pulses is the presence of substantial and rapid healing of local fault shear resistance on time scales much shorter than the duration of rupture propagation. For self-healing pulses resulting from enhanced dynamic weakening due to the thermal pressurization of pore fluids, the healing is governed by the diffusion of pore fluids. The relevant time scale for substantial fluid diffusion depends on the degree of shear localization, related to the shear zone half-width w in our models, and the hydraulic

diffusivity α_{hy}. The diffusion time $t_{diff} \propto w^2/\alpha_{hy}$ can provide an approximation for the time to substantial restrengthening due to pore fluid diffusion over scales comparable to the shear zone width. However, the actual evolution of stress and the duration of slip is a more complicated function of the efficiency of pore fluid diffusion and continued production of heat during sliding, which in turn depends on the evolution of slip rate and shear stress.

Let us consider ruptures in two fault models with the same hydraulic diffusivity $\alpha_{hy} = 10^{-4}$ m^2/s but different shear zone widths (TP5 and TP3). Ruptures in our 2-D simulations fault model TP5 with a more localized shear zone (w = 1 mm) propagate as self-healing pulses (Figure 5.4D), whereas ruptures in 2-D simulations of 1-D fault model TP3 with a broader shear zone (w = 10 mm) propagate as crack-like ruptures (Figure 5.4A). 3-D simulations of these fault models, with 2-D faults and a seismogenic region with aspect ratio of 4, produce ruptures that propagate kinematically as pulses; however, the dynamics and energy partitioning of the two ruptures is distinct (Figure 5.14). The 3-D pulse-like rupture in fault model TP5 with the shorter diffusion time is much sharper than the 3-D pulse in fault model TP3, and produces a notable dynamic undershoot and radiation ratio greater than 1. Thus, the 3-D pulse-like rupture in fault model TP5 exhibits characteristic behavior of a self-healing pulse, qualitatively similar to those in the corresponding 2-D simulations of the same fault model.

In contrast, the pulse-like rupture in 3-D fault model TP3 with the longer diffusion time does not exhibit much undershoot and has the overall energy partitioning generally consistent with a crack-like rupture, including a much larger static stress drop than apparent stress and radiation ratio less than 1. Thus, while the rupture in fault model TP3 is kinematically pulse-like in the 3-D simulation with the elongated fault, the average stress evolution and energy partitioning is more consistent with a crack-like rupture, as exhibited in the 2-D simulations of the same fault model. As such, this pulse-like rupture is more consistent with a geometrically-constrained dynamic crack, which we refer to as a geometric pulse.

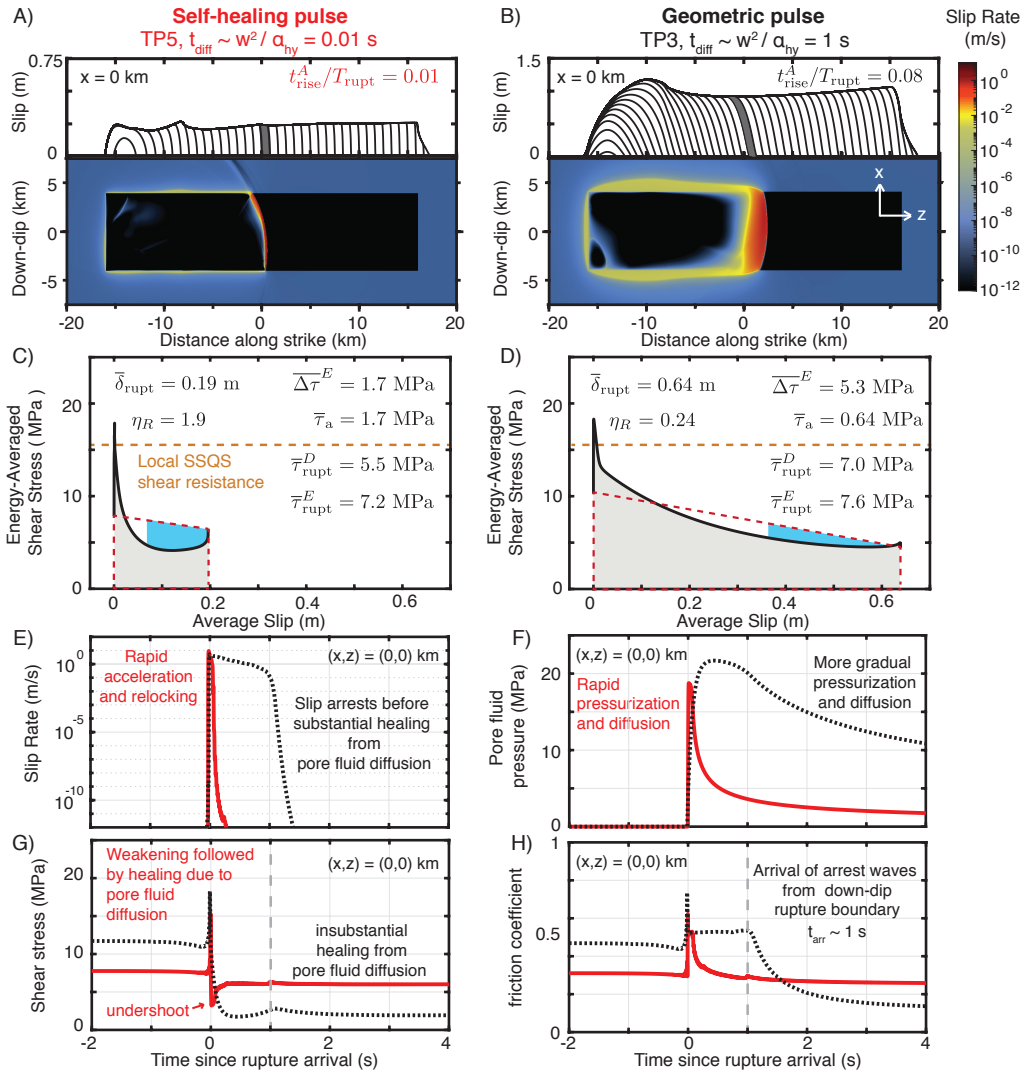

Figure 5.14: Comparison of self-healing versus geometric pulses in 3-D simulations of 2-D faults with the seismogenic zone of 4:1 aspect ratio. (A-B) Evolution of slip at $x = 0$ km (top) and the distribution of slip rate at an instant in time (bottom) for a self-healing pulse (A, TP5) and a geometric pulse (B, TP3). Slip contours are plotted every 0.25 s. Both ruptures exhibit pulse-like slip behavior where a small portion of the fault slips near seismic slip rates at a given instant during the rupture. (C-D) The corresponding average shear stress versus slip diagrams showing that the evolution of stress and energy partitioning of the self-healing pulse are consistent with our 2-D simulations. In contrast, the results for the geometric pulse are consistent with a crack-like rupture, including a mild overshoot. (E-H) Evolution of local slip rate, pore fluid pressure, shear stress, and coeffficient of friction with time in the center of the two ruptures. (E-F) The self-healing pulse exhibits rapid acceleration and relocking due to rapid thermal pressurization and fluid diffusion. In contrast, the evolution of pore fluid pressure is more gradual in the geometric pulse, and sliding continues near seismic slip rates until the arrival of arrest waves from the closer down-dip rupture boundary. (G-H) Rapid healing due to fluid diffusion leads to a considerable dynamic undershoot for the self-healing pulses, whereas most points within the geometric pulse do not exhibit considerable healing from fluid diffusion but rather slip is arrested due to unloading from arrest waves, producing a mild overshoot. The local shear stress considerably decreases for the geometric pulse upon unloading from arrest waves as the friction coefficient drops with the rapid decrease in slip rate (EQ 5.1). The local shear stress is not appreciably altered in the self-healing pulse as the point has already relocked.

Let us further examine the difference in evolution of local shear stress and slip during the self-healing and geometric pulses. The fault model with more localized shear (w = 1 mm, TP5) exhibits more efficient shear heating and thermal pressurization during rupture, but also more efficient diffusion, with a pore fluid diffusion time $t_{\text{diff}} \propto w^2/\alpha_{\text{hy}} = 0.01$ s. Thus points throughout the rupture experience rapid pressurization and healing due to the diffusion of pore fluids, and consequently a rapid acceleration of slip and subsequent relocking (Figure 5.14E-F). The substantial rapid healing due to fluid diffusion for the model with more localized shear (TP5) leads to considerable dynamic undershoot, consistent with a self-healing pulse (Figure 5.14C & G). In contrast, the fault model with the broader shearing layer (w = 10 mm, TP3) results in more gradual pressurization and fluid diffusion, with slip continuing at seismic slip rates until the arrival of arrest waves from the shorter down-dip rupture boundary. Contrary to local behavior in the self-healing pulse, points throughout the geometric pulse do not exhibit substantial healing due to fluid diffusion within the duration of the rupture. Rather, slip is arrested due to unloading from arrest waves, which results in a minor dynamic overshoot at the very end, as in a dynamic crack (TP3, Figure 5.14G). The local shear stress within the geometric pulse decreases upon unloading from arrest waves as the friction coefficient drops with the rapid decrease in slip rate (EQ 5.1, Figure 5.14E & H). The local shear stress in the self-healing pulse is not appreciably altered by the arrest waves as points within the ruptured area have already relocked before their arrival.

The significant distinction between the self-healing pulse and the geometric pulse is thus the manner in which local slip arrests, which is dictated by the mechanism for healing. Let us now compare ruptures in 3-D simulations of three fault models with the same localization of shear (w = 1 mm) but decreasing hydraulic diffusivity, and hence decreasing efficiency of healing indicated by the increasing diffusion times (Figure 5.15). Ruptures in all three models produce pulse-like ruptures with efficient weakening due to thermal pressurization, however models with longer diffusion times produce broader pulses with longer durations of slip that becomes increasingly more influenced by the fault geometry (Figure 5.15A-C). Some points in the center of the ruptures with longer diffusion times may exhibit moderate

restrengthening due to pore fluid diffusion before the arrival of arrest waves from the rupture boundary, and hence a mild undershoot (Figure 5.15I & K). However, as arrest waves arrive sooner at points closer to the rupture boundaries, most points throughout ruptures in fault models with longer diffusion times do not experience sufficiently fast healing, and rather slip is constrained by the dimensions of the rupture by the arrival of arrest waves (Figure 5.15J & L).

Ruptures with less efficient healing produce smaller dynamic undershoots and tend to exhibit larger static stress drops for comparable values of apparent stress, consistent with the previous analysis comparing crack-like and self-healing pulse-like ruptures based on 2-D simulations (Figure 5.15D-F). Hence the ruptures with less efficient healing are more "crack-like," despite appearing kinematically pulse-like. Consistent with the findings of Lambert et al. (2021), sharper self-healing pulses with shorter local sliding durations result in more substantial undershoot and produce higher radiation ratios, greater than 1 (Figure 5.13). Pulses become broader, with larger ratios of average rise time t^A_{rise} to rupture duration T_{rupt}, as the efficiency of both weakening and healing decreases.

5.5.3 Seismological approximation of energy-averaged prestress assuming near-zero residual shear resistance

If the shear resistance drops to near-zero values during large earthquake ruptures, the energy-averaged prestress $\overline{\tau}^E_{\text{ini}}$ can potentially be approximated purely from seismologically inferable quantities, with some input from modeling. The total dissipated energy per unit rupture area can be partitioned further into the average breakdown energy G and residual dissipated energy E_{F}/A below the minimum average shear stress during sliding (Cocco et al., 2004; Kanamori & Brodsky, 2004; Kanamori & Rivera, 2013; Ye et al., 2016b). The sum of the strain energy change available for the breakdown process and radiation is referred to as the available energy $\Delta W_0 = GA + E_R$, which is thought to represent the energy relevant to the dynamics of the rupture (Kanamori & Brodsky, 2004). If the shear resistance drops to near-zero values during rapid slip, then $E_{\text{F}} \approx 0$ and the energy-averaged prestress $\overline{\tau}^E_{\text{ini}}$ can be determined from the available energy ΔW_0, potency $\overline{\delta}_{\text{rupt}}A$, and energy-based static stress

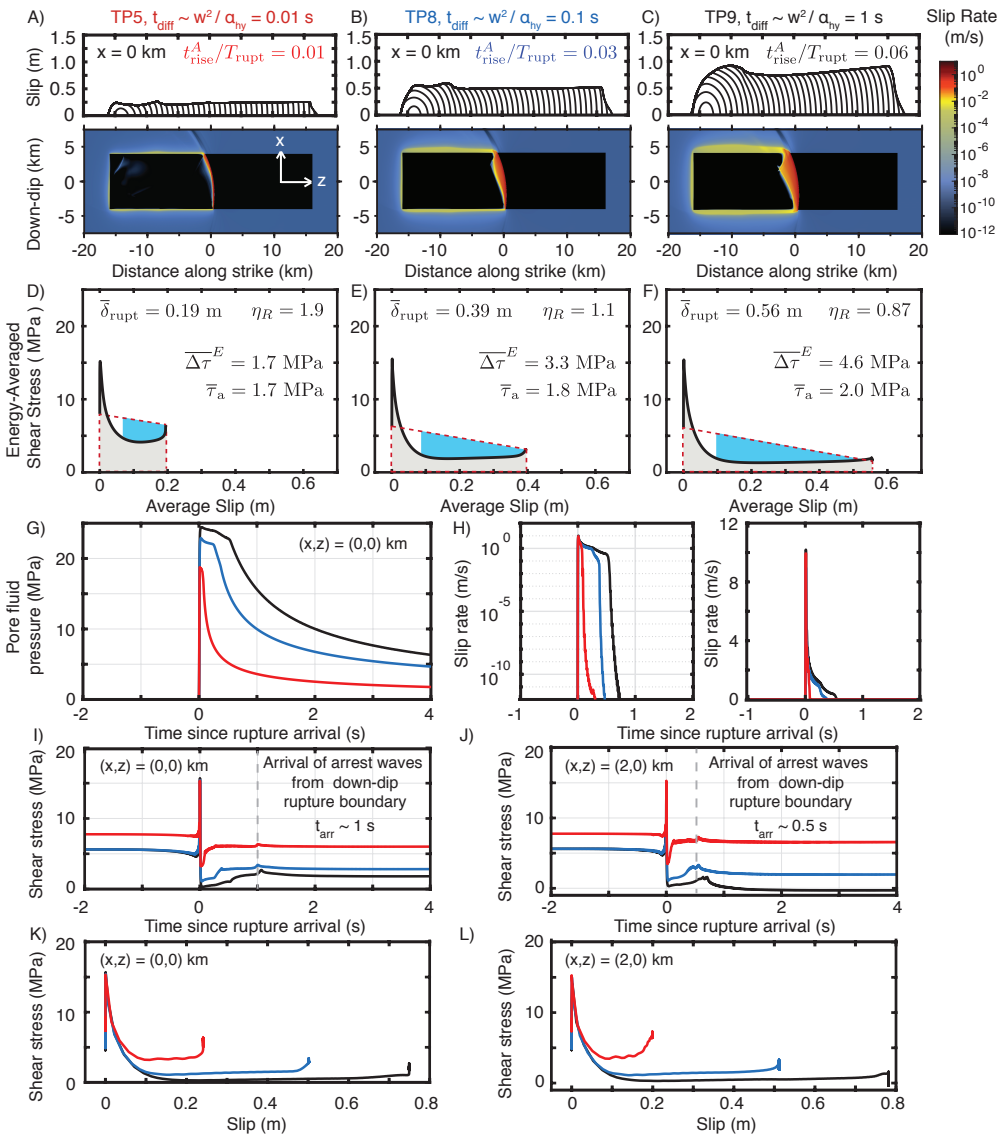

Figure 5.15: Comparison of pulse-like ruptures in 3-D models with 2-D faults with decreasing hydraulic diffusivity. (A-C) Evolution of slip at $x = 0$ km (top) and the distribution of slip rate at an instant in time (bottom) for ruptures in fault models with decreasing hydraulic diffusivity, and hence increasing fluid diffusion time scales. Slip contours are plotted every 0.25 s. (D-F) The corresponding average shear stress versus slip diagrams illustrating the energy partitioning. Fault models with efficient TP and relatively short fluid diffusion time result in self-healing pulses and a substantial stress undershoot (D), whereas models with longer fluid diffusion times produce broader pulses with the duration of slip influenced by rupture geometry. (G-H) The evolution of local pore fluid pressure and slip rate in the center of the fault. Models with efficient TP and short diffusion times exhibit rapid pressurization and healing from fluid diffusion whereas models with lower hydraulic diffusivity exhibit slower healing, resulting in broader pulses with longer seismic slip rate durations. (I-L) Evolution of shear stress with time and slip in the center of the ruptures (I & K) and closer to the rupture boundary (J & L). Healing due to fluid diffusion can be more pronounced in the center of the rupture further from the rupture boundary, resulting in a stress undershoot that is more pronounced for sharper pulses in models with shorter fluid diffusion times. (J & L) Many points in models with longer diffusion time scales are arrested due to arrest waves, which arrive earlier at points closer to the rupture boundary, resulting in rupture propagation being predominantly crack-like.

drop $\overline{\Delta\tau}^E$:

$$\overline{\tau}^E_{\text{ini}} = \overline{\tau}^D_{\text{rupt}} + \overline{\tau}_a + \overline{\Delta\tau}^E/2 \tag{5.28}$$

$$\approx \frac{G}{\overline{\delta}_{\text{rupt}}} + \overline{\tau}_a + \overline{\Delta\tau}^E/2, \quad \text{if } E_{\text{F}} \approx 0 \tag{5.29}$$

$$= \frac{G + E_R/A}{\overline{\delta}_{\text{rupt}}} + \overline{\Delta\tau}^E/2 \tag{5.30}$$

$$= \frac{\Delta W_0}{\overline{\delta}_{\text{rupt}} A} + \overline{\Delta\tau}^E/2. \tag{5.31}$$

The available energy per unit rupture area can be approximated by the energy-based static stress drop $\overline{\Delta\tau}^E$, average slip $\overline{\delta}_{\text{rupt}}$, and dynamic undershoot γ as (Lambert et al., 2021):

$$\Delta W_0/A \approx \left(\frac{1}{2} + \gamma\right) \overline{\Delta\tau}^E \overline{\delta}_{\text{rupt}}, \quad \text{where} \quad \gamma = \left(\overline{\tau}^E_{\text{fin}} - \min(\overline{\tau}^E(\delta'))\right) / \overline{\Delta\tau}^E. \tag{5.32}$$

Here, $\min(\overline{\tau}^E(\delta'))$ is the minimum of the energy-averaged stress versus slip diagram (Figure 5.4). This relation assumes that the fault resistance does not recover appreciably from the minimum level of average dynamic stress before the final slip. Note that, in the absence of any considerable dynamic overshoot or undershoot ($\gamma \approx 0$), the available energy can be estimated from the energy-based static stress drop and average slip. Lambert et al. (2021) have shown that $\overline{\Delta\tau}^E \overline{\delta}_{\text{rupt}}/2$ provides a reasonable estimate of the true available energy ΔW_0 for simulated crack-like ruptures, within a factor of 2. In contrast, simulated self-healing pulses exhibit considerable dynamic undershoot (with γ up to 4), resulting in notably larger available energy than given by $\overline{\Delta\tau}^E \overline{\delta}_{\text{fin}}/2$, as encapsulated in equation (5.32). Following Lambert et al. (2021), we refer to the quantity $\overline{\Delta\tau}^E \overline{\delta}_{\text{fin}}/2$ as the seismologically-inferable available energy, since it can be inferred from seismological observations, yet does not always represent the true available energy (Abercrombie & Rice, 2005; Kanamori & Rivera, 2013; Lambert et al., 2021; Rice, 2006; Venkataraman & Kanamori, 2004; Ye et al., 2016b).

The findings of Lambert et al. (2021) also suggest that a scaling relationship may exist between the dynamic undershoot γ, the radiation ratio η_R, and a scaled measure of the average local rise time, such as the ratio of rise time to rupture duration, $t^A_{\text{rise}}/T_{\text{rupt}}$, i.e.

$\gamma = F(\eta_R, t^A_{\text{rise}}/T_{\text{rupt}})$. Thus, if (i) $E_{\text{F}} \approx 0$, (ii) one can infer the ratio of average local rise time to rupture duration $t^A_{\text{rise}}/T_{\text{rupt}}$, and (iii) the relation $\gamma = F(\eta_R, t^A_{\text{rise}}/T_{\text{rupt}})$ is known (for example, from modeling), the energy-based prestress can then be determined from seismologically-inferable quantities:

$$\overline{\tau}^E_{\text{ini}} \approx (1+\gamma)\,\overline{\Delta\tau}^E, \quad \text{if } E_{\text{F}} \approx 0 \tag{5.33}$$

$$= \left[1 + F(\eta_R, t^A_{\text{rise}}/T_{\text{rupt}})\right] \overline{\Delta\tau}^E. \tag{5.34}$$

In Lambert et al. (2021), the dependence $F(\eta_R, t^A_{\text{rise}}/T_{\text{rupt}})$ has been empirically determined based on 2-D models of a single planar fault segment. These results motivate more detailed study of scaling relationships among source properties of 3-D dynamic rupture scenarios, including more realistic fault geometries and various forms of fault heterogeneity.

5.6 Discussion

As discussed in Lambert et al. (in review), the average shear prestress before rupture represents a measure of the average shear stress that the fault can hold before failing in a rupture over that region, and hence can indicate a measure of the *average fault strength* over the scale of the rupture area. The dissipation-based and energy-based average prestress, τ^D_{ini} and $\overline{\tau}^E_{\text{ini}}$, are more physical interpretations of the average fault strength than the merely spatially-averaged shear prestress τ^A_{ini}, since they are representative of the shear resistance acting against motion, whereas τ^A_{ini} is not.

The dissipation-based average stress measures from our simulated ruptures are consistent with standard notions of shear resistance from laboratory experiments. The average dissipation-based prestress τ^D_{ini} represents the average shear resistance acting against quasi-static motion during rupture nucleation, and it is comparable to the prescribed local steady-state quasi-static resistance as well as average nucleation stress for our simulated ruptures, independent of rupture size (Figures 5.5 and 5.7B). Therefore, it is not necessarily representative of the average prestress over the entire ruptured region. A potential exception may be rupture events where the nucleation region is comparable to the total

rupture size, as considered in some models of slow-slip transients (e.g Y. Liu & Rice, 2005). The dissipation-based rupture stress τ^D_{rupt} represents the average dynamic shear resistance to motion on the fault during rupture and decreases with increasing rupture size and average slip in a manner consistent with observations of enhanced dynamic weakening in the lab.

The energy-based prestress $\overline{\tau}^E_{\text{ini}}$ is most compatible with the notion of average fault strength over the scale of a rupture as it incorporates the shear stress preceding the impending motion of interest over the entire rupture area, weighted by final slip. It is also the most practical definition as it can, in principle, be inferred from field observations (Equation 5.26). The energy-based prestress, as well as the spatially-averaged prestress, in our simulated ruptures decreases with increasing rupture size, which makes the large fault areas appear "weak" or under-stressed with respect to their quasi-static shear resistance required for rupture nucleation, depending on the efficiency of dynamic weakening (Lambert et al., in review). These results are consistent with previous numerical studies demonstrating that fault models with enhanced weakening due to thermal pressurization can result in nearly magnitude-invariant static stress drops, with values consistent with those from natural earthquakes between 1 to 10 MPa, despite exhibiting increased weakening with slip and rupture size (Lambert et al., 2021; Perry et al., 2020). The discrepancy between stress conditions for rupture nucleation and propagation illustrates the importance of considering finite-fault effects and the heterogeneity in motion and shear stress associated with rupture behavior when relating small-scale laboratory friction measurements to larger-scale average shear stress measures on natural faults, such as the static stress drops in earthquake ruptures (Lambert et al., in review; Perry et al., 2020).

We find that rapid fault healing at the end of seismic slip that facilitates self-healing pulses can result in substantial difference between the dissipation-based average dynamic resistance $\overline{\tau}^D_{\text{rupt}}$, which is most related to shear heating, and the average final shear stresses, τ^A_{fin} and $\overline{\tau}^E_{\text{fin}}$, which are one static stress drop away from average fault prestress. This finding highlights the significance of fault healing during dynamic rupture for the relation between thermal

constraints, seismological estimates of average static stress drop, and average shear stress conditions preceding earthquake ruptures. Rapid weakening and healing, consistent with self-healing pulse-like rupture propagation, can allow substantial motion to occur locally at low dynamic resistance (10-20 MPa or less), consistent with low heat production, while larger fault areas away from the slipping zone can maintain higher stress levels perhaps more consistent with the geodynamic estimates of average fault stress (30 MPa or more) required to maintain the surface topography (Fay & Humphreys, 2006; Lamb, 2006). Indeed, let us consider the difference between the average prestress over the rupture –a measure of fault strength –and the dissipation-based average dynamic resistance during rupture that would dominate heat production (Figure 5.16). For self-healing pulse-like ruptures with the energy-based stress drops of 4–5 MPa, typical for natural earthquakes (Ye et al., 2016a), the difference can be 10–15 MPa, implying that the heat-production constraint of 10-20 MPa can correspond to average fault prestress of 25-35 MPa. Crack-like ruptures result in the (much smaller) difference comparable to the static stress drop.

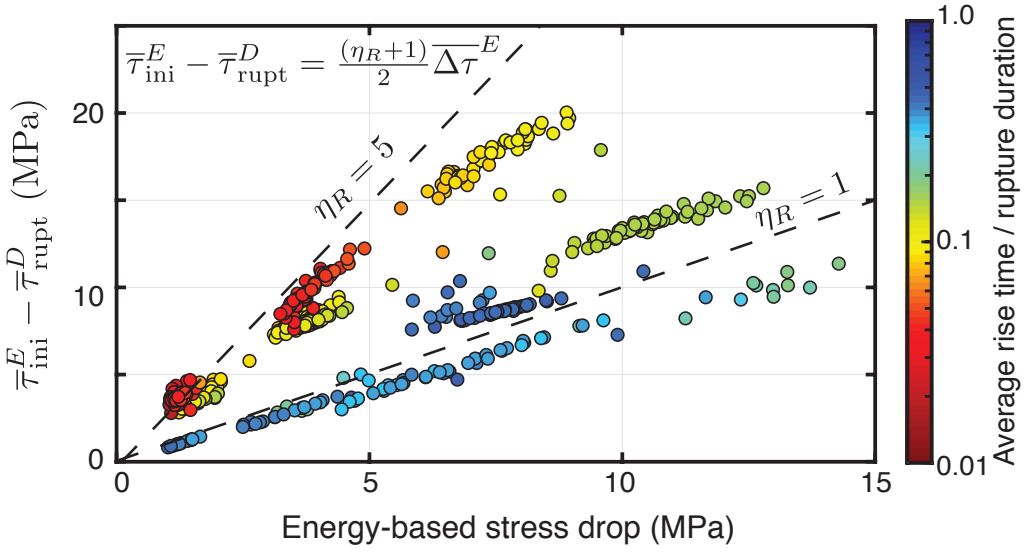

Figure 5.16: Difference between the energy-averaged prestress $\overline{\tau}^E_{\rm ini}$ and dissipation-based average dynamic resistance $\overline{\tau}^D_{\rm rupt}$ versus static stress drop for self-healing pulses and crack-like ruptures. The difference between $\overline{\tau}^E_{\rm ini}$ and $\overline{\tau}^D_{\rm rupt}$ is proportional to the static stress drop through the radiation ration η_R, which is much larger for sharper self-healing pulses with shorter rise time to rupture durations.

If geodynamic considerations, such as maintaining surface topography, indeed require that mature plate boundary faults accommodate spatial or energy-averaged shear stresses larger by more than 4-5 MPa than those inferred from heat flow constraints, this would suggest that either large earthquakes on mature faults propagate predominantly as sharp self-healing pulses or that their static stress drops are substantially underestimated.

If large earthquakes do predominantly propagate as sharp self-healing pulses, then the apparent stress from such ruptures should be notably higher than their inferred energy-based static stress drops. This does not appear to be the case given current seismological estimates, especially for large megathrust earthquakes for which most estimates of radiated energy and energy-based static stress drop are available (Lambert et al., 2021; Ye et al., 2016a). Typical values of apparent stress are 1.5 MPa for interplate strike-slip earthquakes and 0.3 MPa for megathrust earthquakes (Choy & Boatwright, 1995; Ide & Beroza, 2001; Perez-Campos & Beroza, 2001; Ye et al., 2016b), with values inferred to be systematically higher for strike-slip events than thrust events, by up to an order of magnitude (Choy & Boatwright, 1995; Perez-Campos & Beroza, 2001). Current estimates of apparent stress on the order of several MPa in both tectonic settings therefore represent relatively mild to moderate additions in energy-averaged shear stress above shear heating constraints, suggesting that relatively large static stress drops would be required for the energy-averaged (and spatially-averaged) pre-earthquake shear stress to be much higher than the shear heating stress. Higher values of apparent stress around 7 MPa are typical of intraplate strike-slip events, which also tend to achieve larger static stress drops (Allmann & Shearer, 2009; Choy & Boatwright, 1995; Perez-Campos & Beroza, 2001). However, intraplate earthquakes may not occur under low-stress, low-heat conditions that we aim to reproduce by the modeling in this work, since such conditions are predominantly evidenced for mature plate-boundary faults.

The systematic difference in apparent stress between interplate strike-slip and megathrust earthquakes suggests either a dependence of apparent stress on focal mechanism or tectonic settings, or a systematic bias in current seismological estimates. For example, the higher

radiated energy estimates for strike-slip events are typically obtained from regional data, while the lower radiated energy estimates for megathrust events are obtained from teleseismic data. The estimates can be affected by a number of factors, including attenuation, rupture directivity, and focal mechanism (Ide & Beroza, 2001; Kanamori et al., 2020; Ma & Archuleta, 2006; Perez-Campos & Beroza, 2001; Venkataraman & Kanamori, 2004; Ye et al., 2016b). In addition, resolution limitations and the application of smoothing during finite fault slip inversions suggest that seismologically-estimated static stress drops most likely provide lower estimates for the energy-based static stress drops (Adams et al., 2016; Noda et al., 2013).

Our modeling results suggest that re-examining seismological estimates of radiated energy and static stress drop may provide substantial further insight into the rupture style of large earthquakes and the absolute stress conditions on mature faults. Such observations may be particularly useful as finite-fault slip inversions are non-unique and smoothing may make crack-like ruptures appear more pulse-like if the inversions cannot resolve the tails of low slip rates. Moreover, our results indicate that some ruptures can appear kinematically pulse-like, even when the rupture dynamics are more consistent with crack-like ruptures. For example, pulses created by the finite seismogenic depth may essentially be considered geometrically-constrained cracks, in the sense that they do not experience much shear stress undershoot. More detailed studies are warranted to examine how self-healing and geometric pulses differ in terms of stress evolution and energy partitioning, including in models with more complex geometry and heterogeneity. Our results suggest that these two classes of pulses, which can substantially differ with regards to absolute stress conditions on faults, can potentially be differentiated by the relationship between apparent stress and static stress drop.

Our results indicate that the degree of localization of active shear during dynamic rupture can affect the relation between the absolute stress conditions on faults and field observations. The localization of shear dictates the efficiency of shear heating and affects the efficiency of healing mechanisms, such as pore fluid diffusion. A number of laboratory experiments

and theoretical studies suggest that shear localization can evolve during slip, including initial dilation/compaction upon increased slip rate as well as shear localization and damage generation during rupture, which can also alter the pore fluid pressure within the shearing layer and the local effective stress (Faulkner et al., 2018; Lockner & Byerlee, 1994; Marone et al., 1990; K. Okubo et al., 2019; Platt et al., 2015, 2014; Poirier, 1980; Rice et al., 2014; Rudnicki & Rice, 1975; Samuelson et al., 2009; Scuderi et al., 2014, 2017; Segall & Rice, 1995). Dynamically induced changes in rock permeability during dynamic rupture can also increase the rate of pore fluid diffusion, resulting in an increased rate of healing in the case of weakening due to the thermal pressurization of pore fluids. Such effects could alter the evolution of shear stress during ruptures and are important topics for future investigation.

5.7 Conclusions

We have discussed three different definitions for average fault shear stress (Table 5.4), which are all equivalent under uniform and quasi-static slip. Dissipation-based stress measures capture the resistance to most active sliding. Hence the dissipation-based average prestress (or initial stress) captures the typical quasi-static local shear resistance at the end of the nucleation process and the dissipation-based rupture stress captures the typical dynamic shear resistance during dynamic rupture. Energy-based average stress measures capture averages over the entire rupture area. The energy-based average prestress quantifies the average stress that can be sustained before dynamic rupture, and hence can serve as a measure of fault strength. The energy-based average stress measures can, in principle, be inferred from seismological inferences of apparent stress and energy-based static stress drop from earthquakes as well as thermal constraints (Table 5.5).

Fault models with enhanced weakening that produce crack-like ruptures and self-healing pulses exhibit local quasi-statically strong, dynamically weak behavior, while also producing moderate average static stress drops between 1–10 MPa. A critical difference between these two rupture styles is that self-healing pulses experience rapid healing of the local shear resistance within the time scale of the rupture process, resulting in typical dynamic resistance significantly lower than the final stress (aka stress undershoot). Crack-like rup-

tures do not experience such healing and have similar dynamic and final shear stresses, maintaining spatial and energy-averaged shear stress levels within one static stress drop of the dissipation-based rupture stress $\overline{\tau}^{D}_{\text{rupt}}$, whether the efficiency of weakening is relatively mild or efficient (Figure 5.10). Hence large crack-like ruptures require relatively large static stress drops in order to maintain average prestress levels that are substantially higher than the average dynamic shear stress levels associated with shear heating. In contrast, self-healing pulses can maintain higher spatial and energy-averaged shear stresses over the ruptured area, several static stress drops greater than the shear heating stress, throughout periods of both slow and fast sliding.

Our simulations also show that geometric pulses, which arise when slip is arrested due to arrest waves from fault geometry such as limited seismogenic depth, are energetically consistent with crack-like ruptures. Hence the same arguments relating the evolution of average shear stress during rupture and absolute stress conditions on faults for crack-like ruptures apply to geometric pulses. Our modeling results suggest that self-healing pulses, which exhibit larger dynamic changes compared to static stress changes, may be distinguished from crack-like and geometric pulse-like ruptures by their correspondingly larger radiated energy, and hence apparent stress, with respect to the static stress drop. Our findings suggest that re-examining seismological estimates of radiated energy and static stress drop may thus provide better constraints on rupture mode and the average absolute stress levels across seismogenic faults.

Symbol	Definition and physical relation
	Local shear resistance based on laboratory-scale measurements and theories
$\tau(z,t)$	*Local shear resistance*, also equal to *local shear stress* at location z on the fault at time t, which depends on the history of sliding, temperature, and pore pressure evolution (Sec. 5.2).
$\tau_{ss}^{V_{\text{pl}}}(z,t)$	*Local steady-state quasi-static (SSQS) shear resistance* defined as the shear resistance under steady slow sliding at loading rate V_{pl}. $\tau_{ss}^{V_{\text{pl}}}(z,t)$ may generally vary in space and time, but is assumed constant and uniform over the VW region in our models (Sec. 5.2).
	Average shear stress as a function of time
$\tau^A(t)$	*Spatially-averaged shear stress* over domain Ω at time t (Sec. 5.3.1).
$\tau^D(t)$	*Dissipation-averaged shear stress* over domain Ω at time t (Sec. 5.3.2).
$\tau_{\text{vw}}^A(t)$	Spatially-averaged shear stress over VW region at time t.
$\tau_{\text{vw}}^D(t)$	Dissipation-averaged shear stress over VW region at time t.
	Average shear stress as a function of average accumulating slip
$\overline{\tau}^E(\delta')$	*Energy-averaged shear stress* at average slip increment δ' in rupture. Note that $\overline{\tau}^E(\delta')$ requires knowledge of the final slip distribution and thus can only be calculated after the rupture has ended (Sec. 5.3.3).
	Average pre-rupture stress
τ_{nucl}^A	*Spatially-averaged nucleation stress* or spatially-averaged prestress within nucleation region at t_{ini}. Comparable to the spatially-averaged local SSQS shear resistance, $\tau_{\text{nucl}}^A \sim \tau_{\text{ss}}^{V_{\text{pl}}}$.
τ_{nucl}^D	*Dissipation-based nucleation stress* or dissipation-averaged prestress in nucleation region at t_{ini}. Comparable to the spatially-averaged local SSQS shear resistance, $\tau_{\text{nucl}}^D \sim \tau_{\text{nucl}}^A \sim \tau_{ss}^{V_{\text{pl}}}$.
τ_{ini}^A	*Spatially-averaged prestress* over rupture area at t_{ini}.
τ_{ini}^D	*Dissipation-averaged prestress* over the rupture area at t_{ini}. Comparable to the spatially-averaged local SSQS shear resistance, $\tau_{\text{ini}}^D \sim \tau_{\text{nucl}}^D \sim \tau_{\text{nucl}}^A \sim \tau_{ss}^{V_{\text{pl}}}$.
$\overline{\tau}_{\text{ini}}^E$	*Energy-averaged prestress* over the rupture area, $\overline{\tau}_{\text{ini}}^E = \overline{\tau}^E(0)$.
	Average final rupture shear stress
τ_{fin}^A	*Spatially-averaged final stress* over rupture area at t_{fin}.
τ_{fin}^D	*Dissipation-averaged final stress* over rupture area at t_{fin}.
$\overline{\tau}_{\text{fin}}^E$	*Energy-averaged final stress* over rupture area, $\overline{\tau}_{\text{fin}}^E = \overline{\tau}^E(\overline{\delta}_{\text{rupt}})$.
	Average rupture shear stress
$\overline{\tau}_{\text{rupt}}^A$	*Spatially-averaged rupture stress* over the rupture area throughout the rupture process.
$\overline{\tau}_{\text{rupt}}^D$	*Dissipation-averaged rupture stress* or *dissipation-based average dynamic resistance* throughout the rupture process, $\overline{\tau}_{\text{rupt}}^D = E_{\text{Diss}}/(\overline{\delta}_{\text{rupt}}A)$.
$\overline{\tau}_{\text{rupt}}^E$	*Energy-averaged rupture stress* , $\overline{\tau}_{\text{rupt}}^E = \frac{1}{2}\left(\overline{\tau}_{\text{ini}}^E + \overline{\tau}_{\text{fin}}^E\right) = \Delta W/(\overline{\delta}_{\text{rupt}}A) = \overline{\tau}_a + \overline{\tau}_{\text{rupt}}^D$.

Table 5.4: Summary of stress-related quantities discussed in Ch.5.

Symbol	Definition and physical relation
$\overline{\tau}^D_{\text{rupt}}$	*Dissipation-averaged rupture stress* or *dissipation-based average dynamic resistance* throughout the rupture process, $\overline{\tau}^D_{\text{rupt}} = E_{\text{Diss}}/(\overline{\delta}_{\text{rupt}} A)$
$\overline{\tau}_a$	*Apparent stress* or radiation resistance, $\overline{\tau}_a = E_R/(\overline{\delta}_{\text{rupt}} A)$.
$\overline{\tau}^E_{\text{rupt}}$	*Energy-averaged rupture stress*, $\overline{\tau}^E_{\text{rupt}} = \frac{1}{2}\left(\overline{\tau}^E_{\text{ini}} + \overline{\tau}^E_{\text{fin}}\right) = \overline{\tau}_a + \overline{\tau}^D_{\text{rupt}}$
$\overline{\Delta\tau}^E$	*Energy-based static stress drop* or slip-weighted static stress drop relevant to energy partitioning, $\overline{\Delta\tau}^E = \overline{\tau}^E_{\text{ini}} - \overline{\tau}^E_{\text{fin}} = 2\left(\overline{\tau}^E_{\text{ini}} - \overline{\tau}^E_{\text{rupt}}\right) = 2\left(\overline{\tau}^E_{\text{rupt}} - \overline{\tau}^E_{\text{fin}}\right)$
$\overline{\tau}^E_{\text{ini}}$	*Energy-averaged prestress* over the rupture area, $\overline{\tau}^E_{\text{ini}} = \overline{\tau}^D_{\text{rupt}} + \overline{\tau}_a + \overline{\Delta\tau}^E/2$.
$\overline{\tau}^E_{\text{fin}}$	*Energy-averaged final stress* over the rupture area, $\overline{\tau}^E_{\text{fin}} = \overline{\tau}^D_{\text{rupt}} + \overline{\tau}_a - \overline{\Delta\tau}^E/2$.
$\overline{\tau}^D_{\text{heat}}(t)$	*Shear heating stress* or the cumulative dissipation-averaged stress over the VW region up to time t.

Table 5.5: All quantities can be inferred from thermal and seismic observations from individual ruptures, except for $\overline{\tau}^D_{\text{heat}}(t)$, which is related to measurements of long-term thermal signatures around faults. Note that it is not possible, at present, to reliably infer total dissipated energy from a single dynamic rupture, although such inferences may be developed in the future; at present, a useful approximation could be $\overline{\tau}^D_{\text{heat}}(t)$ which has constrains from heat flow measurements.

Chapter 6

RESOLVING SIMULATED SEQUENCES OF EARTHQUAKES AND FAULT INTERACTIONS: IMPLICATIONS FOR PHYSICS-BASED HAZARD ASSESSMENT

This chapter has been adapted from:

Lambert, V. & Lapusta, N. (in review). Resolving simulated sequences of earthquakes and fault interactions: Implications for physics-based seismic hazard assessment. *Journal of Geophysical Research: Solid Earth*. DOI: 10.1002/essoar.10506727.1.

6.1 Introduction

Earthquakes occur in the context of fault networks and many large earthquakes span several fault segments. This reality brings about the issue of fault interaction and highlights the need for simulating earthquake source processes over several fault segments and regional-scale fault networks. How dynamic ruptures navigate fault segmentation has strong implications for seismic hazard analysis (Field, 2019). Earthquakes are capable of jumping fault segments. For example, the 1992 Landers earthquake succeeded in rupturing across at least 4 fault segments, amounting to a Mw 7.3 event (Sieh et al., 1993). The 2016 Mw 7.8 Kaikoura earthquake ruptured at least 21 segments of the Marlborough fault system (Ulrich et al., 2019). Increasingly, seismological observations show that it is not uncommon to see ruptures navigating and triggering subsequent ruptures within fault networks, including the recent 2019 Mw 6.4 and 7.1 Ridgecrest earthquakes (Ross et al., 2019), and the 2012 Mw 8.6 and 8.2 Indian Ocean earthquakes (S. Wei et al., 2013), the largest and second-largest recorded strike-slip earthquakes to date. Yet, in any given seismogenic region, the record of past large events is not long enough to forecast the behavior of ruptures with respect to the existing fault segments, specifically how likely would it be fore the rupture to jump between nearby segments, prompting the discussion on whether and how physics-based models may inform this and other questions important for seismic hazard assessment (Field, 2019).

Determining what conditions allow a dynamic rupture to propagate or arrest are key to understanding the maximum potential magnitude of an earthquake. Previous modeling of single fully dynamic ruptures have shown great success in investigating earthquake propagation in nonplanar and multi-segment fault models, including step-overs and branched geometries (Ando & Kaneko, 2018; Douilly et al., 2015; Duan & Oglesby, 2006; Dunham et al., 2011b; Galvez et al., 2014; Harris et al., 1991; Harris & Day, 1993, 1999; Hu et al., 2016; Kame et al., 2003; Lozos et al., 2015; Ulrich et al., 2019; Withers et al., 2018; Wollherr et al., 2019). In particular, such modeling has shown that the ability of a rupture to propagate across segments depends on the stresses before the rupture and shear resistance assumptions, as well as the geometry of the fault system. However, single-rupture simulations need to select initial conditions and need additional assumptions to incorporate the effect of previous seismic and aseismic slip.

Fault processes involve both sequences of dynamic events and complex patterns of quasi-static slip. Simulating this behavior in its entirety is a fascinating scientific problem. However, even for the more pragmatic goal of physics-based predictive modeling of destructive large dynamic events, it is still important to consider sequences of earthquakes and aseismic slip (SEAS), since prior slip events, including aseismic slip, may determine where earthquakes would nucleate as well as modify stress and other initial conditions before dynamic rupture. Furthermore, such simulations provide a framework for determining physical properties consistent with a range of observations including geodetically recorded surface motions, microseismicity, past (including paleoseismic) events, and thermal constraints, and hence may inform us about the current state of a fault segment or system and potential future rupture scenarios (e.g. Allison & Dunham, 2018; Barbot et al., 2012; Ben-Zion & Rice, 1997; Cattania, 2019; T. Chen & Lapusta, 2009; Erickson & Day, 2016; Erickson & Dunham, 2014; Jiang & Lapusta, 2016; Kaneko et al., 2010; Lambert & Barbot, 2016; Lambert et al., 2021; Lapusta & Rice, 2003; Lapusta et al., 2000; Lin & Lapusta, 2018; Y. Liu & Rice, 2005; Noda & Lapusta, 2013; Perry et al., 2020; Segall et al., 2010).

However, simulating long-term slip histories is quite challenging because of the variety of temporal and spatial scales involved.

Recently, several earthquake simulators have been developed with the goal of simulating millions of earthquake ruptures over regional fault networks for tens of thousands of years (Richards-Dinger & Dieterich, 2012; Shaw et al., 2018; Tullis et al., 2012). The term "simulators" typically refers to approaches that employ significant simplifications, compared to most SEAS simulations, in solution procedures and physical processes, in order to simulate earthquake sequences on complex, regional scale 3-D fault networks for long periods of time. For example, earthquake simulators typically account only for the quasi-static stress transfer due to earthquake events, ignoring wave-mediated stress changes, aseismic slip/deformation, and fluid effects; employ approximate rule-based update schemes for earthquake progression instead of solutions of the governing continuum mechanics equations; and use oversized numerical cells. Such simplifications are currently necessary to permit simulations of hundreds of thousands of events over hundreds of fault segments that comprise the regional networks (Shaw et al., 2018). Earthquake simulators have matched a number of regional-scale statistical relations, including the Gutenberg-Richter frequency-magnitude scaling (Shaw et al., 2018), and highlighted the importance of large-scale fault and rupture interactions.

Here, we examine the sensitivity of the long-term interaction of fault segments to choices in numerical discretization and representations of inertial effects in simulated sequences of earthquakes and aseismic slip, using a relatively simple 2-D model of two co-planar strike-slip fault segments separated by a velocity-strengthening (VS) barrier. We explore how considerations for adequate numerical resolution and convergence depend on the physical assumptions and complexity of earthquake sequences as well as on the modeling outcome of interest. We especially focus on the rate of earthquake ruptures jumping across the VS barrier and examine whether reproducing comparable earthquake frequency-magnitude statistics and static stress drops provides sufficient predictive power for the jump rate, a quantity of interest to seismic hazard studies (Field, 2019).

6.2 Model setup and numerical resolution

Our simulations are conducted following the methodological developments of Lapusta et al. (2000), Noda and Lapusta (2010), and Lambert et al. (2021). We consider a one-dimensional (1-D) fault embedded into a 2-D uniform, isotropic, elastic medium (Figure 6.1). The 2-D model approximates a faulted crustal plate coupled to a moving substrate using the idea of a constrained continuum (Johnson, 1992; Lehner et al., 1981). Fault slip may vary spatially along-strike, but it is depth-averaged through a prescribed seismogenic thickness $\lambda_S = 15$ km, beneath which the elastic domain is coupled to a substrate moving at the prescribed loading rate ($V_{\text{pl}} = 10^{-9}$ m/s). The elastodynamic equation for the depth-averaged displacement along-strike $\overline{u}(x, y, t)$ is given by (Kaneko & Lapusta, 2008; Lehner et al., 1981):

$$Z^2 \frac{\partial^2 \overline{u}}{\partial x^2} + \frac{\partial^2 \overline{u}}{\partial y} + \frac{1}{\lambda_{\text{eff}}^2} \left(\frac{1}{2} \text{sign}(y) V_{\text{pl}} t - \overline{u} \right) = \frac{1}{c_s} \frac{\partial^2 \overline{u}}{\partial t^2}, \tag{6.1}$$

where $\lambda_{\text{eff}} = (\pi/4)\lambda_{\text{S}}$ and $Z = 1/(1 - \nu)$, with ν being the Poisson's ratio. The effective wave speed along-strike for the crustal plane model is $c_L = Zc_s$, where c_s is the shear wave speed. The along-strike slip is then given by $\delta(x, t) = \overline{u}(x, y = 0^+, t) - \overline{u}(x, y^-, t)$.

Our simulations resolve sequences of earthquakes and aseismic slip (SEAS) in their entirety, including the gradual development of frictional instability and spontaneous nucleation, dynamic rupture propagation, post-seismic slip that follows the event, and the interseismic period between events (Figure 6.2). In all models, frictional resistance along the fault interface is governed by the standard laboratory-derived rate-and-state friction law with the state evolution described by the aging law (Dieterich, 1979; Ruina, 1983):

$$\tau = \overline{\sigma} f = (\sigma - p) \left[f_* + a \ln \frac{V}{V_*} + b \ln \frac{V_* \theta}{D_{\text{RS}}} \right], \tag{6.2}$$

$$\frac{d\theta}{dt} = 1 - \frac{V\theta}{D_{\text{RS}}}, \tag{6.3}$$

where $\overline{\sigma} = (\sigma - p)$ is the effective normal stress, σ is the normal stress, p is the pore pressure, τ is the shear stress, f is the friction coefficient, V is the slip velocity, θ is the state variable, D_{RS} is the characteristic slip for the evolution of the state variable, f_* is the

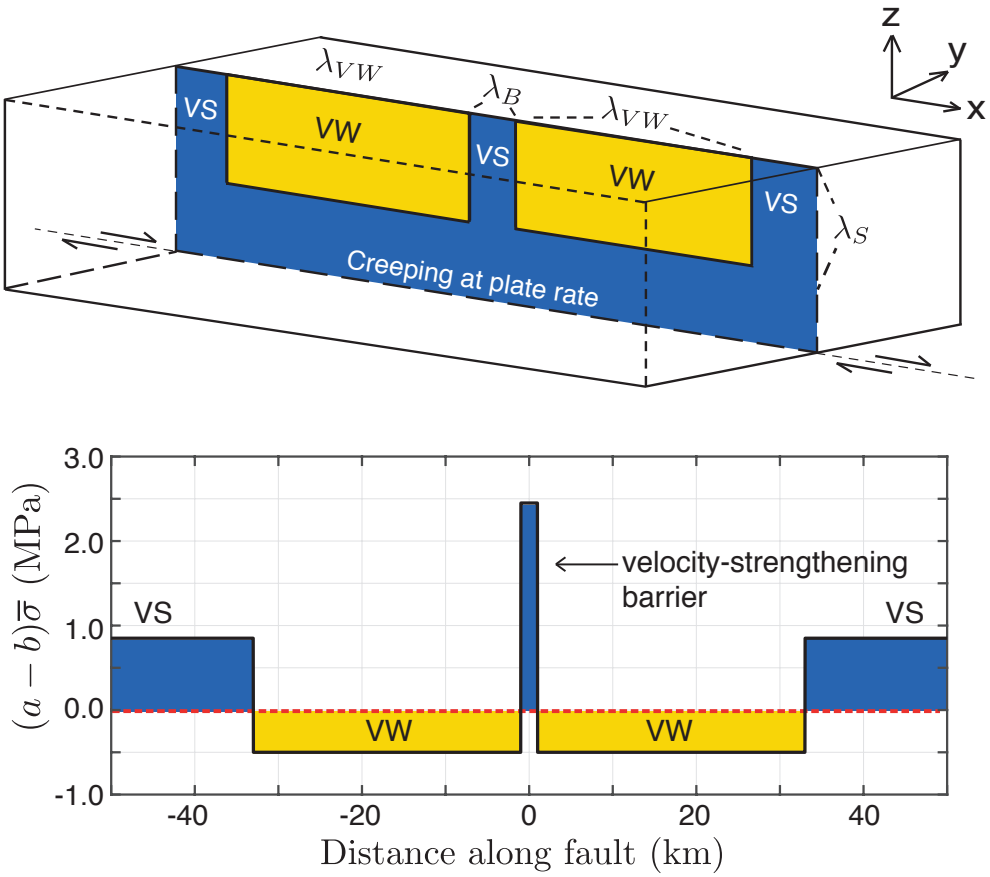

Figure 6.1: Schematic of a strike-slip fault with two co-planar velocity-weakening fault segments separated by a velocity-strengthening barrier. In our simulations, we use a 2-D approximation of the problem with a 1-D along-strike depth-averaged fault, in which the fault is assumed to be creeping at the loading plate rate $V_{\text{pl}} = 10^{-9}$ m/s below the depth of λ_S =15 km.

reference steady-state friction coefficient corresponding to a reference slip rate V_*, and a and b are the direct and evolution effect constitutive parameters, respectively.

At steady-state (constant slip velocity), the shear stress and state variable evolve to their steady-state values τ_{ss} and θ_{ss} given by:

$$\tau_{ss}(V) = (\sigma - p)\left[f_* + (a-b)\ln\frac{V}{V_*}\right], \tag{6.4}$$

$$\theta_{ss}(V) = \frac{D_{\mathrm{RS}}}{V}. \tag{6.5}$$

The combination of frictional properties such that $(a-b) > 0$ results in steady-state velocity-strengthening (VS) behavior, where the shear resistance increases with an increase in slip velocity and where stable slip is expected. If $(a-b) < 0$, then the fault exhibits velocity-weakening (VW) behavior, in which case an increase in slip velocity leads to a decrease in shear resistance, making these regions of the fault potentially seismogenic if their size exceeds a critical nucleation size.

Two theoretical estimates of the nucleation size in mode II are (Rice & Ruina, 1983; Rubin & Ampuero, 2005):

$$h^*_{RR} = \frac{\pi}{4}\frac{\mu L}{(1-\nu)(b-a)(\sigma-p)}; \qquad h^*_{RA} = \frac{2}{\pi}\frac{\mu L b}{(1-\nu)(b-a)^2(\sigma-p)}, \tag{6.6}$$

where μ is the shear modulus. The estimate h^*_{RR} was derived from the linear stability analysis of steady frictional sliding by Rice and Ruina (1983). It also represents the critical cell size for steady-state quasi-static sliding such that larger cells can become unstable on their own. Thus h^*_{RR} represents a key length scale to resolve for slow interseismic processes and earthquake nucleation (Lapusta et al., 2000; Rice & Ruina, 1983). The estimate h^*_{RA} was determined in the parameter regime $a/b > 0.5$ using the energy balance of a quasi-statically expanding crack (Rubin & Ampuero, 2005), and provides an estimate of the minimum size for a slipping region that releases enough stored energy to result in the radiation of waves.

We aim to explore the impact of numerical resolution on the long-term simulated slip behavior of sequences of earthquakes and aseismic slip. The nucleation size, h^*, estimated by either h^*_{RR} or h^*_{RA} from equation (6.6), is one length-scale that clearly needs to be well resolved. Early resolution studies for sequences of events showed that resolution of the nucleation scale h^*_{RR} by 20 to 40 cells is required for stable numerical results (Lapusta et

al., 2000). Later, the need to resolve the nucleation size by at least 20 cells was shown to be due to the more stringent criterion of resolving the region where shear resistance breaks down at the rupture front, often referred to as the cohesive zone. The cohesive zone can be an order of magnitude smaller than the nucleation size, depending on the constitutive description (Day et al., 2005; Lapusta & Liu, 2009). The size of the cohesive zone depends on the weakening rate W of shear stress with slip associated with the constitutive law. The quasi-static estimate Λ_0 of the cohesive zone size at near-zero rupture speed and constant W is given by:

$$\Lambda_0 = C_1 \frac{\mu'}{W}, \tag{6.7}$$

where C_1 is a constant, $\mu' = \mu$ for mode III, and $\mu' = \mu/(1-\nu)$ for mode II (Rice, 1980). For standard rate-and-state friction with the aging form of the state variable evolution, the weakening rate is given by $W = D_{\mathrm{RS}}/(b\overline{\sigma})$ (Lapusta & Liu, 2009) and:

$$\Lambda_0 = C_1 \frac{\mu' D_{\mathrm{RS}}}{b\overline{\sigma}}. \tag{6.8}$$

If one assumes that the traction distribution within the cohesive zone is linear, then the constant C_1 can be approximated as $C_1 = 9\pi/32$ (Rice, 1980).

For fully dynamic rupture simulations, continuously resolving the breakdown process at the rupture front becomes even more challenging as the cohesive zone size Λ exhibits a contraction with increasing rupture speed v_R (e.g Rice, 1980):

$$\Lambda = \Lambda_0 A^{-1}(v_R); \qquad A_{II}^{-1} = \frac{(1-\nu)c_s^2 \mathcal{D}}{v_R^2 (1 - v_R^2/c_s^2)^{1/2}}; \qquad A_{III}^{-1} = (1 - v_R^2/c_s^2)^{1/2}, \tag{6.9}$$

where $\mathcal{D} = 4(1 - v_R^2/c_s^2)^{1/2}(1 - v_R^2/c_p^2)^{1/2} - (2 - v_R^2/c_s^2)^{1/2}$ with $c_p = \sqrt{2(1-\nu)/(1-2\nu)}c_s$. Note that $A^{-1}(0^+) = 1$, giving the quasi-static cohesive zone estimate Λ_0 when $v_R = 0^+$. As the rupture speed approaches the limiting wave speed, $v_R \to c_R$ (Rayleigh wave speed) for mode II and $v_R \to c_s$ (shear wave speed) for mode III, one has $A^{-1}(v_R) \to 0$ and the width of the breakdown region approaches zero. Hence it becomes increasingly more challenging to resolve the rupture front during fully dynamic simulations if the rupture accelerates towards

the limiting speeds. Such acceleration typically occurs during long enough propagation of dynamic rupture over favorable prestress, unless impeded by additional factors such as unfavorable prestress or situations with increasing effective breakdown energy, e.g., due to off-fault inelasticity, thermal pressurization of pore fluids, or navigating fault roughness (Andrews, 2005; Dunham et al., 2011b; Lambert & Lapusta, 2020; K. Okubo et al., 2019; Perry et al., 2020; Poliakov et al., 2002; Rice, 2006). Simulations of faults with rate-and-state friction and the aging form of the state variable evolution embedded in elastic bulk result in ruptures with near-constant breakdown energy (Perry et al., 2020), and this holds for most cases considered in this study. In section 6.7, we show that adding an approximation of off-fault inelasticity to our simulations that reduces the rupture speeds does not alter our conclusions.

In our model, the fault contains a frictional domain consisting of two VW regions of length λ_{VW} = 32 km that are separated by a 2-km-long VS region that impedes rupture propagation. We select large enough values of the velocity strengthening in the central VS region so that the region acts like a barrier, requiring ruptures to jump/renucleate on the other side of the barrier to propagate over the second segment. This region is a proxy for what would be a gap in the fault connectivity, at least at the surface, requiring the ruptures to jump across. The remainder of the frictional region surrounding the VW segments has more mild VS properties (Figure 6.1). At the edges of the model, outside of the frictional domain, fault slip is prescribed at the loading plate rate. Values for the model parameters used in our simulations are provided in Tables 6.1 and 6.2. We first examine models with lower instability ratio λ_{VW}/h^*_{RR} that result in quasi-periodic sequences of events, and then consider models with higher instability ratios that result in more complex earthquake sequences and qualitatively different convergence behavior.

Parameter	Symbol	Value
Loading slip rate	V_{pl}	10^{-9} m/s
Shear wave speed	c_s	3299 m/s
Shear modulus	μ	36 GPa
Poisson's ratio	ν	0.25
Rate-and-state parameters		
Reference friction coefficient	f_*	0.6
Reference slip velocity	V_*	10^{-6} m/s
Direct effect (VS)	a_{VS}	0.02
Evolution effect (VS)	b_{VS}	0.003
Direct effect (barrier)	a_B	0.05
Evolution effect (barrier)	b_B	0.001
Length scales		
Fault length	λ	280 km
Frictional domain	λ_{fr}	258 km
Each VW segment	λ_{VW}	32 km
VS Barrier	λ_B	2 km
Seismogenic depth	λ_S	15 km

Table 6.1: Parameter values for simulations in Ch. 6 unless otherwise specified

Parameter	Symbol	M1	M2	M3	M4	M5
Effective normal stress	$\overline{\sigma} = (\sigma - p)$	50 MPa	60 MPa	40 MPa	30 MPa	50 MPa
Characteristic slip	D_{RS}	20 mm	20 mm	20 mm	18 mm	8 mm
Direct effect (VW)	a_{VW}	0.005	0.005	0.005	0.005	0.005
Evolution effect (VW)	b_{VW}	0.015	0.0135	0.0175	0.02	0.015
Length scales						
Quasi-static cohesive zone	Λ_0	1.1 km	1.0 km	1.2 km	1.3 km	452 m
Nucleation size (R.&A., 2005)	h^*_{RA}	1.8 km	1.9 km	1.7 km	1.6 km	733 m
Nucleation size (R.&R., 1983)	h^*_{RR}	1.5 km	1.5 km	1.5 km	1.6 km	603 m
Instability ratio	λ_{VW}/h^*_{RA}	18	17	19	20	44
Instability ratio	λ_{VW}/h^*_{RR}	21	22	21	21	53

Table 6.2: Parameter values for simulations in Ch. 6 that vary among fault models

6.3 Resolving quasi-periodic fully dynamic sequences of earthquakes and aseismic slip (SEAS)

Let us consider the simulated slip behavior of fault model M1 with instability ratio $\lambda_{VW}/h^*_{RR} = 21$ (Table 6.2). Its quasi-static cohesive zone ($\Lambda_0 = 1.1$ km) should be well-resolved by cell sizes of 12.5 and 25 m, with 88 and 44 cells over Λ_0, respectively; the nucleation size is even larger and hence also well-resolved. Consistently with these considerations, these two well-discretized simulations produce the same relatively simple quasi-periodic sequences

of earthquake events that periodically jump across the VS barrier (Figure 6.2A & B). We clearly see that the results are the same for the two simulations with different resolutions, including the local evolution of slip rate and shear stress during ruptures late in the earthquake sequence (Figure 6.2D-E). Note that the cohesive zone evolves throughout the rupture process, shrinking with the increasing rupture speed by 3-4 times in these simulations (Figure 6.2F-H) and the spatial discretization is fine enough to adequately characterize the rupture front throughout the entire dynamic process. Both simulations have the jump rate as 0.54; we define this rate of ruptures jumping across the VS barrier within a given time period as the total number of ruptures that propagate towards the barrier and result in seismic slip on both fault segments divided by the total number of ruptures that propagate towards the barrier.

The variability between different ruptures in fault model M1 is generally mild, as shown by their frequency-magnitude histograms (Figure 6.2C). To create the frequency-magnitude histograms, we compute the moment for each simulated event in our 2-D models as $M = \mu\bar{\delta}A$ where the rupture area is defined with respect to the rupture length L_R and seismogenic depth λ_S, as $A = (\pi/4)L_R^2$ when $L_R \leq \lambda_S$ and $A = L_R\lambda_S$ when $L_R > \lambda_S$.

The quasi-periodic nature of events observed over the first 4000 years in well-resolved simulations of fault model M1 persists in longer-duration simulations over 20,000 years, resulting in similar long-term jump rates of 0.48 to 0.54 depending on the time interval considered (Figure 6.3). We also examine simulations of fault model M1 with different initial shear stress conditions and find that the long-term sequences of events converge to the same quasi-periodic behavior upon adequate discretization, despite the initial few events being different (Figure 6.3A vs B; details of initial shear stress distributions S1 and S2 are provided in section 6.9). Simulations of fault model M1 thus exhibit *long-term numerical convergence* upon adequate discretization, producing virtually indistinguishable long-term slip behavior and a consistent rate of two-segment ruptures among simulations with differing initial conditions, after a sufficiently large initial sequence of events.

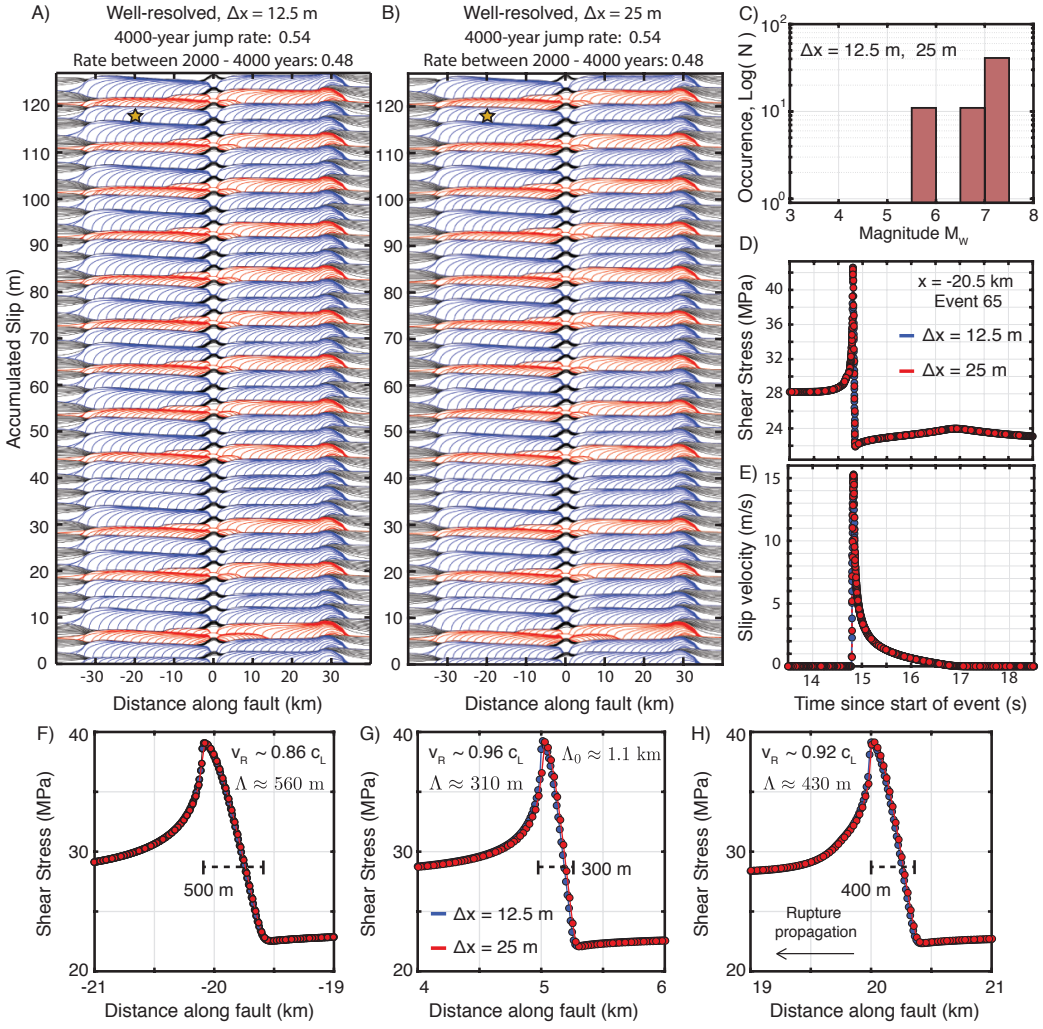

Figure 6.2: Interaction of two co-planar fault segments in well-resolved simulations of model M1 demonstrating convergence of simulated earthquake sequences. (A-B) History of cumulative slip over 4000 years in well-resolved fully-dynamic simulations of fault model M1 with initial conditions S1 using (A) 12.5-m and (B) 25-m cell size. Contours for seismic slip are plotted every 0.5 s, with ruptures that jump across the VS barrier colored blue. The simulated fault behavior is virtually indistinguishable between the two resolutions. (C) Frequency-magnitude histograms of events, on top of each other for the two resolutions. The well-resolved simulations produce the same relatively simple and quasi-periodic behavior. (D-E) The evolution of local shear stress and slip velocity at a point ($x = -20.5$ km, shown by star in A and B), practically indistinguishable even after over 3800 years of simulated time. (F-H) Spatial distribution of shear stress at the rupture front for three locations ($x = -20$ km, 5 km and 20km) throughout the first rupture in (A-B). While the quasi-static estimate of the cohesive zone Λ_0 is about 1.1 km, the actual size of the cohesive zone varies with the local rupture speed throughout the rupture. In these well-resolved simulations, the cohesive zone is always resolved by at least 10 cells.

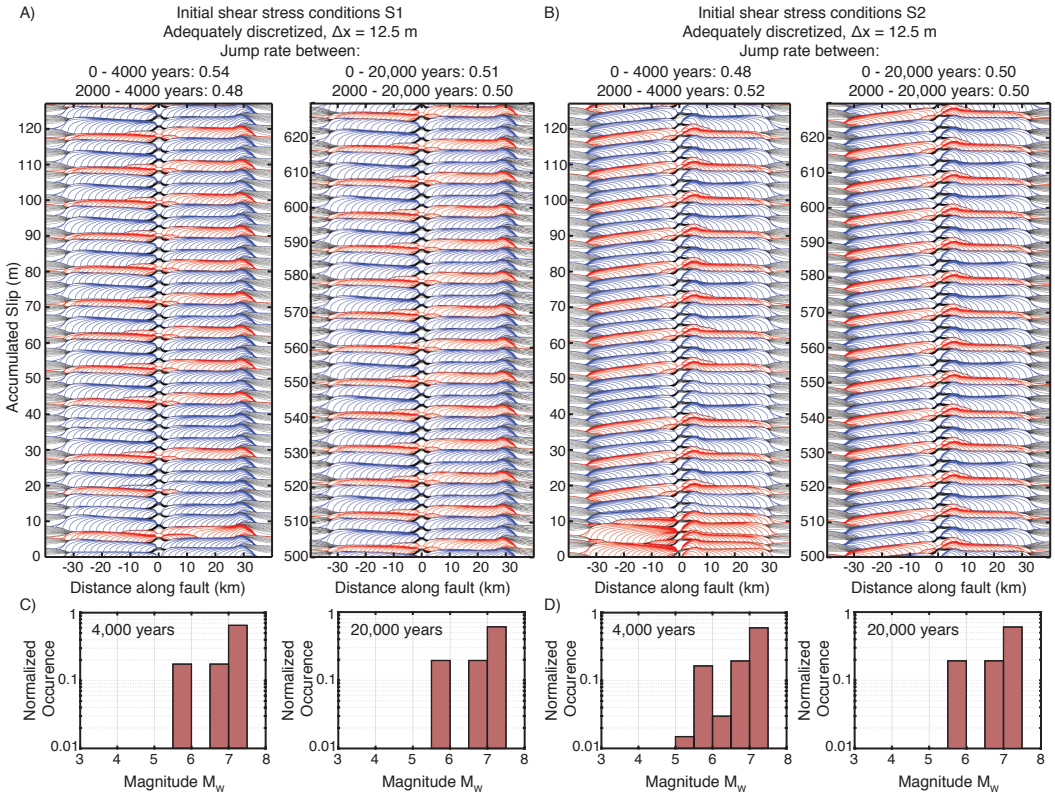

Figure 6.3: Convergence of well-resolved simulated earthquake sequences in model M1 for longer-term simulations and different initial conditions. (A-B) Cumulative slip over 0-4000 years and 16,000-20,000 years in two well-resolved fully-dynamic simulations of fault model M1 with two different initial conditions, S1 and S2. Contours of seismic slip are plotted every 0.5 s with ruptures that jump across the VS barrier colored blue. The quasi-periodic behavior seen in the first 4000 years in well-resolved simulations, including the rate of ruptures jumping across the VS barrier, remains generally consistent throughout longer-term simulations over 20,000 years (Right). Simulations using different initial shear stress conditions produce different initial sequences of events, however, the simulated sequences converge to the same slip behavior and have the same long-term rates of two-segment ruptures (0.50 over 2,000-20,000 years). (C-D) Normalized frequency-magnitude histograms for events from (A) and (B), respectively, over 4000 and 20,0000 years, illustrating that the population statistics in this relatively simple system is the same, apart from the initial start-up period.

Let us now consider simulations that use larger computational cells. The cell sizes of 250 m and 125 m resolve the quasi-static cohesive zone Λ_0 with 4.5-9 cells (Figure 6.4). While this resolution seems adequate (Day et al., 2005), one can anticipate that the dynamic shrinking of the cohesive zone size by 3-4 times would result in a more marginal resolution of 1-3 cells. Indeed, we see that the simulated long-term sequences of events and jump rates differ substantially from those of the well-resolved simulations (Figures 6.2A & B vs. 6.4A & B). Considering even larger cell sizes of 500 m and 1000 m brings further differences in the event sequences and jump rates (Figure 6.6), with the earthquake sequences that look plausible and not obviously numerically compromised even for the largest cell sizes (Figure 6.5). Note that the jump rate in simulations with marginal and oversized cells is neither systematically larger nor smaller than the range 0.48-0.54 from the well-resolved cases, but varies from 0.25 to 0.95 depending on the choice of numerical discretization.

Increasingly poor resolution of the dynamic cohesive zone at the rupture front and, for the largest cell sizes, of the nucleation zone results in an increasing abundance of small events (Figure 6.6), as had been shown in previous studies (Lapusta & Liu, 2009; Rice, 1993; Rice & Ben-Zion, 1996). Inadequate resolution of the dynamic rupture front prevents simulating the actual stress concentration and promotes event arrest. Inadequate resolution of the nucleation size enables individual cells or small number of cells to fail independently due to the inadequate resolution of the stress interactions (Lapusta & Liu, 2009; Rice, 1993; Rice & Ben-Zion, 1996). Using sufficiently oversized cells can result in power-law statistics in terms of the frequency-magnitude distribution of simulated earthquake ruptures (Figure 6.6E-J; Rice, 1993; Rice & Ben-Zion, 1996).

Note that the suggested minimum average resolution of 3 cells of the (variable) cohesive zone from the dynamic rupture study by Day et al. (2005) is not adequate for convergent results in these earthquake sequence simulations. That criterion would be achieved in this model for a cell size between the 250 m and 125 m. Yet the simulated long-term behavior for those cell sizes is clearly different from the better-resolved and convergent results with

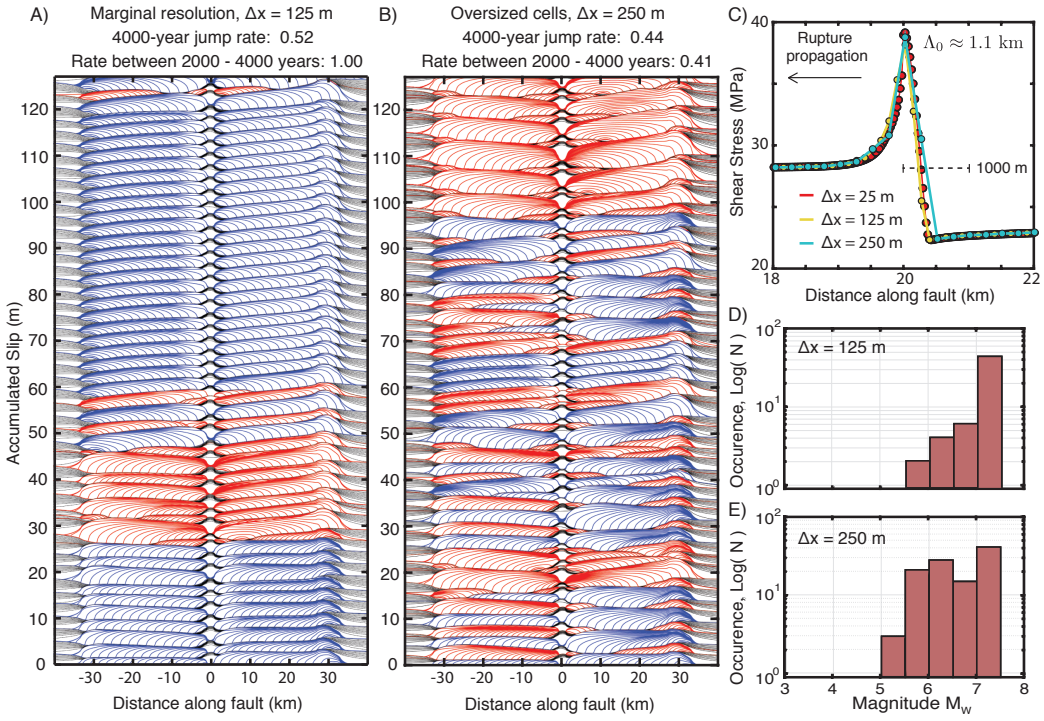

Figure 6.4: Less well-resolved simulations of fault model M1 exhibiting different simulated earthquake sequences and rates of two-segment ruptures. (A-B) History of cumulative slip over 4000 years in fully dynamic simulations of fault model M1 using marginal and oversized cells of (A) 125 m and (B) 250 m, respectively. Contours of seismic slip are plotted every 0.5 s, with ruptures that jump across the VS barrier colored blue. (C) Spatial distribution of shear stress around the rupture front in a well-resolved simulation (Δx = 25 m, red) and the two simulations with larger cells (Δx = 125 and 250 m). As the cell size increases, the resolution of the shear stress evolution at the rupture front decreases, although the resolution would be acceptable in simulations of single ruptures (Day et al., 2005). (D-E) Frequency-magnitude histograms for events in (A-B), respectively. The simulations with larger cells exhibit different long-term sequences of events compared to the well-resolved simulations (Fig. 6.2C), with increased production of small events and significantly different rates of two-segment ruptures.

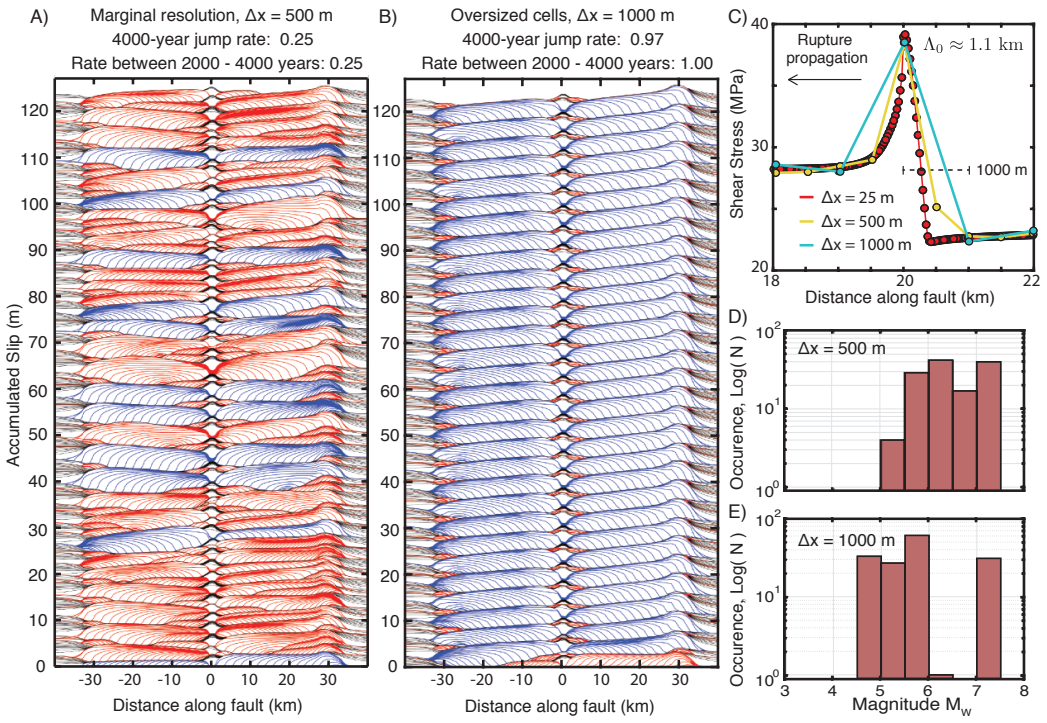

Figure 6.5: Simulations of fault model M1 using more oversized cells exhibiting different simulated earthquake sequences and rates of two-segment ruptures. (A-B) History of cumulative slip over 4000 years in fully dynamic simulations of fault model M1 using oversized cells of (A) 500 m and (B) 1000 m, respectively. Contours of seismic slip are plotted every 0.5 s, with ruptures that jump across the VS barrier colored blue. (C) Spatial distribution of shear stress around the rupture front in a well-resolved simulation (Δx = 25 m, red) and the two simulations with oversized cells (Δx = 500 and 1000 m). As the cell size increases, the breakdown of shear stress at the rupture front is increasingly poorly resolved. (D-E) Frequency-magnitude histograms for events in (A-B), respectively. Simulations with oversized cells exhibit different long-term sequences of events compared to the well-resolved simulations (Figure 6.2), with increased production of small events and significantly different rates of two-segment ruptures.

the cell sizes of 25 m and 12.5 m. At the same time, the criterion by Day et al. (2005) works well for a single dynamic rupture as intended, since the first dynamic events in simulations with cell sizes 12.5 m, 25 m, 125 m, and 250 m are quite similar to each other (Figure 6.7). The events are not identical, however; for example, the average slip with the resolution of 12.5 m and 125 m differs by 0.7%. Clearly, these differences –acceptable for a single event –accumulate in these highly nonlinear solutions, resulting in different event statistics and jump rate (Figure 6.6).

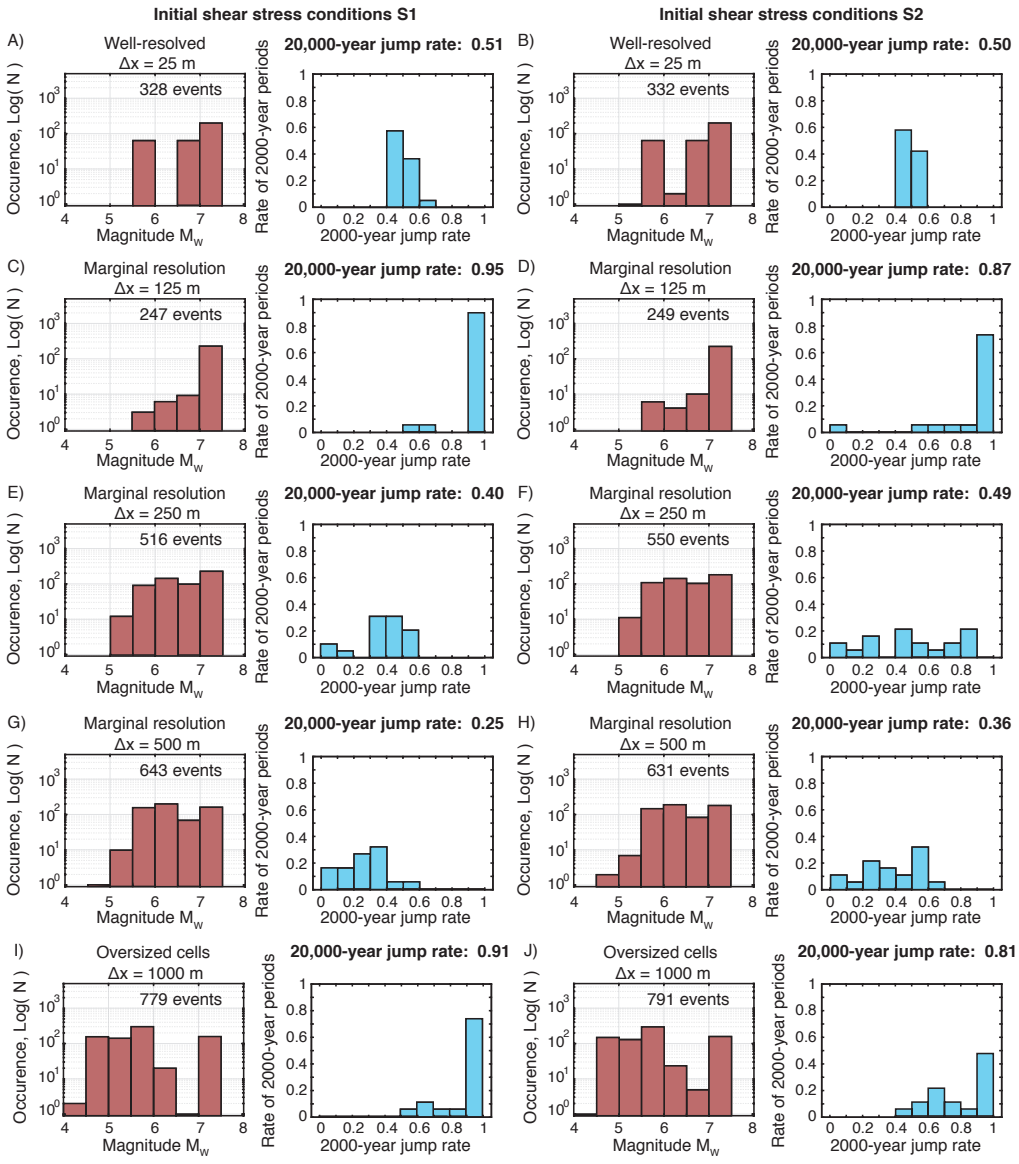

Figure 6.6: Frequency-magnitude (left) and jump-rate (right) statistics for 20,000 years of simulated earthquake sequences in model M1 with different initial conditions and cell sizes. (A-B) Well-resolved simulations with different initial shear stress conditions result in comparable long-term quasi-periodic sequences, and thus comparable frequency-magnitude statistics and 2000-year jump rate statistics that are generally consistent with the 20,000-year jump rate of 0.50. (C-J) As the resolution decreases, the sequences become more complex with greater variability of event sizes and increased production of smaller events. The jump rate during different 2000-year periods also becomes more variable and can considerably differ from the true jump rate of 0.5 in the well-resolved cases.

We find that our fully dynamic 2-D simulations of fault model M1, which include uniform VW properties with relatively mild weakening due to standard rate-and-state friction, converge when the quasi-static cohesive zone estimate Λ_0 is discretized by at least 22 cells, which translates to the average resolution of the dynamically variable cohesive zone size of 10-15 cells. Fault models with additional or different ingredients, such as fault heterogeneity/roughness, more efficient weakening, 3D elastodynamics with 3D faults, or different instability ratio, would require further considerations for resolution requirements that result in convergent simulations. For example, as we discuss in section 6.6, the convergence and resolution properties of models with higher instability ratios, which result in more complex earthquake sequences, are qualitatively different.

In the more complicated earthquake sequences observed in under-resolved simulations of fault model M1, some statistics, such as the rate of two-segment ruptures, depends on the specific period that one considers throughout the simulation. To explore the variability in the event statistics and jump rate across the VS barrier in models with different numerical resolution, we examine the jump rate over different 2000-year periods throughout longer term simulations of 20,000 years, using a sliding window of 1000 years starting at the beginning of the simulation (19 periods total; Figure 6.6). The choice of a 2000-year period allows us to have a sufficient number (~20) of large earthquakes within a period to estimate jump rates. We also consider the outcomes for two different initial conditions S1 and S2, as before. For the well-resolved simulations exhibiting long-term convergence, the frequency-magnitude and 2000-year jump rate statistics for simulations with different initiation conditions are comparable, with the jump rate for all 2000-year periods being consistent with the overall 20,000 year jump rate (Figure 6.6A-B). As the numerical resolution worsens, the sequences of events become more complex with greater variability in rupture sizes and increased production of smaller events (Figure 6.6C-J). The jump rate during any 2000-year period also becomes more variable in marginally-resolved simulations and can considerably differ from both the 20,000-year jump rate of the same simulation as well as from the true jump

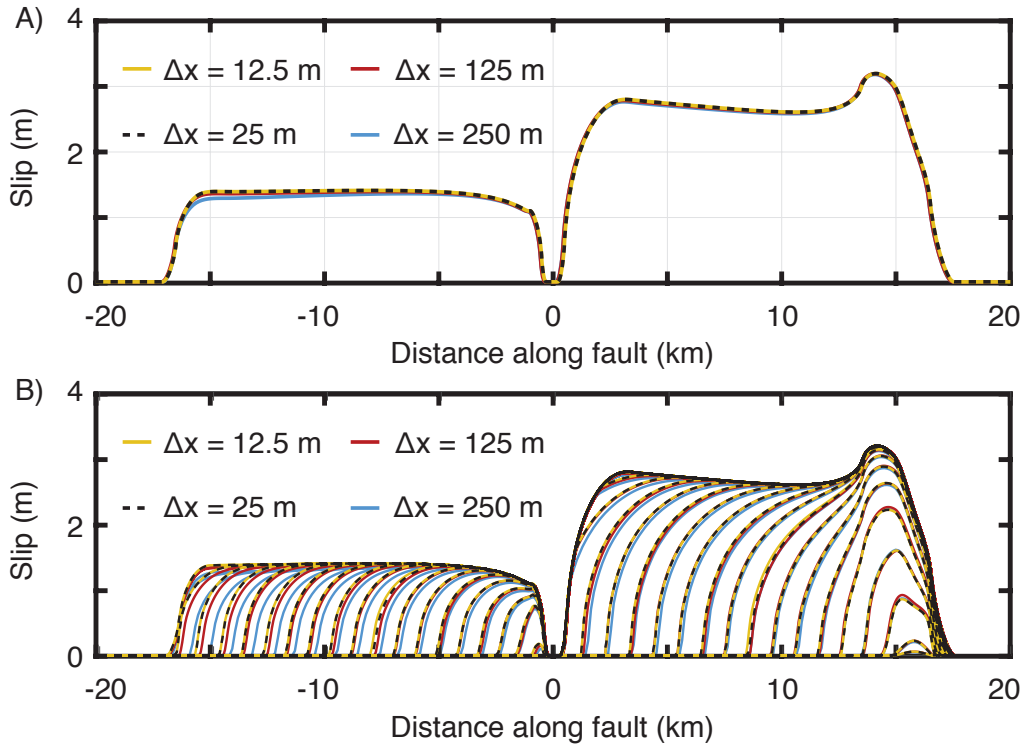

Figure 6.7: Final slip and evolution of slip for the first rupture in simulations of fault model M1 with different numerical resolution. (A) The final slip distribution for the first simulated rupture with the same initial conditions is practically the same for simulations using cell sizes of 12.5, 25, 125, and 250 m. (B) The evolution of slip is contoured every 0.5 s and comparable spacing between contours illustrates that the rupture speed is generally consistent for the first rupture in these well-resolved and marginally-resolved simulations. The evolution of slip and final slip are virtually identical for the two well-resolved simulations using 12.5 and 25 m cells, and the average final slip for simulations with 12.5 and 250 m cell sizes differ by less than 0.8%.

rate in the well-resolved simulations. Note that, despite being clearly affected by numerical resolution, the frequency-magnitude and jump-rate distributions of inadequately resolved simulations can appear generally consistent among simulations with similar cell sizes and different initial conditions (Figure 6.6 left vs. right columns). In other words, even if simulations using marginal or oversized cells produce comparable statistical properties for different initial conditions, these characteristics do not necessarily represent robust features of the physical system, but rather may still be numerical artifacts.

6.4 Interaction of fault segments in simulations with quasi-dynamic approximation for inertial effects

Many numerical studies of long-term fault behavior utilize quasi-dynamic solutions to the equations of motion, in which the wave-mediated stress transfers during the coseismic phase are replaced with a radiation damping approximation (Rice, 1993). The quasi-dynamic approximation substantially reduces the computational expense of the simulation, as the consideration of stress redistribution by waves requires substantial additional storage and computational expense. Considerable insight into fault mechanics has been derived from studies using quasi-dynamic formulations, particularly when such approximations are used to incorporate new physical effects that may otherwise result in prohibitive computational expense, as well as in scenarios where it may be argued that inertial effects are relatively mild, such as during earthquake nucleation or during aseismic slip transients (Allison & Dunham, 2018; Erickson et al., 2017; Lambert & Barbot, 2016; Y. Liu, 2014; Y. Liu & Rice, 2005, 2007; Rice, 1993; Rubin & Ampuero, 2005; Segall & Rice, 1995; Segall et al., 2010). However, as with all approximations, it is important to be aware of how such simplifications modify the outcome of study (Thomas et al., 2014).

Let us review the quasi-dynamic approximation for inertial effects during sliding and study their implications for the long-term interaction of two fault segments. In the 2-D boundary integral formulation, the elastodynamic shear stress along a 1-D fault plane can be expressed as (Cochard & Madariaga, 1994; Perrin et al., 1995):

$$\tau(x,t) = \tau^0(x,t) + \phi_{\text{static}}(x,t) + \phi_{\text{dynamic}}(x,t) - \eta V(x,t), \tag{6.10}$$

where $\tau^0(x,t)$ are the "loading" tractions (i.e. the stress induced on the fault plane if it were constrained against any slip), $\phi_{\text{static}}(x,t)$ and $\phi_{\text{dynamic}}(x,t)$ represent the static and dynamic contributions to the stress transfer along the fault, respectively, and the last term represents radiation damping ($\eta = \mu/(2c_s)$ for mode III).

The static solution for the equations of motion would only contain ϕ_{static}, which depends

only on the current values of slip along the fault. However, the static solution does not exist during dynamic rupture when inertial effects becomes important. ϕ_{dynamic} and ηV both arise due to the inertial effects. ϕ_{dynamic} represents the wave-mediated stress interactions along the interface and this term is challenging to compute as it requires calculating convolutions on time and storing the history of deformation. Radiation damping ηV is much easier to incorporate as it depends on the current slip rate, and represents part of the radiated energy (Rice, 1993). The quasi-dynamic approximation, in which ϕ_{dynamic} is ignored and only ηV is included, allows the solution to exist during inertially-controlled dynamic rupture. However, the solution is altered from the true elastodynamic representation.

Let us consider the long-term behavior of fault model M1, as examined in section 6.3, but now using the quasi-dynamic approximation. For well-resolved quasi-dynamic simulations of fault model M1, we find that the long-term slip behavior of the two fault segment system is even simpler than for the fully dynamic case, with ruptures being exclusively isolated to individual segments and the jump rate being zero (Figure 6.8A). For simulations with the increasing cell size, and thus decreasing spatial resolution, we see increased variability in the size of the individual ruptures, to the point where some marginally-resolved simulations produce ruptures that jump across the VS barrier, whereas well-resolved simulations of the same fault model never do (Figure 6.8B-C). The increasing cell size also leads to increased production of smaller events and more complicated fault behavior, similarly to the fully dynamic simulations (Figure 6.8D-F).

In addition to substantially reducing the computational expense associated with calculating the wave-mediated stress transfers, quasi-dynamic simulations place milder constraints on the spatial resolution since the cohesive zone always remains near the quasi-static estimate, $\Lambda \approx \Lambda_0 = \Lambda(v_R = 0^+)$ (Figure 6.8G-H). This is because the stress transfer calculated for the ruptures is always quasi-static, and the much stronger stress transfer due to waves is ignored (Figure 6.9E). As a result, the quasi-dynamic simulations produce significantly smaller slip velocities and rupture speeds than the fully dynamic ones 6.9A-C, consistent with previous

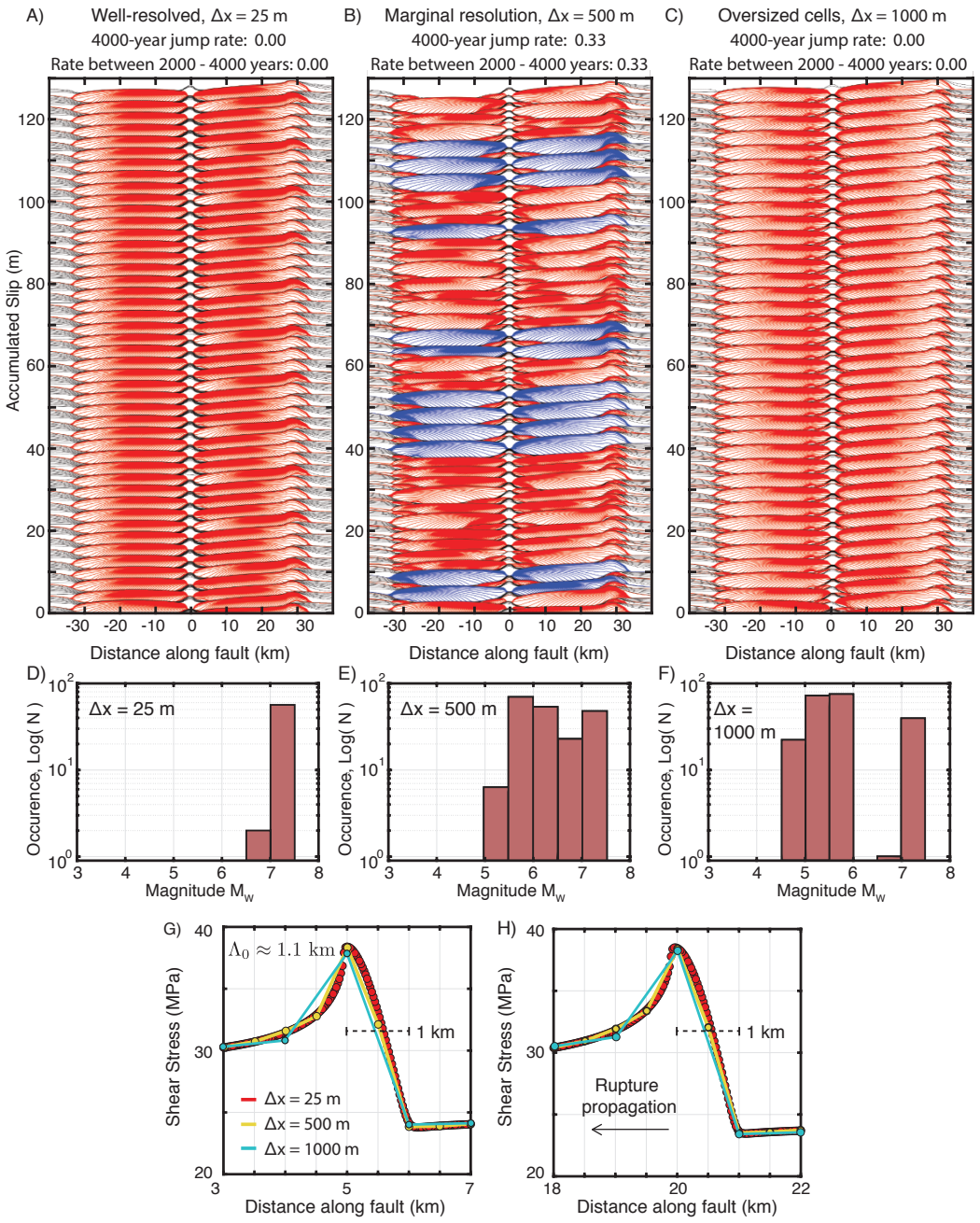

Figure 6.8: Interaction of two co-planar fault segments in quasi-dynamic simulations of fault model M1 with varying discretization. (A-C) History of cumulative slip over 4000 years in quasi-dynamic simulations of fault model M1 with initial conditions S1 using (A) adequate discretization, (B) marginal discretization, and (C) oversized cells. Contours of seismic slip are plotted every 0.5 s, with ruptures that jump across the VS barrier colored blue. (D-F) Frequency-magnitude histograms for events in (A-C). (G-H) Spatial distribution of shear stress illustrating the breakdown of shear resistance at the rupture front during quasi-dynamic simulations in fault model M1 with varying spatial resolution. The cohesive zone does not shrink during quasi-dynamic ruptures. A well-resolved rupture front is shown in red with a cell size of 25 m. The cohesive zone (Λ_0 = 1.1 km) is resolved by at best 1 to 2 cells for cell sizes of 500 to 1000 m.

studies (Lapusta & Liu, 2009; Thomas et al., 2014).

One can attempt to enhance the slip rates and rupture speeds in the quasi-dynamic simulations by reducing the radiation damping term η; this can be interpreted as increasing the effective shear wave speed in the radiation damping term $c_s^{\text{enh.}} = \beta c_s$, thus allowing for higher slip rates (Lapusta & Liu, 2009). We compare the enhanced quasi-dynamic simulations ($\beta = 3$) with the standard quasi-dynamic ($\beta = 1$) and fully dynamic simulations of fault model M1 (Figure 6.10). Decreasing the radiation damping increases the effective rupture speed and slip rate (Figure 6.9A -C) in comparison to the standard quasi-dynamic simulation, however, for the parameters considered, it does not substantially alter the long-term interactions of the two fault segments, nor match the rate of ruptures jumping across the VS barrier in the fully dynamic case (Figure 6.10).

In comparing the three simulations with different treatment of the inertial effects, it is clear that the fully dynamic ruptures result in higher slip rates and narrowing of the cohesive zone (Figure 6.9). For simulations with standard rate-and-state friction, the peak shear stresses vary mildly from fully dynamic versus quasi-dynamic representations, as they are limited by the shear resistance of the fault, which has a relatively mild logarithmic dependence on slip rate. However, the stress transfer along the fault substantially differs for fully dynamic versus quasi-dynamic representations (Figure 6.9E). The difference between the stress transfer term and the shear stress is accommodated by the radiation damping ηV, which results in higher slip rates V to balance the larger dynamic stress stranfers (Figure 6.9C - E). Hence while the resolved peak shear stresses along the fault may be comparable due to the specific choice of the constitutive relationship, the rupture dynamics and kinematics, as seen through the stress transfer, slip rate, and rupture speed along the fault, differ considerably with and without the inclusion of full inertial effects.

These larger dynamic stress transfers facilitate the triggering and continued propagation of slip on the neighboring fault segment, rather than leaving the rupture to always be arrested

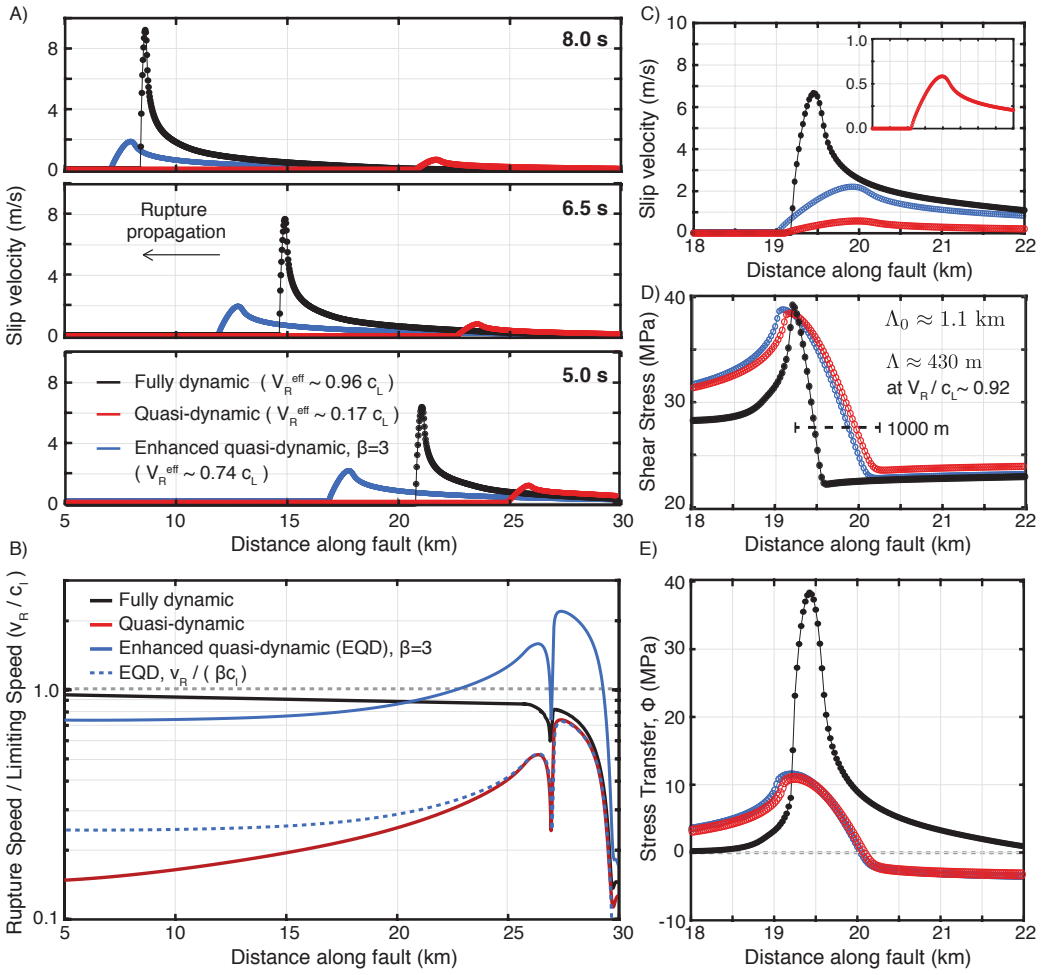

Figure 6.9: Comparison of local slip rate, shear stress, and rupture speed for simulations with different treatment of inertial effects. (A) Spatial distribution of slip rate at three instances of time during the first rupture with the same initial conditions in fully dynamic (black), quasi-dynamic (red), and enhanced quasi-dynamic (blue) simulations of fault model M1. (B) The fully dynamic rupture accelerates to a rupture speed close to the limiting wave speed of $c_L \approx 4.4$ km/s throughout the rupture, whereas the quasi-dynamic ruptures maintain lower effective rupture speeds. Decreasing the radiation damping term for quasi-dynamic ruptures increases the slip rate and rupture speed, but does not truly mimic the acceleration of the fully dynamic rupture. (C-D) A closer look at the spatial distribution of (C) slip velocity and (D) shear stress at a given time highlights how full consideration of inertial effects leads to much higher slip velocities and a more localized stress concentration at the rupture front, which facilitates rupture propagation. Enhancing the quasi-dynamic ruptures with lower radiation damping increases the slip rate, but maintains the same quasi-static spatial pattern of stress at the rupture front. (E) The corresponding values of the stress transfer functional near the rupture front. The radiation damping approximation of the inertial effects results in dramatically reduced stress transfer along the fault. The larger total stress transfer in the fully dynamic simulations is balanced by higher slip rates, as shown in (C).

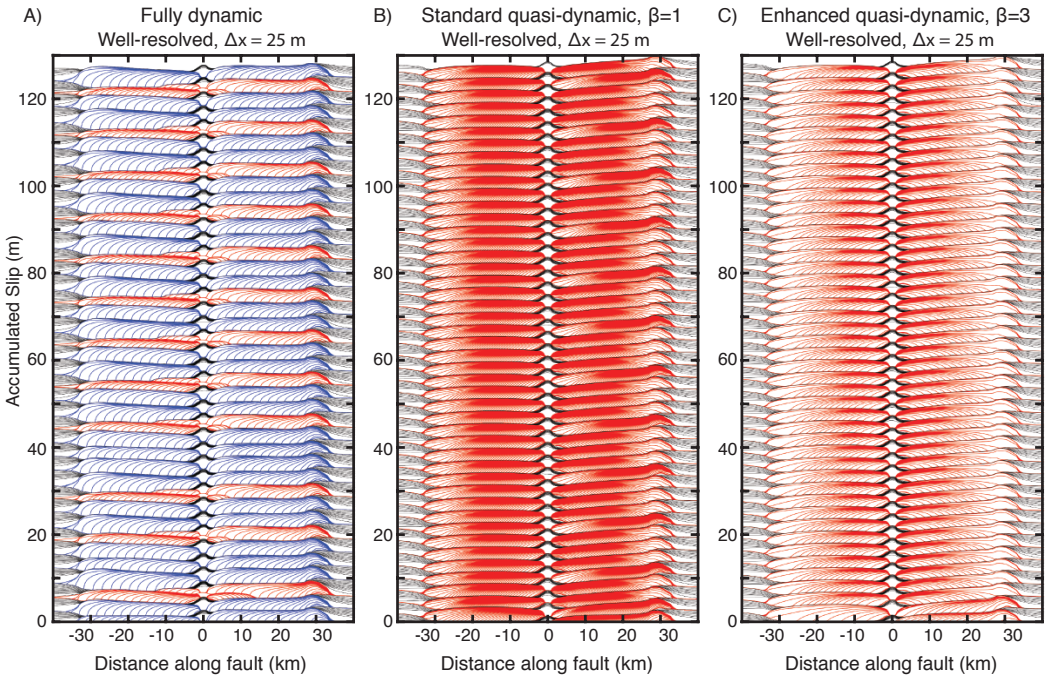

Figure 6.10: Different long-term interaction of co-planar fault segments in simulations with different treatments of inertial effects. (A-C) History of cumulative slip over 4000 years in well-resolved (A) fully dynamic, (B) standard quasi-dynamic (β = 1), and (C) enhanced quasi-dynamic (β = 3) simulations of fault model M1 with initial conditions S1. Contours of seismic slip are plotted every 0.5 s. The increased spacing between contours for the enhanced quasi-dynamic ruptures in (C) illustrate the higher effective rupture speeds that are more comparable to those of the fully dynamic ruptures in (A). Despite the higher rupture speeds and larger slip rates (Figure 6.9), the long-term slip behavior for both quasi-dynamic simulations is qualitatively comparable, with no ruptures jumping across the VS barrier.

by the creeping barrier, as in the well-resolved quasi-dynamic simulations (Figure 6.10). Decreasing the radiation damping term allows for somewhat higher slip rates and arbitrarily higher rupture speeds, but it does not mimic the full effects in the dynamic stress transfer, particularly at the rupture front. As a result, the fully dynamic simulations have higher jump rates. The differences between fully dynamic and quasi-dynamic approximations can be even more substantial for models with enhanced weakening at seismic slip rates from the flash heating of contact asperities or the thermal pressurization of pore fluids (Thomas et al., 2014).

6.5 Constraining rupture jump rates using earthquake frequency-magnitude statistics

Two common observations about natural earthquakes and regional seismicity are the average static stress drops between 1 to 10 MPa independently of the event magnitude (e.g Allmann & Shearer, 2009; Ye et al., 2016b) as well as the frequency-magnitude statistics of earthquakes within a region, which commonly follow the Gutenberg-Richter power-law relation (Field et al., 2013). Earthquake simulators are capable of matching these observations (Shaw et al., 2018). An important question is whether matching these constraints endows simulators with predictive power for other quantities of interest to seismic hazard assessment, such as the probability of multiple fault-segment ruptures, despite using approximations for inertial effects and oversized computational cells.

Let us consider this question using simulations of earthquake sequences in five fault models with the same fault geometry but different friction properties and different assumptions about inertial effects, and one additional model in which the effective seismogenic depth λ_S is slightly reduced from 15 to 14 km (Figure 6.11, Table 6.2). All six models have comparable nucleation and quasi-static cohesive zone sizes (Table 6.2) and use oversized cells of Δx = 1000 m (an example of well-resolved simulations with similar conclusions is given in section 6.7). The six simulations produce comparable frequency-magnitude distributions, characterized by a b-value of 0.3-0.4 for 4000 years of the simulated time. All six simulations also produce ruptures with comparable average static stress drops (Figure 6.12), with values typically between 1 and 10 MPa, as commonly inferred for natural earthquakes (Allmann & Shearer, 2009; Ye et al., 2016b).

However, the probability of a rupture jumping across the VS barrier varies dramatically among the six simulations, ranging from 0 to near 100%. This substantial variability in jump rate for simulations with comparable frequency-magnitude statistics persists in longer-duration simulations over 20,000 years, where both the 20,000-year jump rate and distributions of jump rates within individual 2000-year periods can substantially differ (Figure 6.13).

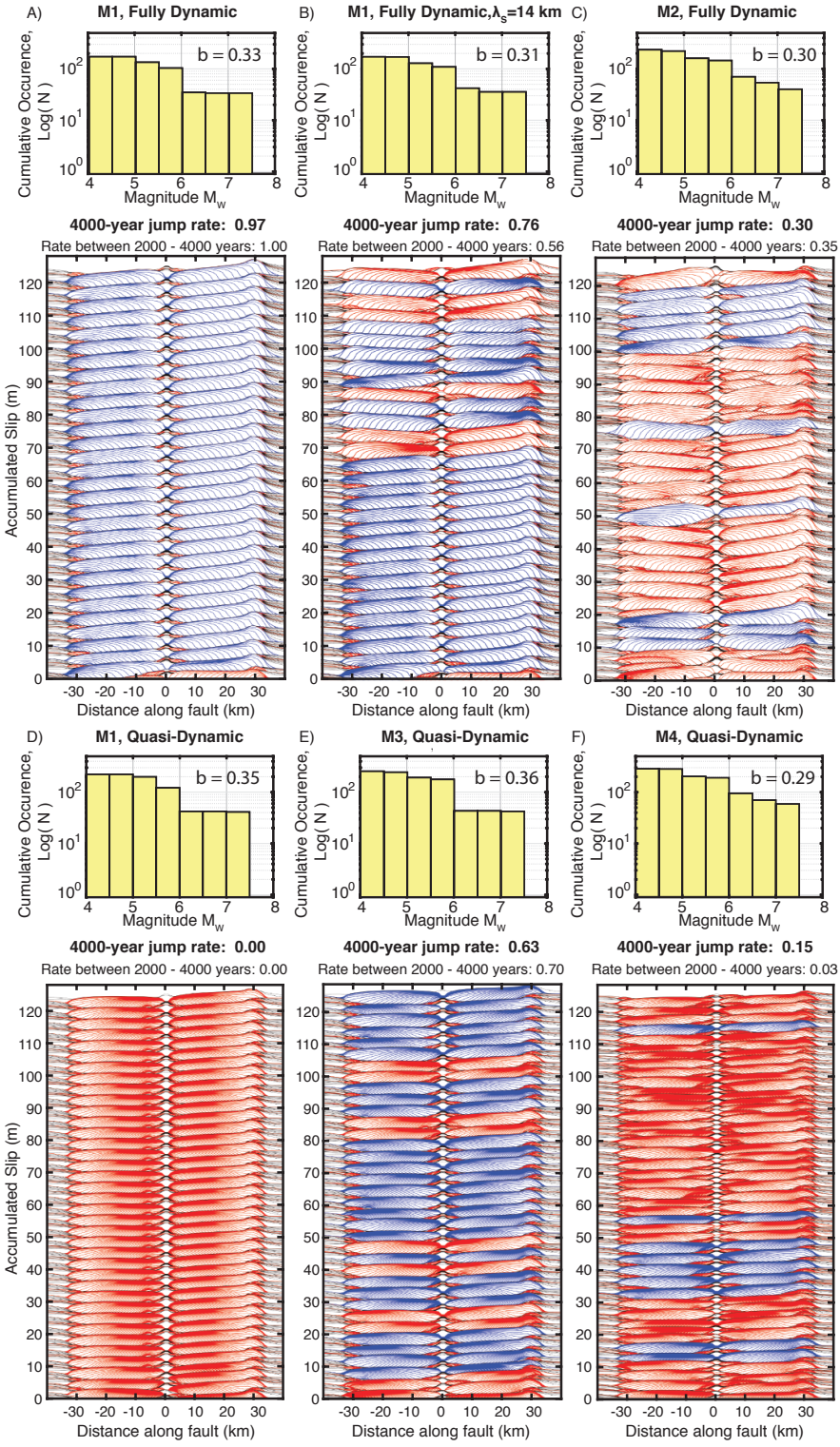

Figure 6.11: Models with comparable frequency-magnitude statistics and static stress drops but very different rates of two-segment ruptures. (A-F) Cumulative frequency-magnitude histograms (top) and history of cumulative slip (bottom) over 4000 years in (A-C) fully dynamic and (D-F) quasi-dynamic SEAS simulations. The simulations assume different physical conditions described in the text. All six simulations produce comparable average static stress drops (Figure 6.12) and comparable population statistics with a b-value around 0.33. However, the rate of two-segment ruptures varies from 0 to 1.

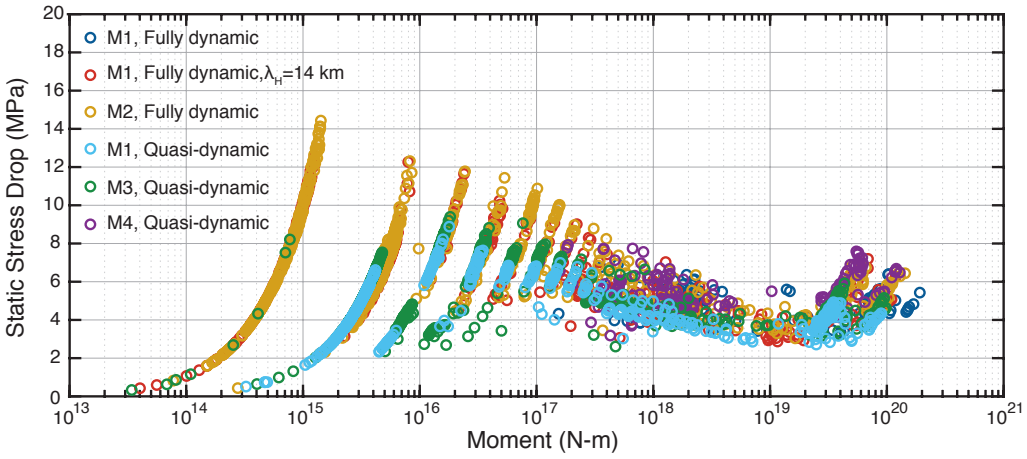

Figure 6.12: Comparable scaling of average static stress drop versus moment with reasonable stress drop values between 1 to 10 MPa for simulated ruptures in the six sets of simulations shown in Figure 6.11. The six models all use oversized cells of $\Delta x = 1000$ m and produce comparable earthquake frequency-magnitude statistics.

In particular, fault model M1 results in a jump rate of 0 for the quasi-dynamic simulation and near 1 for the fully dynamic simulation (Figures 6.11 and 6.13A vs. D), despite having similar frequency-magnitude statistics. This case illustrates how using approximations for inertial effects may considerably bias estimates of the actual rate of multi-segment ruptures, even if the frequency-magnitude statistics and static stress drops are comparable. In addition, the suite of simulations suggest that the probability of ruptures jumping across the VS barrier is sensitive to variations in the frictional parameters, effective normal stress, as well as minor changes in the seismogenic depth.

The results from our simple 2-D modeling suggest that reproducing static stress drops and frequency-magnitude statistics does not provide substantial predictive power for the long-term interaction of fault segments. These results are perhaps not surprising given that many combinations of rate-and-state properties and effective normal stress may produce ruptures with comparable static stress changes (Figure 6.12), but different overall levels of shear resistance. Moreover, numerical studies have shown that fault models including enhanced dynamic weakening may also produce nearly magnitude-invariant static stress drops with reasonable values between 1–10 MPa (Perry et al., 2020). Such models with enhanced

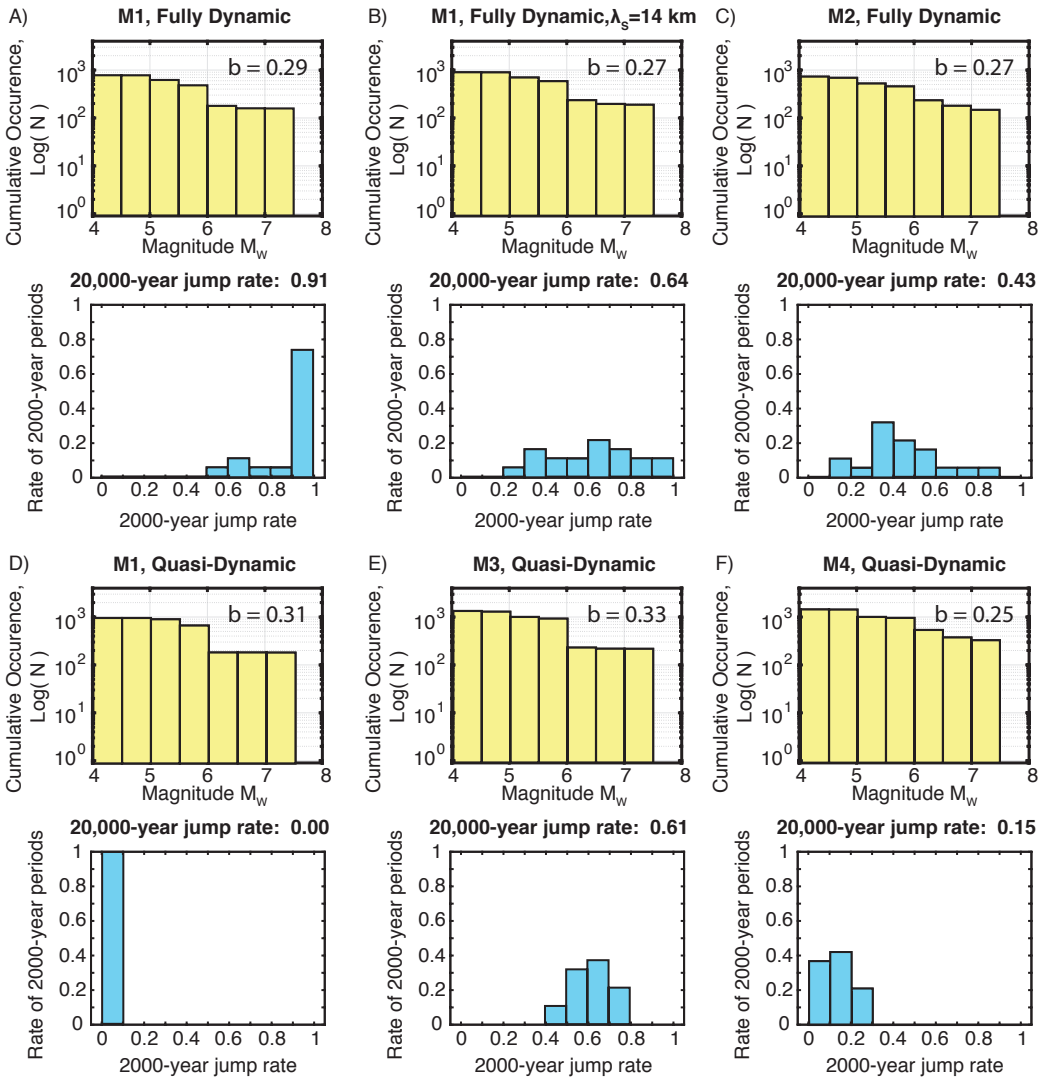

Figure 6.13: Variability of jump rates in models with comparable frequency-magnitude statistics and static stress drops. (A-F) Cumulative frequency-magnitude histograms (Top) and normalized 2000-year jump rate histograms (Bottom) over 20,000 years in (A-C) fully dynamic and (D-F) quasi-dynamic SEAS simulations, as shown in Figure 6.11. The six simulations have comparable frequency-magnitude statistics, but the 20,000-year rate of two-segment ruptures varies from 0 to 0.91. The distribution of 2000-year jump rates is also highly variable among the six simulations.

weakening result in larger dynamic stress variations which may mediate longer-range interactions among faults. However, enhanced weakening can also draw the average stress along the fault further away from nucleation conditions (Jiang & Lapusta, 2016; Lambert et al., 2021), which may produce less favorable conditions for dynamic triggering (Ulrich et al.,

2019).

Similarly, a number of studies have demonstrated that power-law frequency-magnitude statistics can be reproduced in many models, including discrete fault models (Bak & Tang, 1989; Burridge & Knopoff, 1967; Olami et al., 1992), continuum fault models that are inadequately resolved and therefore numerically discrete (Ben-Zion & Rice, 1995), and continuum models with larger instability ratio (Cattania, 2019; Wu & Chen, 2014). In other words, Gutenberg-Richter statistics is consistent with a model having many potential rupture sizes, such as many individual faults of varying size or even a single fault that can host earthquakes of many sizes, between the nucleation size and fault dimensions. Therefore Gutenberg-Richter statistics may be compatible with a range of fault and/or fault network properties, and may not pose a considerable physical constraint on its own.

6.6 Resolution and convergence of SEAS simulations of faults with higher instability ratios

As discussed in section 6.3, we find that the discretization required to achieve long-term numerical convergence in simulations of fault model M1, with instability ratio of $\lambda_{VW}/h^*_{RR} \approx 21$, is more stringent than the current standards based on simulations of single dynamic ruptures and shorter SEAS simulations with lower instability ratios (Day et al., 2005; Lapusta & Liu, 2009). It has been demonstrated that fault models with relatively low instability ratios can result in quasi-periodic behavior, as seen in fault model M1 (Figure 6.2), whereas increasing the instability ratio can lead to more variable sequences of events with partial-segment ruptures of different rupture size, potentially consistent with Gutenberg-Richter scaling (e.g Cattania, 2019; Lapusta & Rice, 2003; Lapusta et al., 2000; Michel et al., 2017; Wu & Chen, 2014). As simulations with higher instability ratios can produce ruptures with a wider variety of rupture sizes, with the rupture size depending on the prestress conditions before rupture nucleation, one could hypothesize that simulations of fault models with higher instability ratios may be more sensitive to how the evolution of shear stress is resolved over long-term fault behavior.

To test that, let us consider sequences of events in fault model M5 (Table 6.2), which has smaller characteristic slip distance, hence smaller nucleation size ($h^*_{RR} \approx 603$ m), and larger instability ratio ($\lambda_{VW}/h^*_{RR} = 53$ vs. 21 in M1). Interestingly, we find that the long-term sequence of simulated events in this model is not the same for finely-discretized simulations with cell sizes of 25, 12.5, and 6.25 m (Figure 6.14), in which the quasi-static cohesive zone Λ_0 is resolved by 18, 36, and 72 cells, respectively. The simulations produce nearly identical fault behavior for the first several hundred years of simulated time, but then eventually begin to differ (Figure 6.14A-C).

Let us consider the first event in the three simulations of model M5 with fine discretization (Figure 6.14A-C), which all have the same initial conditions. If we examine the local evolution of shear stress vs. slip at two spatial points in the simulations, the results are virtually identical (Figure 6.15A-B), suggesting that a single dynamic rupture in these finely-discretized simulations is adequately resolved. The evolution of shear stress and slip rate at the rupture front with time is also well-resolved for each individual simulation. While the different spatial resolutions result in small variations in the timing and magnitude of the resolved properties at specified locations (Figure 6.15C-F), these differences are well within of what is considered well-resolved and convergent in prior studies (e.g Day et al., 2005). Early in the rupture, shortly after nucleation (near $x = 30$ km), the rupture front is almost identical in the three simulations. (Figure 6.15C & E). As the rupture continues, small numerical differences for different resolutions result in minor differences in the rupture, such as less than 0.08% difference in the rupture arrival time and 2% difference in the peak slip rate between the two best-resolved simulations at the location close to the end of the rupture (Figure 6.15D & F). Such minor differences arise even for fine resolutions due to cumulative effects of slightly different representations of the solution by the discrete cells; for example, the fixed computational cells sample slightly different portions of the passing rupture front, leading to small accumulating differences in the magnitude of the shear stress and slip rate.

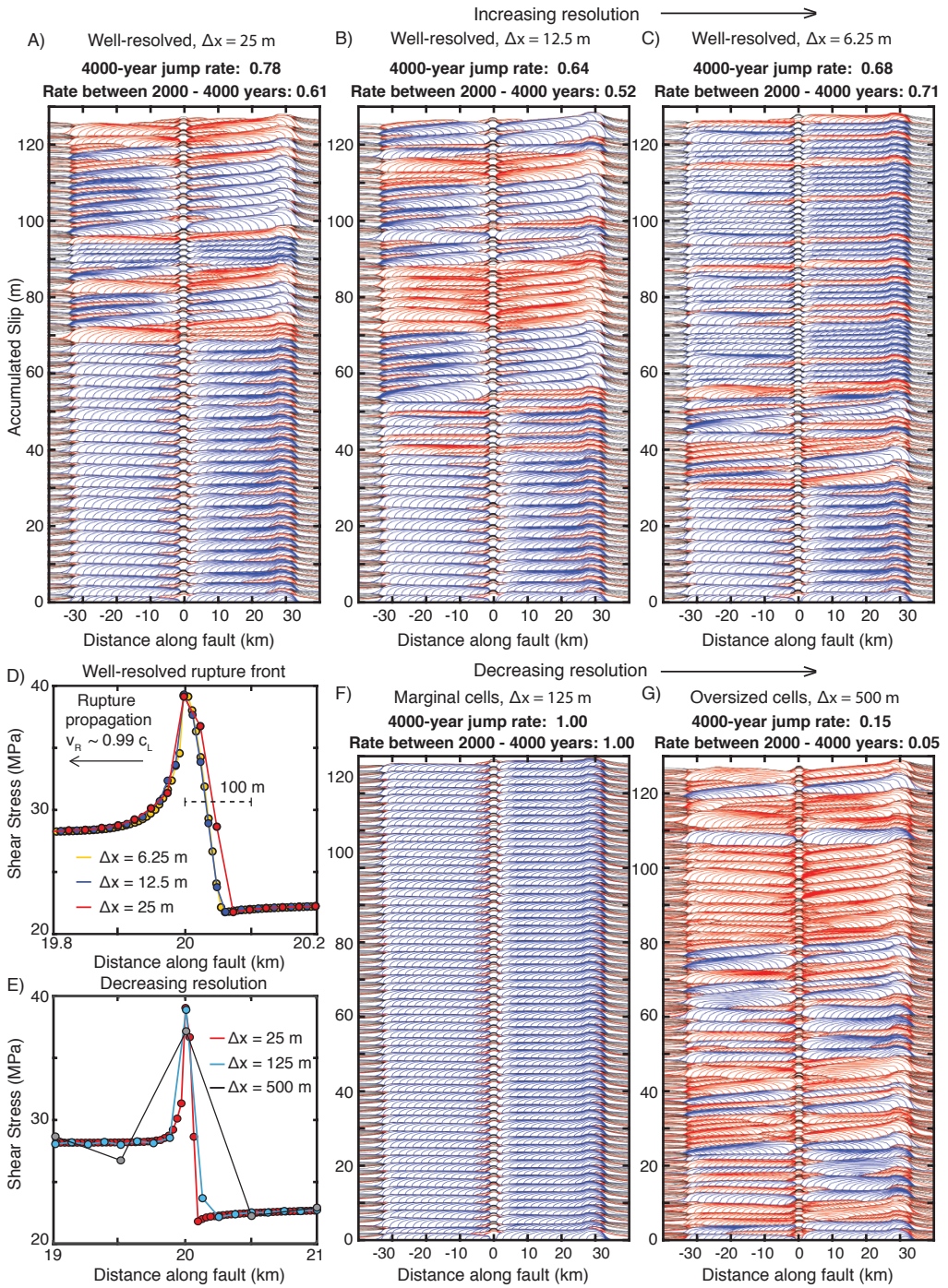

Figure 6.14: Sequences of earthquakes and rates of two-segment ruptures over 4000 years in fully dynamic simulations with different resolution of fault model M5 with higher instability ratio. Seismic slip is contoured every 0.5 s with ruptures jumping across the VS barrier colored blue. (A-C) Slip history for increasingly better-discretized simulations. While the initial 1000 years of simulated behavior appear well resolved and comparable, longer-term simulations begin to diverge due to the compounded effects of small numerical differences, leading to similar but inconsistent jump rates across the barrier. (D-E) The spatial distribution of shear stress at the rupture front. For well-resolved simulations (D), the cohesive zone is resolved by several cells, but is resolved by less than even one cell for poorly-resolved simulations (E). (F-G) Simulations with decreasing numerical resolution can exhibit additional artificial complexity and substantially different long-term fault behavior, including different rates of two-segment ruptures.

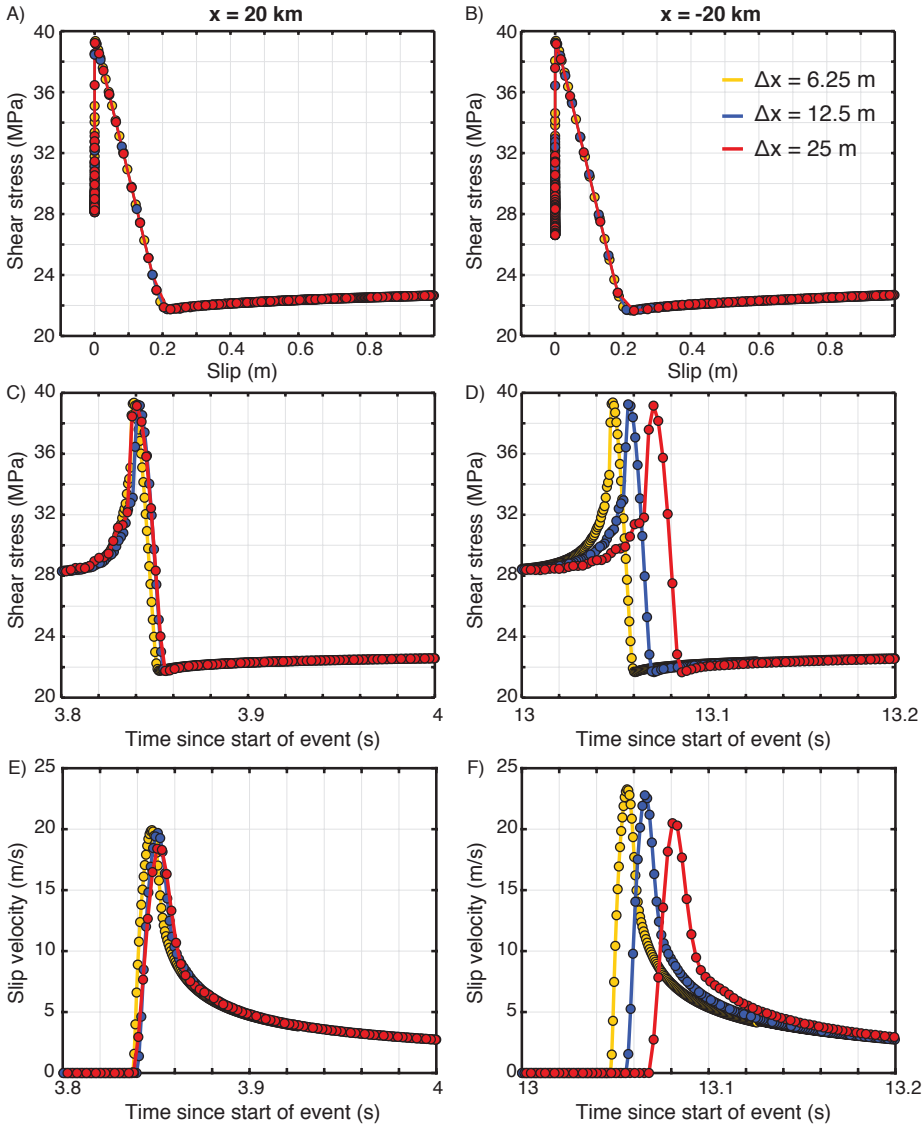

Figure 6.15: Excellent resolution of local shear stress and slip rate for the first rupture of well-resolved fully dynamic simulations of model M5 shown in Figure 6.14. The evolution of local shear stress with slip at (A) $x = 20$ km and (B) $x = -20$ km is virtually identical. Evolution of (C-D) shear stress and (E-F) slip rate with time for the same points. The rupture nucleates near $x = 30$ km. Early in the rupture (A, C & E), the local behavior is comparable among the well-resolved simulations. Near the end of the first rupture (D & F), the simulations begin to deviate very slightly in their local behavior, consistent with the results of Day et al. (2005). While the simulated behavior in the first rupture is very similar, these small differences, resulting from different numerical approximations, compound over many sequences and eventually lead to diverging behavior, as seen in Figure 6.14.

These small differences –that do not substantially alter the resulting rupture characteristics of individual events –do eventually alter the resulting earthquake sequences. For several ruptures early on in finely-discretized simulations, the slip and shear stress distributions before and after individual events are virtually indistinguishable (Figure 6.16A-B). However, eventually the small variations accumulate, resulting in enough differences in prestress conditions to cause more substantial differences in rupture lengths and amounts of slip within individual events, as well as changes in timing and location of earthquake nucleations (Figure 6.16C-E). As a result, the long-term history of sequences of slip events is altered (Figure 6.16F), including the rate of ruptures that jump across the VS barrier. We hypothesize that this alteration occurs for higher but not lower instability ratios due to more complex earthquake sequences in the latter case, although this issue requires further study.

Despite the specific sequences of events being different in the finely-discretized simulations shown in Figure 6.14A-C, we do find that certain outcomes are quite similar between these simulations, such as relationships between average static stress drop and seismic moment, average slip and rupture length, and breakdown energy and average slip, as well as general characteristics of the evolution of average shear stress and shear heating with time (Figure 6.17). Other parameters, such as the rate of ruptures jumping from one fault segment to another, are sensitive to numerical resolution even in these finely-resolved simulations, although they have relatively similar values (from 0.64 to 0.78). This highlights how the criteria for adequate discretization in numerical simulations can depend on both the physical problem being considered and the outcome of interest. Note that while it is plausible that further discretization of fault model M5 would result in eventual convergence, and thus potentially a true rate of two-segment ruptures, the spatial discretization considered in this study is already much finer than those considered in most numerical SEAS studies, especially in more realistic models of 2D faults in 3D media which are often challenged to resolve Λ_0 by even 3 cells.

While the specific rate of ruptures jumping across the VS barrier varies among these finely-

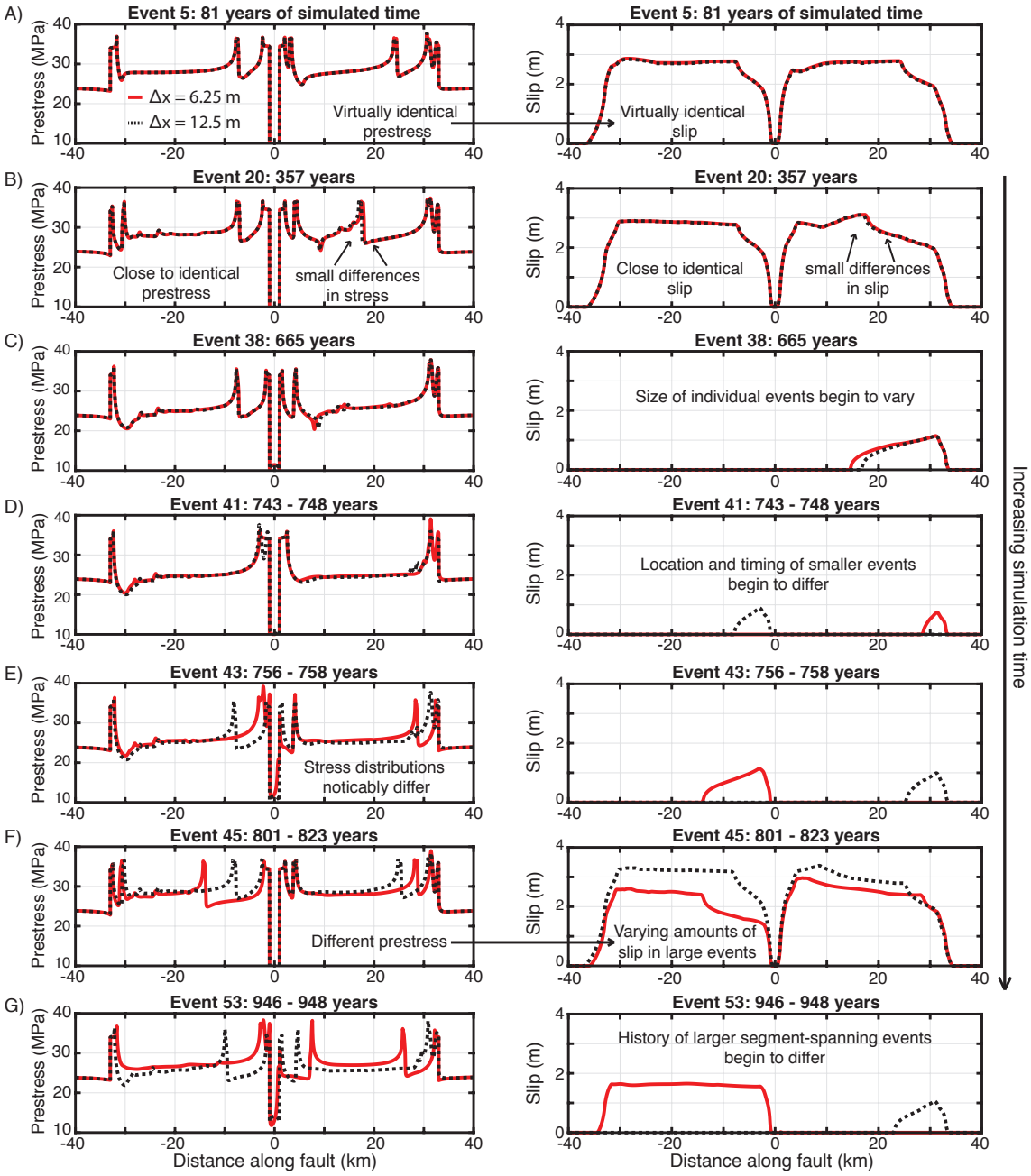

Figure 6.16: Compounded effects of minor numerical differences in well-resolved simulations of model M5 result in diverging long-term earthquake sequences. Comparison of the prestress before rupture (left) and resulting slip distributions (right) for several events over the first 1000 years of simulated time in two fully dynamic simulations of fault model M5 using cell sizes of 6.25 m (red) and 12.5 m (black). (A & B) The evolution of shear stress and accumulation of slip during the first few hundred years of simulated time are virtually identical. (C-E) Eventually, small differences in shear stress before events build up due to different numerical approximations, resulting in small differences in slip and rupture length for individual events, as well as the location and timing for the nucleation of smaller events. (F & G) The differences in shear stress accumulate over sequences of events, resulting in noticeable variations of slip in larger events after 800 years of simulated time and, eventually, different histories of large segment-spanning events between the two well-resolved simulations, as shown in Figure 6.14.

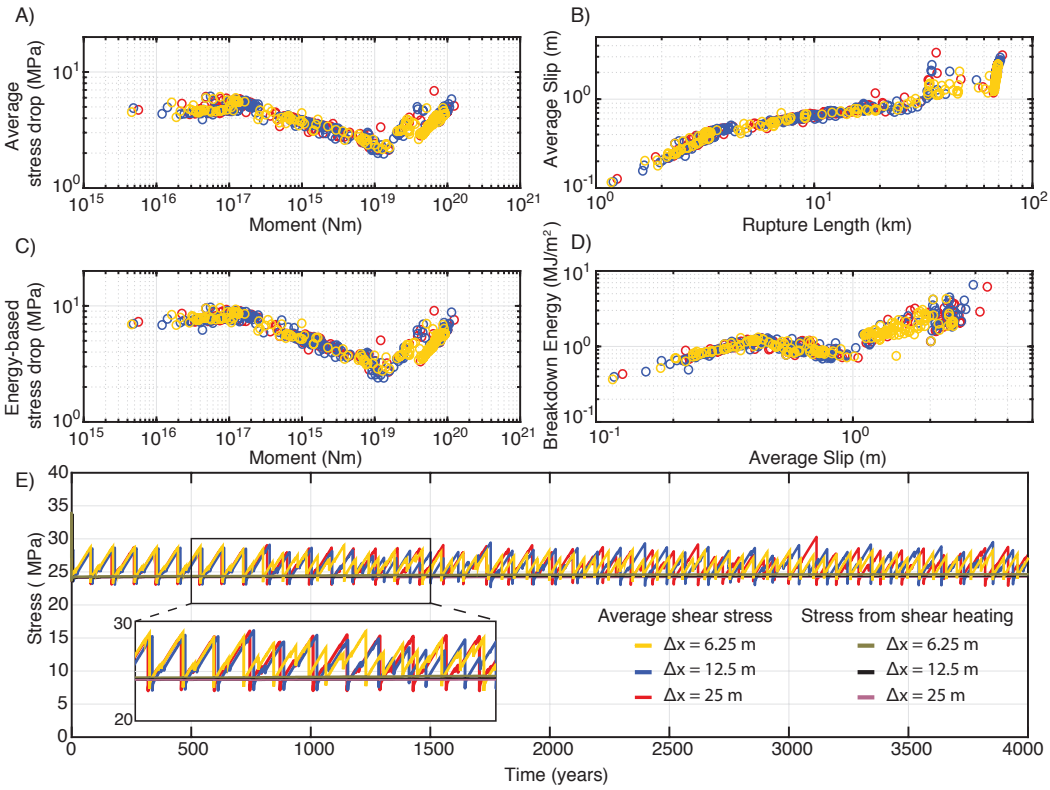

Figure 6.17: Averaged source properties and fault behavior that are generally consistent among well-resolved fully dynamic simulations of fault model M5, despite lack of convergence of slip with finer resolution. (A) Spatially-averaged stress drop versus moment. (B) Average slip versus rupture length. (C) Energy-based average stress drop versus moment. (D) Average breakdown energy versus average slip. (E) Evolution of average shear stress and the shear stress associated with shear heating over 4000 years of simulated sequences of earthquakes. It is apparent that the timing and degree of slip of individual events in the sequences of earthquakes differ. However the general characteristics of the overall average stress evolution, in terms of the maximum and minimum stresses and the average stress drops, are comparable, resulting in virtually indistinguishable shear heating stresses.

discretized simulations of fault model M5, it is possible that some broader statistical features of the jump rate are more robust. We examine the frequency-magnitude and 2000-year jump rate statistics for the long-term sequences of events in simulations of model M5 with different discretization. While the distributions mildly vary among finely-discretized simulations with differing cell sizes (12.5 m and 25 m), they are comparable (Figures 6.18 and 6.19). Thus, one can ascertain information about the probability distribution for the rate of multi-segment ruptures, even if specific results vary due to numerical discretization. Such small numerical perturbations could potentially be considered representative of various sources of physical perturbations on natural faults, and the statistical consistency of the distributions could be explored by producing ensembles of simulations with varying initial conditions. However, our results suggest that it is still important to sufficiently resolve the rupture process as the statistical distributions for rupture properties in simulations using oversized cells can be more substantially impacted by numerical artifacts and considerably vary from simulations with finer discretization (Figures 6.18 and 6.20).

6.7 Resolution and convergence in SEAS simulations with moderate rupture speeds due to an approximation for off-fault plasticity

While the 2-D fault models discussed in this study can be considered relatively simple, in some ways they can be particularly challenging to resolve. In fault models with purely elastic bulk, dynamic ruptures are able to accelerate to rupture speeds close to the limiting values c_L (e.g. Figure 6.9 for fault model M1), making it difficult to resolve the significantly shrinking cohesive zone Λ. For example, during fully dynamic ruptures in simulations of fault model M5, the rupture speed approaches $0.99c_L$ and the cohesive zone shrinks more than 7 times to about 63.5 m. In real rocks, high slip rates and hence high strain rates associated with dynamic rupture would be mitigated by off-fault inelastic behavior around the rupture front, which would contribute to limiting the rupture speed (Andrews, 2004; Dunham et al., 2011a).

In order to examine how conditions for resolution and convergence may differ in long-term SEAS simulations with more moderate rupture speeds, we approximate the effects of off-fault yielding by employing a limit on the slip velocity, as suggested by Andrews (2004)

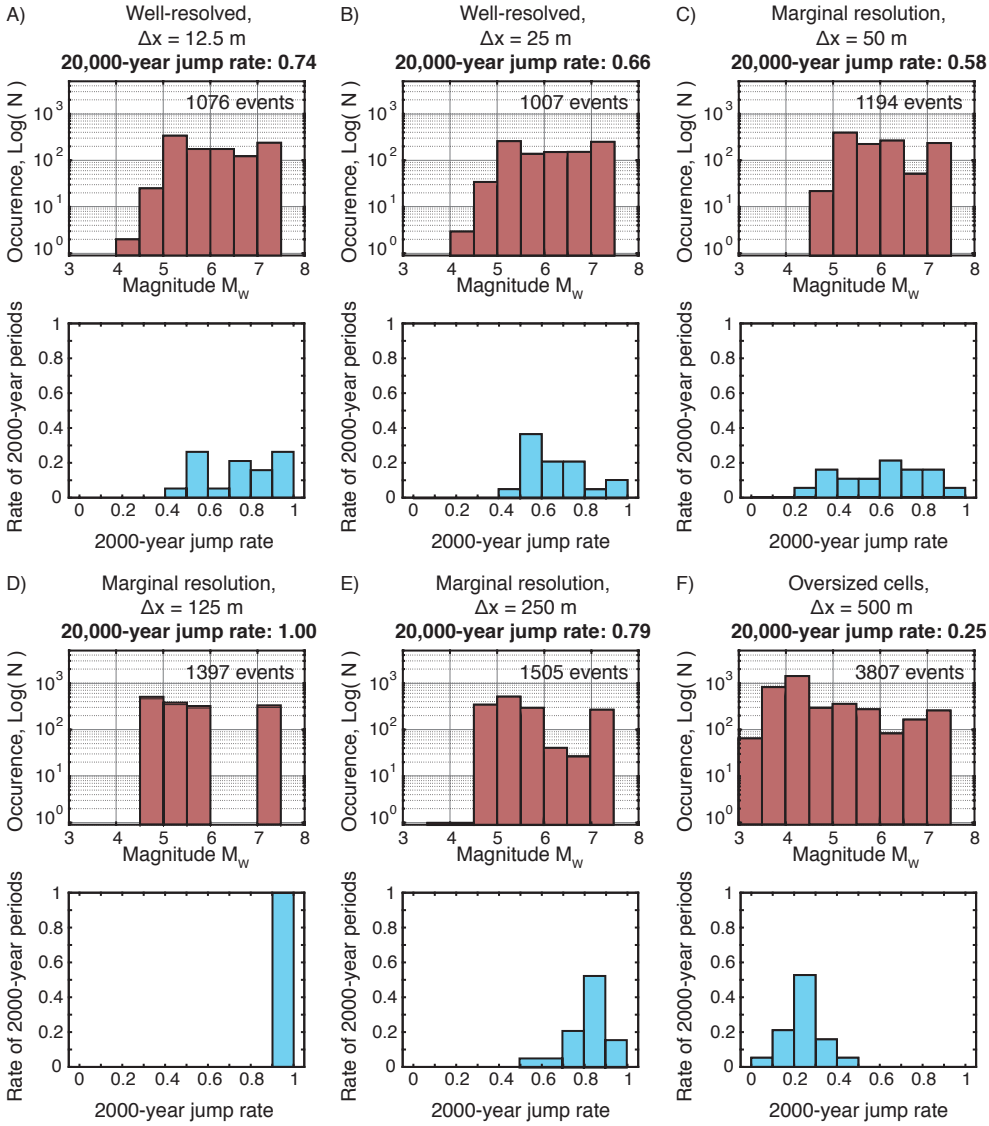

Figure 6.18: Different frequency-magnitude and jump rate statistics for 20,000 years of sequences of earthquakes in fully dynamic simulations of fault model M5 with varying cell sizes. (A-F) Frequency-magnitude histograms (Top) and normalized 2000-year jump rate histograms (Bottom) for 20,000 years of simulated SEAS. (A-B) Even well-resolved simulations exhibit mild differences in long-term event statistics, though the frequency-magnitude histograms are similar. The 2000-year jump rate histograms are different but comparable for well-resolved simulations, with the 20,000-year jump rate varying by approximately 15% among the three simulations. (C-F) Simulations with marginal or inadequate resolution have enhanced production of smaller events, as small groups of cells nucleate into ruptures but fail to propagate substantially due to poorly resolved stress concentration at the rupture front. The 20,000-year jump rates and 2000-year jump rate distributions substantially vary for simulations using oversized cells compared to the well-resolved simulations.

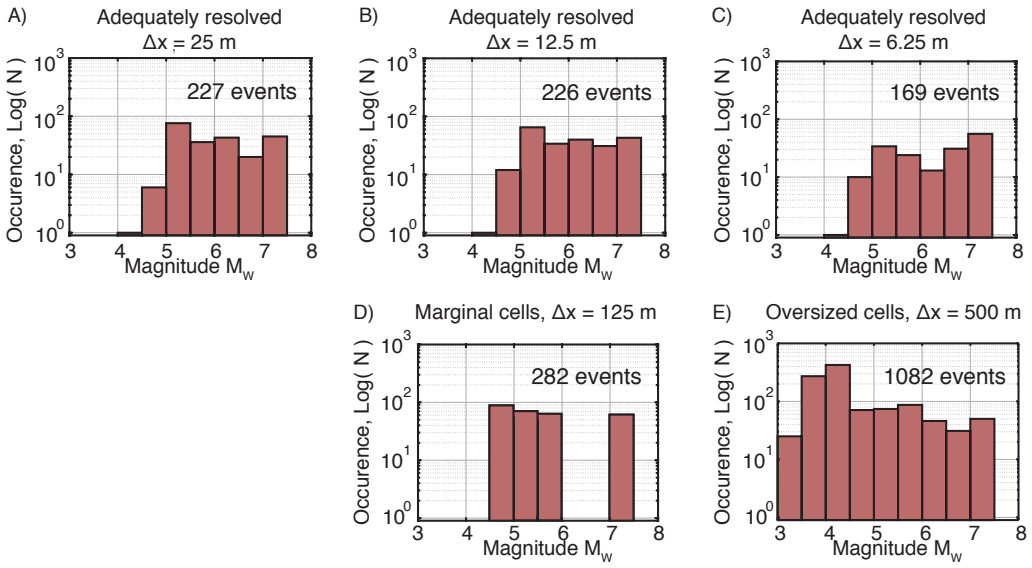

Figure 6.19: Differing frequency-magnitude histograms for 4000 years of sequences of earthquakes in fully dynamic simulations of fault model M5 with varying cell sizes. Simulations are performed using different computational cell sizes of (A) 25 m, (B) 12.5 m, (C) 6.25 m, (D) 125 m, and (E) 500 m. Simulations exhibit differences in long-term behavior, even for well-resolved simulations (A-C) where the stress at the rupture front is spatially described by more than 3 cells. Simulations using oversized cells or with marginal resolution (D & E) produce more smaller events as small groups of cells nucleate into ruptures that fail to propagate due to the stress concentration at the rupture front being poorly resolved.

and discussed in detail in Lambert et al. (2021). We consider long-term fully dynamic simulations of fault model M5 with the slip velocity limited to 2 m/s in order to maintain rupture speeds around $0.8c_L$, consistent with the cohesive zone shrinking by about a factor of 2 from the quasi-static estimate.

Surprisingly, the finely-discretized simulations of fault model M5 with limited rupture speed still produce differing sequences of events, despite the rupture front and local behavior being well-resolved and nearly identical for cell sizes of 6.25 to 25 m (Figures 6.21 and 6.22). As with the standard fully dynamic simulations without the plasticity approximation, well-resolved simulations of fault model M5 with the velocity limit are nearly identical for the initial few sequences (Figure 6.23A-B). However, the sequences of events begin to differ due to slight differences in how the evolution of shear stress is resolved during a slow-slip

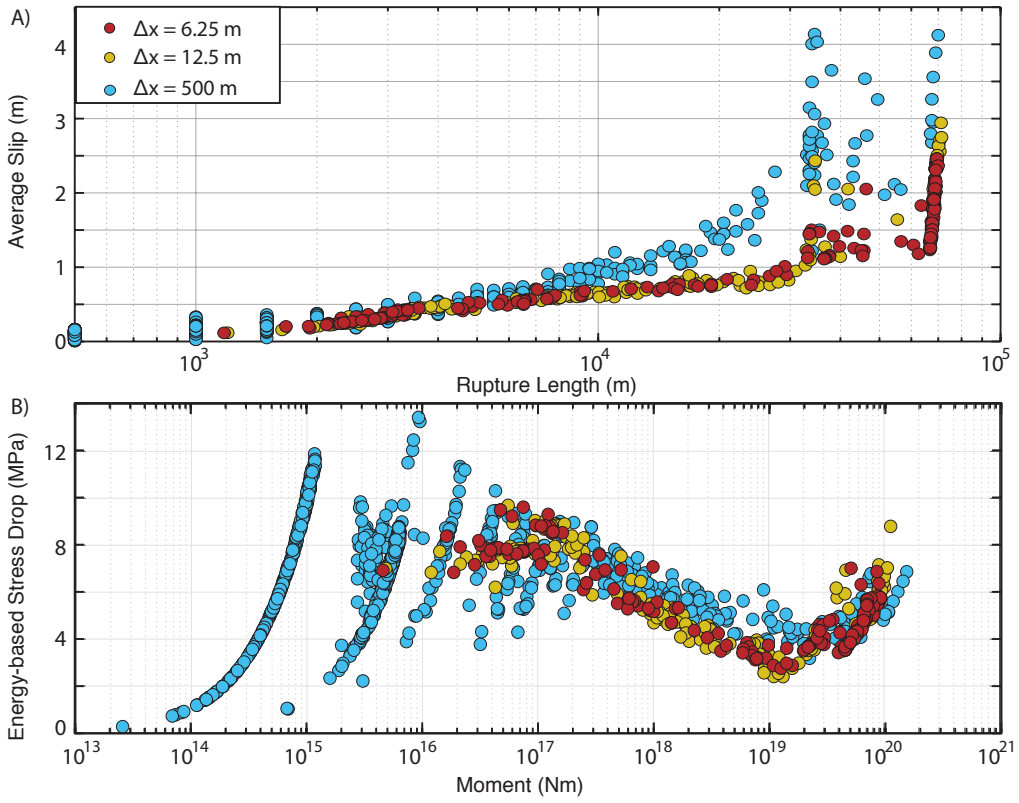

Figure 6.20: Scaling of average slip and stress drop with rupture size for numerically-discrete versus well-resolved ruptures in fault model M5. (A-B) Despite different long-term sequences of events, two well-resolved simulations of fault model M5, with cell sizes Δx = 6.25 m and Δx = 12.5 m, have similar scaling of average slip and static stress drop with rupture size. Simulations using oversized cells produce small numerically-discrete ruptures consisting of only a few cells that fail to propagate due to the poorly resolved stress concentration of the shear stress at the (diffuse) rupture front. This causes large ruptures to occur in poorly-resolved simulations for higher values of shear stress, resulting in large ruptures having greater average slip than in well-resolved simulations (A). The small numerically-discrete ruptures produce variable amounts of slip, despite being restricted to the same rupture size of only 1 to several cells (A), leading to large, upward-sweeping trends in average stress drop with moment, which are purely numerical (B).

transient within the nucleation region of an impending rupture, resulting in a 3-year delay between the nucleation of the subsequent rupture in each simulation (Figure 6.23C-D). As discussed earlier for the standard fully dynamic simulations, the small differences in pre-stress lead to mild differences in slip and rupture size in subsequent events, which eventually compound to produce more substantial variations in the long-term sequences of events (Figure 6.23 E-H). These results once again illustrate the extreme sensitivity of the long-term sequences of events, and rates of two-segment ruptures, in this highly nonlinear problem, as well as the significance of resolving how aseismic processes load, relax, and redistribute stress along faults.

Interestingly, we see similar lack of convergence in quasi-dynamic simulations of fault model M5, where long-term sequences, including the rate of two-segment ruptures, differ in seemingly well-resolved simulations due to the compounded effects of small numerical differences (Figures 6.24 and 6.25). Moreover, despite the rupture front being better resolved in the quasi-dynamic simulations and in fully dynamic simulations withthe plasticity approximation than in the standard fully dynamic simulations, the sequences of events begin to diverge earlier. Specifically, while the standard fully dynamic simulations of fault model M5 with cell sizes of $\Delta x = 6.25$ and $\Delta x = 12.5$ m have the same event sequences through approximately 600 to 700 years of simulated time, fully dynamic simulations with the plasticity approximation begin to substantially differ between 200 to 300 years, and quasi-dynamic simulations begin to noticeably differ between 100 to 200 years.

A potential explanation for this finding is that both the quasi-dynamic approximation and strong limitation on slip rate for fully dynamic simulations also limit the magnitude of the stress transfer along the fault (Figure 6.26), making the simulations more sensitive to small numerical differences. Thus, while the lower stress concentrations in both cases facilitate maintaining slower ruptures and resolving the breakdown of shear resistance at the rupture front, the smaller magnitudes for the stress transfer along the fault makes rupture propagation more sensitive to variations in the pre-existing shear stress ahead of the rupture

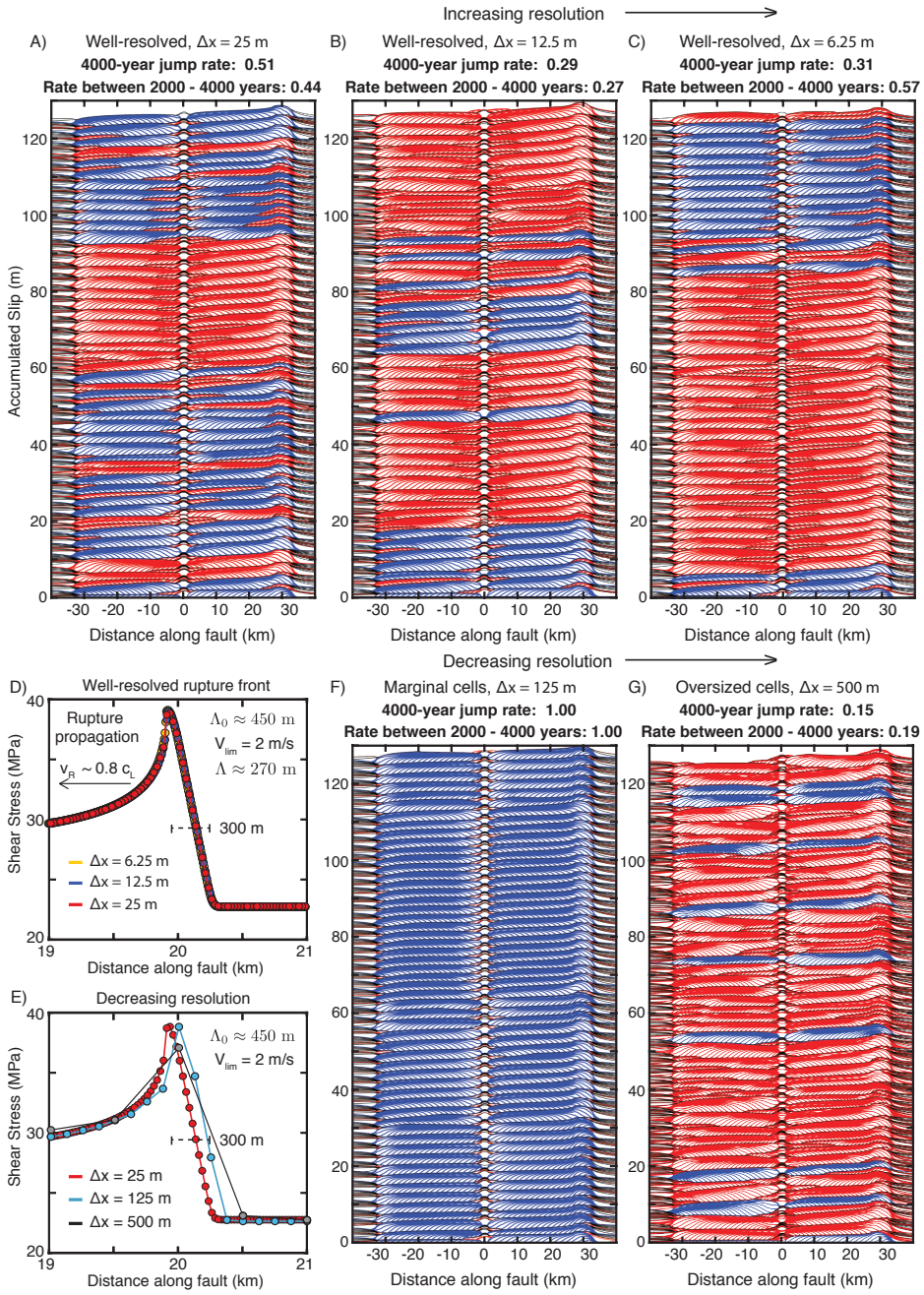

Figure 6.21: Sequences of earthquakes and rate of two-segment ruptures over 4000 years in fully dynamic simulations with different resolution of fault model M5 and an approximation of off-fault plasticity. The rupture speed reduces to 0.8 c_L due to the approximation using a velocity limit of $V_{\text{lim}} = 2$ m/s. Seismic slip is contoured every 0.5 s with ruptures jumping across the VS barrier colored blue. (A-C) Slip history for increasingly well-resolved simulations. The initial few sequences of events appear comparable among well-resolved simulations, however the sequences begin to differ due to the compounded effects of small numerical differences. (D-E) The cohesive zone shrinks by only about a factor of two for rupture speeds below 0.8 c_L, so the rupture front is very well-resolved. (F-G) Simulations with decreasing numerical resolution exhibit additional artificial complexity and substantially different long-term fault behavior, including rates of two-segment ruptures.

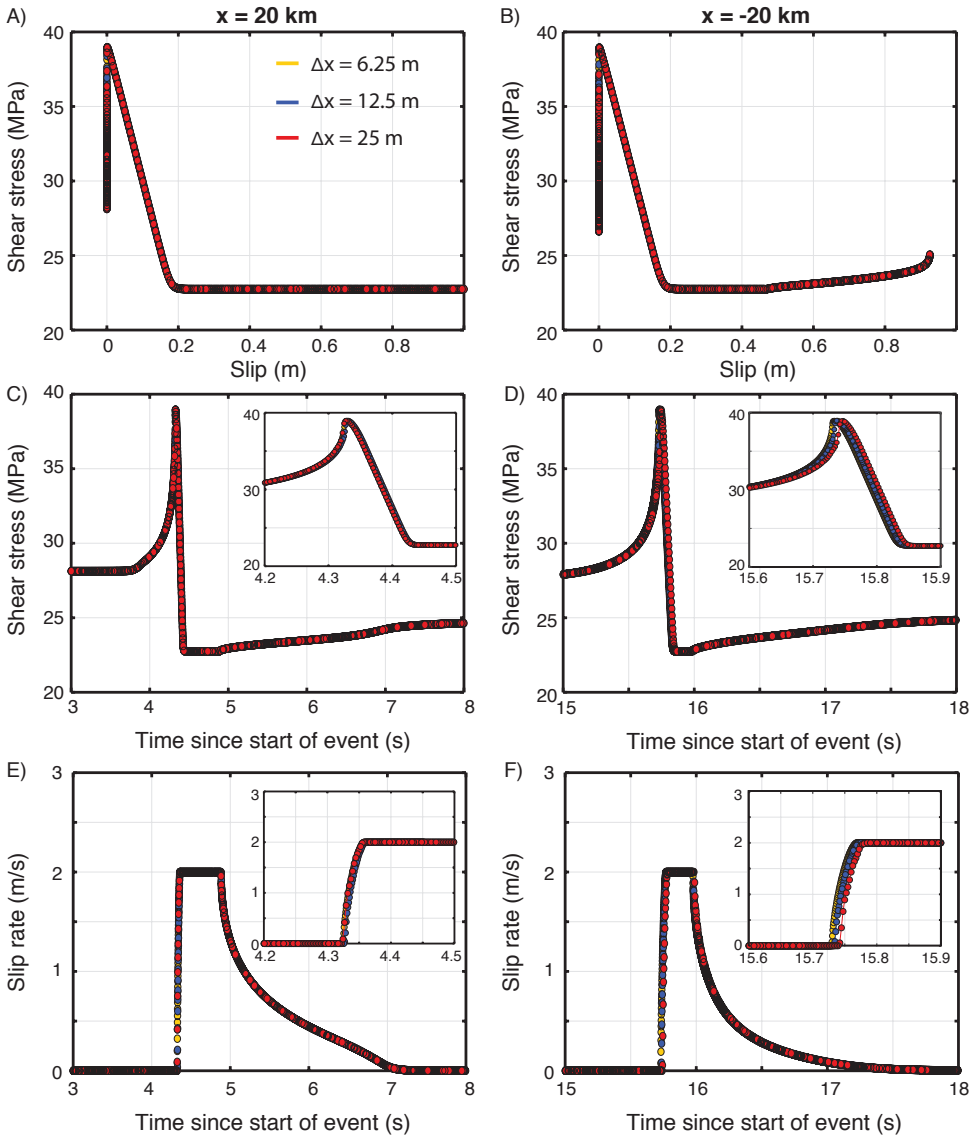

Figure 6.22: Evolution of local slip rate and shear stress with slip and time at two points at (left) $x = 20$ km and (right) $x = -20$ km during the first rupture of adequately-discretized fully dynamic simulations of fault model M5 with the effects of off-fault dissipation approximated using a velocity limit of $V_{\text{lim}} = 2$ m/s, as shown in Figure 6.23. The local behavior is nearly identical for all three simulations with different spatial discretization.

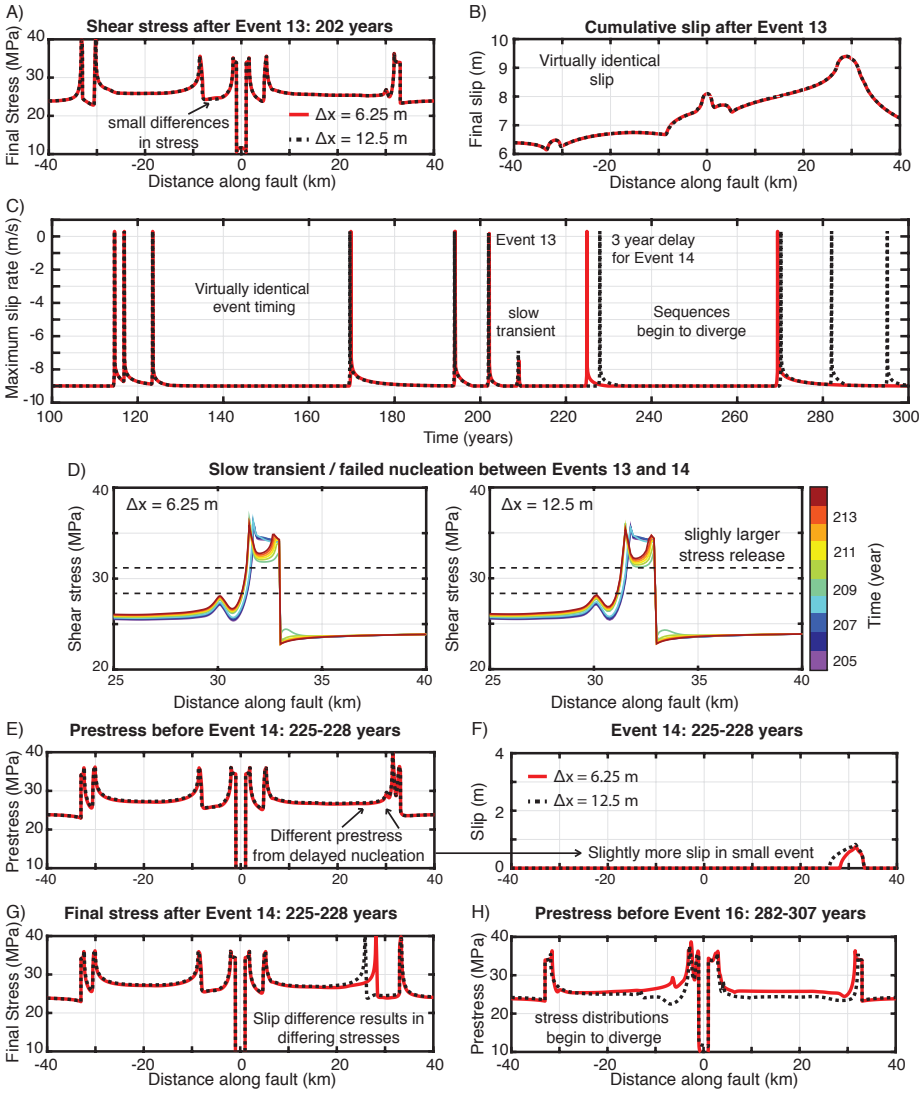

Figure 6.23: Simulations with diverging long-term sequences of earthquakes after small differences in a slow-slip transient. (A-B) Virtually indistinguishable spatial distribution of shear stress and slip after the 13th event in fully dynamic simulations of fault model M5 with the effects of off-fault dissipation approximated using a velocity limit of $V_{\text{lim}} = 2$ m/s, with cell sizes of $\Delta x = 6.25$ (red) and $\Delta x = 12.5$ (black dashed). (C) Evolution of the maximum slip rate between 100 to 300 years of simulated time. Before event 13, the timing of slip events is nearly identical, however after a slow-slip transient following event 13, around $t = 210$ years, the timing of slip events begins to diverge. (D) The resolved shear stress changes due to the slow-slip transient within the nucleation region of event 14 mildly differs between the two simulations of different cell size, resulting in a slightly higher stress release for the simulation with cell size $\Delta x = 12.5$ m. (E-F) Following the slow-slip transient, there is a 3-year difference between the nucleation of event 14, leading to slightly higher prestress before the initiation of the rupture, and hence slightly different resulting slip distributions. (G-H) The different rupture sizes and amount of slip in event 14 results in differing final stress distributions. The timing of subsequent events becomes more disparate between the two simulations and the shear stress distributions and sequences of events begin to differ more substantially (Figure 6.21).

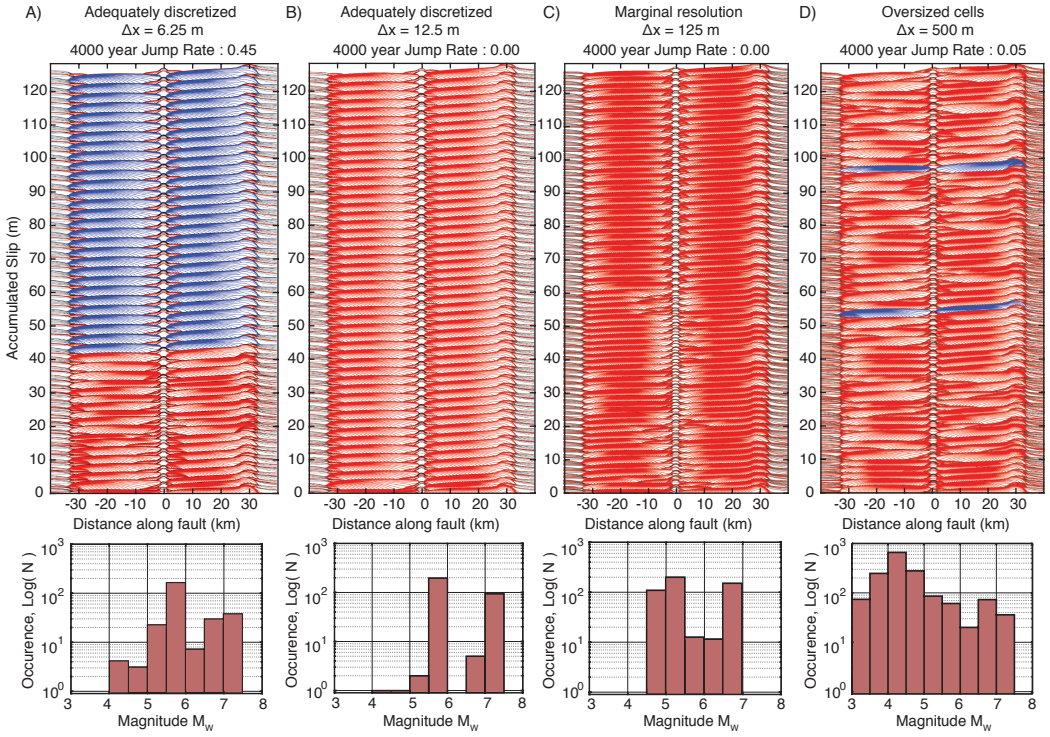

Figure 6.24: Different sequences of earthquakes and rate of two-segment ruptures over 4000 years in quasi-dynamic simulations with different resolution of fault model M5. (Top) Slip history for simulations with varying spatial resolution showing different histories of events depending on the choice of cell size. Seismic slip is contoured every 0.5 s with ruptures jumping across the VS barrier colored blue. (Bottom) Frequency-magnitude statistics for the respective simulations of varying cell size shown above. Simulations using larger cell sizes produce a larger number of small events as small groups of cells nucleate, but ruptures cannot propagate due to the inadequately resolved stress concentration at the rupture front. Even adequately-resolved simulations show different histories of events, including rates of ruptures jumping across the VS barrier.

front. Note that while the approximation for off-fault plasticity substantially limits the peak slip rate and magnitude of the stress transfer along the fault, the overall stress transfer for the fully dynamic rupture including the plasticity approximation is still more pronounced than that of the quasi-dynamic ruptures, and remains more pronounced well behind the rupture front due to the continued arrival of waves from ongoing slip in already-ruptured regions. Both the quasi-dynamic simulations and the fully dynamic simulations with the plasticity approximation produce comparable static stress drops and frequency-magnitude statistics to the standard fully dynamic simulations (Figures 6.19, 6.24 and 6.27). However, the rupture speeds and rates of two-segment ruptures are consistently higher for the fully

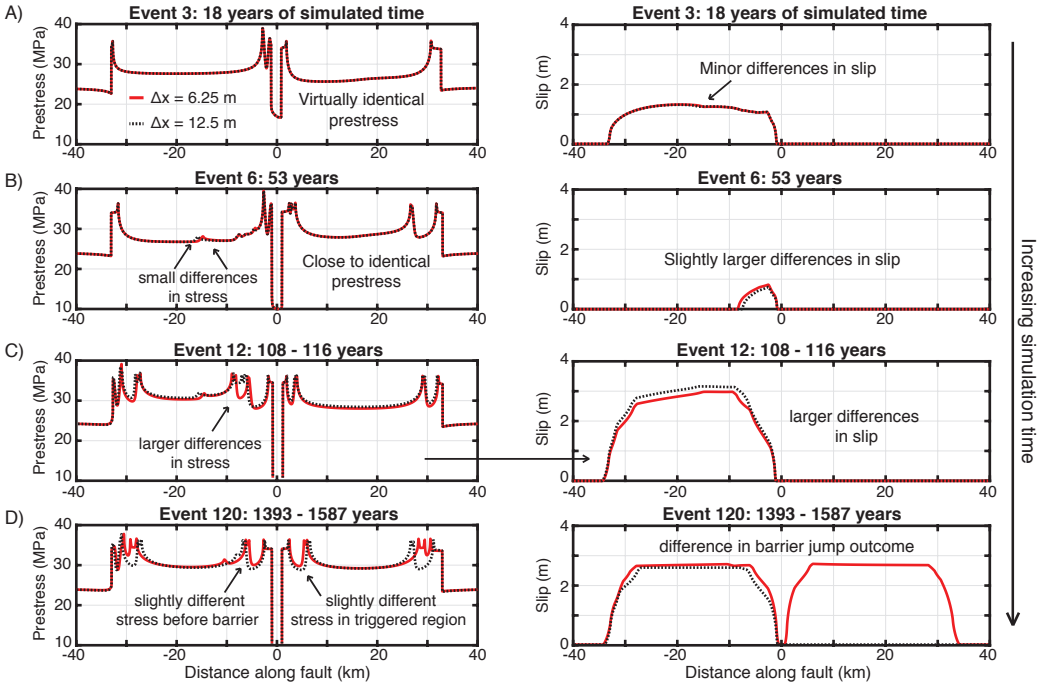

Figure 6.25: Compounded effects of small numerical differences in well-resolved quasi-dynamic simulations result in diverging long-term earthquake sequences. Comparison of prestress before rupture (left) and resulting slip distributions (right) for several events over the first 2000 years of simulated time in two quasi-dynamic simulations of fault model M5 using cell sizes of 6.25 m (red) and 12.5 m (black). (A & B) The evolution of shear stress and accumulated slip during the first few sequences of events is practically identical, however small differences begin to appear due to different numerical approximations. (C) The small differences in shear stress accumulate over sequences of events, resulting in more noticeable variations in the amount of slip in larger events. (D) The accumulation of noticeable differences in shear stress, particularly in regions of rupture nucleation and near the VS barrier, leads to differing sequences of events, rupture sizes, and probabilities of rupture jumping across the VS barrier.

dynamic simulations due to the substantially larger stress transfer. These results emphasize the significance of inertial effects when considering how ruptures navigate various forms of fault heterogeneity.

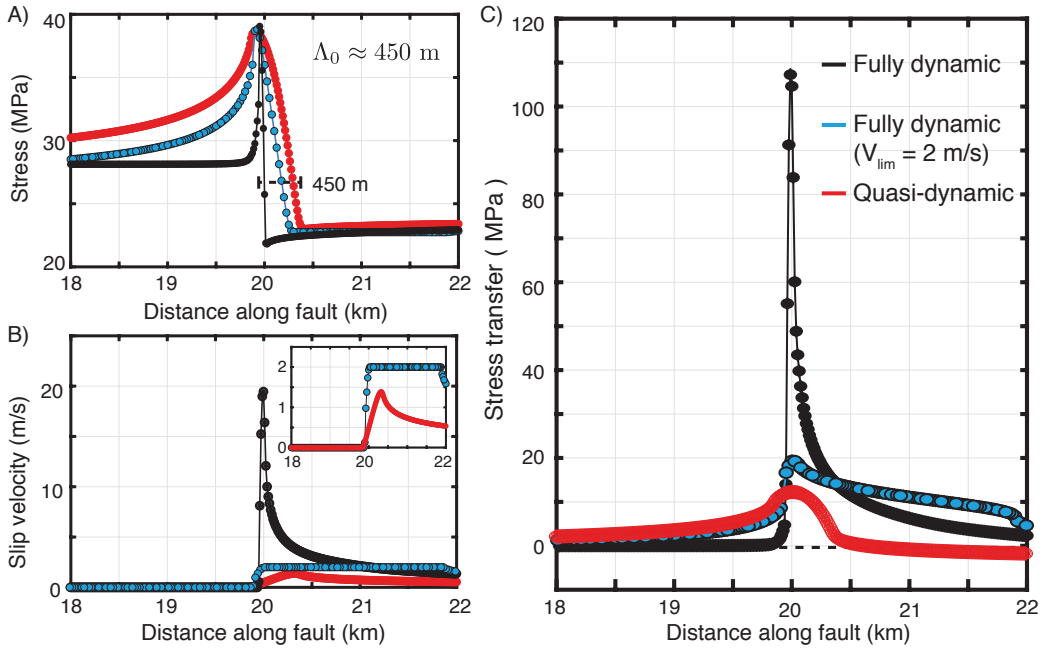

Figure 6.26: Comparison of local slip rate, shear stress and stress transfer with different treatment of inertial effects and considerations for plasticity. (A-B) Spatial distribution of (A) shear stress, (B) slip rate, and (C) stress transfer along the fault during the first rupture with the same initial conditions in fully dynamic (black) and quasi-dynamic (red) simulations of fault model M5, as well as a fully dynamic simulation approximating the effects of off-fault plasticity with a slip velocity limit of 2 m/s. The stress transfer during fully dynamic ruptures is much more pronounced than quasi-dynamic ruptures, resulting in higher slip rates and more focused shear stresses at the rupture front. The approximation for off-fault plasticity limits the peak slip velocity and restricts the magnitude of the peak stress transfer along the fault. However, the stress transfer for the fully dynamic rupture including the plasticity approximation is still more pronounced than that of the quasi-dynamic rupture and remains more pronounced behind the rupture front.

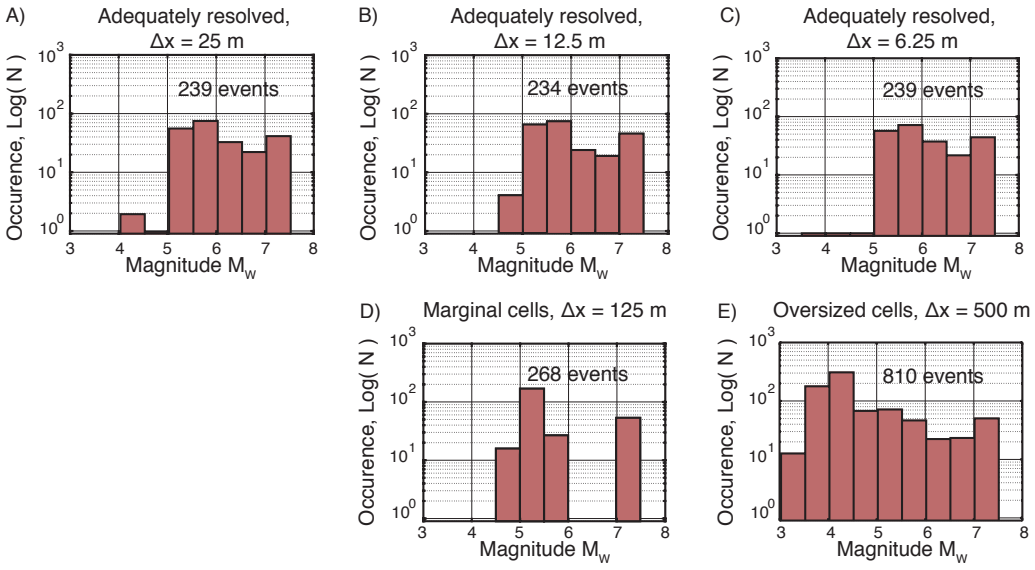

Figure 6.27: Frequency-magnitude histograms for 4000 years of sequences of earthquakes in fully dynamic simulations of fault model M5 with the effects of off-fault dissipation approximated using a slip velocity limit of $V_{\text{lim}} = 2$ m/s. Simulations are performed using different computational cell sizes of (A) 25 m, (B) 12.5 m, (C) 6.25 m, (D) 125 m and (E) 500 m. The increased production of smaller events ($M_{\text{w}} \leq 4$) in simulations with large computations cells (D & E) is qualitatively similar to the fully dynamic simulations of fault model M5 with no velocity limit shown in Figure 6.19.

The simulations of model M5, without and with the plasticity approximation, provide another example of how earthquake sequences with similar frequency-magnitude statistics can result in different jump rates across the velocity-strengthening barrier. While the simulations with cell sizes of 6.25, 12.5, and 25 m have well-resolved cohesive zones (Figures 6.14 and 6.21) and similar event statistics (Figure 6.19 and 6.27), they have jump rates ranging from 0.7-0.8 without the plasticity approximation to 0.3-0.5 with the plasticity approximation (Figures 6.14 and 6.21).

6.8 Discussion

We have investigated the sensitivity of numerical simulations of long-term sequences of earthquakes and aseismic slip (SEAS) to numerical discretization and treatment of inertial effects, using a simplified 2-D model of a 1D fault with two co-planar seismogenic, VW segments separated by a VS barrier. Our focus is, in part, on the resulting rate of rupture jumps across the barrier.

We find that the convergence of long-term simulated earthquake sequences with increasing numerical resolution may not always be achievable. Even if simulations are sufficiently discretized to produce consistent modeling results for individual ruptures or short sequences of events, they may still produce different long-term sequences due to compounded effects of small numerical differences over many events. We have achieved the convergence for fault models with lower instability ratios λ_{VW}/h^*_{RR}, i.e., lower fault lengths in comparison to the nucleation size (Figure 6.3). In contrast, models with higher instability ratios exhibit different long-term behavior even in simulations that are well discretized by standard metrics (Day et al., 2005; Lapusta & Liu, 2009), including different specific sequences of earthquakes and different probability of ruptures jumping across the VS barrier. In the cases with convergent long-term behavior, the criteria for numerical resolution that leads to the same evolution of slip are more stringent than those for individual dynamic ruptures, i.e., the dynamic cohesive zone size needs to be discretized by more cells.

Our results show that numerical convergence in SEAS simulations depends not only on how well important length-scales are discretized but also on the sensitivity of the specific physical problem to small numerical perturbations. In particular, our results suggest that faults with higher instability ratios are more sensitive to accumulating numerical perturbations (Figure 6.28), although that conclusion requires further study. In another example, while quasi-dynamic simulations are easier to resolve and thus should result in smaller numerical discrepancies for sufficiently small cell sizes, the milder stress transfer compared to fully dynamic ruptures can make long-term quasi-dynamic simulations more sensitive to small perturbations in shear stress, as occurs in fault model M5. Hence empirical discretization criteria, such as those of (Day et al., 2005), should be seen as guidelines that may not be universally applicable to all physical models and outcomes of interest. Moreover, for some models, numerical convergence of long-term slip may not be possible, though statistical consistency may hold for some modeling results but not others (Figure 6.28). Overall, these findings highlight the importance for individual numerical studies to examine the sensitiv-

ity of their outcomes of interest to the choice of their numerical procedure and discretization.

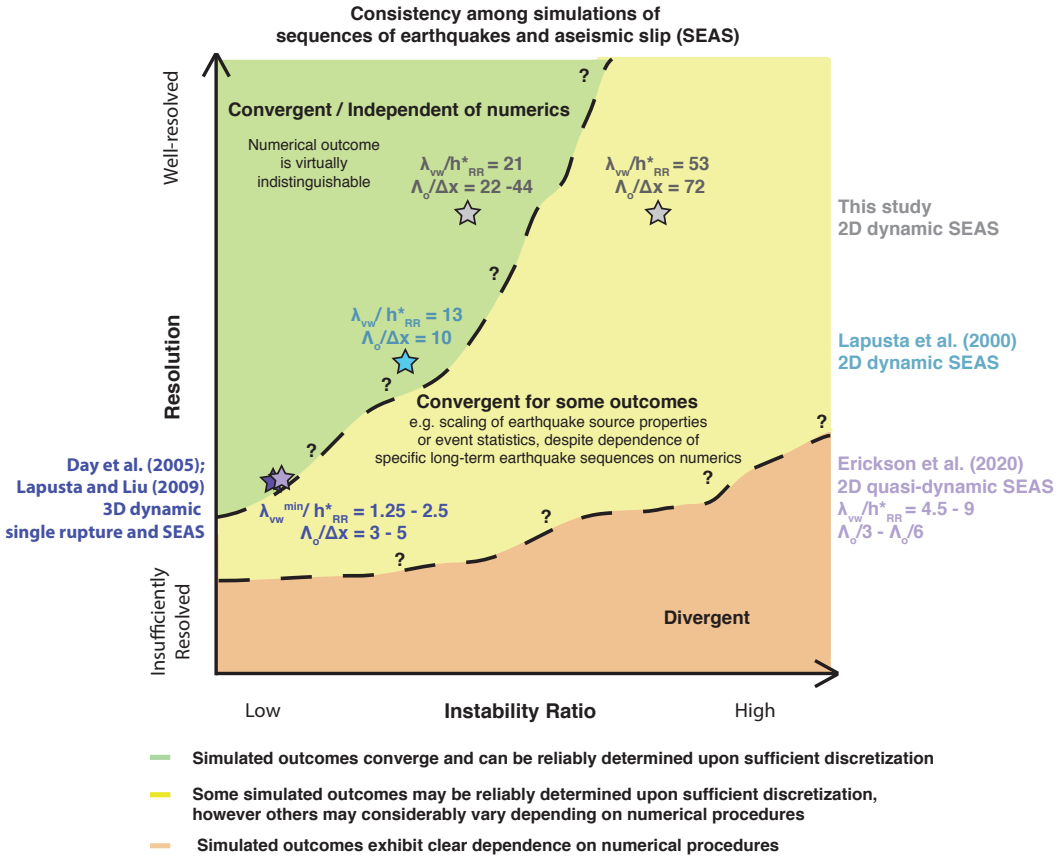

Figure 6.28: Conceptual diagram illustrating potentially convergent versus divergent numerical behavior depending on resolution and model complexity, parameterized by the instability ratio as an example. Well-resolved fault models with low enough instability ratio may potentially be numerically deterministic where adequate discretization results in virtually indistinguishable numerical outcomes. Fault models with higher instability ratio may either have more stringent requirements for numerical discretization in order to achieve long-term convergence, or such convergence may be impossible; either way, achieving numerical convergence in simulations of sufficiently complex fault models, such as with higher instability ratios, would be impractical. In such cases, it may still be possible to achieve statistical consistency among some outcomes within well-resolved simulations, though other properties of the system may be highly sensitive to numerical precision and considerably vary depending on the numerical procedures.

For the fault models considered, we find that the rate of earthquake ruptures jumping across a VS barrier is sensitive to the numerical resolution, representation of inertial effects, as well as minor changes in physical properties, such frictional parameters, confining stress,

seismogenic depth, and barrier size. This suggests that, even in this relatively simple model, the rate of ruptures jumping across a VS barrier is not a stable outcome that can always be reliably estimated from numerical models, unless the barrier is so large or small that the rate is reliably zero or 1 (Figure 6.29). The sensitivity of rupture jump rates to small changes in models suggests that the jump rates across barriers that serve as earthquake gates may also be highly sensitive to small physical perturbations on natural faults, and thus may be impractical to estimate in a reliable manner.

However, even for the models that do not achieve deterministic convergence with finer resolution, we find that some characteristics of well-resolved simulations are preserved, qualitatively and quantitatively. The characteristics include ranges of average source properties such as the average static stress drop, quantities related to energy partitioning such as the average breakdown energy, as well as general features of the average shear stress and shear heating evolution throughout time (Figure 6.17). These results suggest that some aspects of physical systems may be reliably determined from a given physics-based model, while others perhaps cannot, in the sense that they are very sensitive to numerical procedures and initial conditions, and even well-resolved models produce different outcomes with respect to those quantities. Our findings also suggest that it may be possible to discern some statistical aspects of the probability distribution for multi-segment ruptures from well-formulated numerical models, even if they do not exhibit convergence of long-term behavior with numerical resolution. However, as the jump rate appears to be sensitive to small perturbations in numerical and physical properties, it would be prudent to examine the statistical consistency of the jump rate distribution through large ensembles of models. Another route for examining plausible rupture scenarios for large earthquakes navigating key sections of fault networks would be to study detailed dynamic rupture simulations that can handle more realistic fault geometries with full treatment of inertial effects (e.g Ulrich et al., 2019; Wollherr et al., 2019), and produce large ensembles of dynamic rupture scenarios with variations in initial conditions inspired by SEAS simulations.

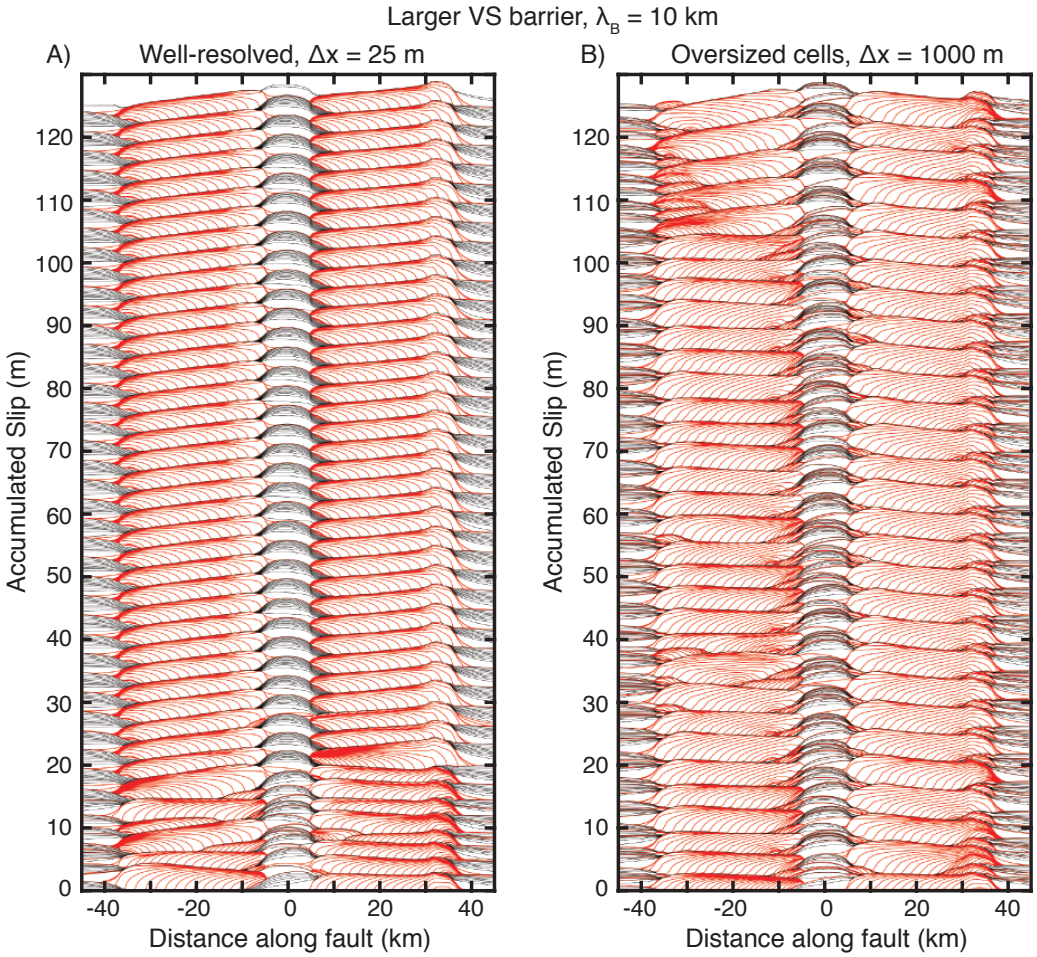

Figure 6.29: Consistent isolation of ruptures on fault segments separated by a larger velocity-strengthening barrier in simulations with adequate discretization and oversized cells. History of cumulative slip over 4000 years in two fully dynamic simulations of fault model M1 that utilize (A) cells that adequately resolve the cohesive zone (Δx = 25 m) and (B) oversized cells (Δx = 1000 m). Seismic slip is contoured every 0.5 s. The VS barrier is increased in width to 10 km such that ruptures are isolated to individual fault segments in both simulations.

Our results confirm that quasi-dynamic simulations that ignore wave-mediated stress transfer during dynamic rupture can lead to qualitative differences in the resolved rupture behavior and long-term sequences of slip events. The wave-mediated stress redistribution not only facilitates long-range interactions among portions of a fault and neighboring segments, but also alters the state of stress at the rupture front, promoting higher slip rates and more focused stress concentrations. In particular, the relatively small static stress transfer in quasi-dynamic simulations makes the rupture front more susceptible to unfavorable conditions, such as those one may expect from frictional heterogeneity, fault roughness, and regions of unfavorably low prestress. In contrast, the larger wave-mediated dynamic stresses in fully dynamic ruptures may assist rupture propagation in navigating unfavorable fault conditions and geometric irregularities (Ando & Kaneko, 2018; Douilly et al., 2015; Duan & Oglesby, 2006; Dunham et al., 2011b; Galvez et al., 2014; Harris et al., 1991; Harris & Day, 1993, 1999; Kame et al., 2003; Lozos et al., 2015; Thomas et al., 2014; Ulrich et al., 2019; Withers et al., 2018; Wollherr et al., 2019). Moreover, the spatial pattern for dynamic stresses, which affects the preferential direction for ruptures to branch or jump to neighboring faults, rotates as a function of the rupture speed, and hence can be considerably different from a quasi-dynamic rupture (Kame et al., 2003). Thus, considering full inertial effects during individual dynamic ruptures and long-term sequences of slip events is particularly important when considering the interaction of multiple fault segments and the likelihood of ruptures propagating through potentially unfavorable conditions.

Our results also confirm that using increasingly oversized cells, with or without wave-mediated stress transfers, results in a progressively more complex slip response, with broader distributions of event sizes, consistent with conclusions from prior studies (Ben-Zion & Rice, 1995). Using oversized cells and/or ignoring wave-mediated stress transfer significantly modifies the probability of two-segment ruptures, as well as the resulting earthquakes sequences.

Finally, we have examined whether the rate of ruptures jumping between two fault segments

can be determined from simulations that reproduce frequency-magnitude statistics and average static stress drops (Field, 2019; Shaw et al., 2018). We find that these observations do not constrain rupture jump rates in our models. This highlights the need to better understand which field observations constrain long-term fault behavior, and thus provide predictive power for potential future hazards. Physics-based modeling is generally well-suited to explore these problems, where the relative contribution of physical mechanisms can be explored for a range of parameters, and intuition can be developed for the relationship among varying observational constraints and source characteristics. Note that a number of physical properties not included in our simplified 2-D models may qualitatively alter the behavior and hence interaction of neighboring fault segments, such as the explicit consideration of depth variations in slip and the depth extent to which ruptures propagate (e.g Jiang & Lapusta, 2016; Ulrich et al., 2019; Wollherr et al., 2019), time-dependent variations in loading from distributed deformation at depth (Allison & Dunham, 2018; Lambert & Barbot, 2016), and enhanced dynamic weakening at seismic slip rates (Di Toro et al., 2011; Dunham et al., 2011b; Lambert et al., 2021; Noda & Lapusta, 2013; Perry et al., 2020; Tullis, 2007). These are just a few physical ingredients that merit detailed study in the long-term interaction of fault segments.

Our results emphasize the need to examine the potential model dependence of simulation outcomes, including to numerical resolution, particularly when assessing their predictive value for seismic hazard assessment. Community initiatives, such as the Southern California Earthquake Center (SCEC) code comparisons for dynamic rupture simulations and simulations of sequences of seismic and aseismic slip (Barall & Harris, 2014; Erickson et al., 2020; Harris et al., 2018, 2009), can provide further insight into how numerically-derived results for different physical quantities may depend on numerical methodologies and computational practices. The significant sensitivity of the rate of multi-segment ruptures to small changes in numerical models implies that such hazard parameters may also be sensitive to physical perturbations on natural faults. This consideration motivates further evaluation of meaningful metrics for describing long-term fault behavior and assessing seismic hazard, tasks for

which physics-based modeling is well-suited.

6.9 Appendix: Description of initial shear stress distributions for numerical simulations of long-term sequences of earthquakes and aseismic slip

In our simulations of sequences of earthquakes and aseismic slip (SEAS), the distributions of shear stress and slip along the fault evolve depending upon the history of previous slip during periods of rapid seismic slip as well as slow aseismic slip and fault locking. We consider how the long-term evolution of fault slip differs among simulations using varying computational cell sizes and considerations of inertial effects, given the same initial conditions for shear stress, slip rate, and the rate-and-state frictional state variable θ.

For all of our simulations, the velocity-strengthening (VS) portions of the fault are set to be initially creeping at steady state with the prescribed tectonic plate rate of $V_{\text{ini}} = V_{\text{pl}}$:

$$\tau_{VS}^{\text{ini}} = \tau_{\text{ss}}(V_{\text{pl}}) = \overline{\sigma}\left[f_* + (a_{\text{VS}} - b_{\text{VS}}) \ln \frac{V_{\text{pl}}}{V_*}\right] \tag{6.11}$$

$$\tau_{B}^{\text{ini}} = \tau_{\text{ss}}(V_{\text{pl}}) = \overline{\sigma}\left[f_* + (a_{\text{B}} - b_{\text{B}}) \ln \frac{V_{\text{pl}}}{V_*}\right]. \tag{6.12}$$

For points within the velocity-weakening (VW) segments of the fault, we first consider the initial shear stress distribution $S1$, which favors the first rupture nucleating along the VW-VS boundary around $x = 33$ km, and then jumping across the VS barrier to produce a two-segment rupture (e.g. Figure 6.2) :

$$\tau_{VW}^{\text{ini}}(x) = \begin{cases} \tau_{\text{ss}}(1 \text{ m/s}) + 3.5\text{MPa} & \text{for} \quad x \in [-33\text{km}, -2\text{km}) \\ \tau_{\text{ss}}(V_{\text{pl}}) + a_{VW} \ln \frac{0.1\text{m/s}}{V_{\text{pl}}} - 1.5\text{MPa} & \text{for} \quad x \in [-2\text{km}, -1\text{km}) \\ \tau_{\text{ss}}(1 \text{ m/s}) + 5\text{MPa} & \text{for} \quad x \in (1\text{km}, 27\text{km}) \\ \tau_{\text{ss}}(V_{\text{pl}}) + a_{VW} \ln \frac{0.1\text{m/s}}{V_{\text{pl}}} & \text{for} \quad x \in [27\text{km}, 33\text{km}]. \end{cases} \tag{6.13}$$

In all of our simulations, points with the VW segments are initially locked with initial slip rate $V_{\text{ini}} = 10^{-10}$ m/s and the initial state variable θ chosen to be consistent with the

corresponding initial shear stress and slip rate, given equation 6.2.

In order to examine the convergence of long-term sequences of earthquakes with different initial conditions, we consider a second initial shear stress distribution $S2$ (Figures 6.3A vs B), which favors the first rupture nucleating near the VS barrier around $x = 1$ km and propagating away from the barrier and spanning the entire right VW segment:

$$\tau_{VW}^{\text{ini}}(x) = \begin{cases} \tau_{\text{ss}}(1 \text{ m/s}) + 3.5\text{MPa} & \text{for} \quad x \in [-33\text{km}, -1\text{km}) \\ \tau_{\text{ss}}(V_{\text{pl}}) + a_{VW} \ln \frac{0.1\text{m/s}}{V_{\text{pl}}} & \text{for} \quad x \in (1\text{km}, 7\text{km}] \\ \tau_{\text{ss}}(1 \text{ m/s}) + 5\text{MPa} & \text{for} \quad x \in (7\text{km}, 33\text{km}]. \end{cases} \tag{6.14}$$

Chapter 7

TIME-DEPENDENT STRESSES FROM FLUID EXTRACTION AND DIFFUSION WITH APPLICATIONS TO INDUCED SEISMICITY

This chapter has been adapted from:

Lambert, V. & Tsai, V.C. (2020). Time-dependent stresses from fluid extraction and diffusion with applications to induced seismicity. *Journal of Applied Mechanics*, 87(8). DOI: 10.1115/1.4047034.

7.1 Introduction

Induced seismicity is a topic of growing scientific interest and societal importance, particularly surrounding practices in resource extraction and waste disposal (Ellsworth, 2013; Lee et al., 2019; McGarr et al., 2015; Zoback, 2013). Many processes considered surrounding induced seismicity focus on solid-fluid interactions governing fault strength and stress. Much attention has been focused on the direct effects of fluid injection and increasing pore pressure in decreasing the effective normal stress across fault surfaces and potentially destabilizing faults under their preexisting stress conditions (Bhattacharya & Viesca, 2019; Frohlich et al., 2014; Frohlich et al., 2011; Guglielmi et al., 2015; Healy et al., 1968; Horton, 2012; Hsieh & Bredehoeft, 1981; Keranen et al., 2014; Kim, 2013; McGarr et al., 2015; Raleigh et al., 1976, 2013; Walsh & Zoback, 2015; Zhang et al., 2013). However, there is continued evidence for the presence of seismicity and aseismic deformation caused by the extraction of pore fluids, particularly in oil and gas fields where pore pressures may be declining by up to several 10's of MPa (Doser et al., 1991; Feignier & Grasso, 1990; Frohlich et al., 2016; Grasso & Feignier, 1989; Grasso & Wittlinger, 1990; Guyoton et al., 1992; Hough & Bilham, 2018; Hough et al., 2017; Pennington et al., 1986; Segall et al., 1994; Wetmiller, 1986; Yerkes & Castle, 1970).

Segall (1989) proposed that the poroelastic stresses resulting from fluid withdrawal can be responsible for triggering earthquakes in producing fields on their own. A key aspect highlighted within his work is that the strain mismatch due to reservoir rocks contracting more than their surroundings generates stresses in areas where no changes in pore-fluid content occur. Segall (1989) produced stress field solutions encompassing a relatively simple reservoir geometry assuming a uniform change in fluid mass content along a horizontal layer. The resulting fields illustrate that, as fluid is extracted, the overlying and underlying layers experience relative horizontal contraction and the neighboring regions on the flanks of the producing zone experience relative tension. Such solutions predict a preference for reverse faulting above and below the producing layer and normal faulting on the flanks of the producing zone, which is qualitatively consistent with observed seismicity around several producing fields (e.g. Goose Creek, Wilmington, Buena Vista Hills, Alberta, and Pau). One drawback of the solutions presented by Segall (1989) is the existence of stress discontinuities at the edges of the reservoir due to the gradient in the change in fluid mass content being undefined at the boundaries of the producing region. Steep gradients in the change in pore fluid content result in local stress concentrations and the finiteness of the resulting solutions depend on the continuity of the fluid distributions (Segall, 1989, 1992). As such, quantitative as well as qualitative predictions for the surrounding stresses caused by fluid extraction and injection may be substantially affected by basic assumptions in the geometry and hydraulic properties of the producing region.

The particular two-dimensional (2-D) problem for fluid extraction from an infinite horizontal layer with uniform diffusivity was introduced by Segall (1985), accounting for the smooth temporal evolution of the change in fluid content through diffusion. However, while considering the effects of varying diffusivity on surface subsidence, he mainly focused on induced stress changes well below the producing zone in order to estimate the stresses imposed on the 1983 Coalinga fault by oil field operations, which is several factors deeper than the corresponding production depth. Since seismicity can also often be observed in the layers overlying and surrounding the producing or injection zone the focus in this study

is to expand the analyses of Segall (1985, 1989) to examine the evolution of the stress field directly surrounding the producing zone in a reservoir including the smooth temporal evolution of the pore fluid distribution through diffusion. While the fixed reservoir model of Segall (1989) was shown to qualitatively agree well with patterns in surface deformation and seismicity surrounding reservoirs with potentially comparable reservoir geometries, we note that the particular example of a laterally unconstrained reservoir with a finite diffusivity may be more quantitatively applicable to other producing fields where changes in fluid mass may not be considered uniform within the producing region (e.g. central Oklahoma (Keranen et al., 2014), North and South Dakota (Keranen & Weingarten, 2018), and Groningen (J. D. Smith et al., 2019)). Moreover, for many reservoir settings the timescale for fluid transport (days to years) within the producing layer may be comparable to the timescale of field observations at relevant distances. For such cases it may be important to account for the nonstationarity of the geometry of the effective producing zone when interpreting field measurements and seismological inferences (Keranen et al., 2013, 2014; Mukuhira et al., 2018). For example, numerical models have illustrated how the temporal evolution of pore pressure and poroelastic stresses due to fluid injection and diffusion can help explain temporal trends in the productivity of triggered seismicity, depending on pre-existing fault geometries and background stress conditions (Segall & Lu, 2015).

The aim of this study is to provide an additional reference model that illustrates the potential importance of considering the nonstationarity of fluid sources when interpreting field observations, and from which exact calculations may be made for quantitative comparison with field data. This model may also serve as a benchmark problem for more complicated numerical studies. While more sophisticated numerical methods have been applied for detailed studies of some well-instrumented reservoirs in which the geometry and hydraulic properties are better constrained, we hope that these relatively simple solutions may prove useful in regions with limited reservoir data. In order to further facilitate such comparisons we provide two potential approximate extensions to 3-D for relevant production quantities such as the volumetric flow rate. In addition, we briefly discuss the implications of our

model results for existing field observations and seismological studies, including inferred temporal variations in the principal stress directions of seismic events around injection wells (Martınez-Garzón et al., 2014; Martıŋnez-Garzón et al., 2013; Schoenball et al., 2014).

7.2 Model description

Segall (1985) showed that for a linear, isotropic poroelastic medium, the solid displacements u_j due to distributed changes in fluid mass content $\Delta m(\mathbf{y}, t)$ can be expressed through a linear integral relationship over the source volume $V_\mathbf{y}$ as,

$$u_j(\mathbf{x}, t) = \frac{(1 + \nu_u)B}{3\pi\rho_0(1 - \nu_u)} \int_V \Delta m(\mathbf{y}, t) g_j(\mathbf{x}, \mathbf{y}) dV_\mathbf{y} \tag{7.1}$$

where ν_u is the undrained Poisson's ratio, B is the Skempton's pore pressure coefficient, and ρ_0 is the fluid density in the reference state. The function $g_j(\mathbf{x}, \mathbf{y})$ represents the displacement in the j direction at $\mathbf{x}$ due to a point center of dilatation at $\mathbf{y}$ with associated change in fluid mass content $\Delta m(\mathbf{y}, t)dV$. Note that $\mathbf{y}$ and $\mathbf{x}$ denote the full position vectors for the source and receiver elements, respectively. The total displacement $u_j(\mathbf{x}, t)$ due to quasi-static changes in a distributed fluid mass at time t is then obtained by integrating the undrained point fluid mass changes within the region for which $\Delta m(\mathbf{y}, t)$ is non-zero.

The change in the fluid mass content is defined as the change in fluid mass per unit solid volume, and can be related to the mean solid stress σ_{kk} and pore fluid pressure p as,

$$\Delta m = \frac{(1 - 2\nu_u)\alpha\rho_0}{2\mu(1 + \nu_u)} \left[\sigma_{kk} + \frac{3}{B}p\right] \tag{7.2}$$

where α relates the bulk modulus of the fluid-saturated rock under drained conditions, K, and that of the solid rock, K_s, as $\alpha = 1 - \frac{K}{K_s}$ (Nur & Byerlee, 1971). Stresses may be related to the displacements and associated strains through the linear isotropic poroelastic constitutive relationship,

$$2\mu\epsilon_{ij} = \sigma_{ij} - \frac{\nu_u}{1 + \nu_u}\sigma_{kk}\delta_{ij} + \frac{2\mu B}{3\rho_0}\Delta m\delta_{ij} \tag{7.3}$$

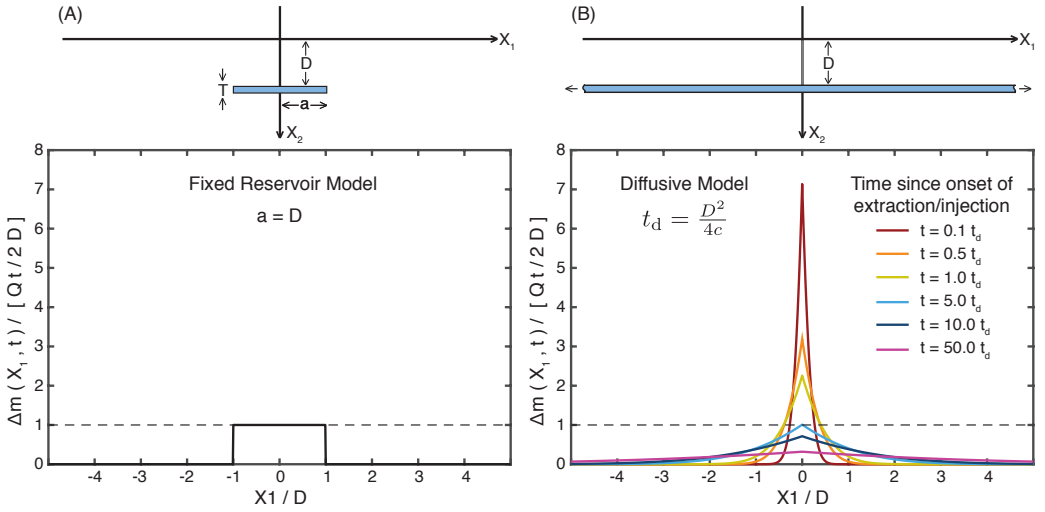

Figure 7.1: Model geometry (top) and distributions for the change in fluid mass content (bottom) for the fixed reservoir model (a) as described in (Segall, 1989) and the diffusive reservoir model (b) as described in (Segall, 1985). The half-width of the fixed reservoir is assumed to be equal to the reservoir depth. Fluid mass content distributions for the diffusive reservoir model are shown at increasing times with relation to the characteristic diffusion timescale, t_d. The spatial distributions of the fluid mass change are scaled by the total mass content divided by twice the reservoir depth.

such that the stress distribution due to the integrated source is given by,

$$\sigma_{ij}(\mathbf{x},t) = \frac{\mu(1+\nu_u)B}{3\pi\rho_0}\int_V \Delta m(\mathbf{y},t)G_{ij}(\mathbf{x},\mathbf{y})dV_\mathbf{y} - \frac{BK_u}{\rho_0}\Delta m(\mathbf{y},t)\delta_{ij} \tag{7.4}$$

where μ is the shear modulus and K_u is the undrained bulk modulus (Segall, 1985). Solutions for displacements and stresses due to the change in fluid mass within a distributed volume can therefore be represented through integral expressions of the prescribed change in fluid mass content and the poroelastostatic Green's functions $G_{ij}(\mathbf{x},\mathbf{y})$ and $g_j(\mathbf{x},\mathbf{y})$ which have been presented by Segall (1985) and included within the Appendix (Section 7.5). Note that in this work, we express solutions for displacements and stresses due to changes in fluid mass content, and do not attempt to solve for the associated pore pressures within the reservoir. However, pore pressure distributions within the producing zone may be calculated from the change in pore fluid mass and the associated solutions for the mean solid stress through Eq. (7.2) (Segall, 1985).

7.2.1 Models for fluid mass distribution

Segall (1989) examined the 2-D poroelastic stress field and surface displacements caused by fluid extraction from a horizontal, permeable layer of thickness T, which was assumed small compared to the reservoir depth D, and enclosed in an otherwise impermeable half-space (Fig. 7.1A). $\Delta m(\mathbf{y}, t)$ is considered uniform over a horizontal interval $-a < y_1 < a$, as well as with depth $D < y_2 < D + T$, reflecting a producing layer of fixed length $2a$ and thickness T. The specific case where $a = D$ was examined by Segall (1989), which we also consider in this study for direct comparison. We set the net mass flux out of the producing zone $-Q$ to be constant for time $t > 0$ and zero for $t < 0$, and thus can express this uniform change in fluid mass distribution as a function of the mass flux and time simply as,

$$\Delta m_f(\mathbf{x}, t) = -\frac{Qt}{2a} B(x_1; -a, a) B(x_2; D, D + T) \tag{7.5}$$

where $B(x; \zeta_1, \zeta_2)$ refers to the boxcar function over x from ζ_1 and ζ_2. We denote this mass distribution as $\Delta m_f(\mathbf{x}, t)$, and will henceforth refer to it as the fixed reservoir model. Note that Q reflects the change in fluid mass per unit time and cross-sectional area transverse to x_1, considering a uniform distribution over T and an additional length scale W not explicitly modeled here out-of-plane along x_3. Two key features of this model are that the reservoir geometry is fixed with length $2a$ and the temporal evolution of the fluid mass distribution neglects the finite timescale for fluid migration towards the extraction site at $x_1 = 0$. In essence, the fixed reservoir model reflects extraction from a geometrically constrained reservoir with effectively infinite internal diffusivity, allowing for instantaneous equilibration of the fluid mass distribution upon further fluid extraction or injection.

In order to account for the redistribution of fluid mass due to diffusion, we consider the case introduced by Segall (1985) of an infinite horizontal layer of thickness T and diffusivity c, similarly buried at a depth of D in an otherwise impermeable medium. The spatio-temporal evolution of the fluid mass distribution within the infinite layer is then governed by the one-dimensional diffusion equation,

$$\frac{\partial \Delta m(\mathbf{x}, t)}{\partial t} = c \frac{\partial^2 \Delta m(\mathbf{x}, t)}{\partial x_1^2} \tag{7.6}$$

with the local fluid mass flux q subject to the boundary conditions,

$$q(x_1 = 0^+) - q(x_1 = 0^-) = -Q \qquad t > 0$$
$$q(x_1 = \pm\infty) = 0 \qquad t > 0.$$

Accounting for diffusion with respect to the plane at $x_1 = 0$, the fluid mass change per unit solid volume can be expressed as (Carslaw & Jaeger, 1959),

$$\Delta m_d(\mathbf{x}, t) = -Q \left(\frac{t}{c}\right)^{1/2} \text{ierfc}\left[\left(\frac{x_1^2}{4ct}\right)^{1/2}\right] B(x_2; D, D + T), \tag{7.7}$$

for $t > 0$, where $\text{ierfc}[x] = \int_0^x \text{erfc}[x]dx = \frac{e^{-x^2}}{\pi^{1/2}} - x\text{erfc}[x]$ is the first integral of the complementary error function. Here we denote the mass distribution accounting for fluid diffusion as $\Delta m_d(\mathbf{x}, t)$ and refer to it as the diffusive model (Fig. 7.1B).

In contrast to the fixed reservoir model given by Eq. (7.5), the diffusive model does not contain a fixed reservoir length scale. Instead one can consider an effective producing zone length approximately equal to the diffusion length $l_d = \sqrt{4ct}$, which describes the spatial extent to which the change in fluid mass concentration due to extraction has propagated with time. Note here that T is assumed small compared to D and l_d such that the mass distribution is considered uniform with depth inside the reservoir. This assumption that $T < l_d$ breaks down as $t \to 0$ during the onset of fluid extraction. However, we will primarily focus on timescales where t approaches or is greater than a reference diffusion timescale, $t_d = \frac{D^2}{4c}$, based on the reservoir depth, and thus where $l_d \gtrsim D > T$, such that this approximation is more appropriate. Assuming a reservoir depth of 1 km, values for t_d would be around 2.9 days after the onset of extraction for a hydraulic diffusivity of 1 m^2/s and 29 days for a diffusivity of 0.1 m^2/s, which represent moderate values of relatively high and low diffusivities for production fields, respectively (Segall, 1985). Since the diffusion length scale increases with the square root of time, l_d approaches 10% of D when t is only at 1% of t_d, meaning that the effective reservoir length is within one order of magnitude of the reservoir depth much earlier than the corresponding reference diffusion timescale.

In considering only the stress distribution outside of the reservoir, where $\Delta m(\mathbf{x}, t) = 0$, Eq. (7.4) reduces to,

$$\sigma_{ij}(\mathbf{x}, t) = C \int_V \Delta m(\mathbf{y}, t) G_{ij}(\mathbf{x}, \mathbf{y}) dV_\mathbf{y} \tag{7.8}$$

where $C = \frac{\mu(1+\nu_u)B}{3\pi\rho_0(1-\nu_u)}$, such that the stresses in the fixed reservoir model (Eq. 7.5) are,

$$\sigma_{ij}(\mathbf{x}, t) = \frac{CQt}{2} \int_V G_{ij}(\mathbf{x}, \mathbf{y}) dV_\mathrm{y} \tag{7.9}$$

and those for the diffusive model (Eq. 7.7) are,

$$\sigma_{ij}(\mathbf{x}, t) = CQ \left(\frac{t}{c}\right)^{1/2} \int_V \mathrm{ierfc}\left[\left(\frac{y_1^2}{4ct}\right)^{1/2}\right] G_{ij}(\mathbf{x}, \mathbf{y}) dV_\mathbf{y}. \tag{7.10}$$

Full expressions for the stresses and displacements for both distributions are presented in the Appendix where full closed form solutions may be expressed for the fixed reservoir model while the diffusive model includes an integral over the horizontal layer which may be computed numerically.

An important distinction between Eq. (7.9) and Eq. (7.10) is the temporal dependence of the stress fields. The fixed reservoir solutions are separable in space and time such that while the total change in fluid mass content increases over time, it is always evenly distributed over the reservoir length $2a$, thereby increasing the magnitude of the same spatial distribution. For the diffusive case, the spatial distribution of the fluid mass is coupled to the temporal evolution with respect to the inception of extraction or injection. In such manner, as the total change in fluid content increases over time, the spatial extent over which this contribution is distributed also grows with the effective diffusion length scale l_d, such that the concentration of the change in fluid mass content is not geometrically fixed throughout time. We explore the implications of the spatio-temporal evolution of the effective producing zone in the next section.

7.3 Results

We consider the cases of fluid extraction from a single site in both the fixed and diffusive reservoir models, and examine the spatial distributions of the displacements and stresses surrounding the reservoirs, as well as the temporal evolution of these fields in the case

of the diffusive model. Figure 7.2 compares the surface displacements and horizontal strain as well as the horizontal normal stress σ_{11} and maximum shear stress fields ($\tau = [(\sigma_{11} - \sigma_{22})^2/4 + \sigma_{12}^2]^{1/2}$) caused by fluid extraction (stresses positive in tension) from the fixed (Fig. 7.2A) and diffusive (Fig. 7.2B-D) reservoir models. The results for the fixed model are the same as those presented by (Segall, 1989). Three cases are shown for the diffusive model with hydraulic diffusivities varying by an order of magnitude $c = 0.1c_D$, $c = c_D$ and $c = 10c_D$ about the reference diffusivity c_D. Each diffusive case is calculated at the same time $t = t_d = \frac{D^2}{4c_D}$. All four examples are scaled to represent instances where the total extracted fluid volume is the same, but the spatial extent and concentration varies based on the reservoir geometry and diffusivity. Simulated focal mechanisms in each case illustrate planes of maximum shear stress ($\phi = \frac{1}{2}\tan^{-1}[(\sigma_{22} - \sigma_{11})/(2\sigma_{12})]$) with black regions denoting quadrants of relative tension and white for quadrants of relative compression, with respect to each representative point.

The spatial distribution of the surface displacements and extensional strain are qualitatively similar among the fixed and diffusive models shown in Fig. 7.2, but they differ quantitatively in both magnitude and localization, reflecting the intensity of the gradient in the change in fluid mass within each reservoir. As pointed out by Segall (1985), the surface expressions depend strongly on the hydraulic diffusivity with more pronounced subsidence for lower diffusivities and relatively small and broadly dispersed subsidence for high diffusivities. Solutions for the fixed reservoir model are most similar to the diffusive model in Fig. 7.2C which has a similar effective producing zone half-length of $l_d = D$, however vertical displacements are 8% more pronounced near the extraction site at $x_1 = 0$ for the diffusive model along with a 32% increase in the horizontal extensional strain (See Figs. 7.2A and 7.2C). Note that the relative contraction and broadening of the surface expressions for the cases where $c = 0.1c_D$ and $c = 10c_D$, respectively, are also consistent with the time dependent evolution of the effective reservoir length.

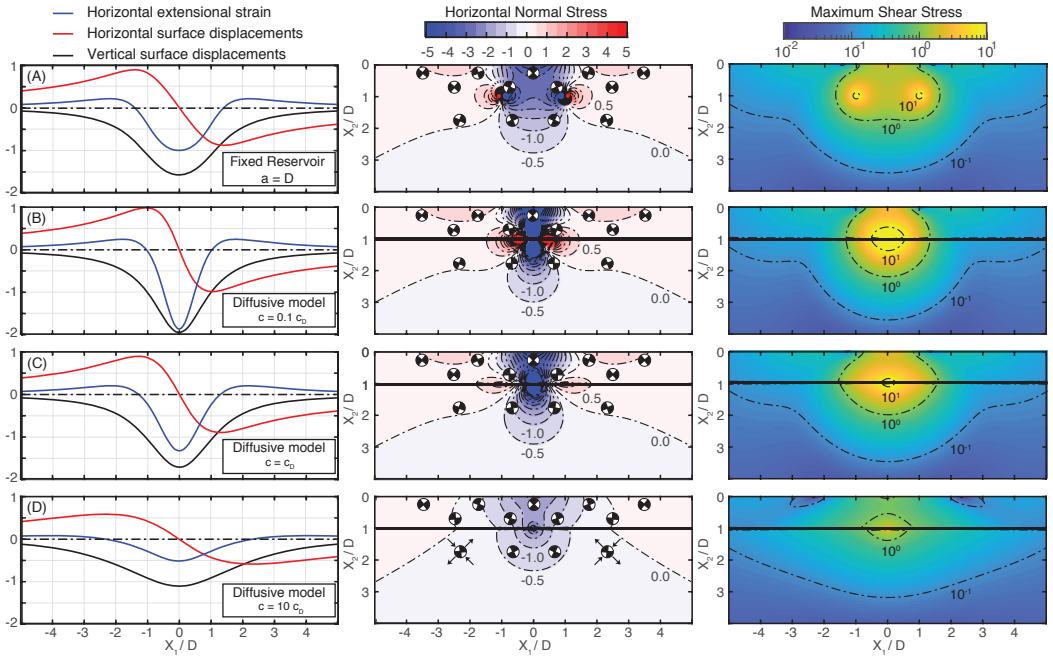

Figure 7.2: Calculated displacements and horizontal extensional strain at the surface (left), change in horizontal normal stress (center), and maximum shear stress (right) due to fluid extraction (relative tension positive) in both the (a) box-car model and (b-d) diffusion models for varying hydraulic diffusivity with respect to c_D at time $t = t_d$, where $t_d = \frac{D^2}{4c_D}$. Note that the convention for x_2 is switched for vertical surface displacements such that negative displacements reflect subsidence. Stresses are contoured outside the producing layer for the diffusive models ($x_2 \in [D, D + T]$). Simulated focal mechanisms indicate planes of maximum shear stress, with arrows indicating the axes of maximum tension and compression. Displacements are normalized by $\frac{(1+\nu_u)BTQt}{3\pi\rho_0 D}$, strains by $\frac{(1+\nu_u)BTQt}{3\pi\rho_0 D^2}$, and stresses by $\frac{\mu(1+\nu_u)BTQt}{6\pi\rho_0 D^2(1-\nu_u)}$.

7.3.1 Geometric and temporal dependence of stress concentrations

An important conclusion about the reservoir geometry is that the intensity of imposed stresses due to injection or extraction depends on the spatial gradient of the change in fluid mass content, such that higher stress concentrations are located around regions with sharper gradients in Δm. This is evident in the fixed reservoir model where discontinuities in the fluid mass distribution at the ends of the producing zone introduce large stress concentrations near the edges of the reservoir (Fig. 7.2A). In the case of the diffusive model, a stress concentration is focused about the extraction site at $x_1 = 0$ due to the localized extraction of fluid, whereas the smooth decay of the distribution away from this point precludes the concentration of stresses elsewhere (Fig. 7.2B-D). This stress concentration at $x_1 = 0$ is not

present in the uniform model as the fluid distribution is assumed to equilibrate rapidly to provide a uniform change in fluid mass content across the reservoir.

In the diffusive model, the intensity of this stress concentration near the extraction point at any given time is a function of the rate of fluid extraction and the reservoir diffusivity, and is governed by the ratio of the volume flux into or out of the reservoir to the rate at which fluid can diffuse away or toward the loading point. For lower diffusivities, the same change in fluid mass is more sharply localized near the injection or extraction point resulting in more concentrated stresses (Fig. 7.2B). For higher diffusivities, sharp gradients in the change in fluid mass are alleviated more rapidly thereby mitigating stress concentrations and resulting in smoother stress distributions (Fig. 7.2D). This emphasizes the significance of the reservoir diffusivity in determining the rate at which concentrated stresses induced by fluid extraction or injection can be relieved.

A more intuitive relationship may be made in terms of the volumetric rate of fluid extraction $\dot{V}$. We consider two simple approximations to extend our 2D model results to three dimension (3D). For Case 1, we assume a fixed producing zone width W in the x_3 direction, and in Case 2, W is assumed to scale with the producing zone length in time. We consider the mass flux per effective producing zone length defined by the diffusion length scale, $\frac{Q}{4\sqrt{ct}} = \frac{\dot{M}}{AT}$ where $\dot{M}$ is the average rate of total fluid mass extraction and A is the horizontal area of the producing zone in the $x_1 \times x_3$ plane. In Case 1, the area can be described as $A = 4\sqrt{ct}W$ with the volumetric rate of extraction $\dot{V} = \frac{\dot{M}}{\rho_0}$, giving the relation $\frac{Q}{\rho_0} = \frac{\dot{V}}{WT}$ for the effective volume flux, as in (Segall, 1985). Alternatively, in Case 2 the producing zone width may be considered to scale with the length through time as $W = \gamma\sqrt{ct}$ for $t > 0$, where γ is a positive constant. The area then is given by $A = 4\gamma ct$ and the effective volume flux is $\frac{Q}{\rho_0} = \frac{\dot{V}}{\pi\gamma\sqrt{ct}T}$. Accordingly, the prefactor $\frac{(1+\nu_u)BQ}{3\pi\rho_0}\sqrt{\frac{t}{c}}$ for the displacements and stresses associated with the diffusive model becomes $\frac{(1+\nu_u)B\dot{V}}{3\pi WT}\sqrt{\frac{t}{c}}$ for Case 1 and $\frac{(1+\nu_u)B\dot{V}}{3\pi^2\gamma cT}$ for Case 2. Here, the trade-off between the volumetric rate of fluid extraction and the diffusivity of the reservoir becomes more apparent, particularly in Case 2 where the assumed linear

increase in extracted fluid volume with time is compensated exactly by the linear increase in the effective producing zone volume. In this case, the prefactor has no temporal dependence, but the spatial distribution of the deformation and stress fields are still coupled to the temporal evolution of the effective producing zone volume. While the 2-D solutions are exact, these extensions to 3-D provide only crude approximations meant to facilitate quantitative comparison with field measurements. The solutions for the special case of an exactly axisymmetric mass distribution have been introduced by Segall (1992).

Figure 7.3 shows the temporal evolution of the spatial distributions of the horizontal normal stress and maximum shear stress in the diffusive reservoir model throughout time. Stresses are normalized by $\frac{\mu(1+\nu_u)BT}{6\pi\rho_0 D(1-\nu_u)}\frac{Qt}{\sqrt{4ct}}$ to reflect the balance between the increasing change in total extracted fluid volume, as well as the increase in the effective producing zone volume with the extension of the diffusion length scale. This normalization factor can also be replaced with the approximate 3-D prefactors introduced in the previous section. In particular for Case 2, this normalization coefficient becomes $\frac{\mu(1+\nu_u)B\dot{V}}{12\pi^2(1-\nu_u)\gamma cD}$ such that the scaling is independent of time and the amplitude depends linearly on the ratio of $\dot{V}$ and c. We see that the stress concentration near the extraction site decreases as the producing zone expands and Δm becomes smoother and more evenly distributed. Additional distributions of the horizontal and vertical normal stresses as well as the shear stresses at similar points in time for the diffusive model are shown in Fig. 7.4.

7.3.2 Rotation of principal stress directions

A notable feature in Figs. 7.2 and 7.3 is that the orientation of the maximum shear stress at a given location, illustrated by the simulated focal mechanisms, is not static, but rotates over time as the reach of the diffusion front advances. For example, in Fig. 7.3 the simulated mechanisms at the outer edges for both $x_1 = \pm 3.5D$ and $x_2 = 0.25D$ rotate from horizontal relative tension to compression between the panels for $t = 10t_d$ and $t = 100t_d$. The temporal evolution of the angle of maximum extensional stress θ and angle of maximum shear stress ϕ are shown in Fig. 7.5 as functions of the lateral distance from the extraction axis at representative depths of $0.25D$ and $0.5D$. As the front of the producing zone expands away from

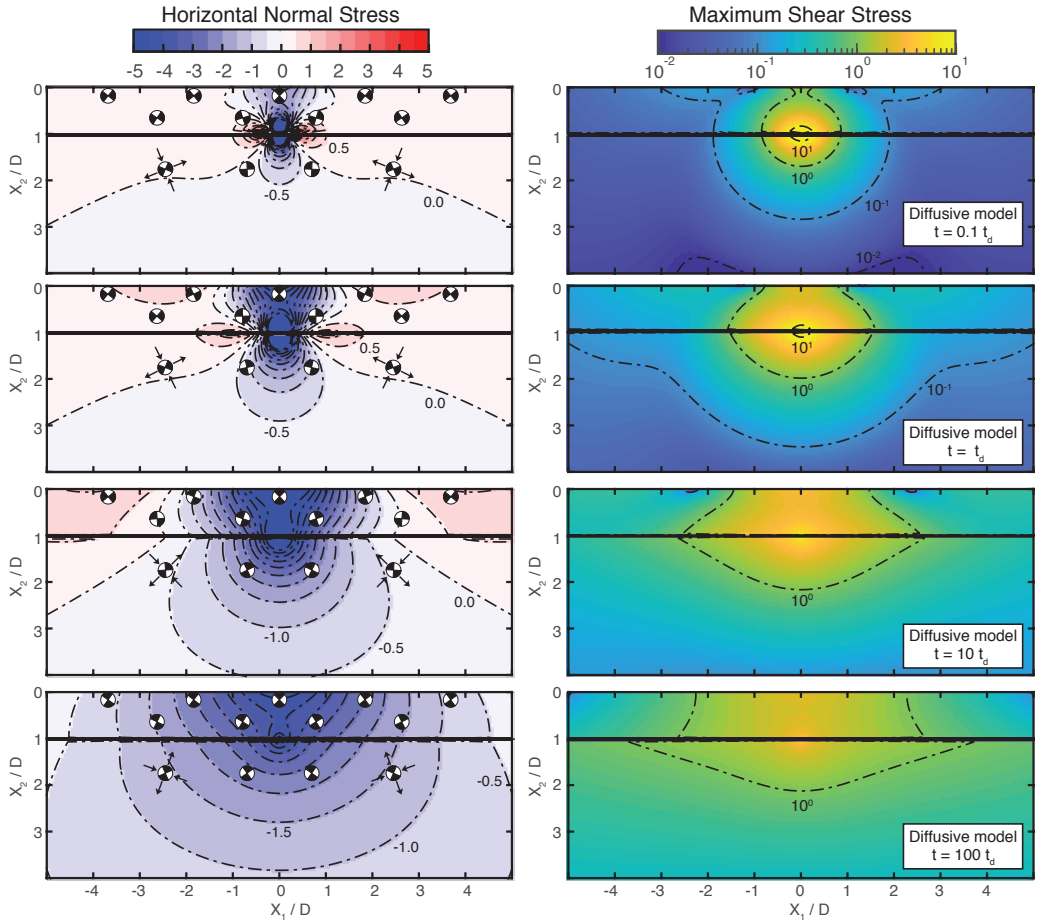

Figure 7.3: Change in horizontal normal stress (left) and maximum shear stress (right) due to fluid extraction (relative tension positive) for diffusion models with progressing time relative to the characteristic diffusion timescale $t_d = \frac{D^2}{4c}$. Stresses are contoured outside the producing zone ($x_2 \in [D, D+T]$). Simulated focal mechanisms indicate planes of maximum shear stress, with arrows indicating the axes of maximum tension and compression, and stresses are normalized by $\frac{\mu(1+\nu_u)BTQ}{12\pi\rho_0 D(1-\nu_u)}\sqrt{\frac{t}{c}}$.

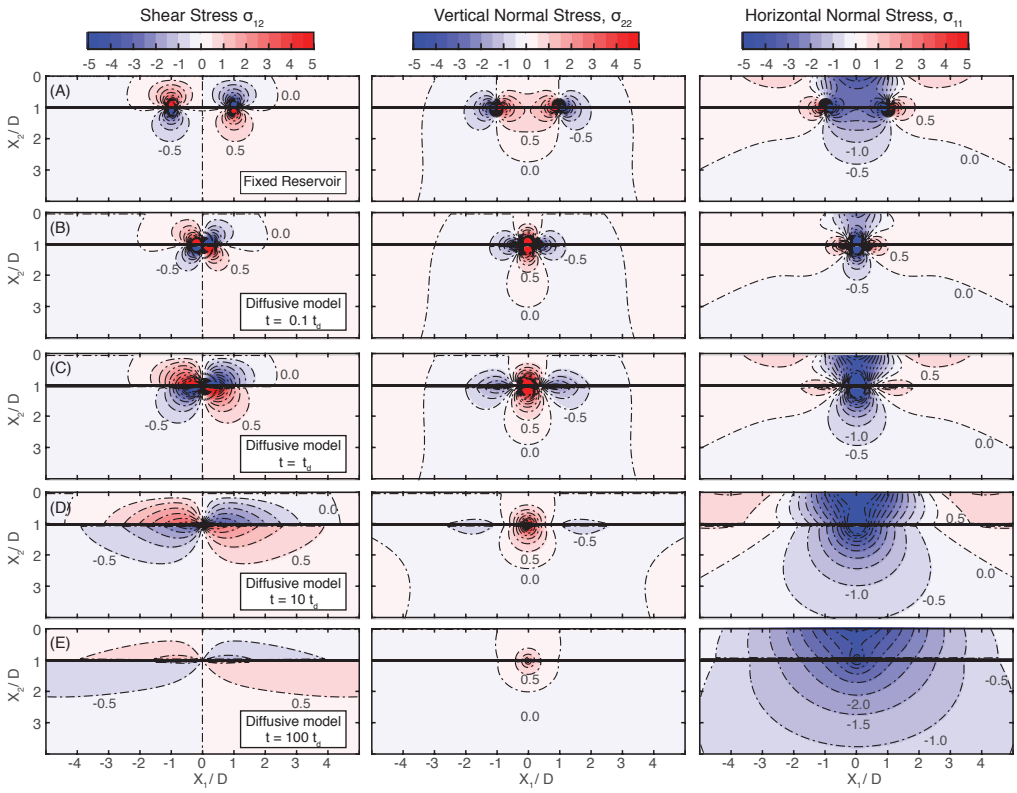

Figure 7.4: Extensional and shear stresses due to fluid extraction for diffusion models for progressing time relative to the characteristic diffusion timescale (relative tension positive) in both the (a) fixed reservoir model of Segall (1989) and (b-e) diffusion models for progressing time relative to the characteristic diffusion timescale. Stresses are normalized for (a) by $\frac{\mu(1+\nu_u)BTQt}{6\pi\rho_0 D^2(1-\nu_u)}$ and for (b-e) by $\frac{\mu(1+\nu_u)BTQ}{12\pi\rho_0 D(1-\nu_u)}\sqrt{\frac{t}{c}}$.

the extraction point, the angle of maximum extensional stress change rotates such that points further away from the extraction site experience a reversal from relative horizontal tension to compression. The angle of maximum shear stress correspondingly rotates from around $-\pi/4$ to $\pi/4$, indicative of a transition from preferred normal faulting to reverse faulting. This is generally consistent with the trend of expected reverse faulting above and below the producing layer and normal faulting at the flanks of the producing layer, as discussed by Segall (1989). However, as the spatial extent of the producing zone grows with time, the preferred mechanism of seismicity at a given location may evolve as the surrounding region transitions into a state of compression. The temporal evolution of the magnitude and direction of the stresses at the locations highlighted in Fig. 7.5 are included in the Appendix (see Figs. 7.7 and 7.8).

Due to the interaction of the stress field with the free surface, the timing of the stress rotations varies slightly with depth but may be estimated given knowledge of the reservoir depth and diffusivity, as well as the depth and distance from the extraction site for the location of interest (Figure 7.6). For a depth of interest around one-half of the reservoir depth, the timescale about which one would expect a transition to relative horizontal compression would be $t \approx t_d$ and $t \approx 5.6t_d$ for lateral locations of $x_1 = D$ and $x_1 = 2D$, respectively. Considering a reservoir at 1 km depth and a diffusivity of $c = 1$ m^2/s, this gives approximate timescales for stress reversal between 1 and 2 kilometers from the extraction site of approximately 3 to 16 days following initiation of extraction. For lower diffusivities, this window can be much broader. For instance, with a diffusivity of $c = 0.1$ m^2/s for otherwise similar considerations, the time window for stress reversal between 1 and 2 kilometers from the extraction site becomes roughly 29 to 145 days, potentially providing a more substantial observation window.

Depending on how the reservoir area scales with time, the magnitude of the stress perturbations may be expected to grow as fluid is continuously extracted. Therefore, the significance of the stress reversal depends on the diffusivity of the reservoir, as well as the ambient stress conditions before extraction. For a given time since initiation of pumping, the orientation of the stress perturbation depends on the diffusivity of the reservoir (Fig. 7.2). For reservoirs with higher diffusivities, locations surrounding the extraction site may experience the rotation in the perturbed stress before the perturbations achieve any notable magnitude. In contrast, lower diffusivities concentrate the change in fluid mass, allowing for more substantial stress perturbations as the diffusion front propagates.

A lower bound for the magnitude of stress perturbations can be estimated in the case that the reservoir length and width scale roughly equivalently over time so that the amplitudes of stresses are independent of time (Case 2, $\gamma = 1$). Assuming values of $\mu = 10$ GPa, $B = 0.6$, $D = 1$ km, and $\dot{V} = 10^6$ m^3/yr, the scaling for the distributions in Figs. 7.3 and 7.4 would

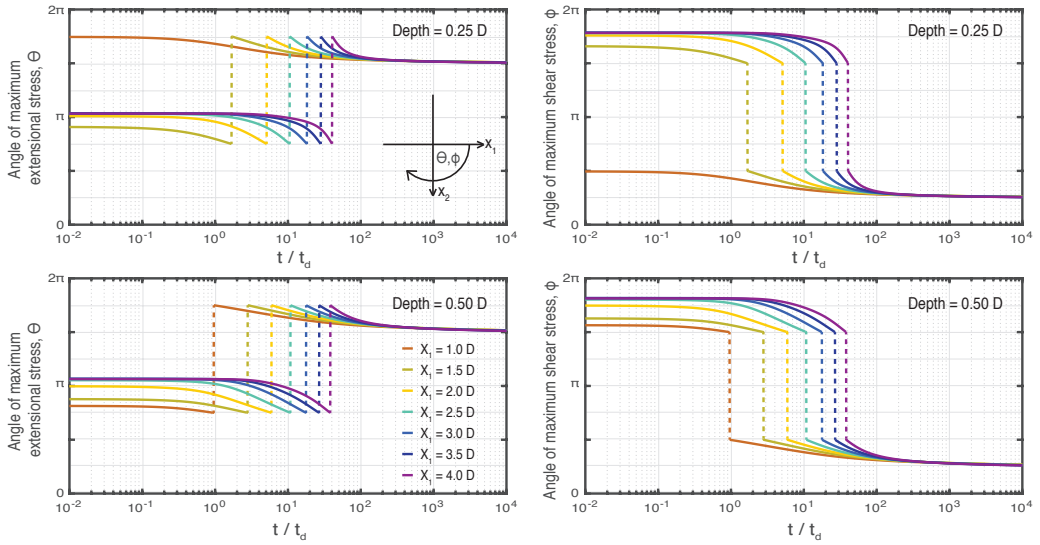

Figure 7.5: Temporal evolution of the angle of maximum shear stress ϕ (left) and angle of maximum extensional stress θ (right) as a function of lateral distance from the extraction site at $x_1 = 0$ for representative depths $x_2 = 0.25D$ (top) and $x_2 = 0.5D$ (bottom). Note that the rotation of the maximums shear stress angle from $-\pi/4$ to $\pi/4$ coincides with the rotation of the horizontal stress from relative tension to compression.

be approximately 3.2 and 32 kPa for $c = 1$ and $c = 0.1$ m^2/s, respectively. If we consider a point at 750 m depth and 1.75 km away from the extraction site, the horizontal normal stress perturbation would correspond to a transition from an extensional stress perturbation of 12.8 kPa at $t_D = 29$ days for $c = 0.1$ m^2/s, to a compressive perturbation of -30 kPa after 289 days. For context, such values are roughly an order of magnitude larger than tidal stresses, typically on the order of 1 kPa, and 0.1% of the potential effective confining stresses around 1 km depth of 15–20 MPa, assuming lithostatic overburden minus hydrostatic pore fluid pressure. The relative significance of such poroelastic perturbations depends heavily on the orientation and existing stress state of faults, including the presence of pore fluid overpressure within the fault gouge which can substantially alter the effective confining stress acting on faults.

7.4 Discussion and conclusions

We have expanded upon the analyses presented by Segall (1985) and Segall (1989), considering the spatio-temporal evolution of the poroelastic response surrounding fluid extraction

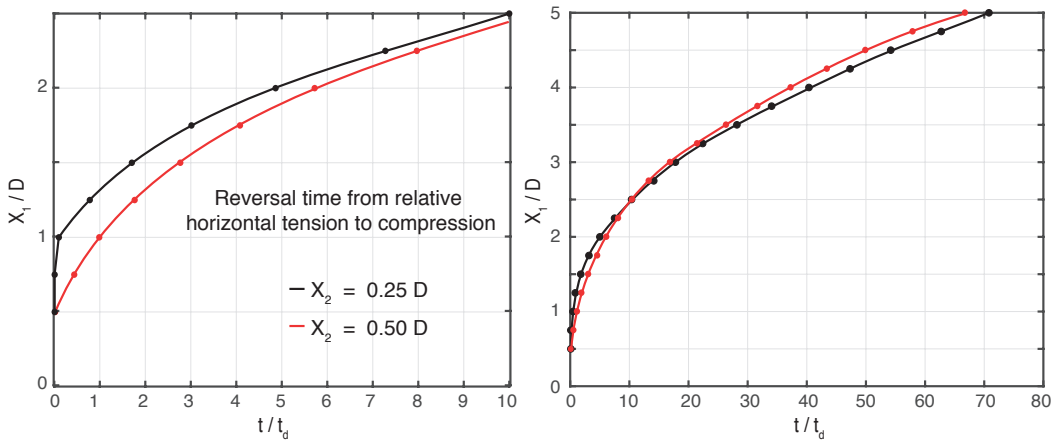

Figure 7.6: Lateral spatio-temporal propagation of reversal from relative horizontal compression to tension at two representative depths of $x_2 = 0.25D$ (black) and $x_2 = 0.5D$ (red).

from a laterally unconstrained horizontal reservoir. We have examined the implications of allowing for the time-dependent spatial evolution of the effective producing zone due to fluid diffusion, in comparison to assuming a fixed producing geometry. Distinctions arise as the intensity of the poroelastic response is influenced by the spatial gradient of the change in fluid mass content within the reservoir with substantial stress concentrations emerging around sharp gradients in Δm. Strong gradients in Δm would be expected surrounding the extraction site as well as any discontinuities in the reservoir geometry or permeability structure. In the particular case considered here with a uniform diffusivity, sharp gradients would be expected to be alleviated over time due to fluid diffusion, but heterogeneity within the geometric or hydrological structure of the producing layer may result in growing stress concentrations over time as the change in fluid mass within the producing zone increases. A potentially important consideration not incorporated within this model is the possible temporal evolution of the permeability structure within the reservoir, particularly if stresses grow large enough to fracture the surrounding rock. In such case, there is the possibility that stress concentrations due to structural or permeability irregularities may be smoothed out over time. Overall, the capability for the reservoir to mitigate stress concentrations depends on the hydraulic diffusivity with respect to the volumetric extraction rate where relatively high diffusivities allow for the timely redistribution of pore fluid.

For many reservoir settings, the timescale of fluid transport within the producing layer may be comparable to the timescale for which field observations and seismological studies are made at relevant distances. For these cases, it may be important to account for the non-stationarity of the geometry of the producing zone when interpreting field measurements. Moreover, the magnitude and distribution of surface expressions depend on the balance between the volumetric rate of extraction and the rate at which changes in fluid content can be redistributed through diffusion. Therefore measurements of the spatio-temporal evolution of surface displacements and strains associated with fluid extraction and injection can allow for the inference of reservoir properties, such as the reservoir diffusivity and thickness.

As introduced by Segall (1989), the spatial distribution of stress fields resulting from fluid extraction from a horizontal layer are consistent with reverse faulting above and below the producing zone and normal faulting along the flanks of the reservoir. However, for a laterally unconstrained reservoir, the effective length of the producing zone is not fixed in time and the progression of the producing front away from the extraction site results in a time-dependent rotation of the planes of maximum imposed shear stress as the stress regime transitions from relative horizontal tension to compression above and below the producing layer. This alone may predict that the preferred mechanism of associated seismicity at a given location transitions from normal faulting to reverse faulting as the effective length of the producing zone increases. In contrast, for fluid injection one may expected a transition from reverse faulting to normal faulting, as inferred for seismicity between 2014 and 2015 in the Crooked Lake and Rocky Mountain House areas in Alberta, Canada, following decades of injection (Eaton & Mahani, 2015). However, it is important to note that this reflects only a change in polarity of the stress perturbation and not the absolute stress levels around the reservoir, whereas the likelihood of triggered seismicity also depends on the criticality of the pre-existing stress conditions as well as the distribution and orientation of available faults. Rather than a visible change in focal mechanism, the stressing conditions may instead transition from favorable to unfavorable conditions, or vice-versa, depending upon the orientation of existing faults

and pre-existing stress state (Segall & Lu, 2015). While general faulting mechanisms may remain consistent, the spatio-temporal evolution of the poroelastic stress field as the effective reservoir expands may be detectable through temporal rotations in the principal stress directions of recorded seismicity, such as those inferred from stress inversions of seismicity in The Geysers geothermal field, California, and the Soultz-sous-Forêts enhanced geothermal system (Martınez-Garzón et al., 2014; Martıŋnez-Garzón et al., 2013; Schoenball et al., 2014). Finally, the stress state surrounding the producing field would also be expected to evolve over time due to stress redistribution from earthquakes as well as aseismic slip within the surrounding region (Bhattacharya & Viesca, 2019; Guglielmi et al., 2015; Keranen et al., 2013). Overall, developing a better understanding of the spatio-temporal evolution of seismicity and their focal mechanisms may provide additional constraints on the geometry and hydraulic properties of the producing zone (Martınez-Garzón et al., 2014; Martıŋnez-Garzón et al., 2013; Mukuhira et al., 2018; Schoenball et al., 2014; Shapiro et al., 2002).

While exploring the conditions for the triggering of seismic and aseismic slip events is beyond the scope of this work, the potential measurement of such temporal transitions in earthquake focal mechanisms or remote activation or deactivation of seismicity may provide constraints on the criticality of regional stress levels. We emphasize the value in the solutions presented by Segall (1985, 1989, 1992) and in this work in providing reference models for which exact calculations may be made for quantitative comparison with field data. Moreover, these solutions may prove useful as reference solutions for more sophisticated numerical methodologies. The 2-D solutions presented here are exact, and we have discussed two approximate extensions to 3-D in order to facilitate direct comparison with field measurements and production data, which should be interpreted with care. Finally, while we have focused on the case of fluid extraction where $Q < 0$, this analysis may also be considered for the case of fluid injection and diffusion where $Q > 0$. Conveniently, the distributions for displacements and stresses will be similar to those shown in this work with only a change in sign due to their linear relationship with the net mass flux Q.

7.5 Appendix

7.5.1 Two-dimensional poroelastic solutions

Segall (1985) presented quasi-static solutions for the displacement and stress fields due to changes in fluid mass content within an infinitesimal volume dV for a 2-D linear isotropic poroelastic half-space. In this study, we calculate these fields resulting from a uniform change in fluid content given by Eq. (7.5), as well as the time-dependent distribution resulting from fluid diffusion given by Eq. (7.7), by convolving the distributions with the poroelastic Green's functions provided in the Appendix of Segall (1985). Here we present these solutions again for completeness.

For the general quasi-static problem of fluid extraction from a half plane, the relation for the solid particle displacements can be expressed in the form,

$$u_j(\mathbf{x}, t) = \frac{C(\mathbf{y}, t)}{\mu} g_j(\mathbf{x}, \mathbf{y}) \tag{7.11}$$

where $g_j(\mathbf{x}, \mathbf{y})$ is the displacement in the j direction at $\mathbf{x}$ due to a point center of dilatation at $\mathbf{y}$ with associated change in fluid mass content $\Delta m(\mathbf{y}, t)dV$:

$$g_1(\mathbf{x}, \mathbf{y}) = \frac{1}{2}\left[\frac{x_1 - y_1}{r_1^2(\mathbf{x}, \mathbf{y})} + \frac{(3 - 4\nu_u)(x_1 - y_1)}{r_2^2(\mathbf{x}, \mathbf{y})} - \frac{4x_2(x_2 + y_2)(x_1 - y_1)}{r_2^4(\mathbf{x}, \mathbf{y})}\right] \tag{7.12}$$

$$g_2(\mathbf{x}, \mathbf{y}) = \frac{1}{2}\left[\frac{x_2 - y_2}{r_1^2(\mathbf{x}, \mathbf{y})} + \frac{2x_2 - (3 - 4\nu_u)(x_2 + y_2)}{r_2^2(\mathbf{x}, \mathbf{y})} - \frac{4x_2(x_2 + y_2)^2}{r_2^4(\mathbf{x}, \mathbf{y})}\right]. \tag{7.13}$$

The prefactor $C(\mathbf{y}, t) = \frac{\mu B(1+\nu_u)}{3\pi\rho_0(1-\nu_u)}\Delta m(\mathbf{y}, t)dV$ has units of force related to the fluid mass source in the infinitesimal volume dV. Here $u_1(\mathbf{x})$ and $u_2(\mathbf{x})$ refer to horizontal and vertical displacements, respectively, and $r_1^2(\mathbf{x}, \mathbf{y}) = (x_2 - y_2)^2 + (x_1 - y_1)^2$ and $r_2^2(\mathbf{x}, \mathbf{y}) = (x_2 + y_2)^2 + (x_1 - y_1)^2$ reflect the source-receiver distances to the true mass source and the image source associated with the free surface at $x_2 = 0$. Note that $\mathbf{y}$ and $\mathbf{x}$ denote the full position vectors for the source and receiver elements, respectively.

The poroelastic stresses caused by points of dilatation may also be calculated from Hooke's law in the form $\sigma_{ij}(\mathbf{x}, t) = C(t)G_{ij}(\mathbf{x}, \mathbf{y})$ where,

$$G_{ij} = \frac{\partial g_i}{\partial x_j} + \frac{\partial g_j}{\partial x_i} + \frac{2\nu_u}{1 - 2\nu_u}\frac{\partial g_k}{\partial x_k}\delta_{ij} \tag{7.14}$$

giving (Segall, 1985),

$$\begin{aligned} G_{11}(\mathbf{x}, \mathbf{y}) = & \frac{(x_2 - y_2)^2 - (x_1 - y_1)^2}{r_1^4(\mathbf{x}, \mathbf{y})} \\ & + \frac{(x_2 + y_2)(3y_2 - x_2) - 3(x_1 - y_1)^2}{r_2^4(\mathbf{x}, \mathbf{y})} \\ & + \frac{16x_2(x_2 + y_2)(x_1 - y_1)^2}{r_2^6(\mathbf{x}, \mathbf{y})} \end{aligned} \tag{7.15}$$

$$\begin{aligned} G_{22}(\mathbf{x}, \mathbf{y}) = & \frac{(x_1 - y_1)^2 - (x_2 - y_2)^2}{r_1^4(\mathbf{x}, \mathbf{y})} \\ & + \frac{(5x_2 + y_2)(x_2 + y_2) - (x_1 - y_1)^2}{r_2^4(\mathbf{x}, \mathbf{y})} \\ & - \frac{16x_2(x_2 + y_2)(x_1 - y_1)^2}{r_2^6(\mathbf{x}, \mathbf{y})} \end{aligned} \tag{7.16}$$

$$\begin{aligned} G_{12}(\mathbf{x}, \mathbf{y}) = & -\frac{2(x_1 - y_1)(x_2 - y_2)}{r_1^4(\mathbf{x}, \mathbf{y})} \\ & - \frac{2(x_1 - y_1)(3x_2 + y_2)}{r_2^4(\mathbf{x}, \mathbf{y})} + \frac{16x_2(x_2 + y_2)^2(x_1 - y_1)}{r_2^6(\mathbf{x}, \mathbf{y})}. \end{aligned} \tag{7.17}$$

7.5.2 Surface displacements and strain due to distributed mass sources

The total displacement due to changes in a distributed fluid mass at time t can be obtained by integrating the undrained changes in fluid mass within the region for which $\Delta m(\mathbf{y}, t)$ is non-zero according to Eq. (7.1). Solutions for the surface displacements and horizontal strains resulting from the fixed reservoir mass distribution given by Eq. (7.5) can be expressed as,

$$u_1(\mathbf{x}, t) = \frac{(1 + \nu_u)BTQt}{6\pi\rho_0 a} \log\left(\frac{1 + \xi_+^2}{1 - \xi_-^2}\right) \tag{7.18}$$

$$u_2(\mathbf{x}, t) = \frac{(1 + \nu_u)BTQt}{3\pi\rho_0 a} \left[\tan^{-1}(\xi_-) - \tan^{-1}(\xi_+)\right] \tag{7.19}$$

$$\epsilon_{11}(\mathbf{x}, t) = \frac{(1 + \nu_u)BTQt}{3\pi\rho_0 a D} \left[\frac{\xi_+}{\xi_+^2 + 1} - \frac{\xi_-}{\xi_-^2 + 1}\right] \tag{7.20}$$

where $\xi_- = \frac{x_1 - a}{D}$ and $\xi_+ = \frac{x_1 + a}{D}$ (Segall, 1989). For the diffusive source represented by Eq. (7.7), the corresponding solutions can be expressed as Eqs. (7.21-7.23), where

$$K_{11}(\mathbf{x}) = \tan^{-1}\left(\frac{x_2-(D+T)}{x_1-a}\right) - \tan^{-1}\left(\frac{x_2-(D+T)}{x_1+a}\right) + \tan^{-1}\left(\frac{x_2-D}{x_1+a}\right) - \tan^{-1}\left(\frac{x_2-D}{x_1-a}\right)$$
$$+ 3\left(\tan^{-1}\left(\frac{x_2+(D+T)}{x_1+a}\right) - \tan^{-1}\left(\frac{x_2+(D+T)}{x_1-a}\right) + \tan^{-1}\left(\frac{x_2+D}{x_1-a}\right) - \tan^{-1}\left(\frac{x_2+D}{x_1+a}\right)\right)$$
$$+ 4ax_2\left(\frac{a^2-x_1^2+(x_2+D+T)^2}{((x_1-a)^2+(x_2+D+T)^2)((x_1+a)^2+(x_2+D+T)^2)}\right.$$
$$\left. - \frac{a^2-x_1^2+(x_2+D)^2}{((x_1-a)^2+(x_2+D)^2)((x_1+a)^2+(x_2+D)^2)}\right). \tag{7.25}$$

$M(y_1,t) = \left[\frac{1}{\sqrt{\pi}}\exp\left(-\frac{y_1^2}{4ct}\right) - \frac{|y_1|}{2\sqrt{ct}}\mathrm{erfc}\left(\frac{|y_1|}{2\sqrt{ct}}\right)\right]$. The integral over y_1 can be computed numerically for the diffusive source.

$$u_1(\mathbf{x},t) = \frac{2(1+\nu_u)BQ}{3\pi\rho_0}\sqrt{\frac{t}{c}}\int M(y_1,t)\left(\tan^{-1}\left(\frac{D+T}{x_1-y_1}\right) - \tan^{-1}\left(\frac{D}{x_1-y_1}\right)\right)dy_1 \tag{7.21}$$

$$u_2(\mathbf{x},t) = \frac{(1+\nu_u)BQ}{3\pi\rho_0}\sqrt{\frac{t}{c}}\int M(y_1,t)\log\left(\frac{(x_1-y_1)^2+D^2)}{(x_1-y_1)^2+(D+T)^2}\right)dy_1 \tag{7.22}$$

$$\epsilon_{11}(\mathbf{x},t) = \frac{(1+\nu_u)TBQ}{3\pi\rho_0}\sqrt{\frac{t}{c}}\int M(y_1,t)\left(\frac{D(D+T)-(x_1-y_1)^2}{(D^2+(x_1-y_1)^2)((D+T)^2+(x_1-y_1)^2)}\right)dy_1. \tag{7.23}$$

7.5.3 Stresses due to distributed mass sources

The stress distributions resulting from the distributed source may also be represented through linear integral relations with the poroelastic Green's functions $G_{nm}(\mathbf{x},\mathbf{y})$. By considering the stress distributions only outside of the reservoir, where $\Delta m(\mathbf{y},t) = 0$, these expressions simplify to the form of Eq. (7.8). Fully analytical expressions for the stress fields associated with the fixed reservoir mass distribution represented by Eq. (7.5) can be solved as,

$$\sigma_{ij}(\mathbf{x},t) = \frac{\mu(1+\nu_u)B}{3\pi\rho_0(1-\nu_u)}\int_V \frac{Qt}{2a}G_{ij}(\mathbf{x},\mathbf{y})dV_\mathrm{y}$$
$$= \frac{\mu(1+\nu_u)BQt}{6\pi\rho_0 a(1-\nu_u)}\int_D^{D+T}\int_{-a}^{a} G_{ij}(x_1,x_2;y_1,y_2)dy_1dy_2. \tag{7.24}$$

These solutions are separable in space and time and can be expressed as $\sigma_{ij}(\mathbf{x},t) = \frac{\mu(1+\nu_u)BQt}{6\pi\rho_0 a(1-\nu_u)}K_{ij}(\mathbf{x})$ where the kernels K_{ij} are expressed as Eqs. (7.25-7.27) (Segall, 1989).

$$
\begin{aligned}
K_{22}(\mathbf{x}) = {} & \tan^{-1}\left(\frac{x_2-(D+T)}{x_1+a}\right) - \tan^{-1}\left(\frac{x_2-(D+T)}{x_1-a}\right) + \tan^{-1}\left(\frac{x_2-D}{x_1-a}\right) - \tan^{-1}\left(\frac{x_2-D}{x_1+a}\right) \\
& + \tan^{-1}\left(\frac{x_2+(D+T)}{x_1+a}\right) - \tan^{-1}\left(\frac{x_2+(D+T)}{x_1-a}\right) + \tan^{-1}\left(\frac{x_2+D}{x_1-a}\right) - \tan^{-1}\left(\frac{x_2+D}{x_1+a}\right) \\
& + 4ax_2\Bigg(\frac{a^2-x_1^2+(x_2+D)^2}{((x_1-a)^2+(x_2+D)^2)((x_1+a)^2+(x_2+D)^2)} \\
& \qquad - \frac{a^2-x_1^2+(x_2+D+T)^2}{((x_1-a)^2+(x_2+D+T)^2)((x_1+a)^2+(x_2+D+T)^2)}\Bigg)
\end{aligned} \tag{7.26}
$$

$$
\begin{aligned}
K_{12}(\mathbf{x}) = {} & \frac{1}{2}\Bigg[\log\left((x_1-a)^2+(x_2-(D+T))^2\right) - \log\left((x_1-a)^2+(x_2-D)^2\right) \\
& + \frac{16ax_1x_2(x_2+D)}{\left((x_1-a)^2+(x_2+D)^2\right)\left((x_1+a)^2+(x_2+D)^2\right)} \\
& - \frac{16ax_1x_2(x_2+D+T)}{\left((x_1-a)^2+(x_2+D+T)^2\right)\left((x_1+a)^2+(x_2+D+T)^2\right)} \\
& + \left((x_1-a)^2+(x_2-D)^2\right)\left((x_1+a)^2+(x_2+D)^2\right)\Bigg(\\
& \qquad \frac{\log((x_1+a)^2+(x_2-D)^2)}{\left((x_1-a)^2+(x_2+D)^2\right)\left((x_1+a)^2+(x_2+D)^2\right)} \\
& \qquad + \frac{\log((x_1-a)^2+(x_2+D)^2)}{\left((x_1-a)^2+(x_2+D)^2\right)\left((x_1+a)^2+(x_2+D)^2\right)} \\
& \qquad - \frac{\log((x_1+a)^2+(x_2+D)^2)}{\left((x_1-a)^2+(x_2+D)^2\right)\left((x_1+a)^2+(x_2+D)^2\right)}\Bigg) \\
& - \left((x_1-a)^2+(x_2-D-T)^2\right)\left((x_1+a)^2+(x_2+D+T)^2\right)\Bigg(\\
& \qquad \frac{\log((x_1+a)^2+(x_2-D-T)^2)}{\left((x_1-a)^2+(x_2+D+T)^2\right)\left((x_1+a)^2+(x_2+D+T)^2\right)} \\
& \qquad + \frac{\log((x_1-a)^2+(x_2+D+T)^2)}{\left((x_1-a)^2+(x_2+D+T)^2\right)\left((x_1+a)^2+(x_2+D+T)^2\right)} \\
& \qquad - \frac{\log((x_1+a)^2+(x_2+D+T)^2)}{\left((x_1-a)^2+(x_2+D+T)^2\right)\left((x_1+a)^2+(x_2+D+T)^2\right)}\Bigg)\Bigg]
\end{aligned} \tag{7.27}
$$

$$J_{11}(\mathbf{x},\mathbf{y},t) = \int M(y_1,t)\Bigg[\frac{x_2+3D}{(x_1-y_1)^2+(x_2+D)^2} + \frac{4x_2(x_1-y_1)^2}{(x_1-y_1)^2+(x_2+D)^2} - \frac{x_2-D}{(x_1-y_1)^2+(x_2-D)^2} - \frac{x_2+3(D+T)}{(x_1-y_1)^2-(x_2+D+T)^2} - \frac{4x_2(x_1-y_1)^2}{(x_1-y_1)^2+(x_2+D+T)^2} + \frac{x_2-D+T}{(x_1-y_1)^2+(x_2-D-T)^2}\Bigg]dy_1 \quad (7.29)$$

$$J_{22}(\mathbf{x},\mathbf{y},t) = 4x_2^2\int M(y_1,t)\Bigg[\frac{D(x_2^2+3(x_1-y_1)^2)+x_2(x_2^2+(x_1-y_1)^2)-x_2D^2-D^3}{\left((x_1-y_1)^2+(x_2-D)^2\right)\left((x_1-y_1)^2+(x_2+D)^2\right)^2} - \frac{(D+T)(x_2^2+3(x_1-y_1)^2)+x_2(x_2^2+(x_1-y_1)^2)-x_2(D+T)^2-(D+T)^3}{\left((x_1-y_1)^2+(x_2-D-T)^2\right)\left((x_1-y_1)^2+\left(x_2+D+T\right)^2\right)^2}\Bigg]dy_1 \quad (7.30)$$

$$J_{12}(\mathbf{x},\mathbf{y},t) = 4x_2\int (x_1-y_1)M(y_1,t)\Bigg[\frac{2D(x_1-y_1)^2+x_2(x_2^2+(x_1-y_1)^2)+x_2D^2+2D^3}{((x_1-y_1)^2+(x_2-D)^2)((x_1-y_1)^2+(x_2+D)^2)^2} - \frac{2(D+T)(x_1-y_1)^2+x_2(x_2^2+(x_1-y_1)^2)+x_2(D+T)^2+2(D+T)^3}{((x_1-y_1)^2+(x_2-D-T)^2)((x_1-y_1)^2+(x_2+D+T)^2)^2}\Bigg]dy_1 \quad (7.31)$$

Solutions resulting from the diffusive mass source represented by Eq. (7.7) can be expressed similarly, however the spatio-temporal evolution of the stress fields are coupled due to the time-dependence of the fluid diffusion process.

$$\begin{aligned}\sigma_{ij}(\mathbf{x},t) &= C\int_V Q\left(\frac{t}{c}\right)^{1/2}\text{ierfc}\left[\left(\frac{y_1^2}{4ct}\right)^{1/2}\right]G_{ij}(\mathbf{x},\mathbf{y})dV_{\mathbf{y}} \\ &= CQ\left(\frac{t}{c}\right)^{1/2}\int_D^{D+T}\int_{-\infty}^{\infty}\text{ierfc}\left[\left(\frac{y_1^2}{4ct}\right)^{1/2}\right] \\ &\quad G_{ij}(x_1,x_2;y_1,y_2)dy_1dy_2 \end{aligned} \quad (7.28)$$

where $C = \frac{\mu(1+\nu_u)B}{3\pi\rho_0(1-\nu_u)}$. Individual stress components can be expressed as $\sigma_{ij}(\mathbf{x},\mathbf{y},t) = \frac{\mu(1+\nu_u)BQ}{3\pi\rho_0(1-\nu_u)}\left(\frac{t}{c}\right)^{1/2}J_{ij}(\mathbf{x},\mathbf{y},t)$, where the kernels J_{ij} expressed in Eqs. (7.29-7.31) can be computed numerically.

The spatial distribution of the horizontal and vertical normal stresses, σ_{11} and σ_{22}, respectively, as well as the shear stress σ_{12} for the fixed reservoir and diffusive models are shown in

Figure 7.4. The temporal evolution of these three stress components as a function of lateral distance from the extraction site are shown in Figure 7.7, where one can note the transition between relative horizontal tension to compression at each site. The amplitudes of the associated principal stresses and maximum shear stresses are given in Figure 7.8. For distances beyond $x_1 = 2D$ an inflection is noticeable in the maximum shear stress which coincides with the transition from relative horizontal tension to compression. The lateral progression of the reversal front to relative compression is shown in Figure 7.6 for representative depths of $x_2 = 0.25D$ and $x_2 = 0.5D$. As the effective producing zone expands as $l_d \propto \sqrt{t}$, the propagation of the reversal front is faster early on at locations closer to the extraction point, but decreases at further distances.

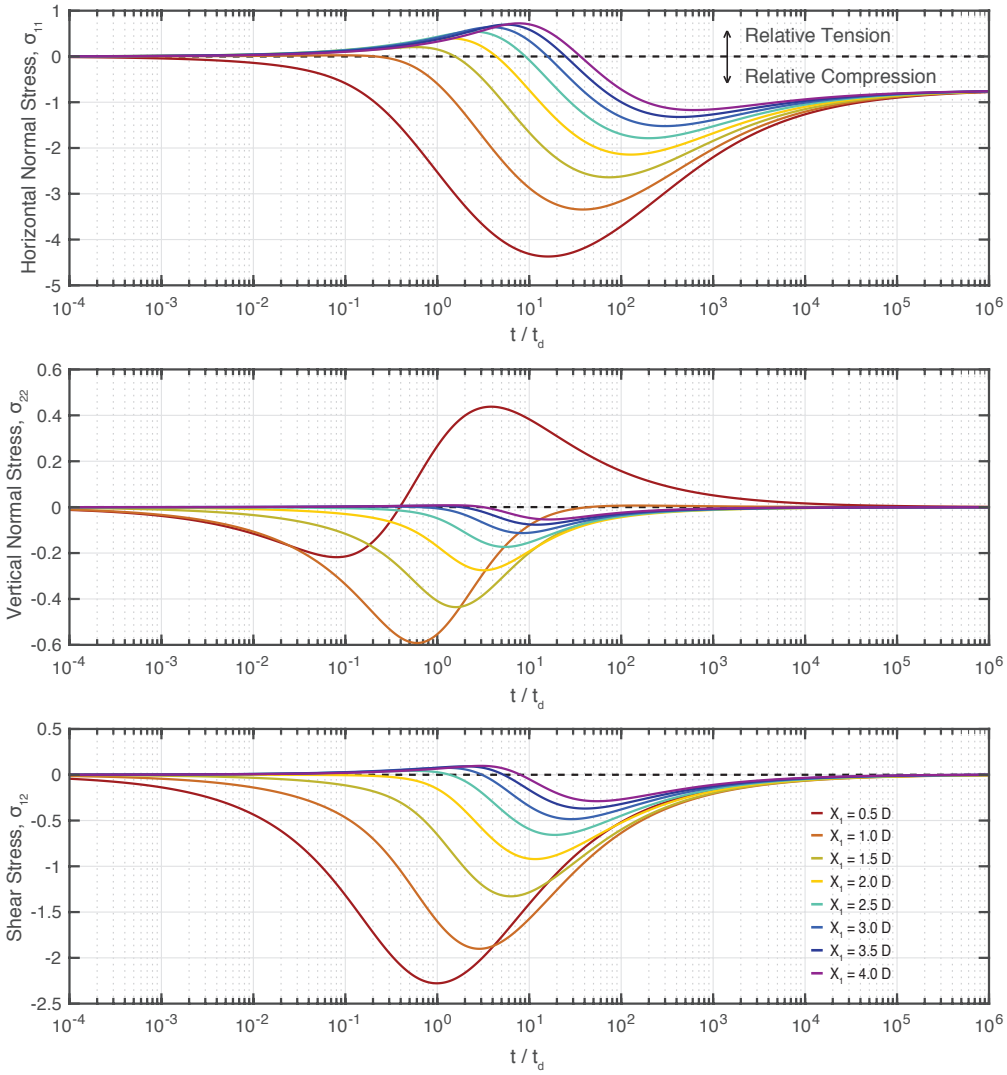

Figure 7.7: Temporal evolution of the horizontal σ_{11} and vertical σ_{22} normal stresses and shear stress σ_{12} as a function of lateral distance from the extraction site at $x_1 = 0$ for the representative depth $x_2 = 0.25D$. Stresses are normalized by $\frac{\mu(1+\nu_u)BTQ}{12\pi\rho_0 D(1-\nu_u)}\sqrt{\frac{t}{c}}$.

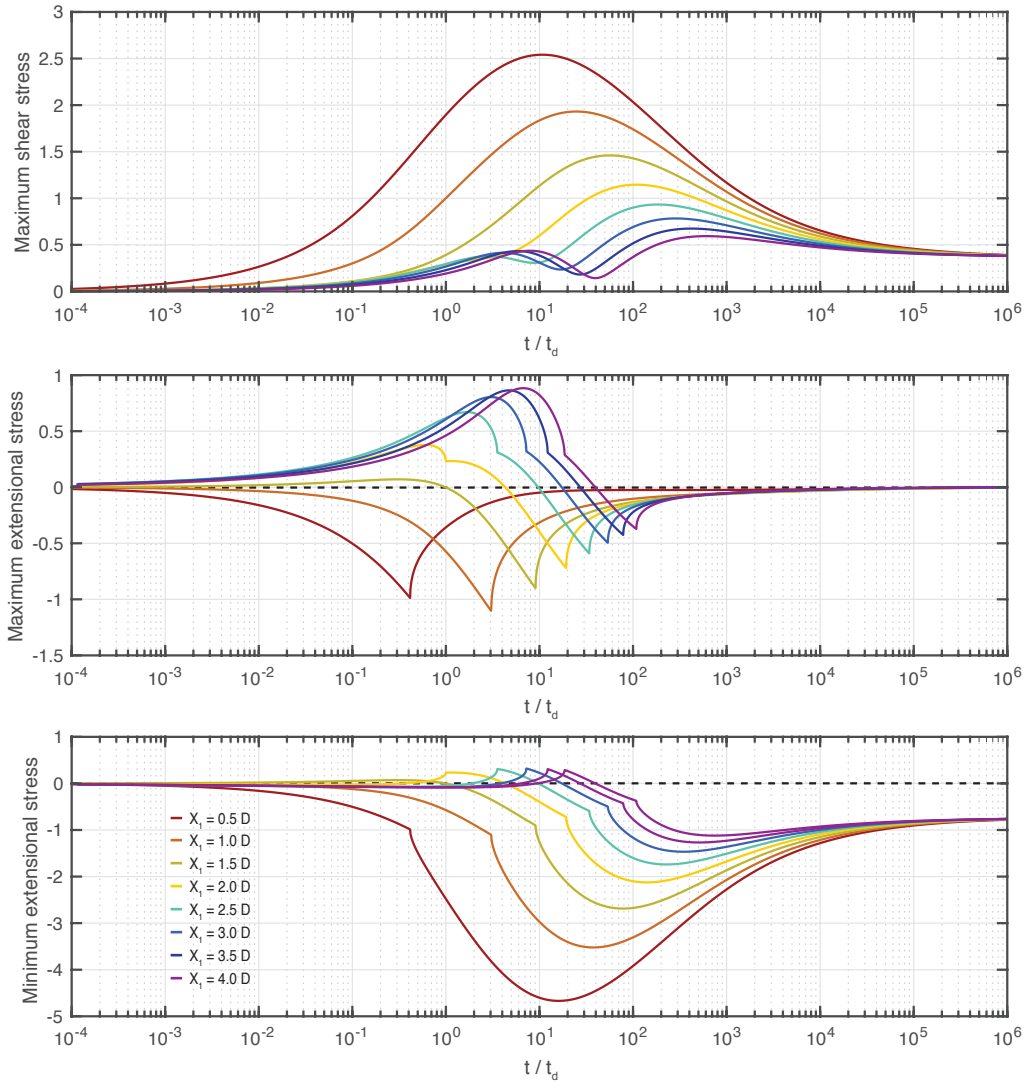

Figure 7.8: Temporal evolution of the maximum shear stress and principal stresses as a function of lateral distance from the extraction site at $x_1 = 0$ for the representative depth $x_2 = 0.25D$. Stresses are normalized by $\frac{\mu(1+\nu_u)BTQ}{12\pi\rho_0 D(1-\nu_u)}\sqrt{\frac{t}{c}}$.

Chapter 8

CONCLUSIONS AND FUTURE RESEARCH DIRECTIONS

8.1 Conclusions

We have used physics-based numerical models to examine the relationship between earthquake source properties and the heterogeneous evolution of motion and stress on faults. In particular, we have utilized SEAS simulations to study different physical models for "weak" mature faults with the goal of determining which fault properties in such models are compatible with a range of available observations taken together, including thermal constraints, earthquake source observations, and earthquake population statistics.

Both end-member models of either chronically weak faults, with mild to moderate enhanced dynamic weakening, or dynamically weak faults, with more efficient weakening, can reproduce magnitude-independent static stress drops with typical values between 1-10 MPa (Perry et al., 2020). In such models, fluids can contribute to apparent fault weakness through persistent fluid overpressure, as well as through transient thermal pressurization during dynamic rupture. We find that even fault models with persistently weak conditions due to chronic fluid overpressure require some mild to moderate enhanced weakening due to thermal pressurization not only to reproduce observed trends of increasing breakdown energy with slip, but also to reproduce moderate static stress drops greater than 1 MPa (Chapter 2; Lambert et al., in review). Our results therefore suggest that some enhanced dynamic weakening is crucial for matching existing seismological observations, which has considerable implications for evaluating the potential stability of different fault segments during future earthquakes (Noda & Lapusta, 2012).

Both chronically weak and dynamically weak faults can operate under low shear stress and with low heat generation, however they present substantially different relations between the shear stress required for rupture nucleation and the average stress conditions over larger

fault areas (Chapter 2; Lambert et al., in review). Our models show that larger ruptures propagate over increasingly under-stressed areas due to dynamic stress concentration, and result in progressively lower average prestress over the entire rupture compared to that for nucleation, with the effect being more significant in models with more efficient weakening. Accordingly, models with increasingly efficient weakening during ruptures tend to produce larger earthquakes, at the expense of smaller earthquakes, resulting in lower b-values and less complex earthquake sequences. Our results suggest that the paucity or absence of smaller events along some mature faults, such as central sections of the San Andreas Fault, may be an observational indication that they undergo considerable dynamic weakening during ruptures, as previously suggested for the brittle-ductile transition region (Jiang & Lapusta, 2016). These considerations may be particularly useful for early warning systems.

Our results highlight the significance of fault heterogeneity for rupture occurrence, particularly in fault models with efficient dynamic weakening. Fault models with more efficient weakening exhibit increasingly notable differences between the stress conditions required for rupture nucleation and the much lower average shear stress over larger rupture areas. Thus, faults that experience more substantial weakening should require the presence of larger amplitudes of heterogeneity to produce small events.

Our simulations illustrate that both critical fault stress required for rupture propagation and earthquake source properties, such as static stress drops, are products of complex finite-fault interactions. The critical stress conditions for earthquake occurrence cannot be described by a single number but rather present as complex spatial distribution with scale-dependent averages. Thus, when considering the critical stress conditions, it is essential to take into account both the size of the rupture and the weakening behavior, and hence the style of motion, that may occur throughout rupture propagation. In addition, our results highlight the importance of accounting for finite-fault effects when relating small lab-scale measurements to larger-scale fault and rupture properties and the need to continue developing a better physical understanding of faulting at various scales through the partnership of laboratory

experiments and finite-fault modeling, constrained by field observations.

We find that persistently weak faults produce predominantly crack-like or mildly pulse-like ruptures and dynamically weak faults typically produce self-healing pulse-like ruptures. Moreover, the two types of rupture styles can be distinguished based on the radiated energy per seismic moment, and hence apparent stress, of the resulting earthquake ruptures (Chapter 4; Lambert et al., 2021). Crack-like ruptures result in radiated energy per moment comparable to teleseismic estimates from large megathrust earthquakes, while self-healing pulses produce radiated energy per moment that is much larger than typical teleseismic estimates for large megathrust earthquakes, yet potentially comparable to limited regional estimates from large crustal earthquakes. Other mechanisms for producing pulse-like rupture propagation, such geometric restrictions of the fault, can result in similar evolution of average shear stress and energy partitioning as crack-like ruptures (Chapter 5; Lambert & Lapusta, in prep). The main difference between self-healing pulses and crack-like ruptures, as well as geometric pulses, is the manner in which local slip arrests via co-seismic healing, which translates into differences between the static and dynamic stress changes. The substantial co-seismic healing exhibited during self-healing pulses is the key feature that allows faults to maintain higher interseismic stress levels, potentially multiple static stress drops above stress constraints from shear heating, and results in higher apparent stress.

If the seismological estimates of radiated energy are reliable, then our findings suggest that the preferred rupture modes for megathrust and mature strike-slip faults would be different, with large megathrust earthquakes propagating as crack-like to mild pulse-like ruptures, while large strike-slip earthquakes propagate as sharper self-healing pulses. The corresponding physical conditions that govern large earthquake ruptures on megathrusts versus mature continental faults such as the San Andreas Fault would then also be different, with megathrusts operating under chronic fluid overpressure and relatively mild dynamic weakening, and continental faults exhibiting much less chronic overpressure but experiencing pronounced dynamic weakening. Our results indicate that re-evaluating seismological es-

timates of radiated energy and static stress drop would thus bring greater insight into the driving physics of large earthquakes and the absolute stress conditions on mature faults. The possible discrepancy in driving mechanisms for large megathrust and continental strike-slip earthquakes raises questions about the relevance of existing inferences from large earthquakes, which are dominated by megathrust events, for informing us about properties of future strike-slip events.

We have found that dynamically weak faults can operate under low stresses but produce crack-like ruptures with radiated energies and static stress drops close to those of natural events (Chapter 4; Lambert et al., 2021). While the radiated energy, average static stress drop and moment may be comparable for crack-like ruptures with mild or extremely efficient weakening, ruptures with more efficient weakening may be potentially distinguished by their production of considerably stronger high-frequency (> 1 Hz) near-fault ground motions. In addition, faults that undergo very efficient weakening during crack-like ruptures should also exhibit a lack of microseismicity or near seismic quiescence other than large earthquakes, as observed on some mature strike-slip faults (Hauksson et al., 2012; Jiang & Lapusta, 2016; Michailos et al., 2019).

We have investigated the sensitivity of long-term SEAS simulations to choices in numerical discretization and found that the criteria for numerical convergence can be considerably more stringent than for simulations of individual dynamic ruptures or shorter sequences, and depend on the sensitivity of the specific physical problem to small numerical perturbations (Chapter 6; Lambert & Lapusta, in review). Longer-term sequences of slip events can eventually diverge due to the subtle accumulation of numerical differences interacting with the highly nonlinear nature of the problem. This is particularly relevant to the parameter regime where the fault dimensions are considerably larger than the nucleation size, which promotes a wider distribution of rupture sizes and is highly relevant to natural faults and fault networks. We find that some physical properties, such as average stress measures, can be reliably determined from well-formulated numerical models even without long-term

convergence of the earthquake sequences, however other quantities, such as the probability of an earthquake rupture jumping from one fault to another, are highly sensitive to modeling choices.

Our results highlight the need to further assess the predictive power of earthquake models for different quantities of interest to seismic hazard assessment, as well as what geophysical observations are needed to constrain the most relevant physics governing earthquake source processes. The extreme sensitivity of some hazard parameters to small perturbations may not be unique to numerical models but also relevant to natural faults, making it challenging, and perhaps impractical, to reliably infer such quantities. As discussed throughout this thesis, physics-based models are valuable exploratory tools, which can be used to probe the sensitivity of existing hazard parameters and help identify reliable metrics for informing long-term fault behavior and future seismic hazards.

Finally, we presented simple physical models that account for the time-dependent diffusion of pore fluids during reservoir fluid extraction, such as due to energy resource practices (Chapter 7; Lambert & Tsai, 2020), We used these solutions to show that the magnitude and spatial distribution of the resulting poroelastic stresses surrounding the reservoir depend not just on the total volume of extracted fluid, but the rate of fluid extraction relative to how fast fluids can be redistributed in the reservoir through diffusion. The spatio-temporal evolution of the perturbed stresses due to fluid extraction may manifest as a rotation in earthquake focal mechanisms or varied sensitivity to poroelastic triggering, depending on the pre-existing stress state and fault orientations, and may explain inferred rotations in principal stress directions associated with some induced seismicity.

8.2 Future directions

The continued development of SEAS simulations and collaborative design of laboratory and field experiments can allow for increasingly detailed explorations of long-term fault behavior, earthquake rupture characteristics and their observable features, with the goal

of developing greater insight into the governing physics of fault zones and earthquake source processes. The resulting insight can inform the assessment of seismic hazards and potentially allow physics-based improvements to mitigation approaches such as earthquake early warning. The following discussions provide an outlook on five areas for continued development in the modeling of earthquake source processes.

8.2.1 Evaluating physical models of earthquake source processes and exploring beyond traditional fracture mechanics

The particular appeal of dynamic fracture theory is that it provides a framework to connect observations of the rupture process, such as rupture speed, to information of the local physics that control the rupture dynamics, such as fracture energy. In principle, such insight is then useful for informing models of future rupture processes. However, the presence of thermo-hydro-mechanical effects in faulting, as well as additional dissipative processes such as damage generation, calls into question the overall analogy between cohesive-zone dynamic fracture theory and frictional ruptures (Chapter 3; Lambert & Lapusta, 2020). In particular, the rupture-dependence of breakdown energy raises questions about how its inferences from previous events may inform future ruptures, and whether such quantity describes the relevant dissipated energy that controls the rupture dynamics. Moreover, our work demonstrates that the physical interpretation of common seismological inferences based on dynamic fracture theory can depend heavily on the earthquake rupture style, and special consideration is needed when relating them to the local evolution of shear stress on faults during rupture.

Further work is warranted to reevaluate physical models of earthquake source processes and examine the physical characteristics that control rupture dynamics, as well as how such quantities may be inferred from geophysical studies. This includes revisiting scaling relations among rupture properties, such as seismic moment, static stress drop, breakdown energy, rupture speed, and rupture duration, for different rupture scenarios and determining where scaling arguments are consistent and where they may be substantially distinct, such as for self-healing pulses. Such insight may be incorporated into seismic hazard scenarios

such as the Uniform California Earthquake Rupture Forecast (UCERF) and Great California Shakeout (Field et al., 2017; Jones et al., 2008).

8.2.2 Reviewing geophysical inferences using in part numerically simulated sources

A substantial challenge for inferring earthquake source characteristics is the lack of ground truth for methodologies aimed at imaging finite-fault aspects of ruptures. Simulated dynamic rupture scenarios of differing rupture styles provide an opportunity to evaluate seismological and geodetic techniques and examine how various layers of source and path complexity contribute to observed features. Such scenarios can be used to calibrate existing observational techniques such as seismic back-projection and finite-fault inversions, and examine what rupture features may be reliably inferred, as well as our current observational limitations. This approach is also well-suited for examining new technologies and the construction of optimal observational arrays for earthquake source imaging. In particular, SEAS simulations can be used to study strategies for resolving the spatial and temporal relationship between seismic and aseismic modes of fault slip, such as slow-slip transients and earthquake ruptures, as well as the earthquake nucleation process (Abercrombie & Mori, 1996; Bouchon et al., 2011; Kato et al., 2016, 2012; McGuire et al., 2005; Schurr et al., 2014; Sugan et al., 2014; Tape et al., 2018).

Our work highlights radiated energy as a valuable seismological observable for inferring fault physics and indicates the need to review the accuracy of radiated energy estimates, especially since regional estimates tend to be higher than the teleseismic estimates for the earthquakes from which both are available. Seismological estimates can be affected by a number of factors, including attenuation, scattering, rupture directivity, focal mechanism, and interactions of the rupture with the free surface (Ide & Beroza, 2001; Kanamori et al., 2020; Ma & Archuleta, 2006; Perez-Campos & Beroza, 2001; Venkataraman & Kanamori, 2004; Venkataraman, Rivera, & Kanamori, 2002; Ye et al., 2016b). Teleseismic studies typically measure only the direct dilatational p-wave and assume a scaling between the p and shear s-wave contributions, though the p-wave typically carries less than 5% of the total radiated energy. Directivity and p-to-s corrections are often determined using simplified

point source or kinematic rupture models, however more complex rupture processes may result in more complicated azimuthal variations in radiated energy as well as different frequency content (Venkataraman & Kanamori, 2004). In addition, teleseismic studies typically consider a limited frequency band below 1 to 2 Hz, whereas the higher radiated energy of self-healing pulses may be distributed at higher frequencies ($\sim$ 10 Hz) that are relevant to strong ground motion, but more attenuated at further distances. Assessing the potential magnitude of these contributions, as well as their compounded effect, is an important topic for future work.

8.2.3 Developing appropriately-scaled fault constitutive relations

In order to assess potential seismic hazards, it is important to evaluate how different physical processes in the Earth contribute to the slip behavior on faults and associated ground motions. The spatial scales relevant to earthquake sources processes span over twelve orders of magnitude from thousands of kilometers to microns. Explicitly incorporating all relevant scales and physical processes into earthquake models is likely not feasible in the foreseeable future, if at all. Our current understanding of frictional behavior and rock failure is largely based on sub-meter-scale (typically centimeters) laboratory experiments, which is directly applied in earthquake models with computational cells on the order of meters to kilometers, with little consideration of how to adjust for differences between laboratory scales and nature.

A promising route for studying scale-dependent behavior of fault materials is through numerical modeling of laboratory experiments and the development of numerical homogenization schemes to produce scale-appropriate fault constitutive relations. Such developments may be essential for incorporating new physical processes and fault attributes in earthquake models. For example, effective scaling relationships in which the rate-and-state characteristic slip distance D_{RS} is not constant, but perhaps evolves with slip rate, may serve as a proxy for additional physical processes as the fault slips, such as the formation of gouge, drag from fault roughness and energy dissipation from off-fault damage generation and bulk plasticity. Such relationships may facilitate resolving relatively small nucleation lengths consistent with microseismicity, while stabilizing the rupture front during the propagation

of large dynamic events. Well-motivated scaling practices for fault constitutive relations may therefore not only introduce new fault physics into earthquake simulations, but also expand the capability of simulating earthquake populations with a wider range of earthquake sizes, while minimizing computational expense.

8.2.4 Integrating insight from earthquake models and geodynamic simulations

The loading of stress on faults and its redistribution through different deformation processes are critical factors controlling the size of earthquake ruptures and seismicity patterns. Mimicking tectonic-like loading by prescribing a fixed loading plate rate can be appropriate when modeling a single planar fault segment, however extending models to long-term motion in geometrically-realistic fault networks requires a better understanding of how stress is loaded on individual faults in the broader picture of plate tectonics and crustal deformation. This highlights the need to improve our understanding of the distribution of forces along faults, as well as throughout the crust and upper mantle, in both the context of individual earthquake source processes and longer-term geodynamics. For example, substantial seismic slip during large earthquakes can transmit stress to more ductile regions, which in turn may alter loading conditions not just on that fault, but also neighboring faults, depending on the rheology of the surrounding bulk. The advancement of SEAS simulations that are able to incorporate off-fault deformation, such as bulk viscoelastic deformation, within earthquake sequences can assist in exploring such processes (Allison & Dunham, 2018; Lambert & Barbot, 2016).

Another plausible route for studying earthquakes in the context of broader crustal deformation is to develop schemes that couple insight from detailed dynamic rupture models with existing larger-scale geodynamic simulations (e.g. Dal Zilio et al., 2018; Sobolev & Muldashev, 2017; van Dinther, Gerya, Dalguer, Corbi, et al., 2013; van Dinther, Gerya, Dalguer, Mai, et al., 2013; van Zelst et al., 2019). For example, earthquake models may assist in formulating better representations of earthquake source processes in geodynamic simulations, such as determining simplified representations of the redistribution of stress during ruptures, accounting for differences between dynamic and static stress changes.

Geodynamic simulations may provide insight into appropriate boundary conditions for fault loading in various geometries and tectonics settings. Such initiatives would be of great value for extending earthquake sequence studies to complex fault networks and intraplate settings, including faults in the accretionary prism and outer-rise of subduction zones, which are of particular relevance for tsunami hazard assessment. Such a partnership may also clarify how long-term geological formations, such as surface topography, and other geodynamic features can be used to constrain fault conditions, such as absolute levels of stress.

8.2.5 Combining techniques from data science with physics-based modeling to distinguish characteristics of fault failure processes

Faults accommodate motion through an array of seismic and aseismic modes of deformation, including earthquakes, slow-slip transients, tectonic tremor, and presumably-steady slow slip. The broad distribution of styles of deformation along faults begs the basic question of how to distinguish an isolated slip event on a fault from the series of complex deformation history both on that fault and in its surroundings.

The conditions governing rupture occurrence depend on the collective interaction of different portions of a fault that can be experiencing varying styles of motion. The lack of well-defined distinctions for when individual slip events start and stop can pose challenges for rigorously comparing properties and scaling features of slip phenomena, including their size and duration. In addition, there is great interest in understanding the relationship among different styles of slip events, such as slow-slip transients and earthquakes, as well as distinguishing characteristics among events within these categories. The potential to identify precursory behavior for large earthquakes is of particular interest in the development of early warning systems, especially with reports of slow-slip transients preceding some recent large events, such as the M_W 9.0 2011 Tohoku and M_W 8.1 2014 Iquique earthquakes (Ito et al., 2013; Kato et al., 2012; Ruiz et al., 2014).

Combining techniques from data science with physics-based numerical modeling is a

promising route for characterizing modes of slip on faults and identifying their observational features. Novel techniques in data science, including methods using unsupervised machine learning, have been successful at extracting rupture features from high-dimensional data structures, such as distinguishing directivity modes of earthquake populations without imposing a kinematic rupture model (Ross et al., 2020). Such techniques have so far not been applied to SEAS simulations, which have the capability of producing large time series data of complex slip behavior, as well as synthetic observables such as seismic waveform and geodetic data.

Identifying the distinguishing characteristics of different failure processes on faults is a crucial step required to examine and quantify how various fault features, such as frictional and structural heterogeneity, as well as the presence of fluids and thermal effects, alter fault stability, the interactions among events, and the nucleation of dynamic earthquake ruptures. Such developments have broad applications for natural and induced seismicity, as well as other natural failure phenomena such as landslides and glacial sliding, and the general failure of rocks and materials.

References

Aben, F. M., Brantut, N., Mitchell, T. M., & David, E. C. (2019). Rupture energetics in crustal rock from laboratory-scale seismic tomography. *Geophysical Research Letters*, *46*(13), 7337-7344. doi: 10.1029/2019GL083040

Abercrombie, R. E., & Mori, J. (1996). Occurence patterns of foreshocks to large earthquakes in the western United States. *Nature*, *381*(6580), 303–307. doi: 10.1038/381303a0

Abercrombie, R. E., & Rice, J. R. (2005). Can observations of earthquake scaling constrain slip weakening? *Geophysical Journal International*, *162*, 406-424. doi: 10.1111/j.1365-246X.2005.02579.x

Acosta, M., Passelègue, F. X., Schubnel, A., & Violay, M. (2018). Dynamic weakening during earthquakes controlled by fluid thermodynamics. *Nature Communications*, *9*(1), 3074. doi: 10.1038/s41467-018-05603-9

Adams, M., Twardzik, C., & Ji, C. (2016, 10). Exploring the uncertainty range of coseismic stress drop estimations of large earthquakes using finite fault inversions. *Geophysical Journal International*, *208*(1), 86-100. doi: 10.1093/gji/ggw374

Ader, T. J., Lapusta, N., Avouac, J.-P., & Ampuero, J.-P. (2014). Response of rate-and-state seismogenic faults to harmonic shear-stress perturbations. *Geophysical Journal International*, *198*(1), 385-413. doi: 10.1093/gji/ggu144

Allison, K. L., & Dunham, E. M. (2018). Earthquake cycle simulations with rate-and-state friction and power-law viscoelasticity. *Tectonophysics*, *733*, 232 - 256. doi: 10.1016/j.tecto.2017.10.021

Allmann, B. P., & Shearer, P. M. (2009). Global variations of stress drop for moderate to large earthquakes. *Journal of Geophysical Research: Solid Earth*, *114*(B1). doi: 10.1029/2008JB005821

Ampuero, J.-P., & Ben-Zion, Y. (2008). Cracks, pulses and macroscopic asymmetry of dynamic rupture on a bimaterial interface with velocity-weakening friction. *Geophysical Journal International*, *173*(2), 674-692. doi: 10.1111/j.1365-246X.2008.03736.x

Ampuero, J.-P., & Rubin, A. M. (2008). Earthquake nucleation on rate and state faults: Aging and slip laws. *Journal of Geophysical Research: Solid Earth*, *113*(B1). doi: 10.1029/2007JB005082

Ando, R., & Kaneko, Y. (2018). Dynamic rupture simulation reproduces spontaneous multifault rupture and arrest during the 2016 Mw 7.9 Kaikoura earthquake. *Geophysical Research Letters*, *45*(23), 12,875-12,883. doi: 10.1029/2018GL080550

Andrews, D. J. (2002). A fault constitutive relation accounting for thermal pressurization of pore fluid. *Journal of Geophysical Research: Solid Earth*, *107*(B12).

Andrews, D. J. (2004, 06). Rupture Models with Dynamically Determined Breakdown Displacement. *Bulletin of the Seismological Society of America*, *94*(3), 769-775. doi: 10.1785/0120030142

Andrews, D. J. (2005). Rupture dynamics with energy loss outside the slip zone. *Journal of Geophysical Research*, *110*. doi: 10.1029/2004JB003191

Andrews, D. J., & Ben-Zion, Y. (1997). Wrinkle-like slip pulse on a fault between different materials. *Journal of Geophysical Research: Solid Earth*, *102*(B1), 553-571. doi: 10.1029/96JB02856

Aochi, H., & Ide, S. (2011). Conceptual multi-scale dynamic rupture model for the 2011 off the Pacific coast of Tohoku earthquake. *Earth, Planets and Space*, *63*(7), 46. doi: 10.5047/eps.2011.05.008

Archuleta, R. J. (1984). A faulting model for the 1979 Imperial Valley earthquake. *Journal of Geophysical Research: Solid Earth*, *89*(B6), 4559-4585. doi: 10.1029/JB089iB06p04559

Asano, K., & Iwata, T. (2006). Source process and near-source ground motions of the 2005 West Off Fukuoka Prefecture earthquake. *Earth, Planets and Space*, *58*, 93-98. doi: 10.1186/BF03351920

Asano, K., & Iwata, T. (2016). Source rupture processes of the foreshock and mainshock in the 2016 Kumamoto earthquake sequence estimated from the kinematic waveform inversion of strong motion data. *Earth, Planets and Space*, *68*(1), 147. doi: 10.1186/s40623-016-0519-9

Asano, K., Iwata, T., & Irikura, K. (2005). Estimation of source rupture process and strong ground motion simulation of the 2002 Denali, Alaska earthquake. *Bulletin of the Seismological Society of America*, *95*(5), 1701-1715. doi: 10.1785/0120040154

Bak, P., & Tang, C. (1989). Earthquakes as a self-organized critical phenomenon.

Journal of Geophysical Research: Solid Earth, *94*(B11), 15635-15637. doi: 10.1029/JB094iB11p15635

Bandis, S., Lumsden, A., & Barton, N. (1981). Experimental studies of scale effects on the shear behaviour of rock joints. *International Journal of Rock Mechanics and Mining Sciences & Geomechanics Abstracts*, *18*(1), 1 - 21. doi: https://doi.org/10.1016/0148-9062(81)90262-X

Bangs, N., Moore, G., Gulick, S., Pangborn, E., Tobin, H., Kuramoto, S., & Taira, A. (2009). Broad, weak regions of the Nankai Megathrust and implications for shallow coseismic slip. *Earth and Planetary Science Letters*, *284*(1), 44 - 49.

Barall, M., & Harris, R. A. (2014). Metrics for comparing dynamic earthquake rupture simulations. *Seismological Research Letters*, *86*(1), 223-235. doi: 10.1785/0220140122

Barbot, S., Lapusta, N., & Avouac, J.-P. (2012). Under the hood of the earthquake machine: Toward predictive modeling of the seismic cycle. *Science*, *336*(6082), 707-710.

Barras, F., Aldam, M., Roch, T., Brener, E. A., Bouchbinder, E., & Molinari, J.-F. (2019, Nov). Emergence of cracklike behavior of frictional rupture: The origin of stress drops. *Physical Review X*, *9*, 041043. doi: 10.1103/PhysRevX.9.041043

Beeler, N. M., Wong, T. F., & Hickman, S. H. (2003). On the expected relationships among apparent stress, static stress drop, effective shear fracture energy, and efficiency. *Bulletin of the Seismological Society of America*, *93*(3), 1381-1389.

Behr, W. M., & Platt, J. P. (2014). Brittle faults are weak, yet the ductile middle crust is strong: Implications for lithospheric mechanics. *Geophysical Research Letters*, *41*(22), 8067-8075. doi: https://doi.org/10.1002/2014GL061349

Ben-David, O., Cohen, G., & Fineberg, J. (2010). The dynamics of the onset of frictional slip. *Science*, *330*(6001), 211–214. doi: 10.1126/science.1194777

Ben-David, O., Rubinstein, S. M., & Fineberg, J. (2010). Slip-stick and the evolution of frictional strength. *Nature*, *463*(7277), 76–79. doi: 10.1038/nature08676

Ben-Zion, Y., & Rice, J. R. (1995). Slip patterns and earthquake populations along different classes of faults in elastic solids. *Journal of Geophysical Research: Solid Earth*, *100*(B7), 12959-12983. doi: 10.1029/94JB03037

Ben-Zion, Y., & Rice, J. R. (1997). Dynamic simulations of slip on a smooth fault in an

elastic solid. *Journal of Geophysical Research: Solid Earth*, *102*(B8), 17771-17784. doi: 10.1029/97JB01341

Beroza, G. C., & Mikumo, T. (1996). Short slip duration in dynamic rupture in the presence of heterogeneous fault properties. *Journal of Geophysical Research: Solid Earth*, *101*(B10), 22449-22460. doi: 10.1029/96JB02291

Bhattacharya, P., Rubin, A. M., Bayart, E., Savage, H. M., & Marone, C. (2015). Critical evaluation of state evolution laws in rate and state friction: Fitting large velocity steps in simulated fault gouge with time-, slip-, and stress-dependent constitutive laws. *Journal of Geophysical Research: Solid Earth*, *120*(9), 6365-6385. doi: 10.1002/2015JB012437

Bhattacharya, P., Rubin, A. M., & Beeler, N. M. (2017). Does fault strengthening in laboratory rock friction experiments really depend primarily upon time and not slip? *Journal of Geophysical Research: Solid Earth*, *122*(8), 6389-6430. doi: 10.1002/2017JB013936

Bhattacharya, P., & Viesca, R. C. (2019). Fluid-induced aseismic fault slip outpaces pore-fluid migration. *Science*, *364*(6439), 464–468. doi: 10.1126/science.aaw7354

Bizzarri, A., & Cocco, M. (2006). A thermal pressurization model for the spontaneous dynamic rupture propagation on a three-dimensional fault: 1. Methodological approach. *Journal of Geophysical Research: Solid Earth*, *111*(B5). doi: 10.1029/2005JB003862

Bletery, Q., Sladen, A., Jiang, J., & Simons, M. (2016). A bayesian source model for the 2004 great Sumatra-Andaman earthquake. *Journal of Geophysical Research: Solid Earth*, *121*(7), 5116-5135. doi: https://doi.org/10.1002/2016JB012911

Boatwright, J., & Choy, G. L. (1986). Teleseismic estimates of the energy radiated by shallow earthquakes. *Journal of Geophysical Research: Solid Earth*, *91*(B2), 2095-2112. doi: 10.1029/JB091iB02p02095

Bolt, B. A. (1986). Seismic energy release over a broad frequency band. *Pure and Applied Geophysics*, *124*, 919-930. doi: 10.1007/BF00879618

Bouchon, M. (1997). The state of stress on some faults of the san andreas system as inferred from near-field strong motion data. *Journal of Geophysical Research: Solid Earth*,

102(B6), 11731-11744. doi: 10.1029/97JB00623

Bouchon, M., & Karabulut, H. (2008). The aftershock signature of supershear earthquakes. *Science*, *320*(5881), 1323–1325. doi: 10.1126/science.1155030

Bouchon, M., Karabulut, H., Aktar, M., Özalaybey, S., Schmittbuhl, J., & Bouin, M.-P. (2011). Extended nucleation of the 1999 Mw 7.6 Izmit Earthquake. *Science*, *331*(6019), 877–880. doi: 10.1126/science.1197341

Bouchon, M., Sekiguchi, H., Irikura, K., & Iwata, T. (1998). Some characteristics of the stress field of the 1995 Hyogo-ken Nanbu (Kobe) earthquake. *Journal of Geophysical Research: Solid Earth*, *103*(B10), 24271-24282. doi: 10.1029/98JB02136

Brantut, N., Garagash, D. I., & Noda, H. (2019). Stability of pulse-like earthquake ruptures. *Journal of Geophysical Research: Solid Earth*, *124*(8), 8998-9020. doi: 10.1029/2019JB017926

Brantut, N., & Viesca, R. C. (2017). The fracture energy of ruptures driven by flash heating. *Geophysical Research Letters*, *44*(13), 6718-6725. doi: 10.1002/2017GL074110

Brodsky, E. E., & Kanamori, H. (2001). Elastohydrodynamic lubrication of faults. *Journal of Geophysical Research: Solid Earth*, *106*(B8), 16357-16374.

Brodsky, E. E., Kirkpatrick, J. D., & Candela, T. (2016, 01). Constraints from fault roughness on the scale-dependent strength of rocks. *Geology*, *44*(1), 19-22. doi: 10.1130/G37206.1

Brown, K., Kopf, A., Underwood, M., & Weinberger, J. (2003). Compositional and fluid pressure controls on the state of stress on the Nankai subduction thrust: A weak plate boundary. *Earth and Planetary Science Letters*, *214*(3), 589 - 603.

Brune, J. N., Henyey, T. L., & Roy, R. F. (1969). Heat flow, stress, and rate of slip along the San Andreas Fault, California. *Journal of Geophysical Research*, *74*(15), 3821-3827.

Burridge, R., & Knopoff, L. (1967). Model and theoretical seismicity. *Bulletin of the Seismological Society of America*, *57*(3), 341-371.

Byerlee, J. (1978). Friction of rocks. *Pure and Applied Geophysics*, *116*(4-5), 615-626. doi: 10.1007/BF00876528

Carslaw, A. R., & Jaeger, C. J. (1959). *Conduction of Heat in Solids*. Oxford.

Cattania, C. (2019). Complex earthquake sequences on simple faults. *Geophysical Research*

Letters, *46*(17-18), 10384-10393. doi: 10.1029/2019GL083628

Causse, M., Dalguer, L. A., & Mai, P. M. (2013, 12). Variability of dynamic source parameters inferred from kinematic models of past earthquakes. *Geophysical Journal International*, *196*(3), 1754-1769. doi: 10.1093/gji/ggt478

Chen, J., Verberne, B. A., & Spiers, C. J. (2015a). Effects of healing on the seismogenic potential of carbonate fault rocks: Experiments on samples from the Longmenshan Fault, Sichuan, China. *Journal of Geophysical Research: Solid Earth*, *120*(8), 5479-5506. doi: https://doi.org/10.1002/2015JB012051

Chen, J., Verberne, B. A., & Spiers, C. J. (2015b). Interseismic re-strengthening and stabilization of carbonate faults by "non-Dieterich" healing under hydrothermal conditions. *Earth and Planetary Science Letters*, *423*, 1 - 12. doi: https://doi.org/10.1016/j.epsl.2015.03.044

Chen, K., Avouac, J.-P., Aati, S., Milliner, C., Zheng, F., & Shi, C. (2020). Cascading and pulse-like ruptures during the 2019 Ridgecrest earthquakes in the Eastern California Shear Zone. *Nature Communications*, *11*(1), 22. doi: 10.1038/s41467-019-13750-w

Chen, T., & Lapusta, N. (2009). Scaling of small repeating earthquakes explained by interaction of seismic and aseismic slip in a rate and state fault model. *Journal of Geophysical Research*, *114*. doi: 10.1029/2008JB005749

Chester, F. M., & Chester, J. S. (1998). Ultracataclasite structure and friction processes of the Punchbowl fault, San Andreas system, California. *Tectonophysics*, *295*(1), 199 - 221. doi: https://doi.org/10.1016/S0040-1951(98)00121-8

Chester, J. S., Chester, F. M., & Kronenberg, A. K. (2005). Fracture surface energy of the Punchbowl Fault, San Andreas system. *Nature*, *437*(7055), 133.

Choy, G. L., & Boatwright, J. (2004). Radiated energy and the rupture process of the Denali Fault earthquake sequence of 2002 from broadband teleseismic body waves. *Bulletin of the Seismological Society of America*, *94*(6B), S269-S277. doi: 10.1785/0120040605

Choy, G. L., & Boatwright, J. (2009). Differential energy radiation from two earthquakes in Japan with identical Mw: The Kyushu 1996 and Tottori 2000 earthquakes. *Bulletin of the Seismological Society of America*, *99*(3), 1815-1826. doi: 10.1785/0120080078

Choy, G. L., & Boatwright, J. L. (1995). Global patterns of radiated seismic energy and

apparent stress. *Journal of Geophysical Research: Solid Earth*, *100*(B9), 18205-18228. doi: 10.1029/95JB01969

Cocco, M., & Bizzarri, A. (2002). On the slip-weakening behavior of rate- and state dependent constitutive laws. *Geophysical Research Letters*, *29*(11). doi: 10.1029/2001GL013999

Cocco, M., Bizzarri, A., & Tinti, E. (2004). Physical interpretation of the breakdown process using a rate-and state-dependent friction law. *Tectonophysics*, *378*(3-4), 241-262.

Cocco, M., & Tinti, E. (2008). Scale dependence in the dynamics of earthquake propagation: Evidence from seismological and geological observations. *Earth and Planetary Science Letters*, *273*(1), 123 - 131. doi: https://doi.org/10.1016/j.epsl.2008.06.025

Cochard, A., & Madariaga, R. (1994). Dynamic faulting under rate-dependent friction. *Pure and Applied Geophysics*, *142*, 419-445. doi: 10.1007/BF00876049

Collettini, C., Niemeijer, A., Viti, C., & Marone, C. (2009). Fault zone fabric and fault weakness. *Nature*, *462*(7275), 907–910. doi: 10.1038/nature08585

Cruz-Atienza, V. M., Olsen, K. B., & Dalguer, L. A. (2009, 12). Estimation of the breakdown slip from strong-motion seismograms: Insights from numerical experiments. *Bulletin of the Seismological Society of America*, *99*(6), 3454-3469. doi: 10.1785/0120080330

Dahlen, F. A. (1977). The balance of energy in earthquake faulting. *Geophysical Journal of the Royal Astronomical Society*, *48*(2), 239-261. doi: 10.1111/j.1365-246X.1977.tb01298.x

Dalguer, L. A., Wu, H., Matsumoto, Y., Irikura, K., Takahama, T., & Tonagi, M. (2020). Development of dynamic asperity models to predict surface fault displacement caused by earthquakes. *Pure and Applied Geophysics*, *177*(5), 1983–2006. doi: 10.1007/s00024-019-02255-8

Dal Zilio, L., Lapusta, N., & Avouac, J.-P. (2020). Unraveling scaling properties of slow-slip events. *Geophysical Research Letters*, *47*(10), e2020GL087477. doi: https://doi.org/10.1029/2020GL087477

Dal Zilio, L., van Dinther, Y., Gerya, T. V., & Pranger, C. C. (2018). Seismic behaviour of mountain belts controlled by plate convergence rate. *Earth and Planetary Science*

Letters, *482*, 81-92. doi: https://doi.org/10.1016/j.epsl.2017.10.053

Day, S. M. (1982). Three-dimensional finite difference simulation of fault dynamics: Rectangular faults with fixed rupture velocity. *Bulletin of the Seismological Society of America*, *72*(3), 705-727.

Day, S. M., Dalguer, L. A., Lapusta, N., & Liu, Y. (2005). Comparison of finite difference and boundary integral solutions to three-dimensional spontaneous rupture. *Journal of Geophysical Research: Solid Earth*, *110*(B12). doi: 10.1029/2005JB003813

De Paola, N., Holdsworth, R. E., Viti, C., Collettini, C., & Bullock, R. (2015). Can grain size sensitive flow lubricate faults during the initial stages of earthquake propagation? *Earth and Planetary Science Letters*, *431*, 48 - 58. doi: https://doi.org/10.1016/j.epsl.2015.09.002

Di Toro, G., Goldsby, D. L., & Tullis, T. E. (2004). Friction falls towards zero in quartz rock as slip velocity approaches seismic rates. *Nature*, *427*(6973), 436–439. doi: 10.1038/nature02249

Di Toro, G., Han, R., Hirose, T., De Paola, N., Nielsen, S., Mizoguchi, K., . . . Shimamoto, T. (2011). Fault lubrication during earthquakes. *Nature*, *471*, 494.

Dielforder, A. (2017). Constraining the strength of megathrusts from fault geometries and application to the Alpine collision zone. *Earth and Planetary Science Letters*, *474*, 49-58. doi: https://doi.org/10.1016/j.epsl.2017.06.021

Dielforder, A., Hetzel, R., & Oncken, O. (2020). Megathrust shear force controls mountain height at convergent plate margins. *Nature*, *582*(7811), 225-229. doi: 10.1038/s41586-020-2340-7

Dieterich, J. H. (1979). Modeling of rock friction 1. Experimental results and constitutive equations. *Journal of Geophysical Research*, *84*(B5), 2161-2168.

Dieterich, J. H. (2007). Applications of rate- and state-dependent friction to models of fault slip and earthquake occurrence. In G. Schubert (Ed.), *Treatise on geophysics* (p. 107 - 129). Amsterdam: Elsevier. doi: https://doi.org/10.1016/B978-044452748-6.00065-1

Dieterich, J. H., & Kilgore, B. D. (1994). Direct observation of frictional contacts: New insights for state-dependent properties. *Pure and Applied Geophysics*, *143*, 283?302.

doi: 10.1007/BF00874332

Doser, D. I., Baker, M. R., & Mason, D. B. (1991). Seismicity in the War-Wink gas field, Delaware Basin, west Texas, and its relationship to petroleum production. *Bulletin of the Seismological Society of America*, *81*(3), 971-986.

Douilly, R., Aochi, H., Calais, E., & Freed, A. M. (2015). Three-dimensional dynamic rupture simulations across interacting faults: The Mw 7.0, 2010, Haiti earthquake. *Journal of Geophysical Research: Solid Earth*, *120*(2), 1108-1128. doi: 10.1002/2014JB011595

Duan, B., & Oglesby, D. D. (2006). Heterogeneous fault stresses from previous earthquakes and the effect on dynamics of parallel strike-slip faults. *Journal of Geophysical Research: Solid Earth*, *111*(B5). doi: 10.1029/2005JB004138

Dunham, E. M., Belanger, D., Cong, L., & Kozdon, J. E. (2011a). Earthquake ruptures with strongly rate-weakening friction and off-fault plasticity, Part 1: Planar faults. *Bulletin of the Seismological Society of America*, *101*(5), 2296-2307. doi: 10.1785/0120100075

Dunham, E. M., Belanger, D., Cong, L., & Kozdon, J. E. (2011b). Earthquake ruptures with strongly rate-weakening friction and off-fault plasticity, Part 2: Nonplanar faults. *The Bulletin of the Seismological Society of America*, *101*, 2308-2322. doi: 10.1785/0120100076

Duputel, Z., Jiang, J., Jolivet, R., Simons, M., Rivera, L., Ampuero, J.-P., ... Minson, S. E. (2015). The Iquique earthquake sequence of April 2014: Bayesian modeling accounting for prediction uncertainty. *Geophysical Research Letters*, *42*(19), 7949-7957. doi: https://doi.org/10.1002/2015GL065402

Eaton, D. W., & Mahani, A. B. (2015, 06). Focal mechanisms of some inferred induced earthquakes in Alberta, Canada. *Seismological Research Letters*, *86*(4), 1078-1085. doi: 10.1785/0220150066

Ellsworth, W. L. (2013). Injection-induced earthquakes. *Science*, *341*(6142). doi: 10.1126/science.1225942

Erickson, B. A., & Day, S. M. (2016). Bimaterial effects in an earthquake cycle model using rate-and-state friction. *Journal of Geophysical Research: Solid Earth*, *121*(4),

2480-2506. doi: 10.1002/2015JB012470

Erickson, B. A., & Dunham, E. M. (2014). An efficient numerical method for earthquake cycles in heterogeneous media: Alternating subbasin and surface-rupturing events on faults crossing a sedimentary basin. *Journal of Geophysical Research: Solid Earth*, *119*(4), 3290-3316. doi: 10.1002/2013JB010614

Erickson, B. A., Dunham, E. M., & Khosravifar, A. (2017). A finite difference method for off-fault plasticity throughout the earthquake cycle. *Journal of the Mechanics and Physics of Solids*, *109*, 50 - 77. doi: https://doi.org/10.1016/j.jmps.2017.08.002

Erickson, B. A., Jiang, J., Barall, M., Lapusta, N., Dunham, E. M., Harris, R., ... Wei, M. (2020). The community code verification exercise for simulating sequences of earthquakes and aseismic slip (SEAS). *Seismological Research Letters*, *91*(2A), 874–890. doi: 10.1785/0220190248

Fang, Z., & Dunham, E. M. (2013). Additional shear resistance from fault roughness and stress levels on geometrically complex faults. *Journal of Geophysical Research: Solid Earth*, *118*(7), 3642-3654. doi: 10.1002/jgrb.50262

Faulkner, D. R., Mitchell, T. M., Behnsen, J., Hirose, T., & Shimamoto, T. (2011). Stuck in the mud? Earthquake nucleation and propagation through accretionary forearcs. *Geophysical Research Letters*, *38*(18). doi: https://doi.org/10.1029/2011GL048552

Faulkner, D. R., Mitchell, T. M., Healy, D., & Heap, M. J. (2006). Slip on 'weak' faults by the rotation of regional stress in the fracture damage zone. *Nature*, *444*(7121), 922–925. doi: 10.1038/nature05353

Faulkner, D. R., Sanchez-Roa, C., Boulton, C., & den Hartog, S. A. M. (2018). Pore fluid pressure development in compacting fault gouge in theory, experiments, and nature. *Journal of Geophysical Research: Solid Earth*, *123*(1), 226-241. doi: https://doi.org/10.1002/2017JB015130

Fay, N., & Humphreys, E. (2006). Dynamics of the Salton block: Absolute fault strength and crust-mantle coupling in Southern California. *Geology*, *34*(4), 261-264. doi: 10.1130/G22172.1

Feignier, B., & Grasso, J. (1990). Seismicity induced by a gas-production: I. Correlation of focal mechanisms and dome structure. *Pure and Applied Geophysics*, *134*(3),

405-426. doi: 10.1007/BF00878740

Fialko, Y., Rivera, L., & Kanamori, H. (2005). Estimate of differential stress in the upper crust from variations in topography and strike along the San Andreas fault. *Geophysical Journal International*, *160*(2), 527-532. doi: 10.1111/j.1365-246X .2004.02511.x

Field, E. H. (2019). How physics based earthquake simulators might help improve earthquake forecasts. *Seismological Research Letters*, *90*(2A), 467-472. doi: 10.1785/0220180299

Field, E. H., Biasi, G., Bird, P., Dawson, T., Felzer, K.R., ... Zeng, Y. (2013). Uniform California Earthquake Rupture Forecast, version 3 (UCERF3): The time-independent model. *U.S. Geological Survey Open-File Report 2013-1165, 97 p., California Geological Survey Special Report 228*. doi: http://pubs.usgs.gov/of/2013/1165/

Field, E. H., Jordan, T. H., Page, M. T., Milner, K. R., Shaw, B. E., Dawson, T. E., ... Thatcher, W. R. (2017). A synoptic view of the third Uniform California Earthquake Rupture Forecast (UCERF3). *Seismological Research Letters*, *88*(5), 1259-1267. doi: 10.1785/0220170045

Fineberg, J., & Bouchbinder, E. (2015). Recent developments in dynamic fracture: Some perspectives. *International Journal of Fracture*, *196*(1), 33–57. doi: 10.1007/s10704 -015-0038-x

Freund, L. B. (1990). *Dynamic fracture mechanics*. Cambridge University Press. doi: 10.1017/CBO9780511546761

Frohlich, C., DeShon, H., Stump, B., Hayward, C., Hornbach, M., & Walter, J. (2016). A historical review of induced earthquakes in Texas. *Seismological Review Letters*, *87*. doi: 10.1785/0220160016

Frohlich, C., Ellsworth, W., Brown, W. A., Brunt, M., Luetgert, J., MacDonald, T., & Walter, S. (2014). The 17 May 2012 M4.8 earthquake near Timpson, East Texas: An event possibly triggered by fluid injection. *Journal of Geophysical Research: Solid Earth*, *119*(1), 581-593. doi: 10.1002/2013JB010755

Frohlich, C., Hayward, C., Stump, B., & Potter, E. (2011). The Dallas-Fort Worth earthquake sequence: October 2008 through May 2009. *The Bulletin of the Seismological Society*

of America, *101*, 327-340. doi: 10.1785/0120100131

Fukuyama, E., & Mizoguchi, K. (2010). Constitutive parameters for earthquake rupture dynamics based on high-velocity friction tests with variable slip rate. *International Journal of Fracture*, *163*(1), 15–26. doi: 10.1007/s10704-009-9417-5

Fulton, P. M., Brodsky, E. E., Kano, Y., Mori, J., Chester, F., Ishikawa, T., . . . Scientists, K.-. (2013). Low coseismic friction on the Tohoku-Oki fault determined from temperature measurements. *Science*, *342*(6163), 1214–1217. doi: 10.1126/science.1243641

Gabriel, A.-A., Ampuero, J.-P., Dalguer, L. A., & Mai, P. M. (2012). The transition of dynamic rupture styles in elastic media under velocity-weakening friction. *Journal of Geophysical Research: Solid Earth*, *117*(B9). doi: 10.1029/2012JB009468

Galetzka, J., Melgar, D., Genrich, J. F., Geng, J., Owen, S., Lindsey, E. O., . . . Maharjan, N. (2015). Slip pulse and resonance of the Kathmandu basin during the 2015 Gorkha earthquake, Nepal. *Science*, *349*(6252), 1091–1095. doi: 10.1126/science.aac6383

Gallovic, F., Valentova, L., Ampuero, J.-P., & Gabriel, A.-A. (2019). Bayesian dynamic finite-fault inversion: 2. Application to the 2016 Mw 6.2 Amatrice, Italy, Earthquake. *Journal of Geophysical Research: Solid Earth*, *124*(7), 6970-6988. doi: 10.1029/2019JB017512

Galvez, P., Ampuero, J.-P., Dalguer, L. A., Somala, S. N., & Nissen-Meyer, T. (2014). Dynamic earthquake rupture modelled with an unstructured 3-D spectral element method applied to the 2011 M9 Tohoku earthquake. *Geophysical Journal International*, *198*(2), 1222-1240. doi: 10.1093/gji/ggu203

Gao, X., & Wang, K. (2014). Strength of stick-slip and creeping subduction megathrusts from heat flow observations. *Science*, *345*(6200), 1038-1041. doi: 10.1126/science.1255487

Goldsby, D. L., & Tullis, T. E. (2002). Low frictional strength of quartz rocks at subseismic slip rates. *Geophysical Research Letters*, *29*(17), 25-1-25-4. doi: 10.1029/2002GL015240

Goldsby, D. L., & Tullis, T. E. (2011). Flash heating leads to low frictional strength of crustal rocks at earthquake slip rates. *Science*, *334*(6053), 216–218. doi: 10.1126/science.1207902

Gori, M., Rubino, V., Rosakis, A. J., & Lapusta, N. (2018). Pressure shock fronts formed by ultra-fast shear cracks in viscoelastic materials. *Nature Communications*, *9*(1), 4754. doi: 10.1038/s41467-018-07139-4

Grasso, J. R., & Feignier, B. (1989). Seismicity induced by gas-production: 2. Lithology correlated events, induced stresses and deformation. *Pure and Applied Geophysics*, *134*, 427-450. doi: 10.1007/BF00878741

Grasso, J. R., & Wittlinger, G. (1990). Ten years of seismic monitoring over a gas field. *Bulletin of the Seismological Society of America*, *80*(2), 450-473.

Greer, J. R., Oliver, W. C., & Nix, W. D. (2005). Size dependence of mechanical properties of gold at the micron scale in the absence of strain gradients. *Acta Materialia*, *53*(6), 1821 - 1830. doi: https://doi.org/10.1016/j.actamat.2004.12.031

Gu, J.-C., Rice, J. R., Ruina, A. L., & Tse, S. T. (1984). Slip motion and stability of a single degree of freedom elastic system with rate and state dependent friction. *Journal of the Mechanics and Physics of Solids*, *32*(3), 167 - 196. doi: https://doi.org/10.1016/0022-5096(84)90007-3

Guatteri, M., & Spudich, P. (2000). What can strong-motion data tell us about slip-weakening fault-friction laws? *Bulletin of the Seismological Society of America*, *90*(1), 98-116. doi: 10.1785/0119990053

Guglielmi, Y., Cappa, Frédéric, Avouac, J.-P., Henry, P., & Elsworth, D. (2015). Seismicity triggered by fluid injection-induced aseismic slip. *Science*, *348*(6240), 1224–1226. doi: 10.1126/science.aab0476

Guyoton, F., Grasso, J.-R., & Volant, P. (1992). Interrelation between induced seismic instabilities and complex geological structure. *Geophysical Research Letters*, *19*(7), 705-708. doi: 10.1029/92GL00359

Hamling, I. J., Hreinsdóttir, S., Clark, K., Elliott, J., Liang, C., Fielding, E., . . . Stirling, M. (2017). Complex multifault rupture during the 2016 Mw 7.8 Kaikoura earthquake, New Zealand. *Science*, *356*(6334). doi: 10.1126/science.aam7194

Han, R., Shimamoto, T., Ando, J.-i., & Ree, J.-H. (2007). Seismic slip record in carbonate-bearing fault zones: An insight from high-velocity friction experiments on siderite gouge. *Geology*, *35*(12), 1131-1134.

Hardebeck, J. L. (2015). Stress orientations in subduction zones and the strength of subduction megathrust faults. *Science*, *349*(6253), 1213–1216. doi: 10.1126/science .aac5625

Hardebeck, J. L., & Hauksson, E. (1999). Role of fluids in faulting inferred from stress field signatures. *Science*, *285*(5425), 236–239. doi: 10.1126/science.285.5425.236

Hardebeck, J. L., & Hauksson, E. (2001). Crustal stress field in Southern California and its implications for fault mechanics. *Journal of Geophysical Research: Solid Earth*, *106*(B10), 21859-21882. doi: https://doi.org/10.1029/2001JB000292

Harris, R., Archuleta, R. J., & Day, S. M. (1991). Fault steps and the dynamic rupture process: 2-D numerical simulations of a spontaneously propagating shear fracture. *Geophysical Research Letters*, *18*(5), 893-896. doi: 10.1029/91GL01061

Harris, R., Barall, M., Aagaard, B., Ma, S., Roten, D., Olsen, K., ... Dalguer, L. (2018). A suite of exercises for verifying dynamic earthquake rupture codes. *Seismological Research Letters*, *89*(3), 1146-1162. doi: 10.1785/0220170222

Harris, R., Barall, M., Archuleta, R., Dunham, E., Aagaard, B., Ampuero, J. P., ... Templeton, E. (2009). The SCEC/USGS dynamic earthquake rupture code verification exercise. *Seismological Research Letters*, *80*. doi: 10.1785/gssrl.80.1.119

Harris, R., & Day, S. M. (1993). Dynamics of fault interaction: Parallel strike-slip faults. *Journal of Geophysical Research: Solid Earth*, *98*(B3), 4461-4472. doi: 10.1029/92JB02272

Harris, R., & Day, S. M. (1999). Dynamic 3D simulations of earthquakes on en echelon faults. *Geophysical Research Letters*, *26*(14), 2089-2092. doi: 10.1029/1999GL900377

Hauksson, E., Yang, W., & Shearer, P. M. (2012). Waveform relocated earthquake catalog for Southern California (1981 to June 2011). *Bulletin of the Seismological Society of America*, *102*(5), 2239-2244. doi: 10.1785/0120120010

Healy, J. H., Rubey, W. W., Griggs, D. T., & Raleigh, C. B. (1968). The Denver earthquakes. *Science*, *161*(3848), 1301–1310. doi: 10.1126/science.161.3848.1301

Heaton, T. H. (1990). Evidence for and implications of self-healing pulses of slip in earthquake rupture. *Physics of the Earth and Planetary Interiors*, *64*(1), 1-20.

Henyey, T. L., & Wasserburg, G. J. (1971). Heat flow near major strike-slip faults in California. *Journal of Geophysical Research (1896-1977)*, *76*(32), 7924-7946. doi: 10.1029/JB076i032p07924

Hickman, S., & Zoback, M. (2004). Stress orientations and magnitudes in the SAFOD pilot hole. *Geophysical Research Letters*, *31*(15).

Horton, S. (2012). Disposal of hydrofracking waste fluid by injection into subsurface aquifers triggers earthquake swarm in Central Arkansas with potential for damaging earthquake. *Seismological Research Letters*, *83*(2), 250-260. doi: 10.1785/gssrl.83.2 .250

Hough, S. E., & Bilham, R. (2018). Revisiting earthquakes in the Los Angeles, California, basin during the early instrumental period: Evidence for an association with oil production. *Journal of Geophysical Research: Solid Earth*, *123*(12), 10,684-10,705. doi: 10.1029/2017JB014616

Hough, S. E., Tsai, V. C., Walker, R., & Aminzadeh, F. (2017). Was the Mw 7.5 1952 Kern County, California, earthquake induced (or triggered)? *Journal of Seismology*, *21*, 1613-1621. doi: 10.1007/s10950-017-9685-x

Hsieh, P. A., & Bredehoeft, J. D. (1981). A reservoir analysis of the Denver earthquakes: A case of induced seismicity. *Journal of Geophysical Research: Solid Earth*, *86*(B2), 903-920. doi: 10.1029/JB086iB02p00903

Hu, F., Zhang, Z., & Chen, X. (2016). Investigation of earthquake jump distance for strike-slip step overs based on 3-D dynamic rupture simulations in an elastic half-space. *Journal of Geophysical Research: Solid Earth*, *121*(2), 994-1006. doi: 10.1002/2015JB012696

Hulikal, S., Bhattacharya, K., & Lapusta, N. (2015). Collective behavior of viscoelastic asperities as a model for static and kinetic friction. *Journal of the Mechanics and Physics of Solids*, *76*, 144 - 161. doi: https://doi.org/10.1016/j.jmps.2014.10.008

Husseini, M. I., & Randall, M. J. (1976). Rupture velocity and radiation efficiency. *Bulletin of the Seismological Society of America*, *66*(4), 1173-1187.

Ida, Y. (1972). Cohesive force across the tip of a longitudinal-shear crack and Griffith's specific surface energy. *Journal of Geophysical Research*, *77*(20), 3796-3805.

Ide, S., & Aochi, H. (2005). Earthquakes as multiscale dynamic ruptures with heterogeneous fracture surface energy. *Journal of Geophysical Research: Solid Earth*, *110*(B11). doi: 10.1029/2004JB003591

Ide, S., Baltay, A., & Beroza, G. C. (2011). Shallow dynamic overshoot and energetic deep rupture in the 2011 Mw 9.0 Tohoku-Oki earthquake. *Science*. doi: 10.1126/science.1207020

Ide, S., & Beroza, G. C. (2001). Does apparent stress vary with earthquake size? *Geophysical Research Letters*, *28*(17), 3349-3352.

Ide, S., & Takeo, M. (1997). Determination of constitutive relations of fault slip based on seismic wave analysis. *Journal of Geophysical Research: Solid Earth*, *102*(B12), 27379-27391. doi: 10.1029/97JB02675

Ikari, M. J., Marone, C., & Saffer, D. M. (2011). On the relation between fault strength and frictional stability. *Geology*, *39*(1), 83-86. doi: 10.1130/G31416.1

Ishibe, T., & Shimazaki, K. (2012). Characteristic earthquake model and seismicity around late quaternary archive faults in Japan. *Bulletin of the Seismological Society of America*, *102*(3), 1041-1058. doi: 10.1785/0120100250

Ishii, M., Shearer, P. M., Houston, H., & Vidale, J. E. (2005). Extent, duration and speed of the 2004 Sumatra-Andaman earthquake imaged by the Hi-Net array. *Nature*, *435*(7044), 933–936. doi: 10.1038/nature03675

Ito, Y., Hino, R., Kido, M., Fujimoto, H., Osada, Y., Inazu, D., . . . Ashi, J. (2013). Episodic slow slip events in the Japan subduction zone before the 2011 Tohoku-Oki earthquake. *Tectonophysics*, *600*, 14-26. doi: https://doi.org/10.1016/j.tecto.2012.08.022

Jaeger, J., & Cook, N. (1976). *Fundamentals of rock mechanics*. London, UK: Chapman and Hall.

Jeffreys, H. (1959). *The Earth: Its origin, history, and physical constitution*. Cambridge, UK: Cambridge University Press.

Ji, C., Wald, D. J., & Helmberger, D. V. (2002). Source description of the 1999 Hector Mine, California, earthquake, part II: Complexity of slip history. *Bulletin of the Seismological Society of America*, *92*(4), 1208-1226. doi: 10.1785/0120000917

Jiang, J., & Lapusta, N. (2016). Deeper penetration of large earthquakes on seismically

quiescent faults. *Science*, *352*(6291), 1293–1297. doi: 10.1126/science.aaf1496

Johnson, E. (1992). The influence of the lithospheric thickness on bilateral slip. *Geophysical Journal International*, *108*(1), 151-160. doi: 10.1111/j.1365-246X.1992.tb00846.x

Jones, L. M., Bernknopf, R., Cox, D., Goltz, J., Hudnut, K., Mileti, D., . . . Wein, A. (2008). The ShakeOut scenario. *U.S. Geological Survey Open-File Report 2008-1150 and California Geological Survey Preliminary Report 25*. doi: http://pubs.usgs.gov/of/2008/1150/

Kagan, Y. Y., Jackson, D. D., & Geller, R. J. (2012). Characteristic earthquake model, 1884−2011, RIP. *Seismological Research Letters*, *83*(6), 951-953. doi: 10.1785/0220120107

Kame, N., Rice, J. R., & Dmowska, R. (2003). Effects of prestress state and rupture velocity on dynamic fault branching. *Journal of Geophysical Research: Solid Earth*, *108*(B5). doi: 10.1029/2002JB002189

Kanamori, H. (1994). Mechanics of earthquakes. *Annual Review of Earth and Planetary Sciences*, *22*(1), 207-237. doi: 10.1146/annurev.ea.22.050194.001231

Kanamori, H., & Brodsky, E. E. (2004). The physics of earthquakes. *Reports on Progress in Physics*, *67*(8), 1429-1496. doi: 10.1088/0034-4885/67/8/R03

Kanamori, H., & Heaton, T. H. (2000). Geocomplexity and the physics of earthquakes. In *Microscopic and macroscopic physics of earthquakes* (p. 147-163). doi: 10.1029/GM120p0147

Kanamori, H., & Rivera, L. (2013). Energy partitioning during an earthquake. In *Earthquakes: Radiated energy and the physics of faulting* (p. 3-13). American Geophysical Union (AGU). doi: 10.1029/170GM03

Kanamori, H., & Ross, Z. E. (2019). Reviving mB. *Geophysical Journal International*, *216*(3), 1798-1816. doi: 10.1093/gji/ggy510

Kanamori, H., Ross, Z. E., & Rivera, L. (2020). Estimation of radiated energy using the KiK-net downhole records - Old method for modern data. *Geophysical Journal International*. doi: 10.1093/gji/ggaa040

Kaneko, Y., Avouac, J.-P., & Lapusta, N. (2010). Towards inferring earthquake patterns from geodetic observations of interseismic coupling. *Nature Geoscience*, *3*, 363-369.

doi: 10.1038/NGEO843

Kaneko, Y., Fukuyama, E., & Hamling, I. J. (2017). Slip-weakening distance and energy budget inferred from near-fault ground deformation during the 2016 Mw 7.8 Kaikura earthquake. *Geophysical Research Letters*, *44*(10), 4765-4773. doi: 10.1002/2017GL073681

Kaneko, Y., & Lapusta, N. (2008). Variability of earthquake nucleation in continuum models of rate-and-state faults and implications for aftershock rates. *Journal of Geophysical Research*, *113*, B12312. doi: 10.1029/2007JB005154

Kato, A., Fukuda, J., Nakagawa, S., & Obara, K. (2016). Foreshock migration preceding the 2016 Mw 7.0 Kumamoto earthquake, Japan. *Geophysical Research Letters*, *43*(17), 8945-8953. doi: https://doi.org/10.1002/2016GL070079

Kato, A., Obara, K., Igarashi, T., Tsuruoka, H., Nakagawa, S., & Hirata, N. (2012). Propagation of slow slip leading up to the 2011 Mw 9.0 Tohoku-Oki earthquake. *Science*, *335*(6069), 705–708. doi: 10.1126/science.1215141

Ke, C.-Y., McLaskey, G. C., & Kammer, D. S. (2018). Rupture termination in laboratory-generated earthquakes. *Geophysical Research Letters*, *45*(23), 12,784-12,792. doi: https://doi.org/10.1029/2018GL080492

Keranen, K. M., Savage, H. M., Abers, G. A., & Cochran, E. S. (2013). Potentially induced earthquakes in Oklahoma, USA: Links between wastewater injection and the 2011 Mw 5.7 earthquake sequence. *Geology*, *41*(6), 699-702. doi: 10.1130/G34045.1

Keranen, K. M., & Weingarten, M. (2018). Induced seismicity. *Annual Review of Earth and Planetary Sciences*, *46*(1), 149-174. doi: 10.1146/annurev-earth-082517-010054

Keranen, K. M., Weingarten, M., Abers, G. A., Bekins, B. A., & Ge, S. (2014). Sharp increase in Central Oklahoma seismicity since 2008 induced by massive wastewater injection. *Science*, *345*(6195), 448–451. doi: 10.1126/science.1255802

Kim, W.-Y. (2013). Induced seismicity associated with fluid injection into a deep well in Youngstown, Ohio. *Journal of Geophysical Research: Solid Earth*, *118*(7), 3506-3518. doi: 10.1002/jgrb.50247

Kostrov, B. (1964). Selfsimilar problems of propagation of shear cracks. *Journal of Applied Mathematics and Mechanics*, *28*(5), 1077 - 1087.

Kostrov, B. (1974). Seismic moment and energy of earthquakes and seismic flow of rock. *Izv. Acad. Sci. USSR Phys. Solid Earth*, *1*, 23-44.

Kostrov, B., & Das, S. (1988). *Principles of earthquake source mechanics*. Cambridge, England ; New York : Cambridge University Press.

Lachenbruch, A. H., & Sass, J. H. (1980). Heat flow and energetics of the San Andreas Fault zone. *Journal of Geophysical Research: Solid Earth*, *85*(B11), 6185-6222. doi: 10.1029/JB085iB11p06185

Lamb, S. (2006). Shear stresses on megathrusts: Implications for mountain building behind subduction zones. *Journal of Geophysical Research: Solid Earth*, *111*(B7). doi: 10.1029/2005JB003916

Lambert, V., & Barbot, S. (2016). Contribution of viscoelastic flow in earthquake cycles within the lithosphere-asthenosphere system. *Geophysical Research Letters*, *43*(19), 10,142-10,154. doi: 10.1002/2016GL070345

Lambert, V., & Lapusta, N. (2020). Rupture-dependent breakdown energy in fault models with thermo-hydro-mechanical processes. *Solid Earth*, *11*(6), 2283-2302. doi: 10 .5194/se-11-2283-2020

Lambert, V., & Lapusta, N. (in prep). Absolute stress levels on numerically simulated faults: Definitions, links to seismological observables, and differences for crack-like vs. pulse-like ruptures. *Journal of Geophysical Research: Solid Earth*.

Lambert, V., & Lapusta, N. (in review). Resolving simulated sequences of earthquakes and fault interactions: Implications for physics-based seismic hazard assessment. *Journal of Geophysical Research: Solid Earth*. doi: 10.1002/essoar.10506727.1

Lambert, V., Lapusta, N., & Faulkner, D. (in review). Scale dependence of earthquake rupture prestress in models with enhanced weakening: Implications for event statistics and inferences of fault stress. *Journal of Geophysical Research: Solid Earth*, 55. doi: 10.1002/essoar.10506240.1

Lambert, V., Lapusta, N., & Perry, S. (2021). Propagation of large earthquakes as self-healing pulses or mild cracks. *Nature*, *591*(7849), 252–258. doi: 10.1038/s41586 -021-03248-1

Lambert, V., & Tsai, V. C. (2020). Time-dependent stresses from fluid extraction and

diffusion with applications to induced seismicity. *Journal of Applied Mechanics*, *87*(8). doi: 10.1115/1.4047034

Lapusta, N., & Liu, Y. (2009). Three-dimensional boundary integral modeling of spontaneous earthquake sequences and aseismic slip. *Journal of Geophysical Research*, *114*, B09303. doi: 10.1029/2008JB005934

Lapusta, N., & Rice, J. (2003). Low-heat and low-stress fault operation in earthquake models of statically strong but dynamically weak faults. *AGU Fall Meeting Abstracts*.

Lapusta, N., Rice, J. R., Ben-Zion, Y., & Zheng, G. (2000). Elastodynamic analysis for slow tectonic loading with spontaneous rupture episodes on faults with rate- and state-dependent friction. *Journal of Geophysical Research*, *105*, 765-789. doi: 10.1029/2000JB900250

Lee, K.-K., Ellsworth, W. L., Giardini, D., Townend, J., Ge, S., Shimamoto, T., ... Langenbruch, C. (2019). Managing injection-induced seismic risks. *Science*, *364*(6442), 730–732. doi: 10.1126/science.aax1878

Lehner, F. K., Li, V. C., & Rice, J. R. (1981). Stress diffusion along rupturing plate boundaries. *Journal of Geophysical Research: Solid Earth*, *86*(B7), 6155-6169. doi: 10.1029/JB086iB07p06155

Lin, Y.-Y., & Lapusta, N. (2018). Microseismicity simulated on asperity-like fault patches: On scaling of seismic moment with duration and seismological estimates of stress drops. *Geophysical Research Letters*, *45*(16), 8145-8155. doi: 10.1029/2018GL078650

Litchfield, N. J., Villamor, P., Dissen, R. J. V., Nicol, A., Barnes, P. M., A. Barrell, D. J., ... Zinke, R. (2018). Surface rupture of multiple crustal faults in the 2016 Mw 7.8 Kaikura, New Zealand, earthquake. *Bulletin of the Seismological Society of America*, *108*(3B), 1496-1520. doi: 10.1785/0120170300

Liu, P., & Archuleta, R. (2000). Inversions for kinematic source parameters of the 1994 Northridge earthquake using a three dimensional velocity structure. *Seismological Research Letters*, *71*, 220.

Liu, Y. (2014). Source scaling relations and along-strike segmentation of slow slip events in a 3-D subduction fault model. *Journal of Geophysical Research: Solid Earth*, *119*(8),

6512-6533. doi: 10.1002/2014JB011144

Liu, Y., & Rice, J. R. (2005). Aseismic slip transients emerge spontaneously in three-dimensional rate and state modeling of subduction earthquake sequences. *Journal of Geophysical Research: Solid Earth*, *110*(B8). doi: 10.1029/2004JB003424

Liu, Y., & Rice, J. R. (2007). Spontaneous and triggered aseismic deformation transients in a subduction fault model. *Journal of Geophysical Research: Solid Earth*, *112*(B9). doi: 10.1029/2007JB004930

Lockner, D. A., & Byerlee, J. D. (1994). Dilatancy in hydraulically isolated faults and the suppression of instability. *Geophysical Research Letters*, *21*(22), 2353-2356. doi: https://doi.org/10.1029/94GL02366

Lockner, D. A., Morrow, C., Moore, D., & Hickman, S. (2011). Low strength of deep San Andreas fault gouge from SAFOD core. *Nature*, *472*(7341), 82–85. doi: 10.1038/nature09927

Lozos, J. C., Oglesby, D. D., Brune, J. N., & Olsen, K. B. (2015). Rupture and ground-motion models on the Northern San Jacinto Fault, incorporating realistic complexity. *Bulletin of the Seismological Society of America*, *105*(4), 1931-1946. doi: 10.1785/0120140327

Lu, X., Lapusta, N., & Rosakis, A. J. (2007). Pulse-like and crack-like ruptures in experiments mimicking crustal earthquakes. *Proceedings of the National Academy of Sciences*, *104*(48), 18931-18936.

Lu, X., Rosakis, A. J., & Lapusta, N. (2010). Rupture modes in laboratory earthquakes: Effect of fault prestress and nucleation conditions. *Journal of Geophysical Research: Solid Earth*, *115*(B12). doi: 10.1029/2009JB006833

Luttrell, K. M., & Smith-Konter, B. (2017). Limits on crustal differential stress in Southern California from topography and earthquake focal mechanisms. *Geophysical Journal International*, *211*(1), 472-482. doi: 10.1093/gji/ggx301

Luttrell, K. M., Tong, X., Sandwell, D. T., Brooks, B. A., & Bevis, M. G. (2011). Estimates of stress drop and crustal tectonic stress from the 27 February 2010 Maule, Chile, earthquake: Implications for fault strength. *Journal of Geophysical Research: Solid Earth*, *116*(B11). doi: 10.1029/2011JB008509

Ma, S., & Archuleta, R. J. (2006). Radiated seismic energy based on dynamic rupture models of faulting. *Journal of Geophysical Research: Solid Earth*, *111*(B5). doi: 10.1029/2005JB004055

Madariaga, R. (1976). Dynamics of an expanding circular fault. *Bulletin of the Seismological Society of America*, *66*(3), 639-666.

Marone, C. (1998). Laboratory-derived friction laws and their application to seismic faulting. *Annual Review of Earth and Planetary Sciences*, *26*(1), 643-696. doi: 10.1146/annurev.earth.26.1.643

Marone, C., Raleigh, C. B., & Scholz, C. H. (1990). Frictional behavior and constitutive modeling of simulated fault gouge. *Journal of Geophysical Research: Solid Earth*, *95*(B5), 7007-7025. doi: https://doi.org/10.1029/JB095iB05p07007

Martınez-Garzón, P., Kwiatek, G., Sone, H., Bohnhoff, M., Dresen, G., & Hartline, C. (2014). Spatiotemporal changes, faulting regimes, and source parameters of induced seismicity: A case study from The Geysers geothermal field. *Journal of Geophysical Research: Solid Earth*, *119*(11), 8378-8396. doi: 10.1002/2014JB011385

Martıŋnez-Garzón, P., Bohnhoff, M., Kwiatek, G., & Dresen, G. (2013). Stress tensor changes related to fluid injection at The Geysers geothermal field, California. *Geophysical Research Letters*, *40*(11), 2596-2601. doi: 10.1002/grl.50438

Mase, C. W., & Smith, L. (1987). The role of pore fluids in tectonic processes. *Reviews of Geophysics*, *25*(6), 1348-1358. doi: 10.1029/RG025i006p01348

McGarr, A. (1999). On relating apparent stress to the stress causing earthquake fault slip. *Journal of Geophysical Research: Solid Earth*, *104*(B2), 3003-3011.

McGarr, A., Bekins, B., Burkardt, N., Dewey, J., Earle, P., Ellsworth, W., ... Sheehan, A. (2015). Coping with earthquakes induced by fluid injection. *Science*, *347*(6224), 830–831. doi: 10.1126/science.aaa0494

McGuire, J. J., Boettcher, M. S., & Jordan, T. H. (2005). Foreshock sequences and short-term earthquake predictability on East Pacific Rise transform faults. *Nature*, *434*(7032), 457–461. doi: 10.1038/nature03377

McLaskey, G. C., Kilgore, B. D., & Beeler, N. M. (2015). Slip-pulse rupture behavior on a 2 m granite fault. *Geophysical Research Letters*, *42*(17), 7039-7045. doi:

10.1002/2015GL065207

McLaskey, G. C., Kilgore, B. D., Lockner, D. A., & Beeler, N. M. (2014). Laboratory generated M-6 earthquakes. *Pure and Applied Geophysics*, *171*(10), 2601–2615. doi: 10.1007/s00024-013-0772-9

McLaskey, G. C., & Lockner, D. A. (2014). Preslip and cascade processes initiating laboratory stick slip. *Journal of Geophysical Research: Solid Earth*, *119*(8), 6323-6336. doi: 10.1002/2014JB011220

Mclaskey, G. C., & Yamashita, F. (2017). Slow and fast ruptures on a laboratory fault controlled by loading characteristics. *Journal of Geophysical Research: Solid Earth*, *122*(5), 3719-3738. doi: 10.1002/2016JB013681

Michailos, K., Smith, E. G., Chamberlain, C. J., Savage, M. K., & Townend, J. (2019). Variations in seismogenic thickness along the Central Alpine Fault, New Zealand, revealed by a decade's relocated microseismicity. *Geochemistry, Geophysics, Geosystems*, *20*(1), 470-486. doi: 10.1029/2018GC007743

Michel, S., Avouac, J.-P., Lapusta, N., & Jiang, J. (2017). Pulse-like partial ruptures and high-frequency radiation at creeping-locked transition during megathrust earthquakes. *Geophysical Research Letters*, *44*(16), 8345-8351. doi: 10.1002/2017GL074725

Minson, S. E., Simons, M., & Beck, J. L. (2013). Bayesian inversion for finite fault earthquake source models I: theory and algorithm. *Geophysical Journal International*, *194*(3), 1701-1726. doi: 10.1093/gji/ggt180

Minson, S. E., Simons, M., Beck, J. L., Ortega, F., Jiang, J., Owen, S. E., ... Sladen, A. (2014). Bayesian inversion for finite fault earthquake source models II: the 2011 great Tohoku-oki, Japan earthquake. *Geophysical Journal International*, *198*(2), 922-940. doi: 10.1093/gji/ggu170

Mukuhira, Y., Fuse, K., Naoi, M., Fehler, M., Moriya, H., Ito, T., ... Häring, M. (2018). Hybrid focal mechanism determination: Constraining focal mechanisms of injection induced seismicity using in situ stress data. *Geophysical Journal International*, *215*(2), 1427-1441. doi: 10.1093/gji/ggy333

Nankali, H. R. (2011, April). Slip rate of the Kazerun Fault and Main Recent Fault (Zagros, Iran) from 3D mechanical modeling. *Journal of Asian Earth Sciences*, *41*, 89-98. doi:

10.1016/j.jseaes.2010.12.009

Nielsen, S., Spagnuolo, E., Violay, M., Smith, S., Di Toro, G., & Bistacchi, A. (2016). G: Fracture energy, friction and dissipation in earthquakes. *Journal of Seismology*, *20*(4), 1187–1205. doi: 10.1007/s10950-016-9560-1

Noda, H. (2008). Frictional constitutive law at intermediate slip rates accounting for flash heating and thermally activated slip process. *Journal of Geophysical Research: Solid Earth*, *113*(B9).

Noda, H., Dunham, E. M., & Rice, J. R. (2009). Earthquake ruptures with thermal weakening and the operation of major faults at low overall stress levels. *Journal of Geophysical Research: Solid Earth*, *114*(B7). doi: 10.1029/2008JB006143

Noda, H., & Lapusta, N. (2010). Three-dimensional earthquake sequence simulations with evolving temperature and pore pressure due to shear heating: Effect of heterogeneous hydraulic diffusivity. *Journal of Geophysical Research*, *115*, B123414. doi: 10.1029/2010JB007780

Noda, H., & Lapusta, N. (2012). On averaging interface response during dynamic rupture and energy partitioning diagrams for earthquakes. *Journal of Applied Mechanics*, *79*. doi: 10.1115/1.4005964

Noda, H., & Lapusta, N. (2013). Stable creeping fault segments can become destructive as a result of dynamic weakening. *Nature*, *493*, 518.

Noda, H., Lapusta, N., & Kanamori, H. (2013). Comparison of average stress drop measures for ruptures with heterogeneous stress change and implications for earthquake physics. *Geophysical Journal International*. doi: 10.1093/gji/ggt074

Nur, A., & Byerlee, J. D. (1971). An exact effective stress law for elastic deformation of rock with fluids. *Journal of Geophysical Research (1896-1977)*, *76*(26), 6414-6419. doi: 10.1029/JB076i026p06414

Okubo, K., Bhat, H. S., Rougier, E., Marty, S., Schubnel, A., Lei, Z., ... Klinger, Y. (2019). Dynamics, radiation, and overall energy budget of earthquake rupture with coseismic off-fault damage. *Journal of Geophysical Research: Solid Earth*, *124*(11), 11771-11801. doi: 10.1029/2019JB017304

Okubo, P. G. (1989). Dynamic rupture modeling with laboratory-derived constitutive

relations. *Journal of Geophysical Research: Solid Earth*, *94*(B9), 12321-12335. doi: 10.1029/JB094iB09p12321

Olami, Z., Feder, H. J. S., & Christensen, K. (1992). Self-organized criticality in a continuous, nonconservative cellular automaton modeling earthquakes. *Physics Review Letters*, *68*, 1244–1247. doi: 10.1103/PhysRevLett.68.1244

Olsen, K. B., Madariaga, R., & Archuleta, R. J. (1997). Three-dimensional dynamic simulation of the 1992 Landers earthquake. *Science*, *278*(5339), 834–838. doi: 10.1126/science.278.5339.834

Page, M. T., & Felzer, K. (2015). Southern San Andreas Fault seismicity is consistent with the Gutenberg-Richter magnitude-frequency distribution. *Bulletin of the Seismological Society of America*, *105*(4), 2070-2080. doi: 10.1785/0120140340

Page, M. T., & van der Elst, N. J. (2018). Fault-tolerant b-values and aftershock productivity. *Journal of Geophysical Research: Solid Earth*, *123*(12), 10,880-10,888. doi: https://doi.org/10.1029/2018JB016445

Palmer, A. C., & Rice, J. (1973). The growth of slip surfaces in the progressive failure of over-consolidated clay. *Proceedings of the Royal Society of London A: Mathematical, Physical and Engineering Sciences*, *332*(1591), 527-548.

Passelegue, F. X., Goldsby, D. L., & Fabbri, O. (2014). The influence of ambient fault temperature on flash-heating phenomena. *Geophysical Research Letters*, *41*, 828-835. doi: 10.1002/2013GL058374

Pennington, W. D., Davis, S. D., Carlson, S. M., DuPree, J., & Ewing, T. E. (1986). The evolution of seismic barriers and asperities caused by the depressuring of fault planes in oil and gas fields of South Texas. *Bulletin of the Seismological Society of America*, *76*(4), 939-948.

Perez-Campos, X., & Beroza, G. C. (2001). An apparent mechanism dependence of radiated seismic energy. *Journal of Geophysical Research: Solid Earth*, *106*(B6), 11127-11136. doi: 10.1029/2000JB900455

Perrin, G., Rice, J. R., & Zheng, G. (1995). Self-healing slip pulse on a frictional surface. *Journal of the Mechanics and Physics of Solids*, *43*(9), 1461 - 1495. doi: https://doi.org/10.1016/0022-5096(95)00036-I

Perry, S. M., Lambert, V., & Lapusta, N. (2020). Nearly magnitude-invariant stress drops in simulated crack-like earthquake sequences on rate-and-state faults with thermal pressurization of pore fluids. *Journal of Geophysical Research: Solid Earth*, *125*(3), e2019JB018597. doi: 10.1029/2019JB018597

Pharr, G. M., Herbert, E. G., & Gao, Y. (2010). The indentation size effect: A critical examination of experimental observations and mechanistic interpretations. *Annual Review of Materials Research*, *40*(1), 271-292. doi: 10.1146/annurev-matsci-070909-104456

Platt, J. D., Brantut, N., & Rice, J. R. (2015). Strain localization driven by thermal decomposition during seismic shear. *Journal of Geophysical Research: Solid Earth*, *120*(6), 4405-4433. doi: https://doi.org/10.1002/2014JB011493

Platt, J. D., Rudnicki, J. W., & Rice, J. R. (2014). Stability and localization of rapid shear in fluid-saturated fault gouge: 2. Localized zone width and strength evolution. *Journal of Geophysical Research: Solid Earth*, *119*(5), 4334-4359. doi: https://doi.org/10.1002/2013JB010711

Poirier, J. (1980). Shear localization and shear instability in materials in the ductile field. *Journal of Structural Geology*, *2*, 135-142.

Poliakov, A. N. B., Dmowska, R., & Rice, J. R. (2002). Dynamic shear rupture interactions with fault bends and off-axis secondary faulting. *Journal of Geophysical Research: Solid Earth*, *107*(B11), ESE 6-1-ESE 6-18. doi: 10.1029/2001JB000572

Pritchard, M. E., Ji, C., & Simons, M. (2006). Distribution of slip from 11 Mw > 6 earthquakes in the northern Chile subduction zone. *Journal of Geophysical Research: Solid Earth*, *111*(B10). doi: https://doi.org/10.1029/2005JB004013

Ragon, T., & Simons, M. (2020). Accounting for uncertain 3-D elastic structure in fault slip estimates. *Geophysical Journal International*, *224*(2), 1404-1421. doi: 10.1093/gji/ggaa526

Ragon, T., Sladen, A., & Simons, M. (2019). Accounting for uncertain fault geometry in earthquake source inversionsĂŞ II: Application to the Mw 6.2 Amatrice earthquake, central Italy. *Geophysical Journal International*, *218*(1), 689-707. doi: 10.1093/gji/ggz180

Raleigh, C. B., Healy, J. H., & Bredehoeft, J. D. (1976). An experiment in earthquake control at Rangely, Colorado. *Science*, *191*(4233), 1230–1237. doi: 10.1126/science .191.4233.1230

Raleigh, C. B., Healy, J. H., & Bredehoeft, J. D. (2013). Faulting and crustal stress at Rangely, Colorado. In *Flow and fracture of rocks* (p. 275-284). American Geophysical Union (AGU). doi: 10.1029/GM016p0275

Rempel, A. W., & Rice, J. R. (2006). Thermal pressurization and onset of melting in fault zones. *Journal of Geophysical Research: Solid Earth*, *111*(B9).

Rice, J. R. (1980). The mechanics of earthquake rupture. *Physics of Earth's Interior*, 555-649.

Rice, J. R. (1993). Spatio-temporal complexity of slip on a fault. *Journal of Geophysical Research: Solid Earth*, *98*(B6), 9885-9907. doi: 10.1029/93JB00191

Rice, J. R. (1999). Flash heating at asperity contacts and rate-dependent friction. *Eos Transactions American Geophysical Union*, *80*(46), F471.

Rice, J. R. (2000). Fracture energy of earthquakes and slip-weakening rupture parameters. *EOS, Transactions America Geophysical Union*, *81*(48), F1227.

Rice, J. R. (2006). Heating and weakening of faults during earthquake slip. *Journal of Geophysical Research*, *111*, B05311. doi: 10.1029/2005JB004006

Rice, J. R., & Ben-Zion, Y. (1996). Slip complexity in earthquake fault models. *Proceedings of the National Academy of Sciences of the United States of America*, *93*(9), 3811–3818. doi: 10.1073/pnas.93.9.3811

Rice, J. R., Lapusta, N., & Ranjith, K. (2001). Rate and state dependent friction and the stability of sliding between elastically deformable solids. *Journal of the Mechanics and Physics of Solids*, *49*(9), 1865-1898.

Rice, J. R., Rudnicki, J. W., & Platt, J. D. (2014). Stability and localization of rapid shear in fluid-saturated fault gouge: 1. Linearized stability analysis. *Journal of Geophysical Research: Solid Earth*, *119*(5), 4311-4333. doi: https://doi.org/10.1002/2013JB010710

Rice, J. R., & Ruina, A. L. (1983). Stability of steady frictional slipping. *Journal of Applied Mechanics*, *50*(2), 343-349.

Rice, J. R., Sammis, C. G., & Parsons, R. (2005). Off-fault secondary failure induced by a dynamic slip pulse. *Bulletin of the Seismological Society of America*, *95*(1), 109-134. doi: 10.1785/0120030166

Richards-Dinger, K., & Dieterich, J. H. (2012). RSQSim earthquake simulator. *Seismological Research Letters*, *83*(6), 983-990. doi: 10.1785/0220120105

Rockwell, T., Sisk, M., Girty, G., Dor, O., Wechsler, N., & Ben-Zion, Y. (2009). Chemical and physical characteristics of pulverized tejon lookout granite adjacent to the San Andreas and Garlock faults: Implications for earthquake physics. *Pure and Applied Geophysics*, *166*(10), 1725–1746. doi: 10.1007/s00024-009-0514-1

Ross, Z. E., Trugman, D. T., Azizzadenesheli, K., & Anandkumar, A. (2020). Directivity modes of earthquake populations with unsupervised learning. *Journal of Geophysical Research: Solid Earth*, *125*(2), e2019JB018299. doi: https://doi.org/10.1029/2019JB018299

Ross, Z. E., Trugman, D. T., Hauksson, E., & Shearer, P. M. (2019). Searching for hidden earthquakes in Southern California. *Science*, *364*(6442), 767–771. doi: 10.1126/science.aaw6888

Roten, D., Olsen, K. B., & Day, S. M. (2017). Off-fault deformations and shallow slip deficit from dynamic rupture simulations with fault zone plasticity. *Geophysical Research Letters*, *44*(15), 7733-7742. doi: 10.1002/2017GL074323

Rubin, A., & Ampuero, J.-P. (2005). Earthquake nucleation on (aging) rate and state faults. *Journal of Geophysical Research: Solid Earth*, *110*(B11).

Rubino, V., Rosakis, A. J., & Lapusta, N. (2017). Understanding dynamic friction through spontaneously evolving laboratory earthquakes. *Nature Communications*, *8*(1), 15991. doi: 10.1038/ncomms15991

Rubinstein, S. M., Cohen, G., & Fineberg, J. (2004). Detachment fronts and the onset of dynamic friction. *Nature*, *430*(7003), 1005–1009. doi: 10.1038/nature02830

Rubinstein, S. M., Cohen, G., & Fineberg, J. (2006). Contact area measurements reveal loading-history dependence of static friction. *Physics Review Letters*, *96*, 256103. doi: 10.1103/PhysRevLett.96.256103

Rudnicki, J., & Rice, J. (1975). Conditions for the localization of deformation in pressure-

sensitive dilatant materials. *Journal of the Mechanics and Physics of Solids*, *23*(6), 371-394. doi: https://doi.org/10.1016/0022-5096(75)90001-0

Ruina, A. (1983). Slip instability and state variable friction laws. *Journal of Geophysical Research*, *88*(B12), 10359-10370.

Ruiz, S., Metois, M., Fuenzalida, A., Ruiz, J., Leyton, F., Grandin, R., ... Campos, J. (2014). Intense foreshocks and a slow slip event preceded the 2014 Iquique Mw 8.1 earthquake. *Science*, *345*(6201), 1165–1169. doi: 10.1126/science.1256074

Samuelson, J., Elsworth, D., & Marone, C. (2009). Shear-induced dilatancy of fluid-saturated faults: Experiment and theory. *Journal of Geophysical Research: Solid Earth*, *114*(B12). doi: https://doi.org/10.1029/2008JB006273

Savage, J. C., & Wood, M. D. (1971). The relation between apparent stress and stress drop. *Bulletin of the Seismological Society of America*, *61*(5), 1381-1388.

Schmitt, S. V., Segall, P., & Dunham, E. M. (2015). Nucleation and dynamic rupture on weakly stressed faults sustained by thermal pressurization. *Journal of Geophysical Research: Solid Earth*, *120*(11), 7606-7640. doi: 10.1002/2015JB012322

Schoenball, M., Dorbath, L., Gaucher, E., Wellmann, J. F., & Kohl, T. (2014). Change of stress regime during geothermal reservoir stimulation. *Geophysical Research Letters*, *41*(4), 1163-1170. doi: 10.1002/2013GL058514

Scholz, C. H. (2000). Evidence for a strong San Andreas fault. *Geology*, *28*(2), 163-166. doi: 10.1130/0091-7613(2000)28<163:EFASSA>2.0.CO;2

Schurr, B., Asch, G., Hainzl, S., Bedford, J., Hoechner, A., Palo, M., ... Vilotte, J.-P. (2014). Gradual unlocking of plate boundary controlled initiation of the 2014 Iquique earthquake. *Nature*, *512*(7514), 299–302. doi: 10.1038/nature13681

Schwartz, D. P., & Coppersmith, K. J. (1984). Fault behavior and characteristic earthquakes–examples from the Wasatch and San Andreas fault zones. *Journal of Geophysical Research*, *89*, 5681-5698.

Scuderi, M. M., Carpenter, B. M., & Marone, C. (2014). Physicochemical processes of frictional healing: Effects of water on stick-slip stress drop and friction of granular fault gouge. *Journal of Geophysical Research: Solid Earth*, *119*(5), 4090-4105. doi: https://doi.org/10.1002/2013JB010641

Scuderi, M. M., Collettini, C., Viti, C., Tinti, E., & Marone, C. (2017). Evolution of shear fabric in granular fault gouge from stable sliding to stick slip and implications for fault slip mode. *Geology*, *45*(8), 731-734. doi: 10.1130/G39033.1

Segall, P. (1985). Stress and subsidence resulting from subsurface fluid withdrawal in the epicentral region of the 1983 Coalinga earthquake. *Journal of Geophysical Research: Solid Earth*, *90*(B8), 6801-6816. doi: 10.1029/JB090iB08p06801

Segall, P. (1989). Earthquakes triggered by fluid extraction. *Geology*, *17*(10), 942-946. doi: 10.1130/0091-7613(1989)017<0942:ETBFE>2.3.CO;2

Segall, P. (1992). Induced stresses due to fluid extraction from axisymmetric reservoirs. *Pure and Applied Geophysics*, *139*, 535-560. doi: 10.1007/BF008799502

Segall, P., Grasso, J.-R., & Mossop, A. (1994). Poroelastic stressing and induced seismicity near the Lacq gas field, southwestern France. *Journal of Geophysical Research: Solid Earth*, *99*(B8), 15423-15438. doi: 10.1029/94JB00989

Segall, P., & Lu, S. (2015). Injection-induced seismicity: Poroelastic and earthquake nucleation effects. *Journal of Geophysical Research: Solid Earth*, *120*(7), 5082-5103. doi: 10.1002/2015JB012060

Segall, P., & Rice, J. R. (1995). Dilatancy, compaction, and slip instability of a fluid-infiltrated fault. *Journal of Geophysical Research: Solid Earth*, *100*(B11), 22155-22171. doi: 10.1029/95JB02403

Segall, P., & Rice, J. R. (2006). Does shear heating of pore fluid contribute to earthquake nucleation? *Journal of Geophysical Research: Solid Earth*, *111*(B9). doi: 10.1029/2005JB004129

Segall, P., Rubin, A. M., Bradley, A. M., & Rice, J. R. (2010). Dilatant strengthening as a mechanism for slow slip events. *Journal of Geophysical Research: Solid Earth*, *115*(B12). doi: 10.1029/2010JB007449

Selvadurai, P. A. (2019). Laboratory insight into seismic estimates of energy partitioning during dynamic rupture: An observable scaling breakdown. *Journal of Geophysical Research: Solid Earth*, *124*(11), 11350-11379. doi: 10.1029/2018JB017194

Shapiro, S., Rothert, E., Rath, V., & Rindschwentner, J. (2002). Characterization of fluid transport properties of reservoirs using induced microseismicity. *Geophysics*, *67*. doi:

10.1190/1.1451597

Shaw, B. E., Milner, K. R., Field, E. H., Richards-Dinger, K., Gilchrist, J. J., Dieterich, J. H., & Jordan, T. H. (2018). A physics-based earthquake simulator replicates seismic hazard statistics across California. *Science Advances*, *4*(8). doi: 10.1126/sciadv.aau0688

Shreedharan, S., Riviere, J., Bhattacharya, P., & Marone, C. (2019). Frictional state evolution during normal stress perturbations probed with ultrasonic waves. *Journal of Geophysical Research: Solid Earth*, *124*(6), 5469-5491. doi: 10.1029/2018JB016885

Sibson, R. H. (1973). Interactions between temperature and pore-fluid pressure during earthquake faulting and a mechanism for partial or total stress relief. *Nature*, *243*(126), 66-68.

Sibson, R. H. (1975). Generation of pseudotachylyte by ancient seismic faulting. *Geophysical Journal of the Royal Astronomical Society*, *43*(3), 775-794. doi: 10.1111/j.1365-246X.1975.tb06195.x

Sieh, K. E. (1978). Central California foreshocks of the great 1857 earthquake. *Bulletin of the Seismological Society of America*, *68*(6), 1731-1749.

Sieh, K. E., Jones, L., Hauksson, E., Hudnut, K., Eberhart-Phillips, D., Heaton, T., ... Zachariasen, J. (1993). Near-field investigations of the Landers Earthquake Sequence, April to July 1992. *Science*, *260*(5105), 171–176. doi: 10.1126/science.260.5105.171

Simons, M., Minson, S. E., Sladen, A., Ortega, F., Jiang, J., Owen, S. E., ... Webb, F. H. (2011). The 2011 magnitude 9.0 Tohoku-Oki earthquake: Mosaicking the megathrust from seconds to centuries. *Science*, *332*(6036), 1421–1425. doi: 10.1126/science.1206731

Smith, J. D., Avouac, J.-P., White, R. S., Copley, A., Gualandi, A., & Bourne, S. (2019). Reconciling the long-term relationship between reservoir pore pressure depletion and compaction in the Groningen region. *Journal of Geophysical Research: Solid Earth*, *124*(6), 6165-6178. doi: 10.1029/2018JB016801

Smith, K. D., Brune, J. N., & Priestley, K. F. (1991). The seismic spectrum, radiated energy, and the savage and wood inequality for complex earthquakes. *Tectonophysics*, *188*(3),

303 - 320.

Sobolev, S. V., & Muldashev, I. A. (2017). Modeling seismic cycles of great megathrust earthquakes across the scales with focus at postseismic phase. *Geochemistry, Geophysics, Geosystems*, *18*(12), 4387-4408. doi: https://doi.org/10.1002/2017GC007230

Sone, H., & Shimamoto, T. (2009). Frictional resistance of faults during accelerating and decelerating earthquake slip. *Nature Geoscience*, *2*(10), 705–708. doi: 10.1038/ngeo637

Subarya, C., Chlieh, M., Prawirodirdjo, L., Avouac, J.-P., Bock, Y., Sieh, K., . . . McCaffrey, R. (2006). Plate-boundary deformation associated with the great Sumatra-Andaman earthquake. *Nature*, *440*(7080), 46–51. doi: 10.1038/nature04522

Sugan, M., Kato, A., Miyake, H., Nakagawa, S., & Vuan, A. (2014). The preparatory phase of the 2009 Mw 6.3 ĂĽL'Aquila earthquake by improving the detection capability of low-magnitude foreshocks. *Geophysical Research Letters*, *41*(17), 6137-6144. doi: https://doi.org/10.1002/2014GL061199

Sulem, J., & Famin, V. (2009). Thermal decomposition of carbonates in fault zones: Slip-weakening and temperature-limiting effects. *Journal of Geophysical Research: Solid Earth*, *114*(B3).

Suppe, J. (2007). Absolute fault and crustal strength from wedge tapers. *Geology*, *35*(12), 1127-1130. doi: 10.1130/G24053A.1

Svetlizky, I., & Fineberg, J. (2014). Classical shear cracks drive the onset of dry frictional motion. *Nature*, *509*(7499), 205–208. doi: 10.1038/nature13202

Tanikawa, W., & Shimamoto, T. (2009). Frictional and transport properties of the chelungpu fault from shallow borehole data and their correlation with seismic behavior during the 1999 Chi-Chi earthquake. *Journal of Geophysical Research: Solid Earth*, *114*(B1). doi: 10.1029/2008JB005750

Tape, C., Holtkamp, S., Silwal, V., Hawthorne, J., Kaneko, Y., Ampuero, J. P., . . . West, M. E. (2018). Earthquake nucleation and fault slip complexity in the lower crust of central Alaska. *Nature Geoscience*, *11*(7), 536–541. doi: 10.1038/s41561-018-0144-2

Tenthorey, E., & Cox, S. F. (2006). Cohesive strengthening of fault zones during the interseismic period: An experimental study. *Journal of Geophysical Research: Solid Earth*, *111*(B9). doi: https://doi.org/10.1029/2005JB004122

Terzaghi, K. (1923). Die berechnung der durchassigkeitsziffer des tones aus dem verlauf der hydrodynamischen spannungsercheinungen. *Akademie der Wissenschaften, Mathematish-naturwissenschaftliche, Klasse Wien, Abt. 2A*, *132*(105), 125-138.

Thom, C. A., Brodsky, E. E., Carpick, R. W., Pharr, G. M., Oliver, W. C., & Goldsby, D. L. (2017). Nanoscale roughness of natural fault surfaces controlled by scale-dependent yield strength. *Geophysical Research Letters*, *44*(18), 9299-9307. doi: 10.1002/2017GL074663

Thomas, M. Y., Lapusta, N., Noda, H., & Avouac, J.-P. (2014). Quasi-dynamic versus fully dynamic simulations of earthquakes and aseismic slip with and without enhanced coseismic weakening. *Journal of Geophysical Research*, *119*, 1986-2004. doi: 10 .1002/2013JB010615

Tinti, E., Scognamiglio, L., Michelini, A., & Cocco, M. (2016). Slip heterogeneity and directivity of the ML 6.0, 2016, Amatrice earthquake estimated with rapid finite-fault inversion. *Geophysical Research Letters*, *43*(20).

Tinti, E., Spudich, P., & Cocco, M. (2005). Earthquake fracture energy inferred from kinematic rupture models on extended faults. *Journal of Geophysical Research: Solid Earth*, *110*(B12). doi: 10.1029/2005JB003644

Tormann, T., Wiemer, S., & Mignan, A. (2014). Systematic survey of high-resolution b value imaging along Californian faults: Inference on asperities. *Journal of Geophysical Research: Solid Earth*, *119*(3), 2029-2054. doi: https://doi.org/10.1002/2013JB010867

Townend, J., & Zoback, M. D. (2000). How faulting keeps the crust strong. *Geology*, *28*(5), 399-402. doi: 10.1130/0091-7613(2000)28<399:HFKTCS>2.0.CO;2

Townend, J., & Zoback, M. D. (2004). Regional tectonic stress near the San Andreas fault in Central and Southern California. *Geophysical Research Letters*, *31*(15). doi: 10.1029/2003GL018918

Tsutsumi, A., & Shimamoto, T. (1997). High-velocity frictional properties of gabbro. *Geophysical Research Letters*, *24*(6), 699-702. doi: 10.1029/97GL00503

Tullis, T. (2007). Friction of rock at earthquake slip rates. *Treatise on Geophysics*, *4*, 131-152. doi: 10.1016/B978-044452748-6.00064-X

Tullis, T., & Goldsby, D. (2003). Flash melting of crustal rocks at almost seismic slip rates. *Eos Transactions AGU*, *84*(46). doi: AbstractS51B-05

Tullis, T., Richards-Dinger, K., Barall, M., Dieterich, J. H., Field, E. H., Heien, E. M., ... Yikilmaz, M. B. (2012). Generic earthquake simulator. *Seismological Research Letters*, *83*(6), 959-963. doi: 10.1785/0220120093

Uchic, M. D., Dimiduk, D. M., Florando, J. N., & Nix, W. D. (2004). Sample dimensions influence strength and crystal plasticity. *Science*, *305*(5686), 986–989. doi: 10.1126/science.1098993

Ulrich, T., Gabriel, A.-A., Ampuero, J.-P., & Xu, W. (2019). Dynamic viability of the 2016 Mw 7.8 Kaikoura earthquake cascade on weak crustal faults. *Nature Communications*, *10*(1), 1213. doi: 10.1038/s41467-019-09125-w

van Dinther, Y., Gerya, T. V., Dalguer, L. A., Corbi, F., Funiciello, F., & Mai, P. M. (2013). The seismic cycle at subduction thrusts: 2. Dynamic implications of geodynamic simulations validated with laboratory models. *Journal of Geophysical Research: Solid Earth*, *118*(4), 1502-1525. doi: https://doi.org/10.1029/2012JB009479

van Dinther, Y., Gerya, T. V., Dalguer, L. A., Mai, P. M., Morra, G., & Giardini, D. (2013). The seismic cycle at subduction thrusts: Insights from seismo-thermo-mechanical models. *Journal of Geophysical Research: Solid Earth*, *118*(12), 6183-6202. doi: https://doi.org/10.1002/2013JB010380

van Zelst, I., Wollherr, S., Gabriel, A.-A., Madden, E. H., & van Dinther, Y. (2019). Modeling megathrust earthquakes across scales: One-way coupling from geodynamics and seismic cycles to dynamic rupture. *Journal of Geophysical Research: Solid Earth*, *124*(11), 11414-11446. doi: https://doi.org/10.1029/2019JB017539

Venkataraman, A., & Kanamori, H. (2004). Observational constraints on the fracture energy of subduction zone earthquakes. *Journal of Geophysical Research: Solid Earth*, *109*(B5).

Venkataraman, A., Rivera, L., & Kanamori, H. (2002, 05). Radiated energy from the 16 October 1999 Hector Mine earthquake: Regional and teleseismic estimates. *Bulletin of*

the Seismological Society of America, *92*(4), 1256-1265. doi: 10.1785/0120000929

Viesca, R. C., & Garagash, D. I. (2015). Ubiquitous weakening of faults due to thermal pressurization. *Nature Geoscience*, *8*, 875-879. doi: 10.1038/NGEO2554

Wald, D. J. (1995). A preliminary dislocation model for the 1995 Kobe (Hyogo-ken Nanbu), Japan, earthquake determined from strong motion and teleseismic waveforms. *Seismological Research Letters*, *66*(4), 22-28. doi: 10.1785/gssrl.66.4.22

Wald, D. J., & Heaton, T. H. (1994). Spatial and temporal distribution of slip for the 1992 Landers, California, earthquake. *Bulletin of the Seismological Society of America*, *84*(3), 668-691.

Wald, D. J., Heaton, T. H., & Hudnut, K. W. (1996). The slip history of the 1994 Northridge, California, earthquake determined from strong-motion, teleseismic, GPS, and leveling data. *Bulletin of the Seismological Society of America*, *86*(1B), S49-S70.

Wald, D. J., Helmberger, D. V., & Heaton, T. H. (1991). Rupture model of the 1989 Loma Prieta earthquake from the inversion of strong-motion and broadband teleseismic data. *Bulletin of the Seismological Society of America*, *81*(5), 1540-1572.

Walsh, F., & Zoback, M. D. (2015). Oklahoma's recent earthquakes and salt water disposal. *Science Advances*, *1*(5). doi: 10.1126/sciadv.1500195

Wei, M., & McGuire, J. J. (2014). The Mw 6.5 offshore Northern California earthquake of 10 January 2010: Ordinary stress drop on a high-strength fault. *Geophysical Research Letters*, *41*(18), 6367-6373. doi: 10.1002/2014GL061043

Wei, S., Helmberger, D., & Avouac, J.-P. (2013). Modeling the 2012 Wharton basin earthquakes off-Sumatra: Complete lithospheric failure. *Journal of Geophysical Research: Solid Earth*, *118*(7), 3592-3609. doi: 10.1002/jgrb.50267

Wesnousky, S. G. (1994). The Gutenberg-Richter or characteristic earthquake distribution, which is it? *Bulletin of the Seismological Society of America*, *84*(6), 1940-1959.

Wetmiller, R. J. (1986). Earthquakes near Rocky Mountain House, Alberta, and their relationship to gas production facilities. *Canadian Journal of Earth Sciences*, *23*(2), 172-181. doi: 10.1139/e86-020

Wibberley, C. A. J., & Shimamoto, T. (2003). Internal structure and permeability of major strike-slip fault zones: The Median Tectonic Line in Mie prefecture, southwest

Japan. *Journal of Structural Geology*, *25*(1), 59-78. doi: https://doi.org/10.1016/S0191-8141(02)00014-7

Wibberley, C. A. J., & Shimamoto, T. (2005). Earthquake slip weakening and asperities explained by thermal pressurization. *Nature*, *436*(7051), 689-692.

Wibberley, C. A. J., Yielding, G., & Toro, G. D. (2008). Recent advances in the understanding of fault zone internal structure: A review. In *The Internal Structure of Fault Zones: Implications for Mechanical and Fluid-Flow Properties.* Geological Society of London. doi: 10.1144/SP299.2

Williams, C. F., Grubb, F. V., & Galanis, S. P. (2004). Heat flow in the SAFOD pilot hole and implications for the strength of the San Andreas Fault. *Geophysical Research Letters*, *31*(15).

Withers, K. B., Olsen, K. B., Day, S. M., & Shi, Z. (2018). Ground motion and intraevent variability from 3D deterministic broadband (0-7.5 Hz) simulations along a nonplanar strike-slip fault. *Bulletin of the Seismological Society of America*, *109*(1), 229-250. doi: 10.1785/0120180006

Wollherr, S., Gabriel, A.-A., & Mai, P. M. (2019). Landers 1992 reloaded: Integrative dynamic earthquake rupture modeling. *Journal of Geophysical Research: Solid Earth*, *124*(7), 6666-6702. doi: 10.1029/2018JB016355

Wu, Y., & Chen, X. (2014). The scale-dependent slip pattern for a uniform fault model obeying the rate- and state-dependent friction law. *Journal of Geophysical Research: Solid Earth*, *119*(6), 4890-4906. doi: 10.1002/2013JB010779

Wyss, M., & Brune, J. N. (1968). Seismic moment, stress, and source dimensions for earthquakes in the California-Nevada region. *Journal of Geophysical Research (1896-1977)*, *73*(14), 4681-4694. doi: 10.1029/JB073i014p04681

Yagi, Y., & Kikuchi, M. (2000). Source rupture process of the Kocaeli, Turkey, earthquake of August 17, 1999, obtained by joint inversion of near-field data and teleseismic data. *Geophysical Research Letters*, *27*(13), 1969-1972. doi: 10.1029/1999GL011208

Yamashita, F., Fukuyama, E., Mizoguchi, K., Takizawa, S., Xu, S., & Kawakata, H. (2015). Scale dependence of rock friction at high work rate. *Nature*, *528*(7581), 254–257. doi: 10.1038/nature16138

Yasuhara, H., Marone, C., & Elsworth, D. (2005). Fault zone restrengthening and frictional healing: The role of pressure solution. *Journal of Geophysical Research: Solid Earth*, *110*(B6). doi: https://doi.org/10.1029/2004JB003327

Ye, L., Lay, T., Kanamori, H., & Rivera, L. (2016a). Rupture characteristics of major and great (Mw > 7.0) megathrust earthquakes from 1990 to 2015: 1. Source parameter scaling relationships. *Journal of Geophysical Research: Solid Earth*, *121*(2), 826-844. doi: 10.1002/2015JB012426

Ye, L., Lay, T., Kanamori, H., & Rivera, L. (2016b). Rupture characteristics of major and great (Mw >7.0) megathrust earthquakes from 1990 to 2015: 2. Depth dependence. *Journal of Geophysical Research: Solid Earth*, *121*(2), 845-863. doi: 10.1002/2015JB012427

Yerkes, R., & Castle, R. (1970). Surface deformation associated with oil and gas field operations in the United States, in Land subsidence. *International Association of the Science of Hydrology, UNESCO Publication*, *89*(1), 55-66.

Yoo, S.-H., Rhie, J., Choi, H., & Mayeda, K. (2010). Evidence for non-self-similarity and transitional increment of scaled energy in the 2005 west off Fukuoka seismic sequence. *Journal of Geophysical Research: Solid Earth*, *115*(B8). doi: 10.1029/2009JB007169

Zhan, Z., Helmberger, D. V., Kanamori, H., & Shearer, P. M. (2014). Supershear rupture in a Mw 6.7 aftershock of the 2013 Sea of Okhotsk earthquake. *Science*, *345*(6193), 204–207. doi: 10.1126/science.1252717

Zhang, Y., Person, M., Rupp, J., Ellett, K., Celia, M. A., Gable, C. W., ... Elliot, T. (2013). Hydrogeologic controls on induced seismicity in a crystalline basement rocks due to fluid injection into basal reservoirs. *Groundwater*, *51*(4), 525-538. doi: 10.1111/gwat.12071

Zheng, G., & Rice, J. R. (1998). Conditions under which velocity-weakening friction allows a self-healing versus a crack-like mode of rupture. *Bulletin of the Seismological Society of America*, *88*(6), 1466-1483.

Zoback, M. D. (2013). Managing the seismic risk posed by wastewater disposal. *Earth Magazine*, *57*, 38-42.

Zoback, M. D., Hickman, S., & Ellsworth, W. (2010). Scientific drilling into the San Andreas fault zone. *Eos, Transactions American Geophysical Union*, *91*, 197-199. doi: 10.1029/2010EO220001

Zoback, M. D., Zoback, M. L., Mount, V. S., Suppe, J., Eaton, J. P., Healy, J. H., ... Wentworth, C. (1987). New evidence on the state of stress of the San Andreas fault system. *Science*, *238*(4830), 1105–1111. doi: 10.1126/science.238.4830.1105